



## ***Modeling and Simulation in Science, Engineering and Technology***

### ***Series Editor***

Nicola Bellomo  
Politecnico di Torino  
Italy

### ***Advisory Editorial Board***

*M. Avellaneda* (Modeling in Economics)  
Courant Institute of Mathematical Sciences  
New York University  
251 Mercer Street  
New York, NY 10012, USA  
avellaneda@cims.nyu.edu

*K.J. Bathe* (Solid Mechanics)  
Department of Mechanical Engineering  
Massachusetts Institute of Technology  
Cambridge, MA 02139, USA  
kjb@mit.edu

*P. Degond* (Semiconductor & Transport Modeling)  
Mathématiques pour l'Industrie et la Physique  
Université P. Sabatier Toulouse 3  
118 Route de Narbonne  
31062 Toulouse Cedex, France  
degond@mip.ups-tlse.fr

*A. Deutsch* (Complex Systems  
in the Life Sciences)  
Center for Information Services  
and High Performance Computing  
Technische Universität Dresden  
01062 Dresden, Germany  
andreas.deutsch@tu-dresden.de

*M.A. Herrero Garcia* (Mathematical Methods)  
Departamento de Matematica Aplicada  
Universidad Complutense de Madrid  
Avenida Complutense s/n  
28040 Madrid, Spain  
herrero@sunma4.mat.ucm.es

*W. Kliemann* (Stochastic Modeling)  
Department of Mathematics  
Iowa State University  
400 Carver Hall  
Ames, IA 50011, USA  
kliemann@iastate.edu

*H.G. Othmer* (Mathematical Biology)  
Department of Mathematics  
University of Minnesota  
270A Vincent Hall  
Minneapolis, MN 55455, USA  
othmer@math.umn.edu

*L. Preziosi* (Industrial Mathematics)  
Dipartimento di Matematica  
Politecnico di Torino  
Corso Duca degli Abruzzi 24  
10129 Torino, Italy  
luigi.preziosi@polito.it

*V. Prottopopescu* (Competitive Systems,  
Epidemiology)  
CSMD  
Oak Ridge National Laboratory  
Oak Ridge, TN 37831-6363, USA  
vvp@epmns.epm.ornl.gov

*K.R. Rajagopal* (Multiphase Flows)  
Department of Mechanical Engineering  
Texas A&M University  
College Station, TX 77843, USA  
KRajagopal@mengr.tamu.edu

*Y. Sone* (Fluid Dynamics in Engineering Sciences)  
Professor Emeritus  
Kyoto University  
230-133 Iwakura-Nagatani-cho  
Sakyo-ku Kyoto 606-0026, Japan  
sone@yoshio.mbox.media.kyoto-u.ac.jp

# Mathematical Modeling of Biological Systems, Volume II

*Epidemiology, Evolution and Ecology,  
Immunology, Neural Systems and the Brain,  
and Innovative Mathematical Methods*

Andreas Deutsch  
Rafael Bravo de la Parra  
Rob J. de Boer  
Odo Diekmann  
Peter Jagers  
Eva Kisdi  
Mirjam Kretzschmar  
Petr Lansky  
Hans Metz  
*Editors*

Birkhäuser  
Boston • Basel • Berlin

Andreas Deutsch  
Center for Information Services  
and High Performance Computing  
Technische Universität Dresden  
01062 Dresden  
Germany

Rafael Bravo de la Parra  
Departamento de Matemáticas  
Universidad de Alcalá  
28871 Alcalá de Henares  
Spain

Rob J. de Boer  
Department of Theoretical  
Biology  
Utrecht University  
Padualaan 8  
3584 CD Utrecht  
The Netherlands

Odo Diekmann  
Mathematisch Instituut  
Utrecht University  
Budapestlaan 6  
3584 CH Utrecht  
The Netherlands

Peter Jagers  
Mathematical Sciences  
Chalmers University of Technology  
Göteborg University  
412 96 Göteborg  
Sweden

Eva Kisdi  
Department of Mathematics  
and Statistics  
University of Helsinki  
Gustaf Hällströmin katu 2b  
00014 Helsinki  
Finland

Mirjam Kretzschmar  
Fakultät für Gesundheitswis-  
senschaften  
Universität Bielefeld  
Universitätsstr. 25  
33615 Bielefeld  
Germany

Petr Lansky  
Institute of Physiology  
Academy of Sciences of  
the Czech Republic  
Videnska 1083  
142 20 Prague 4  
Czech Republic

Hans Metz  
Section Theoretical  
Evolutionary Biology  
Institute of Evolutionary and  
Ecological Sciences  
Rijksuniversiteit Leiden  
Kaiserstraat 63  
2311 GP Leiden  
The Netherlands

Mathematics Subject Classification: 00A71, 37N25, 46N60, 47N60, 62P10, 76Zxx, 78A70, 92-XX, 92Bxx, 92B05, 92Cxx, 92C05, 92C15, 93A30

**Library of Congress Control Number:** 2007925791

ISBN-13: 978-0-8176-4555-7      e-ISBN-13: 978-0-8176-4556-4

Printed on acid-free paper.

©2008 Birkhäuser Boston

All rights reserved. This work may not be translated or copied in whole or in part without the written permission of the publisher (Birkhäuser Boston, c/o Springer Science+Business Media LLC, 233 Spring Street, New York, NY 10013, USA), except for brief excerpts in connection with reviews or scholarly analysis. Use in connection with any form of information storage and retrieval, electronic adaptation, computer software, or by similar or dissimilar methodology now known or hereafter developed is forbidden.

The use in this publication of trade names, trademarks, service marks and similar terms, even if they are not identified as such, is not to be taken as an expression of opinion as to whether or not they are subject to proprietary rights.

9 8 7 6 5 4 3 2 1

[www.birkhauser.com](http://www.birkhauser.com)

(LM/EB)



---

## Preface

This edited volume contains a selection of chapters that are an outgrowth of the European Conference on Mathematical and Theoretical Biology (ECMTB05, Dresden, Germany, July 2005). The peer-reviewed contributions show that mathematical and computational approaches are absolutely essential to solving central problems in the life sciences, ranging from the organizational level of individual cells to the dynamics of whole populations.

The contributions indicate that theoretical and mathematical biology is a diverse and interdisciplinary field, ranging from experimental research linked to mathematical modelling to the development of more abstract mathematical frameworks in which observations about the real world can be interpreted and with which new hypotheses for testing can be generated. Today, much attention is also paid to the development of efficient algorithms for complex computations and visualization, notably in molecular biology and genetics. The field of theoretical and mathematical biology and medicine has profound connections to many current problems of great relevance to society. The medical, industrial, and social interests in its development are in fact undisputable. Insights and predictions from mathematical modelling are used increasingly in decision support in medicine (e.g., immunology and spread of infectious diseases, cancer research, cardiovascular research, neurological research, optimization of medical treatments, imaging), environmental and nature management, climate problems, agriculture and management of natural resources. Fast developments in areas such as biotechnology (e.g., genome projects, genetic modification, tissue engineering) continue to add new focal points of activity to the field. The contributions of this volume capture some of these developments.

The volume contains five parts: epidemiology, evolution and ecology, immunology, neural systems and the brain, and, finally, innovative mathematical methods and education.

**Part I** deals with epidemiology and contains three chapters.

*Smith* discusses implications of new malaria vaccines. Recent breakthroughs in malaria vaccines have given new hope that a safe, effective malaria vaccine may be found. In particular, the following epidemiological questions are addressed: 1. What

level of vaccination coverage is required to offset the limitations of an imperfect disease-modifying vaccine? 2. Could the introduction of a low-efficacy malaria vaccine lead to an increase in the number of secondary infections? 3. What characteristics of such a vaccine will have the greatest effect on the outcome? A mathematical model is developed for a disease-modifying malaria vaccine that is given once prior to infection, and the minimum coverage level for disease eradication is established. It is shown that there is a threshold depending on the relative rate of infection, the efficacy of the vaccine, and the duration of infection. Vaccines which reduce the rate and duration of infection will always result in a decrease in secondary infections. More surprisingly, there is a duration “shoulder,” such that vaccines that increase the duration of infection slightly will still lead to a decrease in secondary infections, even if the rate of infection is unchanged. Beyond this, the number of secondary infections will increase unless the rate of infection is sufficiently lowered. This is critical for low-efficacy vaccines.

*Burie, et al.* introduce a model for the invasion of a fungal disease over a vineyard. In particular, the spatiotemporal spreading of a fungal disease over a vineyard is investigated using a SEIR-type model coupled with a set of partial differential equations describing the dispersal of the spores. The model takes into account both short and long range dispersal of spores and growth of the foliar surface. Results of numerical simulations are presented, and a mathematical result for the asymptotic behavior of the solutions is given.

*Stollenwerk and Mikolajczyk* present an algorithm for parameter estimation in nosocomial infections. Parameter estimation in nosocomial infections poses specific problems for estimation techniques. The mathematical description of the spread of nosocomial infections incorporates transmission as the dynamic part; the outcome is discrete, and the amount of available information is usually small. The authors transfer an estimation technique developed previously for plant epidemics to nosocomial infections and demonstrate its application to a data set related to methicillin-resistant *Staphylococcus aureus* (MRSA).

**Part II** focuses on evolution and ecology and consists of eight chapters.

*Broom, et al.* discuss evolutionarily stable investment in anti-predatory defenses and aposematic signalling. Many species possess defenses (such as toxins) against predator attack which cannot be observed by the predator prior to attack, but which might be beneficial for the predator to avoid. Often, such animals are brightly colored or have some other way of signalling that they are defended (aposematism). In an earlier paper the authors examined the evolution and maintenance of defense and conspicuousness, the brightness of the defense signal, in such prey species using a game theoretic model. Here, they develop the model further, and, in particular, expand on the more theoretical results with examples demonstrating the type of solutions which can occur. The authors categorize eight possible configurations of solution states for simple solutions. Finally, it is shown that there is another class of solutions possible where there is strong between-individual variation in appearance between conspicuous, poorly defended prey, and one example of this complex solution is demonstrated.

*Laird, et al.* introduce an overview of the Tangled Nature model of evolutionary ecology. The model focuses on the effect of evolution and multiple interactions on

ecological and evolutionary observables. Furthermore, the model is individual based, and ecological structures, such as species, are emergent quantities. The dynamics consists of a simplistic mutation-prone multiplication in which the probability of producing an offspring is determined by the occupancy in genotype space. The macroscopic long-time dynamics is intermittent and exhibits a slow decrease in the macroscopic extinction rate. Ecological quantities such as the species-abundance distribution and the species-area relationship compare qualitatively well with observations, as does the relation between interaction and diversity. The effect of correlations between parents and mutants has been studied, as well as the effect of a conserved resource.

*Garay* discusses the relative advantage and fundamental theorems of natural selection. According to the tenet of Darwinian selection, a phenotype will spread only if its fitness is greater than the mean fitness of the entire population. It is therefore natural to introduce the notion of relative advantage of a replicator, which is defined as the expected fitness of this replicator minus the average fitness of the entire replicator population. For general replicator dynamics, it is shown that the relative advantage of an offspring population over its parent population is proportional to the variance in fitness. The relationship between the proposed and earlier versions of the fundamental theorem of natural selection is also discussed.

*Kon* considers competitive exclusion between year-classes in a semelparous biennial population. In particular, competitive exclusion between two reproductively isolated year-classes in the Leslie matrix model for a semelparous biennial population is investigated. The results show that competitive exclusion occurs if competition is more severe between than within year-classes. A criterion is suggested which is applicable even if the model exhibits complex behavior.

*Nedorezov, et al.* study the impact of winter conditions on the dynamics of an isolated population. In particular, this chapter is devoted to the analysis of single-species population dynamics models with overlapping and nonoverlapping generations. It is assumed that there are no activities of individuals during the winter time (as, for example, is the case for forest insect populations in the boreal zone), and changes in population size at these moments are described with a broken trajectory (“jump down”). Furthermore, it is assumed that the fecundity of individuals is constant and that the quota of individuals surviving winter depends on the within-year population dynamics. The dynamics of the models, which are determined by the influence of winter conditions on the survival of individuals and by the influence of intra-population self-regulative mechanisms, are analyzed. For some particular cases the conditions for population extinction and for stabilization at a nonzero level are determined; it is shown numerically that chaotic regimes exist in some models. In addition, the conditions for the reduction of the models to some well-known discrete models are obtained.

*Fuller, et al.* consider the topic of planning for biodiversity conservation using stochastic programming. Rapid species extinctions and the loss of other biodiversity features worldwide have prompted the development of a systematic planning framework for the conservation of biodiversity. Limited resources ( $\sim 40$  million USD annually) are available for conservation, particularly in the developing countries that contain many of the world’s hotspots of species diversity. Thus, conservation planning problems are often represented as mathematical programs in which the objective is to

select sites to serve as conservation areas so that the cost of the plan is as small as possible and adequate habitat is protected for each species. Here, the authors generalize this approach to allow for uncertainty in the planning process. In particular, it is assumed that the species to be protected disperse after the conservation areas are established and that planners cannot anticipate with certainty the species' future locations when selecting the conservation areas. This uncertainty is modeled by including random variables in the mathematical program. The approach is illustrated by designing a network of conservation areas for birds in southern Quebec.

*Eberl and Schraft* present a diffusion-reaction model of a mixed culture biofilm arising in food safety studies. Bacterial biofilms are communities of microorganisms that develop on interfaces in aqueous environments. The authors formulate a density-dependent diffusion-reaction model for the growth of a dual-species biofilm. Both bacteria respond differently to their environment and develop different types of biofilms: one is a classical aerobic biofilm former that produces the characteristic cluster-and-channel biofilm morphology; the other one also develops under anaerobic conditions and tends to form flat, creeping biofilms. A previously developed nonstandard finite-difference scheme is adapted for computer simulation. In a numerical experiment it is shown how variations of a single parameter (growth rate) can trigger different spatial patterns and organization of the biofilm community.

*Iwata, et al.* discuss the periodical population dynamics of lottery models with undeveloped seeds. The mechanism that promotes coexistence of species has not been completely clarified yet. The authors propose that the amount of nutrient can be one of the factors that promotes coexistence of species. Plant species have to reproduce seeds to produce descendants. Even if plant species do reproduce seeds, it is not ensured that every seed will bud. The amount of seeds that can bud successfully depends on the amount of nutrient: if the nutrient is scarce, then not every seed can bud, but if the nutrient is rich, then every seed can bud. It is also assumed that the amount of seeds reproduced by one plant individual depends on the amount of nutrient. It is shown that in this situation the population dynamics of plants exhibits a complex behavior, which promotes coexistence of species.

**Part III** deals with the immune system and has four chapters.

*Zanlungo, et al.* present an automata-based microscopic model for the clonal expansion process. The model is based on a repertoire of antigens and T lymphocytes interacting via the APC cells which present the antigen peptides. Each cell is represented by an automaton moving randomly on a two-dimensional lattice. This simplified model is used in order to introduce local and spatial considerations in the mathematical models of clonal expansion based on differential equations, and at the same time to attempt an analytical interpretation of the results of computer simulations. Furthermore, a mean field theory is derived, whose results are in good agreement with the solutions of the microscopic model, at least for situations that are not too far from equilibrium. This model may be used as the basis of a more realistic one that could follow the clonal expansion process on a simplified version of the lymphatic network.

*Vogel and Behn* focus on Th1–Th2 regulation and allergy and present a bifurcation analysis of the nonautonomous system. A previously proposed mathematical model

based on a simplified scheme of Th1–Th2 regulation mediated by the cytokine network which describes the population dynamics of allergen-specific naive T cells, Th1 and Th2 cells, autocrine and cross-suppressive cytokines, and allergen is further investigated. The model provides a theoretical explanation of the switch from a Th2-dominated response to a Th1-dominated response to allergen in allergic individuals as a result of a hyposensitization therapy. The authors focus here on the bifurcation analysis of the nonautonomous dynamical system driven by periodic allergen injections. The stability of the fixed points of a stroboscopic map is investigated. The set of unstable fixed points forms the dynamical separatrix between the regions of Th2-dominated response and Th1-dominated response which is crossed during a successful therapy. The maintenance phase of the therapy holds the system near the stable fixed point of the stroboscopic map.

*Schmidtchen and Behn* discuss the architecture of randomly evolving idiotypic networks. B lymphocytes express on their surface receptors (antibodies) of a given specificity (idiotypic). Crosslinking these receptors by complementary structures, antigens or antibodies, stimulates the lymphocyte. Thus, a large functional network of interacting lymphocytes, the idiotypic network, emerges. Idiotypic networks, conceived by Niels Jerne 30 years ago, experience a renewed interest, e.g., in the context of autoimmune diseases. In a previously proposed minimalistic model, idiotypes are represented by bit strings. The population dynamics of the idiotypic clones is reduced to a zero-one scheme. An idiotypic clone survives only if it meets enough but not too many complementary structures. The authors investigate the random evolution of the network towards a highly organized functional architecture which is driven by the influx of new idiotypes, randomly generated in bone marrow. The vertices can be classified into different groups, which are clearly distinguished, e.g., by the mean lifetime of the occupied vertices. They include densely connected core groups and peripheral groups of isolated vertices, resembling the central and peripheral parts of the biological network. The authors have determined the construction principles of the observed patterns and propose a description of their architecture, which is easily transferable to other patterns and applicable to different system sizes.

*Sannikova* presents an analysis of infectious mortality by means of the individualized risk model. The goal of the work is to describe the mechanism underlying the age-specific increase in death risk related to immunosenescence and to determine the cause-specific hazard rate as a function of immune system characteristics. Therefore, a mathematical model that allows for the estimation of the age-specific risk of death caused by infectious diseases has been developed. The model consists of three parts: (1) a model of immunosenescence, (2) a model of infectious disease, and (3) a model giving the relationship between disease severity and the risk of death. The proposed model makes it possible to analyze age-specific mortality from infectious diseases and to predict future changes in mortality due to public health activity. At the same time it can be used for individualized risk assessment.

**Part IV** deals with neural systems and the brain and includes nine chapters.

*Schierwagen, et al.* focus on neuromorphological phenotyping in transgenic mice. 3D morphological data have been used to quantitatively characterize the morpholog-

ical phenotype of pyramidal neurons in transgenic mice. The authors calculated the multiscale fractal dimension (MFD) of reconstructed neuronal cells. Changes in the complexity of neuronal morphology due to permanent activation of p21Ras in the primary somatosensory cortex of transgenic mice correlate with changes in the MFD of dendrites of pyramidal neurons. Transgenic neurons seem slightly less complex (i.e., have lower peak fractal dimension) if compared with the wild type. On the other hand, it is shown that the enhanced p21Ras activity in transgenic mice may lead to greater variety in the cell morphological phenotype.

*Gibson, et al.* introduce a quantitative model of ATP-mediated calcium wave propagation in astrocyte networks. In the past, attention has mainly been focused on neurons and the role they play, both individually and as parts of networks, in the functioning of the brain and nervous system. However, glial cells outnumber neurons in the brain, and it is now becoming apparent that, far from just performing supportive and housekeeping tasks, they are also actively engaged in information processing and possibly even learning. Communication in glial cells is manifested by waves of calcium ions ( $\text{Ca}^{2+}$ ) that are released from internal stores, and these waves are observed experimentally using fluorescent markers attached to the ions. The waves can be initiated by stimulation of a single cell, and initially it was assumed that the transmission mechanism involved the passage of an intercellular signalling agent through gap junctions connecting the cells. However, a surprising feature is that in many cases the calcium waves can cross cell-free zones, thus indicating the presence of an extracellular messenger. The authors have constructed a mathematical model of calcium wave propagation in networks of model astrocytes, these being a subclass of glial cells. The extracellular signalling agent is ATP (adenosine triphosphate), and it acts on metabotropic purinergic receptors on the astrocytes, initiating a G-protein cascade leading to the production of inositol trisphosphate ( $\text{IP}_3$ ) and the subsequent release of  $\text{Ca}^{2+}$  from intracellular stores via  $\text{IP}_3$ -sensitive channels. Stimulation of one cell (by a pulse of ATP or by raising the  $\text{IP}_3$  level) leads to the regenerative release of ATP both from this cell and from neighboring cells, and hence a  $\text{Ca}^{2+}$  wave. Results are given for the propagation of  $\text{Ca}^{2+}$  waves in two-dimensional arrays of model astrocytes and also in lanes with cell-free zones in between. These theoretical considerations support the concept of extracellular purinergic transmission in astrocyte networks.

*Atay and Hutt* analyze the dynamics of neural fields with distributed transmission speeds. In particular, the continuous field model of neural populations is considered with the addition of a distribution of transmission speeds. The speed distribution arises as a result of the natural variability of the properties of axons, such as their degree of myelination. The authors analyze the stability and bifurcations of equilibrium solutions for the resulting field dynamics. Using a perturbation approach, it is shown that the speed distribution affects the frequency of bifurcating periodic solutions and the phase speed of traveling waves. The theoretical findings are illustrated by numerical calculations.

*Hampel* focuses on the estimation of differential entropy for positive random variables and its application in computational neuroscience. This chapter takes essential steps toward the goal of a differential entropy concept and provides a set of methods related to differential entropy estimation. At the beginning, the author defines the basic

terms: entropy, differential entropy, Kullback–Leibler distance, and refractory periods. Relations between differential entropy and the Kullback–Leibler distance are demonstrated. Hereafter a detailed description of the used methods is provided. These methods can be divided into three groups: parametric methods of entropy estimation, “plug-in” entropy estimators based on nonparametric density estimation, and direct entropy estimators. The formulas for direct entropy estimation based on the first four sample moments are introduced. The results are illustrated by comparison of the methods of entropy estimation, combined with two refractory period estimates. In particular, the author compares the estimates based on the histogram, the kernel density estimator, the sample spacing method, Vasicek’s method, the nearest neighbor distance method, and the methods based on sample moments.

*Tyrcha* discusses the dynamics of integrate-and-fire models. In particular, a model for the generation of action potentials by a neuron is presented. This model is based on standard and commonly accepted properties of excitable cells (neurons). The novelty is that under quite natural assumptions the generation of action potentials is described as a special case of a general model for systems generating recurrent biological events. A formula for a density function of the membrane potential distribution in the firing times of the neuron is derived. An analysis of time intervals between spikes is of special interest. Three different interspike interval distributions are found, where one of them is close to the stable distribution. This is consistent with the known literature hypothesis that stable interspike intervals form part of the neural chain in which information is being preserved.

*Kotti and Rigas* present a Monte Carlo method for the identification of the muscle spindle. In particular, the behavior of the muscle spindle is described by using a logistic regression model. The system receives input from a motoneuron and fires through the Ia sensory axon that transfers the information to the spinal cord and from there to the brain. Three functions, which are of special interest, are included in the model: the threshold, the recovery, and the summation functions. The most favorable method of estimating the parameters of the muscle spindle is the maximum likelihood approach. However, there are cases when this approach fails to converge because some of the model’s parameters are considered to be perfect predictors. In this case, the exact likelihood can be used, which succeeds in finding the estimates and the exact confidence intervals for the unknown parameters. This method has the main drawback that it is computationally very demanding, especially with large data sets. A good alternative in this case is a specific application of the Monte Carlo technique.

*Marsalek and Drapal* discuss mechanisms of coincidence detection in the auditory brainstem. The auditory brainstem in mammals contains a neural circuit for sound localization. The exact functioning of this circuit is still under controversy. Two spike generation mechanisms studied previously, excitatory coincidence detection and inhibitory coincidence detection, are studied here regarding the input-output relationship of the spike time densities. The authors propose that synchronous binary multiplication operation on spikes is the underlying process of these two variants of coincidence detection. A derivation of time to the spike is shown, which allows us to estimate the contribution of the neural circuit in the auditory brainstem to the overall reaction time of sound localization. The brainstem contribution is minute compared to the conduc-



tion delays in the mammalian neocortex. Finally, the skewness of the resulting output spike time densities is discussed in both the excitatory and inhibitory cases, and the inhibitory case is shown to be close to the normal density with a standard goodness-of-fit test for the normal probability density function.

*Hübsch and Tittgemeyer* present a multi-scale analysis of brain surface data. The human brain is characterized by complex convolution patterns. Analyzing the variability of these patterns among human subjects can reveal information for the detection of diseases that affect the human brain. This chapter presents a novel method to visualize the brain surface and its folding pattern at different scales. The analysis steps involve the transformation of the cortical surface from high resolution MRT images to an initial representation as a triangulated mesh, and finally to a representation as a series of spherical harmonic basis functions. The spherical harmonic parameterization of the surface is translation, rotation, and scaling invariant. The parametric representation gives a multidimensional coefficient vector for each cortical surface. The technique allows easier recognition of convolutional patterns. The method is a first step toward a statistical multi-scale analysis of the brain surface.

*Scheper* focuses on spike generation processes. Over the last years, the focus of the computational aspects of neurons has moved from synaptic weight and firing rate encoding to temporal firing encoding. On the other hand, several elements of these models have been based on some conceptual assumptions that imply relatively simple dynamic behavior of neuronal membrane activity in an active-passive process. In line with recent advances that yielded a better understanding of the biochemical processes that occur within cells, it is proposed that the processes that are involved in a membrane depolarization cascade are less static than has been assumed so far. In particular, the possibilities of low-level computation at the membrane level need to be explored more extensively. In this chapter some computational properties of the spike generation processes are explored using phenomenological models.

**Part V** focuses on innovative mathematical methods and education and consists of eight chapters.

*Claussen* introduces Offdiagonal Complexity (OdC) as a computationally quick network complexity measure and applies it to protein networks and cell division. Many complex biological, social, and economic networks show topologies drastically differing from random graphs. But what is a complex network, i.e., how can one quantify the complexity of a graph? Here the OdC, a new, and computationally cheap, measure of complexity is defined, based on the node-node link cross-distribution, whose nondiagonal elements characterize the graph structure beyond link distribution, cluster coefficient, and average path length. The OdC approach is applied to the *Helicobacter pylori* protein interaction network and randomly rewired surrogates thereof. In addition, OdC is used to characterize the spatial complexity of cell aggregates. The author investigates the earliest embryo development states of *Caenorhabditis elegans*. The development states of the premorphogenetic phase are represented by symmetric binary-valued cell connection matrices with dimension growing from 4 to 385. These matrices can be interpreted as adjacency matrices of an undirected graph or network. The OdC approach allows us to describe quantitatively the complexity of the cell aggregate geometry.



*Simitev and Biktashev* present an analytically solvable asymptotic model of atrial excitability. In particular, a three-variable simplified model of excitation fronts in human atrial tissue is introduced. The model is derived by novel asymptotic techniques from a previously introduced biophysically realistic model. An iterative analytical solution of the model is presented, which is in excellent quantitative agreement with the realistic model. This opens new possibilities for analytical studies as well as for efficient numerical simulation of this and other cardiac models of similar structure.

*Lalam and Jacob* introduce a Bayesian approach to the quantitative polymerase chain reaction. This reaction aims at determining the initial amount of a specific portion of DNA molecules from the observation of the amplification process of the DNA molecules' quantity. This amplification process is achieved through successive replication cycles and depends on the efficiency of the replication of the molecules. Modelling the amplification process by a branching process, the authors estimate the unknown parameter using Markov chain Monte Carlo methods under a Bayesian framework.

*Buck-Sorlin, et al.* present a model of poplar (*Populus* sp.) physiology and morphology based on relational growth grammars. Functional-structural plant models (FSPMs), combining the physiological function of a plant with its architecture, require precise and transparent specifications. This can be viewed as a new challenge to the design of programming languages. Here the authors introduce, exemplarily, a model of young poplar trees, based on the new formalism of relational growth grammars (RGGs), which extend the well-known Lindenmayer (L-)systems to a specific type of node- and edge-labelled graph grammars. The model has been written in the programming language XL, which extends standard Java by rule-based programming with RGGs and overcomes many of the disadvantages of L-systems. RGGs can bridge different scales: In the presented model, morphogenetic rules in L-system style are combined with rules describing a regulatory network of hormone biosynthesis and rules updating photosynthate concentrations of shoot modules, all in one and the same formalism.

*Calvez and Dolak-Struß* analyze the asymptotic behavior of a two-dimensional Keller–Segel model with and without density control. In particular, the authors study the Keller–Segel model for chemotaxis, consisting of a drift-diffusion equation describing the evolution of the cell density coupled to an equation for the chemoattractant. It is known that in the classical Keller–Segel model, solutions can become unbounded in finite time. The authors present recent analytical results for this model, and compare its behavior in two space dimensions numerically to the behavior of a model accounting for the finite volume of cells. This modified Keller–Segel model relies on the assumption that cells stop aggregating when their density is too high, and thus allows for the global existence of solutions. The authors characterize the slow movement of a certain class of plateau-shaped solutions and perform numerical experiments for both models, showing that solutions of the classical (before blow-up) and of the density control model share common features: regions of high cell density are attracted by each other and, under suitable boundary conditions, by the domain boundaries.

*Jacob* discusses saturation effects in population dynamics. The chapter deals with the behavior of a branching population undergoing saturation effects when it becomes too large. The author studies, in particular, the limits of the prediction given in the

setting of the deterministic dynamical system related to the stochastic branching process modelling the evolution of the population. Furthermore, *Jacob* also generalizes the usual Markovian branching processes of order one to size-dependent branching processes that may have a longer memory and gives conditions leading to an almost sure extinction of the process while the dynamical system is persistent. The notion of reproductive rate is explained and generalized. Finally, some examples are given, in particular, the amplification process in the PCR (polymerase chain reaction).

*Klauß and Voß-Böhme* consider modelling and simulation by stochastic interacting particle systems. Stochastic interacting particle systems (IPSS) are individual-based models, which include stochastic local interactions on a spatial lattice. In this respect an IPS works similarly to a cellular automaton. However, IPSs are continuous-time Markov processes, hence there is a large background of analytical methods. Furthermore, one has the possibility to simulate the system on a finite lattice. The authors explain the modelling steps and describe the core of a simulation algorithm. The idea is to convince the reader that IPSS can be used to set up and simulate sophisticated and applicable models, but allow an analytical approach as well.

*De Vries and Hillen* present mathematical biology teaching experiences from a summer school for undergraduates. For the past four years, the University of Alberta has hosted a summer school on mathematical biology, aimed at undergraduate students who have completed 2–3 years of study in mathematics or a similar quantitative science. The aim of this summer school is to introduce the students to mathematical modelling and analysis applied to real biological systems. In the span of 10 days, students attend lectures and exercise sessions, learn how to set up mathematical models, and use analytical and computational tools to relate them to biological data. Furthermore, they experience the modelling process by working on a research project. In this chapter, the authors explain their teaching philosophy, share some unique features of the summer school, and exemplify the key course components.

Finally, the volume owes its existence to the support of many colleagues. First of all, thanks go to the authors of the various contributions. We would also like to express our gratitude to the members of the ECMTB05 scientific committee and to a significant number of other colleagues for providing reviews and suggestions. ECMTB05 and these peer-reviewed proceedings have only become possible thanks to the strong institutional support provided by the Centre for Information Services and High Performance Computing (Technical University of Dresden). Particular thanks go to Professor Wolfgang E. Nagel, the head of this Centre and many colleagues at the Centre, particularly Niloy Ganguly, Christian Hoffmann, Samatha Kottha, Claudia Schmidt, Jörn Starruß, and Sabine Vollheim. Finally, we would like to thank Tom Grasso of Birkhäuser for making this project possible.

Dresden, January 2007  
Andreas Deutsch (for the editors)

---

# Contents

<b>Preface</b> .....	v
<hr/>	
<b>Part I Epidemiology</b>	<b>1</b>
<hr/>	
1 Could Low-Efficacy Malaria Vaccines Increase Secondary Infections in Endemic Areas? <i>Robert J. Smith?</i> .....	3
2 Modeling of the Invasion of a Fungal Disease over a Vineyard <i>Jean-Baptiste Burie, Agnès Calonnec, Michel Langlais</i> .....	11
3 An Algorithm for Parameter Estimation in Nosocomial Infections <i>Nico Stollenwerk, Rafaël Mikolajczyk</i> .....	23
<hr/>	
<b>Part II Evolution and Ecology</b>	<b>35</b>
<hr/>	
4 Evolutionarily Stable Investment in Anti-Predatory Defences and Aposematic Signalling <i>Mark Broom, Graeme D. Ruxton, Michael P. Speed</i> .....	37
5 The Tangled Nature Model of Evolutionary Ecology: An Overview <i>Simon Laird, Daniel Lawson, Henrik Jeldtoft Jensen</i> .....	49
6 Relative Advantage and Fundamental Theorems of Natural Selection <i>József Garay</i> .....	63
7 Competitive Exclusion Between Year-Classes in a Semelparous Biennial Population <i>Ryusuke Kon</i> .....	75

8 On the Impact of Winter Conditions on the Dynamics of an Isolated Population  
*Lev V. Nedorezov, E.V. Volkova, Alexandr M. Sadykov* ..... 87

9 Planning for Biodiversity Conservation Using Stochastic Programming  
*Trevon Fuller, David P. Morton, Sahotra Sarkar* ..... 101

10 A Diffusion-Reaction Model of a Mixed-Culture Biofilm Arising in Food Safety Studies  
*Hermann J. Eberl, Heidi Schraft* ..... 109

11 The Periodical Population Dynamics of Lottery Models Including the Effect of Undeveloped Seeds  
*Shigehide Iwata, Ryusuke Kon, Yasuhiro Takeuchi* ..... 121

---

**Part III Immunology** **131**

---

12 An Automata-Based Microscopic Model Inspired by Clonal Expansion  
*Francesco Zanlungo, Sandro Rambaldi, Giorgio Turchetti* ..... 133

13 Th1–Th2 Regulation and Allergy: Bifurcation Analysis of the Non-Autonomous System  
*Reinhard Vogel, Ulrich Behn* ..... 145

14 Architecture of Randomly Evolving Idiotypic Networks  
*Holger Schmidtchen, Ulrich Behn* ..... 157

15 Analysis of Infectious Mortality by Means of the Individualized Risk Model  
*Tatiana E. Sannikova* ..... 169

---

**Part IV Neural Systems and the Brain** **183**

---

16 Neuromorphological Phenotyping in Transgenic Mice: A Multiscale Fractal Analysis  
*Andreas Schierwagen, Luciano da Fontoura Costa, Alan Alpar, Ulrich Gärtner, Thomas Arendt* ..... 185

17 A Quantitative Model of ATP-Mediated Calcium Wave Propagation in Astrocyte Networks  
*William G. Gibson, Les Farnell, Max R. Bennett* ..... 193

18 Dynamics of Neural Fields with Distributed Transmission Speeds  
*Fatihcan M. Atay, Axel Hutt* ..... 205

19 Estimation of Differential Entropy for Positive Random Variables and Its Application in Computational Neuroscience  
*David Hampel* . . . . . 213

20 Dynamics of Integrate-and-Fire Models  
*Joanna Tyrcha* . . . . . 225

21 A Monte Carlo Method Used for the Identification of the Muscle Spindle  
*Vassiliki K. Kotti, Alexandros G. Rigas* . . . . . 237

22 Mechanisms of Coincidence Detection in the Auditory Brainstem: Examples  
*Petr Marsalek, Marek Drapal* . . . . . 245

23 Multi-Scale Analysis of Brain Surface Data  
*Thomas Hübsch, Marc Tittgemeyer* . . . . . 255

24 The Spike Generation Processes: A Case for Low Level Computation  
*Tjeerd olde Scheper* . . . . . 265

---

**Part V Innovative Mathematical Methods and Education** **277**

---

25 Offdiagonal Complexity: A Computationally Quick Network Complexity Measure—Application to Protein Networks and Cell Division  
*Jens Christian Claussen* . . . . . 279

26 An Analytically Solvable Asymptotic Model of Atrial Excitability  
*Radostin D. Simitev, Vadim N. Biktashev* . . . . . 289

27 A Bayesian Approach to the Quantitative Polymerase Chain Reaction  
*Nadia Lalam, Christine Jacob* . . . . . 303

28 A Model of Poplar (*Populus* sp.) Physiology and Morphology Based on Relational Growth Grammars  
*Gerhard Buck-Sorlin, Ole Kniemeyer, Winfried Kurth* . . . . . 313

29 Asymptotic Behavior of a Two-Dimensional Keller–Segel Model with and without Density Control  
*Vincent Calvez, Yasmin Dolak-Struß* . . . . . 323

30 Saturation Effects in Population Dynamics: Use Branching Processes or Dynamical Systems?  
*Christine Jacob* . . . . . 339

31 Modelling and Simulation by Stochastic Interacting Particle Systems  
*Tobias Klauß, Anja Voß-Böhme* . . . . . 353

32 Teaching Mathematical Biology in a Summer School for Undergraduates  
*Gerda de Vries, Thomas Hillen* ..... 369

**Index** ..... 379

**Epidemiology**

# Could Low-Efficacy Malaria Vaccines Increase Secondary Infections in Endemic Areas?

Robert J. Smith?

Department of Mathematics and Faculty of Medicine, The University of Ottawa,  
585 King Edward Ave, Ottawa, Ontario, K1N 6N5, Canada; rsmith43@uottawa.ca

**Summary.** Recent breakthroughs in malaria vaccines have given new hope that a safe, effective malaria vaccine may be found. The following epidemiological questions are addressed: 1. What level of vaccination coverage is required to offset the limitations of an imperfect disease-modifying vaccine? 2. Could the introduction of a low-efficacy malaria vaccine lead to an increase in the number of secondary infections? 3. What characteristics of such a vaccine will have the greatest effect on the outcome? A mathematical model is developed for a disease-modifying malaria vaccine that is given once prior to infection, and the minimum coverage level for disease eradication is established. There is a threshold depending on the relative rate of infection, the efficacy of the vaccine and the duration of infection. Vaccines which reduce the rate and duration of infection will always result in a decrease in secondary infections. More surprisingly, there is a duration “shoulder,” such that vaccines that increase the duration of infection slightly will still lead to a decrease in secondary infections, even if the rate of infection is unchanged. Beyond this, the number of secondary infections will increase unless the rate of infection is sufficiently lowered. This is critical for low-efficacy vaccines.

**Key words:** Malaria, vaccines, coverage, rate of infection, duration of infection, efficacy.

## 1.1 Introduction

Malaria remains one of the most important human diseases throughout the tropical and subtropical regions of the world and causes more than 300 million acute illnesses and at least one million deaths annually [18]. 90% of deaths due to malaria occur in sub-Saharan Africa, mostly among young children [17]. The search for a malaria vaccine is now over seventy years old [6], and a great deal of effort and funding has been put into the task [11]. Recent vaccine findings [1] have renewed the interest in the potential role of vaccines within malaria-control programs by focusing on the possibility of an anti-malarial vaccine delivered to infants prior to infection.

In this chapter, a model of malaria infection is developed which combines the classic Aron models [2,3] with those of vaccine models [8], but includes disease-modifying effects based on theoretical HIV vaccine models [4, 15]. The following epidemiological questions are addressed: 1. What level of vaccination coverage is required to offset



the limitations of an imperfect disease-modifying vaccine? 2. Could the introduction of a low-efficacy malaria vaccine lead to an increase in the number of secondary infections? 3. What characteristics of such a vaccine will have the greatest effect on the outcome?

## 1.2 The Model

A malaria vaccine could have different potential effects, including (a) reducing mortality due to malaria, (b) increasing the recovery rate, (c) increasing the acquired immunity rate or d) reducing the rate of infection. Possible limitations of a vaccination program include (i) the vaccine may only be delivered to a proportion  $p$  of the population, (ii) the vaccine may only “take” in a proportion  $\epsilon$  of people vaccinated, (iii) the vaccine may wane over time ( $\omega$  is the rate of waning of immunity) and (iv) the vaccine may have a suboptimal efficacy  $\psi$ . It is assumed that all vaccinated individuals are vaccinated before infection, reflecting the situation in [1]. Furthermore, unlike in HIV models (but in common with other models of vaccination; eg pertussis [16]), the vaccine may wane before, during or after infection.

It follows that “*successfully vaccinated*” individuals consist of those who received the vaccine, for whom the vaccine “took” and for whom the vaccine did not wane prior to infection. All other individuals shall be referred to as *unprotected individuals*, regardless of whether they received the vaccine or not, since the net effect prior to infection is identical. (See [4] and [15] for more detailed discussions.) Note that “*successfully vaccinated*” individuals have the potential to become infected (if the vaccine efficacy  $\psi$  is less than 100%, or if vaccine-induced immunity wanes subsequently) and cause secondary infections. These individuals may have a reduced rate of infection, but will have an increased life expectancy. They may recover faster from the disease and their disease-induced mortality will be lower. Consequently, their total duration of infection may either decrease (due to higher recovery rates) or increase (due to fewer deaths from infection).

It can be assumed that mosquitos are either susceptible ( $M$ ) or infected ( $N$ ), have birth rate  $\Omega$  and that their death rate ( $\mu_M$ ) does not vary significantly if they are infected. Individuals who have experienced infection may recover (without substantial gain in immunity) at *recovery rate*  $h_k$  ( $k = U, V$ ;  $U =$  unvaccinated,  $V =$  vaccinated) or may become temporarily immune at *acquired immunity rate*  $\alpha_k$  ( $k = U, V$ ). See [5, 9, 10, 12] for further details. Temporarily immune individuals will become susceptible again at rate  $\delta_k$  ( $k = U, V$ ). The rate of infection of an infected individual in class  $X_k$  is  $\beta_k$  ( $k = U, V$ ) and the rate of infecting a mosquito is  $\beta_M$  (assumed identical from either class of individual, since mosquitos are not vaccinated). The birth rate is  $\pi$ , the background death rate is  $\mu$  and  $\gamma_k$  is the death rate due to malaria ( $k = U, V$ ). Thus, the model is

$$\begin{aligned}\frac{dM}{dt} &= \Omega - \beta_M Y_U M - \beta_M Y_V M - \mu_M M \\ \frac{dN}{dt} &= \beta_M Y_U M + \beta_M Y_V M - \mu_M N\end{aligned}$$

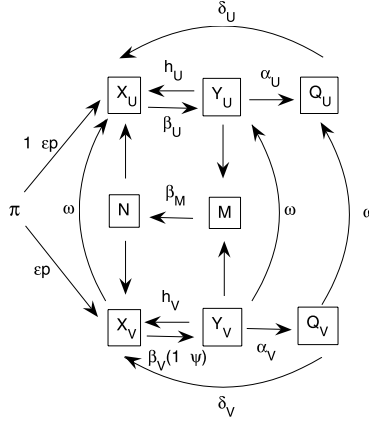


**Fig. 1.1.** Schematic representation of the model, representing both unprotected and “successfully vaccinated” individuals, as well as mosquitos. The background mortalities for humans  $\mu$  (in all compartments) and mosquitos  $\mu_M$  (in both compartments), as well as disease-induced mortality for humans  $\gamma_U, \gamma_V$  (in the infected compartments) are not drawn in, for conciseness.

$$\begin{aligned} \frac{dX_U}{dt} &= (1 - \epsilon p)\pi - \mu X_U - \beta_U N X_U + \omega X_V + h_U Y_U + \delta_U Q_U \\ \frac{dX_V}{dt} &= \epsilon p \pi - \mu X_V - (1 - \psi)\beta_V N X_V - \omega X_V + h_V Y_V + \delta_V Q_V \\ \frac{dY_U}{dt} &= \beta_U N X_U - (\mu + \gamma_U + \alpha_U + h_U) Y_U + \omega Y_V \\ \frac{dY_V}{dt} &= (1 - \psi)\beta_V X_V - (\mu + \gamma_V + \alpha_V + h_V) Y_V - \omega Y_V \\ \frac{dQ_U}{dt} &= \alpha_U Y_U - (\mu + \delta_U) Q_U + \omega Q_V \\ \frac{dQ_V}{dt} &= \alpha_V Y_V - (\mu + \delta_V) Q_V - \omega Q_V . \end{aligned}$$

The model is illustrated in Fig. 1.1.

With the notation  $\xi_k = \mu + \gamma_k + \alpha_k + h_k$  ( $k = U, V$ ),  $1/\xi_K$  is the total duration of the infectious period for unprotected and “successfully vaccinated” individuals, respectively. It is expected that the recovery rates  $\alpha_V, h_V$  will increase due to the vaccine, but that the disease-induced death rate  $\gamma_V$  will decrease. It follows that the total duration of the infectious period for vaccinated individuals may either increase or decrease. It is also expected that the rate of infection  $\beta_V$  will not increase.

### 1.3 Analysis

The disease-free equilibrium satisfies  $\bar{M} = \Omega/\mu_M$ ,  $\bar{X}_U = [\pi(\mu(1 - \epsilon p) + \omega)]/[\mu(\mu + \omega)]$ ,  $\bar{X}_V = \epsilon p \pi/(\mu + \omega)$  and  $\bar{N} = \bar{Y}_U = \bar{Y}_V = \bar{Q}_U = \bar{Q}_V = 0$ .

Thus, the proportion of the population that is successfully vaccinated,  $S$ , satisfies  $S = \bar{X}_V / (\bar{X}_U + \bar{X}_V) = \epsilon p \mu / (\mu + \omega)$ . In particular,  $\bar{X}_U = (\pi / \mu)(1 - S)$  and  $\bar{X}_V = (\pi / \mu)S$ .

At the disease-free equilibrium, the Jacobian matrix is  $J =$

$$\begin{bmatrix} \mu_M & 0 & 0 & 0 & -\beta_M \bar{M} & -\beta_M \bar{M} & 0 & 0 \\ 0 & -\mu_M & 0 & 0 & \beta_M \bar{M} & \beta_M \bar{M} & 0 & 0 \\ 0 & -\beta_U \bar{X}_U & -\mu & \omega & h_U & 0 & \delta_U & 0 \\ 0 & -(1 - \psi)\beta_V \bar{X}_V & 0 & -\mu - \omega & 0 & h_V & 0 & \delta_V \\ 0 & \beta_U \bar{X}_U & 0 & 0 & -\xi_U & \omega & 0 & 0 \\ 0 & (1 - \psi)\beta_V \bar{X}_V & 0 & 0 & 0 & -\xi_V - \omega & 0 & 0 \\ 0 & 0 & 0 & 0 & \alpha_U & 0 & -\mu - \delta_U & \omega \\ 0 & 0 & 0 & 0 & 0 & \alpha_V & 0 & -\mu - \delta_V - \omega \end{bmatrix}.$$

Thus,  $\det(J - \Lambda I) = -(\mu_M + \Lambda)(\mu + \Lambda)(\mu + \omega + \Lambda)(\mu + \delta_U + \Lambda)(\mu + \delta_V + \omega + \Lambda) \det M$ , where

$$M = \begin{bmatrix} -\mu_M - \Lambda & \beta_M \bar{M} & \beta_M \bar{M} \\ \beta_U \bar{X}_U & -\xi_U - \Lambda & \omega \\ (1 - \psi)\beta_V \bar{X}_V & 0 & -\xi_V - \omega - \Lambda \end{bmatrix}.$$

Thus, the largest eigenvalue for  $J$  will be the largest eigenvalue for  $M$ . The vanishing determinant condition gives  $-\mu_M \xi_U (\xi_V + \omega) + (1 - \psi)\beta_V \beta_M \omega \bar{X}_V \bar{M} + (1 - \psi)\xi_U \beta_V \beta_M \bar{X}_V \bar{M} + (\xi_V + \omega)\beta_U \beta_M \bar{X}_U \bar{M} = 0$ . Hence,

$$\frac{(1 - \psi)\beta_V \beta_M \bar{M} (\xi_U + \omega)}{\mu_M \xi_U (\xi_V + \omega)} \bar{X}_V + \frac{\beta_U \beta_M \bar{M}}{\mu_M \xi_U} \bar{X}_U = 1.$$

Individuals who are vaccinated with disease-modifying vaccines have the potential to become infected and cause secondary infections. Such individuals may have a reduced rate of infection, but will have an increased survival time. The reproduction number in a population with vaccination is  $R_V$ , in contrast to  $R_0$ , the basic reproduction number in an unvaccinated population.

If there is no vaccine,  $S = 0$ , so  $\bar{X}_V = 0$ ,  $\bar{X}_U = \pi / \mu$  and hence the vanishing determinant condition gives  $R_0 = \pi \Omega \beta_U \beta_M / \mu \mu_M^2 \xi_U$ . If the entire population is successfully vaccinated,  $S = 1$  and  $\omega = 0$ , so  $\bar{X}_V = \pi / \mu$ ,  $\bar{X}_U = 0$  and hence the vanishing determinant condition gives  $R_V = (1 - \psi)(\pi \Omega \beta_V \beta_M / \mu \mu_M^2 \xi_V)$ . Thus, the population reproduction number is  $R_P = (1 - S)R_0 + SR_V$ . See [4, 7, 13–15].

To estimate the minimum coverage levels  $p_c$  for an imperfect disease-modifying vaccine, when  $R_P = 1$ , this last equation can be rearranged to produce

$$S = \frac{\epsilon p_c \mu}{\mu + \omega} = \frac{1 - R_0}{R_V - R_0}.$$

Thus, the threshold disease-modifying vaccine coverage level is

$$p_c = \frac{(\mu + \omega)(\mu + \gamma_V + \alpha_V + h_V)[\mu \mu_M^2 (\mu + \gamma_U + \alpha_U + h_U) - \beta_U \beta_M \Omega \pi]}{\epsilon \mu \beta_M \Omega \pi [(1 - \psi)\beta_V (\mu + \gamma_U + \alpha_U + h_U) - \beta_U (\mu + \gamma_V + \alpha_V + h_V)]}. \quad (1.1)$$

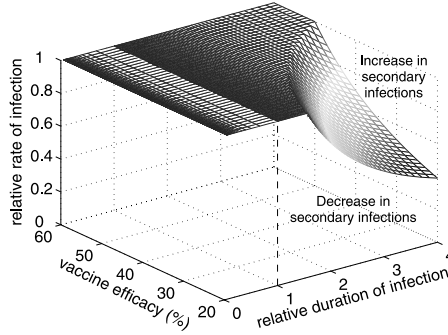


**Fig. 1.2.** The relationship between the relative rate of infection, the relative duration of infection and the vaccine efficacy. A disease-modifying vaccine which reduces the duration of infection will always lead to a decrease in secondary infections, regardless of the efficacy of the vaccine. More surprisingly, a vaccine which increases the duration of infection can still result in an overall decrease in secondary infections, but the outcome depends on the rate of infection and the efficacy of the vaccine. There is a duration “shoulder,” such that vaccines that increase the duration of infection slightly will still result in a net decrease in secondary infections. However, as the duration of infection increases, the number of secondary infections will increase, unless the rate of infection is lowered accordingly. This is critical for low-efficacy vaccines.

Vaccination programs whose coverage levels exceed this proportion of the population are likely to eradicate the disease.

Once a vaccine is introduced, the number of secondary infections will increase if  $R_P > R_0$  (i.e., if the population reproduction number after the introduction of a vaccine is greater than the reproduction number currently). This occurs when

$$(1 - S)R_0 + SR_V > R_0$$

$$\frac{\beta_V}{\beta_U} > \frac{\xi_V}{(1 - \psi)^2 \xi_U}.$$

This is illustrated in Fig. 1.2.

Clearly, if the rate of infection and the duration of infection both decrease, then there will always be a decrease in the number of secondary infections. More surprisingly, for a given efficacy of the vaccine, there is a duration “shoulder,” such that a small increase in the duration of infection will still decrease the number of secondary infections, even if the rate of infection is unchanged. However, if the duration of infection is increased beyond this shoulder, then it is crucial that the rate of infection be decreased accordingly. This is critical for low-efficacy vaccines.

The “shoulder” occurs when the relative duration of infection satisfies

$$\frac{1/\xi_V}{1/\xi_U} = \frac{1}{(1 - \psi)^2}$$

for a given vaccine efficacy  $\psi$ . For example, a 20% efficacious vaccine could accommodate an increase in the duration of infection by as much as 1.5625 times the current

duration of infection, with no reduction in the rate of infection and still result in a decrease in secondary infections. However, a 20% efficacious vaccine that increased the duration of infection by a factor of 4 would lead to an increase in secondary infections unless the rate of infection for the vaccinated population were reduced to 40% of the current rate of infection.

## 1.4 Discussion

A vaccination program implementing a disease-modifying malaria vaccine in an endemic area should have a minimum coverage level  $p_c$ , as estimated by (1.1). If the proportion of the population that can be vaccinated exceeds  $p_c$ , then such a vaccination program is likely to result in the eradication of the disease.

Furthermore, reducing the transmission probability of such a disease-modifying vaccine is crucial, for vaccines whose duration of infection increases significantly. While it is expected that a disease-modifying vaccine would increase the recovery rates, it would also decrease the rate of disease-induced mortality, so the total duration of the infectious period for a vaccinated individual may either increase or decrease. If this duration decreases, then the number of secondary infections will always decrease, regardless of the vaccine efficacy, so long as the rate of infection does not increase.

There is a duration “shoulder,” such that the number of secondary infections will always decrease if the duration increases within this shoulder. However, an increase beyond the “shoulder” will lead to an increase in secondary infections, unless the rate of infection of the vaccine is lowered accordingly. This is critical for low-efficacy vaccines.

It should be noted that these results primarily apply to areas in which malaria is endemic. A disease-modifying malaria vaccine with a high duration of infection (for example, one which drastically reduced disease-induced mortality, but which had negligible effect on the recovery rates) might be quite desirable for a temporary outbreak of malaria in the developed world, if the prospect of reinfection is negligible. In endemic areas however, such a vaccine would likely make the situation worse. It follows that low-efficacy vaccines which result in high durations of infection but which do not significantly lower the rate of infection should not be used in endemic areas.

## Acknowledgments

The author is grateful to Shoshana Magnet, Helen Kang, Anne Conway and Celia Abood for technical discussions, as well as to Mirjam Kretzschmar and three anonymous referees for helpful comments that greatly improved the manuscript.

## References

1. Alonso, P. L., Sacarlal, J., Aponte, J. J., Leach, A., Macete, E., Milman, J., Mandomando, I., Spiessens, B., Guinovart, C., Espasa, M., Bassat, Q., Aide, P., Ofori-Anyinam, O., Navia, M.

- M., Corachan, S., Ceuppens, M., Dubois, M. C., Demoitie, M. A., Dubovsky, F., Menendez, C., Tornieporth, N., Ballou, W. R., Thompson, R., Cohen, J.: Efficacy of the RTS,S/AS02A vaccine against *Plasmodium falciparum* infection and disease in young African children: randomised controlled trial. *Lancet*, **364**, 1411–20 (2004).
2. Aron, J. L.: Mathematical modeling of immunity to malaria. *Math. Biosci.*, **90**, 385–396 (1988).
  3. Aron, J. L., May, R. M.: The population dynamics of malaria. In: Anderson, R.M. (ed) *The Population Dynamics of Infectious Diseases: Theory and Applications*. Chapman & Hall, London (1982).
  4. Blower, S. M., Koelle, K., Mills, J.: Health Policy Modeling: Epidemic Control, HIV Vaccines and Risky Behavior. In: Kaplan, E., Brookmeyer, R. (eds) *Quantitative Evaluation of HIV Prevention Programs*. Yale University Press, New Haven, CT (2002).
  5. Boyd, M. F. (ed): *Malariaology, Saunders*, Philadelphia (1949).
  6. Desowitz, R. S.: *Federal Bodysnatchers and the New Guinea Virus: Tales of Parasites, People and Politics*. W.W. Norton & Company, New York (2002).
  7. Heffernan, J. M., Smith, R. J., Wahl, L. M.: Perspectives on the basic reproductive ratio. *J. R. Soc. Interface*, **2**, 281–293 (2005).
  8. Koella, J.: On the use of mathematical models of malaria transmission. *Acta Trop.*, **49**, 1–25 (1991).
  9. Mackinnon, M. J., Read, A. F.: The effects of host immunity on virulence-transmissibility relationship in the rodent malaria parasite *Plasmodium chabaudi*. *Parasitology*, **126**, 103–112 (2003).
  10. Molineaux, L., Gramiccia, G.: *The Garki Project: Research on the Epidemiology and Control of Malaria in the Sudan Savannah of West Africa*. World Health Organization, Geneva (1980).
  11. Moorthy, V. S., Good, M. F., Hill, A. V.: Malaria vaccine developments. *Lancet.*, **363**, 150–6 (2004).
  12. Pérignon, J. L., Druilhe, P.: Immune mechanisms underlying the premunition against *Plasmodium falciparum* malaria. *Mem. Inst. Oswaldo Cruz, Rio de Janeiro*, **89**, Suppl. II (1994).
  13. Porco, T. C., Blower, S. M.: Designing HIV vaccination policies: Subtypes and cross-immunity. *Interfaces*, **28**, 167–190 (1998).
  14. Porco, T. C., Blower, S. M.: HIV vaccines: The effect of the mode of action on the coexistence of HIV subtypes. *Math. Pop. Studies*, **8**, 205–229 (2000).
  15. Smith, R. J., Blower, S. M.: Could disease-modifying HIV vaccines cause population-level perversity? *Lancet Inf. Dis.*, **4**, 636–639 (2004).
  16. van Boven, M., de Melker, H. E., Schellekens, J. F., Kretzschmar, M.: Waning immunity and sub-clinical infection in an epidemic model: Implications for pertussis in The Netherlands. *Math Biosci.*, **164**, 161–82 (2000).
  17. van de Perre, P., Dedet, J.-P.: Vaccine efficacy: winning a battle (not war) against malaria. *Lancet*, **364**, 1411–1420 (2004).
  18. World Health Organisation, Roll Back Malaria infosheet: What is Malaria? [http://malaria.who.int/cmc\\_upload/0/000/015/372/RBMInfosheet\\_1.htm](http://malaria.who.int/cmc_upload/0/000/015/372/RBMInfosheet_1.htm) (accessed 26 May 2007).

# Modeling of the Invasion of a Fungal Disease over a Vineyard

Jean-Baptiste Burie,<sup>1</sup> Agnès Calonnec,<sup>2</sup> and Michel Langlais<sup>1</sup>

<sup>1</sup> UMR CNRS 5466, Mathématiques Appliquées de Bordeaux, INRIA futurs, Equipe Anubis, case 26, Université Victor Segalen Bordeaux 2, 146 rue Léo Saignat, 33076 Bordeaux Cedex, France; burie@sm.u-bordeaux2.fr

<sup>2</sup> INRA-CR de Bordeaux, UMR INRA-ENITA en Santé végétale, BP 81, 33883 Villenave d'Ornon, France; calonnec@bordeaux.inra.fr

**Summary.** The spatiotemporal spreading of a fungal disease over a vineyard is investigated using a susceptible-exposed-infected-removed (SEIR)-type model coupled with a set of partial differential equations describing the dispersal of the spores. The model takes into account both short and long range dispersal of spores and growth of the foliar surface. Results of numerical simulations are presented. A mathematical result for the asymptotic behavior of the solutions is given as well.

**Key words:** SEIR model, dispersal, diffusion, large time behavior.

## 2.1 Introduction

Integrated pest management offers an attractive alternative to routine chemical application by treating only in response to disease risk indicators. Powdery mildew, caused by the fungus *Uncinula necator*, is the most economically important and widespread disease of grapevines. For this disease, the main factor of risk is a timing of the attack early in the season combined with the phenological stage of the host. The leaves are the first to be infected, and there is a spatial relationship between maps of frequency of leaves diseased early in the season with maps of frequency of bunches with high severity [4,8]. A better knowledge of the mechanisms of the disease propagation could help to improve its control at the plot scale by tailoring treatments to local specific needs, or at the estate scale by treating only specific plots.

We aim at building a mathematical model of this fungal epidemic with a particular stress on the dispersal mechanism of the spores produced by the colonies of fungus. Already much work has been done on the subject of dispersal for various kinds of dispersers such as animals, seeds and spores (see, e.g., [6,10,11] and references therein).

In particular, we want to investigate the role of a dual dispersal mechanism in which the spores produced may either disperse inside the vine stock and germinate near the colony (short range dispersal) or may be lifted up above the vine rows and fall far from the colony (long range dispersal).

Our goal is to build a model which is a simpler version, and consequently easier to analyse, of a much more elaborate one [5]. This latter model couples a mechanistic model for the growth of each vine stock in the vineyard with a dispersal model using ray-tracing-like techniques at the vine stock scale and a distribution law at the vineyard scale for the spores escaping the vine stock.

In [13], the authors considered a two-dimensional (2D) spatial model based upon such a dual dispersal mechanism using diffusion theory coupled with a Vanderplank equation [12]. Using this Vanderplank equation leads to delay equations that complicate the mathematical analysis of the model. Instead, in this chapter, we will use a susceptible, exposed, infectious, removed (SEIR) compartmental model as used in classical epidemiology (see, e.g., [1, 3]) to take into account the local extension of the disease. In the nonspatial case, a comparison between these two approaches can be found in [9].

During an epidemic lasting a whole season from bud break until grape maturation, the growth of the host cannot be neglected. We include a description of the host growth in our model. We also take into consideration the specific spatial organisation of vineyards that are made of several separate rows.

This chapter is organised as follows. After having described the model, we perform a mathematical analysis and present numerical simulations.

## 2.2 The Model

The vectors of a fungal disease are the spores produced by the colonies of fungus that lie on the vegetal tissue, which may be leaves, buds, fruits, etc. We assume for simplicity that the time variation of the surface of a colony can be neglected. Then as in [9] we consider the unit of disease to be a colony and the host to be a site, that is the surface occupied by a colony.

The cycle of the epidemic is as follows: when spores fall upon the vegetal tissue, they may create a new colony which will produce spores after some latency period and during some sporulating period.

Let  $\Omega$  be a regular 2D spatial domain. Let  $t$  be the time and let  $x$  denote the position of some point in  $\Omega$ . We will use the following notation for the state variables.

As in the case of a SEIR model, the total density  $N$  of sites susceptible to host a colony of fungus at  $(x, t)$  is subdivided into healthy  $H$ , latent  $L$ , sporulating  $I$  and removed (postinfectious)  $R$ .

We want to devise a model that takes into account multiple ranges of dispersal for the spores in order to investigate their different roles for the spreading of the epidemic. Spores may disperse separately or as infection units (packages of spores). For simplicity, we only take into account two ranges for dispersal: a short range (spores disperse inside the vine stock where they come from), and a longer range (spores disperse at the vineyard scale). Let  $S(x, t)$  denote the density of spores produced by the colonies. The spores' total density  $S$  is subdivided according to the range of dispersal; the short range dispersal spore density  $S_1$  and the longer range one  $S_2$ . They are produced by a



sporulating colony with rate  $r_p > 0$  and may disperse at short range with a constant probability  $F \in [0, 1]$  and at longer range with probability  $(1 - F)$ .

We assume that the spores disperse according to a diffusion process with Fickian diffusion coefficient  $D_1 > 0$  (short range) or  $D_2 > D_1 > 0$  (longer range) as in [13]. Using Fickian diffusion for long range dispersal may seem unrealistic at first. But the spores are not necessarily taken away along dominating wind directions. The dispersal is also due to turbulence that provides the energy to tear off the spores from the leaves.

Spores fall upon the vineyard with some deposition rate  $\delta_1 > 0$  or  $\delta_2 > 0$ ; we will set  $\delta_1 = \delta_2$  in the numerical simulations. We thus find the first set of equations of our model that describes the production of spores by the colonies and their dispersal:

$$\begin{cases} \frac{\partial S_1}{\partial t}(x, t) = \nabla \cdot (D_1 \nabla S_1(x, t)) - \delta_1 S_1(x, t) + r_p F I(x, t) \\ \frac{\partial S_2}{\partial t}(x, t) = \nabla \cdot (D_2 \nabla S_2(x, t)) - \delta_2 S_2(x, t) + r_p (1 - F) I(x, t) \end{cases} \quad (2.1)$$

for  $x \in \Omega$  and  $t > 0$ .

Moreover, we assume that no spores come from outside the vineyard. The spores produced by the fungus colonies should freely escape from the vineyard. To simulate this, we choose a computing domain  $\Omega$  with vine rows located at the center and surrounded by a region with no vines. Then, if  $\Omega$  is large enough with respect to diffusion coefficients, spores do not reach the boundary and their densities at these points should be equal to 0. Thus, we impose Dirichlet conditions on the boundary

$$S_1(x, t) = S_2(x, t) = 0 \text{ for } x \in \partial\Omega \text{ and } t > 0. \quad (2.2)$$

We also set nonnegative initial conditions

$$S_1(x, 0) = S_1^0(x) \geq 0, \quad S_2(x, 0) = S_2^0(x) \geq 0 \text{ for } x \in \Omega. \quad (2.3)$$

Let  $\Omega_r \subset \Omega$  denote the area covered by the vine rows. We devise our model in such a way that for all  $t > 0$  and  $x \in \Omega$ ,  $N(x, t)$  equals 0 if  $x \notin \Omega_r$ .

The powdery mildew epidemic has no impact upon the growth of the host. This growth brings new sites available for colonization. We study the epidemic during one single season; then we assume that the time variation of the total number of colony sites inside the rows obeys a logistic law

$$\frac{\partial N}{\partial t}(x, t) = r N(x, t) \left( 1 - \frac{N(x, t)}{K} \right), \text{ for } x \in \Omega_r, \quad (2.4)$$

where  $r > 0$  is the growth rate and  $K > 0$  the carrying capacity. Although  $r$  and  $K$  are constant for simplicity, we could introduce spatial heterogeneities for the host growth assuming  $r$  and  $K$  depend on  $x$ . Provided  $r, K$  are bounded, our results can be easily extended to handle this.

Next, the local evolution of the disease at some point  $x \in \Omega_r$  (inside a row) obeys the classical SEIR model, whereas we set  $N(x, t) = L(x, t) = I(x, t) = R(x, t) = 0$  for  $t \geq 0$  if  $x \notin \Omega_r$ . Let  $p$  and  $i$  denote the mean duration of the latency and infectious period respectively. Let  $E$  be the inoculum effectiveness (probability for the spores to

succeed in creating a new colony upon a site). Taking into account (2.4), this yields the second set of equations of our model for  $x \in \Omega_r$ :

$$\begin{cases} \frac{\partial H}{\partial t}(x, t) = -E(\delta_1 S_1(x, t) + \delta_2 S_2(x, t)) \frac{H(x, t)}{N(x, t)} + rN(x, t) \left(1 - \frac{N(x, t)}{K}\right) \\ \frac{\partial L}{\partial t}(x, t) = +E(\delta_1 S_1(x, t) + \delta_2 S_2(x, t)) \frac{H(x, t)}{N(x, t)} - \frac{1}{p}L(x, t) \\ \frac{\partial I}{\partial t}(x, t) = +\frac{1}{p}L(x, t) - \frac{1}{i}I(x, t) \\ \frac{\partial R}{\partial t}(x, t) = +\frac{1}{i}I(x, t) \end{cases} \quad (2.5)$$

supplemented with nonnegative initial conditions

$$\begin{aligned} H(x, 0) = H^0(x) \geq 0, \quad L(x, 0) = L^0(x) \geq 0, \\ I(x, 0) = I^0(x) \geq 0, \quad R(x, 0) = R^0(x) \geq 0 \text{ for } x \in \Omega_r \end{aligned} \quad (2.6)$$

The contact term in (2.5) is based upon a proportionate mixing assumption. Though our model includes host growth, this assumption is in agreement with the underlying hypothesis of classical epidemiologic models in phytopathology (see Vanderplank [12]) that states that the rate of increase of diseased tissue is proportional to the amount of spores multiplied by the probability that these spores fall upon healthy tissues. A similar approach for including host growth in a model of phytopathology but with nonspatial delay equations can be found in [2].

## 2.3 Theoretical Results

We have the following existence result for our model.

**Theorem 1** *The system (2.1),(2.5) is well posed: let  $H^0, L^0, I^0, R^0$  be in  $L^\infty(\Omega)$  and  $S_1^0, S_2^0$  be in  $L^2(\Omega)$ ; the system possesses a unique componentwise nonnegative solution that exists globally in time.*

The proof of this theorem follows standard arguments (see, e.g., [7]) and will not be detailed here.

The large time behavior of the solutions can be described as follows.

**Theorem 2** *If the hypothesis of the previous existence theorem is satisfied, then as  $t$  goes to infinity,  $S_1(x, t)$  and  $S_2(x, t)$  converge to 0 in the  $L^2(\Omega)$  and  $H_0^1(\Omega)$  norms. And there are nonnegative functions  $H_\infty$  and  $R_\infty$  such that for all  $x \in \Omega_r$ ,  $H^\infty(x) + R^\infty(x) = K$  and*

$$\begin{aligned} \lim_{t \rightarrow +\infty} H(x, t) &= H_\infty(x) \\ \lim_{t \rightarrow +\infty} L(x, t) &= \lim_{t \rightarrow +\infty} I(x, t) = 0 \\ \lim_{t \rightarrow +\infty} R(x, t) &= R_\infty(x). \end{aligned}$$

This result must be carefully interpreted since our model is valid for only one single season. It means that the epidemic finally dies out at the end of the season when the growth of the host is achieved.

*Proof* It is easy to show that for all  $x, t, N, H, L, I, R$  are nonnegative and bounded by  $K$ .

As  $\partial N/\partial t = rN(1 - N/K)$  we have  $\lim_{t \rightarrow +\infty} N(x, t) = K$ .

From (2.5) we have  $\partial R/\partial t = (1/i)I \geq 0$ , hence for all  $x, R(x, t)$  converges to some limit  $R_\infty(x)$  as  $t$  goes to infinity. Moreover,  $I(x, t) \in L^1(0, +\infty)$  for all  $x$ .

Next, as  $\partial I/\partial t = +(1/p)L - (1/i)I$ , we also have  $\partial I(x, t)/\partial t \in L^\infty(0, +\infty)$  for all  $x$ . This classically proves that for all  $x, \lim_{t \rightarrow +\infty} I(x, t) = 0$ .

By integrating over  $\Omega$  the last two equations in (2.5), we similarly prove that  $\lim_{t \rightarrow +\infty} \int_\Omega I(x, t) = 0$ . And as  $I(t, x)$  is bounded by  $K$  uniformly in  $x, t$ , for any integer  $p \geq 1$ , we also have  $\lim_{t \rightarrow +\infty} \int_\Omega I^p(x, t) = 0$ .

Let  $|\cdot|_2$  denote the  $L^2(\Omega)$  norm. Multiplying the first equation in system (2.1) by  $S_1$ , integrating over  $\Omega$  and using Young's inequality, we find

$$\frac{d|S_1|_2^2}{dt} + D_1|\nabla S_1|_2^2 + \frac{1}{2}\delta_1|S_1|_2^2 \leq c|I|^2,$$

where  $c$  is some constant.

Since  $\lim_{t \rightarrow +\infty} \int_\Omega I^2(x, t) = 0$  and  $\delta_1 > 0$ , it can be proven easily that  $\lim_{t \rightarrow +\infty} |S_1|_2(t) = 0$ . Similarly, by multiplying the first equation in system (2.1) by  $\nabla^2 S_1$ , we have  $\lim_{t \rightarrow +\infty} |\nabla S_1|_2(t) = 0$  and the same results hold true for  $S_2$ .

Adding the last three equations of (2.5), since  $S_1$  and  $S_2$  are nonnegative,  $D = L + I + R$  is increasing with respect to  $t$  and converges to some limit. We thus find that  $L(x, t)$  converges to some limit  $L_\infty(x)$  as  $t$  goes to infinity. And as  $N = H + L + I + R$  converges to  $K$ ,  $H(x, t)$  converges to some limit  $H_\infty(x)$  as well.

It remains to prove that  $L_\infty(x) = 0$ . Since  $rN(1 - N/K) = N'$ , adding the first two equations of (2.5) and integrating with respect to  $t$  yields

$$H(x, t) + L(x, t) + \frac{1}{p} \int_0^t L(x, s) ds + N(x, 0) = H(x, 0) + L(x, 0) + N(x, t).$$

Hence,  $L(x, t) \in L^1(0, +\infty)$  for all  $x$ , hence for all  $x, L_\infty(x) = 0$ .  $\square$

We also give a threshold condition for successful establishment of the disease but only in the nonspatial case. We thus investigate the linear stability of the nontrivial equilibrium point  $(S_1, S_2, H, L, I, R) = (0, 0, K, 0, 0, 0)$  of the set of differential equations (2.1) (with  $\nabla \cdot (D_i \nabla S_i(x, t)) = 0$ ) coupled with equations (2.5).

From the Routh–Hurwitz criterion, we find the following basic reproductive rate of the disease:  $R_0 = Er_p i$ , and the threshold condition is  $R_0 > 1$ .

The biological interpretation is straightforward.  $R_0$  equals the number of spores  $r_p$  produced by a single colony during the duration of the infectious period  $i$  multiplied by the probability that these spores succeed in creating a new colony.

## 2.4 Numerical Experiments

An example of field data is available (Calonnec et al., personal communication) of a powdery mildew epidemic over a 5-row vineyard. It shows that without fungicide treatment the disease invades the entire vineyard within 3 months. We make a simulation of this particular vineyard. Each row is 66 m long and 0.5 m wide, and the distance between two rows is 1.5 m.

We choose a rectangular computing domain  $\Omega$  such that the 5 rows are located at the center of the domain and  $\Omega$  is 3 times larger than the vineyard. As mentioned before, by doing so, the Dirichlet conditions at the boundary of  $\Omega$  describe the fact that the spores may freely disperse out of  $\Omega$ .

The parameters of the model as well as roughly realistic values are listed in Table 2.1. With these parameters, the basic reproductive rate of the disease in the homogeneous case is  $R_0 = 10$ . We now explain how the values of the dispersal parameters  $\delta_a = \delta_2$  and  $D_i$  were estimated.

All spores lifted up in the atmosphere fall within half an hour so the deposition rates  $\delta$  are more or less equal to  $50 \text{ day}^{-1}$ .

To estimate the diffusion coefficients  $D_1$  and  $D_2$ , we focus on the spore dispersal mechanism alone. Let  $D$  be a diffusion coefficient and  $\delta$  a deposition rate; the density  $S$  of spores dispersed in the atmosphere and produced by a single source obeys the following equation:

$$\begin{cases} \frac{\partial S}{\partial t}(x, t) = \nabla \cdot (D \nabla S(x, t)) - \delta S(x, t), & \forall (x, t) \in \mathbb{R}^2 \times \mathbb{R}^+ \\ S(x, 0) = \text{Dirac}(x), & \forall x \in \mathbb{R}^2 \end{cases},$$

where  $\text{Dirac}(x)$  is the Dirac function. Then the total amount of fallen spores upon the vineyard at some point  $x \in \mathbb{R}^2$  is

$$d(x) = \int_0^{+\infty} \delta S(x, t) dt,$$

where  $d(x)$  is the the probability density of fallen spores. It can be explicitly computed and its variance is  $\sigma = \sqrt{D/\delta}$ . The values of  $D_1$  and  $D_2$  in Table 2.1 have been chosen so that  $\sigma = 1$  m for the short range dispersal, and  $\sigma = 20$  m for the long range dispersal.

We start the infection at  $t = 0$  with one latent colony at the center of the vineyard over one vine stock. For simplicity, we take an initial uniform site density for all the vine stocks. Hence, the initial conditions are  $H^0(x) = 4 \text{ m}^{-2}$  colony sites and  $L^0(x) = I^0(x) = R^0(x) = 0$  for  $x$  in the rows except for  $x \in [-1/4; 1/4]^2$  where  $H^0(x) = I^0(x) = R^0(x) = 0$  and  $L^0(x) = 4 \text{ m}^{-2}$  colony site density. We also set  $S_1^0(x) = S_2^0(x) = 0$  for all  $x$ .

The duration of the simulation is 90 days.

Results of the simulation for these parameters are displayed on Fig. 2.1–2.5. They show the proportion of diseased colony sites with respect to spatial location  $P(x) = D(x)/N(x) = (L(x) + I(x) + R(x))/N(x)$  30, 60 and 90 days after the beginning of the infection (Fig. 2.1–2.3). The epidemic first invades the central row of

**Table 2.1.** Model parameters.

Parameter	Description	Value
$\delta_1$	short range deposition rate	50 day <sup>-1</sup>
$\delta_2$	long range deposition rate	50 day <sup>-1</sup>
$D_1$	short range diffusion coefficient	50 m <sup>2</sup> day <sup>-1</sup>
$D_2$	long range diffusion coefficient	20,000 m <sup>2</sup> day <sup>-1</sup>
$r_p$	spore production	10 <sup>4</sup> spores day <sup>-1</sup> colony site <sup>-1</sup>
$F$	short range vs. long range dispersion	0.8
$E$	inoculum effectiveness	0.1%
$p$	latency period duration	10 days
$i$	infectious period duration	10 days
$K$	carrying capacity of the colony sites	40 m <sup>-2</sup> colony sites
$r$	growth rate of the colony sites	0.1 day <sup>-1</sup>

the vineyard (day 30) then it reaches the other rows until almost all the vineyard has been contaminated at day 90.

We also display the short and long range spore density with respect to the spatial location at day 90 in Fig. 2.4 and 2.5. Short range spores mostly stay over the row where they are produced whereas the distribution of long range spores is more uniform. The lower spore density in the central row is due to the fact that the corresponding colonies have attained the postsporulating phase.

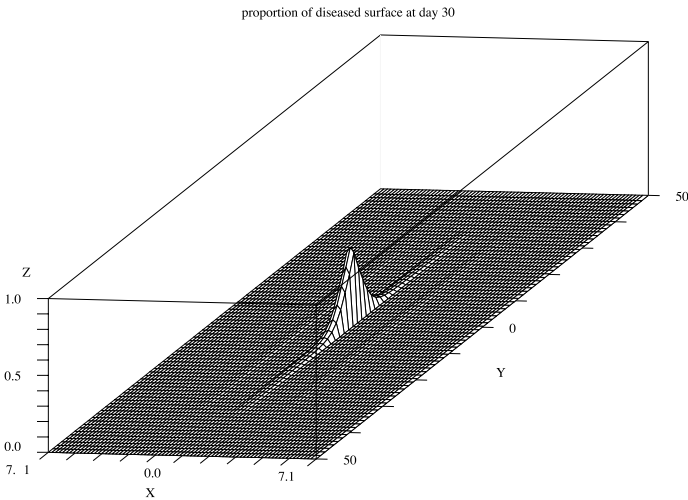


**Fig. 2.1.** Proportion of diseased colony sites in the vineyard at day 30.

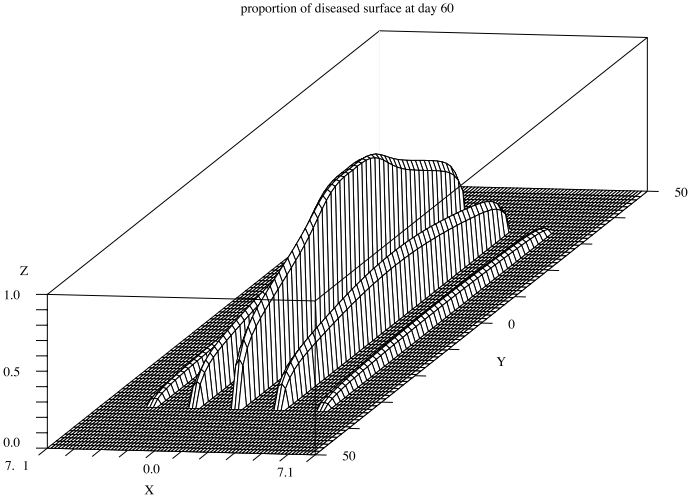


**Fig. 2.2.** Proportion of diseased colony sites in the vineyard at day 60.

Finally, we investigate the influence of the parameter  $F$  over the intensity of the epidemic, keeping other parameters of the simulation at the same values as above. If  $F = 0$  only long range dispersion takes place. The proportion of diseased colony sites is displayed in Fig. 2.6 at day 90. Compared with Fig. 2.3, the disease intensity is very low in each row. If  $F = 1$  only short range dispersion takes place. As shown in Fig. 2.7, the epidemic has attained its maximum intensity but only in the main part of the central row whereas the other rows have not been contaminated.

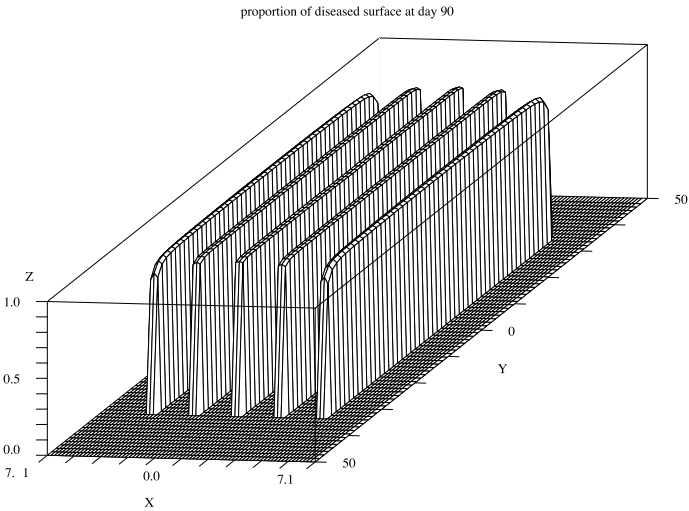


**Fig. 2.3.** Proportion of diseased colony sites in the vineyard at day 90.

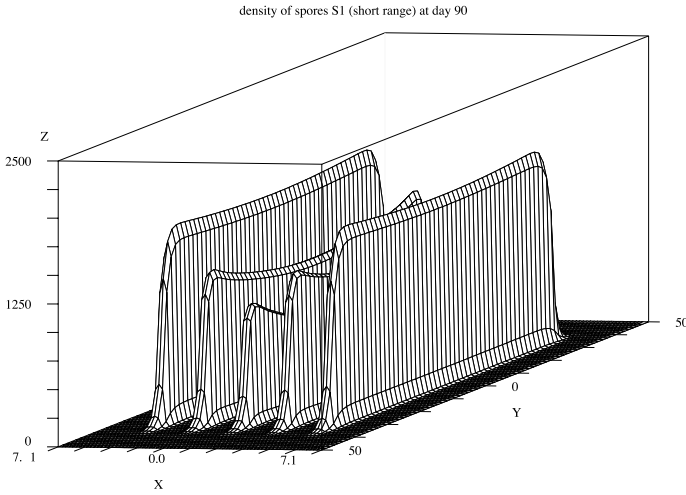


**Fig. 2.4.** Density  $S_1$  of short range dispersal spores over the vineyard at day 90.

As pointed out in [11, 13], the rate of expansion of the epidemic needs both short and long range dispersal of its vectors to reach an optimal value. This is even more evident in the case of separate rows of vine: without long distance dispersal, the disease hardly reaches the rows where the initial contamination did not take place, while without short distance dispersal, local extension of the disease is not strong enough to ensure a high level of contamination.

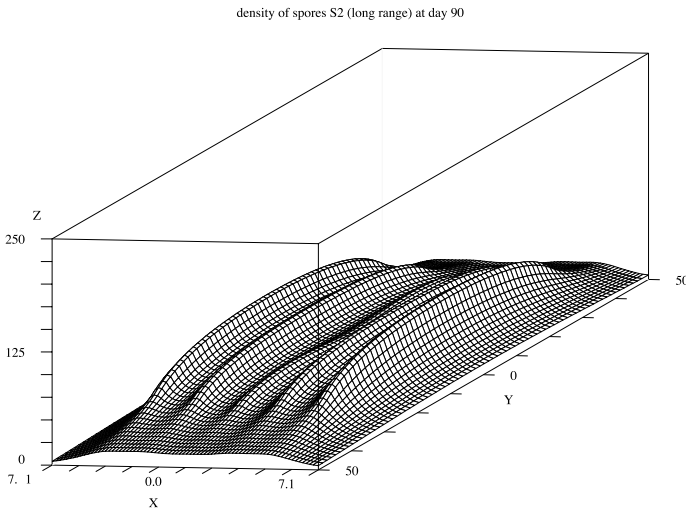


**Fig. 2.5.** Density  $S_2$  of long range dispersal spores over the vineyard at day 90.

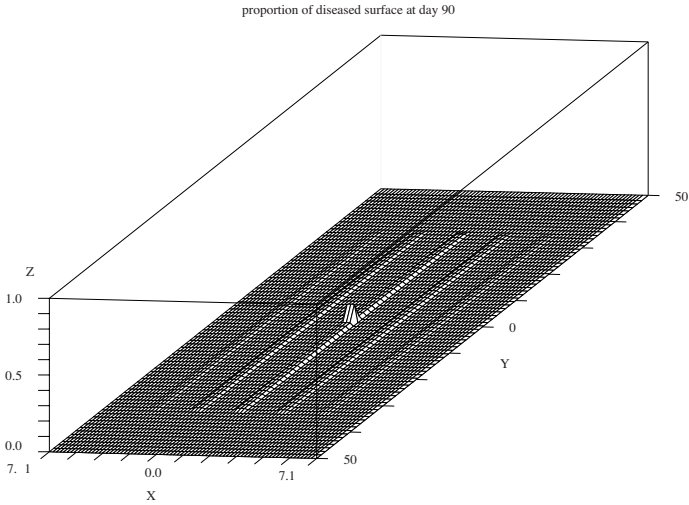


Fig. 2.6. Proportion of diseased colony sites at day 90—long range dispersal only.

## 2.5 Conclusion

We have designed a mathematical model for a fungal disease of the vine. It takes into account the host growth occurring during the epidemic and a dual dispersal mechanism of the spores together with the spatial organization in rows of vine of the vineyards.

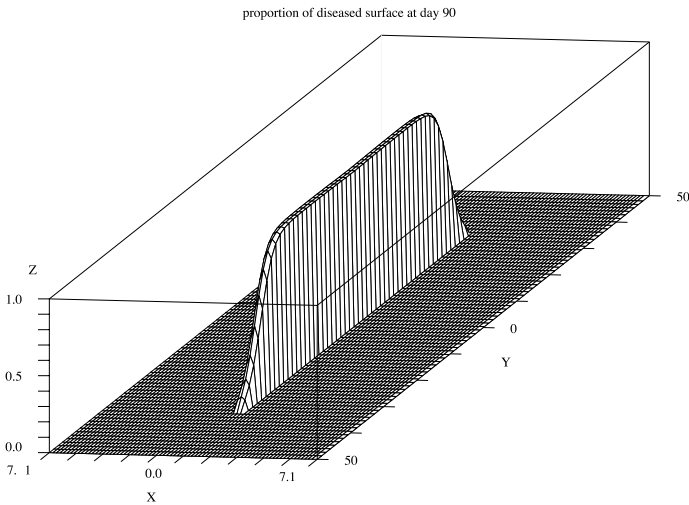


Fig. 2.7. Proportion of diseased colony sites at day 90—short range dispersal only.



We were able to give an existence result for the solutions of the model, a description of the long time behavior of the solutions and a threshold theorem in the homogeneous case.

Numerical simulations show how short and long range dispersal interact with the row structure of the vineyard to allow the epidemic to reach an optimal rate of infection.

In future work, we plan to investigate the existence of traveling waves for this kind of model and, if they exist, to find how the different parameters of the model influence the speed of these waves. We also plan to design a more mechanistic and biologically realistic description of the dispersal mechanism which would allow us to compare our results with the field data available and perform a parameter identification

## References

1. Bailey, N. T. J.: *The Mathematical Theory of Infectious Disease and Its Applications*. Second edition, Hafner Press, New York (1975).
2. Blaise, P., Gessler, C.: An extended Progeny Parent Ratio Model. 1. Theoretical Development, *Journal of Phytopathology—Phytopathologische Zeitschrift*, **134**, 39–52 (1992).
3. Brauer, F., Castillo-Chavez, C.: *Mathematical Models in Population Biology and Epidemiology*, Texts in Applied Mathematics 40. Springer-Verlag, Berlin, Heidelberg, New York (2001).
4. Calonnec, A., Cartolarao, P., Deliere, L., Chadoeuf, J.: Powdery mildew on grapevine: the date of primary contamination affects disease development on leaves and damage on grape. *IOBC/wbrs Bulletin*, **29**(11), 67–73 (2006).
5. Calonnec, A., Latu, G., Naulin, J., Roman, J., Tessier, G.: Parallel Simulation of the Propagation of Powdery Mildew in a Vineyard. *Proceedings of Euro-Par 2005, Lecture Notes in Computer Science*, **3648**, 1254–1264 (2005).
6. Clark, J. S., Fastie, C., Hurr, G., et al.: Reid's paradox of rapid plant migration. *Bioscience*, **48**, 13–24 (1998).
7. Henry, D.: *Geometric Theory of Semilinear Parabolic Equations*, Lecture Notes in Mathematics 840. Springer-Verlag, Berlin, Heidelberg, New York (1981).
8. Peyrard, N., Calonnec, A., Bonnot, F., Chadoeuf, J.: Explorer un jeu de données sur grille par tests de permutation. *Revue Statistique Appliquée*, **LIII**, 59–78 (2005).
9. Segarra, J., Seger, M. J., van den Bosch, F.: Epidemic dynamics and patterns of plant diseases. *Phytopathology*, **91**, 1001–1010 (2001).
10. Shigesada, N., Kawasaki, K.: *Biological Invasions: Theory and Practice*. Oxford Series on Ecology and Evolution. Oxford University Press, Oxford (1997).
11. Shigesada, N., Kawasaki, K.: Invasion and the range expansion of species: effects of long-distance dispersal. In: Bullock, J., Kenward, R., Hails, R. (eds) *Dispersal Ecology*, 350–373, Blackwell Science, Malden, MA (2002).
12. Vanderplank, J. E.: *Plant Diseases: Epidemics and Control*. Academic Press, New York (1963).
13. Zawolek, M. W., Zadoks, J. C.: Studies in focus development: an optimum for the dual dispersal of plant pathogens. *Phytopathology*, **82**, 1288–1297 (1992).

# An Algorithm for Parameter Estimation in Nosocomial Infections

Nico Stollenwerk<sup>1</sup> and Rafael Mikolajczyk<sup>2</sup>

<sup>1</sup> Centro de Matemática da Universidade do Porto, Departamento de Matemática Pura, Porto, Portugal and Gulbenkian Institute of Science, Theoretical Epidemiology Group, Oeiras, Portugal; nks22@cam.ac.uk

<sup>2</sup> Department of Public Health Medicine, School of Public Health, University of Bielefeld, Bielefeld, Germany; rmikolajczyk@uni-bielefeld.de

**Summary.** Parameter estimation in nosocomial infections poses specific problems for estimation techniques. The mathematical description of the spread of nosocomial infections incorporates transmission as a dynamic part; the outcome is discrete and the amount of available information is usually small. We transfer an estimation technique developed previously for plant epidemics to nosocomial infections and demonstrate its application to a data set related to methicillin-resistant *Staphylococcus aureus*.

**Key words:** Nosocomial infections, parameter estimation, eta-ball ( $\eta$ -ball) method.

## 3.1 Introduction

Estimation of parameters with dynamic dependency between variables in stochastic processes is lacking standard established techniques. In many cases analytic expressions for the likelihood can only be obtained under crude simplifying and hence unrealistic assumptions. In other cases analytic expressions cannot be obtained at all. A technique based on minimizing the Euclidian distances between observations and multiple simulations was described for plant epidemics and animal infections [1, 2]. The transmission processes of infections within hospitals is another field for a possible application of this methodology.

There is an increasing interest in the epidemiology of pathogens that are resistant against antibiotics and their spread in hospitals [3–7]. Mathematical modelling was used for the estimation of the importance of different transmission routes relative to each other and for the estimation of the impact of different interventions on the spread of the infection [8–10].

We obtained clinical data on methicillin-resistant *Staphylococcus aureus* (MRSA), which is one of the most important multiresistant pathogens [11, 12]. We use the data for a demonstration of the application of the estimation algorithm to nosocomial transmission data and seek to estimate the prevalence of MRSA in the patient population at admission and the transmission probability within the hospital.

In an intensive care unit the number of patients with MRSA per week was recorded over a period of 40 weeks. During this period at most seven patients with MRSA were observed at a time. We develop a master equation for a stochastic transmission model for MRSA within this intensive care unit. We use this equation for the generation of random realizations of the transmission model. The fit between simulations and observations is measured with the  $\eta$ -ball method described in the next section. The log likelihood function is used to identify best fit values and their confidence intervals.

We seek to estimate two parameters of the transmission model: the baseline prevalence of MRSA in patients at admission fraction  $\rho$  and the transmission rate  $\beta$ . In separate estimations of each parameter with the other being fixed, clear log likelihood maxima within the considered parameter interval could be seen, but in a joint estimation the transmission parameter approached the low boundary of zero. Given this result, the observed aggregation of MRSA cases in the intensive care unit could be explained by a random fluctuation in the admission process solely. This counterintuitive result may be easily explained by the omission of previous periods of observation where no outbreaks were recorded, but these data were not available. We use the data solely for the presentation of the potential usability of the  $\eta$ -ball method and we do not claim any substantial interpretation of the results.

### 3.2 Parameter Estimation with the $\eta$ -Ball Method

In a previously considered epidemiological problem several data sets were given (Fig. 3.1 a) which were compared to simulations from a suitable model with three model parameters (Fig. 3.1 b) [1].

A likelihood function estimator was evaluated numerically (Fig. 3.2) by comparing how many simulation trajectories fall into an  $\eta$ -neighborhood (of Euclidian distance, hence  $\eta$ -ball) of the data when varying model parameters, here fixing two parameters and varying one. The curve shows the results for various  $\eta$ -values. The results compare well with analytic results obtained from that model for the likelihood based on the evaluation of a matrix exponential function [1].

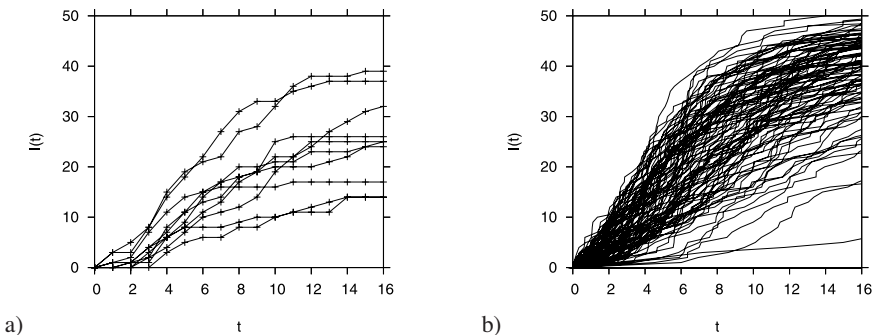


**Fig. 3.1.** a) Data for a previously considered system with three parameters. b) Simulations for a previously considered system with three parameters.

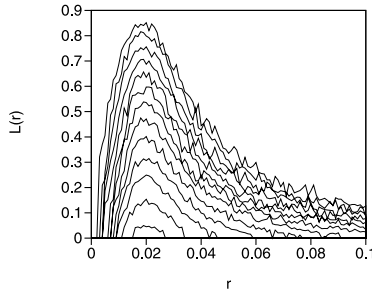


**Fig. 3.2.** Empirical likelihood curves for the parameter  $r$  for various values of  $\eta$ -neighborhoods. The maximum does not change much with varying  $\eta$ , showing that the estimate for the parameter is rather robust.

Varying two parameters simultaneously (Fig. 3.3) shows typical features of a non-linear parameter estimation problem: The maximum does not have just an ellipsoid shape as in typical multivariate Gaussian estimations, but around the maximum there is a curved region with a rather shallow decline.

In similar data sets from the above-mentioned plant scientific experiments we sometimes found a maximum for either unrealistically large values of one parameter or an unrealistically high value of the other parameter, when adding or subtracting a single data point to/from the estimation.

We will now apply the  $\eta$ -ball method to observations regarding records of colonization with a methicillin-resistant *Staphylococcus aureus* in an intensive care unit (ICU), using a suitable stochastic model.

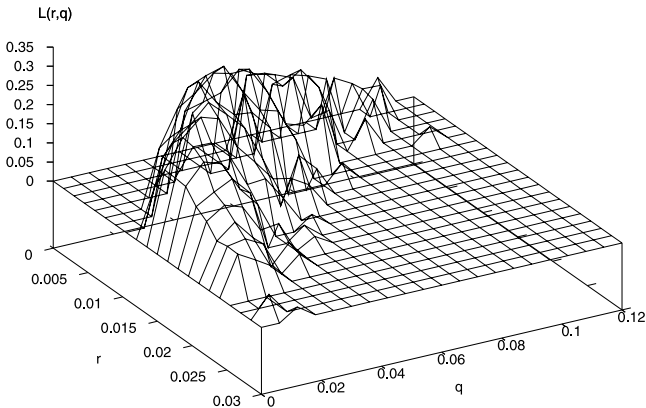


**Fig. 3.3.** Parameter estimation for two parameters in a previously considered model.

### 3.3 Methicillin-Resistant *Staphylococcus aureus*

MRSA is a common name for several strains of *Staphylococcus aureus*, which developed a resistance against methicillin and usually some other antibiotics [13]. Several phenotypes and, among them, genotypes with several clones exist [14], but new MRSA cases are unlikely to result from the development of the resistance de novo [15]. Although an increased incidence of community acquired MRSA has been observed in some places [16, 17], at present MRSA is mainly a hospital transmitted infection [18]. In patients with compromised immunity the colonization can be fairly persistent and therefore MRSA can be reintroduced to hospitals by these patients. Within hospitals, because of the selection advantage in comparison with nonresistant strains and several medical interventions which increase the risk of MRSA acquisition, transmission can occur, depending on the level of precautions taken.

The number of MRSA cases detected with screening of all patients in an ICU with 14 beds during a period of 40 weeks was recorded [12]. There was no screening at admission to this ward and therefore the prevalence at admission has to be estimated from the data. During the stationary stay, no treatment for MRSA was offered and standard hygienic procedures were used. Although transmissions in the ICU most often occur indirectly via the hands of the medical staff instead of a direct patient-to-patient transmission, we use a single parameter for the description of the transmission process. The data are shown in Fig. 3.4. The formal model is described in the following sections.

### 3.4 Parameter Estimation for MRSA Using the SIB-Model

To describe the spreading of MRSA in a hospital we model the epidemiology by what we call an SIB-model, explained in the next subsection. Running many simulations with the stochastic version of the SIB-model we are able to perform parameter estimation with the  $\eta$ -ball method as previously described. Finally, we can perform a joint estimation of both parameters.

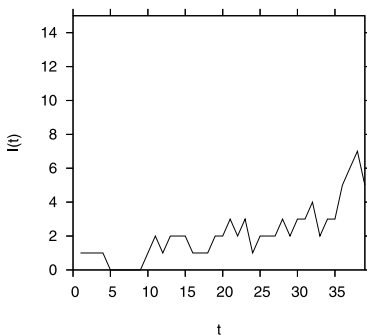


**Fig. 3.4.** Data from an intensive care unit in a hospital in Bielefeld over 40 weeks. Note that these data are recorded weekly whereas the simulation data are on a continuous scale due to the Gillespie algorithm. The time unit is one week.

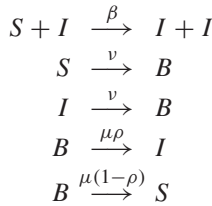
### 3.4.1 Epidemic Model: SIB

With  $N$  denoting the total number of beds in a hospital station, of which  $S$  denotes beds with susceptible patients,  $I$  those infected with MRSA, and  $B$  the number of empty beds, such that  $S + I + B = N$  at all times, the dynamic variables are  $S, I, B$ . An ordinary differential equation (ODE) model for the system would be

$$\begin{aligned} \frac{dS}{dt} &= -\beta \frac{I}{N} S + \mu(1 - \rho)B - \nu S \\ \frac{dI}{dt} &= \beta \frac{I}{N} S + \mu\rho B - \nu I \\ \frac{dB}{dt} &= -\mu B + \nu(S + I), \end{aligned} \tag{3.1}$$

where the transitions are explicitly given as follows:  $\beta(I/N)S$  is the infection of susceptible patients with MRSA through contact with infected patients.  $\nu S$  are the susceptible patients who are discharged from hospital, and  $\nu I$  the MRSA-infected patients who are released from hospital, such that  $\nu(S + I)$  beds become free again. Free beds can be filled with  $\mu B$ , from which a proportion of  $\rho$  patients already have the MRSA, hence  $\mu\rho B$  new infected patients come from the outside of the hospital into the hospital station under investigation, whereas  $\mu(1 - \rho)B$  new patients coming into the hospital are uninfected with MRSA.

The reaction scheme for transitions is given by



and can be translated into a stochastic model as shown below.

### 3.4.2 Stochastic Modelling

We include demographic stochasticity into the description of the epidemic. For the basic SIB-model we consider the dynamics of the probability  $p(S, I, B, t)$  of the system to have  $S$  susceptibles,  $I$  infected, and  $B$  empty beds at time  $t$ , which is governed by a master equation [19,20].

For state vectors  $\underline{n}$ , here for the SIB-model we have  $\underline{n} = (S, I, B)$ , and the master equation reads

$$\frac{dp(\underline{n})}{dt} = \sum_{\tilde{\underline{n}} \neq \underline{n}} w_{\underline{n}, \tilde{\underline{n}}} p(\tilde{\underline{n}}) - \sum_{\tilde{\underline{n}} \neq \underline{n}} w_{\tilde{\underline{n}}, \underline{n}} p(\underline{n}) \tag{3.2}$$

with transition probabilities corresponding to the ones described above for the ODE system. Here the rates  $w_{\underline{n},\underline{n}}$  are

$$\begin{aligned}
 w_{(S-1,I+1,B),(S,I,B)} &= \beta \frac{I}{N} S \\
 w_{(S-1,I,B+1),(S,I,B)} &= \nu S \\
 w_{(S,I-1,B+1),(S,I,B)} &= \nu I \\
 w_{(S,I+1,B-1),(S,I,B)} &= \mu \rho B \\
 w_{(S+1,I,B-1),(S,I,B)} &= \mu(1-\rho)B
 \end{aligned} \tag{3.3}$$

from which the rates  $w_{\underline{n},\underline{n}}$  follow immediately as

$$\begin{aligned}
 w_{(S,I,B),(S+1,I-1,B)} &= \beta \frac{I-1}{N} (S+1) \\
 w_{(S,I,B),(S+1,I,B-1)} &= \nu(S+1) \\
 w_{(S,I,B),(S,I+1,B-1)} &= \nu(I+1) \\
 w_{(S,I,B),(S,I-1,B+1)} &= \mu \rho (B+1) \\
 w_{(S,I,B),(S-1,I,B+1)} &= \mu(1-\rho)(B+1) \quad .
 \end{aligned} \tag{3.4}$$

This formulation defines the stochastic process completely.

Initial parameter values (as rough guesses given by experienced medical personnel) for the simulations are as follows.  $\nu := (1/1.5)$  per week, since patients stay on average 10 days in the station.  $\mu := (1/0.2)$ , since beds stay empty on average for one-fifth of a week, between one and two days.  $\rho := 0.02$ , since 2% of the incoming patients are already infected with MRSA.  $\beta := 0.5$  can only be guessed to obtain a realistic number of infected during the simulation period of 52 weeks. In the simulations a transient of several weeks was discarded before data were sampled, to obtain stationary values for  $S$  and  $B$ . This was achieved to a great extent, as can be seen in Fig. 3.5.

Simulations were performed with the Gillespie algorithm [21–23], essentially using exponential waiting times between events, where events are transitions into other states.

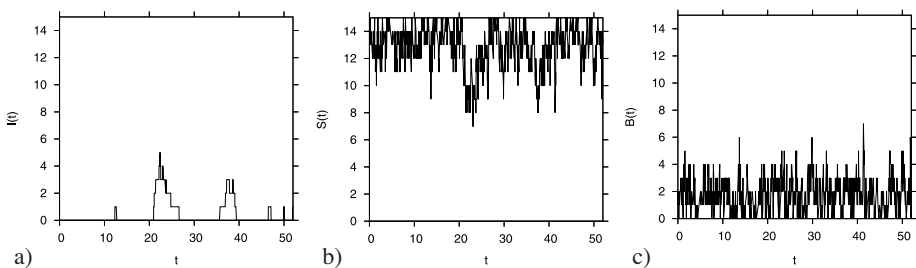


**Fig. 3.5.** a) Weekly number of MRSA-infected in a simulation of length one year, b) weekly number of susceptibles, and c) weekly number of free beds on the hospital station under simulation.

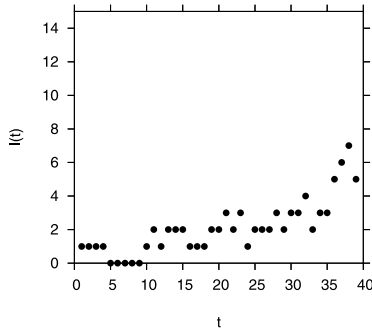


Fig. 3.6. Data for 40 weeks of observation.

### 3.4.3 Comparing Data and Simulations

We now apply the  $\eta$ -ball method to the MRSA data set described above. As a first step we compare the data (Fig. 3.6) with many simulations (Fig. 3.7) for one set of parameters.

Looking at time steps, e.g.,  $t_1 = 35$ , the 35th week, and  $t_2 = 36$ , with  $I(t_1) = 3$  and  $I(t_2) = 5$ , shows the data set  $a = s$  (the full dot) surrounded by the cloud of simulations (Fig. 3.8). The simulation cloud is essentially an estimation of the joint probability at the two consecutive time steps.

For a full parameter estimation we have to obtain the joint probability estimate for all 40 time steps, and compare it with the data set, and then vary the parameters under investigation. As a measure of proximity we use the Euclidian distance between the data point and simulation points in the 40 dimensional space defined by 40 time steps for the data. The number of simulation points in a neighborhood with radius  $\eta$  is counted. This is the basis for the term “ $\eta$ -ball method.”

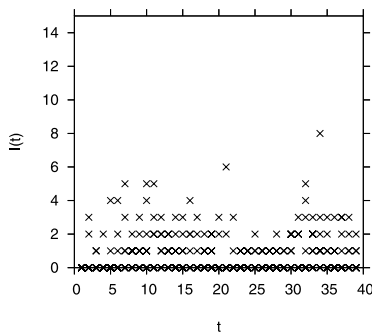
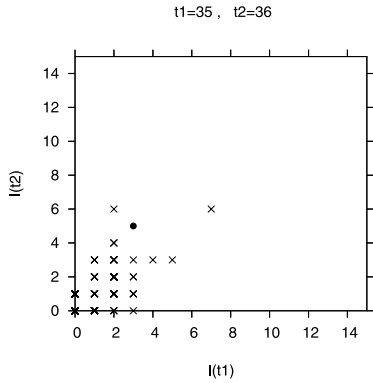


Fig. 3.7. 10 simulations, sampled at the same time points as the observed data.





**Fig. 3.8.** Data (full dot) compared with 200 simulations (crosses). The simulations with the initial parameters can describe the data well at these two time slices, since the data dot is surrounded by some simulation crosses.

### 3.4.4 Measuring $\eta$ -Ball Distances

The number of simulation points in an  $\eta$ -ball around the data set in a high-dimensional space gives an estimation of the quality of the parameter set used. An appropriate  $\eta$  size has to be chosen from first inspection. In Fig. 3.9 the number of points in the ball of size  $\eta$  around the data set is counted for various values of  $\eta$ , for one set of parameters, here the parameter set of first guess. From this curve we choose a value of  $\eta = 15$  for the variation of parameters that now follows.

### 3.4.5 Variation of $\beta$ and Joint Parameter Estimation

In Fig. 3.10 we present results for parameter estimation where one parameter was fixed at a specified value and the other one was estimated using the  $\eta$ -ball method. In the first case  $\beta$  was estimated using the starting value of 0.02 for the prevalence at admission. In the second case the result from the first estimation for  $\beta$  (0.8) was used as a fixed

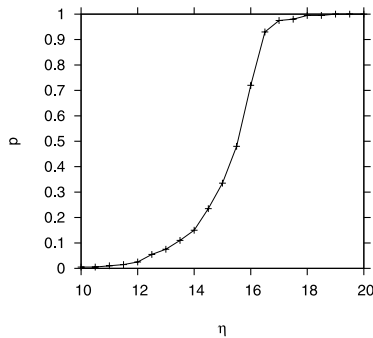


**Fig. 3.9.** Ratio of points inside the  $\eta$ -ball as function of  $\eta$ . 200 simulations are used.

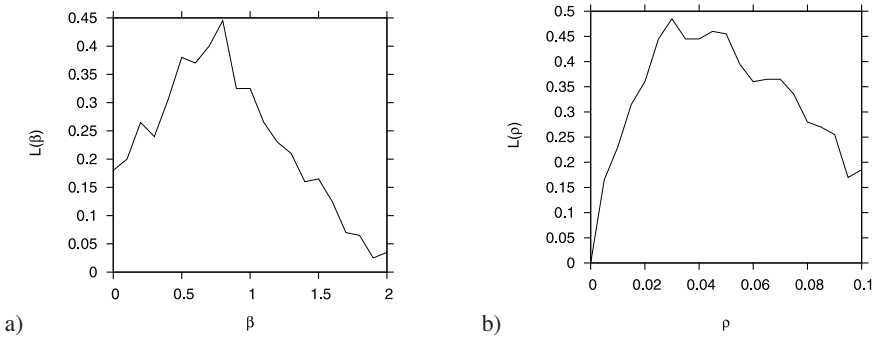


**Fig. 3.10.** a) Variation of  $\beta$  with fixed  $\rho = 0.02$ ,  $\eta = 15$ . 200 simulations for each  $\beta$ -value were used. The maximum is reached at  $\beta = 0.8$ . b) Variation of  $\rho$  with fixed  $\beta = 0.8$ ,  $\eta = 15$ . 200 simulations for each  $\rho$ -value were used.

parameter value. The location of the maximum at about 0.03 was slightly higher than the starting parameter of 0.02. Both estimations lead to a clear maximum for a middle range value of the estimated parameter.

In Fig. 3.11 we show the joint estimation of  $\beta$  and  $\rho$ . Very small values of  $\beta$  have a high likelihood of describing the data. We suspect that this result is a consequence of fitting the model to a relatively short chain of data. The noise on the estimates is quite high due to the relatively small number of simulations used for comparison with the sparse data.

The contour plot Fig. 3.11 shows the typical features of nonlinear parameter estimation: There is a curved maximal region, which has a high likelihood for small  $\rho$ -values combined with large  $\beta$ -values as well as a high likelihood for large  $\eta$ -values combined with small  $\rho$ -values (see also Fig. 3.3 from the previous study with a pro-

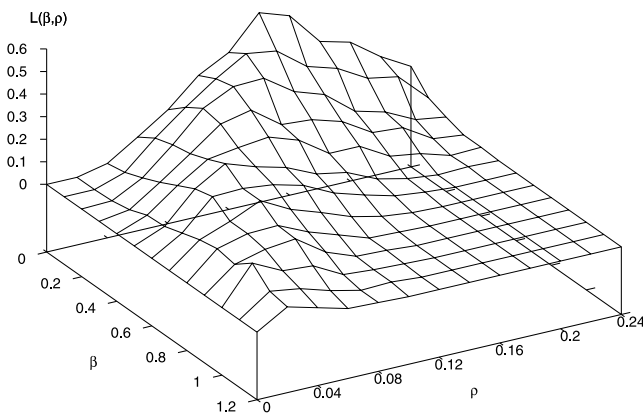


**Fig. 3.11.** Parameter estimation for the MRSA model for two parameters from data obtained at an intensive care station in Bielefeld hospital.

nounced curved maximum area). The experience with the previous plant-scientific problem tells us that the maximum of the likelihood might be very sensitive to a little additional information as a single data point. Confidence intervals around one or the other parameter do not capture this feature well, since the high values of likelihood around the maximum are located on a nonlinear curve in parameter space (see Fig. 3.3). For a rigorous model selection (as, e.g., performed by Stollenwerk, Drepper and Siegel [24]) more data points are definitely needed. Such data sets could be obtained through a longer period of observation.

### 3.5 Summary and Discussion

We have presented a model for the spreading of MRSA in an ICU of a hospital and have estimated the crucial transmission parameters via a numerical simulation method using our model. The maximum of the likelihood was obtained from our present data at zero transmission parameter and a finite import ratio. However, the present data set is very limited and the likelihood sensitive to minor changes, as demonstrated in a previous work. Hence, any substantial findings have to be obtained in future applications of this method to larger data sets.

Recently, evolutionary aspects of pathogen strains have been studied (for MRSA for example see [15]) and can lead to new stochastic effects [25]. In such situations parameter estimation can be performed along the lines described by Jansen et al. [26]. Future research may combine stochastic strain dynamic models with the parameter estimation demonstrated in this paper.

### Acknowledgments

We thank Keith Briggs, Ipswich, Vincent Jansen, London, Alberto Pinto, Porto, and Friedhelm Drepper, Jülich, for many useful discussions on the topics mentioned here. Further, we would like to thank Elio Coutinho, Porto, for computer support during the simulations presented and throughout, and the referees for improving the text.

### References

1. Stollenwerk, N., Briggs, K.M.: Master equation solution of a plant disease model. *Phys. Lett. A*, **274**, 84–91 (2000).
2. Stollenwerk, N.: Parameter estimation in nonlinear systems with dynamic noise. In: Matthies M., Malchow H. & Kriz J. (eds) *Integrative Systems Approaches to Natural and Social Sciences—System Science 2000*. Springer, Berlin Heidelberg New York (2001).
3. Escolano, S., Golmard, S.L. et al.: A multi-state model for evolution of intensive care unit patients: prediction of nosocomial infections and deaths. *Stat. Med.*, **19**, 3465–82 (2000).
4. Meyer, E., Schwab, F. et al.: Temporal changes in bacterial resistance in German intensive care units, 2001–2003: data from the SARI (surveillance of antimicrobial use and antimicrobial resistance in intensive care units) project. *J. Hosp. Infect.*, **60**, 348–52 (2005).

5. Cooper, B.S., Stone, S.P. et al.: Isolation measures in the hospital management of methicillin resistant *Staphylococcus aureus* (MRSA): systematic review of the literature. *BMJ*, **329**, 533 (2004).
6. Farrington, M., Trundle, C. et al.: Effects on nursing workload of different methicillin-resistant *Staphylococcus aureus* (MRSA) control strategies. *J. Hosp. Infect.*, **46**, 118–22 (2000).
7. Cooper, B., Lipsitch, M.: The analysis of hospital infection data using hidden Markov models. *Biostatistics*, **5**, 223–37 (2004).
8. Pelupessy, I., Bonten, M.J. et al.: How to assess the relative importance of different colonization routes of pathogens within hospital settings. *Proc. Natl. Acad. Sci. USA*, **99**, 5601–5. Epub 2002 Apr 9. (2002).
9. Austin, D.J., Anderson, R.M.: Transmission dynamics of epidemic methicillin-resistant *Staphylococcus aureus* and vancomycin-resistant enterococci in England and Wales. *J. Infect. Dis.*, **179**, 883–891 (1999).
10. Lipsitch, M., Bergstrom, C.T. et al.: The epidemiology of antibiotic resistance in hospitals: paradoxes and prescriptions. *Proc. Natl. Acad. Sci. USA*, **97**, 1938–43 (2000).
11. Sagel, U., Mikolajczyk, R.T. et al.: Using mandatory data collection on multiresistant bacteria for internal surveillance in a hospital. *Biom. J.*, **46**, 93 (2004).
12. Sagel, U., Mikolajczyk, R.T. et al.: Using mandatory data collection on multiresistant bacteria for internal surveillance in a hospital. *Methods Inf. Med.*, **43**, 483–485 (2004).
13. Farrington, M., Redpath, C. et al.: Winning the battle but losing the war: methicillin-resistant *Staphylococcus aureus* (MRSA) infection at a teaching hospital. *QJM*, **91**, 539–48 (1998).
14. Grundmann, H., Hori, S. et al.: Determining confidence intervals when measuring genetic diversity and the discriminatory abilities of typing methods for microorganisms. *J. Clin. Microbiol.*, **39**, 4190–2 (2001).
15. Enright, M.C., Robinson, D.A., Randler, G., Feil, E.J., Grundmann, H., Spratt, B.G. The evolutionary history of methicillin-resistant *Staphylococcus aureus* (MRSA), *Proc. Natl. Acad. Sci. USA*, **99**, 7687–7692 (2002).
16. Robinson, D.A., Kearns, A.M. et al.: Re-emergence of early pandemic *Staphylococcus aureus* as a community-acquired methicillin-resistant clone. *Lancet*, **365**, 1256–8 (2005).
17. Cooper, B.S., Medley, G.F. et al.: Methicillin-resistant *Staphylococcus aureus* in hospitals and the community: stealth dynamics and control catastrophes. *Proc. Natl. Acad. Sci. USA*, **101**, 10223–8 (2004).
18. Fridkin, S.K., Hageman, J.C. et al.: Methicillin-resistant *Staphylococcus aureus* disease in three communities. *N. Engl. J. Med.*, **352**, 1436–44 (2005).
19. van Kampen, N.G.: *Stochastic Processes in Physics and Chemistry*. North-Holland, Amsterdam (1992).
20. Gardiner, C.W.: *Handbook of Stochastic Methods*. Springer, Berlin Heidelberg New York (1985).
21. Gillespie, D.T.: A general method for numerically simulating the stochastic time evolution of coupled chemical reactions. *J. Comp. Phys.*, **22**, 403–434 (1976).
22. Gillespie, D.T.: Monte Carlo simulation of random walks with residence time dependent transition probability rates. *J. Comp. Phys.*, **28**, 395–407 (1978).
23. Feistel, R.: Betrachtung der Realisierung stochastischer Prozesse aus automatentheoretischer Sicht. *Wiss. Z. WPU Rostock*, **26**, 663–670 (1977).
24. Stollenwerk, N., Drepper, F., Siegel, H.: Testing nonlinear stochastic models on phytoplankton biomass time series. *Ecological Modelling*, **144**, 261–277 (2001).
25. Stollenwerk, N., Maiden, M.C.J., Jansen, V.A.A.: Diversity in pathogenicity can cause outbreaks of meningococcal disease. *Proc. Natl. Acad. Sci. USA*, **101**, 10229–10234 (2004).

26. Jansen, V.A.A., Stollenwerk, N., Jensen, H.J., Ramsay, M.E., Edmunds, W.J., Rhodes, C.J.: Measles outbreaks in a population with declining vaccine uptake. *Science*, **301**, 804 (2003).

**Evolution and Ecology**

## Evolutionarily Stable Investment in Anti-Predatory Defences and Aposematic Signalling

Mark Broom,<sup>1</sup> Graeme D. Ruxton,<sup>2</sup> and Michael P. Speed<sup>3</sup>

<sup>1</sup> Department of Mathematics, Mantell Building, University of Sussex, Falmer, Brighton, BN1 9RF, UK; M.Broom@sussex.ac.uk

<sup>2</sup> Division of Environmental & Evolutionary Biology, Institute of Biomedical and Life Sciences, Graham Kerr Building, University of Glasgow, Glasgow G12 8QQ, UK; G.Ruxton@bio.gla.ac.uk

<sup>3</sup> School of Biological Sciences, University of Liverpool, Liverpool L69 7ZB, UK; speedm@liverpool.ac.uk

**Summary.** Many species possess defences (such as toxins) against predator attack which cannot be observed by the predator prior to attack, but which it might be beneficial for the predator to avoid. Often, such animals are brightly coloured or have some other way of signalling that they are defended (aposematism). In one of our papers we examined the evolution and maintenance of defence and conspicuousness, the brightness of the defence signal, in such prey species using a game theoretic model. In this chapter we develop the model further and in particular expand on the more theoretical results with examples demonstrating the type of solutions which can occur. We categorise eight possible configurations of solution states for simple solutions. Finally there is another class of solutions possible where there is strong between-individual variation in appearance between conspicuous, poorly defended prey, and we demonstrate one example of this complex solution.

**Key words:** ESS, secondary defence, conspicuousness, aversiveness, coevolution.

### 4.1 Introduction

Prey species possess various types of defence against predators. Some of these defences are highly visible, such as sharp spines or strong legs, indicating fast running speed. Other defences are non-visible, the most prominent example being the possession of dangerous or unpalatable toxins. Some potential prey with non-visible defences seek not to hide from their predators, but rather advertise their anti-predatory defences by bright signals: gaining by deterring attacks, rather than avoiding them through adopting a cryptic appearance; a cryptic individual is one that adopts a colouration or patterning which makes it hard to see. The existence of bright signals of defence (so-called aposematic signals) was seen by Darwin and Wallace as an interesting challenge to evolutionary theory, and remains so to this day (Chapter 8, Ruxton et al. [1]). For algebraic or computational simplicity, most theories on the evolution of such sig-

nals assume that the defence itself is a fixed trait throughout the evolutionary process. This approach is difficult to justify biologically, and so an approach that considers the coevolution of both investment in defences and external appearance of individuals to potential predators is required. Furthermore, the theoretical literature on aposematism has been strongly focussed on how aposematic display could evolve in the first instance, ignoring the broader questions about how conspicuous a display should become, and how much should be invested in costly secondary defences. We shall use the term conspicuousness to mean the brightness of the signal given to the predator. The minimum possible level of conspicuousness will be referred to as crypsis.

In [2] we examined the evolution and maintenance of defence and conspicuousness in prey species using a game theoretic model (see also [3]). An important earlier model [4] considers a group of naive predators who initially attack all individuals, but learn to avoid unpalatable types over time. Our model considers a group of predators in equilibrium (i.e., having fixed proportions of the predatory population at all levels of learning), where individuals can both raise and lower their aversiveness to given appearances (see [5]). We investigated the interaction between defence and conspicuousness in a theoretical way, with general functions, which resulted in a number of predictions and conjectures, but which required some assumptions. In this chapter we adapt the model to make the analysis more tractable and examine some example functions in detail, showing that for these functional forms our predictions hold and providing a much clearer picture of the relationship between solutions and specific parameters. In [2] and in the following sections, we shall use the term toxin to represent non-visible defences, although the results are more widely applicable.

## 4.2 The Original Model

In [2] we considered a single population of prey individuals, where each prey individual  $i$  is described by three parameters  $(t_i, r_i, \theta_i)$ . The parameter  $t_i$  is the toxicity of individual  $i$ , with increasing values indicating increasing toxicity, and  $t_i = 0$  indicating minimal investment in toxicity. The parameter  $r_i$  describes the conspicuousness of individual  $i$ , increasing values of  $r_i$  indicate increasing conspicuousness, with  $r_i = 0$  indicating maximum crypsis. The final parameter  $\theta_i$  also describes the appearance of the individual, but such that changes in  $\theta$  affect the appearance of the individual without affecting its conspicuousness. Thus two prey types can be equal in conspicuousness against the background (have identical  $r$  values) but be very different in appearance from each other (have different  $\theta$  values). We were interested in finding the evolutionarily stable values of  $t_i, r_i, \theta_i$ . The parameters and functions used in the model are summarised in Table 4.1.

We assumed that  $F$  is a decreasing function of  $t$ , as is  $K$  (high toxicity individuals may be released unharmed by a predator which finds them distasteful). There is another way that toxicity can affect survivorship, namely by influencing the probability  $Q(I)$ .  $Q(I)$  declines with the aversiveness of the experiences that the predator has previously had (and subsequently remembered) on attacking similar-looking prey items,  $I$ . Positive values of  $H$  indicate an aversive experience; the higher the toxicity, the



**Table 4.1.** The parameters and functions of the model.

Parameter	Meaning
$t$	the toxicity of an individual
$r$	the level of conspicuousness of an individual
$\theta$	the patterning parameter of an individual
$N$	the size of the prey population
$n$	the size of the predator population
$F(t)$	the fecundity of an individual of toxicity $t$
$K(t)$	the probability that an individual of toxicity $t$ dies in an attack
$H(t)$	the aversiveness of an individual of toxicity $t$
$t_c$	the toxicity for which $H(t_c) = 0$
$D(r)$	the rate at which individuals of conspicuousness $r$ are detected
$L(r)$	the rate at which $r$ -individuals are detected and recalled
$S(x)$	the similarity function of individuals differing in appearance by $x$
$I$	the level of aversive information of an individual
$Q(I)$	the probability that a predator will attack an $I$ -individual
$a$	the average relatedness of individuals in the population
$\lambda$	the rate of death of individuals not due to predation

more positive  $H$  and so the more aversive the experience. If an individual's investment in toxins is low then the experience of attacking it may not be aversive at all, indeed the predator may treat it as a beneficial experience. We described such situations by a negative value of  $H$ .

$D$  (the rate at which an individual is encountered by a predator multiplied by the probability that it is detected when it encounters it) is an increasing function of  $r$ . Note that even maximally cryptic prey have some chance of being detected (i.e.,  $D(0) > 0$ ).  $L$  too is an increasing function of  $r$ . If the predator has perfect recollection of all encounters then  $L = D$ , which is what we shall assume here.

The function  $S(r_i, \theta_i, r_j, \theta_j)$  is a measure of the visual similarity between individuals  $i$  and  $j$ .  $S$  increases as the points  $(r_i, \theta_i)$  and  $(r_j, \theta_j)$  get closer together; in particular in [2] and this chapter we treat  $S$  as a univariate function of the Euclidian distance between the two species.  $S(0)$  is thus the similarity between two identical individuals and is given the maximum value 1. On encountering individual  $i$ , the available information to the predators (scaled by the total number of predators  $n$ ) on the aversiveness of that prey item (denoted  $I_i$ ) was calculated as follows:

$$I_i = \frac{1}{n} \sum_{i \neq j}^N L(r_j) H(t_j) S(r_i, \theta_i, r_j, \theta_j).$$

We assume that any changes in the prey population are mirrored in the predator population, so that the ratio  $N/n$  remains constant. It should be noted that as the pop-

ulations increase, it could be the case that the functions  $D$  and  $L$  increase, so that changing population size may well complicate our analysis. We, rather, envisage a situation where the population has reached an equilibrium size so that such changes do not occur.  $I_i$  is thus the sum over all individuals of the rate at which any given individual is encountered and remembered multiplied by the aversiveness of that individual and a measure of the similarity of that individual to our focal individual.  $I_i$  is larger the more aversive similar-looking individuals to our focal individual are. The payoff to such an individual is

$$P(t_i, r_i, \theta_i) = \frac{F(t_i)}{\lambda + D(r_i)K(t_i)Q(I_i)}.$$

$Q(I)$  is a decreasing function of  $I$ , so that if  $I$  is large and positive there is little chance of the individual being attacked, and if it is large and negative it is almost certain to be attacked. The parameter  $a$  affects the model through the information function  $I_i$  (see below).

We compared the fitness of a small mutant group with values  $(t, r, \theta)$  against that of the majority of the population with values  $(t_1, r_1, \theta_1)$ . The payoff function for such a small group will be written  $P(t, r, \theta; t_1, r_1, \theta_1)$ . The mutant group made up a significant proportion of individuals in their own locality  $a$ , but a negligible proportion of the total population. This gave the information function of the mutant group

$$I = (aL(r)H(t) + (1 - a)L(r_1)H(t_1)S(r, r_1, \theta, \theta_1))N/n$$

and that of the majority as  $L(r_1)H(t_1)N/n$ . The conditions for evolutionarily stable strategies (ESSs), where no such mutant group could invade, were as follows. The population described by  $(t_1, r_1, \theta_1)$  is in equilibrium in the direction of  $t$ , for  $t_1 > 0$ , if

$$\frac{\partial P(t, r, \theta; t_1, r_1, \theta_1)}{\partial t} \Big|_{t=t_1, r=r_1, \theta=\theta_1} = 0. \quad (4.1)$$

(If  $t_1 = 0$  then it is in stable equilibrium if the above expression is negative.) This value  $t_1 > 0$  was stable if the following condition was satisfied:

$$\frac{\partial^2 P(t, r, \theta; t_1, r_1, \theta_1)}{\partial t^2} \Big|_{t=t_1, r=r_1, \theta=\theta_1} < 0. \quad (4.2)$$

It was shown under certain assumptions that this value of  $t$ ,  $t(r)$ , was unique and increased with  $r$ . Thus we had a unique value of  $t$  which was stable given a particular value of  $r$ .

The derivative of the payoff function with respect to  $r$  was shown to be discontinuous at  $r = r_1$ . This meant that any given value of  $r_1$  was in equilibrium if and only if it was stable. Thus for a stable pair, we needed conditions (4.1) and (4.2) met at the same time as the stability condition for  $r$ . For  $r = 0$  the condition was that the right-hand side derivative of  $P(t, r, \theta; t_1, 0, \theta_1)$  with respect to  $r$  at  $r = 0$  is negative. For  $r > 0$  the condition became that the left-hand side derivative of  $P(t, r, \theta; t_1, r_1, \theta_1)$  with respect to  $r$  at  $r = r_1$  is positive (we also needed the right-hand side derivative to be negative, but this was a weaker condition).

Conditions (4.1),(4.2) and the appropriate condition for the stability in the  $r$ -direction being satisfied was necessary and sufficient for any  $(t, r)$  in the vicinity of  $(t_1, r_1)$  to be unable to invade. It was shown that there was generally an infinite number of such ESSs, and we hypothesised that these would often be in the range  $r > R$ , for some constant  $R$ .

We refer to the above solutions as point solutions, because we have a monomorphic solution with all individuals in the population having identical parameter values. We do not specify a value for the parameter  $\theta$  as any value of  $\theta$  will give an ESS; it does not matter which  $\theta$  is chosen, as long as all individuals choose the same value (any that choose a different value will do worse). It was also hypothesised that there could be non-point solutions, defined by individuals with different values of  $r$  and  $\theta$ , where  $C(r)$  is the density of the population of conspicuousness  $r$ , the density is uniform over  $\theta$  and the solution satisfies the following conditions. Such solutions needed to satisfy  $C(r) = 0$   $r \geq r_m$  for some value of  $r_m$  and the two following equations. The first equation is the condition for the population to be in equilibrium (where all have identical payoffs), and the second gives an expression for the information function  $I(w)$  needed in the first. We have as yet not been able to prove stability for this solution.

$$D(w)Q(I(w)) = D(0)Q(I(0)) \quad w \in (0, r_m), \quad (4.3)$$

$$I(w) = \frac{1}{n}H(t_1) \int_0^{r_m} L(r)C(r) \int_0^{2\pi} \frac{1}{2\pi} S((w^2 + r^2 - 2wr \cos(\theta))^{0.5}) d\theta dr \quad (4.4)$$

### 4.3 The Adapted Model and ESS Conditions

In this chapter we use the same model as in [2] but make two simplifying assumptions, which may well hold in many cases. We allow perfect recollection of encounters, so that  $L(r) = D(r)$  and we disregard the possibility of mortality not due to predation,  $\lambda = 0$ . This leads to the payoff function

$$\frac{F(t)}{D(r)K(t)Q(I_1)}, \quad (4.5)$$

where the information term  $I_1 = NH(t_1)D(r_1)/n$ . The key ESS conditions from above can now be rearranged as follows.

The equilibrium value of  $t$  is given by

$$\frac{F'(t_1)}{F(t_1)} - \frac{K'(t_1)}{K(t_1)} - a \frac{I_1 Q'(I_1)}{Q(I_1)} \frac{H'(t_1)}{H(t_1)} = 0 \quad (4.6)$$

if the root of the equation  $t_1$  is positive (otherwise  $t_1 = 0$ ), which is stable if

$$-\frac{F''(t_1)}{F(t_1)} + \frac{K''(t_1)}{K(t_1)} + 2a \frac{K'(t_1)}{K(t_1)} \frac{I_1 Q'(I_1)}{Q(I_1)} \frac{H'(t_1)}{H(t_1)}$$

$$+ a^2 \frac{Q''(I_1)}{Q(I_1)} \left( I_1 \frac{H'(t_1)}{H(t_1)} \right)^2 + a \frac{I_1 Q'(I_1)}{Q(I_1)} \frac{H''(t_1)}{H(t_1)} > 0. \quad (4.7)$$

Maximum crypsis ( $r = 0$ ) is stable if

$$\frac{D'(0)}{D(0)} + \left( a \frac{D'(0)}{D(0)} + S'(0)(1-a) \right) \frac{I_1 Q'(I_1)}{Q(I_1)} > 0 \quad (4.8)$$

and  $r > 0$  is stable if

$$\frac{D'(r_1)}{D(r_1)} + \left( a \frac{D'(r_1)}{D(r_1)} - S'(0)(1-a) \right) \frac{I_1 Q'(I_1)}{Q(I_1)} < 0. \quad (4.9)$$

## 4.4 Results

We shall use the following example functions in the above conditions to find the ESSs for our model. These have been chosen to represent plausible real situations and maintain mathematical tractability.

$$F(t) = f_0 e^{-ft}, \quad K(t) = k_0/(1+kt), \quad H(t) = t - t_c,$$

$$S(x) = \max(1 - vx, 0), \quad Q(i) = \min(1, q_0 e^{-qi}).$$

We will keep the detection function  $D(r)$  in general form. In the analysis that follows, we assume that  $I_1 > \log(q_0)/q$ , i.e., the level of information of toxicity is not sufficiently large and negative to make  $Q(I_1) = 1$ , so that the predators have some reluctance to attack prey.

To find the equilibrium  $t$  we substitute into (4.6)

$$\begin{aligned} -f + \frac{k}{1+kt} + \frac{aiq}{t-t_c} = 0 &\Rightarrow \frac{k}{1+kt} + \frac{aqND(r)}{n} = f \\ \Rightarrow t(r) &= \frac{1}{f - aqND(r)/n} - \frac{1}{k} \end{aligned} \quad (4.10)$$

(if this is negative, then  $t(r) = 0$ ). Since  $D(r)$  increases with  $r$ , this means that there is a unique value of  $t(r)$  for every  $r$ , which increases as  $r$  does, provided that  $a > 0$ . This increase is very slight if the level of relatedness in the population is small.

To check stability we substitute into (4.7)

$$-f^2 + \frac{2k^2}{(1+kt)^2} + \frac{2ak}{1+kt} \frac{qD(r)N}{n} + a^2 q^2 \left( \frac{ND(r)}{n} \right)^2 + 0 > 0.$$

Using equation (4.10) above this gives  $k^2/(1+kt)^2 > 0$  so that the solution is always stable.

The stability condition for  $r = 0$  is found by substituting into (4.8), giving

$$1 - \frac{qN}{n}(t - t_c)D(0) \left( a - (1 - a)v \frac{D(0)}{D'(0)} \right) > 0. \quad (4.11)$$

The stability condition for  $r > 0$  is found by substituting into (4.9), giving

$$1 - \frac{qN}{n}(t - t_c)D(r) \left( a + (1 - a)v \frac{D(r)}{D'(r)} \right) < 0. \quad (4.12)$$

If  $t(r) < t_c$  for all values of  $r$ , then inequality (4.12) is never satisfied, so that there can be no solution with  $r > 0$ . That is, if prey are perceived by the predators as being beneficial to them, then the prey should be maximally cryptic. If  $t(r) > t_c$  for some  $r$ , then this is true for all  $r$  larger than this value. Such a solution occurs if

$$d_m = \lim_{r \rightarrow \infty} D(r) > \frac{n}{aqN} \left( f - \frac{k}{1 + kt_c} \right), \quad (4.13)$$

where we assume that  $D(r)$  is bounded above by  $d_m$ , so that there is an upper limit to the encounter rate for individuals, irrespective of how conspicuous they are. Provided that  $D(r)/D'(r)$  does not decrease with  $r$  (and for any sensible function this is likely to be true) then if stability in  $r$  is satisfied at some value of  $r$ , it is for all larger values, so that solutions are of the form  $r > R$ . If there is a maximum value of  $r$  allowable there may be no such solution, otherwise if (4.13) is satisfied such a solution is guaranteed.

There are eight conceivable configurations of point solutions (collections of all solutions for a given set of parameters; this includes the case where there are no such solutions). There can either be a set of aposematic solutions  $r > R$  or not, combined with each of four possibilities for  $r = 0$ , namely a)  $t(0) = 0$  and so there is no investment in defence, b)  $0 < t(0) < t_c$  and so there is some investment in defence but insufficient to make the prey aversive, c)  $t_c < t(0)$  and so there is sufficient investment in defence to make the prey aversive, and d) no solution. From (4.10) the conditions for (a)–(c) are

$$\begin{aligned} \text{(a)} \quad & \frac{1}{f - aqND(0)/n} - \frac{1}{k} < 0 \Rightarrow t(0) = 0 \\ \text{(b)} \quad & 0 < \frac{1}{f - aqND(0)/n} - \frac{1}{k} < t_c \Rightarrow 0 < t(0) < t_c \\ \text{(c)} \quad & t_c < \frac{1}{f - aqND(0)/n} - \frac{1}{k} \Rightarrow t_c < t(0). \end{aligned}$$

For each of the above cases, for the point solution to be stable (in the  $r$  direction) we also need equation (4.11) to be satisfied. No solution at  $r = 0$  occurs if equation (4.11) is not satisfied for whichever of the above would be the evolutionarily stable value.

Supposing that  $r$  is not bounded above, then there is a stable set of  $r > R$  solutions if (4.13) is satisfied, i.e.,

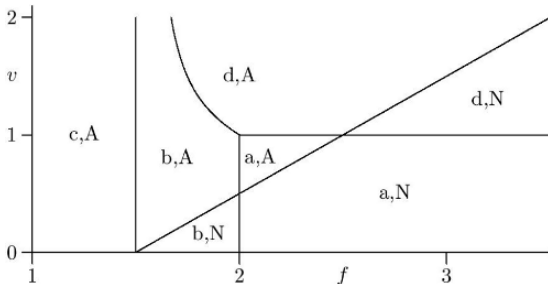


**Fig. 4.1.** ESS configurations using our example functions with  $A_1 = A_2 = k = d_0 = t_c = 1$ ,  $d_m = 1 + v$ . Which of the four types of solution occurs at  $r = 0$  is indicated by one of a–d, and the presence (absence) of aposematic solutions is indicated by A (N).

$$\frac{1}{f - aqNd_m/n} - \frac{1}{k} - t_c > 0.$$

We shall now demonstrate that all eight combinations are possible. If  $a$  is sufficiently small, the stability condition reduces to

$$1 + A_1v(t - t_c) > 0$$

for  $A_1 = qN(1 - a)D(0)^2/nD'(0)$ . Thus depending on the size of  $v$ , if the evolutionarily stable value is less than  $t_c$  stability may or may not occur, but if it is larger than  $t_c$  stability occurs.

The evolutionarily stable values depend on the relative size of the expression  $1/(f - A_2d_0) - 1/k$  compared to 0 and  $t_c$ , where  $d_0 = D(0)$  and  $A_2 = aqN/n$ , from above. There is a stable set of  $r > R$  solutions if  $1/(f - A_2d_m) - 1/k > t_c$ .

Consider an example where  $A_1 = A_2 = k = d_0 = t_c = 1$ . Using the above expressions means that condition (a) occurs if  $v < 1, 2 < f$ ; (b) occurs if  $v < (f - 1)/(2f - 3), 1.5 < f < 2$ ; (c) occurs if  $f < 1.5$ ; (d) occurs if  $v > 1, 2 < f$  or  $v > (f - 1)/(2f - 3), 1.5 < f < 2$ .

There is a stable set of aposematic solutions if  $d_m > f - 0.5$  (we know that  $d_m > d_0 = 1$ ). In Fig. 4.1, where we set  $d_m = 1 + v$  and vary the two remaining free variables  $f$  and  $v$ , we can see seven of the eight possible combinations.

For case c, we automatically have a stable set. However, if  $r$  has a maximum value  $r_{max}$  then such a set need not occur. Such a maximum  $r_{max}$  will yield no such stable set if inequality (4.11) holds and inequality (4.12) does not hold at  $r = 0$ , so that we have the following inequality:

$$1 - \frac{qN}{n}(t - t_c)D(0) \left( a + (1 - a)v \frac{D(0)}{D'(0)} \right) > 0.$$

This will hold for values of  $v$  below a critical value provided  $t > t_c$ . We can thus have all eight possibilities.

## 4.5 Non-Point Solutions

Suppose that there is no point solution at maximum crypsis ( $r = 0$ ). We look for a solution where the population is dispersed over a range of appearances, as conjectured in [2]. In particular, we seek one where density is uniform over  $\theta$ , has density in the  $r$  direction of  $C(r)$ , with  $C(r_m) = 0$  at some critical value and

$$\int_0^{r_m} C(r)dr = N. \quad (4.14)$$

Substituting into (4.4) we obtain the following expression for  $I(w)$ :

$$I(w) = H(t_1) \frac{1}{n} \int_0^{r_m} D(r)C(r)Y(r, w)dr, \quad (4.15)$$

where

$$Y(r, w) = \int_0^{2\pi} \frac{1}{2\pi} \left(1 - v(w^2 + r^2 - 2wr \cos(\theta))^{0.5}\right) d\theta. \quad (4.16)$$

We shall first try to obtain an expression for  $Y(r, w)$ , and then consider an approximation. Choosing  $v = 1$  we get

$$\begin{aligned} Y(r, w) &= 1 - \int_0^\pi \frac{1}{2\pi} \left( (w^2 + r^2 - 2wr \cos(\theta))^{0.5} + (w^2 + r^2 - 2wr \cos(\theta + \pi))^{0.5} \right) d\theta \\ &= 1 - \frac{1}{2\pi} (w^2 + r^2)^{0.5} \int_0^\pi \left( 1 - \frac{2wr \cos(\theta)}{w^2 + r^2} \right)^{0.5} + \left( 1 + \frac{2wr \cos(\theta)}{w^2 + r^2} \right)^{0.5} d\theta \\ &= 1 - (w^2 + r^2)^{0.5} \\ &\quad \times \left( 1 - \frac{(w/r)^2}{4(1 + w^2/r^2)^2} - \frac{15(w/r)^4}{64(1 + w^2/r^2)^4} - \frac{105(w/r)^6}{256(1 + w^2/r^2)^6} \dots \right). \end{aligned} \quad (4.17)$$

We shall consider the simplest non-trivial approximation to  $Y(r, w)$  namely,

$$Y(r, w) \approx 1 - (w^2 + r^2)^{0.5}.$$

We thus have the equation

$$I(w) \approx \frac{1}{n} H(t_1) \int_0^{r_m} D(r)C(r)(1 - (w^2 + r^2)^{0.5})dr. \quad (4.18)$$

We need to satisfy the condition (4.3) that

$$\begin{aligned} D(w)Q(I(w)) &= D(w) \exp(-qI(w)) = k \\ \Rightarrow D'(w) \exp(-qI(w)) - D(w)qI'(w) \exp(-qI(w)) &= 0 \\ \Rightarrow \frac{d}{dw}(I(w)) &= \frac{D'(w)}{qD(w)} = (-H(t_1)) \frac{1}{n} \int_0^{r_m} wD(r)C(r)(w^2 + r^2)^{-0.5}dr. \end{aligned} \quad (4.19)$$

Note that since the right-hand term is positive and so is the integral, then there can only be a solution if  $H(t_1) < 0$  so that the equilibrium toxin level is insufficient to be aversive.

To find a solution that satisfies (4.19) above, we need

$$\frac{d}{dw} \log(D(w)) \propto w \int_0^{r_m} D(r)C(r)(w^2 + r^2)^{-0.5} dr.$$

We first look for a solution where  $r_m = 1$  and  $D(r)C(r) = 1 - r$ :

$$\begin{aligned} \int_0^{r_m} D(r)C(r)(w^2 + r^2)^{-0.5} dr &= \int_0^1 \frac{1}{(w^2 + r^2)^{0.5}} - \frac{r}{(w^2 + r^2)^{0.5}} dr \\ \Rightarrow \frac{d}{dw} \log(D(w)) &= B_1 w (\log(1 + (1 + w^2)^{0.5}) - \log(w) - (1 + w^2)^{0.5} + w) \\ \Rightarrow \log(D(w)) &= \int B_1 w (\log(1 + (1 + w^2)^{0.5}) - \log(w) - (1 + w^2)^{0.5} + w) dw \\ &= B_1 \left( B_2 + \frac{w^3}{3} - \frac{(1 + w^2)^{1.5}}{3} + \frac{w^2}{2} \log \left( \frac{1}{w} + \sqrt{1 + \frac{1}{w^2}} \right) \right. \\ &\quad \left. + \frac{1}{2}(1 + w^2)^{0.5} \right). \end{aligned}$$

Thus

$$\begin{aligned} D(w) &= \exp \left[ B_1 \left( B_2 + \frac{w^3}{3} - \frac{(1 + w^2)^{1.5}}{3} \right. \right. \\ &\quad \left. \left. + \frac{w^2}{2} \log \left( \frac{1}{w} + \sqrt{1 + \frac{1}{w^2}} \right) + \frac{1}{2}(1 + w^2)^{0.5} \right) \right] \end{aligned} \quad (4.20)$$

and so

$$\begin{aligned} C(w) &= (1 - w) / \exp \left[ B_1 \left( B_2 + \frac{w^3}{3} - \frac{(1 + w^2)^{1.5}}{3} \right. \right. \\ &\quad \left. \left. + \frac{w^2}{2} \log \left( \frac{1}{w} + \sqrt{1 + \frac{1}{w^2}} \right) + \frac{1}{2}(1 + w^2)^{0.5} \right) \right]. \end{aligned} \quad (4.21)$$

We can see that  $D(w)$  is increasing in the range  $(0,1)$ , and so  $C(w)$  is decreasing in that range, with  $C(1) = 0$ . The constant  $B_1$  is a specific number which satisfies equation (4.18), and  $B_2$  is a constant which attains its value when the integral of  $C(w)$  from 0 to 1 is  $N$ . Thus for the given values of the example functions, including the complicated function  $D(w)$ , we have a non-point solution of the envisaged type.



## 4.6 Discussion

In this chapter we have developed the model of [2] to try to clarify and elaborate on some important results from that paper. In particular we have shown for our chosen functions that there is an equilibrium level of toxicity  $t(r)$  for any given appearance  $r$ , that this level increases with  $r$  (as predicted by [6]; the strength of this relationship depends upon the relatedness of individuals amongst other factors) and that stability in the direction of  $t$  always occurs. The set of point ESSs thus falls into one of eight categories, each of which is possible. In particular it is possible for heavily defended prey to be cryptic in our model. We have also demonstrated a case where the complex non-point equilibrium hypothesised in [2] occurs, and have shown the form of the solution. In summary we have shown that all of the solutions from [2] occur for reasonable parameter values and confirmed that the hypothesised results do indeed occur. We believe that such results are likely to generalise to most reasonable forms.

The theoretical literature concerning secondary defences is divided on the extent to which we can expect cryptic prey to be defended. Both [4] and [7] suggest that when predation pressure is low, cryptic prey should not invest in secondary defences. Others (e.g., [8], [9], [10], [11], [12]) contend that cryptic prey can be highly defended. One important consequence is that aposematic coloration is not necessarily optimal for prey that possess substantial defences.

From a practical point of view, the most important development of this chapter is the ability to quantify the relationship between parameter values and the range of possible solutions, as exemplified by Fig. 4.1. This should allow effective testing of the theory by studying gradients of appropriate parameter values, either in comparative analyses such as [6] or by means of manipulative laboratory experiments utilising species with short generation times. Fig. 4.1 also makes clear that alternative strategies can exist, with the ESS selected by a given system depending not simply on current parameter values, but also on the evolutionary history of the population. There is a challenge to empiricists here to explore whether there is any evidence for such alternate steady states in nature.

At present expectation in many theoretical models is that pro-apostatic selection favours diversity in edible, undefended prey populations but that as soon as there is any level of defence selection becomes anti-apostatic, favouring uniformity ([13]). However we indicate here that one class of stable evolutionary result is a combination of some moderate investment in secondary defence with high levels of diversity in the prey appearance. Evidence for such non-point solutions in the natural world is currently lacking, however this may be due to a lack of focussed study. The type of exploration typified by Fig. 4.1 can allow clear predictions to be made about necessary circumstances for the maintenance of non-point solutions and so allow more focussed exploration of the natural world for empirical support for this predicted outcome of evolution.

We have not explored the dynamics of our model, but they could be complex. It is likely that when there is a unique cryptic ESS then this will be globally stable, but when there are aposematic ESSs, there are an infinite number of them, and the situation will be more complicated. It is not clear that all ESSs will be reachable by

repeated localised mutations. Perhaps starting from crypsis, the lower bound  $R$  will always be attained. It is also possible that there will be a non-point solution as well as the aposematic point solutions, so that none of these aposematic ESSs can be reached from crypsis. It is unclear what dynamic behaviour will occur from a starting point where  $r > 0$ . Note that close to any point solution evolution in the direction of  $r$  is stronger than that in the direction of  $t$  because of the discontinuity in the derivative in this direction so that analysis may effectively reduce to one dimension.

## References

1. Ruxton, G. D., Sherratt, T. N., Speed, M. P.: *Avoiding Attack: The Behavioural Ecology of Crypsis, Mimicry and Aposematism*. Oxford University Press (2004).
2. Broom, M., Speed, M. P., Ruxton, G. D.: Evolutionarily stable defence and signalling of that defence. *J. Theor. Biol.*, **242**, 32–43 (2006).
3. Broom, M., Speed, M. P., Ruxton, G. D.: Evolutionarily stable investment in secondary defences. *Funct. Ecol.*, **19**, 836–843 (2005).
4. Leimar, O., Enquist, M. Sillén-Tullberg, B.: Evolutionary stability of aposematic coloration and prey unprofitability—a theoretical-analysis. *American Naturalist*, **128**, 469–490 (1986).
5. Sherratt, T. N., Speed, M. P. Ruxton, G. D.: Natural selection on unpalatable species imposed by state-dependent foraging behaviour. *J. Theor. Biol.*, **228**, 217–226 (2004).
6. Summers, K., Clough, M. E.: The evolution of coloration and toxicity in the poison frog family (Dendrobatidae). *Proceedings of the National Academy of Sciences of the United States of America*, **98**, 6227–6232 (2001).
7. Speed, M. P., Ruxton, G. D.: Aposematism: what should our starting point be? *Proceedings of the Royal Society of London Series B*, **272**, 431–438 (2005).
8. Harvey, P. H., Bull, J. J., Pemberton, M. Paxton, R. J.: The evolution of aposematic coloration in distasteful prey—a family model. *American Naturalist*, **119**, 710–719 (1982).
9. Yachi, S., Higashi, M.: The evolution of warning signals. *Nature*, **394**, 882–884 (1998).
10. Servedio, M. R.: The effects of predator learning, forgetting, and recognition errors on the evolution of warning coloration. *Evolution*, **54**, 751–763 (2000).
11. Speed, M. P.: Can receiver psychology explain the evolution of aposematism? *Animal Behaviour*, **61**, 205–216 (2001).
12. Brodie, E. D., Agrawal, A. F.: Maternal effects and the evolution of aposematic signals. *Proceedings of the National Academy of Sciences of the United States of America*, **98**, 7884–7887 (2001).
13. Mallet, J., Joron, M.: Evolution of diversity in warning color and mimicry: Polymorphisms, shifting balance, and speciation. *Annual Review of Ecology and Systematics*, **30**, 201–233 (1999).

# The Tangled Nature Model of Evolutionary Ecology: An Overview

Simon Laird, Daniel Lawson, and Henrik Jeldtoft Jensen

Department of Mathematics, Imperial College London, South Kensington campus, SW7 2AZ, UK; simion.laird02@imperial.ac.uk; daniel@bioss.ac.uk; h.jensen@imperial.ac.uk

**Summary.** We present a review of the Tangled Nature model. The model is developed to focus on the effect of evolution and multiple interactions on ecological and evolutionary observables. The model is individual based and ecological structures, such as species, are emergent quantities. The dynamics consists of a simplistic mutation-prone multiplication in which the probability of producing an offspring is determined by the occupancy in genotype space. The macroscopic long time dynamics is intermittent and exhibits a slow decrease in the macroscopic extinction rate. Ecological quantities such as the species abundance distribution and the species-area relationship compare qualitatively well with observations, as does the relation between interaction and diversity. The effect of correlations between parents and mutants has been studied, as has the effect of a conserved resource.

**Key words:** Evolution, ecology, network of interactions, species-area relationship (SAR), species abundance distribution (SAD).

## 5.1 Introduction

Can we establish a general framework for the description of ecosystems consisting of many interacting and evolving organisms? We seek a description which will enable us to bridge the span from microscopic to macroscopic time. The model is to be defined at the level of individuals so that ecological and taxonomic structures emerge as a result of the dynamics. The description should be logically simple and cover broad classes of observed facts.

Much work is done on the regime of strongly separated time scales, using, e.g., “adaptive dynamics” [1] or game theory [2,3]. One can incorporate evolution by considering that evolutionary dynamics occurs much more slowly than ecological dynamics, so that at all times the system is in an equilibria (e.g., the Webworld model, [4,5]). However, the time scales may overlap when long-lived species interact with short-lived ones, and additionally there is evidence [6] that the evolutionary dynamics can affect ecological stability, and vice versa. These are not insurmountable problems, e.g., the “Streetcar theory of evolution” [7] addresses this problem, but assumes that the system equilibrates between mutations. Such models are essential to understand

individual cases but we wish to also address the broad picture. Individual-based models [8] are an appropriate tool to combine fast and *usually* predictable ecological processes with the highly stochastic evolutionary behaviour in a controlled and realistic manner. Our model falls into the category (e) in DeAngelis and Mooij’s classification system [9]: “Genetic Variability and Evolution,” although arguably the most important feature gained from an individual-based approach at such a simple level is “demographic stochasticity,” that is, representing the inherent noise in the population in an accurate way. Our approach is inspired by statistical mechanics and complex systems theory, looking for overall general structures instead of specific details of the organisms comprising the system.

Our model consists of asexually reproducing individuals all subject to the same killing probability (per time unit). The multitude of interactions between coexisting organisms is included through a weight function which determines the reproduction rate of individuals. Our philosophy is that a simple statistical model may help to identify the important mechanisms behind macroscopic observed ecological measures. the same,

## 5.2 A Simple Introductory Model

The Tangled Nature model is an individual based model of evolutionary ecology. We give a brief outline of the model here, with more details available in [10–13]. This version of the model is an attempt to address systems with many interactions between species in the simplest possible way, with detail and realism added in stages. We start with the bare model, to which we will add spatial effects and consider more realistic forms of the fitness.

### 5.2.1 Uncorrelated Non-Spatial Model

An individual is represented by a vector  $\mathbf{S}^\alpha = (S_1^\alpha, S_2^\alpha, \dots, S_L^\alpha)$  in the genotype space  $\mathcal{S}$ , where the “genes”  $S_i^\alpha$  may take the values  $\pm 1$ , i.e.,  $\mathbf{S}^\alpha$  denotes a corner of the  $L$ -dimensional hypercube. Here we take  $L = 20$ , giving a reasonable sized space (over a million genotypes) whilst not being computationally prohibitive. We think of the genotype space  $\mathcal{S}$  as containing all possible ways of combining the genes into genome sequences. Many sequences may not correspond to viable organisms. The viability of a genotype is determined by the evolutionary dynamics. All possible sequences are available for evolution to select from. We will see that a natural species concept arises from the dynamics, in which each species is separated in genotype space.

The system consists of  $N(t)$  individuals, and a time step consists of *one* annihilation attempt followed by *one* reproduction attempt. A reproduction event is successful with varying probability  $p_{\text{off}}$ , defined below, and an annihilation attempt is successful with constant probability  $p_{\text{kill}}$ .<sup>1</sup> One generation consists of  $N(t)/p_{\text{kill}}$  time steps,

---

<sup>1</sup> The restriction of constant killing probability can be shown to be qualitatively irrelevant in this model, as we do not include individual aging.

which is the time taken (on average) to kill all currently living individuals. The dynamics lead to an (approximately) constant population size, on short time scales.

The ability of an individual to reproduce,  $p_{\text{off}}$ , is ultimately controlled by a weight function  $H(\mathbf{S}^\alpha, t)$ :

$$H(\mathbf{S}^\alpha, t) = \frac{c}{N(t)} \left( \sum_{\mathbf{S} \in \mathcal{S}} \mathbf{J}(\mathbf{S}^\alpha, \mathbf{S}) n(\mathbf{S}, t) \right) - \mu N(t), \quad (5.1)$$

where  $c$  controls the strength of interaction (large  $c$  means large interaction),  $N(t)$  is the total number of individuals at time  $t$ , the sum is over the  $2^L$  locations in  $\mathcal{S}$  and  $n(\mathbf{S}, t)$  is the number of individuals (or occupancy) at position  $\mathbf{S}$ . Two positions  $\mathbf{S}^a$  and  $\mathbf{S}^b$  in genome space are coupled with fixed but random strength  $\mathbf{J}(\mathbf{S}^a, \mathbf{S}^b)$  ( $= J^{ab}$  in matrix notation) which can be positive, negative or zero. This link exists (in both directions) with probability  $\theta$  ( $= 0.2$  in Sect. 5.2.1), i.e.,  $\theta$  is simply the probability that any two sites are interacting. If the link exists, then  $\mathbf{J}(\mathbf{S}^a, \mathbf{S}^b)$  and  $\mathbf{J}(\mathbf{S}^b, \mathbf{S}^a)$  are both generated random and independent  $\in (-1, 1)$ . To study the effects of interactions *between* species, we exclude self-interaction so that  $\mathbf{J}(\mathbf{S}^a, \mathbf{S}^a) = 0$ .

The conditions of the physical environment are simplistically described by the term  $\mu N(t)$  in Eq. (5.1), where  $\mu$  determines the average sustainable total population size, i.e., the carrying capacity of the environment. An increase in  $\mu$  corresponds to harsher physical conditions. We use asexual reproduction consisting of one individual being replaced by two copies mimicking the process of binary fission seen in bacteria. Successful reproduction occurs with a probability per unit time given by

$$p_{\text{off}}(\mathbf{S}^\alpha, t) = \frac{\exp[H(\mathbf{S}^\alpha, t)]}{1 + \exp[H(\mathbf{S}^\alpha, t)]} \in [0, 1]. \quad (5.2)$$

This function is chosen for convenience, the specific functional form having no effect on the dynamics of the model—any smoothly varying function that maps  $H(\mathbf{S}^\alpha, t)$  to the interval  $[0, 1]$  will do. We allow for mutations in the following way: with probability  $p_{\text{mut}}$  per gene we perform a change of sign  $S_i^\alpha \rightarrow -S_i^\alpha$  during reproduction.

Eq. (5.1) can be understood as the average interaction for an individual with all others, with a normalisation condition given by the  $\mu N$  term, which determines the total population and controls fluctuations. The interaction strength  $c$  gives the magnitude of the total interactions, regardless of density; i.e., we choose to represent systems in which the population size has saturated.<sup>2</sup> We can tune the effective “resource” density (and hence population density) with the parameters  $c$  and  $\mu$ . The total population remains approximately constant over ecological time scales (and actually increases over evolutionary time scales). Setting self-interaction to zero is equivalent to considering that all types interact equally with their own species (one can rescale  $p_{\text{kill}}$  and  $\mu$  to accommodate this); we relax this constraint in Sect. 5.2.3.

Initially, we place  $N(0) = 500$  individuals with randomly chosen genotype. Their initial location in genotype space does not affect the nature of the dynamics. A two-phase switching dynamic is seen, consisting of long periods of relatively stable configurations (quasi-evolutionarily stable strategies or q-ESSs) (Fig. 5.1) interrupted by

<sup>2</sup> One could easily consider the case of density dependent interactions by allowing  $c = c(N)$ .

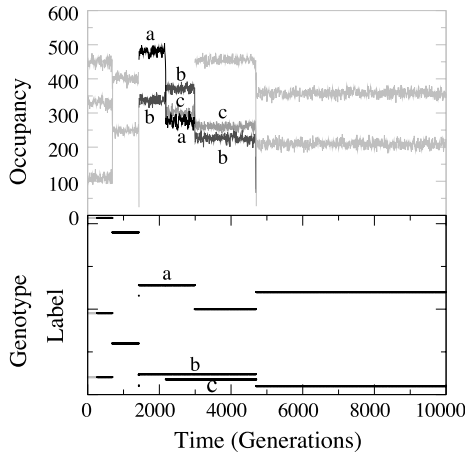


**Fig. 5.1.** q-ESS in a single run, both graphs have the same time axis. Top: Occupancy of wild type species vs. time. Horizontal lines constitute q-ESS and the changes between q-ESS are transitions, too fast to see on this time scale. Labels are placed only on species that survive q-ESS transitions. Bottom: A sample plot of species existence vs. time. The Genotype Label axis is not meaningfully ordered, and is included for comparison to the correlated phenotype space model in Sect. 5.3 (Fig. 5.4).

brief spells of reorganisation of occupancy called transitions. Transition periods are terminated when a new q-ESS is found, as discussed in [10]. A “species” can be well defined as the highly occupied genotype points called “wild types,” which are separated in genotype space. Each wild type is surrounded by a “cloud” of mutant genotypes with low occupancy. Thus we can take a natural definition of diversity: the number of wild types in the system.

The q-ESSs themselves consist of a number of wild type species, which are ecologically stable and stable to mutations from the neighbouring genotype space. The absolute stability of a q-ESS depends on both the stability against invasion by mutants, and against ecological “accidents” such as the extinction of a keystone species. The two cannot be separated in our model, as, for example, the probability of an accident eliminating a wild type will depend on the interaction properties of all individuals in the system.

The observed species abundance distribution (SAD) is log-normal like [10] with a log-series like tail, consistent with many observations and similar to that found in neutral theory [14]. The log-normal portion is made up of wild type species only. These have evolved so that the number of births in a given species exactly cancels the number of deaths (and mutations). The log-series section is made up of “mutant” sub-species, that is, species who have experienced deleterious mutations from a wild type. They are less successful and short lived, as their population is only supported by a constant influx of mutants from the neighbouring wild type.

The long term dynamics of this model are essentially the same as the extension in Sect. 5.2.3. The stability of the q-ESS found increases slowly with time, as does

the mean total population  $\langle N(t) \rangle$ . The waiting time for extinction events (occurring at transitions) decreases with time (close to  $1/t$ ), and the species lifetime distribution compares well with much fossil data [10]. Results which support these conclusions are presented in [15, 16] for a very similar model but with simplified dynamics.

### 5.2.2 Uncorrelated Spatial Model

To add spatial extension to the Tangled Nature model, we consider a number of sites on a spatial lattice, with a number of individuals in each. We now consider that individuals interact only with other individuals at the same site, and hence compete only locally for space via the  $\mu$  term. Migration moves an individual to a randomly chosen neighbouring lattice point and occurs with constant probability  $p_{\text{move}}$ . Spatial boundaries are periodic to prevent the complication of edge effects.

Each site on the spatial lattice behaves similarly to the non-spatial model, spending most time in a q-ESS. However, in the spatial case a small number of migrants are present in each site. This acts as an additional pressure to enter a transition phase, *unless* the site is in the same type of q-ESS as its neighbours. This gives rise to spatial patches of q-ESS types. These patches grow and shrink on a very slow time scale, except when the migration probability  $p_{\text{move}}$  is high.

Patches form in sizes that appear to be power-law distributed, and species-area curves close to a power law are observed (Fig. 5.2). The species-area curve has a slight s-shape produced by the periodic boundary. This same shape was found in a “neutral” (non-interacting) model [17] of Durrett and Levin. In their neutral model the  $z$ -value (the slope in the log-log plot of diversity vs. area) decreases with decreasing speciation rate. However, their speciation rate can be thought of as a migration rate from an external pool as there is no genotype space. In our model with interactions and explicit genotype space, we find that the  $z$ -value decreases with *increasing* migration

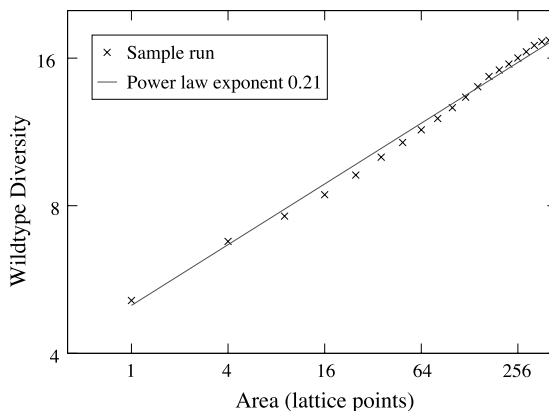


**Fig. 5.2.** Sample species-area relationship (from a single run), which is very close to a power law, with a slight S shape due to the periodic boundaries.

rate inside the system. This is because mutation occurs at constant speed, therefore increasing migration rate increases the competition faced by a new species.

In general it is logical that *immigration* (from outside the system) and *migration* (within the system) are correlated. However, increased internal migration rate reduces the chances of mutations surviving, and so produces the inverse effect of the immigration rate (i.e., mutation rate in models without genotype space) of new species from outside the system. High mobility (i.e., migration and immigration rates) for a family of species may mean better mixing and so less chance for spatial segregation of species within a single family—the standard explanation for why bird families generally have lower  $z$ -values than land-dwelling families. Conversely, e.g., on islands, it allows species from elsewhere to arrive, thus possibly increasing diversity (as argued in [17]). Which effect dominates will depend on the geography in question, i.e., the size of the local groups of individuals, and the separation between them.

Magurran and Henderson [18] noted that permanent fish species have a log-normal SAD whilst transient species have a log-series distribution. Our local q-ESS has the same distribution, with a log-normal like distribution for the wild types and a log-series like distribution for mutants and migrants. For low mutation rates and high migration rates, clearly migrants will outnumber local mutants and we will observe the exact same distribution near the q-ESS patch borders. In our spatial model, the distinction between the two types is of fitness. The wild types with a log-normal like SAD are all equally fit in that they have a reproduction rate exactly balancing the death rate; the migrants with a log-series like SAD are all less fit and rely on repopulation from an external pool (and, hence, are transient).

Full details for the spatial model are available in [19].

### 5.2.3 Diversity and Fitness in the Non-Spatial Model

The restriction that all species are uniform with respect to their own members is approximately valid for many circumstances but is in general unrealistic. We therefore introduce different values of “intrinsic fitness” to each genotype, which can be formed in many ways. The cases are considered separately for clarity, but are easily combined.

A fitness landscape can be uncorrelated or correlated. The correlation we choose is a type of *Fujiyama* landscape (because it has a single, large peak) [2] defined as follows. One type  $\alpha$  has a fitness of 1, and with each mutational step away from this type we subtract  $\Delta$  ( $= 0.1$  in simulations), down to a minimum of 0. An uncorrelated landscape is generated with each type having a fitness drawn uniformly from  $(0, 1)$ . This results in the following modified weight functions:

1. Density dependent fitness, which is the varying interaction of an individual with its own type, defined by

$$H_d(\mathbf{S}^\alpha, t) = H(\mathbf{S}^\alpha, t) + \frac{\epsilon}{N(t)} n(\mathbf{S}^\alpha, t) E(\mathbf{S}^\alpha). \quad (5.3)$$

Here,  $\epsilon$  is the magnitude of the density dependent part of the “intrinsic fitness strength” and  $\epsilon E(\mathbf{S}^\alpha)$  is the intrinsic fitness of individual  $\alpha$ .  $E(\mathbf{S}^\alpha)$  is determined



according to the case studied. 1(a): Uncorrelated, density dependent intrinsic fitness landscape, 1(b): Correlated, density dependent intrinsic fitness using a Fujiyama landscape.

2. Density independent fitness, defined by

$$H_i(\mathbf{S}^\alpha, t) = H(\mathbf{S}^\alpha, t) + \epsilon_I E(\mathbf{S}^\alpha). \quad (5.4)$$

Here,  $\epsilon_I$  is the magnitude of the density independent part of the intrinsic fitness strength.  $E_i$  is again determined by the case studied. 2(a): Uncorrelated, density dependent intrinsic fitness landscape, 2(b): Correlated, density dependent intrinsic fitness using a Fujiyama landscape.

Fig. 5.3 shows the behaviour of the wild type diversity. Cases 1(a), 1(b) and 2(b) are qualitatively the same, with a rise in density above some characteristic interaction strength  $c$ . The density independent case produces diverse states at much smaller values of  $c$  because only the *difference* in fitness needs to be overcome; in the density dependent case, it is the absolute fitness that provides a barrier to diversification. In the uncorrelated density independent case, there are many species with (approximately) the same high fitness within a couple of mutation steps. This means that, for low  $c$ , neutral drift can occur between the numerous fit types, and for larger  $c$  interaction is the dominant form of selection; in each case, multiple species can be supported (although not in q-ESS for the case of drift).

Interestingly, case 1(b) allows the fittest species to be replaced at a lower interaction than that for which a diverse state can be supported. However, case 2(b) allows diverse states at a lower interaction than that for which replacement of a fittest type is possible. These claims can all be shown with a simple mean field approximation of our model; see [20] for details.

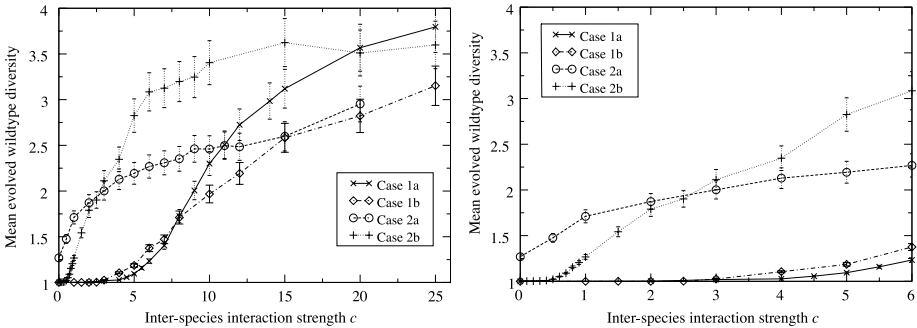


**Fig. 5.3.** Left:  $c$  dependence of the average wild type diversity of an evolved system, taken for 40000–50000 generations and 500 runs per data point for the separate cases of density dependent (case 1) and density independent (case 2) fitness, both on a rugged random fitness landscape (cases (a)) and a Fujiyama landscape (cases (b)). Right: A closer look at the low- $c$  region, showing the qualitative similarity in  $D$  vs.  $c$  for all cases except case 2(a).

### 5.3 Correlated Non-Spatial Model

In the original model, mutated offspring acquired interaction properties that were uncorrelated with those of the parent. This was unrepresentative of a real biological system where correlations are vital to the evolutionary process. Efforts have since been made to rectify the issue [21] but the limited size and hypercubic geometry of the genotype space have proven to be very restrictive. The problems were finally resolved by disregarding the hypercubic geometry entirely. Correlations were then successfully incorporated so that mutated offspring had interactions comparable with those of the parent [22]. To achieve this goal we use a phenotype description of  $L = 16$  traits,  $\mathbf{T}^a = (T_1^a, T_2^a, \dots, T_L^a)$ , with each trait taking a value from the periodically bounded range,  $[0, 99999]$ . A proportion,  $\theta$ , of the entries of the greatly enlarged interaction matrix,  $\mathbf{J}(\mathbf{T}^a, \mathbf{T}^b)$  are assigned normally distributed values that are locally correlated within the  $\mathbf{J}$ -matrix. All other values of the remaining proportion of the matrix,  $1 - \theta$ , are assigned zeroes which are treated as a lack of interaction between the two relevant phenotypes. As well as being locally correlated in value, the non-zero entries, as a set, are also distributed with a local correlation. By this we mean the  $\mathbf{J}$ -matrix exhibits a clustering of non-zero entries so correlated phenotypes will interact with similar sets of other phenotypes. The result is that given a mutation of one trait value we have an exponential decay in the correlation between parent and offspring interaction set values that is dependent upon the distance mutated in the trait value,  $\Delta(\mathbf{T}^\alpha, \mathbf{T}^\beta)$ ,

$$\mathbf{c}(\mathbf{J}(\mathbf{T}^\alpha, \mathbf{T}^\gamma), \mathbf{J}(\mathbf{T}^\beta, \mathbf{T}^\gamma)) = \exp[-\Delta(\mathbf{T}^\alpha, \mathbf{T}^\beta)/\xi] \in (0, 1]. \quad (5.5)$$

Here,  $\xi$  is the correlation length and  $\alpha, \beta$  and  $\gamma$  are indices used to represent individuals as opposed to  $a$  and  $b$ , which would indicate points in phenotype space—multiple individuals may exist with the same phenotype vector. As phenotypes are essentially defined by their interaction sets we shall herein refer to the correlation measure between two phenotypes as  $\mathbf{C}(\mathbf{T}^\alpha, \mathbf{T}^\beta)$ , i.e., as an entry in the correlation matrix,  $\mathbf{C}$ . The clustering of non-zero  $\mathbf{J}$ -matrix entries also exhibits a short range correlation length similar to (5.5). The probability of a random phenotype  $\alpha$  having an interaction with another phenotype  $\gamma$  is  $\theta$ , but if  $\alpha$  has a vector similar to another  $\beta$  that has an interaction with  $\gamma$ , then this probability is elevated by virtue of the correlation (and therefore we have clustering). Importantly, interacting uncorrelated phenotypes take values  $\mathbf{J}(\mathbf{T}^a, \mathbf{T}^b)$  and  $\mathbf{J}(\mathbf{T}^b, \mathbf{T}^a)$  that are uncorrelated thus permitting any interaction type (predator-prey, mutualistic, etc.) to exist in principle. The process with which we achieve these quantifiable correlations is quite involved, so we have elected to give an overview here whilst referring the reader to the original paper for a fuller explanation [22].

In order to more truly represent evolution in a real ecosystem several changes were made to the original model. These changes can best be described via the modifications made to the weight function shown previously in (5.1),

$$H(\mathbf{T}^\alpha, t) = a_1 \frac{\sum_{\mathbf{T} \in \mathcal{T}} \mathbf{J}(\mathbf{T}^\alpha, \mathbf{T})n(\mathbf{T}, t)}{\sum_{\mathbf{T} \in \mathcal{T}} \mathbf{C}(\mathbf{T}^\alpha, \mathbf{T})n(\mathbf{T}, t)} - a_2 \sum_{\mathbf{T} \in \mathcal{T}} \mathbf{C}(\mathbf{T}^\alpha, \mathbf{T})n(\mathbf{T}, t) - a_3 \frac{N(t)}{R(t)}. \quad (5.6)$$

The sums are made over the points in phenotype space,  $\mathcal{T}$ , and the occupancies (population associated with each phenotype),  $n(\mathbf{T}, t)$  are used to account for the multiplicity of individuals with the same phenotype vector. We consider here a well mixed system of constant spatial size, although spatial extent is not explicitly considered. For clarity we reiterate at this point that the phenotype space is a pre-defined, complete set of all possible phenotypes and it is evolution and contingency that select the actualised phenotypes in the evolved system. The  $\mathbf{J}$ -matrix is similarly a pre-defined complete set of all possible interactions for all possible phenotypes that may exist *in potentia*.

The correlation measure is used in the first term of the weight function to restrict the impact of the interaction sum. It represents the fact that interactions are shared amongst members of the same species. For example, a tree may provide a volume of fruit to a solo member of a species but the provision must be shared with reduced efficacy if there are many members. So the overall effect of this denominator on an individual is to dampen its interaction sum as a whole, thus representing the effect of distributing all interaction effects amongst the individual's own species members. Another example could be a wildebeest in proximity to a lion. The negative predatory effect (or predation probability) of the single lion on that specific wildebeest is decreased if there are many wildebeest about to select from. The interaction is damped by the presence of other members of the individual's own species. This aspect is not ubiquitous in species interactions but does feature in many cases. It is less applicable at low population densities but our system generally maintains significant species populations even at low resource levels. Lowering the resource tends to reduce diversity rather than distinct species populations so this limitation was deemed to be acceptable. In recognition of the phenotypic variation inherent in a species, the sum over the correlation values,  $\mathbf{C}(\mathbf{T}^a, \mathbf{T}^b)$ , accounts for the fact that species members have different but similar phenotypes. This can be seen as a species description in itself.

When referring to diversity we specifically mean the wild type diversity but all interaction effects from all extant phenotypes, mutants included, are accounted for in every interaction sum. The mutant cloud itself is in fact very sparse as we have elected to use a low mutation rate,  $P_{\text{mut}} = 0.0002$ . As a consequence, the phenotype distribution is essentially a set of delta points of high occupancy with infrequent mutants existing with low occupancy. This makes the recognition of the wild type diversity very simple as each species is massively dominated by the population of the wild type.

The second term of the weight function represents intra-specific competition and uses the same correlation measure as before. Similar but distinct phenotypes are likely to be in competition for resources, space, etc. that are specific to their niche. The correlation measure accounts for this similarity. The original model operated without such a term, but it was deemed essential here to allow sufficient wild type diversity to develop. Otherwise, mutualistic pairs of phenotypes dominate the system, competitively excluding all others.

The third term represents competition for a conserved vital resource that all phenotypes require for survival. Any successful reproduction event produces an offspring that assumes a unit of resource from the bath,  $R(t)$ . The conservation requirement,  $R(t) + N(t) = \text{constant}$  means we have a carrying capacity for the system as a whole.

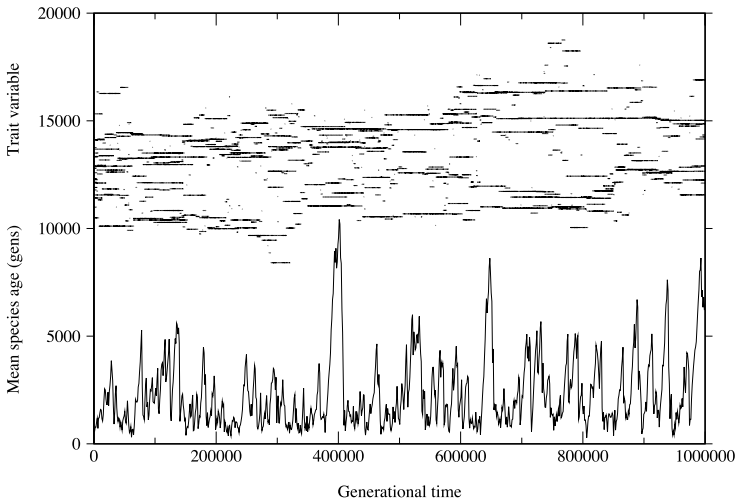


**Fig. 5.4.** The upper plot represents the time evolution of the extant phenotype distribution projected onto one of the 16 trait variables. The lower plot represents the mean age of the extant phenotypes weighted according to population. Stable periods can be seen where the mean age increases nearly linearly until a collapse occurs and new species are introduced.

Its functional form represents the number of system members competing per unit of available resource.

The parameters,  $a_1 = 0.5$ ,  $a_2 = 0.01$ ,  $a_3 = 0.2$  are the selection, conspecific competition and resource competition parameters respectively. These are subjectively chosen to allow interaction controlled dynamics and a sufficient wild type diversity to develop. A value of  $\theta = 0.05$  is used throughout the simulations.

### 5.3.1 Lifetimes and Extinctions

The macroscopic dynamics of the system have similarities with the original model as intermittency occurs, but the phases of stability are not so disjoint. Fig. 5.4 shows the evolution of the occupancy in phenotype space where phenotypes can be seen to drift, speciate and often go extinct. The transitions are there to some degree as demonstrated in the accompanying plot of the mean age of the system wild type phenotypes. There are regular collapses of the system where long term phenotypes go extinct and the extant set becomes partially reset. Many phenotypes survive these transitions, however.

The lifetime distribution associated with these extinctions has a near power-law form,  $P(s) \sim s^{-\gamma}$  as can be seen in Fig. 5.5. It has often been suggested that such real system distributions are power laws with proposed exponents around  $\gamma \simeq 2$ , but this is still an open debate. Our data implies a near power law form that is exhibited both in other models and the original Tangled Nature model itself [10, 23–25] (and also [26] in reference to [27]). By increasing the resource in our system we can shift the mean lifetime to lower values which is a consequence of an increase in the mean

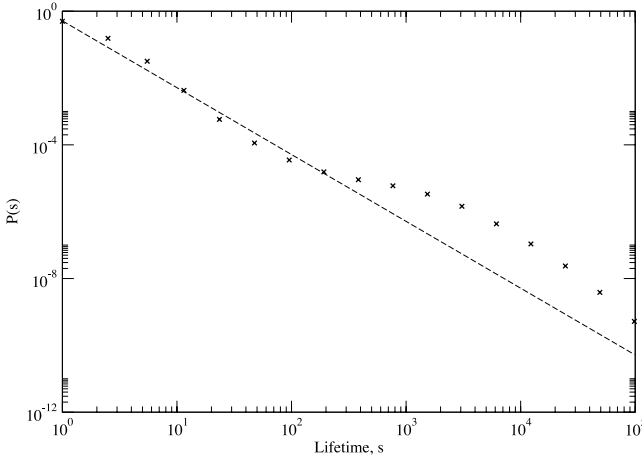


**Fig. 5.5.** An example of a lifetime distribution for a low resource system. The form is nearly a power law with a distinct deviation. Dotted line represents a functional power law,  $P(s) \sim s^{-\gamma}$  with exponent,  $\gamma=2$ .

population density. This phenomenon arises as a population density increase leads to an elevation in the rate of mutant offspring per generational time step, resulting in the system destabilising more frequently. It has recently been discovered that species diversity may negatively correlate with average species duration, thus implying a greater species turnover rate [28]. The population density and wild type diversity are positively correlated in our model due to the presence of the intra-specific competition term in (5.6). As this aspect is an arguably realistic portrayal of niches within an ecosystem we can provide agreement that wild type diversity does incur a greater species turnover rate.

### 5.3.2 Species Interaction Network

The species interaction network is defined by the realised adjacency matrix of the wild type diversity,  $D$ . The structural formation of the network arises from evolutionary processes occurring at the level of individuals but it has dynamic global properties as a result of this. The evolutionary pressure to achieve positive interactions leads to a global increase in the mean degree  $\langle k \rangle$  of the extant species set. Here the mean degree  $\langle k \rangle$  is the number of interactions of any type a species has with other species, averaged over all species. We can compare the evolved system to a “null” one consisting of a *random* species set. For this set, the connectance values will conform on average to the value of  $\theta$ , the proportion of non-zero interactions in the  $\mathbf{J}$ -matrix. Fig. 5.6 shows the mean degree versus wild type diversity taken at the highest resource level,  $R = 30000$  (all other resource levels exhibit similar behaviour). In comparison to the null system mean degree,  $\langle k \rangle_{\theta} = \theta(D - 1) = 0.05(D - 1)$ , it is obvious that the network achieves a status that far exceeds this value. It is generally unclear whether greater stability

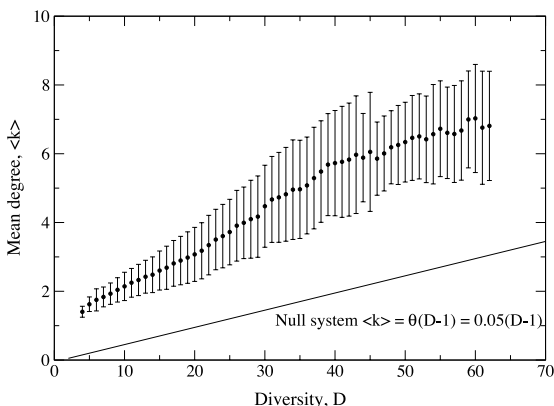


**Fig. 5.6.** Plot of mean degree,  $\langle k \rangle$ , against wild type diversity,  $D$ . Each point is an ensemble average of data taken at each instance of each diversity achieved at the resource level,  $R = 30000$ , with error bars representing the standard error. Fifty simulation runs of a million generations each were made, so given the fluctuations involved, a large range of diversities were repeatedly encountered. The lower line is the mean degree of the null system  $\langle k \rangle = \theta(D-1) = 0.05(D-1)$ .

is achieved through mean degrees that are either lower than the network percolation threshold or higher [29–32], but here the system naturally evolves towards the latter. The mean interaction strength also increases to a positive value that is diversity dependent, but around one standard deviation of the normal distribution values of the null system. Our system therefore has a global response whereby it evolves to assume networks involving greater numbers of positive interactions. This process is strongly enhanced by mutualistic interaction types, and whilst the interactions are generally asymmetric their strengths are more positively biased in the evolved systems.

The correlations in inheritance have an unusual effect on the degree distributions of the assumed networks. They all conform closely to exponential,  $P(k) \sim e^{-k/\langle k \rangle}$ , as opposed to the null system binomial distributions. We attribute this degree form to the inheritance process which directs the evolution of the network. Simulations performed with zero correlations lead to networks that display enhanced mean degrees but without any deviation from the binomial degree distribution. The correlation appears to be a necessary requirement for these longer tailed distributions to appear.

## 5.4 Discussion

Our focus has been on emergence and large numbers of interdependent organisms. We have described a set of minimalistic models in which reproduction probability is the only explicit phenotypical property of individuals, and is not defined as an intrinsic property but rather determined for each type of organism through its interaction with other extant types. Basic properties, such as the existence and formation of separate

species, and the existence of quasi-stable states separated by periods of mutation, are emergent from the dynamics.

In the simple model in Sect. 5.2.1, transitions between q-ESS are rare events, even though mutations are common. On transition, all species perform an evolutionary random walk *with an effective selection gradient due to interactions*, meaning the distance covered is much larger than predicted by a standard random walk of equal time (i.e., the jumps resemble Lévy flights [33]).

The Tangled Nature model, and similar approaches, should be considered as complementary to more detailed models such as those in adaptive dynamics, in which ecosystems are established with many shared features with observations on real biological systems. The sort of questions which can be asked of our model are very different. In particular, we do not intend to model a specific situation, but to capture features common to a great many evolving systems, such as the effect of interaction on the stability of an ecosystem, and the time dependence of properties such as stability, average population, the form of interactions, etc.

By allowing evolution to select the network of interacting species from a potential configuration space we are able to study issues concerning functionality and stability. Our approach allow us to consider the network properties of the ecosystem as collectively selected quantities.

## References

1. Abrams, P.A.: ‘Adaptive dynamics’ vs. ‘adaptive dynamics’. *J. Evol. Biol.*, **18**, 1162–1165 (2005).
2. Drossel, B.: Biological evolution and statistical physics. *Adv. in Phys.*, **50**, 209–295 (2001).
3. Maynard Smith, J.: *Evolution and the Theory of Games*. Cambridge University Press, Cambridge CB2 2RU (1982).
4. Drossel, B., Higgs, P.G., McKane, A.J.: The influence of predator-prey population dynamics on the long-term evolution of food web structure. *J. Theor. Biol.*, **208**, 91–107 (2001).
5. Caldarelli, G., Higgs, P.G., McKane, A.J.: Modelling coevolution in multispecies communities. *J. Theor. Biol.*, **193**, 345–358 (1998).
6. Thompson, J.N.: The evolution of species interactions. *Science*, **284**, 2116–2118 (1999).
7. Hammerstein, P.: Darwinian adaptation, population genetics and the streetcar theory of evolution. *J. Math. Biol.*, **34**, 511–532 (1996).
8. DeAngelis, D.L., Gross, L.J.: *Individual-based models and approaches in ecology: populations, communities and ecosystems*. Chapman & Hall, New York (1992).
9. DeAngelis, D.L., Mooij, W.M.: Individual-based modelling of ecological and evolutionary processes. *Ann. Rev. of Ecol., Evol., and Sys.*, **36**, 147–168 (2005).
10. Christensen, K., di Collobiano, S.A., Hall, M., Jensen, H.J.: Tangled nature: A model of evolutionary ecology. *J. Theor. Biol.*, **216**, 73–84 (2002).
11. Anderson, P., Jeldtoft Jensen, H.: Network properties, species abundance and evolution in a model of evolutionary ecology. *J. Theor. Biol.*, **232**, 551–558 (2005).
12. Avogadro di Collobiano, S., Christensen, K., Jensen, H.J.: The tangled nature model as an evolving quasi-species model. *J. Phys. A*, **36**, 883–891 (2003).
13. Hall, M., Christensen, K., di Collobiano, S.A., Jensen, H.J.: Time-dependent extinction rate and species abundance in a tangled-nature model of biological evolution. *Phys. Rev. E*, **66**, 011904 (2002).

14. Hubbell, S.: The Unified Neutral Theory of Biodiversity and Biogeography. Princeton University Press, Princeton, NJ 08540 (2001).
15. Rikvold, P.A., Zia, R.K.P.: Punctuated equilibria and  $1/f$  noise in a biological coevolution model with individual-based dynamics. *Phys. Rev. E*, **68**, 031913 (2003).
16. Zia, R.K.P., Rikvold, P.A.: Fluctuations and correlations in an individual-based model of evolution. *J. Phys. A*, **37**, 5135–5155 (2004).
17. Durrett, R., Levin, S.: Spatial models for species-area curves. *J. Theor. Biol.*, **179**, 119–127 (1996).
18. Magurran, A.E., Henderson, P.A.: Explaining the excess of rare species in natural species abundance distributions. *Nature*, **422**, 714–716 (2003).
19. Lawson, D., Jensen, H.J.: The species-area relationship and evolution. arXiv:q-bio.PE, 0412024 (2005).
20. Lawson, D., Jensen, H.J., Kaneko, K.: Diversity as a product of interspecific interactions. arXiv:q-bio.PE, 0505019 (2005).
21. Sevim, V., Rikvold, P.A.: Effects of correlated interactions in a biological coevolution model with individual-based dynamics. arXiv:q-bio.PE, 0507040 (2005).
22. Laird, S., Jensen, H.J.: The tangled nature model with inheritance and constraint: Evolutionary ecology restricted by a conserved resource. arXiv:q-bio.PE, 0510008 (2005).
23. Standish, R.K.: Ecolab: where to now? *Complexity International*, 3, (1996). (See <http://parallel.hpc.unsw.edu.au/rks/docs/newman-model/newman-model.html> for a plot of the full lifetime distribution.)
24. Chowdhury, D., Stauffer, D., Kunwar, A.: Unification of small and large time scales for biological evolution: deviations from power law. *Phys. Rev. Lett.*, **90**, 068101 (2003).
25. Chowdhury, D., Stauffer, D.: Food web based unified model of macro- and microevolution. *Phys. Rev. E*, **68**, 041901 (2003).
26. Chowdhury, D., Stauffer, D.: Sole-manrubia model of biological evolutions: some new insights. *Physica A*, **318**, 461–468 (2003).
27. Sole, R.V., Manrubia, S.C.: Extinction and self-organised criticality in a model of large scale evolution. *Phys. Rev. E*, **54**, 42–45 (1996).
28. Emerson, B.C., Kolm, N.: Species diversity can drive speciation. *Nature*, **434**, 1015–1017 (2005).
29. May, R.M. (ed): *Stability and Complexity in Model Ecosystems* in *Monographs in Population Biology*. Princeton University Press, Princeton, NJ (1974).
30. McCann, K.S.: The diversity stability debate. *Nature*, **405**, 228–233 (2000).
31. Haydon, D.T.: Maximally stable model ecosystems can be highly connected. *Ecology*, **81**, 2631–2636 (2000).
32. Dunne, J.A., Williams, R.J., Martinez, N.D.: Food web structure and network theory: the role of connectance and size. *Proc. Natl. Acad. Sci. USA*, **99**, 12917–12922 (2002).
33. Metzler, R., Klafter, J.: The random walk's guide to anomalous diffusion: a fractional dynamics approach. *Physics Reports*, **339**, 1–77 (2000).



## Relative Advantage and Fundamental Theorems of Natural Selection

József Garay

Research Group of Ecology and Theoretical Biology, Hungarian Academy of Sciences and L. Eötvös University, Department of Plant Taxonomy and Ecology, Pázmány P. sétány 1/C, H-1117 Budapest, Hungary; garayj@ludens.elte.hu

**Summary.** According to the tenet of Darwinian selection, a phenotype will spread only if its fitness is greater than the mean fitness of the entire population. It is, therefore, natural to introduce the notion of relative advantage of a replicator, which is defined as the expected fitness of this replicator minus the average fitness of the entire replicator population. For the general replicator dynamics, it is shown that the relative advantage of an offspring population over its parent population is proportional to the variance in fitness. The relationship between the proposed and earlier versions of the fundamental theorem of natural selection is also discussed.

**Key words:** Fitness variance, fundamental theorem of natural selection, relative advantage, replicator dynamics.

### 6.1 Introduction

In this chapter, we consider a sufficiently large population in which the individual phenotypes are uniquely determined genetically. We consider only the frequency-dependent selection process.

This chapter is centered around the following question: what function is optimized during natural selection such that its rate of increase equals the variance of the fitnesses?

Fisher's fundamental theorem of natural selection states that "*the rate of increase in the average fitness of a population is equal to the genetic variance of that population*" [5]. This theorem has been the subject of controversy and exegesis.<sup>1</sup> For instance, this theorem does not hold in evolutionary game theory where genotypic fitness is frequency dependent. For example, infanticide is a successful evolutionary strategy among lions and langurs [9]. This kind of phenotype, obviously, decreases the mean fitness of the population.

Ewens [3] redrafted the fundamental theorem of natural selection in the following way: *the partial change in mean fitness is equal to the additive genetic variance in*

---

<sup>1</sup> The historical details of this controversy can be traced from the references in [2,4,13,14].

*fitness divided by the mean fitness* (see also [13]). Ewens has substituted the average fitness by the partial change in the mean fitness.

The aim of this chapter is to reveal the relationship between selection and variance in a replicator population. We will see the simplest version of a fundamental theorem of natural selection which can be given in terms of the relative advantage. Moreover, in special cases we also see the connection between one version of Fisher's theorem and the proposed theorem, and that the notion of the partial change in mean fitness contains the notion of the relative advantage.

For this purpose, we have to recall the dynamics of the selection of proper replicators. Let us consider  $n$  different types of a given proper replicator. A replicator is proper if the principle of "*i-type from an i-type*" is valid. In other words, for the production of an  $i$ -type replicator the contribution of a parent  $i$ -type replicator is a must. Here we can think about an asexual population without mutation or a sexual diploid population where two alleles at a single locus determine the individual fitness and there is no mutation, either. In both cases replication is proper. Consider, for example, the first situation. Now the gamete distributions are the same as the allele distributions, and the gamete dynamics is nothing else than the replicator dynamics of the alleles. This is no surprise, because now each individual only reproduces its parental gametes.

Denote by  $F_i(x)$  the frequency-dependent fitness of an  $i$ -replicator and by  $F(x) := (F_1(x), F_2(x), \dots, F_n(x))$  the fitness vector of the population in state  $x \in S_n$ .<sup>2</sup> Using this notation, the average fitness of the population is  $x F(x) = \sum_{i=1}^n x_i F_i(x)$ , where  $x_i$  is the frequency of the  $i$ -replicator.

In the course of selection, the frequencies of the replicators will change. This change can be given by the *replicator dynamics* [10] formulated in discrete time as

$$x_i(t+1) = x_i \frac{F_i(x)}{x F(x)}, \quad (6.1)$$

and in continuous time as

$$\dot{x}_i = x_i (F_i(x) - x F(x)). \quad (6.2)$$

We have to emphasise that these dynamics are strictly based on proper replicators. This explains that the right-hand side of dynamics (6.1) and (6.2) are linearly proportional to the relative frequency of the replicator.

Now let us recall the definition of the relative advantage function [11]. According to the classical Darwinian theory, a phenotype will spread if it has greater fitness than the others. Based on this, the definition of *relative advantage function* for a proper replicator population is the following:

$$A : S_n \times S_n \rightarrow \mathbb{R}, \quad A(y, z) := y F(z) - z F(z). \quad (6.3)$$

This function describes the relative advantage of state  $y$  over state  $z$ , since it is positive only if the average fitness of a subpopulation,  $y F(z)$ , in which the distribution of replicators is  $y$ , is greater than the average fitness of the whole population with distribution

<sup>2</sup>  $S_n$  denotes the standard simplex of the  $n$ -dimensional space.

$z, zF(z)$ . This implies that the frequency of subpopulation  $y$  increases.<sup>3</sup> Finally, observe that the right-hand side of the replicator dynamics (6.2) is the frequency of the  $i$ -replicator multiplied by their relative advantage.

## 6.2 The Fundamental Theorem of Natural Selection Based on Relative Advantage

We are in a position to formulate a new and the simplest possible fundamental theorem of natural selection. First, let us consider proper replicators.

### 6.2.1 Discrete Case

Assume that we have a discrete time scale. In this case, we have the following statement: *the relative advantage of the offspring generation over its parent generation is always positive and is proportional to the variance of the fitness of its parent population.* Indeed, according to the discrete replicator dynamics (6.1), after the operation of selection, in the offspring generation the distribution of the replicator can be given by

$$x(t+1) = \left( \frac{x_1(t)F_1(x(t))}{x(t)F(x(t))}, \frac{x_2(t)F_2(x(t))}{x(t)F(x(t))}, \dots, \frac{x_n(t)F_n(x(t))}{x(t)F(x(t))} \right).$$

We have to assume that the number of offspring of an  $i$ -replicator, i.e.,  $F_i(x(t))$  is positive to avoid division by zero. Now the relative advantage of the offspring generation over its parental one can be calculated as

$$\begin{aligned} (x(t+1) - x(t))F(x(t)) &= \sum_{i=1}^n \frac{x_i(t)F_i(x(t))}{x(t)F(x(t))} F_i(x(t)) - \sum_{i=1}^n x_i(t)F_i(x(t)) \\ &= \frac{1}{x(t)F(x(t))} \left[ \sum_{i=1}^n x_i(t) (F_i(x(t)))^2 - (x(t)F(x(t)))^2 \right] \\ &= \frac{\text{Var}(F(x(t)))}{x(t)F(x(t))}. \end{aligned} \quad (6.4)$$

In particular, in an asexual population offspring are fitter than their parents when competing against the parents' state.

### 6.2.2 Continuous Case

The above statement is true for the continuous-time version of the replicator dynamics as well. More specifically, we claim an analogue of the fundamental theorem for the

<sup>3</sup> The relative advantage can be used in evolutionary game theory to define an evolutionarily stable state (ESS): an  $x^* \in S_n$  is an ESS if and only if  $A(x^*, x) = x^*F(x) - xF(x) > 0$  for all  $x^* \in S_n$ ,  $x^* \neq x$  near  $x^*$  [16]. Let us observe that the relative advantage of an ESS as a function of its second variable attains a local minimum at  $x^*$ , the ESS.

continuous-time version of the replicator dynamics (6.2): *the instantaneous rate of increase in the population's relative advantage over its current state is equal to the variance of the replicators' fitnesses.*<sup>4</sup> Indeed, for a fixed  $z$  and time-dependent  $x$ ,

$$\frac{d}{dt}A(x, z) = \dot{x}F(z).$$

Putting  $z = x$

$$\begin{aligned} \dot{x}F(z)|_{z=x} &= \sum_{i=1}^n x_i [F_i(x) - xF(x)]F_i(x) \\ &= \sum_{i=1}^n x_i [F_i(x) - xF(x)]^2 = \text{Var}(F(x)). \end{aligned} \quad (6.5)$$

The above two arguments are obviously true for the evolutionary matrix game, the classical Fisher's selection model and the single autosomal locus model when the individual's fitness can be given by an evolutionary game-theoretical model. In the third model, the fitness of  $A_i$  allele  $F_i(x) := \sum_j p_j \sum_{k,l} a_{ij,kl} p_k p_l$ , where  $p_i$  is the frequency of allele  $A_i$  and  $a_{ij,kl}$  is the  $A_i A_j$  zygote's pay-off when it interacts with  $A_k A_l$  zygote [7]. We emphasise that in all models it is supposed that there is no mutation during the selection process, and this is why the replicators are proper in these examples.

### 6.2.3 General Replicators with Panmixis

To see that the above reasoning can be extended beyond proper replicator, let us consider  $n$  different types of a given general replicator. A replicator is general if the principle of  $i$ -type from an  $i$ -type does not hold. Let us consider a sufficiently large, panmictic diploid sexual population where the phenotypes are genetically determined by multiple loci with recombination and/or mutation between existing alleles. Recombination produces chromosomes different from those in parental zygotes. Moreover, mutation injures the principle of  $i$ -types gamete from  $i$ -types gamete.

Now we introduce some notation. Let  $x_i$  be the relative frequency of the  $G_i$  gamete types. Let  $w_{ij}(x)$  be an arbitrary frequency-dependent fitness (viability) function of zygote  $G_i G_j$  ( $i, j = 1, 2, \dots, n$ ),  $m_{i,kl}$  be the probability that zygotes  $G_k G_l$  produce gamete  $G_i$ . Of course,  $\sum_i m_{i,kl} = 1$  for all zygotes  $G_k G_l$ . Since we assume that the population is panmictic, the relative frequency of the ordered genotype  $G_i G_j$  is  $x_i x_j$ . Thus, we get the following discrete gamete dynamics:

$$x_i(t+1) = \frac{\sum_{k,l} m_{i,kl} w_{kl}(x(t)) x_k(t) x_l(t)}{\sum_i \sum_{k,l} m_{i,kl} w_{kl}(x(t)) x_k(t) x_l(t)}$$

<sup>4</sup> This statement is a generalization of an earlier result [8]: the relative advantage of an ESS decreases in the course of replicator selection and the rate of decrease is proportional to the variance of the fitnesses of the replicators.

$$= \frac{\sum_{k,l} m_{i,k,l} w_{kl}(x(t)) x_k(t) x_l(t)}{\sum_{k,l} w_{kl}(x(t)) x_k(t) x_l(t)}. \quad (6.6)$$

For continuous time we have the following dynamics:

$$\dot{x}_i = x_i \sum_{k,l} m_{i,k,l} w_{kl}(x) x_k x_l - x_i \sum_{k,l} w_{kl}(x) x_k x_l. \quad (6.7)$$

In general, such an equation describes a multiplication process in which a replicator may also be produced by a replicator of a different type [1, 12, 17].

For the generalization of the concept of fitness, it is suitable to introduce the notation of *production rate of a gamete type* present in the parental population. Let the production rate of an  $i$ -gamete be the number of  $i$ -gametes in the offspring generation divided by the number of  $i$ -gametes in the parental generation. Formally, for all  $x \in S_n$  and  $i = 1, 2, \dots, n$  with  $x_i > 0$ , we define the production rate of the  $i$ -gamete as

$$f_i(x(t)) = \frac{\sum_{k,l} m_{i,k,l} w_{kl}(x(t)) x_k(t) x_l(t)}{x_i(t)}. \quad (6.8)$$

Observe in the definition of production rate that the assumption of a large enough population is important. If we have a small population and a huge number of different gamete types then all possible gamete types cannot exist at any point of time, thus  $x_i(t) = 0$  may occur. Moreover, if the population is small then genetic drift can mask the effect of selection.

Using the production rate, we rewrite the dynamics (6.6) and (6.7) as follows:

$$x_i(t+1) = x_i(t) \frac{f_i(x(t))}{\sum_k x_k(t) f_k(x(t))}. \quad (6.9)$$

For the continuous-time scale, we have the following dynamics:

$$\dot{x}_i = x_i \left( f_i(x) - \sum_k x_k f_k(x) \right). \quad (6.10)$$

Based on the notion of production rate, the relative advantage function for a gamete population can be defined as

$$A : S_n \times S_n \rightarrow \mathbb{R}, \quad A(y, z) := yf(z) - zf(z). \quad (6.11)$$

Using the notion of production rate, the fundamental theorems of natural selection proposed in (6.4) and (6.5) are valid without any change for general replicators, as well.

### 6.3 Connection to Fisher's Theorem

In order to see the connection between Fisher's fundamental theorem of natural selection and the one proposed here (6.5), we have to recall the well-known proof of the

continuous version of Fisher's theorem (see, e.g., [10]). Let us consider the classical Fisher's selection model, which considers a diploid, panmictic sexual population, in which abiotic selection takes place at the zygotic level. The marginal fitness of alleles is given by  $F_i(x) := (Ax)_i$ , where the viability matrix  $A$  is symmetric (i.e.,  $a_{ij} = a_{ji}$  for all  $i, j$ ) and  $(Ax)_i$  denotes the  $i$ th coordinates of vector  $Ax$ . Using these notions, the average fitness of the allele population is given by  $xAx$  and the replicator dynamics (6.2) is rewritten as

$$\dot{x}_i = x_i((Ax)_i - xAx). \quad (6.12)$$

In this case, the average fitness is a Lyapunov function with respect to Fisher's selection model, and its derivative with respect to Fisher's selection equation (6.12) is the variance of the marginal fitness of alleles. Indeed, since the viability matrix  $A$  is symmetric, the gradient of the average fitness is  $\text{grad } xAx = 2((Ax)_1, (Ax)_2, \dots, (Ax)_n)$ . Thus, its derivative with respect to dynamics (6.12) is

$$\begin{aligned} (\text{grad } xAx)\dot{x} &= 2 \sum_i x_i((Ax)_i - xAx)(Ax)_i = 2 \sum_i x_i((Ax)_i - xAx)^2 \\ &= 2\text{Var}(Ax). \end{aligned} \quad (6.13)$$

If the viability matrix  $A$  is not symmetric then this proof does not work.

Now, let us compare (6.5) and the above proof of Fisher's fundamental theorem (6.13). We recognize first that the proposed version of the fundamental theorem is based strictly on Fisher's theorem, since the proof of the proposed version is part of the proof of Fisher's theorem. Second, observe that  $\sum_i x_i((Ax)_i - xAx)(Ax)_i$  is, in essence, the relative advantage of the offspring generation over its parents. Indeed, according to the dynamics (6.3),  $x_i(t + \Delta t) - x_i(t) \approx \Delta t x_i((Ax)_i - xAx)$ , thus the relative advantage in  $\Delta t$  is  $\sum_i (x_i(t + \Delta t) - x_i(t))(Ax)_i \approx \Delta t \sum_i x_i((Ax)_i - xAx)(Ax)_i$ .

## 6.4 Relative Advantage Versus Partial Change in Mean Fitness

Here the connection between the proposed fundamental theorem (6.4) and Ewens's theorems will be investigated. We will do this in three steps. First, we recall the concept of partial change in mean fitness. Second, we will study the residual of average effects. Third, we will see that the notion of partial change of mean fitness "contains" the concepts of relative advantage.

### 6.4.1 Ewens's Concept

To get insight into the connection between the partial change in mean fitness and the relative advantage we have to recall the notion of partial change in mean fitness. We will follow the derivation of Ewens's version of the fundamental theorem for one locus [3] and briefly recall all points of [3] used here. Let  $p_i$  denote the frequency of allele

$A_i$ , and  $P_{ij}$  denote the frequency and  $w_{ij}$  the fitness (viability) of zygote  $A_i A_j$  ( $i, j = 1, 2, \dots, n$ ). Ewens [3] considered Mendelian systems, thus  $w_{ij} = w_{ji}$ . The current frequency of allele  $A_i$  is

$$p_i = \sum_j P_{ij} \quad (6.14)$$

and, in the next generation, this frequency

$$p'_i = \frac{\sum_j P_{ij} w_{ij}}{w(p)}, \quad (6.15)$$

where  $\bar{w}(P) = \sum_{i,j} P_{ij} w_{ij}$  is the mean fitness of the population. Using this notation, Ewens [3] introduced the following notions, based on [6, 15]. The *average excess* of allele  $A_i$  is defined by

$$a_i(p) = \frac{\sum_j P_{ij} (w_{ij} - \bar{w}(P))}{p_i}. \quad (6.16)$$

In Ewens's version of the fundamental theorem, even more important is the notion of the average effect of allele  $A_i$  which is defined by a least squares procedure. Let  $\alpha_i$  denote the *average effect* of allele  $A_i$ . Then  $\alpha_1, \alpha_2, \dots, \alpha_n$  are chosen so as to minimize

$$\sum_{i,j} P_{ij} (w_{ij} - \bar{w}(P) - \alpha_i - \alpha_j)^2, \quad (6.17)$$

subject to

$$\sum_j p_j \alpha_j = 0. \quad (6.18)$$

Of course, the average effect depends on the parental allele distribution. Moreover, Ewens [3] noted that if  $P_{ij} = p_i p_j$  then the average effect and the average excess are equal.

Now we are at the basic concept of the Ewens version, namely the concept of the *partial change in mean fitness* which is defined as follows:

$$\sum_{i,j} P_{ij} (\bar{w}(P) + \alpha_i + \alpha_j). \quad (6.19)$$

The additive genetic variance is given by Ewens as

$$\sigma^2 = 2 \sum_i p_i a_i \alpha_i = 2 \bar{w}(P) \sum_i (\Delta p_i) \alpha_i,$$

where  $\Delta p_i = p_i(t+1) - p_i(t)$ . Ewens' version of the fundamental theorem reads

$$\begin{aligned}
\sum_{i,j} (P'_{ij} - P_{ij})(\bar{w}(P) - \alpha_i - \alpha_j) &= 2 \sum_i \alpha_i \sum_j (P'_{ij} - P_{ij}) \\
&= 2 \sum_i (\Delta p_i) \alpha_i = \frac{\sigma^2}{w(p)}. \quad (6.20)
\end{aligned}$$

This says that the *partial change in mean fitness is proportional to the fitness variance of the alleles*.

In what follows we make a few remarks on the average effect and partial change in the mean fitness.

#### 6.4.2 Residual of Average Effect

To demonstrate the background of the average effect let us see a case where the minimization problem defined by (6.17), (6.18) is without residual for all allele distributions. Function (6.17) is equal to zero if and only if  $w_{ij} = \bar{w}(P) + \alpha_i + \alpha_j$  for all  $i, j$ . This equality means that the fitness components of the alleles are additive.<sup>5</sup> The widely used fitness additivity condition is rather restrictive since it reduces the degree of freedom of the symmetric fitness matrix and excludes, for instance, the case of overdominance. Moreover, in this additive case the fitness of an allele is  $w_i(p) = \bar{w}(P) + \alpha_i$ , so the relative advantage of an allele (i.e.,  $w_i(p) - \bar{w}(P) = \alpha_i$ ) does not depend on the allele distribution, which is a very special frequency dependence. Thus, the minimization problem defined by (6.17), (6.18) is with residual in general.

Let us consider a panmictic but non-additive case, where the residual of (6.17) is given in the following.

*Remark 1* When  $P_{ij} = p_i p_j$  using the previous notation and observation (recall  $P_{ij} = p_i p_j$  implies  $\alpha_i = a_i(p) = w_i(p) - \bar{w}(P)$  for all  $i = 1, 2, \dots, n$ ) it is not hard to see that (6.17) becomes

$$\begin{aligned}
\sum_{i,j} P_{ij} (w_{ij} - \bar{w}(P) - \alpha_i - \alpha_j)^2 \\
= \sum_{i,j} P_{ij} (w_{ij} - \bar{w}(P))^2 - 2 \sum_{i,j} p_i (w_i(p) - \bar{w}(P))^2. \quad (6.21)
\end{aligned}$$

This means that the residual of (6.17) for the minimizing values of  $\alpha_i$  under the constraint (6.18) can be given as a difference of the fitness variance at the zygote level and two times the fitness variance at the allelic level. To my knowledge, the residual of the minimalization problem of (6.17), (6.18) is not given in the literature.

Observe that optimization model (6.17), (6.18) is an additive estimation of the effects of alleles, which is surprising, since it is unusual to base a theoretical setup on a statistical approach. In my view, the intuitive strength of the optimization model (6.17), (6.18) is that it provides a fundamental theorem in a general genetic situation. Then the question is what the theoretical interpretation of constraint (6.18) is in the case of non-additive fitness.

<sup>5</sup> An easy calculation shows that the constraint (6.18) must hold in this case.



## 6.5 Connection Between Partial Change and Relative Advantage

In this subsection, we will see a possible interpretation of partial change in mean fitness. For this purpose, we will see first, in Remarks 2 and 3, two important connections between the notions of relative advantage and of partial change in mean fitness.

*Remark 2* Let us assume that  $w_{ij} = \alpha_i + \alpha_j$  for all  $i, j = 1, 2, \dots, n$ . Then we have

$$\sum_{i,j} (P'_{ij} - P_{ij})(\bar{w}(P) + \alpha_i + \alpha_j) = \sum_{i,j} (P'_{ij} - P_{ij})(\alpha_i + \alpha_j) = \sum_{i,j} (P'_{ij} - P_{ij})w_{ij}, \quad (6.22)$$

so the partial change in the mean fitness is equal to the relative advantage of the offspring zygote population over the parent zygote population.

*Remark 3* Let us assume  $P_{ij} = p_i p_j$ . Then the average excess of allele  $A_i$  is, apart from the multiplication by 2, equal to the relative advantage of allele  $A_i$  over the population  $p$ . Formally,  $A_i$  is identified with the  $i$ -replicator and  $F_i(p) = w_i(p) = \sum_j w_{ij} p_j$  denotes the fitness of allele  $A_i$ . Using  $P_{ij} = p_i p_j$  and  $\bar{w}(p) = \sum_{i,j} w_{ij} p_j$  we get the definition of average excess rewritten as follows:

$$\begin{aligned} a_i(p) &= \sum_j \frac{p_i p_j (w_{ij} - \sum_{k,l} w_{kl} p_k p_l)}{p_i} = \sum_j p_j \left( w_{ij} - \sum_{k,l} w_{kl} p_k p_l \right) \\ &= w_i(p) - \bar{w}(p). \end{aligned} \quad (6.23)$$

Moreover, under the condition that  $P_{ij} = p_i p_j$ , we already know that the average effect and the average excess are equal; thus, the average effect and the relative advantage are equal as well. Therefore, for the partial change in mean fitness we obtain

$$\begin{aligned} &\sum_{i,j} (P'_{ij} - P_{ij})(\bar{w}(p) + \alpha_i + \alpha_j) \\ &= \sum_{i,j} (p'_i p'_j - p_i p_j)(\bar{w}(p) + w_i(p) - \bar{w}(p) + w_j(p) - \bar{w}(p)) \\ &= \sum_{i,j} (p'_i p'_j - p_i p_j)(w_i(p) + w_j(p)) = 2 \sum_{i,j} (p'_i - p_i)w_i(p). \end{aligned} \quad (6.24)$$

Thus, apart from the multiplication by 2, the partial change in mean fitness is equal to the relative advantage of the offspring generation of alleles over its parental allele population. Thus, Ewens's version and the proposed version of the fundamental theorem are essentially the same under random mating.

Based on Remarks 2 and 3 it is intuitively clear that there is a deep connection between the partial change in mean fitness and the relative advantage. Now, from the viewpoint of the notion of relative advantage, a possible interpretation of partial change in the mean fitness is given. In the definition of Ewens's partial change in the mean fitness, there are two points.

1. What is the connection between the average fitness of the whole population and the average effects of alleles? We have the following:

$$\bar{w}(P) = \sum_{i,j} P_{ij} w_{ij} = \sum_{i,j} P_{ij} (\bar{w}(P) + \alpha_i + \alpha_j) = \bar{w}(P) + 2 \sum_i p_i \alpha_i. \quad (6.25)$$

Thus, equality (6.25) strictly depends on constraint (6.18). It seems that this is the only biological relevance of constraint (6.18).

2. The second point concerns the relative advantage of the offspring zygote generation over its parents,  $\sum_{i,j} (P'_{ij} - P_{ij}) w_{ij}$ . Similarly to (6.25), if  $w_{ij}$  is replaced by  $\bar{w}(P) + \alpha_i + \alpha_j$ , then we get the concept of Ewens's formula (6.19). In other words, if we take the relative advantage of zygotes but we approximate fitness with the average effects, then we obtain the partial change in mean fitness. In this sense, the notion of partial change in mean fitness includes that of relative advantage. In general, however, we have

$$\sum_{i,j} P_{ij} (\bar{w}(P) + \alpha_i + \alpha_j) \neq \sum_{i,j} (P'_{ij} - P_{ij}) w_{ij}, \quad (6.26)$$

due to the residual of the average effect (see Remark 1).

Let us observe that Ewens's approach is "zygote centered," as was the original concepts of Fisher, in the sense that the definition of partial change in the mean fitness is based on the relative frequencies of the zygotes.

There is, however, another possibility. Let us consider Fisher's selection equation (6.12), which is "allele centered," in the sense that the state of the population is described in terms of the allele distribution. If we try to follow Ewens's setup but at the level of alleles we need neither the average excess nor the average effect of alleles, since in Fisher's selection equation (6.12) the allelic fitness determines the whole process of selection. Following Ewens's setup, the partial change in mean fitness at the allelic level could be defined as  $\sum_{i,j} (p'_i - p_i) w_i(p)$  which is nothing else than the relative advantage of the offspring allele generation over its parental population (cf. second point above).

Summing up, the notion of partial change of the zygote mean fitness contains the notion of relative advantage of the offspring allele population over its parent one. Furthermore, Ewens's version is "zygote centered" while the proposed version is "allele centered."

## 6.6 Summary

In this chapter, the simplest fundamental theorem of natural selection is given: the relative advantage of the offspring generation over its parent generation is always positive and is proportional or equal to the variance of fitness in the parent population in the discrete- or continuous-time model, respectively.

Now a game-theoretical interpretation of this statement is given. During Darwinian selection, a phenotype will spread only if its fitness is greater than the mean fitness of

the whole population. Thus, it is natural to ask: What kind of improvement can happen during natural selection? Now let us consider a frequency-dependent individual fitness. In this chapter, we see that from generation to generation, the offspring generation is better against its parental population than the parental population against itself. In this sense, natural selection improves competition ability from generation to generation. Moreover, we also see that this improvement is proportional to the variance of the marginal fitness of replicators.

Moreover, we have shown that the relative advantage plays an important rule in Fisher's (see Section 6.3) and Ewens's version (see Section 6.4) of the fundamental theorems of natural selection, as well.

## Acknowledgments

The author expresses his gratitude to Éva Kisdi, to an anonymous referee, to János Podani and to Ross Cressman for their comments. This research was supported by the National Scientific Research Fund (OTKA No. T029320, No. T037271). The final version of this chapter was completed while the author was a fellow at Konrad Lorenz Institute for Evolution and Cognition Research. The author is a grantee of the János Bolyai Scholarship.

## References

1. Akin, E.: *The Geometry of Population Genetics*. Springer-Verlag, Berlin, Heidelberg, New York (1979).
2. Edwards, A. W. F.: The fundamental theorem of natural selection. *Biol. Rev.*, **69**, 443–474 (1994).
3. Ewens, W. J.: An interpretation and proof of the fundamental theorem of natural selection. *Theor. Pop. Biol.*, **36**, 167–180 (1989).
4. Ewens, W. J.: An optimizing principle of natural selection in evolutionary population genetics. *Theor. Pop. Biol.*, **42**, 333–346 (1992).
5. Fisher, R. A.: *The Genetical Theory of Natural Selection*. Clarendon Press, Oxford (1930).
6. Fisher, R. A.: Average excess and average effect of a gene substitution. *Ann. Eugen.*, **11**, 53–63 (1941).
7. Garay, J., Varga, Z.: Evolutionarily stable allele distributions. *J. Theor. Biol.*, **191**, 163–172 (1998).
8. Garay, J., Varga, Z.: Relative advantage: a substitute for mean fitness in Fisher's fundamental theorem? *J. Theor. Biol.*, **201**, 215–218 (1999).
9. Hausfater, G., Aref, S., Cairns, S. J.: Infanticide as an alternative male reproductive strategy in langurs: a mathematical model. *J. Theor. Biol.*, **94**, 391–412 (1982).
10. Hofbauer, J., Sigmund, K.: *Evolutionary Games and Population Dynamics*. Cambridge University Press, London (1998).
11. Hofbauer, J., Sigmund, K.: Adaptive dynamics and evolutionary stability. *Appl. Math. Lett.*, **3**, 75–79 (1990).
12. Kimura, M.: On the change of population fitness by natural selection. *Heredity*, **12**, 145–167 (1958).
13. Lessard, S.: Fisher's fundamental theorem of natural selection. *Theor. Pop. Biol.*, **52**, 119–136 (1997).

14. Nagylaki, T.: Evolution under fertility and viability selection. *Proc. Nat. Acad. Sci. U.S.A.*, **88**, 2402–2406 (1991).
15. Price, G. R.: Fisher's fundamental theorem made clear. *Ann. Hum. Genet.*, **36**, 129–140 (1972).
16. Pohley, H. J., Thomas, B.: Non-linear ESS-models and frequency dependent selection. *BioSystems*, **16**, 87–100 (1983).
17. Shahshahani, S.: *A New Mathematical Framework for the Study of Linkage and Selection*. Memoirs Series of Amer. Math. Soc. **17(211)** (1979).

# Competitive Exclusion Between Year-Classes in a Semelparous Biennial Population

Ryusuke Kon

Faculty of Mathematics, Kyushu University, Hakozaki 6-10-1, Higashi-ku, Fukuoka 812-8581, Japan; kon-r@math.kyushu-u.ac.jp

**Summary.** We investigate competitive exclusion between two reproductively isolated year-classes in the Leslie matrix model for a semelparous biennial population. Our results show that competitive exclusion occurs if competition is more severe between than within year-classes. Our criterion is applicable even if the model exhibits complex behavior.

**Key words:** Leslie matrix, permanence, average Lyapunov function.

## 7.1 Introduction

A species is said to be semelparous if it reproduces only once during its lifetime. There are numerous examples of semelparous species. Pacific salmon and many insects such as cicadas are typical examples of semelparous species.

If, in addition to semelparity, the individuals reproduce at the same chronological age, then the population can be divided into reproductively isolated year-classes according to the year of birth. For example, consider the 17-year periodical cicada, inhabiting the Eastern United States. The life cycle of this cicada has a fixed length of 17 years and the adults reproduce at the end of their life [18, 19] (see also [20, 22]). Therefore, the 17-year periodical cicada can be divided into 17 reproductively isolated year-classes according to the year of birth. None of the year-classes contributes to the reproduction of the others. We can find many other examples of semelparous species with several reproductively isolated year-classes.

It is known that the existence of reproductively isolated year-classes plays a key role in the synchronous behavior of insect emergence. For example, consider again the 17-year periodical cicada. In a given region, the adults emerge synchronously from the ground every seventeenth year. Thus, in intervening years, we cannot see any adults above the ground. Such synchronous emergence results from elimination of all but one year-class because once a reproductively isolated year-class is eliminated, it cannot reappear spontaneously. On the other hand, if year-classes are not reproductively isolated, then temporally eliminated year-classes can reappear due to the reproduction of the others. There are many other examples of insects whose adults emerge synchronously (see [1, 10]).

We have to note that existence of reproductively isolated year-classes is a necessary but not a sufficient condition for synchronous emergence. Competition between year-classes is regarded as one of the important factors leading to synchronous emergence. Bulmer [1] studied the Leslie matrix model with  $n$  year-classes and found a stable solution corresponding to synchronous emergence when competition is more severe between than within year-classes. Davydova et al. [8] concentrated on the case  $n = 2$ , i.e., the case of biennials, and obtained a mathematical condition for stability of periodic solutions corresponding to synchronous emergence. There are several studies addressing the stability of such interesting solutions (e.g., see [6, 7, 23]). However, we have few criteria that can properly evaluate the possibility of synchronization even if the model has a complex solution (but see [21]). In this chapter, we concentrate on the biennial case and obtain a criterion for synchronous emergence that is applicable irrespective of the dynamical complexity of the model.

This chapter is organized as follows. In the next section, we introduce the Leslie matrix model for a semelparous population with  $n$  reproductively isolated year-classes. Furthermore, by addressing the biennial case, we show some important properties of the Leslie matrix model for a semelparous population. In Section 7.4, we obtain the main results of this paper. Our main results give sufficient conditions both for coexistence and for competitive exclusion between two reproductively isolated year-classes. The final section includes concluding remarks. Some mathematical results that are necessary for proving our main results are given in the Appendix.

## 7.2 Leslie Matrix Model for a Semelparous Population

Let us consider the following Leslie matrix model for a semelparous population (see [2, 3] for the Leslie matrix model):

$$\mathbf{x}(t+1) = A(\mathbf{x}(t))\mathbf{x}(t), \quad t \in \mathbb{Z}_+ := \{0, 1, 2, \dots\}, \quad (7.1)$$

where  $\mathbf{x} = (x_0, x_1, \dots, x_{n-1})^\top$  and

$$A(\mathbf{x}) = \begin{pmatrix} 0 & 0 & \cdots & 0 & \phi s_{n-1} \sigma_{n-1}(\mathbf{x}) \\ s_0 \sigma_0(\mathbf{x}) & 0 & \cdots & 0 & 0 \\ 0 & s_1 \sigma_1(\mathbf{x}) & \cdots & 0 & 0 \\ \vdots & \vdots & \ddots & \vdots & \vdots \\ 0 & 0 & \cdots & s_{n-2} \sigma_{n-2}(\mathbf{x}) & 0 \end{pmatrix}.$$

In this model, the population is divided into  $n$  age-classes according to the chronological age. The density (or number) of each age-class  $i$  is denoted by  $x_i$ . The parameter  $s_i$  denotes the probability of surviving the  $i$ th age-class in the absence of density dependence. The function  $\sigma_i(\mathbf{x})$  represents the intensity of density dependence on  $s_i$ . The parameter  $\phi$  denotes the number of offspring produced by one individual of the last age-class  $n - 1$ . It is assumed that these parameters and functions satisfy

$$s_i \in (0, 1], \quad \phi > 0, \quad \sigma_i : \mathbb{R}_+^n \rightarrow (0, 1],$$

where  $\mathbb{R}_+^n$  is the non-negative cone, i.e.,  $\mathbb{R}_+^n = \{\mathbf{x} \in \mathbb{R}^n : x_0 \geq 0, x_1 \geq 0, \dots, x_{n-1} \geq 0\}$ . The above assumption for the function  $\sigma_i$  implies that the population density always reduces the survival probability. Note that the function  $\sigma_{n-1}$  can also be regarded as the density dependence function for the fertility  $\phi$  or for both  $s_{n-1}$  and  $\phi$ . It is clear that this model assumes that the individuals can reproduce only once at the end of their life.

For mathematical reasons, we focus on the case where the functions  $\sigma_i$  are defined by

$$\sigma_i(\mathbf{x}) = \exp \left[ - \sum_{j=0}^{n-1} a_{ij} x_j \right].$$

Then the survival probability decreases as the population density increases. This implies that there exists competition between year-classes. The intensity of competition is determined by the positive constants  $a_{ij} > 0, i, j \in \{0, 1, \dots, n-1\}$ . As  $a_{ij}$  increases, the survival probability of the year-class  $i$  is strongly reduced by the year-class  $j$ . Under this assumption on  $\sigma_i$ , our model is identical to the model studied by Bulmer [1].

If  $n = 2$ , the Leslie matrix model is reduced to

$$\begin{cases} x_0(t+1) = \phi s_1 x_1(t) \exp[-a_{10} x_0(t) - a_{11} x_1(t)] \\ x_1(t+1) = s_0 x_0(t) \exp[-a_{00} x_0(t) - a_{01} x_1(t)] \end{cases} \quad (7.2)$$

If  $a_{10} = \alpha a_{11}$  and  $a_{00} = \alpha a_{01}$  for some  $\alpha > 0$ , then this model is reduced to the model studied by Davydova et al. [8]. Let  $f : \mathbb{R}_+^2 \rightarrow \mathbb{R}_+^2$  be the right-hand side of (7.2). Define  $S_0$  and  $S_1$  as follows:

$$S_0 = \{\mathbf{x} \in \mathbb{R}_+^2 : x_0 = 0\}, \quad S_1 = \{\mathbf{x} \in \mathbb{R}_+^2 : x_1 = 0\}.$$

The sets  $S_0$  and  $S_1$  correspond to the  $x_1$ - and  $x_0$ -axes, respectively. We can recognize from (7.2) that if  $\mathbf{x} \in S_0$  (resp.  $\mathbf{x} \in S_1$ ), then  $f(\mathbf{x}) \in S_1$  (resp.  $f(\mathbf{x}) \in S_0$ ). Moreover, if  $\mathbf{x} \in \mathbb{R}_+^2 \setminus (S_0 \cup S_1)$ , then  $f(\mathbf{x}) \in \mathbb{R}_+^2 \setminus (S_0 \cup S_1)$ . Therefore, both  $\mathbb{R}_+^2 \setminus (S_0 \cup S_1)$  and  $S_0 \cup S_1$  are forward invariant. The interesting feature of (7.2) is that  $f(S_0) \subset S_1$  and  $f(S_1) \subset S_0$ . This implies that every orbit  $\{\mathbf{x}(t)\}_{t \in \mathbb{Z}_+}$  with  $\mathbf{x}(0) \in S_0 \cup S_1$  visits  $S_0$  and  $S_1$  alternately. This kind of orbit is called a synchronous orbit (e.g., see [4, 15]). A synchronous orbit corresponds to the periodical emergence of insects since along a synchronous orbit we observe the adults only every other year.

By the linearization of (7.2) at the trivial fixed point  $\mathbf{0}$ , we have

$$\begin{cases} x_0(t+1) = \phi s_1 x_1(t) \\ x_1(t+1) = s_0 x_0(t) \end{cases}.$$

This linear system is stable if every eigenvalue  $\lambda$  of the non-negative matrix

$$\begin{pmatrix} 0 & \phi s_1 \\ s_0 & 0 \end{pmatrix}$$

satisfies  $|\lambda| < 1$  and unstable if  $|\lambda| > 1$ . Define  $\mathcal{R}_0 := \phi_{s_0 s_1}$ . We can show that  $|\lambda| > 1$  if  $\mathcal{R}_0 > 1$  and  $|\lambda| < 1$  if  $\mathcal{R}_0 < 1$ . Hence, the trivial fixed point (7.2) is locally stable if  $\mathcal{R}_0 < 1$  and unstable if  $\mathcal{R}_0 > 1$ . The number  $\mathcal{R}_0$  is called the basic reproduction ratio and it is identical to the number of offspring per individual per lifetime.

### 7.3 Preliminary Results

In this section, we list some preliminary results. These results are necessary to show our main results, which appear in Section 7.4.

First, we consider the boundedness of solutions. The following lemma shows that all solutions of (7.2) are attracted by some bounded set.

**Proposition 1 (Lemma 4.1 [16])** *Let  $C = [0, \mathcal{R}_0/(a_{00}e)] \times [0, \mathcal{R}_0/(a_{11}e)]$ . Then the compact set  $B = C \cup f(C)$  is an absorbing set for  $\mathbb{R}_+^2$ , i.e.,  $f(B) \subset B$  and for every  $\mathbf{x} \in \mathbb{R}_+^2$  there exists a  $T > 0$  such that  $f^T(\mathbf{x}) \in B$  holds.*

The following lemma shows that if the basic reproduction ratio  $\mathcal{R}_0$  is less than one or equal to one, then the population goes extinct irrespective of the initial population densities.

**Proposition 2 (Lemma 4.2 [16])** *If  $\mathcal{R}_0 \leq 1$  holds, then*

$$\lim_{t \rightarrow \infty} (x_0(t), x_1(t)) = (0, 0)$$

*holds for all  $(x_0(0), x_1(0)) \in \mathbb{R}_+^2$ .*

If  $\mathcal{R}_0 > 1$ , then we can show that the population can survive in the sense of permanence, which is defined as follows.

**Definition 1** *System (7.2) is said to be permanent if there exist positive constants  $\delta > 0$  and  $D > 0$  such that*

$$\delta \leq \liminf_{t \rightarrow \infty} (x_0(t) + x_1(t)) \leq \limsup_{t \rightarrow \infty} (x_0(t) + x_1(t)) \leq D$$

*holds for all  $(x_0(0), x_1(0)) \in \mathbb{R}_+^2$  with  $x_0(0) + x_1(0) > 0$ .*

In fact, by using the above two propositions with Theorem 3 [17], we can obtain the following proposition.

**Proposition 3 (Theorem 4.4 [16])** *System (7.2) is permanent if and only if  $\mathcal{R}_0 > 1$  holds.*



## 7.4 Main Results

Since the population cannot persist under the assumption  $\mathcal{R}_0 \leq 1$  (see Proposition 2), we concentrate on the case  $\mathcal{R}_0 > 1$ .

Let  $\gamma_+(\mathbf{x}) = \{\mathbf{x}, f(\mathbf{x}), f^2(\mathbf{x}), \dots\}$ . Proposition 3 ensures that if  $\mathcal{R}_0 > 1$ , then there exists a compact set  $M \subset \mathbb{R}_+^2$  such that  $M \cap \{\mathbf{0}\} = \emptyset$  and  $\gamma_+(\mathbf{x}) \cap M \neq \emptyset$  for every  $\mathbf{x} \in \mathbb{R}_+^2 \setminus \{\mathbf{0}\}$ . In this case, by using Lemma 2.1 of [13], we can construct a forward invariant compact set  $X \subset \mathbb{R}_+^2$  such that  $X \cap \{\mathbf{0}\} \neq \emptyset$  and  $\gamma_+(\mathbf{x}) \cap X \neq \emptyset$  for every  $\mathbf{x} \in \mathbb{R}_+^2 \setminus \{\mathbf{0}\}$ . Therefore, for understanding the ultimate behavior of  $\gamma_+(\mathbf{x})$ , it is enough to investigate  $\gamma_+(\mathbf{x})$  with  $\mathbf{x} \in X$ . So, in this section, we investigate the dynamics in  $X$ . In particular, we investigate the attractivity of  $S$  defined by  $S = \{\mathbf{x} \in X : x_0 x_1 = 0\}$ , i.e.,  $S = (S_0 \cup S_1) \cap X$ . Since the compact set  $X$  does not contain the trivial fixed point, the attractivity of  $S$  does not imply extinction of the population, but extinction of one of the two year-classes. If  $S$  is attractive, then all orbits starting in a neighborhood of  $S$  converge to  $S$  visiting the neighborhoods of  $S_0$  and  $S_1$  alternately. It is clear that if  $S$  is a repellor, then two year-classes coexist.

The following lemma will be used below to consider the attractivity of  $S$ .

**Lemma 1** *Suppose that  $\mathcal{R}_0 > 1$  holds. Then for every  $(0, x_1(0)) \in S_0$  with  $x_1(0) > 0$  there exists a sequence  $t_j \rightarrow \infty$  such that*

$$\ln \mathcal{R}_0 = a_{00} \lim_{j \rightarrow \infty} \frac{1}{t_j} \sum_{i=0}^{t_j-1} \tilde{x}_0(2i) + a_{11} \lim_{j \rightarrow \infty} \frac{1}{t_j} \sum_{i=0}^{t_j-1} x_1(2i), \quad (7.3)$$

and for every  $(x_0(0), 0) \in S_1$  with  $x_0(0) > 0$  there exists a sequence  $t_j \rightarrow \infty$  such that

$$\ln \mathcal{R}_0 = a_{00} \lim_{j \rightarrow \infty} \frac{1}{t_j} \sum_{i=0}^{t_j-1} x_0(2i) + a_{11} \lim_{j \rightarrow \infty} \frac{1}{t_j} \sum_{i=0}^{t_j-1} \tilde{x}_1(2i),$$

where  $\tilde{x}_0(t) = \phi_{S_1} x_1(t) e^{-a_{11} x_1(t)}$  and  $\tilde{x}_1(t) = s_0 x_0(t) e^{-a_{00} x_0(t)}$ .

*Proof* Let  $(0, x_1(0)) \in S_0$  with  $x_1(0) > 0$ . Then it follows from (7.2) that

$$\frac{x_1(t+2)}{x_1(t)} = \mathcal{R}_0 \exp[-a_{00} \tilde{x}_0(t) - a_{11} x_1(t)]$$

holds for every even number  $t \geq 0$ . Note that  $x_0(t) = 0$  for all even numbers  $t \geq 0$ . Consequently, we have

$$\frac{1}{t} \sum_{i=0}^{t-1} \ln \frac{x_1(2i+2)}{x_1(2i)} = \frac{1}{t} \sum_{i=0}^{t-1} (\ln \mathcal{R}_0 - a_{00} \tilde{x}_0(2i) - a_{11} x_1(2i)).$$

The sum on the left-hand side tends to 0 as  $t \rightarrow \infty$  since (7.2) is permanent (i.e.,  $x_1(2i)$  is bounded away from 0 and  $\infty$ ). We choose a subsequence  $t_j \rightarrow \infty$  such that both  $\lim_{j \rightarrow \infty} \sum_{i=0}^{t_j-1} \tilde{x}_0(2i)/t_j$  and  $\lim_{j \rightarrow \infty} \sum_{i=0}^{t_j-1} x_1(2i)/t_j$  converge (this is possible since they are bounded). Then we obtain (7.3). The case  $(x_0(0), 0) \in S_1$  with  $x_0(0) > 0$  can be proved similarly.  $\square$

By using this lemma, we can prove the following two theorems.

**Theorem 1** *Suppose that  $\mathcal{R}_0 > 1$  holds. If  $a_{00} < a_{10}$  and  $a_{11} < a_{01}$  hold, then  $S$  is an attractor of the system  $f : X \rightarrow X$ , i.e., there exists a neighborhood  $U$  of  $S$  such that  $\omega(\mathbf{x}) \subset S$  for every  $\mathbf{x} \in U$ .*

*Proof* We shall prove this theorem by using the average Lyapunov function  $P : X \rightarrow \mathbb{R}_+$  defined by  $P(\mathbf{x}) = x_1 x_2$ . This continuous function satisfies  $P(\mathbf{x}) = 0$  if and only if  $\mathbf{x} \in S$ . The theory of average Lyapunov functions ensures that  $S$  is an attractor if for all  $\mathbf{x} \in S$ ,  $\inf_{t \geq 0} \prod_{i=0}^{t-1} \psi(f^i(\mathbf{x})) < 1$ , where  $\psi : X \rightarrow \mathbb{R}_+$  is a continuous function with  $P(f(\mathbf{x})) \leq \psi(\mathbf{x})P(\mathbf{x})$  (see Appendix).

Define  $\psi : X \rightarrow \mathbb{R}_+$  by  $\psi(\mathbf{x}) = \mathcal{R}_0 \exp[-(a_{00} + a_{10})x_0 - (a_{01} + a_{11})x_1]$ . Then  $P(f(\mathbf{x}))/P(\mathbf{x}) = \psi(\mathbf{x})$  holds. Let  $\Lambda(\mathbf{x}, t) = \sum_{i=0}^{2t-1} \ln \psi(f^i(\mathbf{x}))/2t$ . Then we have

$$\Lambda(\mathbf{x}(0), t) = \ln \mathcal{R}_0 - (a_{00} + a_{10}) \frac{1}{2t} \sum_{i=0}^{2t-1} x_0(i) - (a_{01} + a_{11}) \frac{1}{2t} \sum_{i=0}^{2t-1} x_1(i),$$

where  $(x_0(t), x_1(t)) = f^t(\mathbf{x}(0))$ . Let  $\mathbf{x}(0) \in S_0 \cap S$ . Then  $x_0(2t) = x_1(2t + 1) = 0$  for all  $t \in \mathbb{Z}_+$ . Hence, we have

$$\Lambda(\mathbf{x}(0), t) = \ln \mathcal{R}_0 - \frac{a_{00} + a_{10}}{2} \frac{1}{t} \sum_{i=0}^{t-1} \tilde{x}_0(2i) - \frac{a_{01} + a_{11}}{2} \frac{1}{t} \sum_{i=0}^{t-1} x_1(2i).$$

Note that  $x_0(2i + 1) = \phi_{s_1} x_1(2i) e^{-a_{11} x_1(2i)} = \tilde{x}_0(2i)$ . Since  $X$  is compact and  $X \cap \{\mathbf{0}\} \neq \emptyset$ , there exists a positive  $\Delta > 0$  such that

$$\ln \mathcal{R}_0 - \frac{a_{00} + a_{10}}{2} x_0 - \frac{a_{01} + a_{11}}{2} x_1 \leq \ln \mathcal{R}_0 - a_{00} x_0 - a_{11} x_1 - \Delta$$

for all  $\mathbf{x} \in X$ . Therefore, by using Lemma 1, we can show that there exists a subsequence  $t_j \rightarrow \infty$  such that

$$\lim_{j \rightarrow \infty} \Lambda(\mathbf{x}(0), t_j) < 0.$$

This implies that  $\inf_{t \geq 1} \prod_{i=0}^{2t-1} \psi(f^i(\mathbf{x})) < 1$  for all  $\mathbf{x} \in S_0 \cap S$ . The case  $\mathbf{x}(0) \in S_1 \cap S$  can be checked similarly.  $\square$

**Theorem 2** *Suppose that  $\mathcal{R}_0 > 1$  holds. If  $a_{00} > a_{10}$  and  $a_{11} > a_{01}$  hold, then  $S$  is a repeller of the system  $f : X \rightarrow X$ , i.e., there exists a neighborhood  $U$  of  $S$  such that for all  $\mathbf{x} \notin S$  there exists  $T = T(\mathbf{x}) > 0$  satisfying  $f^T(\mathbf{x}) \notin U$  for all  $t \geq T$ .*

*Proof* We again use  $P(\mathbf{x}) = x_0 x_1$  as an average Lyapunov function. The theory of average Lyapunov functions ensures that  $S$  is a repeller if for all  $\mathbf{x} \in S$ ,

$$\sup_{t \geq 0} \prod_{i=0}^{t-1} \psi(f^i(\mathbf{x})) > 1,$$

where  $\psi : X \rightarrow \mathbb{R}_+$  is a continuous function with  $P(f(\mathbf{x})) \geq \psi(\mathbf{x})P(\mathbf{x})$  (see [12] and Appendix). We again use the function  $\psi$  defined in Theorem 1 since  $P(f(\mathbf{x}))/P(\mathbf{x}) = \psi(\mathbf{x})$  holds. Let  $\mathbf{x}(0) \in S_0 \cap S$ . Then by a similar argument as that above, we obtain

$$\Lambda(\mathbf{x}(0), t) = \ln \mathcal{R}_0 - \frac{a_{00} + a_{10}}{2} \frac{1}{t} \sum_{i=0}^{t-1} \tilde{x}_0(2i) - \frac{a_{01} + a_{11}}{2} \frac{1}{t} \sum_{i=0}^{t-1} x_1(2i),$$

where  $(x_0(t), x_1(0)) = f^t(\mathbf{x}(0))$ . Note that  $x_0(2i + 1) = \phi_{s_1} x_1(2i) e^{-a_{11} x_1(2i)} = \tilde{x}_0(2i)$ . By using Lemma 1, we can show that there exists a subsequence  $t_j \rightarrow \infty$  such that

$$\lim_{j \rightarrow \infty} \Lambda(\mathbf{x}(0), t_j) > 0.$$

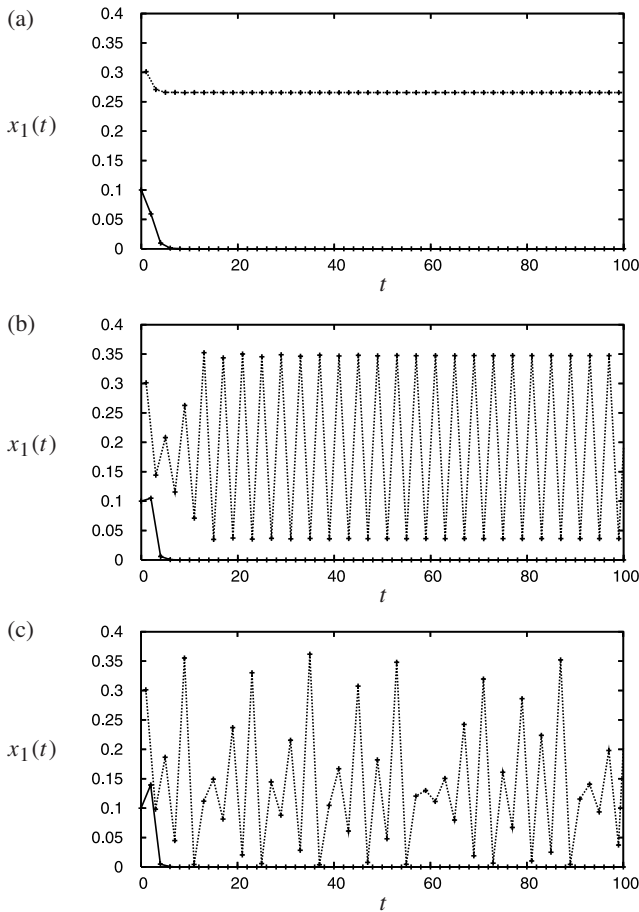
This implies that  $\sup_{t \geq 1} \prod_{i=0}^{2t-1} \psi(f^i(\mathbf{x})) > 1$  for all  $\mathbf{x} \in S_0 \cap S$ . The case  $\mathbf{x}(0) \in S_1 \cap S$  can be checked similarly.  $\square$

Fig. 7.1 and 7.2 illustrate the above two theorems. In these figures,  $x_1(t)$  is plotted against  $t$  and the solid and dotted lines connect  $(x_1(t), t)$  to  $(x_1(t + 2), t + 2)$  with even  $t$  and odd  $t$ , respectively. These lines represent the population dynamics of two different year-classes. In Fig. 7.1, the condition of Theorem 1 holds. Hence, two year-classes do not coexist and one of the two year-classes goes extinct. The orbits in Fig. 7.1 (a), (b) and (c) converge to the 2-periodic, 4-periodic and chaotic orbits on  $S_0 \cup S_1$ , respectively. In Fig. 7.2, the condition of Theorem 2 holds. Hence, two year-classes coexist. In Fig. 7.2 (a), two year-classes coexist at a stable fixed point. In Fig. 7.2 (b), two year-classes coexist with chaotic oscillation. Although the population densities oscillate with large amplitude, Theorem 2 ensures that any orbits do not approach the boundary of  $\mathbb{R}_+^2$ .

### 7.5 Concluding Remarks

In this paper, we have investigated competitive exclusion between two year-classes. This investigation gave a sufficient condition for competitive exclusion. More precisely, we have showed that competitive exclusion occurs in system (7.2) if the inequalities  $a_{00} < a_{10}$  and  $a_{11} < a_{01}$  hold. This condition implies that competition is more severe between than within year-classes. Furthermore, we have shown that two-year classes coexist if competition is more severe within than between year-classes, i.e.,  $a_{00} > a_{10}$  and  $a_{11} > a_{01}$ . The numerical investigations show that our results properly evaluate the possibility of competitive exclusion even if the system composed of a single year-class exhibits complex behavior (see Fig. 7.1 (b)). However, note that our results do not cover the following two cases: (i)  $a_{00} \geq a_{10}$  and  $a_{11} \leq a_{01}$  and (ii)  $a_{00} \leq a_{10}$  and  $a_{11} \geq a_{01}$ . It is known that in these cases the competitive exclusion depends also on the remaining parameters  $\phi$ ,  $s_0$  and  $s_1$  (see [5, 8, 16]).

There are a few studies of the higher dimensional case. For example, Mjølhus et al. [21] studied system (7.1) with  $\sigma_i(\mathbf{x}) \equiv 1, i = 0, 1, \dots, n - 2$  and  $\sigma_{n-1}(\mathbf{x}) = F(x_0 +$



**Fig. 7.1.** The dynamics of system (7.2) with the initial condition  $x_0(0) = 1, x_1(0) = 0.1$ . The solid (resp. dotted) line represents  $x_1(t)$  at even (resp. odd) years  $t$  (i.e., the population densities of two different year-classes). The parameters are  $a_{00} = a_{11} = 1, a_{12} = a_{21} = 2, s_0 = 1, s_1 = 0.5$ , (a)  $\phi = 20$  ( $\mathcal{R}_0 = 10$ ), (b)  $\phi = 40$  ( $\mathcal{R}_0 = 20$ ) and (c)  $\phi = 60$  ( $\mathcal{R}_0 = 30$ ).

$x_1 + \dots + x_{n-1}$ ), where  $F$  is a continuous function of the total population density. That is, they assumed that the survival probabilities are constant and the fecundity decreases with the total population density. It is a future problem to relax these assumptions. As reported by Bulmer [1], system (7.1) can have a heteroclinic orbit connecting periodic points on the coordinates if  $n \geq 3$  (see [4] for a mathematical proof concerning the existence of heteroclinic orbits in the Leslie matrix model). Hence, it is expected that the higher dimensional Leslie matrix model exhibits various dynamical behavior. It is interesting to challenge the higher dimensional case (see [9]).

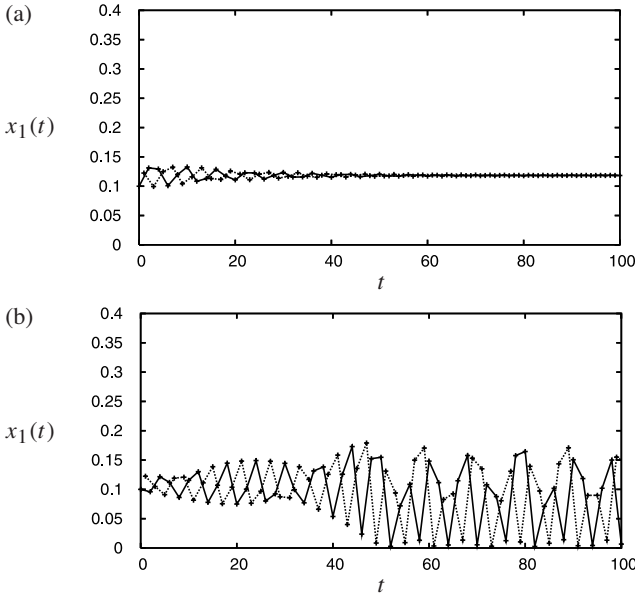


**Fig. 7.2.** The dynamics of system (7.2) with the initial condition  $x_0(0) = 1, x_1(0) = 0.1$ . The solid (resp. dotted) line represents  $x_1(t)$  at even (resp. odd) years  $t$  (i.e., the population densities of two different year-classes). The parameters are  $a_{00} = a_{11} = 2, a_{12} = a_{21} = 1, s_0 = 1, s_1 = 0.5$ , (a)  $\phi = 60$  ( $\mathcal{R}_0 = 30$ ) and (b)  $\phi = 80$  ( $\mathcal{R}_0 = 40$ ).

### Acknowledgments

This research was partially supported by the 21st Century COE Program “Development of Dynamic Mathematics with High Functionality (Kyushu University)” and the Grant-in-Aid for Young Scientists (B), 17740060, 2005, the Ministry of Education, Culture, Sports, Science and Technology, Japan.

### Appendix

In this appendix, we consider the semi-dynamical system generated by the continuous map  $f : X \rightarrow X$ , where  $X$  is a compact metric space.

Let  $M \subset X$  be a compact forward invariant set, i.e.,  $f(M) \subset M$ . The set  $M$  is said to be a repeller if there exists a neighborhood  $U$  of  $M$  such that for all  $\mathbf{x} \notin M$  there exists  $T = T(\mathbf{x}) > 0$  satisfying  $f^t(\mathbf{x}) \notin U$  for all  $t \geq T$ .  $M$  is said to be an attractor if there exists a neighborhood  $U$  of  $M$  such that  $\omega(\mathbf{x}) \subset M$  for all  $\mathbf{x} \in U$ , where  $\omega(\mathbf{x})$  is the omega-limit set of  $\mathbf{x}$  defined by  $\omega(\mathbf{x}) := \{\mathbf{y} \in X : \lim_{j \rightarrow \infty} f^{t_j}(\mathbf{x}) = \mathbf{y} \text{ for some sequence } t_j \rightarrow \infty\}$ .

The following theorem of average Lyapunov functions is utilized to show that the compact forward invariant set  $M$  is a repeller (see also Theorem 2.2 [13] and Theorem 2.17 [14]).

**Theorem 3 (Corollary 2.3 [12])** Let  $X \setminus M$  be forward invariant. Then  $M$  is a repeller if there exists a continuous function  $P : X \rightarrow \mathbb{R}_+$  such that (i)  $P(\mathbf{x}) = 0$  if and only if  $\mathbf{x} \in M$ , (ii) for all  $\mathbf{x} \in M$ ,  $\sup_{t \geq 1} \prod_{i=0}^{t-1} \psi(f^i(\mathbf{x})) > 1$ , where  $\psi : X \rightarrow \mathbb{R}_+$  is a continuous function with  $P(f(\mathbf{x})) \geq \psi(\mathbf{x})P(\mathbf{x})$ .

By using the same technique, we can prove the following theorem, which is used to show that the compact forward invariant set  $M$  is an attractor (see also Theorem 2.7 [11] and Theorem 2.18 [14])

**Theorem 4** Let  $X \setminus M$  be forward invariant. Then  $M$  is an attractor if there exists a continuous function  $P : X \rightarrow \mathbb{R}_+$  such that (i)  $P(\mathbf{x}) = 0$  if and only if  $\mathbf{x} \in M$ , (ii) for all  $\mathbf{x} \in M$ ,  $\inf_{t \geq 1} \prod_{i=0}^{t-1} \psi(f^i(\mathbf{x})) < 1$ , where  $\psi : X \rightarrow \mathbb{R}_+$  is a continuous function with  $P(f(\mathbf{x})) \leq \psi(\mathbf{x})P(\mathbf{x})$ .

*Proof* For  $p \in (0, 1)$  and  $t \geq 1$ , define

$$U(p, t) = \left\{ \mathbf{x} \in X : \prod_{i=0}^{t-1} \psi(f^i(\mathbf{x})) < p \right\}.$$

Then  $U(p, t)$  is open. Since  $\inf_{t \geq 1} \prod_{i=0}^{t-1} \psi(f^i(\mathbf{x})) < 1$  for all  $\mathbf{x} \in M$ ,

$$M \subset \bigcup_{p \in (0, 1), t \geq 1} U(p, t)$$

holds. Since  $M$  is compact, there exist  $\bar{p} \in (0, 1)$  and  $t_1, \dots, t_m \geq 1$  such that  $M \subset \bigcup_{i=1}^m U(\bar{p}, t_i) =: W$ . Let  $\bar{t} = \max\{t_1, \dots, t_m\}$ .

Let  $W_p = \{\mathbf{x} \in X : P(\mathbf{x}) < p\}$ . Choose  $p \in (0, 1)$  such that  $\overline{W_p} \subset W$ , where  $\overline{W_p}$  is the closure of  $W_p$ . Let  $\mathbf{x} \in W_p \subset W$ . Then there exists  $T \in [1, \bar{t}]$  such that  $x \in U(\bar{p}, T)$ . Furthermore,  $P(f^T(\mathbf{x})) < \bar{p}P(\mathbf{x})$  holds. This implies that  $f^T(\mathbf{x}) \in W_p$ . Therefore, by iteration we obtain a sequence  $T_j \rightarrow \infty$  with  $T_{j+1} - T_j \leq \bar{t}$  such that  $f^{T_j}(\mathbf{x}) \in W_p$  and  $P(f^{T_j}(\mathbf{x})) \rightarrow 0$  as  $j \rightarrow \infty$ . Since  $P(f^t(\mathbf{x})) \leq \alpha P(f^{T_j}(\mathbf{x}))$  holds for all  $t$  with  $T_j \leq t \leq T_{j+1}$ , where  $\alpha = \max\{\prod_{i=0}^{t-1} \psi(f^i(\mathbf{x})) : 1 \leq t \leq \bar{t}, x \in X\}$ , we conclude that  $P(f^t(\mathbf{x})) \rightarrow 0$  as  $t \rightarrow \infty$ . This completes the proof.  $\square$

## References

1. Bulmer, M. G.: Periodical insects. *Amer. Natur.*, **111**, 1099–1117 (1977).
2. Caswell, H.: *Matrix Population Models*, 2nd Ed. Sinauer Associates, Sunderland, MA (2001).
3. Cushing, J. M.: *An Introduction to Structured Population Dynamics*. CBMS-NSF Regional Conference Series in Applied Mathematics, 71. Society for Industrial and Applied Mathematics (SIAM), Philadelphia, PA (1998).
4. Cushing, J. M.: Cycle chains and the LPA model. *J. Difference Equ. Appl.*, **9**, 655–670 (2003).
5. Cushing, J. M.: Nonlinear semelparous Leslie models. *Math. Biosci. Eng.*, **3**, 17–36 (2006).

6. Cushing, J. M., Li, J.: Intra-specific competition and density dependent juvenile growth. *Bull. Math. Biol.*, **54**, 503–519 (1992).
7. Cushing, J. M., Li, J.: The dynamics of a size-structured intraspecific competition model with density dependent juvenile growth rates. In: DeAngelis, D. L., Gross, L. J. (eds) *Individual-Based Models and Approaches in Ecology: Populations, Communities and Ecosystems*. Routledge Chapman & Hall, New York (1992).
8. Davydova, N. V., Diekmann, O., van Gils, S. A.: Year class coexistence or competitive exclusion for strict biennials? *J. Math. Biol.*, **46**, 95–131 (2003).
9. Diekmann, O., Davydova N. V., van Gils, S. A.: On a boom and bust year class cycle. *J. Difference Equ. Appl.*, **11**, 327–335 (2005).
10. Heliövaara, K., Väisänen, R., Simon, C.: Evolutionary ecology of periodical insects. *Trends in Ecology & Evolution*, **9**, 475–480 (1994).
11. Hofbauer, J., Hutson, V., Jansen, W.: Coexistence for systems governed by difference equations of Lotka-Volterra type. *J. Math. Biol.*, **25** 553–570 (1987).
12. Hofbauer, J., So, J. W.-H.: Uniform persistence and repellers for maps. *Proc. Amer. Math. Soc.*, **107**, 1137–1142 (1989).
13. Hutson, V.: A theorem on average Liapunov functions. *Monatsh. Math.*, **98**, 267–275 (1984).
14. Hutson, V., Schmitt, K.: Permanence and the dynamics of biological systems. *Math. Biosci.*, **111**, 1–71 (1992).
15. Kon, R.: Non-existence of synchronous orbits and class coexistence in matrix population models. *SIAM J. Appl. Math.*, **66**, 616–626 (2005).
16. Kon, R.: Invasibility of missing year-classes in Leslie matrix models for a semelparous biennial population. *Proceedings of the Czech–Japanese Seminar in Applied Mathematics 2005*, COE Lecture Notes Vol. 3, Faculty of Mathematics, Kyushu University, 64–75 (2006).
17. Kon, R., Saito, Y., Takeuchi, Y.: Permanence of single-species stage-structured models. *J. Math. Biol.*, **48**, 515–528 (2004).
18. Lloyd, M., Dybas, H. S.: The periodical cicada problem. I. population ecology. *Evolution*, **20**, 133–149 (1966).
19. Lloyd, M., Dybas, H. S.: The periodical cicada problem. II. evolution. *Evolution*, **20**, 466–505 (1966).
20. May, R. M.: Periodical cicadas, *Nature*, **277**, 347–349 (1979).
21. Mjølhus, E., Wikan, A., Solberg, T.: On synchronization in semelparous populations. *J. Math. Biol.*, **50**, 1–21 (2005).
22. Powlledge, T. M.: The 17-year itch. *Sci. Amer.*, **290**, 32–33 (2004).
23. Wikan, A., Mjølhus, E.: Overcompensatory recruitment and generation delay in discrete age-structured population models. *J. Math. Biol.*, **35**, 195–239 (1996).

## On the Impact of Winter Conditions on the Dynamics of an Isolated Population

Lev V. Nedorezov, E.V. Volkova, and Alexandr M. Sadykov

International Centre of Insect Physiology and Ecology, Nairobi, Kenya;  
l.v.nedorezov@gmail.com

**Summary.** This chapter is devoted to the analysis of single-species population dynamics models with overlapping and non-overlapping generations. Within the framework of all models it is assumed that there are no activities of individuals during the wintertime (as, for example, is the case for forest insect populations in the boreal zone), and changes in population size at these moments are described with a broken trajectory (“jump down”). Also, it is assumed that the fecundity of individuals is constant and that the quota of individuals surviving winter depends on the within-year population dynamics. The dynamics of the models, which are determined by the influence of winter conditions on the survival of individuals and by the influence of intra-population self-regulative mechanisms, are analyzed. For some particular cases the conditions for population extinction and for stabilization at a non-zero level are determined; it is shown numerically that chaotic regimes can also be realized in some models. The conditions for the reduction of the models under consideration to some well-known discrete models are obtained.

**Key words:** Population dynamics, ordinary differential equations with impulses, discrete models.

### 8.1 Introduction

In insect populations in the boreal zone there are no activities of individuals during winter. This makes it possible not to use special equations for the description of the population decrease during this time, but to describe this decrease with a trajectory of a differential equation ([39], [1], [34], [10], [15], [16], [17]) interspersed with jumps at selected time moments. Similar situations are typical for populations under periodic harvesting and periodic use of chemical poisons against pests if the latter are realized without any after-effect influencing the population dynamics ([18], [19]).

It is possible to find in the modern literature (see, for example, [47], [22], [23], [25], [38], [3], [4], [35], [42]) an opinion that winter conditions play a very important role in the beginning and development of forest insect outbreaks. An analysis of the real role of winter conditions in insect population dynamics cannot take place within the framework of traditional ecological models (recurrence equations or ordinary differential equations). It requires the use of another mathematical apparatus where we can



separate the influence of winter conditions from the influences of all other population mechanisms.

For these reasons it is better to use ordinary differential equations with impulses ([26], [39], [1], [32], [34], [16], [17], [10] and others). First, the use of models of that type allows us to separate the influences of all mechanisms on the population dynamics and, hence, to find the real dependence of the birth rate on the parameters that characterize the impacts of winter conditions on the changes in population size. For some species of forest insects (for example, for *Dendrolimus sibiricus superans* Tschetv., *Ips subelongatus* Mosch., *Monogamus urussovi* Fisch. and some others) it was assumed that the influence of weather conditions on population birth rates can be presented in a linear multiplicative form ([11], [49], [24], [21], [20]). Using discrete-continuous models allows us to determine the conditions when this assumption (linear dependence of birth rate on weather parameters) is truthful, and provides a faithful limiting description of such assumptions.

Second, as pointed out by several authors ([36], [10], [14], [15], [16], [44]) the construction and analysis of models of this type (ordinary differential equations with impulses) can allow us to determine the domains over which discrete time models can be applied to establish the relation between within-year population dynamics and long-term population fluctuations. Consequently, sometimes it gives us more adequate biological interpretations of model parameters. Third, using this approach to the modeling of population dynamics allows us to obtain new discrete models which are based on various assumptions about the functioning of intra-population mechanisms during within-year periods ([10], [32]).

This chapter considers mathematical models of single-species population dynamics which can be considered modifications and generalizations of the well-known [48] model. Within the framework of the considered models it is assumed that trajectories are “broken” periodically in a manner that corresponds to the decrease of population size during wintertime and the increase of population size at the appearance of new generations. It is also assumed that the quota of surviving individuals in a population depends on the “food conditions” during the time period under consideration. This dependence is taken into account as a dependence of the respective coefficient on the average population size during this time interval.

## 8.2 Model with Discrete Birth Process

Let us consider the situation when there are no activities in the population during wintertime and let  $t_k, k = 0, 1, 2, \dots, t_{k+1} - t_k = h = \text{const} > 0$ , be the moments of the beginning of winter periods (respectively, the moments of the beginning of the next “vegetative periods”). Denote as  $x(t)$  the population size at moment  $t$ , as  $x(t_k - 0)$  the number of individuals surviving to moment  $t_k$ , as  $x_k = x(t_k)$  the population size at the beginning of the next vegetative period, and as  $Q, 0 < Q < 1$ , the quota of individuals surviving the winter. The amount  $p = 1 - Q$  is equal to the probability of dying during this period. Thus, at moments  $t_k$  we have the following relation:

$$x(t_k) = Qx(t_k - 0). \quad (8.1)$$

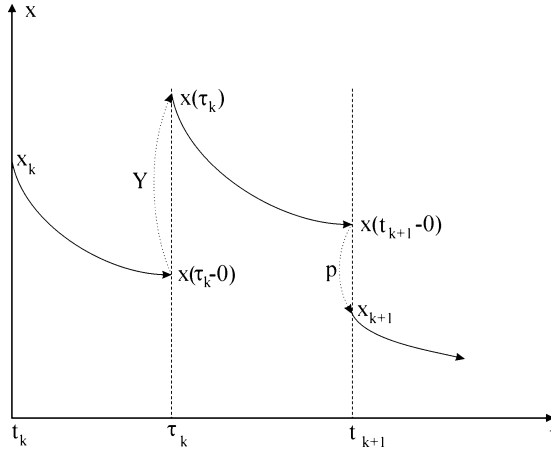


**Fig. 8.1.** Change of population size with time.  $x_k$  is population size of  $k$ th generation (after winter period).  $x(\tau_k - 0)$  is number of individuals surviving up to moment  $\tau_k$ .  $x(\tau_k)$  is initial size of the  $k+1$ -th generation.  $Y$  is productivity,  $Y = const > 1$ .  $Q$  is winter survival,  $Q = 1 - p$ .

Within the framework of the model we shall assume that the appearance of new individuals is realized at fixed time moments  $\tau_k$ ,  $\tau_k \in (t_k, t_{k+1})$ , thus allowing us to describe the changes in population size with a broken trajectory (Fig. 8.1). Denote as  $x(\tau_k - 0)$  the number of individuals surviving up to moment  $\tau_k$ . Let  $Y = const$ ,  $Y > 1$ , be the coefficient of productivity:  $Y$  is equal to the average number of new individuals that can be produced by one surviving individual. Thus, at moments  $\tau_k$  the following relation holds:

$$x(\tau_k) = Yx(\tau_k - 0). \tag{8.2}$$

We shall describe the population dynamics during time intervals  $[t_k, \tau_k)$  and  $[\tau_k, t_{k+1})$  with the following equation:

$$\frac{dx}{dt} = -xR(x), \tag{8.3}$$

where the per capita death rate  $R(x)$  satisfies the following conditions, which are common for various models ([45], [46], [23], [37]):

$$R(0) > 0, \quad \frac{dR}{dx} > 0, \quad R(\infty) = \infty. \tag{8.4}$$

$R(0)$  is an intensity of natural deaths, and increases of values of  $R(x)$  are a result of the strengthening of the influence of intra-population self-regulative mechanisms with increasing population size.

In the model we shall assume that the coefficient  $Q$  depends on the average population size during the period  $[t_k, t_{k+1})$ ,  $Q = Q(u)$ , where

$$u = \frac{1}{h} \int_{t_k}^{t_{k+1}} x(s) ds.$$

The interpretation of the coefficient  $Q(u)$  lets us assume that  $Q$  is a monotonically decreasing function (increase of population size leads to an increase of intra-population competition for food):

$$Q(u) \in [0, 1], \quad \frac{dQ}{du} < 0. \tag{8.5}$$

Relations (8.1)–(8.5) give us a model of population dynamics with a discrete time birth process and continuous-discrete time death process. Note that if the coefficient of productivity  $Y < 1$ , then the time series  $\{x(t_k)\}, k = 0, 1, 2, \dots$ , in model (8.1)–(8.5) is a monotone decreasing sequence for all initial values of the population size (the population goes extinct for all initial values).

### 8.2.1 Reduction of Model (8.1)–(8.5) to a Recurrence Equation

Let  $\psi(x)$  be the following function:

$$\psi(x) = \int \frac{dx}{xR(x)} + C,$$

where  $C$  is a constant of integration for equation (8.3). From conditions (8.4) we have

$$\psi'(x) > 0, \quad \psi''(x) < 0.$$

It means that there exists an inverse monotonically increasing function  $\psi^{-1}$ . Solution of the Cauchy problem on the interval  $[t_k, \tau_k)$  with  $x(t_k) = x_k$  gives the following relation:

$$x(t) = \psi^{-1}(-t + c_1), \tag{8.6}$$

where  $c_1 = t_k + \psi(x_k)$ . Hence, equation (8.6) can be presented in the form

$$x(t) = \psi^{-1}(t_k - t + \psi(x_k)) \quad \forall t \in [t_k, \tau_k).$$

Using relation (8.2) gives the balance relation

$$x(\tau_k) = Yx(\tau_k - 0) = Y\Psi^{-1}(\Psi(x_k) - h_1), \tag{8.7}$$

where  $h_1 = \tau_k - t_k$ . Equation (8.7) gives the initial condition for the Cauchy problem for (8.3) on the interval  $[\tau_k, t_{k+1})$ . Finally we have

$$x_{k+1} = x(t_{k+1}) = Q \left( \frac{1}{h} \int_{t_k}^{t_{k+1}} x(s) ds \right) \psi^{-1}(c_2 - t_{k+1}), \tag{8.8}$$

where

$$c_2 = \tau_k + \psi(x(\tau_k)).$$

Denote as  $F(x_k)$  the function on the right-hand side of equation (8.7). If

$$0 \leq x_k < \psi^{-1} \left( \psi \left( \frac{\psi^{-1}(h_2)}{Y} \right) + h_1 \right),$$

where  $h_2 = t_{k+1} - \tau_k$ , the  $F(x)$  is a monotonically increasing function on this interval. For all non-negative initial values the solutions of equation (8.8) are non-negative. From conditions (8.4) it follows that solutions of model (8.8) are bounded.

### 8.2.2 Particular Cases

1. If  $R(x) = b = \text{const} > 0$  (this means that self-regulating mechanisms do not work during the vegetative period; not all the conditions (8.4) are realized for this assumption) and  $Q(u) = e^{-pu}$ ,  $p = \text{const} > 0$ , model (8.8) has the following form:

$$x_{k+1} = \alpha x_k e^{-\beta x_k}, \quad (8.9)$$

where the positive constants  $\alpha$  and  $\beta$  depend on  $b$ ,  $Y$ ,  $h_1$ ,  $h_2$ , and  $p$ . The parameter  $p$  describes the influence of winter conditions on the population dynamics: an increase of the value of this parameter leads to a decreasing quota of individuals surviving the winter for the same within-year population dynamics.

Equation (8.9) is the well-known Moran–Ricker model ([30], [40]). Analysis of this model is presented in diverse publications (see, for example, [9], [41], [50], [27], [28], [29], [42], [6]). Thus, the Moran–Ricker model (8.9) can be deduced from model (8.1)–(8.5) but under the assumption that there are no self-regulative mechanisms ( $R = \text{const}$ ) during the vegetative period and productivity is constant.

Population size is regulated by winter conditions only. But it is very important to note that changing the value of the parameter  $p$  leads only to a change of the population stationary level; it cannot lead to changing the character of any population fluctuations (in other words, it cannot lead to a bifurcation of a dynamical regime). This means that in the situation under consideration we have reasons for assuming that winter conditions play the role of stabilizing factor in the population dynamics.

2. If  $R(x) \equiv b = \text{const} > 0$ ,  $Q(u) = 1/(1 + pu)$ , equation (8.8) is the well-known Beverton–Holt model ([5]):

$$x_{k+1} = \frac{\alpha x_k}{\beta x_k + \gamma}, \quad (8.10)$$

where  $\alpha$ ,  $\beta$ ,  $\gamma$  are positive parameters. Thus, the Beverton–Holt model (8.10) can also (like the Moran–Ricker model (8.9)) be deduced within the framework of model (8.1)–(8.5). Model (8.10) can also be obtained in (8.1)–(8.5) under the condition that the action of the self-regulative mechanisms correspond to a Verhulst law ([48]), and the productivity,  $Y$ , and the coefficient of surviving,  $Q$ , are constant ([34]).

In the case under consideration the influence of winter conditions leads to a decrease of the population stationary state only. This means that, as in the previous situation, these conditions play the role of stabilizing factor.

3. If  $R(x) = ax + b$ ,  $a, b = \text{const} > 0$ ,  $Q(u) = e^{-pu}$ , model (8.8) has the following form:

$$x_{k+1} = \frac{K_1 x_k}{K_2 x_k + K_3} \left( \frac{K_4 x_k + K_5}{K_6 x_k^2 + K_7 x_k + K_5} \right)^{p/ha}, \quad (8.11)$$

where the “macrocoefficients”  $K_i = \text{const} \geq 0, i = 1, \dots, 7$ , are determined by the following formulas:

$$\begin{aligned} K_1 &= bY, \\ K_2 &= a(Ye^{bh_2} + (e^{bh_1} - 1)e^{bh_2} - Y), \\ K_3 &= be^{bh}, \\ K_4 &= ab(e^{bh_1} - 1), \\ K_5 &= b^2 e^{bh_1}, \\ K_6 &= a^2(Y(1 - e^{-bh_1})(1 - e^{-bh_2}) + (1 - e^{-bh_1})(e^{bh_1} - 1)), \\ K_7 &= ab(2(e^{bh_1} - 1) + Y(1 - e^{-bh_2})). \end{aligned}$$

It is very important to note that equation (8.11) was obtained under the assumption that the action of the intra-population self-regulative mechanisms follow the Verhulst law ([48]) when  $R$  is a linear function.

The stationary states of model (8.11) can be found from the equation

$$x = \frac{K_1 x}{K_2 x + K_3} \left( \frac{K_4 x + K_5}{K_6 x^2 + K_7 x + K_5} \right)^{p/ha}. \quad (8.12)$$

Obviously,  $x_0 = 0$  is a root of this equation. If  $K_3/K_1 < 1$ , equation (8.12) has positive solutions. If  $K_3 > K_1$ , which is equivalent to  $e^{bh} > Y$ , the origin is a globally stable equilibrium for model (8.11). Under this condition the population goes extinct for all initial values of the population size.

Analysis of the bifurcation diagram (Fig. 8.2) shows that various cyclic regimes can be realized for model (8.11). Numerical analysis of Diamond’s conditions ([8]) at  $Y = 224$  shows that in the  $(a, b)$ -plane there is a domain (Fig. 8.3) that corresponds to dynamic regimes with chaotic trajectories ([43]).

### 8.3 Model with Continuous Birth Process

Let us consider the situation where the population has overlapping generations. We shall assume that the population dynamics on the intervals  $[t_k, t_{k+1})$  is described by the equation

$$\frac{dx}{dt} = xR(x), \quad (8.13)$$

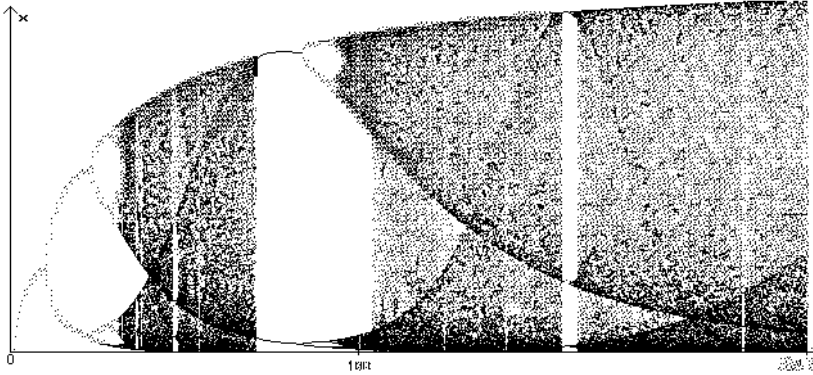


**Fig. 8.2.** Bifurcation diagram for model (8.11).  $a = 0.2, b = 0.4$ .

where the function  $R(x)$  describes the death process of individuals, the birth process, and the influence of intra-population self-regulative mechanisms on the population dynamics. The following assumptions are typically made for the function  $R(x)$  ([2], [45], [46], [12], [13], [7], [31] and others):

$$R(0) > 0, \quad \frac{dR}{dx} < 0, \quad R(\infty) = -\infty. \tag{8.14}$$

The quantity  $R(0)$  is the Malthusian parameter for population.

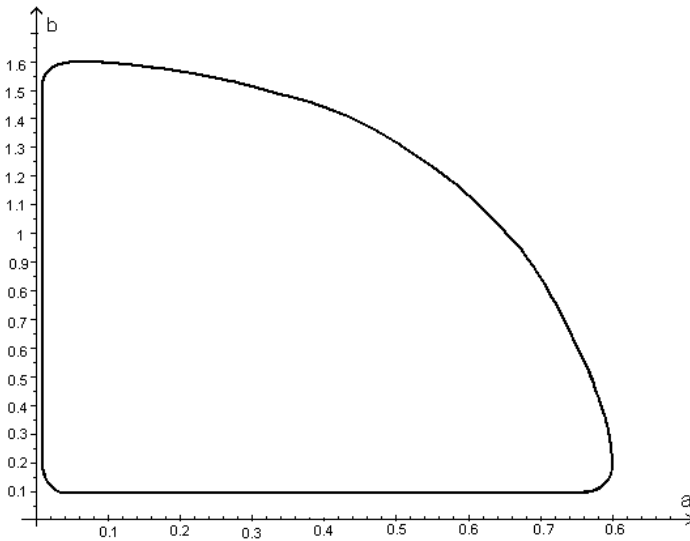


**Fig. 8.3.** Domain in a space of parameters where conditions of Diamond's theorem are realized.  $Y = 224$ .

As previously, we shall assume that the quota  $Q$  of individuals that survive the winter is determined by the food supply of the individuals during a certain time interval:

$$Q = Q \left( \frac{1}{h} \int_{t_k}^{t_{k+1}} x(s) ds \right). \tag{8.15}$$

Additionally, it is natural to assume that an increase in the average population size leads to a decrease in the food supply for the individuals. Hence, it leads to an increase in the death rate during wintertime, and the derivative of the function (8.15) must be negative.

**8.3.1 Properties of Model (8.13)–(8.15) for  $Q \equiv const$**

1. Let  $K$  be a solution of the equation  $R(x) = 0$ . If  $x_0 = x(0) > K$ , it is obvious that the trajectory  $\{x_k = x(t_k)\}$  of model (8.13)–(8.15) will belong to the domain  $x \leq K$  after a finite number of time steps. If  $x_0 = x(0) < K$ , the sequence  $\{x_k\}$  cannot intersect the boundaries of interval  $[0, K]$ . This means that for every time moment the population size is bounded and non-negative.

Further we will assume that the inequality  $x_0 = x(0) < K$  is always realized.

2. When

$$Q e^{R(0)h} < 1, \tag{8.16}$$

the origin is globally attracting. In other words, if (8.16) holds true the population goes extinct for all initial values of the population size. Further we shall assume that the inverse inequality in (8.16) is always satisfied.

3. Let  $\psi(x)$  be the following function:

$$\psi(x) = \int \frac{dx}{xR(x)}.$$

If  $0 < x < K$  then  $\psi(x)$  is a monotonically increasing function,  $\psi'(x) > 0$ . When  $x$  changes from 0 to  $K$  the value of  $\psi(x)$  changes from  $-\infty$  to  $+\infty$ . Thus, there exists an inverse function  $\psi^{-1}$ , which is defined on the interval  $(-\infty, +\infty)$  and bounded,  $0 \leq \psi^{-1} \leq K$ .

Formally, it is possible to present the solution of model (8.13)–(8.15) in the following form (with initial condition  $x_k = x(t_k)$ ):

$$x_{k+1} = Q\psi^{-1}(\psi(x_k) + h). \tag{8.17}$$

The function on the right-hand side of equation (8.17) is monotonically increasing. Thus, in model (8.13)–(8.15) there are only the regimes of monotone population change.

The number of non-trivial stationary states in (8.17) is determined by the number of positive solutions of the functional equation

$$\psi\left(\frac{x}{Q}\right) = \psi(x) + h,$$

which is defined on the interval  $0 < x < QK$ . Taking into account that the second derivative of  $\psi(x)$  can change the sign, in general the last equation has several non-zero solutions.

### 8.3.2 Particular Cases

1. Let us consider the case when  $R$  takes a linear form,  $R(x) = \tilde{\alpha} - \tilde{\beta}x$ , where all parameters are positive,  $\tilde{\alpha}, \tilde{\beta} \equiv \text{const} > 0$ . The coefficient  $\tilde{\alpha}$  is a Malthusian parameter of the population and  $\tilde{\beta}$  is a parameter of the self-regulatory mechanism. After integrating we get model (8.10) with parameters

$$\alpha = Qe^{\tilde{\alpha}h}, \quad \beta = \frac{\tilde{\beta}}{\tilde{\alpha}}(e^{\tilde{\alpha}h} - 1), \quad \gamma = 1.$$

In the deduction of this model from a continuous-discrete model (8.13)–(8.15), we assumed that the sequence  $\{x_k\}$  contains the values of the population size at moments  $t_k$  (population sizes at the beginning of vegetative periods). For various insect populations in the boreal zone the most suitable moments for population measurements are at the end of vegetative periods. Consequently, there exists the important question about the relation between the type of discrete time model (which we use for fitting of experimental time series) and the moments at which the population is sampled.

Let  $\tau, \tau \leq h$ , be the time after the beginning of the vegetative period and, respectively, let  $t_k + \tau$  be the time moment at which the population is sampled,  $x_k = x(t_k + \tau)$ . Taking into account all the assumptions we made above, in the end we get the following discrete model:

$$x_{k+1} = \frac{\alpha x_k}{1 + Cx_k}, \quad (8.18)$$

where

$$C = \frac{\beta}{\alpha} \left( e^{\alpha(h-\tau)} - 1 + Q(e^{\alpha\tau} - 1)e^{\alpha(h-\tau)} \right). \quad (8.19)$$

Finally, in the situation under consideration there is no relation between the kinds of model (in all situations we have model (8.10)) and the moments of population size measurement. However, it is very important to note that if  $\tau = 0$ , the parameter  $C$  does not depend on the value of parameter  $Q$  (it does not depend on survival of individuals over the winter periods).

2. Let us consider the situation when

$$Q = \exp\left(-b \int_{t_k}^{t_{k+1}} x(s) ds\right). \quad (8.20)$$



The coefficient  $b$  is a positive parameter corresponding to the “sensitivity” of the individuals to the food conditions. After some calculations formula (8.20) can be presented in the form

$$Q = \frac{1}{\left(1 - \frac{\beta}{\alpha}x_k + \frac{\beta}{\alpha}e^{\alpha h}x_k\right)^{b/\beta}}.$$

In the end, we get the following discrete model of population dynamics

$$x_{k+1} = \frac{Ax_k}{(1 + Bx_k)^{(b/\beta)+1}}, \tag{8.21}$$

where

$$A = e^{\alpha h}, \quad B = \frac{\beta}{\alpha}(e^{\alpha h} - 1).$$

Equation (8.21) is the well-known Hassell model ([12], [13]). Model (8.21) was obtained under the assumption that the population size can be measured at the beginning of the vegetative period. If the population size can be estimated at the beginning of wintertime we have

$$x_{k+1} = \frac{(q + 1) \cdot x_k}{\frac{\beta}{\alpha}qx_k + \left(\frac{\beta}{\alpha}qx_k + 1\right)^{b/\beta}}, \tag{8.22}$$

where  $x_k = x(t_k - 0)$  and  $q = e^{\alpha h} - 1$ . Thus, we can conclude that the type of discrete time model depends on the time of the population size measurement. It means that if we have a dataset on population dynamics with the measurements taken just before wintertime, there are no reasons to use model (8.21) for an approximation of the experimental trajectories.

Formally, models (8.21) and (8.22) are different. However, it is obvious that for the same values of the parameters these models have the same dynamic regimes. Hence, these models have similar structures of their parameter spaces.

Let  $\tau, \tau \leq h$ , be the time after the beginning of the vegetative period and, respectively, let  $t_k + \tau$  be the moments at which the population is sampled,  $x_k = x(t_k + \tau)$ . If  $Q$  is determined by (8.20) we have

$$Q = \left( \frac{\alpha e^{\alpha \tau} - \beta x_k (e^{\alpha \tau} - 1)}{\alpha e^{\alpha \tau} + \beta x_k (e^{\alpha h} - e^{\alpha \tau})} \right)^{b/\beta}.$$

This expression gives us a one-parameter ( $\tau$ ) family of discrete time models that are “produced” by model (8.13)–(8.15) under the assumptions considered above.

## 8.4 Conclusion

Analysis of single-species population dynamics under periodic impacts that lead to decreases in population size shows that, at a constant value of the coefficient of surviving after the impacts, only regimes of monotone stabilization of population size can

be realized. In the general case regimes with several stationary states can be realized within the framework of the analyzed model. This result can be considered as additional support for the hypothesis that winter conditions play a very important role in the beginning and development of population outbreaks.

For some particular cases of populations with non-overlapping generations we found that winter conditions can play the role of stabilizing regulator. Also, we found that even in the simplest cases when there is no self-regulation in population and the impacts of winter conditions are described by an exponential or fractional-linear function, we have a non-linear dependence of the birth rate on the parameter describing the influence of winter conditions on the population dynamics. Consequently, all models ([11], [49], [24], [21], [20]) of population dynamics that were constructed under the assumption of linear dependence of the birth rate on weather parameters need serious modifications.

Analysis of two other particular cases (for populations with overlapping generations) where the within-year population dynamics is described by the Verhulst model showed that there are no trigger regimes in the phase space of the system if the quota of surviving individuals during the wintertime is constant or an exponentially decreasing function of the average population size. Also, analysis of these particular cases allowed us to obtain one-parametric sets of discrete time models which can be “produced” by one continuous-discrete model, and to show that the type of discrete model of population dynamics can depend on the time moments of the population size measurements. It is very important to take the latter into account when choosing a discrete time dynamic model for the fitting of experimental time series.

## References

1. Aagaard-Hansen, H., Yeo, G.F.: A stochastic discrete generation birth, continuous death population growth model and its approximate solution. *J. Math. Biol.*, **20**, 69–90 (1984).
2. Bazykin, A.D.: *Mathematical Biophysics of Interacting Populations*. Moscow, Nauka (1985), in Russian.
3. Berryman, A.A.: *Population Systems: A General Introduction*. Plenum Press, New York (1981).
4. Berryman, A.A.: Population cycles: a critique of maternal effects and allometric hypotheses. *J. Anim. Ecol.*, **64**, 290–293 (1995).
5. Beverton, R.J., Holt, S.J.: The theory of fishing. In: Graham, M.: *Sea Fisheries. Their Investigation in the United Kingdom*. Edward Arnold, London, 372–441 (1956).
6. Davidova, N.V.: *Old and Young. Can They Coexist?* Univ. Utrecht, The Netherlands (2004).
7. De Roos, A.M.: *Modeling Population Dynamics*. Univ. of Amsterdam, The Netherlands (2004).
8. Diamond, P.: Chaotic behaviour of systems of difference. *Int. J. Syst. Sci.*, **7**, 953–956 (1976).
9. Frisman, E.Ya., Shapiro, A.P.: *Selected Mathematical Models of Divergent Population Evolution*. Nauka, Moscow (1977), in Russian.
10. Geritz, S.A.H., Kisdi, E.: On the mechanistic underpinning of discrete-time population models with complex dynamics. *J. Theor. Biol.*, **228**, 261–269 (2004).

11. Golubev, A.V., Insarov, G.E., Strakhov, V.V.: *Mathematical Models in Forest Protection*. Forest Industry, Moscow (1980), in Russian.
12. Hassell, M.P.: *The Dynamics of Arthropod Predator-Prey Systems*. Princeton University Press, Princeton, NJ (1978).
13. Hassell, M.P.: Some consequences of habitat heterogeneity for population dynamics. *Oikos*, **35**, 150–160 (1980).
14. Il'ichev, V.G.: Delta-functions and theory of biological competition in periodically changing environment. *Automatics and Telemechanics*, **11**, 115–127 (1996), in Russian.
15. Il'ichev, V.G.: Hereditary properties of non-autonomous dynamical systems and its application to models of competition. *Izvestia VUZov, Mathematics*, **6**, 26–36 (2002), in Russian.
16. Il'ichev, V.G.: Evolution-stable parameters in a periodically changing environment. *Automation and Remote Control.*, **65**, 612–624 (2004).
17. Il'ichev, V.G.: The concept of evolutionary stability in ecological models. *Differential Equations*, **42**, 1–12 (2006).
18. Isaev, A.S., Nedorezov, L.V., Khlebopros, R.G.: *The Boomerang-Effect in Models of Pest Population Control. Pest and Pathogen Control*, John Wiley, IIASA, 29–39 (1984).
19. Isaev, A.S., Nedorezov, L.V., Khlebopros, R.G.: *Qualitative Analysis of the Phenomenological Model of the Forest Insect Number Dynamics. Pest and Pathogen Control*, V. 9, IIASA, Austria, 1–44 (1980).
20. Isaev, A.S., Khlebopros, R.G.: Lag effects in regulation of forest insect populations. *Doklady AS USSR*, **232**, 1448–1451 (1977).
21. Isaev, A.S., Khlebopros, R.G., Kondakov, Yu.P.: Laws of forest insect population dynamics. *Lesovedenie*, **3**, 27–42 (1974).
22. Isaev, A.S., Khlebopros, R.G., Nedorezov, L.V., Kondakov, Yu.P., Kiselev, V.V.: *Population Dynamics of Forest Insects*. Nauka, Novosibirsk (1984), in Russian.
23. Isaev, A.S., Khlebopros, R.G., Nedorezov, L.V., Kondakov, Yu.P., Kiselev, V.V., Soukhovol'sky, V.G.: *Forest Insect Population Dynamics*. Nauka, Moscow (2001), in Russian.
24. Isaev, A.S., Rozhkov, A.S., Kiselev, V.V.: *Monogamus urussovi Fisch*. Nauka, Novosibirsk (1988), in Russian.
25. Konikov, A.S.: *Forest Insect Number Regulators*. Nauka, Novosibirsk (1978), in Russian.
26. Kostitzin, V.A.: *La Biologie Mathématique*. A. Colin, Paris (1937).
27. May, R.M.: Stability in multispecies community models. *Math. Biosc.*, **12**, 59–79 (1977).
28. May, R.M.: Biological populations obeying difference equations: stable points, stable cycles and chaos. *J. Theor. Biol.*, **51**, 511–524 (1975).
29. May, R.M.: *Stability and Complexity in Model Ecosystems*. Princeton Univ. Press, Princeton and Oxford (2001).
30. Moran, P.A.P.: Some remarks on animal population dynamics. *Biometrika*, **6**, 250–258 (1950).
31. Murray, J.D.: *Mathematical Biology. I. An Introduction*. Springer-Verlag, Berlin, Heidelberg (2002).
32. Nedorezov, L.V.: *Modeling of Forest Insect Outbreaks*. Nauka, Novosibirsk (1986), in Russian.
33. Nedorezov, L.V., Nazarov, I.N., Nazarov, O.N.: The Continuous-Discrete Models for Competition of Two Species. *Int. J. Chaos Theory and Appl.*, **3**, 39–51 (1998).
34. Nedorezov, L.V., Nedorezova, B.N.: Correlation between models of population dynamics in continuous and discrete time. *Ecological Modelling*, **82**, 93–97 (1995).
35. Nedorezov, L.V., Sadykov, A.M.: Influence of winter conditions on the dynamics of an isolated population dynamics. *Euro-Asian Entomological Journal*, **3**, 169–172 (2004), in Russian.

36. Pichugin, B.Yu.: Stochastic model of isolated population with seasonal birth process and self-limitation. *Siberian Journal of Industrial Mathematics*, **6**, 75–81 (2003), in Russian.
37. Pielou, E.C.: *Mathematical Ecology*. John Wiley & Sons, New York (1977).
38. Pleshanov, A.S.: *Insects-Defoliators of Larix Forests in Eastern Siberia*. Nauka, Novosibirsk (1982), in Russian.
39. Poulsen, E.T.: A model for population regulation with density- and frequency-dependent selection. *J. Math. Biol.*, **8**, 325–348 (1979).
40. Ricker, W. E.: Stock and recruitment. *J. Fish. Res. Board of Canada*, **11**, 559–623 (1954).
41. Shapiro, A.P., Luppov, S.P.: *Recurrent Equations in a Theory of Population Biology*. Nauka, Moscow (1982), in Russian.
42. Sharov, A.A.: Insect population dynamics modeling. *VINITI: Entomology*, **6**, 1–115 (1986), in Russian.
43. Shuster, G.: *Deterministic Chaos*. Mir, Moscow (1988), in Russian.
44. Sicheva, E.V.: Reasons of appearance of non-regular dynamics for fish commercial populations. in *Theoretical Analysis and Modeling*. DVO RAN, Vladivostok (1999), in Russian.
45. Smith, J.M.: *Models in Ecology*. Cambridge University Press (1974),
46. Svirezhev, Yu.M., Logofet, D.O.: *Stability of Biological Communities*. Nauka, Moscow, 352pp. (1978), in Russian.
47. Varley, G.C., Gradwell, G.R., Hassell, M.P.: *Insect Population Ecology, an Analytical Approach*. Blackwell Scientific, Oxford, 212 pp. (1973), in Russian.
48. Verhulst, P.F.: Notice sur la loi que la population suit dans son accroissement. *Corresp. Math. et Phys.*, **10**, 113–121 (1938).
49. Vorontsov, A.I.: *Forest Pathology*. Forest Industry, Moscow, 272 pp. (1978), in Russian.
50. Yakobson, M.V.: About properties of one-parametric family of dynamic systems  $x \rightarrow Ax * e^{-x}$ . *UMN*, **31**, 239–240 (1976), in Russian.

# Planning for Biodiversity Conservation Using Stochastic Programming

Trevon Fuller,<sup>1</sup> David P. Morton,<sup>2</sup> and Sahotra Sarkar<sup>1</sup>

<sup>1</sup> Section of Integrative Biology, University of Texas at Austin, 1 University Station, C0390, Austin, Texas 78712–1180, USA; [tfuller@mail.utexas.edu](mailto:tfuller@mail.utexas.edu), [sarkar@mail.utexas.edu](mailto:sarkar@mail.utexas.edu)

<sup>2</sup> Graduate Program in Operations Research, University of Texas at Austin, 1 University Station, C2200, Austin, Texas 78712–0292, USA; [morton@mail.utexas.edu](mailto:morton@mail.utexas.edu)

**Summary.** Rapid species extinctions and the loss of other biodiversity features worldwide have prompted the development of a systematic planning framework for the conservation of biodiversity. Limited resources (~ 40 million USD annually) are available for conservation, particularly in the developing countries that contain many of the world’s hotspots of species diversity. Thus, conservation planning problems are often represented as mathematical programs in which the objective is to select sites to serve as conservation areas so that the cost of the plan is as small as possible and adequate habitat is protected for each species. Here, we generalize this approach to allow for uncertainty in the planning process. In particular, we assume that the species to be protected disperse after the conservation areas are established and that planners cannot anticipate with certainty the species’ future locations when selecting the conservation areas. This uncertainty is modeled by including random variables in the mathematical program. We illustrate the approach by designing a network of conservation areas for birds in southern Quebec.

**Key words:** Conservation areas, reserve selection, stochastic programming, conservation biology, biodiversity.

## 9.1 Introduction

Conservation areas are broadly defined as sites administered for the protection of threatened species and other features of biodiversity. However, many conservation areas throughout the world were created not because of their biodiversity content but because they had little economic value when established [9]. As a consequence, there is growing evidence at the global scale that existing conservation areas do not represent threatened species adequately [11]. Thus, tools are needed for selecting and refining conservation areas worldwide. Globally, approximately 40 million USD is spent annually to protect biodiversity hotspots [10]. To make the best use of this limited funding, conservation areas must be selected in such a way that the cost of acquiring and managing the land and the foregone opportunity cost to local human communities are as small as possible.

An effective way to formulate this planning problem is to represent it as a linear integer mathematical program. In general, a mathematical program is an optimization model that takes as input data parameters. Solving the mathematical program amounts to selecting values for decision variables that optimize an objective function while obeying one or more constraints. In our setting, the objective is to minimize the cost of the selected sites. Alternatively, the objective may be to maximize the number of species (or other biodiversity surrogates) protected subject to a budgetary constraint. Typically, the program includes constraints to ensure that the selected sites contain sufficient habitat for each species. Though this approach has proven useful in many planning contexts [15], it makes two unrealistic assumptions: that there is no uncertainty in the data parameters of the mathematical program and that the conservation areas are selected all at once.

Here, we relax these assumptions by modeling conservation planning problems using stochastic programming, which is a branch of operations research concerned with optimization under uncertainty [1]. The uncertainty is represented by having some of the data parameters in the mathematical program be random variables whose values are determined by a random experiment. Formally, each random variable is a mapping from the sample space  $\Omega$  to  $\mathbb{R}$  and the outcomes of the random experiment constitute a  $\sigma$ -algebra  $F$  on  $\Omega$  in the probability space  $(\Omega, F, P)$ , where  $P$  is a probability measure on  $F$  [7]. In a two-stage stochastic program, the first-stage decision must be taken before the specific values of the random variables are known. Then a random experiment is conducted and the values of the random variables are disclosed. In the second stage, a recourse decision is taken to respond to, or compensate for, the results of the random experiment. The objective of the stochastic program is to minimize the cost of the first-stage decision plus the expected value of some function of the first-stage decision and the random variables. This two-stage framework has been used profitably in many areas of environmental planning, including acid rain control [14], water supply reliability modeling [8], and biodiversity conservation [6, 13].

In our two-stage stochastic integer program, sites are selected, based on their species composition, to be included in a network of conservation areas in stage one (Appendix, Fig. 9.1). There is no uncertainty about the locations of the species in stage one. However, the stochastic program includes random variables that represent the locations of the species after the first stage. After the stage-one decision, a random experiment is conducted and the species' new locations are disclosed. This models the relocation of species due, e.g., to anthropogenic habitat disturbance. The sample space  $\Omega$  of the stochastic program consists of all possible scenarios of species dispersal.  $F$  is a collection of subsets of  $\Omega$  and the function  $P : F \rightarrow [0, 1]$  assigns probabilities to the dispersal scenarios. In the second stage, we determine whether the sites selected in the first stage still cover each species adequately. If the species are no longer covered, the stage-one decision incurs a penalty based on the "site shortage" for each species. The site shortage is the targeted number of sites for the species less the number of selected sites that contain the species. The objective is to minimize the expected value of this penalty. The stochastic program requires a particular decision-making sequence—stage-one decision, random experiment, recourse decision—but places no restrictions on the duration of the stage-one activities or the elapsed time between the first and

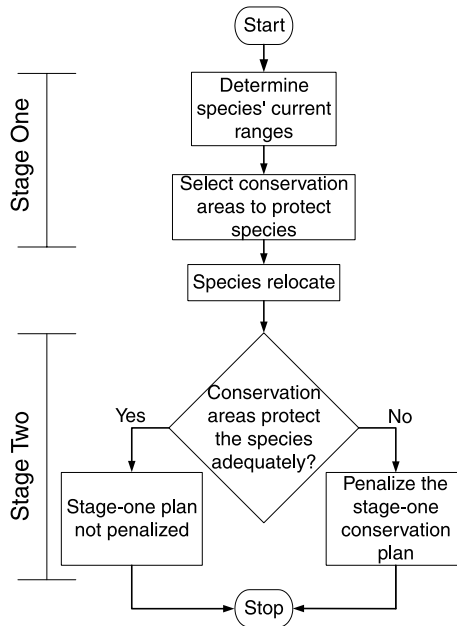


**Fig. 9.1.** Flowchart of conservation planning with species relocation.

second stages. This is particularly useful in conservation planning because it may take several years to establish the conservation areas (the stage-one decision) and to assess their performance (the stage-two decision).

This chapter makes two contributions. First, our stochastic program allows general targets of representation. The target of representation for a species is the number of populations of the species that should be included in the conservation areas. Previous models for conservation planning under uncertainty assume that a target of one representation is adequate [3, 6, 13]. However, if only one population of a species is protected and some conservation areas are destroyed or subject to poaching, the species may go extinct. For this reason, targets of 20 to 50 representations may be suitable for at-risk species [12]. Our stochastic program permits planners to select a suitable target for each species from one population up to all populations of the species. Second, we find the optimal solution for a substantially larger conservation planning problem that involves uncertainty than has been reported in the literature. In the context of deterministic conservation planning, decision problems with up to 1,906 sites have been solved optimally [5]. In the context of conservation planning under uncertainty, optimal solutions have been found only for much smaller problems (up to 146 sites, 116 species, and 100 scenarios of species relocation [13]). We report results for a stochastic programs that is substantially larger with respect to the number of sites, species, and species relocation scenarios.

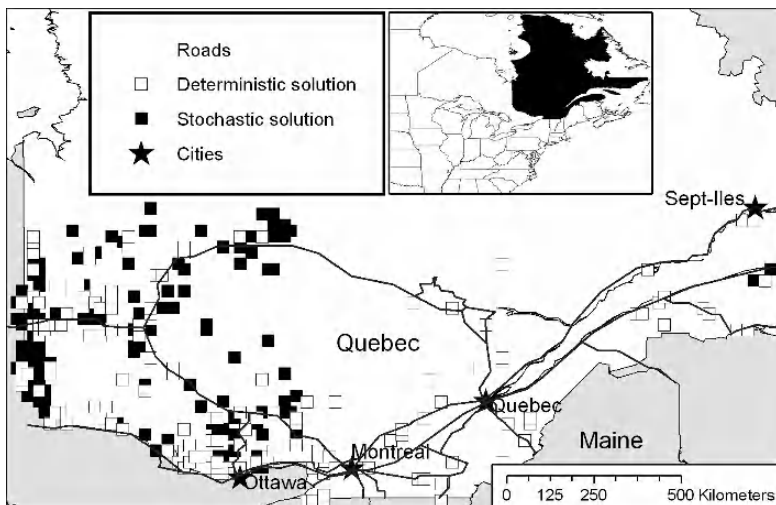


**Fig. 9.2.** Conservation areas for birds in southern Quebec selected using linear integer programming (white squares) and stochastic programming (black squares).

## 9.2 Case Study: Bird Conservation in Quebec

As part of an effort to expand the network of conservation areas of the Canadian province of Quebec, breeding bird nesting data was collected in southern Quebec between 1984 and 1994 [12]. At the  $0.02^\circ \times 0.02^\circ$  scale of longitude and latitude, the data set contains 2,049 sites and 242 bird species. First, we solved the integer linear program with deterministic input parameters to find the minimum set of sites required to represent 10% of the habitat of each bird species. The optimal set of conservation areas contained 156 sites (Fig. 9.2, white squares). Next, we simulated 500 scenarios of bird dispersal after stage one and solved the resulting stochastic program with a stage-one budget of 156 sites (Appendix). The solution to the stochastic program contains more sites in southwestern Quebec (Fig. 9.2, black squares) than the solution to the deterministic planning problem. However, both solutions contain many sites adjacent to roads in western Quebec. This may be due to a bias toward roads in the bird data set because sites adjacent to roads are easier to survey. We solved the stochastic program both (i) by converting it into a mixed-integer program and solving it using a branch-and-bound algorithm and (ii) using the L-shaped method [1]. The L-shaped method decomposes the two-stage program into a master program and several sub-programs, each of which corresponds to a different scenario of relocation for the bird species. At each iteration of the algorithm, the solution of the subproblems is used to construct a piecewise linear approximation of the stage-one objective function. The mixed-integer program had 121,242 constraints and 123,049 decision variables but the L-shaped method required solving a master program with 2,049 binary decision variables and 242 initial constraints. One new constraint was added to the master program at each iteration and the algorithm converged after 7 iterations. Both methods obtained



the same optimal solution but the L-shaped method was 1.77 times faster (running time: 4,325 seconds on a 1.7GHz Dell Xeon computer with 1 GB of RAM). The mathematical program was coded in the GAMS modeling language and solved with the CPLEX 9.0 solver.

### 9.3 Conclusion

Unlike our two-stage program, previous models for conservation planning under uncertainty [3, 6, 13] contain integer decision variables in the second (and subsequent) stages and therefore cannot be solved with the L-shaped method. In some previous optimization models [3, 13], the objective was to maximize the number of species covered, whereas our objective is to minimize the shortage of each species from its target. Whether the min or max formulation is more suitable depends on the planning context.

Here, we represent conservation area selection problems that include uncertainty as stochastic programs. Alternatively, such conservation planning problems can be formulated as stochastic dynamic programs [3]. However, the decision-making structure encountered in conservation planning may be more amenable to solution by stochastic programming than by stochastic dynamic programming. In conservation planning, decisions are made infrequently because the establishment of a new conservation area requires years of effort, and stochastic dynamic programming is often better suited for problems with many time stages in which decisions are made in each stage. We refer the reader to [2, 4] for further discussion comparing stochastic programming and approaches in stochastic dynamic programming and optimal control.

## Appendix

### Sets

- $i \in I$  species
- $j \in J$  sites
- $\omega \in \Omega$  species dispersal scenarios

### Data Parameters

- $c_j$  cost of site  $j$  in stage 1.  $c \in \mathbb{R}_+^{|J|}$
- $t_i$  target for species  $i$ .  $t_i \in [0, 1, 2, \dots, |J|]$
- $b_1$  stage 1 budget.

### Random Data

- $p^\omega$  probability of scenario  $\omega$ .  $p^\omega \in [0, 1]$ ,  $\sum_{\omega \in \Omega} p^\omega = 1$
- $b_{ij}^\omega$  1 if species  $i$  is in site  $j$  in scenario  $\omega$ . 0 otherwise
- $b^\omega \in \{0, 1\}^{|I| \times |J|}$

### Decision Variables

- $x_j$  1 if site  $j$  is selected in stage one. 0 otherwise.  $x \in \{0, 1\}^{|J|}$
- $y_i^\omega$  tally the site shortage for species  $i$  in scenario  $\omega$ .  $y_i^\omega \in [0, t_i]$

### Formulation

$$\min_x \sum_{\omega \in \Omega} p^\omega Q(x, b^\omega) \quad (9.1)$$

$$\text{s.t. } \sum_{j \in J} c_j x_j \leq b_1 \quad (9.2)$$

$$x_j \in \{0, 1\}, \quad j \in J, \quad (9.3)$$

where

$$Q(x, b^\omega) = \min_{y^\omega} \sum_{i \in I} y_i^\omega \quad (9.4)$$

$$\text{s.t. } y_i^\omega \geq t_i - \sum_{j \in J} b_{ij}^\omega x_j, \quad i \in I \quad (9.5)$$

$$y_i^\omega \geq 0, \quad i \in I. \quad (9.6)$$

The stochastic program (9.1)–(9.3) is expressed in terms of the stage-one decision variables, which select sites to be protected. Constraint (9.2) ensures that the cost of the sites selected in stage one does not exceed the budget. Constraint (9.3) states that each site must be selected or not selected in stage one. The objective function in (9.4) sums the tallies of site shortages for each species, i.e., the (positive) amount by which the species' target exceeds the number of sites selected in stage one that contain the species under scenario  $\omega$ . The overall objective function in (9.1) then takes the expected value of the number of species-site shortages over all  $b^\omega$  scenarios. Together, constraints (9.5) and (9.6) capture  $\max\{t_i - \sum_{j \in J} b_{ij}^\omega x_j, 0\}$ . This is the total number of sites short species  $i$  is relative to its target. For the Quebec data set, we generated scenarios of species dispersal by having each bird species randomly select one of the sites adjacent to its location in stage one and relocate to the selected site in stage two.

## References

1. Birge, J. R., Louveaux, F.: *Introduction to Stochastic Programming*. Springer, Berlin (1997).
2. Cheng, L., Subrahmanian, E., Westerberg, A.: A comparison of optimal control and stochastic programming from a formulation and computation perspective. *Computers and Chemical Engineering*, **29**, 149–164 (2004).
3. Costello, C., Polasky, S.: Dynamic reserve site selection. *Resource and Energy Economics*, **26**, 157–174 (2004).
4. Dupačová, J., Sladký, K.: Comparison of multistage stochastic programs with recourse and stochastic dynamic programs with discrete time. *Zeitschrift für angewandte Mathematik und Mechanik*, **82**, 753–765 (2002).
5. Fischer, D. T., Church, R. L.: The SITES reserve selection system: a critical review. *Environmental Modeling and Assessment*, **10**, 215–228 (2005).
6. Haight, R. G., Snyder, S. A., Revelle, C. S.: Metropolitan open-space protection with uncertain site availability. *Conservation Biology*, **19**, 327–337 (2005).
7. Karr, A. F.: *Probability*. Springer, Berlin (1993).
8. Lund, J. R.: Derived estimation of willingness to pay to avoid probabilistic shortage. *Water Resources Research*, **31**, 1367–1372 (1995).

9. Margules, C., Pressey, R.: Systematic conservation planning. *Nature*, **405**, 243–253 (2000).
10. Myers, N., Mittermeier, R. A., Mittermeier, C. G., da Fonseca, G. A. B., Ken, J.: Biodiversity hotspots for conservation priorities. *Nature*, **403**, 853–858 (2000).
11. Rodrigues, A. S., and twenty others.: Effectiveness of the global protected area network in representing species diversity. *Nature*, **428**, 640–643 (2004).
12. Sarakinos, H., Nicholls, A. O., Tubert, A., Aggarwal, A., Margules, C. R., Sarkar, S.: Area prioritization for biodiversity conservation in Québec on the basis of species distributions. *Biodiversity and Conservation*, **10**, 1419–1472 (2001).
13. Snyder, S. A., Haight, R. G., ReVelle, C. S.: Scenario optimization model for dynamic reserve site selection. *Environmental Modeling and Assessment*, **9**, 179–187 (2004).
14. Watanabe, T., Ellis, H.: Stochastic programming models for air quality management. *Computers and Operations Research*, **20**, 651–663 (1993).
15. Williams, J. C., ReVelle, C. S., Levin, S. A.: Using mathematical optimization models to design nature reserves. *Frontiers in Ecology and the Environment*, **2**, 98–105 (2004).

## A Diffusion-Reaction Model of a Mixed-Culture Biofilm Arising in Food Safety Studies\*

Hermann J. Eberl<sup>1</sup> and Heidi Schraft<sup>2</sup>

<sup>1</sup> Department of Mathematics and Statistics, University of Guelph, Guelph, Ontario, Canada; heberl@uoguelph.ca

<sup>2</sup> Department of Biology, Lakehead University, Thunder Bay, Ontario, Canada; heidi.schraft@lakeheadu.ca

**Summary.** Bacterial biofilms are communities of microorganisms that develop on interfaces in aqueous environments. We formulate a density-dependent diffusion-reaction model for the growth of a dual-species biofilm. Both bacteria respond differently to their environment and develop different types of biofilms: One is a classical aerobic biofilm former that produces the characteristic cluster-and-channel biofilm morphology, the other one also develops under anaerobic conditions and tends to form flat, creeping biofilms. A previously developed nonstandard finite-difference scheme is adapted for the computer simulation. In a numerical experiment it is shown how variations of a single parameter (growth rate) can trigger different spatial structure and organisation of the biofilm community.

**Key words:** Biofilm, mathematical model, nonlinear diffusion, computer simulation.

### 10.1 Introduction

The vast majority of bacteria live in microbial biofilm communities, adhered to surfaces in aqueous environments. Biofilm formation has been described as a complex dynamic process. Planktonic cells attach to the surface and excrete a glue-like substance of exopolysaccharides (EPS). In this layer of EPS the bacteria live a protected life. The growth of the biofilm depends on environmental conditions such as nutrient and oxygen availability, hydrodynamic stress, or pH value. While these factors are largely determined by the environmental conditions, they are affected in return by the biofilm bacteria themselves. For example, sufficient availability of nutrients leads to growth of the population and a growing population diminishes the nutrient resources. This leads to a complicated nonlinear interaction between the microbial community and its environment. Biofilms can be formed by a single bacterial species or they can develop as mixed-culture communities. Not all species show the same ability to form biofilms and neither do all species respond in the same way to the external stimuli.

---

\* Supported by the Advanced Foods and Materials Network (NCE).

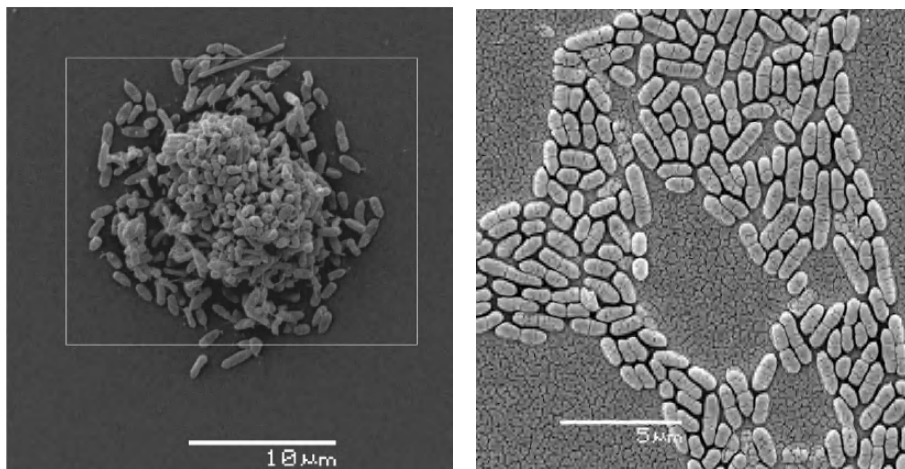


**Fig. 10.1.** SEM images of early stage (1 day) biofilm colonies of *P. putida* (left) and *L. monocytogenes* (right).

Biofilm communities can develop highly complex behavior and properties. For example, oxygen-consuming aerobic bacteria can create oxygen-free niches for anaerobic bacteria.

Although the term biofilm indicates a homogeneous flat structure, many biofilms grow in highly complex spatial architectures. Of fame are mushroom shaped, complicated cluster-and-channel arrangements. The spatial organisation is an important property of many biofilm systems; in the example above, the aerobes will form a protecting rim around the anaerobes. Therefore, the function and dynamics of biofilms cannot be studied without also studying the spatial structure.

Biofilm research has been traditionally motivated by environmental engineering and medical applications. Only recently has it been understood that biofilms also play a detrimental role in food safety and food processing (e.g., [2], [11], [12]). Our attention will be on the biofilms formed by *Listeria monocytogenes*, a hardy, harmful food-borne pathogen that causes the often-fatal infection listeriosis [3]. *L. monocytogenes* biofilms develop in thin layers of cells across the substratum, without extensive EPS production [9]; see Fig. 10.1. This is quite different from classical, EPS-prolific biofilm formers such as *Pseudomonas putida*, which develop in colonies that eventually form the characteristic cluster-and-channel morphologies. While *L. monocytogenes* in pure cultures is intensively studied, in many instances it appears together with other, biofilm-producing bacteria; see Fig. 10.2. These mixed-culture systems are far less understood (e.g., [9]). In this theoretical modeling and simulation study we will investigate the coexistence of the facultative anaerobic *L. monocytogenes* with a classical aerobic biofilm former like *P. putida*, in a system that is controlled by oxygen availability.

Different mathematical models have been proposed for spatio-temporal biofilm formation in recent years, ranging from stochastic cellular automata and individual-

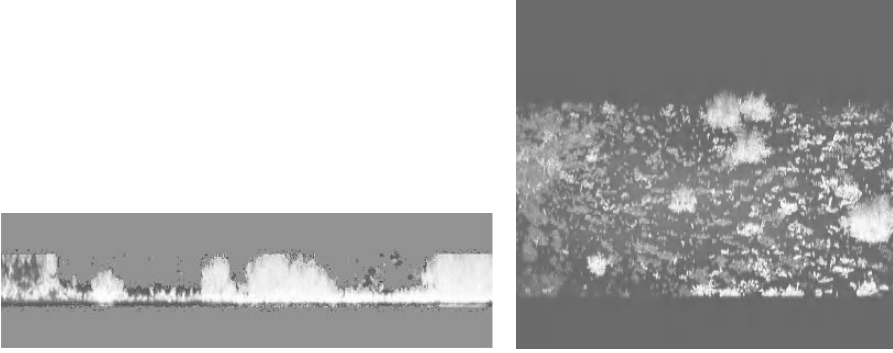


**Fig. 10.2.** Confocal laser scanning microscopy (CLSM) images of an early stage (1 day) mixed-culture biofilm, taken in the entry region of a flow cell. The original green-red images were modified to a greyscale presentation. *L. monocytogenes* is represented by darker cells, *P. putida* by lighter cells.

based models to deterministic continuum formulations. Only the latter has been accessible to mathematical analysis so far, while the first two mentioned groups are solely used as computer simulation tools. Since they are complex stochastic processes, they require many simulation runs per scenario, which makes them computationally quite expensive.

We will present here the extension of a continuous prototype biofilm, originally developed for mono-culture systems, to a binary biofilm system. This model takes the dynamic systems approach of classical mathematical biology. We will adapt a numerical method for the mono-species model to solve the dual-species model. The model consists of a system of highly nonlinear partial differential equations. The numerical scheme is based on finite difference discretisation in space and nonlocal treatment of time derivatives.

## 10.2 Mathematical Model

We follow the modeling approach proposed in [7] for a prototype mono-species biofilm, a density-dependent diffusion-reaction model, formulated in terms of the concentration of a limiting dissolved substrate  $C$  and the density of biomass  $M$ . The latter is normalised with respect to the maximum possible cell density, i.e., it is equivalent to the unit volume fraction occupied by the biofilm. The model is formulated in an open and bounded domain  $\Omega \subset \mathbb{R}^d$ . Later on we will carry out two-dimensional simulations, i.e.,  $d = 2$ . The biofilm itself is the region  $\Omega_2(t) = \{x \in \Omega : M(t, x) > 0\}$ , while the surrounding aqueous environment is denoted by  $\Omega_1(t) = \{x \in \Omega : M(t, x) = 0\}$ , cf. also Fig. 10.3.

$$\begin{cases} \partial_t M = \nabla(D_M(M)\nabla M) + g(C, M) \\ \partial_t C = \nabla(D_C(M)\nabla C) - f(C, M) \end{cases} . \quad (10.1)$$

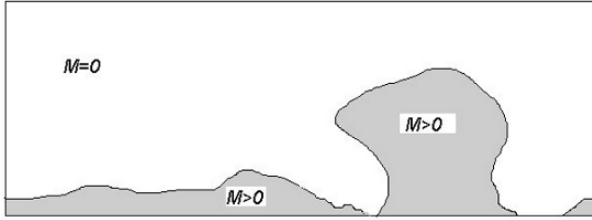


**Fig. 10.3.** Schematic representation of the biofilm system: The actual biofilm is the region where  $M > 0$ ; the surrounding aqueous environment is defined by  $M = 0$ . Both regions change according to the evolution equation (10.1).

The reaction terms in (10.1) describe the growth of new biomass and the decay of substrate due to bacterial growth. In the simplest case this is modeled by a Monod reaction, stating that for low substrate concentrations the growth rate is proportional to the available substrate but that saturation occurs if the substrate is available in abundance. In addition to this substrate-dependent growth we include a natural constant decay rate describing bacterial deactivation. This is expressed by

$$f(C, M) = \frac{k_1 C M}{k_2 + C}, \quad g(C, M) = \frac{k_3 C M}{k_2 + C} - k_4 M, \quad (10.2)$$

where all constants  $k_i$  are nonnegative and  $k_3/(k_2 + 1) - k_4 > 0$  (otherwise decay would outweigh growth for all levels of substrate supply). Since the growth function  $g(C, M)$  in (10.2) implies that new biomass is produced as long as there is substrate available, the upper bound on the biomass  $M < 1$  must be guaranteed by the spatial spreading mechanism and, hence, by the density-dependent diffusion coefficient  $D_M(M)$  in (10.1). It reads

$$D_M(M) = \delta \frac{M^\beta}{(1 - M)^\alpha}, \quad \alpha, \beta \geq 1, \quad \delta > 0. \quad (10.3)$$

The power law nonlinearity  $M^\beta$  leads to a sharp biofilm/water interface that spreads with finite speed of propagation, as in the porous medium equation. Notable spatial spreading only occurs for  $M \gg 0$ . The nonlinearity  $(1 - M)^\alpha$  guarantees the upper bound  $M \leq 1$  (squeezing property). The interplay of both nonlinear effects in (10.3) is required to describe biofilm formation. In case  $\beta = 0$  the biomass would be instantaneously distributed evenly over the domain, while  $\alpha = 0$  could lead to  $M > 1$ .

For small molecules, like oxygen, many authors assume that the difference in the diffusion coefficient of a solute in water and in the polymeric biofilm matrix is negligible. We follow this argument for the sake of simplicity and, hence, we have

$$D_C(M) = D_C = \text{const}, \quad D_C > 0.$$

Model (10.1) is to be completed by appropriate initial and boundary conditions: We prescribe mixed Dirichlet–Neumann conditions at the boundary of  $\Omega$ . More specifically, let  $\partial\Omega = \partial_1\Omega \cup \partial_2\Omega$ ; then we have

$$\begin{cases} C(t, x) = C_{\text{bulk}}, & x \in \partial_1 \Omega, t > 0 \\ \partial_n C(t, x) = 0, & x \in \partial_2 \Omega, t > 0 \end{cases}.$$

At  $t = 0$  we have the initial data for  $C$ ,  $C(0, x) = C_0(x)$  with  $C_0 \in \mathcal{C}^0(\Omega)$ .

Similarly we will allow for homogeneous Neumann or Dirichlet or mixed boundary conditions to be imposed on  $M$ . In our simulations later on we will always choose

$$\partial_n M = 0, \quad x \in \partial \Omega.$$

For the initial data we have to require that they obey the maximum cell density. We have therefore

$$M(0, x) = M_0(x), \quad x \in \Omega$$

with  $\|M_0\|_\infty < 1$ . Since continuity is not required for the initial data, we only ask for  $M_0 \in \mathcal{L}^2(\Omega)$ . Since we are interested in describing a developing biofilm,  $M_0(x) = 0$  will hold for most  $x$  and  $M_0(x) > 0$  will hold only in very small subdomains (not connected with each other) close to the substratum. These subdomains are the inoculum  $\Omega_2(0)$ .

The mono-species model (10.1) was studied in a series of papers, both analytically and numerically. Existence and uniqueness results were proved in [8]. In particular, it could be shown that the model solution indeed obeys the threshold imposed by the maximum cell density, i.e., that  $M \leq 1$ . It was shown that the long-time behavior depends on the boundary condition imposed on the biomass component  $M$ . If (homogeneous) Dirichlet conditions are prescribed somewhere on the boundary of  $\Omega$ , the solution  $M < 1$  (almost everywhere) exists for all  $t > 0$ . On the other hand, if homogeneous Neumann conditions are imposed everywhere on the boundary of  $\Omega$  (i.e., no biomass leaves the system), there exist initial data and model parameters such that  $M = 1$  (almost everywhere) in finite time. This describes the situation of a biofilm growing in a closed pot with a steady supply of nutrients. In this case the vessel will eventually be filled with biomass. A further result of [8] is the existence of a global attractor. If the substrate  $C$  is nowhere limited, i.e.,  $C \gg k_2$ , one obtains the simplification  $g(C, M) = g(M) = kM$ . For this model, which still captures the essential features of spatio-temporal spreading of biomass, a Lyapunov functional was found in [4]. Fully three-dimensional computer simulations in [7] showed that the model is able to predict cluster-and-channel and mushroom-type biofilm structures that can be observed in laboratory experiments of fully developed biofilms. An improved numerical scheme, based on a nonlocal (in time) representation of the nonlinear diffusion operator in the biomass spreading equation of (10.1) was proposed and discussed in [5]. It could be shown that the numerical solution renders important properties of the solution of the continuous model (10.1) such as positivity, boundedness, and speed of interface propagation.

The model (10.1) describes classical biofilm formers such as *P. putida*. For the second species in our system (e.g., *L. monocytogenes*) the model must be adapted to the specific properties as described above. First, one has to account for the possibility of both aerobic and anaerobic growth. To this end, the growth rate is modified as



$$\tilde{g}(C, M) = \tilde{k}_3 \frac{CM}{\tilde{k}_2 + C} + k_5 \frac{k_6 M}{k_6 + C} - k_4 M \tag{10.4}$$

The additional inhibition term  $k_5/(k_6 + C)$  has the property that it is biggest if  $C \ll k_6$  and vanishes as  $C \gg k_6$ . Hence, it acts in exactly the opposite way as the Monod term describing aerobic growth. Note that one obtains the simplified model  $\tilde{g}(C, M) = kM$  discussed above if the saturation constants of aerobic and anaerobic growth are equal, i.e.,  $\tilde{k}_2 = k_6$ , and if the maximum specific growth rates of aerobic and anaerobic growth are the same, i.e.,  $k_5 = \tilde{k}_3$ . In this special case, the production of biomass is independent of the available oxygen. However, the aerobic production of biomass still affects the oxygen balance.

The second model modification is due to the preferred biomass spreading direction across the substratum. This is expressed by a biased density-dependent diffusive flux with direction

$$j = \begin{pmatrix} 1 & 0 \\ 0 & \tilde{\delta} \end{pmatrix} \cdot \nabla M, \quad 0 < \tilde{\delta} \leq 1, \tag{10.5}$$

where the first component indicates the direction parallel to the substratum. Combining (10.4) and (10.5) one obtains the model for *L. monocytogenes* biofilms,

$$\begin{cases} \partial_t M = \partial_x (D(M)\partial_x M) + \partial_y (\tilde{\delta} D(M)\partial_y M) + \tilde{g}(C, M) \\ \partial_t C = D_C(\partial_{xx} C + \partial_{yy} C) - f(C, M) \end{cases} \tag{10.6}$$

Since we are primarily interested in a mixed-culture biofilm system, the models of both species must be combined into one model and the simulation techniques must be adapted.

### 10.2.1 The Mixed-Culture Biofilm Model Formulation

If two different types of biofilm formers are present in one biofilm, they compete for space. The total unit volume is locally available to both species. We denote the volume fractions occupied by the species by  $X$  (say, *P. putida*) and by  $Y$  (say, *L. monocytogenes*). In order to incorporate the space competition and the boundedness of available volume in the framework set by the nonlinear diffusion model, the squeezing term is modified to  $(1 - X - Y)^{-\alpha}$ , i.e., spatial spreading intensifies as  $X + Y \rightarrow 1$ . This leads to the following mixed-culture variant of the mono-species biofilm model:

$$\begin{cases} \partial_t X = \partial_x (D_X(X, Y)\partial_x X) + \partial_y (D_X(X, Y)\partial_y X) + g(C, M) \\ \partial_t Y = \partial_x (D_Y(X, Y)\partial_x Y) + \partial_y (\tilde{\delta} D_Y(X, Y)\partial_y Y) + \tilde{g}(C, M) \\ \partial_t C = D_C(\partial_{xx} C + \partial_{yy} C) - f_X(C, X) - f_Y(C, Y) \end{cases} \tag{10.7}$$

where

$$D_X(X, Y) = \delta_X \frac{X^\beta}{(1 - X - Y)^\alpha}, \quad D_Y(X, Y) = \delta_Y \frac{Y^\beta}{(1 - X - Y)^\alpha} \tag{10.8}$$

with reaction terms

$$f_X(C, X) = k_1 \frac{CX}{k_2 + C}, \quad f_Y(C, Y) = \tilde{k}_1 \frac{CY}{\tilde{k}_2 + C}.$$

This model is to be completed by appropriate initial and boundary conditions as discussed above. Note that in the absence of one species, i.e., either  $X \equiv 0$  or  $Y \equiv 0$ , the model (10.7) reduces to the single-species model of the previous section. If both species are present but in disjoint subdomains, i.e.,  $\Omega_X \cap \Omega_Y = \emptyset$  with  $\Omega_X(t) := \{x \in \Omega : X(t, x) > 0\}$ ,  $\Omega_Y(t) := \{x \in \Omega : Y(t, x) > 0\}$ , then each individual population behaves like a mono-species population and they influence each other only indirectly through the effect they have on the availability of  $C$ . Thus, the model develops distinct multi-species features only if in one colony both species are present.

### 10.2.2 Numerical Method

The method that we adapt for the numerical solution of (10.7) is a nonstandard finite difference scheme that was originally developed and analysed for the simpler mono-species problem (10.1) in [4]. According to the definition given in [1], a finite difference scheme is nonstandard if (i) either the difference approximation is nonlinear or (ii) nonlinear terms are evaluated nonlocally, i.e., at neighboring grid points. Our scheme falls under this latter definition (ii). Nonstandard schemes aim at numerical solutions that show the same qualitative behavior as the solutions of the underlying continuous problem. In the context of (10.7) these are in particular solutions with a finite speed of interface propagation. The discretisation method is derived following two rules for the construction of nonstandard finite difference schemes, as given in [10]: The order of approximation of a derivative is of the same order as the derivative; the nonlinear diffusion operator is evaluated nonlocally in time. To introduce the numerical scheme we rewrite (10.7) as an ordinary differential equation on an appropriate function space  $V$ ,

$$\partial_t u = A(u)u, \tag{10.9}$$

where  $u$  is the vector valued dependent variable  $u = (X, Y, C)^T$ . The diffusion-reaction operator  $A(u) : V \rightarrow V$  is derived from (10.7) such that it is linear for a given  $u$ . The nonlocal time discretisation of (10.9) is then

$$u(t^{n+1}) = u(t^n) + \Delta t A(u(t^n))u(t^{n+1}). \tag{10.10}$$

The spatial discretisation of  $u$  is carried out using standard second-order finite differences on a rectangular grid. Thus, in every time step of a simulation three linear systems must be solved consecutively, one for each component  $X$ ,  $Y$ , and  $C$  of  $u$ . The system matrices in (10.10) are sparse and banded but not symmetric, albeit structurally symmetric. It was proved in [5] that this numerical scheme applied to the mono-species model (10.1) (a) is positivity preserving and free of spurious oscillations, (b) renders a finite speed of interface propagation where the discrete interface satisfies a discretised

version of the continuous interface condition, (c) is able to describe the merging of biofilm colonies, and (d) results in a small diffusive interface smearing. Furthermore, it was shown in simulations that the computed interface quickly converges as the grid is refined. In fact, the interface location is accurate within  $\Delta x$ .

As pointed out above, the model for mono-species biofilms is a special case of the mixed-culture model (10.7). Accordingly the properties of the numerical scheme also naturally hold for mono-species colonies in a mixed-culture biofilm system. Moreover, the proofs of properties (a), (b), (c), and (d) directly carry over to the mixed-culture biofilm.

### 10.3 Simulation Results and Discussion

We use numerical simulations to show that the spatial organisation of both populations in a biofilm depends on the model parameters. It is known from single-species biofilm simulations of (10.1) that under given environmental conditions and, hence, given conditions of nutrient supply, the maximum specific growth rate  $\mu$  determines the morphology of the biofilm ([7]). This physiological parameter enters our model (10.4) as  $k_1 = \mu$  and  $k_3 = \mu/\Upsilon$ , where  $\Upsilon = \text{const}$  is a yield factor. In the binary biofilm model (10.7) the situation is more complex since we have different maximum specific growth rates for both species. In our experiment we investigate how the biofilm morphology and the spatial organisation of the bacteria in the biofilm depend on these growth rates. To this end we carry out a number of simulations in which  $k_1$  (and accordingly  $k_3$ ) is varied and all other parameters are kept unchanged.

The computer simulations were carried out on a rectangular grid of  $200 \times 60$  cells. The initial distribution of biomass on the substratum (i.e., in the first layer of grid cells in the  $y$  direction),  $X(0, \cdot)$ ,  $Y(0, \cdot)$ , is chosen randomly, where the total amount as well as the number of initial colonies are specified as input data. The same initial data were used for all simulations in order to allow a better comparison. The model parameters were chosen in the range of typical values reported in the literature. As a reference data set we chose the same maximum specific growth rate for both populations, i.e.,  $k_1 = \tilde{k}_1$ . In the numerical experiment the parameter  $k_1$  was chosen to vary over one order of magnitude,  $0.5\tilde{k}_1 \leq k_1 \leq 5\tilde{k}_1$  (where  $\tilde{k}_1 = 10$  in dimensionless units). In order to allow a better comparison we also imposed  $k_2 = \tilde{k}_2 = k_6$  and  $k_5 = \tilde{k}_3$  to make the actual growth of  $Y$  independent of  $C$  as noted above.

Some lumped simulation results are shown in Fig. 10.4. As expected, higher maximum growth rates  $k_1$  imply that the total biomass of  $X$  in the system grows faster. In all cases the  $X$  growth curves lie clearly below the corresponding exponential growth curve (straight line), due to oxygen limitation. As can be seen from the graph of  $\min_{x \in \Omega} C(t, x)$ , higher aerobic maximum growth rates imply an earlier depletion of oxygen. Accordingly the observed growth rates slow down more quickly, the higher  $k_1$  is (albeit on a higher level). Since the production of  $Y$  does not depend on oxygen, the same (exponential) growth curves of  $Y$  are obtained for all simulations. It is observed that higher maximum specific growth rates  $k_1$  also lead to a faster compression of the

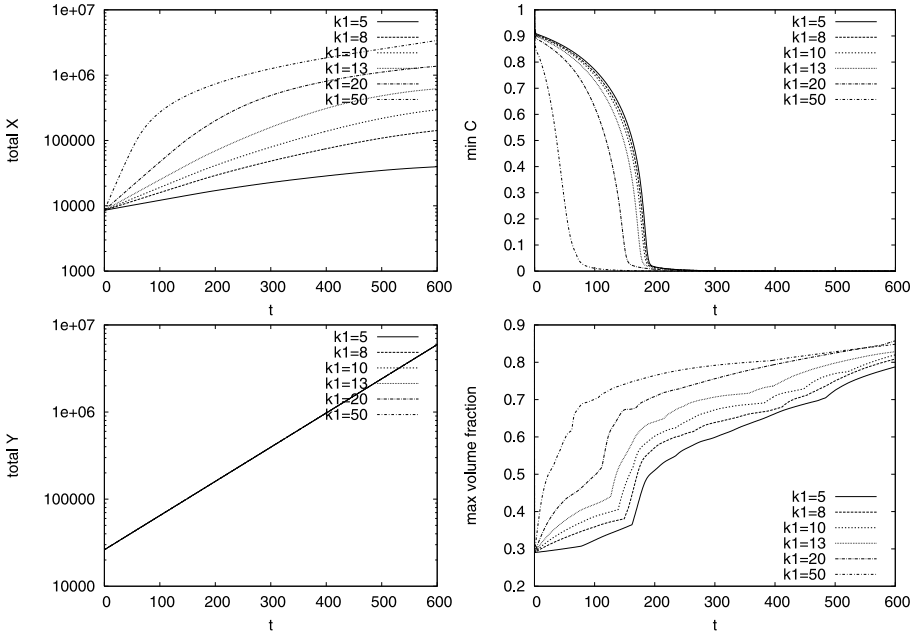


**Fig. 10.4.** Lumped simulation results for varying values of parameter  $k_1$  (keeping  $\tilde{k}_3 = 10$  fixed). Shown are the total amount of  $X$  and of  $Y$ , as well as the minimum concentration value of  $C$  in the reactor and the maximum volume fraction occupied by biomass.

biomass, as shown by the graph of  $\max_{x \in \Omega} [X(t, x) + Y(t, x)]$ . While for low values of  $k_1$  a population lag phase is observed initially, this is not the case for high values.

The impact of variations in  $k_1$  on the spatial morphology of the biofilm and on the spatial organisation of the populations in the biofilm is shown in Fig. 10.5 for the choices  $k_1 = 0.5\tilde{k}_3$ ,  $k_1 = \tilde{k}_3$ , and  $k_1 = 5\tilde{k}_3$ . In the case of lowest  $k_1$  the biofilm is dominated by species  $Y$ . Despite not necessarily depending on oxygen,  $Y$  consumes it faster than the strictly aerobic  $X$ . Hence,  $X$  is hindered in its development. The resulting biofilm is a homogeneous layer of  $Y$ , in which isolated niches of  $X$  are captured. A qualitatively similar, albeit less drastic, picture is obtained for the case  $k_1 = \tilde{k}_3$ . In this situation the oxygen consumption by the facultative anaerobic species also dominates the growth of the aerobes by controlling the oxygen in the system. Only if  $k_1$  is clearly higher than  $\tilde{k}_3$  (e.g.,  $k_1 = 5\tilde{k}_3$ ), can the aerobes develop unhindered. One obtains a two-layered biofilm morphology, with a mixed flat base layer containing  $X$  and  $Y$  and a top layer of fast-growing aerobic  $X$ . The latter develops in the well-known mushroom-type cluster-and-channel architecture, which is characteristic for strong aerobic biofilm formers in substrate limited regimes (i.e., in the case of high growth number  $\mathcal{G}$ , cf. [7], as it is the case for high maximum specific growth rates). This is in good agreement with the CLSM figures in Fig. 10.2. These were taken in the entrance region of a flow channel in which the growth conditions are best for the aerobic bacteria. In all cases it is observed that the species  $Y$  forms a creeping biofilm, i.e., preferably spreads flat across

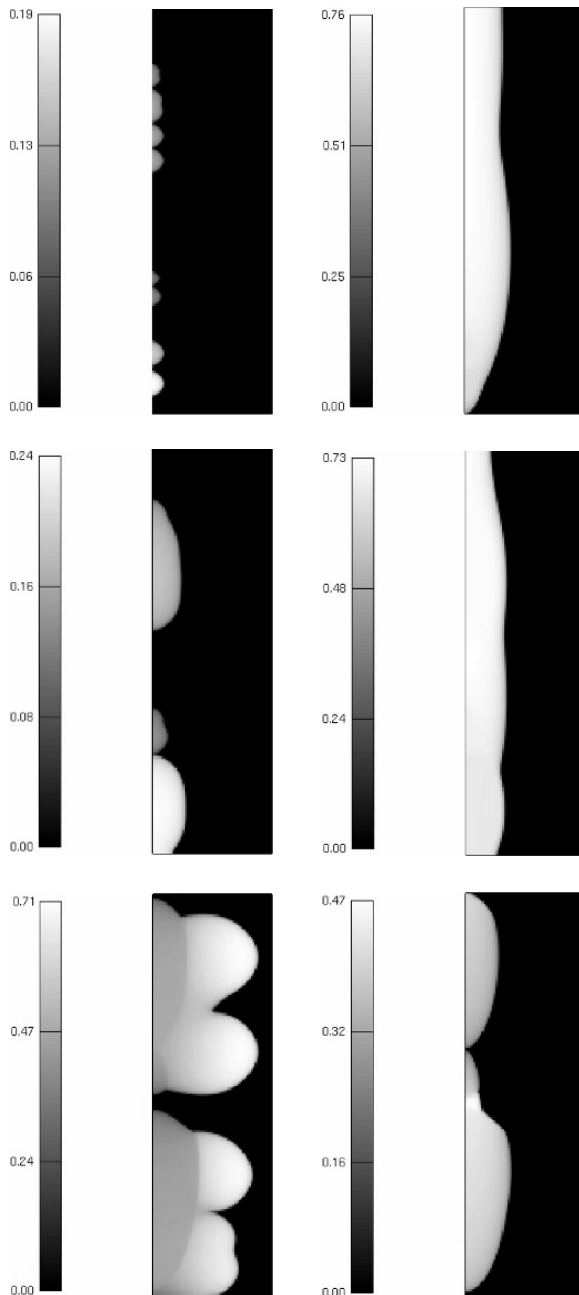


**Fig. 10.5.** Simulation snapshots of developed biofilms (sufficiently large  $t$ ) for model parameter  $k_1 : \tilde{k}_3 = 0.5$  (top),  $k_1 : \tilde{k}_3 = 1$  (middle),  $k_1 : \tilde{k}_3 = 5$  (bottom) that evolve from the same inoculum. Shown are the spatial biomass distributions of  $X$  (left) and  $Y$  (right), normalised to the maximum biomass density. The biofilm is the superposition of both figures.

the substratum, in both experiments and simulations. The classical aerobic biofilm former *X* tends to develop colonies that are initially almost spherical (see also Fig. 10.1 and 10.2).

## 10.4 Conclusion

This qualitative modeling and simulation study is a first attempt to understand spatio-temporal formation and population dynamics of biofilms formed by *L. monocytogenes* and *P. putida*, based on diffusion-reaction principles. It was shown that both the structure of the biofilm and the spatial distribution of the bacteria in the colony are determined by local growth conditions. In favorable conditions, *P. putida* biofilms form a layer of characteristic mushroom-shaped cell clusters on top of a mixed flat layer of both bacteria. The implications for disinfection with sanitizers or antimicrobial agents is that *P. putida* in the top clusters will take the largest hit, while the harmful *L. monocytogenes* at the substratum remains protected and difficult to remove. A closer analysis of this shall be the subject of a further study.

## Acknowledgment

The microscopy images were produced by Greg Kepka as part of his B.S. honors project at Lakehead University. The authors also acknowledge the financial support received from NSERC through individual Discovery Grants.

## References

1. Anguelov, R., Lubuma J.M.S.: Contributions to the mathematics of the nonstandard finite difference method and its applications. *Num. Meth. PDE*, **17**, 518–543 (2001).
2. Chmielewski, R.A.N., Frank, J.F.: Biofilm formation and control in food processing facilities. *Compr. Revs. Food Sc. and Food Saf.*, **2**, 22–32 (2003).
3. Dept. of Health and Human Services, Centers for Disease Control and Prevention, USA, <http://www.cdc.gov/ncidod/dbmd/diseaseinfo/listeriosis.g.htm>, Date: October 2005.
4. Duvnjak, A., Eberl, H.J.: Time-discretization of a degenerate reaction-diffusion equation arising in biofilm modeling. *El. Trans. Num. Analysis*, **23**, 15–37 (2006).
5. Eberl, H.J., Demaret, L.: A finite difference scheme for a degenerate diffusion equation arising in microbial ecology. *El. J. Diff. Equ.*, **CS15**, 77–95 (2007).
6. Eberl H.J., Efendiev, M.A.: A transient density dependent diffusion-reaction model for the limitation of antibiotic penetration in biofilms. *El. J. Diff. Equ.*, **CS10**, 123–142 (2003).
7. Eberl H.J., Parker D.F., van Loosdrecht M.C.M.: A new deterministic spatio-temporal continuum model for biofilm development. *J. Theor. Med.*, **3**, 161–175 (2001).
8. Efendiev, M.A., Eberl, H.J., Zelik, S.V.: Existence and longtime behaviour of solutions of a nonlinear reaction-diffusion system arising in the modeling of biofilms. *RIMS Kyoto*, **1258**, 49–71 (2002).

9. Hassan, A.N., Birt, D.M., Frank, J.F.: Behavior of *Listeria monocytogenes* in a *Pseudomonas putida* biofilm on a condensate-forming surface. *J. Food Prot.*, **67**, 322–327 (2004).
10. Mickens, R.E.: Nonstandard finite difference schemes. In: Mickens, R.E. (ed) *Applications of Nonstandard Finite Difference Schemes*, World Scientific (2000).
11. Trachoo, N.: Biofilms and the food industry. *Songklanakarin J. Sci. Tech.*, **25**, 807–815 (2003).
12. Verran, J.: Biofouling in food processing: Biofilm or biotransfer potential? *Trans. IChemE*, **80**, 292–298 (2002).

## The Periodical Population Dynamics of Lottery Models Including the Effect of Undeveloped Seeds

Shigehide Iwata,<sup>1</sup> Ryusuke Kon,<sup>2</sup> and Yasuhiro Takeuchi<sup>3</sup>

<sup>1</sup> Graduate School of Science and Technology, Shizuoka University. Johoku 3-5-2, Hamamatsu, Japan; f5645023@ipc.shizuoka.ac.jp

<sup>2</sup> Faculty of Mathematics, Kyushu University. Hakozaki 6-10-1, Higashi-ku Fukuoka, Japan; kon-r@math.kyushu-u.ac.jp

<sup>3</sup> Department of Systems Engineering, Faculty of Engineering, Shizuoka University. Johoku 3-5-2, Hamamatsu, Japan; takeuchi@sys.eng.shizuoka.ac.jp

**Summary.** The mechanism that promotes coexistence of species has not been completely clarified yet. We propose that the amount of nutrient can be one of the factors that promote coexistence of species. Plant species have to reproduce seeds to produce descendants. Even if plant species do reproduce seeds, it is not ensured that every seed will bud. The amount of seeds that can bud successfully depends on the amount of nutrient: if the nutrient is scarce, then every seed cannot bud, but if the nutrient is rich, then every seed can bud. We also assume that the amount of seeds reproduced by one plant individual depends on the amount of nutrient. We show that, in this situation, the population dynamics of plants exhibits a complex behavior, which promotes coexistence of species.

**Key words:** Space, nutrient, reproduction function, effective availability, undeveloped seed.

### 11.1 Introduction

Based on the lottery model proposed by Chesson and Warner [1,2], we consider the effect of undeveloped seeds on the population dynamics. Most plant species are influenced by an abiotic or biotic environment in the reproduction phase (Lambers [8]). The amount of nutrient may be insufficient for plants to grow their sprouts or seedlings. We consider the situation where plants reproduce both undeveloped and developed seeds depending on the amount of nutrient.

The standard lottery model (Chesson and Warner [1], Chesson [2]) is given by the following nonautonomous difference equation:

$$P_i(t+1) = (1 - \delta_i(t))P_i(t) + S(P_1(t), \dots, P_n(t)) \frac{\beta_i(t)P_i(t)}{\sum_{j=1}^n \beta_j(t)P_j(t)}, \quad i = 1, \dots, n, \quad (11.1)$$

where  $S(P_1(t), \dots, P_n(t)) = 1 - \sum_{j=1}^n (1 - \delta_j(t))P_j(t)$ . The vital coefficients  $\beta_i(t)$  and  $\delta_i(t)$  depend on time  $t$ , so the equation (11.1) is a nonautonomous system. The



initial condition satisfies  $P_i(0) \geq 0$ ,  $i = 1, \dots, n$ , and  $\sum_{j=1}^n P_j(0) = 1$ . The variable  $P_i(t)$  denotes the occupation rate of space by plant species  $i$  at year  $t$ . There are  $n$  plant species in a single habitat. Every year, each plant species  $i$  reproduces the developed seeds, the amount of which is given by  $\beta_i(t)P_i(t)$ . Additionally, every year adult plants are removed at the rate  $\delta_i(t)$ , and this removal creates the vacant space  $S(P_1(t), \dots, P_n(t)) = 1 - \sum_{j=1}^n (1 - \delta_j(t))P_j(t)$ , which is immediately occupied by the individuals randomly chosen from the pool of the developed seeds. In model (11.1), it is implicitly assumed that nutrients are always sufficiently available for all plant species. The studies of Chesson and Warner [1] and Chesson [2] show that the temporal fluctuation of the natality rates  $\beta_i(t)$  promotes coexistence of species, but the temporal fluctuation of the mortality rates  $\delta_i(t)$  does not. Furthermore, coexistence cannot be achieved for almost every pair of the parameters  $\beta_i$  and  $\delta_i$  as long as they are constant. Therefore, we see that the temporal heterogeneity promotes coexistence in the lottery model.

Following these seminal papers, the effects of temporal fluctuations in the recruitment process have been analyzed intensively (e.g., see Hatfield and Scheibling [6], Chesson and Huntly [3]). The lottery model also provides a basis for understanding the coexistence of multiple species in terrestrial systems (Laurie et al. [9]). Additionally, Dewi and Chesson [5] studied a lottery model with a stage structure and Comins and Noble [4] studied a lottery model with different patches. The recent works of Muko and Iwasa [10, 11] considered the other mechanism which promotes coexistence. They incorporated the spatial heterogeneity into the standard lottery model (11.1). Their model includes multiple habitats, each of which has different mortality and natality rates of the species. Their study shows that the heterogeneity of mortality rates promotes coexistence of species, but natality rates does not (Muko and Iwasa [10]). By these two studies, we see that the spatial heterogeneity promotes coexistence in a lottery model.

Besides a lottery model, Neuhauser and Pacala [12] studied a Lotka–Volterra equation with explicit spatial factors. By using a chemostat model, Huisman and Weissing [7] showed that nine species can coexist under three kinds of resources.

This paper is organized as follows. In Section 11.2, we derive a new lottery model, which incorporates the effect of undeveloped seeds, and show some basic properties of the model. In Section 11.3, we show the results of simulations for two or three species cases. The final section includes our discussion.

## 11.2 Model

Our model is the following autonomous difference equation:

$$\begin{cases} P_i(t+1) = (1 - \delta_i)P_i(t) \\ \quad + S(P_1(t), \dots, P_n(t)) \frac{\beta_i(x(t))P_i(t)}{\sum_{j=1}^n \beta_j(x(t))P_j(t)} & i = 1, \dots, n, \\ x(t+1) = (x(t) - \sum_{j=1}^n \alpha_j(x(t))P_j(t))q + s, \end{cases} \quad (11.2)$$

where  $S(P_1, \dots, P_n) = 1 - \sum_{j=1}^n (1 - \delta_j) P_j$ . The parameters  $\delta_i$  ( $0 \leq \delta_i \leq 1$ ) and the variables  $P_i(t)$  have the same meaning as those in model (11.1). Let us first consider the second equation in (11.2). The function  $\alpha_i(x)$  is the amount of nutrient consumed through the space occupied by plant species  $i$ :

$$\alpha_i(x) = \frac{m_i x}{a_i + x}, \tag{11.3}$$

where  $x$  is the amount of a limiting nutrient contained in a unit area of the habitat,  $m_i$  is the maximum number of seeds reproduced from the space occupied by an individual of plant species  $i$ , and  $a_i$  is the Michaelis–Menten (or half-saturation) constant. Since plant species can uptake only the nutrient in soil,  $x(t) - \sum_{j=1}^n \alpha_j(x(t)) > 0$  must hold for  $t > 0$ . This is ensured if  $m_i/a_i \leq 1$ . The parameter  $s$  ( $s > 0$ ) denotes a constant inflow and  $q$  ( $0 < q < 1$ ) denotes washout rate. The total amount of the nutrient consumed through the space occupied by the plants is given as follows:

$$\sum_{j=1}^n \alpha_j(x) P_j.$$

The function  $\beta_i(x)$  is the number of the developed seeds reproduced from the space occupied by plant species  $i$ . In this chapter, we assume

$$\beta_i(x) = \begin{cases} c_i \rho_i \alpha_i(x) & (l_i \leq x) \\ 0 & (0 < x < l_i), \end{cases}$$

where  $c_i > 0$  denotes the conversion rate from nutrient to the number of seeds of species  $i$ .  $\rho_i > 0$  denotes the rate of nutrient used to produce seeds of plant species  $i$ .  $l_i \geq 0$  is a positive constant. We assume  $l_n = 0$ . This assumption shows that species  $n$  does not reproduce any undeveloped seeds. Under the condition  $0 < x < l_i$  any seeds of species  $i \neq n$  cannot bud. This means that if the nutrient is scarce (i.e.,  $0 < x < l_i$ ), then any seeds are not able to bud. Therefore, if the nutrient in the soil is scarce, species  $i \neq n$  reproduces only undeveloped seeds. All parameters ( $\delta_i, m_i, a_i, c_i, \rho_i, l_i, q, s$ ) in (11.2) are constant. Therefore, (11.2) is an autonomous system.

### 11.2.1 The Basic Properties of Model (11.2)

We define  $\Omega := \{(P_1, \dots, P_n, x) \in \mathbf{R}^{n+1} \mid P_1 \geq 0, \dots, P_n \geq 0, \sum_{j=1}^n P_j = 1, x > 0\}$ . Then we can show that  $\Omega$  is forward invariant.

**Proposition 1** *If  $(P_1(0), \dots, P_n(0), x(0)) \in \Omega$ , then  $(P_1(t), \dots, P_n(t), x(t)) \in \Omega$  for all  $t \geq 0$ .*

*Proof* Let  $(P_1(t), \dots, P_n(t), x(t)) \in \Omega$ . Then it follows from (11.2) that

$$\sum_{j=1}^n P_j(t+1) = 1.$$

Since  $\beta_i(x)$  and  $S(P_1, P_2, \dots, P_n)$  are nonnegative,  $P_i(t+1) \geq 0$  holds for all  $i = 1, 2, \dots, n$ . Finally, we prove  $x(t+1) \geq 0$ . In fact,  $\max_{x \geq 0} (m_i/(a_i + x)) = m_i/a_i$ , and we have the following inequalities:

$$\begin{aligned} x(t+1) &= x(t) - \sum_{j=1}^n \alpha_j(x(t))P_j(t)q + s \\ &\geq x(t) - \sum_{j=1}^n \frac{m_j}{a_j} x(t)P_j(t)q + s \\ &\geq x(t)\left(1 - \sum_{j=1}^n P_j(t)\right)q + s \\ &= s. \end{aligned}$$

This completes the proof.  $\square$

From the second equation of (11.2),  $x(t+1) \leq x(t)q + s$  is satisfied for all  $t \geq 0$ . This implies that  $x(t) \leq 2s/(1-q)$  for sufficiently large  $t > 0$ . Hence by combining with Proposition 1, we have the following proposition.

**Proposition 2** *Every solution of system (11.2) with the initial condition  $(P_1(0), \dots, P_n(0), x(0)) \in \Omega$  is bounded.*

*Proof* From Proposition 1, if  $(P_1(0), \dots, P_n(0), x(0)) \in \Omega$ , then  $(P_1(t), \dots, P_n(t), x(t)) \in \Omega$  for all  $t \geq 0$ . So, we consider the boundedness of  $x$ . If  $(P_1(t), \dots, P_n(t), x(t)) \in \Omega$ , then  $(x(t) - \sum_{j=1}^n \alpha_j(x(t))P_j(t))q + s < qx(t) + s$  holds. Therefore, we have

$$x(t+1) \leq qx(t) + s.$$

If we reduce both sides of the inequality by  $s/(1-q)$ , we obtain

$$\begin{aligned} x(t+1) - \frac{s}{1-q} &\leq qx(t) + s - \frac{s}{1-q} \\ &= q \left( x(t) - \frac{s}{1-q} \right) \\ &\leq q^{t+1} \left( x(0) - \frac{s}{1-q} \right). \end{aligned}$$

This implies the boundedness of  $x$ . This completes the proof.  $\square$

These propositions imply that the occupation rate  $P_i$  always satisfies  $0 \leq P_i \leq 1$  and the amount of nutrient is always positive and is bounded above.

### 11.3 Simulations

In this section, we show the simulation results for the cases with two and three species.

### 11.3.1 The Case with Two Species ( $n = 2$ )

Fig. 11.1 is the result of the numerical simulations of system (11.2) with two species ( $n = 2$ ). In Fig. 11.1, there are two types of area: in AREA I and AREA III, one species survives; in AREA II and AREA IV, two species coexist.

In AREA I (resp. AREA III), species 2 (resp. species 1) survives and species 1 (resp. species 2) is excluded (see Fig. 11.2 (a) and (c)). In AREA I and III, one of the boundary fixed points  $E_2(P_1, P_2, x) = (0, 1, x_2)$  and  $E_1(P_1, P_2, x) = (1, 0, x_1)$  is stable, respectively.

In AREA II, species can coexist (see Fig. 11.2 (b)) and there exists one positive fixed point to which all solutions of system (11.2) tend. In this situation, two boundary fixed points are unstable.

In AREA IV, species can coexist with sustained oscillations (see Fig. 11.2 (d)). In this area of parameters,  $x$  oscillates between the intervals  $0 < x < l_1$  and  $l_1 \leq x$ . The solution tends to the boundary fixed point  $E_2$  when  $x$  is located in the interval  $0 < x < l_1$ . The solution tends to  $E_1$  when  $x$  is located in the interval  $x \geq l_1$ .

### 11.3.2 The Case with Three Species ( $n = 3$ )

In Fig. 11.3, we can find three types of area: in AREA I, II and IV, two species survive with sustained oscillations; in AREA III, one species survives; in AREA V, three species coexist with sustained oscillations.

In AREA I, species 2 and 3 can survive with sustained oscillations (see Fig. 11.4 (a)). In this region, species 1 cannot invade the  $P_2 - P_3$  subsystem, since species 1 cannot reproduce a sufficient amount of developed seeds. Note that  $m_1$  is small or  $l_1$  is large in AREA I.

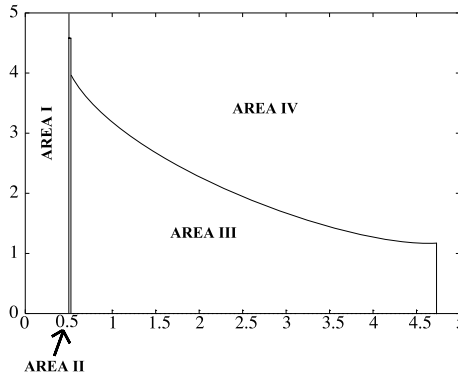


**Fig. 11.1.** The  $(m_1, l_1)$  parameter plane. In AREA I, only species 2 survives. In AREA II, two species coexist without oscillation. In AREA III, only species 1 survives. In AREA IV, species 1 and 2 coexist with a sustained oscillation. The parameters are  $m_1 \in [0, 5]$ ,  $l_1 \in [0, 4.7]$ ,  $\delta_1 = \delta_2 = 0.12$ ,  $m_2 = 0.3$ ,  $a_1 = 4.7$ ,  $a_2 = 1$ ,  $l_2 = 0$ ,  $q = 0.8$ ,  $s = 1$ ,  $\rho_1 = \rho_2 = 0.8$ ,  $c_1 = c_2 = 2.5$ . The initial condition is  $(P_1(0), P_2(0), x(0)) = (0.3, 0.6, 0.9)$ .

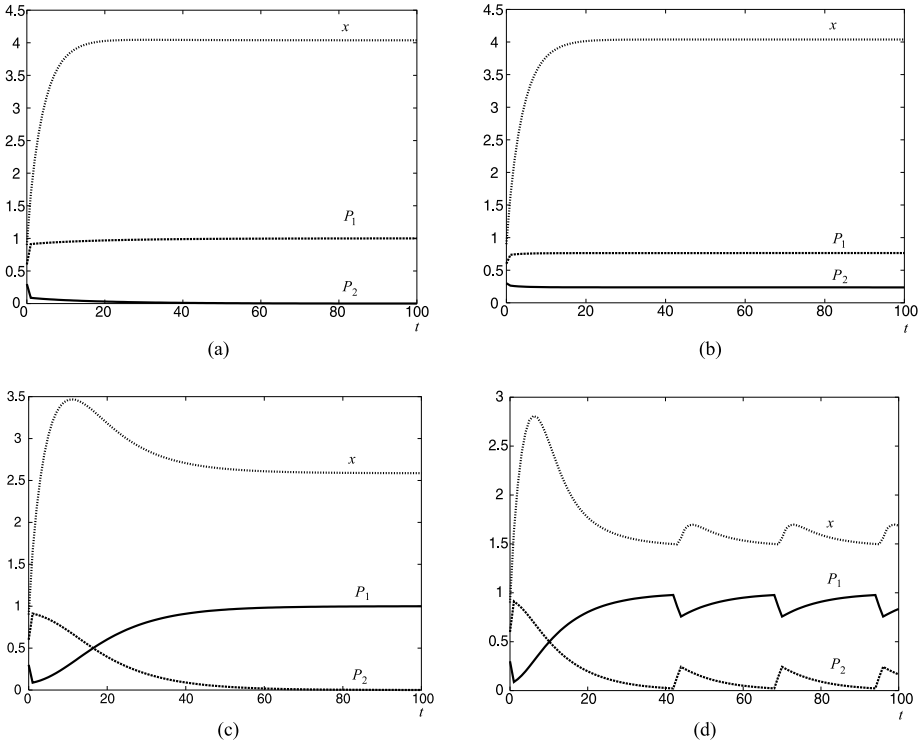


**Fig. 11.2.** The temporal sequence of  $P_1$ ,  $P_2$  and  $x$  with the initial condition  $(P_1(0), P_2(0), x(0)) = (0.3, 0.6, 0.9)$ . The parameters are  $\delta_1 = \delta_2 = 0.12$ ,  $m_2 = 0.3$ ,  $a_1 = 4.7$ ,  $a_2 = 1$ ,  $l_1 = 1.5$ ,  $l_2 = 0$ ,  $q = 0.8$ ,  $s = 1$ ,  $\rho_1 = \rho_2 = 0.8$ ,  $c_1 = c_2 = 2.5$ , (a)  $m_1 = 0.3$  (AREA I in Fig. 11.1), (b)  $m_1 = 0.52$  (AREA II in Fig. 11.1), (c)  $m_1 = 1.7$  (AREA III in Fig. 11.1), (d)  $m_1 = 3.7$  (AREA IV in Fig. 11.1).

In AREA II, species 1 and 2 can survive (see Fig. 11.4 (b)). In this region, species 1 invades the  $P_2 - P_3$  subsystem and eliminates species 3.

In AREA III, only species 1 survives (see Fig. 11.4 (c)). In this region, species 1 can reproduce a sufficient number of developed seeds. Note that  $m_1$  is large and  $l_1$  is small in AREA III and species 1 is the strongest there.

In AREA IV, species 1 and 3 can survive with sustained oscillations (see Fig. 11.4 (d)). In this region, species 1 can invade the  $P_2 - P_3$  subsystem. After the invasion of species 1, species 2 is eliminated and species 3 survives. Note that  $l_2 > l_3$  and  $m_3 < m_2$  in AREA IV.

Finally, in AREA V, three species can survive with sustained oscillations (see Fig. 11.4 (e)). Although we need future investigations, we think that the temporal fluctuation of  $x$  plays a crucial role for the coexistence.

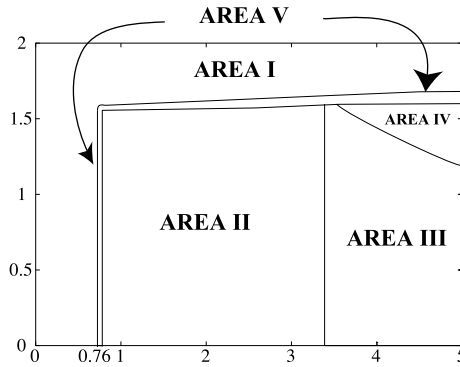


**Fig. 11.3.** The  $(m_1, l_1)$  parameter plane. In AREA I, species 2 and 3 coexist with sustained oscillations. In AREA II, species 1 and 2 coexist with sustained oscillations. In AREA III, only species 1 survives. In AREA IV, species 1 and 3 coexist with sustained oscillation. In AREA V, three species coexist with sustained oscillations. The parameters are  $m_1 \in [0, 5], l_1 \in [0, 2], m_2 = 3.2, m_3 = 0.3, a_1 = 5, a_2 = 4.7, a_3 = 1, l_2 = 1.6, l_3 = 0, \delta_1 = \delta_2 = \delta_3 = 0.12, \rho_1 = \rho_2 = \rho_3 = 0.8, c_1 = c_2 = c_3 = 2.5, q = 0.8, s = 1$ . The initial condition is  $(P_1(0), P_2(0), P_3(0), x(0)) = (0.2, 0.4, 0.3, 0.9)$ .

### 11.4 Discussion

In this chapter, we have considered the effect of undeveloped seeds. In Section 11.2, we proposed model (11.2), which is based on the lottery model (11.1). We investigated model (11.2) to understand the effect of undeveloped seeds on population dynamics.

From the result of numerical simulations, we see that three species coexist in a wide range of the parameter space (see Fig. 11.3). For (11.2) with two species, in AREA II of Fig. 11.1, two species can coexist at an interior fixed point. On the other hand, in system (11.2) with three species, an interior fixed point does not exist. That is, even if three species coexist, there are no interior fixed points. For this case, it is shown that three species can coexist with a sustained oscillation (see AREA V of Fig. 11.3 and Fig. 11.4 (e)). It is known that the sustained oscillations do not exist in the lottery model (11.1) if all coefficients are constants. Furthermore, it is known that in the original lottery model, species coexist under the temporal fluctuation of vital coefficients. Our results show that the incorporation of undeveloped seeds leads to the temporal fluctuation of populations and ensures the coexistence of three species with a sustained oscillation.

### Acknowledgments

The authors thank Professor T. Takada and Professor K. Sato for their very valuable comments and help.

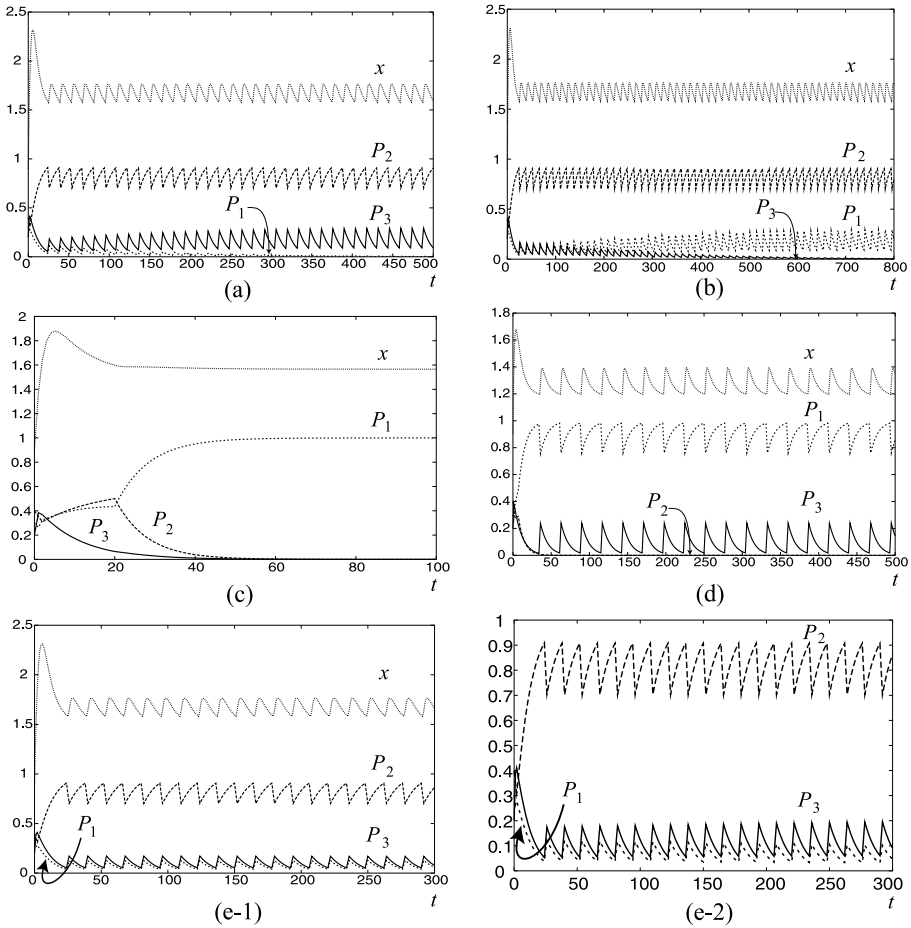


**Fig. 11.4.** The temporal sequence of  $P_1$ ,  $P_2$ ,  $P_3$  and  $x$  with the initial condition  $(P_1(0), P_2(0), P_3(0), x(0)) = (0.2, 0.4, 0.3, 0.9)$ . The parameters are  $\delta_1 = \delta_2 = \delta_3 = 0.12$ ,  $m_2 = 3.2$ ,  $m_3 = 0.3$ ,  $a_1 = 5$ ,  $a_2 = 4.7$ ,  $a_3 = 1$ ,  $l_1 = 1.2$ ,  $l_2 = 1.6$ ,  $l_3 = 0$ ,  $q = 0.8$ ,  $s = 1$ ,  $\rho_1 = \rho_2 = \rho_3 = 0.8$ ,  $c_1 = c_2 = c_3 = 2.5$ , (a)  $m_1 = 0.7$  (AREA I in Fig. 11.3), (b)  $m_1 = 0.8$  (AREA II in Fig. 11.3), (c)  $m_1 = 3.6$  (AREA III in Fig. 11.3), (d)  $m_1 = 5$  (AREA IV in Fig. 11.3), (e-1) and (e-2)  $m_1 = 0.76$  (AREA V in Fig. 11.3). (e-2) gives the expanded temporal sequence of  $P_1$ ,  $P_2$ ,  $P_3$ .

## References

1. Chesson, P., Warner, R. R.: Environmental variability promotes coexistence in lottery competitive system. *Am. Nat.*, **117**, 923–943 (1981).
2. Chesson, P.: The stabilizing effect of a random environment. *J. Math. Biol.*, **15**, 1–36 (1982).
3. Chesson, P., Huntly, N.: The roles of harsh and fluctuating conditions in the dynamics of ecological communities. *Am. Nat.*, **150**, 519–553 (1997).

4. Comins, H. N., Noble, I. R.: Dispersal, variability and transient niches: Species coexistence in a uniformly variable environment. *Am. Nat.*, **126**, 706–723 (1985).
5. Dewi, S., Chesson, P.: The age-structured lottery model. *Theor. Popul. Biol.*, **117**, 923–943 (1981).
6. Hatfield, J. S., Scheibling, R. E.: Diffusion analysis and stationary distribution of the two-species lottery competition model. *Theor. Popul. Biol.*, **36**, 251–266 (1989).
7. Huisman, J., Weissing, F. J.: Biodiversity of plankton by species oscillations and chaos. *Nature.*, **402**, 407–410 (1999).
8. Lambers, H., Chapin III, F. S., Pons, T. L.: *Plant Physiological Ecology*. Springer-Verlag, New York (1998).
9. Laurie, H., Mustart, P. J., Cowling, R. M.: A shared niche? The case of the species pair, *Protea obtusifolia* *Leucadendron meridianum*. *Oikos.*, **79**, 127–136 (1997).
10. Muko, S., Iwasa, Y.: Species coexistence by permanent spatial heterogeneity in a lottery model. *Theor. Popul. Biol.*, **57**, 273–284 (2000).
11. Muko, S., Iwasa, Y.: Incomplete mixing promotes species coexistence in a lottery model with permanent spatial heterogeneity. *Theor. Popul. Biol.*, **64**, 359–368 (2003).
12. Neuhauser, C., Pacala, W.: An explicitly spatial version of the Lotka–Volterra model with interspecific competition. *Ann. Appl. Probab.*, **9**, 1226–1259 (1999).



**Immunology**

## An Automata-Based Microscopic Model Inspired by Clonal Expansion

Francesco Zanlungo,<sup>1,2</sup> Sandro Rambaldi,<sup>1,2</sup> and Giorgio Turchetti<sup>1,2</sup>

<sup>1</sup> Department of Physics, Via Irnerio 46, 40126 Bologna, Italy and Centro Interdipartimentale L. Galvani, Università di Bologna, Bologna, Italy

<sup>2</sup> Istituto Nazionale di Fisica Nucleare, sezione di Bologna, Italy; turchetti@bo.infn.it

**Summary.** We present a simple model based on microscopic automata to describe the clonal expansion process. The model is based on a repertoire of antigens and T lymphocytes interacting via antigen-presenting cells which present the antigens peptides. Each cell is represented by an automaton moving randomly on a two-dimensional lattice. We use this simplified model in order to introduce local and spatial considerations in the mathematical models of clonal expansion based on differential equations, and at the same time to attempt an analytical interpretation of the results of computer simulations. For this reason we also derive a mean field theory, whose results are in good agreement with the solutions of the microscopic model, at least for situations that are not too far from equilibrium. This model may be used as the basis of a more realistic one that could follow the clonal expansion process on a simplified version of the lymphatic network.

**Key words:** Clonal expansion, automata, agent model, differential equations, competitive exclusion.

### 12.1 Introduction

In this chapter we try to create a bridge between two different ways to study the clonal expansion in the immune system (IS). One kind of approach consists in studying the concentrations of the different species of cells, whose behaviour and interaction is modelled through a system of differential equations (DEs), the other one in studying the microscopic interactions between the single cells, which are usually modelled as cellular automata (CA).

It is our opinion that in immunology as in other fields of research the languages of microscopic (CA or agent) and macroscopic (DE) models could be integrated, in order to use the analytical result to explain and partially predict the behaviour of the simulated models, and also to utilise the simulations to enrich the assumptions of the macroscopic models with microscopic details.

In this chapter we present a simplified model of the clonal expansion, in which we stress the spatial interaction between T cells and antigen-presenting cells (APCs), while omitting the details of the T cell-antigen and APC-antigen interactions, and ignoring many other important agents of the IS. The aim here is thus not to present a new

model for the clonal expansion, but to start a project of work in which two different ways to model it could be combined.

## 12.2 Description of the Model

### 12.2.1 Differential Equations Model

One of the major open questions in immunology is the problem of understanding clonal expansion, i.e., how the T cells, which belong to a very large repertoire, are selected in response to a specific threat (the presence of an antigen) and proliferate to form a large clone, and how this proliferation is regulated.

De Boer and Perelson presented a model that justifies the maintenance of diversity in the periphery through the concept of competitive exclusion ([1]). This competition between T cells (between the different clones and inside the same clone) arose as competition for the peptides presented on the surface of an APC. In fact, these peptides can be freely available on the surface of an APC, or be captured in the receptor of a T cell bound to an APC; in the second occurrence they are no longer available to other T cells.

De Boer and Perelson imposed a quasi-steady-state condition for the number of complexes given the number of peptides, and obtained a system of differential equations for the different clone sizes, which corresponded to the well-known principle of competitive exclusion in biology (two different species cannot co-exist in equilibrium if they use just the same resource) and also introduced a capacity (equilibrium size for a single clone).

In this model the number of peptides is considered to be proportional to the antigen concentration, which is assumed as fixed. This assumption is well justified in the case of self antigens, while for pathogens they assumed this fixed concentration to be the equilibrium value of a prey equation for the antigens, in which T cells had the role of predators. Using this assumption, immune memory is attained through the persistence of antigen at a controlled concentration. (See [2] and the Appendix for a treatment of prey-predator equations, and [3] for an application to the immune system.)

This is one of the many models that describe the clonal expansion using a system of differential equations (see for example [4]) and it has been further studied and improved by the authors ([5]). Our interest in this version of the model is due to its simplicity and to the fact that its basic assumptions concern the microscopic spatial interactions between T cells and APC, averaged in the quasi-steady-state condition.

Since there are many experimental results concerning how these interactions happen [6–9], we think that this model is well suited to a microscopic formulation, in which the different individual cells are represented as automata in a computer simulation. (We use the term automaton referring to the original definition by Von Neumann, and not just to cellular automata; i.e., we do not necessarily identify a biological cell with a site of a discrete grid, even if it is the case of the model that we are going to present.)

These are the differential equations that describe our version of the De Boer-Perelson model:

$$\dot{A}_i = aA_i - bA_i^2 - \sum_j c_{ij}A_iT_j \quad (12.1)$$

$$\dot{P}_i = dA_i - rP_i \quad (12.2)$$

$$\dot{N}_{APC} = 0 \quad (12.3)$$

$$\dot{T}_i^N = 2gT_i^A - hT_i^N - \sum_j k_{ij}T_i^NT_j - lf \left( \sum_j m_{ij}P_j \right) FT_i^N + oC_i + s \quad (12.4)$$

$$\dot{T}_i^A = qC_i - gT_i^A \quad (12.5)$$

$$\dot{C}_i^A = -qC_i - oC_i + lf \left( \sum_j m_{ij}P_j \right) FT_i^N \quad (12.6)$$

$$\dot{F} + \sum_i \dot{C}_i = 0. \quad (12.7)$$

Equation 12.1 tells us that the  $n_A$  species of antigens  $A_i$  follow a logistic prey equation in which the  $n_T$  T cell clones  $T_i$  have the role of predators. Equation 12.2 gives the average number of peptides of species  $i$ ,  $P_i$ , (we assume for simplicity a one-to-one correspondence between peptides and antigens) presented on a site of an APC cell. This number grows with the number of antigens and follows a decay rule (peptides remain on the APC's surface for a finite average time). With equation 12.3 we fix the number of APC cells.

Equations 12.4 and 12.5 concern the number of non-activated  $T_i^N$  and activated  $T_i^A$  T cells ( $T_i \equiv T_i^N + T_i^A$ ). Non-activated T cells are produced by duplication of activated ones with a rate  $g$  and die by apoptosis with rate  $h$ . The probability rate  $s$  represents an external source (thymus).  $F$  is the total number of free sites on the APC's surface, to which T cells can bind with a probability rate that depends on a function  $f$  of the probability to find a given species of peptides multiplied by its affinity  $m_{ij}$  to it ( $l$  is the probability of binding in case of maximum affinity). We call  $C_i$  a complex formed by a T cell  $T_i$  and a site of an APC. These complexes can unbind with probability rate  $q$  in the case of successful activation (equation 12.5) and with probability rate  $o$  in the case of unsuccessful activation (equation 12.4). The terms  $k_{ij}$  in equation 12.4 rule the fratricide competition between the T cells (see for example [10]).

The number of complexes and free sites is governed by equations 12.6, 12.7 coherently with the assumptions of equations 12.4, 12.5 and with the request that their sum has to be fixed as the total number of sites ( $n_s N_{APC}$  if  $n_s$  is the number of sites on a single cell).

### 12.2.2 Microscopic Model

In the differential equations based model we tried to write explicitly an equation for each agent of the process, and we defined a probability rate for each interaction between these agents, since we want these equations to be the mean field version of a microscopic model. Given the high number of equations and parameters we won't try an analytical treatment and we will rely on numerical integration for their solution. Our microscopic model is realized on two superposed two-dimensional (2D) squared grids, one on which antigens move and one for APC and T cells. The physical region corresponding to each layer will be the same (creating a correspondence between sites "located in the same physical space") while the step of the grids and thus the number of sites could be different.

All the cells move by random walk obeying an exclusion principle (no more than a single cell on a given site of a layer), and the interaction between cells can occur by superposition when they are located on different layers, or by contact (i.e., if they are located on first neighbour sites) if they are on the same layer. We call these events that allow an interaction between the cells "encounters." An encounter between an antigen  $A_i$  and a T cell  $T_j$  leads to the elimination of the antigen with probability  $p^c_{ij}$ , while an encounter between an antigen and an APC leads with probability  $p^d$  to the presentation of a peptide on the "surface" (i.e., on one of the four sides) of the APC (in our convention we associate to the probabilistic rate  $x$  in the continuous macroscopic model the probability  $p^x$  in the discrete microscopic one). Encounters between a T cell  $T_i$  and an APC can form a complex, with a probability  $p^l$  multiplied by the affinity to the site  $f(\sum_j m_{ij} \Pi_j)$  (a function of the averaged affinity to the peptides  $\Pi_j$  presented on the site, where  $\Pi_j$  is the number of peptides in species  $j$  present on the site). Encounters between the antigens lead to an overpopulation due to "logistic" elimination of the antigen with probability  $p^b$ , while those between T cells in clones  $i$  and  $j$  lead to fratricide apoptosis with probability  $p^k_{ij}$ . These fratricide terms are in a certain sense "ad hoc" in our model (they are not present in the original formulation by De Boer and Perelson, even if they are present in other models, as in [10]), since we need them to avoid a filling of the grid. They should be chosen in such a way that they are not relevant under normal conditions (i.e., when the number of occupied sites is low with respect to the total number of sites). All the other processes are encounter independent and can occur with given probabilities at each time step.

It is quite clear that this model is too simple to describe all the complex processes that concern the clonal expansion in the immune system. A more complete formulation should use at least two different 2D grids to describe the site of infection and the lymph nodes (connected in some way to allow the displacement of T and dendritic cells), while for a realistic description of immunological memory a differentiation between naive and memory T cells is necessary.

### 12.2.3 Mean Field Equations

All the probability rates in a macroscopic model have to be chosen on the base of macroscopic observations, in such a way that the behaviour of the solutions will correspond to the behaviour of the biological species under some given assumptions.

According to the ideas of this work, the probabilities of the microscopic model should be given on the basis of microscopic observations, as reported for example in [6–9]. The time step should be chosen smaller than the shorter characteristic time of the processes involved, and all these characteristic times should be expressed as probabilities. An average process would be necessary to describe three-dimensional (3D) cells with a complex shape as 2D squared objects, and probably also minor changes in the geometry (allowing for example APC and T cells to have different sizes) could be necessary.

Given the preliminary stage of this work and its general purposes, and considering also our limits in the interpretation of experimental data given our scientific formation, we are just making simple considerations that allow us to have some qualitative result, without any claim to quantitative or predictive results.

We can obtain the mean field equations for the microscopic model in the following way. Let us assume for example that the average time for antigen duplication is one day. If we choose a time step of 15 minutes, the probability for antigen duplication is fixed to  $p^a = 0.01$ . Defining  $N_A$  as the number of sites of the antigen's grid and assuming random distribution for all the cells, the probability for an antigen to have an encounter with another antigen on one of its 4 sides is  $A/N_A$ , and thus the time evolution of the number of antigens in the absence of T cells is given by

$$A(t + \Delta t) = A(t) + p^a A(t) - p^b A(t)^2/N_A. \quad (12.8)$$

The value of  $p^b$  can be fixed given the wanted maximum density of antigens (the capacity),

$$A_{\max}/N_A = p^a/p^b \quad (12.9)$$

and in the continuous limit we obtain equation 12.1 through the identifications  $a = p^a/\Delta t$ ,  $b = p^b/(N_A \Delta t)$ .

The discrete version of equation 12.2 is, referring to  $\Pi_i$  as the number of peptides of species  $i$  on a single side of an APC,

$$\sum_{APC} \Pi_i(t + \Delta t) = \sum_{APC} \Pi_i(t) + p^d A_i(t) N_{APC}/N_T - p^r \sum_{APC} \Pi_i(t) \quad (12.10)$$

or, averaging over all the sides,

$$P_i(t + \Delta t) = P_i(t) + p^d A_i(t)/(4N_T) - p^r P_i(t), \quad (12.11)$$

where  $N_T$  is the number of sites of the APC-T cell grid. The continuous version of 12.11 is equation 12.2, through the identification  $d = p^d/(4\Delta t N_T)$ ,  $r = p^r/\Delta t$ . Equation 12.2 has the solution

$$P_i(t) = e^{-rt} \left[ \int A_i(t') e^{rt'} dt + const \right] \quad (12.12)$$

that reduces to

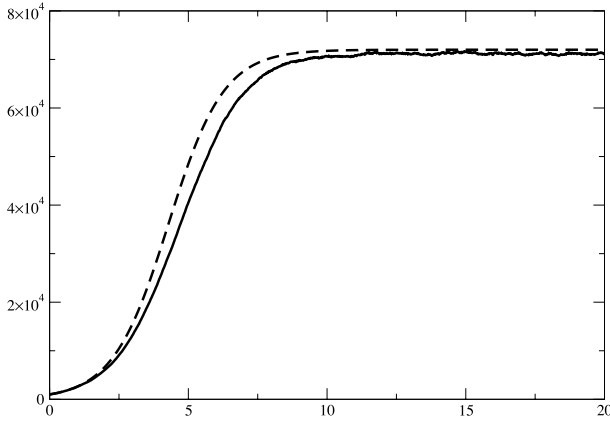


**Fig. 12.1.** Comparison between the free growth of the antigen number  $A(t)$  as obtained from the microscopic model (continuous line) and the mean field equations. The time unit is one day, as in all the figures to follow.

$$P_i(t) = \frac{A_i d}{r} + \left[ P_i(0) - \frac{A_i d}{r} \right] e^{rt} \tag{12.13}$$

in the case of constant  $A_i$  concentration. We use  $p^d = 1$  (the APC always recognises the antigen) and  $p^r = 0.02$ , corresponding to a permanence of the peptide on the antigen surface for an average time of 12 hours.

In Fig. 12.1, we compare the numerical integration of equation 12.1 (for a single species) with the corresponding results given by the microscopic model, and in Fig. 12.2 we present the same comparison for the analytical result of equation 12.13. (We

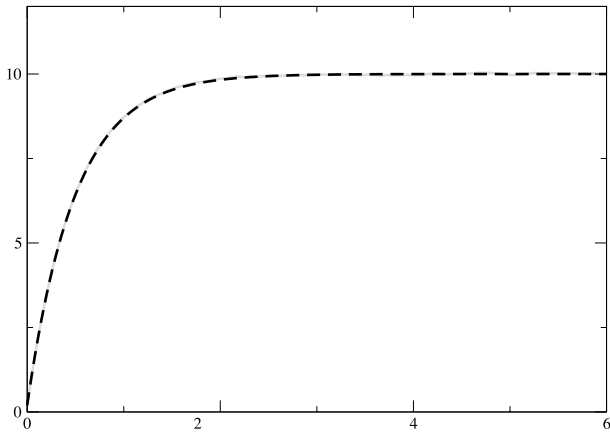


**Fig. 12.2.** Average number of peptides as obtained by the microscopic model (continuous line in grey) and the mean field equations. The two lines are almost indistinguishable.

have used for these simulations  $N_T = 9 \times 10^4$ ,  $N_A = 3.6 \times 10^5$  and  $p^b = 0.05$  which corresponds, according to equation 12.9, to a capacity of an antigen every 5 sites.)

While there is an almost perfect correspondence between the curves in Fig. 12.2, there is a slight difference between those in Fig. 12.1. This effect is due to the fact that while the behaviour described by equation 12.10 depends on the interaction between cells located on different layers, and thus is not actually based on microscopic spatial interactions, the behaviour described by equation 12.8 relies on and influences the spatial distribution of antigens. For this reason the mean field equation describes well the microscopic model in the initial configuration, when a uniform distribution is imposed, and at the equilibrium, while the discrepancy is stronger during the expansion.

The local effects are obviously stronger when we consider the spatial T-APC interaction. Let us fix  $N_{APC} = 2 \times 10^3$  on the  $N_T = 9 \times 10^4$  grid, use the sigmoid function

$$f \left( \sum_j m_{ij} P_j \right) = \frac{1 - e^{-\sum_j m_{ij} P_j}}{1 + e^{-\sum_j m_{ij} P_j}} \tag{12.14}$$

to obtain the affinity of a T cell to a site on the APC surface, and let  $p^s = 0.05$  (an activated T cell needs 5 hours to split referring to the time step of 15 minutes),  $p^h = 0.001$  (a life span of 10 days for the T cells),  $p^l = 0.25$  (an hour to form a complex in case of maximum affinity),  $p^a = 0.2$ , and  $p^o = 0.04$ . (These last two parameters are the probabilities to unbind with and without activation in the case of maximum affinity. The dependence of these microscopic probabilities on the affinity has been chosen “ad hoc” in such a way that the first one grows and the second one decreases with affinity.)

If now we consider a single clone  $T$  with maximum affinity to a single species of antigen  $A$  ( $m \equiv m_{11} = 1$ ) and fix  $A$  to its maximum capacity ( $c \equiv c_{11} = 0$ , i.e., antigens are not removed), we can obtain in the usual way the discrete mean field equations for  $T$ ,  $F$  and  $C$  whose continuous limit leads to equations 12.4–12.6, redefining the parameters on the basis of the microscopic probabilities.

Fig. 12.3 refers to the growth of the clone, and compares the integration of the mean field equation with the results given by the microscopic model (the fratricide term value is fixed to  $p^k = 0.1$ ). In this case the discrepancy is stronger, and is also qualitative. The growth in the microscopic model is lower at the beginning, while the equilibrium value is higher. Two different effects are present, both due to the presence of zones around the APC in which T cells reproduce: the fratricide effect is enforced because of the higher density in these zones, but also the probability to meet an APC and thus to be activated is enhanced. Since these effects depend strongly on the density of cells, it is possible to obtain the parameters of equations 12.1–12.7 by a process of best-fitting only on regions in which the values of  $A$  and  $T$  are almost constant (this means that those equations can describe properly the behaviour of the microscopic system only if we introduce a dependence of the parameters on  $A$  and  $T$ ).



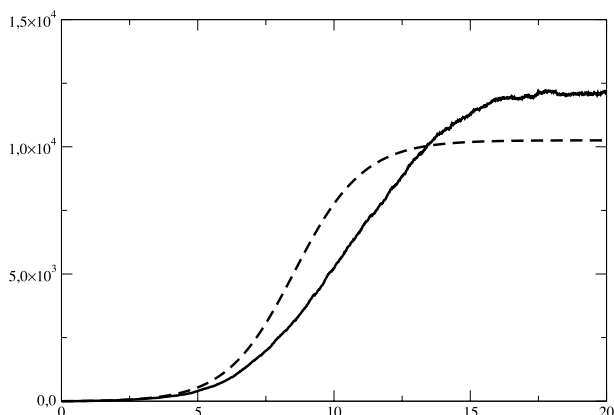


**Fig. 12.3.** T clone expansion in response to a fixed number of antigens in the microscopic (continuous line) and mean field models.

## 12.3 Results of the Simulations

### 12.3.1 Acute Antigenic Impulse

In order to complete the model we have to fix the value of the parameters  $c_{ij} \equiv c m_{ij}$  (we are assuming that the ability of a T cell to remove an antigen is proportional to its affinity to it). We have used  $c = 0.2$  in order to obtain a realistic time scale for the response of the immune system to the infection.

In Fig. 12.4 we plot the evolution of the clone size  $T$  and antigen  $A$  populations, comparing the results of the microscopic model with the solutions of the mean field equations. In agreement with the previous discussion the results are very similar at equilibrium values, while the agreement is only qualitative during the transient part. Damped oscillations are present in both models, and both the period and the height of

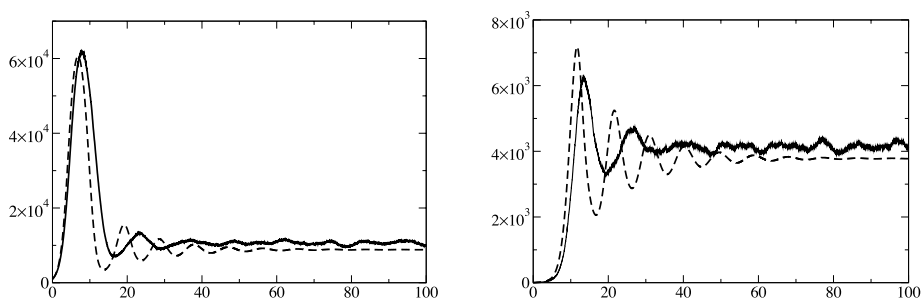


**Fig. 12.4.** Evolution of the system under an acute antigenic stimulus. The evolution of the antigen number in the microscopic (continuous line) and mean field models is shown at left, while the size of the T cell clone is reported on the figure at right (the continuous line corresponds to the microscopic model).

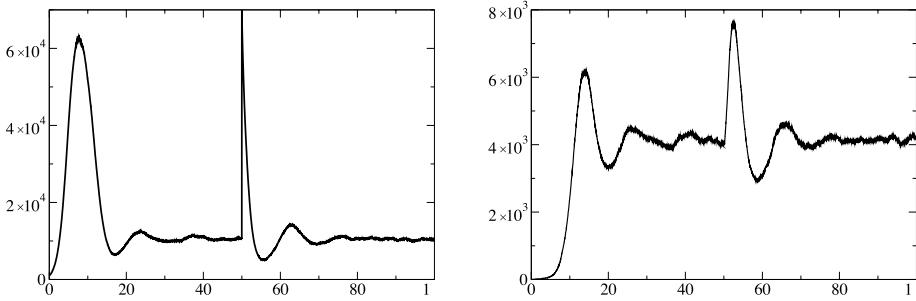


**Fig. 12.5.** Left: evolution of the antigen population after a secondary impulse occurring 50 days after the primary; microscopic model. Right: corresponding evolution of the T cells clone.

peaks and valleys are of the same order of magnitude (the damping rate and the period of oscillations are higher in the microscopic model).

This behaviour corresponds to that of a prey-predator system (see the Appendix and [2]). To an equilibrium value with  $A \neq 0$ ,  $B \neq 0$  corresponds a “memory” effect due to the permanence of the antigen. In this situation the response to a secondary stimulus is obviously quicker (Fig. 12.5).

### 12.3.2 The Clonal Repertoire Model

We finally consider the effects of both fratricide and spatial competition terms between different clones in the presence of a differentiated antigen repertoire. By using a fratricide term in which the decrease is proportional to the overall size of the clones,  $\Delta_-T_i = -kT_i \sum_j T_j$ , we obtain a mutual exclusion principle. In fact, if we summarise the growth terms with  $\Delta_+T_i$ , the relative variation of the clone size is

$$\frac{\dot{T}_i}{T_i} = \frac{\Delta_+T_i}{T_i} - \frac{\Delta_-T_i}{T_i}.$$

Since  $\Delta_-T_i/T_i$  is the same for all the clones, supposing that there is a unique antigen with the highest affinity to the clone  $T_j$  (namely  $\Delta_+T_j/T_j > \Delta_+T_i/T_i \forall i \neq j$ ), if the clone  $j$  reaches an equilibrium  $\Delta_+T_j = \Delta_-T_j$  then any other clone extinguishes since  $\Delta_+T_i - \Delta_-T_i < 0$ . (These are the basics of competitive exclusion, see [2].)

To show that in our model there is competition for peptides presented at the APC surface (the mechanism investigated in [1]), we can use a “pure fratricide” term  $-kT_i^2$ . This is actually a “non-competitive” one since it favours the small clones. In fact, studying the expansion of three clones under the stimulus of a single antigen, using an affinity matrix  $m_{i,1}$  such that  $m_{i,1} \ll m_{1,1} = 1$  if  $i \neq 1$  we have an equilibrium with  $T_2 \neq 0$  (Fig. 12.6).

Nevertheless, even in this situation the competition for the peptides on the APC surface leads to a control in the overall number of T cells, at least when the number of clones is large. To study this effect we introduce an antigen with constant concentration, to which 10 clones have maximal affinity. Once these clones have reached their

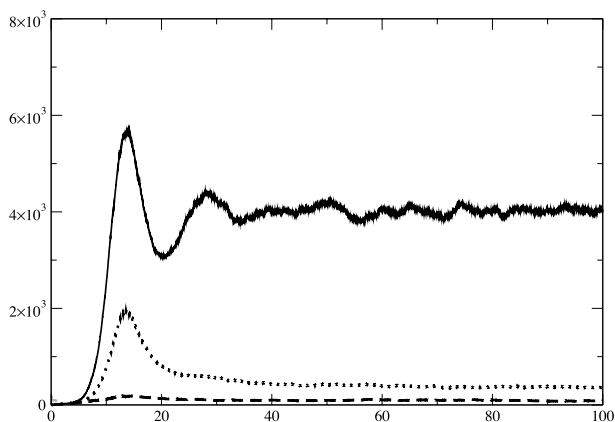


**Fig. 12.6.** Time evolution of the size of three clones one of which (continuous line) has higher affinity to a given antigen.

equilibrium size, we introduce three different additional antigens at which three new clones are highly affine. The results of Fig. 12.7 show that the size of the “old” clones shrinks as a reaction to the growth of the new ones.

## 12.4 Conclusions

Analytical models and simulations are usually treated as completely distinct fields of research, even when they approach the same problem. We have presented a microscopic dynamical model inspired by the clonal expansion in the immune system, together with a system of differential equations that could be interpreted as its mean field theory. We have shown how the mean field equation can be used to interpret the

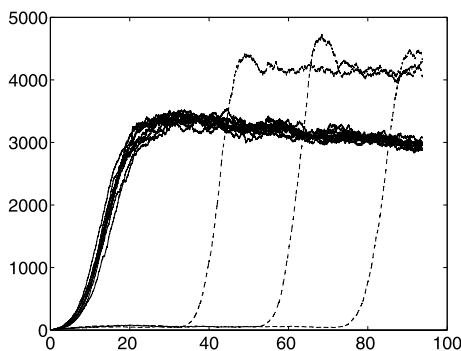


**Fig. 12.7.** Time evolution of the size of 10 clones (continuous curves) stimulated by a single antigen and shrinkage due to the expansion of three new clones (dashed curves).

results of simulations, while the microscopic model can be used to add a local and spatial character to a macroscopic system based on differential equations.

We do not claim that the results of our model are biologically relevant, but we present it as a starting point for a more complex model and as a solution for a compromise between pure analytical and pure simulated models that could be used in different fields of research.

## Appendix

The dynamics of the model can be described by a simplified system of differential equations for  $A$  and  $T$ . We assume that the antigen-APC-T average interaction consists of a growth term for the  $T$  clone proportional to  $A$ . The equations become

$$\dot{A} = A(a(1 - cA) - bT) \quad \dot{T} = T(-d + eA - fT). \quad (12.15)$$

These Lotka–Volterra equations with a logistic term have been extensively investigated and if  $e > cd$  they exhibit a critical stable point:

$$T_c = \frac{a(e - cd)}{eb + caf} \quad A_c = \frac{af + db}{eb + caf}. \quad (12.16)$$

Every solution in the positive sector  $T > 0$   $A > 0$  is attracted by this point which is topologically a focus. Convergence rate to equilibrium and the oscillations period are determined by the eigenvalues of the Jacobian matrix.

From its trace and determinant,

$$\text{Tr } J = -a \frac{acf + bcd + ef - cdf}{eb + caf} < 0 \quad \det J = \frac{a(e - cd)(bd + af)}{eb + caf} > 0, \quad (12.17)$$

we obtain the eigenvalues  $\lambda_{\pm} = (1/2)[\text{Tr } J \pm \sqrt{\text{Tr } J^2 - 4\det J}]$  which are real negatives or complex with a negative real part. We have oscillations if  $\Delta = \text{Tr } J^2 - 4\det J = -\omega^2 < 0$  and their period is  $2\pi/\omega$ .

## Acknowledgment

We are indebted to Fabio Luciani for useful discussion and advice.

## References

1. De Boer, R., Perelson, A.S.: T cells repertoires and competitive exclusion. *J. Theor. Biol.*, **169**, 375–390 (1994).
2. Hofbauer, J., Sigmund, K.: *Evolutionary Games and Population Dynamics*. Cambridge University Press, London (1998).

3. Novak, M., May, R., Sigmund, K.: Immune responses against multiple epitopes. *J. Theor. Biol.*, **175**, 325–350 (1994).
4. Antia, R., Ganusov, V., Ahmed, R.: The role of models in understanding CD8<sup>+</sup> T-cell memory. *Nature Reviews Immunology* (published online 20 January 2005).
5. De Boer, R., Perelson, A.S.: Competitive control of the self renewing T cell repertoire. *International Immunology*, Vol. 9, No. 5, p. 779, Oxford University Press, London (1997).
6. Lanzavecchia, A., Sallustio, F.: Lead and follow: the dance of the dendritic cell and T cell. *Nature Immunology*, **5**, 1201–1202 (2004).
7. Huges, S., Fetler, L., Bonifaz, L., Helft, J., Amblard, F., Amigorena, S.: Distinct T cell dynamics in lymph nodes during the induction of tolerance and immunity. *Nature Immunology*, **5**, 1235–1242 (2004).
8. Lindquist, R., Shakhar, G., Dudziak, D., Wardemann, H., Eisenreich, T., Dustin, M., Nussenzweig, M.: Visualizing dendritic cell networks in vivo. *Nature Immunology*, **5**, 1243–1247 (2004).
9. Germain, R., Jenkins, M.: In vivo antigen presentation. *Current Opinion in Immunology*, **16**, 120–125.
10. Callard, R., Stark, J., Yates, A.: Fratricide: a mechanism for T memory-cell homeostasis. *Trends in Immunology*, **24**, 370–375 (2003).

---

## Th1–Th2 Regulation and Allergy: Bifurcation Analysis of the Non-Autonomous System

Reinhard Vogel and Ulrich Behn

Institute for Theoretical Physics, University Leipzig, POB 100 920, 04009 Leipzig, Germany;  
Ulrich.Behn@itp.uni-leipzig.de

**Summary.** A previously proposed mathematical model based on a simplified scheme of Th1–Th2 regulation mediated by the cytokine network which describes the population dynamics of allergen-specific naive T cells, Th1 and Th2 cells, autocrine and cross-suppressive cytokines, and allergen is more closely investigated. The model provides a theoretical explanation of the switch from a Th2-dominated response to a Th1-dominated response to allergen in allergic individuals as a result of a hyposensitization therapy. We focus here on the bifurcation analysis of the non-autonomous dynamical system driven by periodic allergen injections. The stability of the fixed points of a stroboscopic map is investigated. The set of unstable fixed points forms the dynamical separatrix between the regions of Th2-dominated response and Th1-dominated response which is crossed during a successful therapy. The maintenance phase of the therapy holds the system near the stable fixed point of the stroboscopic map.

**Key words:** Th1–Th2 regulation, allergy, venom immunotherapy, hyposensitization, non-autonomous dynamical systems, bifurcation analysis.

### 13.1 Th1–Th2 Regulation, Allergy, and Hyposensitization

In the last two decades it became clear that for T-helper cells subsets can be defined, which differ in the spectrum of cytokines they secrete [1]. Th1 cells producing cytokines such as IL-2 and IFN- $\gamma$  are involved in the response against intracellular pathogens, whereas Th2 cells producing mainly IL-3, IL-4, IL-5, and IL-13 play a role in combatting extracellular pathogens. The cytokines secreted by one subset have an autocrine effect on their own population and a suppressive effect on the population of the other subset, thus providing a balance between Th1 and Th2 cells, see Fig. 13.1 for a simplified scheme. Several diseases are connected with a perturbation of this balance [2]. For example, an allergy of type I is a typical Th2-dominated response.

A widespread and successful therapy of allergy, hyposensitization, e.g., against bee venom, pollen, or house dust mites, consists in the initial phase in subcutaneous injections of increasing doses of allergen in varying intervals following empirical protocols. In the maintenance phase high doses of antigen are injected every 4 weeks for a period of several years [3]. During a venom immunotherapy a shift from a Th2-dominated

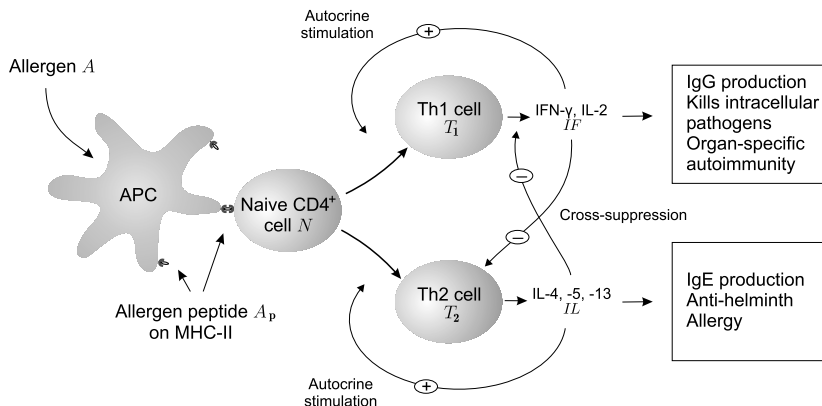


**Fig. 13.1.** Simplified scheme of Th1–Th2 regulation reduced to processes described in the model. Antigen is taken up by antigen-presenting cells (APCs) and presented with a concentration  $A_p$  to naive cells  $N$ , which differentiate into either Th1 or Th2 cells of concentration  $T_1$  and  $T_2$ , respectively. Cytokines produced by Th2 cells ( $IL$ ) stimulate proliferation of Th2 cells and suppress  $IFN-\gamma$  production in Th1 cells. Th1 cytokines ( $IF$ ) on the other hand have an autocrine effect on production of Th1 cells and suppress proliferation of Th2 cells.

to a Th1-dominated profile and an increase of the specific IgG4/IgE ratio has been observed [4–7].

Hyposensitization was first introduced in 1911 by Noon, who treated patients suffering from hay fever by injecting them with pollen extracts [8]. Since then this method has been adopted as the treatment of choice for allergic hypersensitivity.

A mathematical model describing the regulation of Th1–Th2 balance was proposed by Behn et al. [9] and supplemented in [10] by a model describing the desensitization of mast cells and basophils, cf. also [11].

The original equations describe the dynamics of six variables, the concentrations of naive cells, of Th1 and Th2 cells, of cytokines  $IF$  and  $IL$  produced by Th1 and Th2 cells respectively, and of allergen. They take into account the asymmetry in the cross-suppression sketched in Fig. 13.1. The proliferation of Th2 cells is stimulated by  $IL$  and suppressed by  $IF$ , which is reflected by a production term proportional to  $NA_p IL/(1 + \text{const } IF)$  in the equation for  $T_2$ . The production of  $IF$  by Th1 cells is suppressed by  $IL$ , which leads to a term proportional to  $T_1/(1 + \text{const } IL)$  in the equation for  $IF$ .

Since cytokines evolve on a shorter time scale than lymphocytes they can be adiabatically eliminated, which results in  $IF \propto T_1/(1 + \text{const } IL)$  and  $IL \propto T_2$ . For a detailed derivation see [10].

Taking into account a small cytokine background  $c$  originating from other immunological processes assumed to be constant in time amounts to  $IF \rightarrow IF + c$  and  $IL \rightarrow IL + c$ . Up to first order in  $c$  one arrives after a rescaling to suitable units at

$$\frac{dT_1}{dt} = -T_1 + vNA_p \left( \frac{T_1}{1 + \mu_2 T_2} + c \right), \quad (13.1)$$

$$\frac{dT_2}{dt} = -T_2 + v\phi NA_p \frac{T_2 + c}{1 + \mu_1 \frac{T_1}{1 + \mu_2 T_2}}, \quad (13.2)$$

$$\frac{dN}{dt} = -N + \alpha - NA_p \left( \frac{T_1}{1 + \mu_2 T_2} + c \right) - \phi NA_p (T_2 + c), \quad (13.3)$$

$$\frac{dA_p}{dt} = \xi_p(t) - A_p (T_1 + T_2). \quad (13.4)$$

Here  $T_{1/2}$ ,  $N$ , and  $A_p$  denote the concentrations of Th1 and Th2 cells, naive cells, and allergen presented by antigen-presenting cells (APCs), respectively.

The parameter  $\alpha$  is the production rate of the naive T cells,  $v$  is the proliferation rate of the T cells, and  $\xi_p(t)$  is the rate at which allergen peptide is presented by APCs after an allergen injection. The parameters  $\mu_1$  and  $\mu_2$  control the cross-suppression of Th1 and Th2 cells mediated by their cytokines and become important at high concentrations. The parameter  $\phi$  regulating the balance of the autocrine effects of the Th1–Th2 system is relevant at low concentrations. For  $\phi \lesssim 1$  the response to small doses of antigen is Th2-dominated, cf. [9], whereas for  $\phi \gtrsim 1$  it is Th1-dominated, cf. [10]. The latter choice is appropriate considering more recent experimental findings [12]. A small cytokine background  $c$  originating from other immunological processes is assumed to be constant in time. All parameters are dimensionless, as well as the time, which is measured in units of the half-life of lymphocytes. In numerical simulations we use  $\alpha = 10$ ,  $v = 8$ ,  $c = 10^{-5} \dots 10^{-4}$ ,  $\phi = 1.02$ ,  $\mu_1 = 0.2$ , and  $\mu_2 = 0.1$ .

The analysis of the non-linear dynamics of the model has shown that the system is driven by the injection of antigens from a region in the state space where the response to allergen is Th2-dominated to a region where it is Th1-dominated [10]. These regions are separated by a dynamical separatrix. The dynamical separatrix was determined as follows. The trajectories of the system (13.1)–(13.4) starting with an injection of an allergen dose  $D_p = 1$  have been tracked for initial conditions of  $N = \alpha$  and different points in the  $T_1$ – $T_2$  plane. Some points in the  $T_1$ – $T_2$  plane are distinguished because the trajectory returns to the initial point after a certain time  $\tau$ . If  $\tau$  is not too small compared with the half-life of the T cells the allergen is almost eliminated and the naive cells have almost returned to their initial value. Periodic injections of the same dose of antigen  $D_p$  with the period  $\tau$  will therefore induce a periodic trajectory ever returning to the initial point, which clearly is a fixed point of a stroboscopic map.

In the paper [9] we have numerically compared the present model with an extended version which includes long-lived Th1- and Th2-memory cells. Since no essential differences in the qualitative behaviour were found, here we restrict the mathematical analysis to the simpler model.

In this chapter we investigate more closely the dynamical separatrix mentioned above by analyzing the fixed points of a stroboscopic map for the case of periodic injections of allergen. The dynamical separatrix is just the line of unstable fixed points. We first present results for a simplified two-dimensional (2D) stroboscopic map in the  $T_1$ – $T_2$  plane where periodically the values for  $A_p$  and  $N$  are reset to 0 and  $\alpha$ , respec-



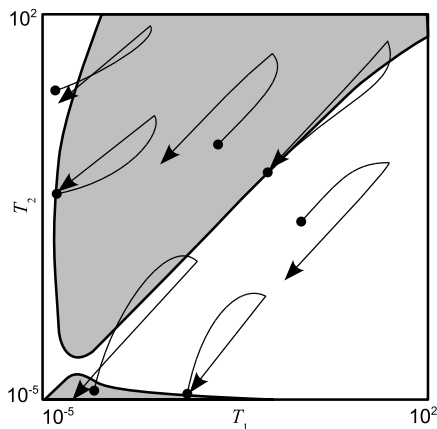


**Fig. 13.2.** Schematic illustration of the concept of dynamical separatrix. The response to the injection of a given dose of allergen is shown in the  $T_1$ – $T_2$  plane for different initial conditions. The trajectories starting from points on the separatrix return to their starting point. The  $T_1$ – $T_2$  plane is divided in regions in which an injection of  $D_p$  will either improve the ratio  $T_1/T_2$  (white) or impair it (grey).

tively. The stability of the fixed points and the bifurcations of the manifold of fixed points are determined. We then show that the 4D stroboscopic map corresponding to the complete dynamics of (13.1)–(13.4) leads to practically the same results provided the period of injections is not too small. Finally, we look at the influence of changes of the background cytokines  $c$  and the dose of allergen injections  $D_p$ .

## 13.2 Dynamical Separatrix and Stroboscopic Maps

In numerical investigations of the response to the injection of a given dose of allergen for different initial conditions it was found [9, 10] that there exist points in the  $T_1$ – $T_2$  plane which are reached again by the trajectory after a certain time  $\tau$ . Repeating injections of the same dose with a period  $\tau$  produces a process of periodic returns to the initial point, which is naturally a fixed point of the stroboscopic map of just this period  $\tau$ . The manifold of those fixed points is a line in the  $T_1$ – $T_2$  plane parametrized by  $\tau$ . The fixed points may be stable or unstable. The manifold of unstable fixed points is a dynamical separatrix: For initial points left or right of the separatrix the response to a certain dose of allergen leads into regions of different Th1–Th2 balance. See Fig. 13.2.

We consider the case of periodic injections of a certain allergen dose  $D_p$ ,  $\xi_p(t) = \sum_n D_p \delta(t - t_n)$ . We first analyze the stroboscopic map for a simplified dynamics describing the projection on the  $T_1$ – $T_2$  subspace with the idealization that the allergen has completely disappeared after  $\tau$ , and that the population of naive cells has returned to the fixed point  $N^* = \alpha$  of the situation without allergen. This proves an excellent approximation for a not too small  $\tau$ , see below.

Introducing the abbreviations  $T = (T_1, T_2)^T$  and  $A = (N, A_p)^T$  we denote by  $\theta(T_0, A_0; t)$  the solution of the autonomous system (13.1)–(13.4) at time  $t$  for  $\xi_p = 0$  with initial conditions  $T_0 = (T_1^0, T_2^0)^T$  and  $A_0 = (\alpha, D_p)^T$ .  $\theta_T$  denotes the projection of  $\theta$  on the  $T_1$ – $T_2$  subspace. Note that starting with the initial condition  $A_p(0) = D_p$  corresponds to  $\xi_p(t) = D_p\delta(t)$ .

The stroboscopic map  $\mathbf{S}_\tau(n) : \mathbb{N} \times \mathbb{R}_+^2 \rightarrow \mathbb{R}_+^2$  with period  $\tau$  looking just before the  $n$ th periodic injection of the dose  $D_p$  at the systems projection on the  $T_1$ – $T_2$  plane is defined by

$$\mathbf{S}_\tau(n + 1) = \theta_T(\mathbf{S}_\tau(n), A_0; \tau - 0), \quad n = 0, 1, 2, \dots \tag{13.5}$$

with initial condition  $\mathbf{S}_\tau(0) = T_0$ . The fixed points  $S(\tau)$  of the stroboscopic map (13.5) obey  $S(\tau) = \theta_T(S(\tau), A_0; \tau - 0)$ . Differentiation with respect to  $\tau$  yields

$$\frac{dS}{d\tau} = \left(1 - \frac{\partial\theta_T}{\partial S}\right)^{-1} \frac{\partial\theta_T}{\partial\tau}, \tag{13.6}$$

provided the matrix  $(1 - \partial\theta_T/\partial S)$  can be inverted. If this is not the case, i.e., for  $\det(1 - \partial\theta_T/\partial S) = 0$ , by the implicit function theorem a bifurcation occurs at a critical value of  $\tau$ . For the numerical evaluation we observe that

$$\frac{\partial\theta_T}{\partial S} = \left. \frac{\partial\theta_T}{\partial T_0} \right|_{T_0=S(\tau)} \quad \text{and} \quad \frac{\partial\theta_T}{\partial\tau} = \left. \frac{dT}{dt} \right|_{T=S(\tau), A=(\alpha,0)} = -S(\tau). \tag{13.7}$$

Fig. 13.3 shows the manifolds of stable and unstable fixed points parametrized by the period of injections  $\tau$  numerically obtained from (13.6). Furthermore,  $\det(1 - \partial\theta_T/\partial S)$  is shown as a function of  $\tau$  evaluated along the stable and unstable manifolds, and the ratio  $T_1/T_2$  which undergoes a perturbed backward pitchfork (saddle-node) bifurcation with increasing  $\tau$ .

The preceding analysis of the simplified 2D stroboscopic map corresponds to the numerical determination of the dynamical separatrix directly applied to the system (13.1)–(13.4) in [10]. To clarify whether these simplifications making the system effectively two dimensional and the bifurcation analysis are justified, we now investigate the complete stroboscopic map for the 4D non-autonomous dynamical system for  $(T_1, T_2, N, A_p)^T$ .

We denote by  $\theta(T_0, A_0; t)$  the solution of the autonomous system (13.1)–(13.4) at time  $t$  for  $\xi_p = 0$  with initial conditions  $T_0 = (T_1^0, T_2^0)^T$  and  $A_0 = (N^0, A_p^0)^T$ . The 4D stroboscopic map  $\mathbf{S}_\tau(n) : \mathbb{N} \times \mathbb{R}_+^4 \rightarrow \mathbb{R}_+^4$  with period  $\tau$  is defined as

$$\mathbf{S}_\tau(n + 1) = \theta(\mathbf{S}_\tau(n) + (0, 0, 0, D_p)^T; \tau - 0), \quad n = 0, 1, 2, \dots \tag{13.8}$$

with initial condition  $\mathbf{S}_\tau(0) = (T_0, A_0)^T$ . Analogously to the 2D case we denote the fixed points by  $S(\tau)$  and obtain

$$\frac{dS}{d\tau} = \left(1 - \frac{\partial\theta}{\partial S}\right)^{-1} \frac{\partial\theta}{\partial\tau}, \tag{13.9}$$

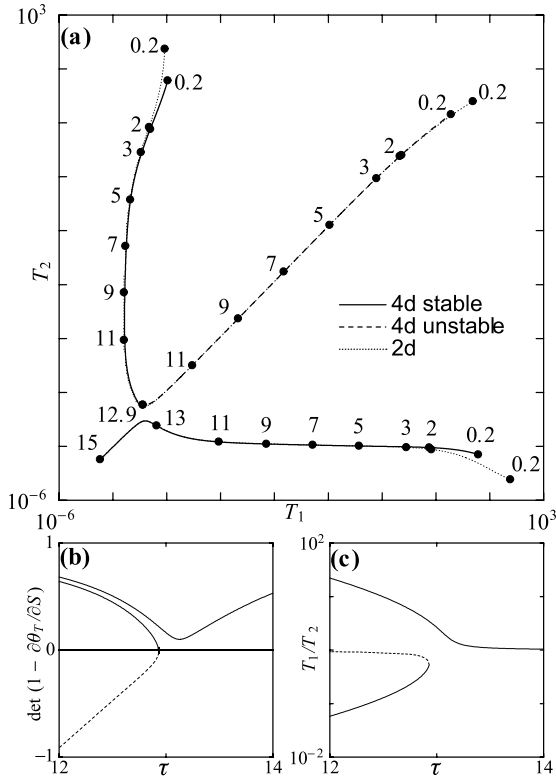


**Fig. 13.3.** The manifolds of stable and unstable fixed points of the stroboscopic maps for the simplified case (2D model, *dotted lines*) and the complete 4D model (*solid and dashed lines*) are shown in (a). The curves are parametrized by the period of injections  $\tau$ . Values of  $\tau$  in the range from 0.2 to 15 are indicated in the figure. It can be seen that only for small periods  $\tau < 1$  differences between the simplified and the complete model exist,  $D_p = 1, c = 10^{-4}$ . In (b) a plot of  $\det(1 - \partial\theta_T/\partial S)$  which equals the product of eigenvalues is shown as a function of  $\tau$ . The bifurcation is associated with the occurrence of a zero eigenvalue. Near the bifurcation there are no differences between the 2D and the 4D mapping. In (c) the corresponding bifurcation diagram of the ratio  $T_1/T_2$  with control parameter  $\tau$  is depicted. Stable and unstable cases are distinguished by *solid* and *dashed lines*, respectively.

provided the matrix  $(1 - \partial\theta/\partial S)$  can be inverted. If this is not the case, a bifurcation occurs at a critical value of  $\tau$ . Again, for numerical evaluation we exploit

$$\frac{\partial\theta}{\partial S} = \frac{\partial\theta}{\partial(T_0, A_0)^T} \Big|_{S(\tau)} \quad \text{and} \quad \frac{\partial\theta}{\partial\tau} = \frac{d(T, A)^T}{dt} \Big|_{S(\tau)}. \quad (13.10)$$

For sufficiently large  $\tau$  (for our parameter setting it is  $\tau \gtrsim 2$ ) the manifolds of fixed points agree with those of the simplified map; in particular, the bifurcation analysis gives the same results for both cases, see Fig. 13.3. This is easily understood: If the

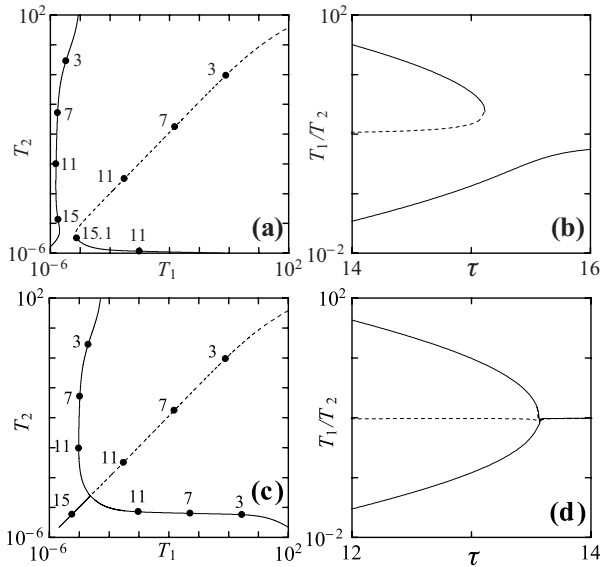


**Fig. 13.4.** Manifold of fixed points of the stroboscopic map (13.8) parametrized by the period of injections  $\tau$  and the corresponding bifurcation diagram of  $T_1/T_2$  for  $D_p = 1$  and different concentrations of background cytokines. Values of  $\tau$  in the range from 3 to 15.1 are indicated in (a) and (b). Again, stable and unstable cases are distinguished by *solid* and *dashed* lines, respectively.  $c = 10^{-5}$  in (a) and (b), and  $c = 6 \times 10^{-5}$  in (c) and (d).

period between the injections of allergen is long enough, allergen is eliminated and the naive cells recover to their baseline value  $\alpha$  while the T-helper cells reach their initial value (since we consider fixed points of the stroboscopic map). Of course, without further injections of allergen T-helper cells would return to their zero baseline. For smaller  $\tau$  ( $\tau < 2$ ), allergen is not completely eliminated before the next injection and the naive cells have not yet recovered; thus the assumptions of the 2D model are not fulfilled and the differences between the 2D and 4D models become visible.

For smaller values of  $\alpha$  and  $\nu$ , the production of T-helper cells is smaller and the elimination of allergen less efficient, and differences between the 2D and 4D models occur for larger values of  $\tau$ .

We also investigated the dependence on the small cytokine background  $c$  and the dose of the periodic allergen injections  $D_p$ . Fig. 13.4 shows the manifold of fixed points and the corresponding bifurcation diagram for two different values of  $c$ . It can be seen that for  $c \approx 6 \times 10^{-5}$  there is a perfect backward pitchfork bifurcation. Even small deviations from this critical value (cf. for  $c = 10^{-5}$  Fig. 13.4b, and for  $c = 10^{-4}$  Fig. 13.3c) lead to a perturbation of the perfect bifurcation. Note however that the bifurcations occur for very small concentrations of  $T_1$  and  $T_2$  on the order of  $10^{-5}$  to  $10^{-4}$ . For larger concentrations the line of unstable fixed points, i.e., the dynamical separatrix, that determines the qualitative behaviour of the system is not affected.

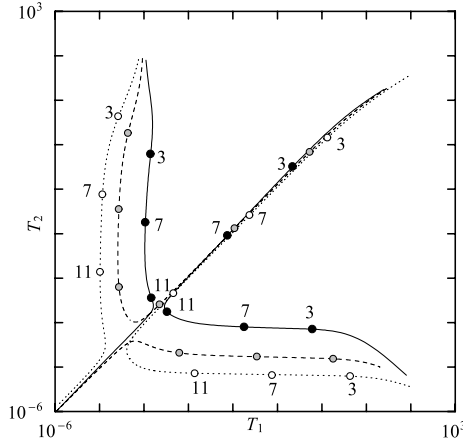


**Fig. 13.5.** Manifold of fixed points of the stroboscopic map (13.8) for  $c = 10^{-4}$  and different doses  $D_p$  parametrized by the period of injections  $\tau$ . Values of  $\tau$  in the range from 3 to 11 are indicated. Solid line  $D_p = 0.1$ , dashed line  $D_p = 0.5$ , and dotted line  $D_p = 10$ . The qualitative behaviour of the fixed point manifolds depends on  $D_p$ . For small ( $D_p = 0.1$ ) and large ( $D_p = 10$ ) values they appear similar to those in Fig. 13.4a, for intermediate values ( $D_p = 5$ ) similar to Fig. 13.3a. Correspondingly, the character of bifurcations occurring for small T cell concentrations is different. However, for T cell concentrations that are not too small the unstable manifold is practically the same for all  $D_p$ .

The manifolds of fixed points for different values of the dose  $D_p$  of periodic injections are shown in Fig. 13.5. Similarly, we see changes in the location of the stable manifolds and in the character of the bifurcation, whereas the location of the dynamical separatrix for T cell concentrations larger than  $10^{-3}$  is practically the same for all values of  $D_p$ .

### 13.3 Concluding Remarks

Venom immunotherapy consists in the initial phase in injections of increasing doses of allergen administered in increasing intervals following empirical protocols. As described in detail in [10] the gradual increasing doses of allergen desensitize the effector cells, mast cells, and basophils of the early phase reactions. Having reached this desensitized state it is possible to apply high doses of allergen to perform a Th2–Th1 switch. In the maintenance phase of the therapy, carried out for 3 to 5 years or even longer, periodic injections of high doses hold the system in a state of Th1-dominated response to the allergen.

In this chapter we investigated the second phase of the therapy by analyzing a stroboscopic map of the period of the injections driving a non-linear dynamical system describing Th1–Th2 regulation. Using the tool of stroboscopic maps reduces the complexity of the non-autonomous system, allowing a thorough analysis, and puts the notion of dynamical separatrix on a firm mathematical ground.

We determined the manifolds of stable and unstable fixed points parametrized by the period  $\tau$  between successive injections. The manifold of unstable fixed points is the dynamical separatrix which has to be crossed during a successful Th2–Th1 switch. The periodic injections of the maintenance phase hold the system near the stable fixed point of the stroboscopic map where  $T_1/T_2 \gg 1$ .

The bifurcation analysis of the manifolds of fixed points of the stroboscopic map of a simplified system, corresponding to the numerical study in [10], and of the complete non-autonomous system leads to the same results provided the period of allergen injections is not too small.

As shown in [10] the present model describes the Th1–Th2 switch not only for the conventional protocol, where the maintenance dose is reached in about 50 days, but also for rush- and ultra-rush protocols, cf. [3], where the dose must be reached in only a few days.

Assuming that for an allergic individual initially  $T_2/T_1 > 1$ , three regions in the  $T_1$ – $T_2$  plane can be distinguished. *Region 1*, located to the right of the separatrix, is the region where successive injections of  $D_p = 1$  will continuously improve the ratio  $T_1/T_2$  independent of the time interval between injections. *Region 2*, located left of the separatrix, is where the trajectory after injection of  $D_p = 1$  transiently crosses the separatrix, cf. Fig. 13.2. If a next dose of allergen is injected while the system is beyond the separatrix, it is possible to further improve the ratio  $T_1/T_2$ . Success or failure of the Th2–Th1 switch depends on the schedule of injections. The further the initial state is from the separatrix the shorter the trajectory is on the other side of the separatrix. In this phase, shorter intervals between injections will increase the chance of success. Empirical protocols already follow this strategy by increasing the intervals between injections of  $D_p = 1$  from initially one week to eventually four weeks. Finally, in *Region 3*, left of *Region 2*, the Th2 dominance is so pronounced that every injection of allergen will only impair  $T_1/T_2$ .

A more detailed discussion of the timing of subsequent injections can be found in [10]. For example, the Th2–Th1 switch may fail if the intervals between injections are too long. Furthermore, a few injections of allergen corresponding to lower dose wasp stings may induce a switch from Th1 to Th2 prevalence—a possible scenario for sensitization.

The location of the dynamical separatrix is not influenced by changes of the allergen dose  $D_p$  or by small changes in the cytokine background  $c$ , provided the T cell concentrations are larger than  $10^{-3}$ . The bifurcations occurring for smaller values of the T cell concentrations may change however varying  $c$  or  $D_p$ . We do not exclude that this property could be relevant during the process of sensitization.

We also considered periodic injections of small doses of allergen  $D_p$  for which  $\tau$  also becomes small. The fixed points then converge to the fixed point of the autonomous system with a constant supply (infusion) of allergen at a rate  $\xi = D_p/\tau$  as expected. To minimize the inconvenience for the patients, it seems feasible to maintain a large ratio  $T_1/T_2$  by an infusion of allergen at minute rates applied, e.g., by an implantable nanopump.

On the other hand, in the maintenance phase of the therapy when the trajectory is not able to cross the separatrix, it is also possible to extend the intervals between

injections. Fig. 13.5 shows that the same ratio  $T_1/T_2$  can be achieved for different pairs of maintenance dose and injection period. A recent clinical study reported that the conventional interval of 4 to 6 weeks can be safely extended to 3 months [13].

The present model describing Th1–Th2 regulation is, of course, a crude simplification of a very complex system. Nevertheless, it exhibits essential features of venom immunotherapy. Future investigations aim at proceeding with the mathematical analysis, for example generalizing the bifurcation analysis for non-periodic, or stochastic, injections of allergen adopting the concept of pull-back attractors [14]. A second necessary line is to make the model more realistic, including, e.g., T cell memory, the recently rediscovered regulatory T cells, see, e.g., [15, 16], or the interaction with the B-cell system, where very recently internal images of allergen have been identified [17].

## References

1. Romagnani, S.: Human Th1 and Th2: doubt no more. *Immunology Today*, **12**, 256–257 (1991).
2. Romagnani, S. (ed): Th1 and Th2 cells in health and disease. *Chemical Immunology*, **63**, Karger, Basel (1996).
3. Heppt, W., Reuz, H., Roecken, M. (eds): *Allergologie*. Springer, Berlin (1998).
4. Blaser, K., Carballido, J., Faith, A., Cramer, R., Akdis, C.: Determinants and mechanisms of human immune responses to bee venom phospholipase A2. *Int. Arch. Allergy Immunol.*, **117**, 1–10 (1998).
5. McHugh, S.M., Deighton, J., Stewart, A.G., Lachmann, P.J., Ewan, P.W.: Bee venom immunotherapy induces a shift in cytokine response from a Th2 to a Th1 dominant pattern: comparison of rush and conventional immunotherapy. *Clin. Exp. Allergy*, **25**, 828–838 (1995).
6. Schuerwegh, A.J., Cluck, L.S.D., Bridts, C.H., Stevens, W.J.: Wasp venom immunotherapy induces a shift from IL-4-producing towards interferon-gamma-producing CD4+ and CD8+ T lymphocytes. *Clin. Exp. Allergy*, **31**, 740–746 (2001).
7. Tari, M.G., Mancino, M., Madonna, F., Buzzoni, L., Parmiani, S.: Immunologic evaluation of 24 month course of sublingual immunotherapy. *Allergol. Immunopathol. (Madr)*, **22**, 209–216, (1994).
8. Noon, L., Cantab, B.C.: Prophylactic inoculation against hay fever. *Lancet* **1**, 1572–1574 (1911).
9. Behn, U., Dambeck, H., Metzner, G.: Modeling Th1–Th2 regulation, allergy, and hyposensitization. In: Bagnoli, F., Ruffo, S. (eds) *Dynamical Modeling in Biotechnologies (Lectures presented at the EU Advanced Workshop, Torino, May 27–June 9, 1996)*. World Scientific, Singapore, 227–244 (2001).
10. Richter, J., Metzner, G., Behn, U.: Venom immunotherapy: A mathematical model. *J. Theor. Med.*, **4**, 119–132 (2002).
11. Richter, J., Behn, U., Metzner, G.: Modelling of Th1–Th2 regulation, allergy and venom immunotherapy. In: Marone, G. (ed) *Clinical Immunology and Allergy in Medicine*, Proc. 21st EAACI Congress 2002, Naples. JGC Editions, Naples, 257–262 (2003).
12. Ruedl, C., Bachmann, M.F., Kopf, M.: The antigen dose determines T helper subset development by regulation of CD40 ligand. *Eur. J. Immunol.*, **30**, 2056–2064 (2000).
13. Goldberg, A., Confino-Cohen, R.: Maintenance venom immunotherapy administered at 3-month intervals is both safe and efficacious. *J. Allergy Clin. Immunol.*, **107**, 902–906 (2001).

14. Langa, J.A., Robinson, J.C., Suárez, A.: Stability, instability, and bifurcation phenomena in non-autonomous differential equations. *Nonlinearity*, **15**, 887–903 (2002).
15. Akdis, M., Blaser, K., Akdis, C.A.: T<sub>Reg</sub> cells and allergy: a question of balance and antigen specificity. *Nature Rev. Immunol.*, **3** Viewpoint (online only), doi:10.1038/nri1047 (2003).
16. Ngoc, L.P., Gold, D.R., Tzianabos, A.O., Weiss, S.T., Celedón, J.C.: Cytokines, allergy, and asthma. *Curr. Opin. Allergy Clin. Immunol.*, **5**, 161–166 (2005).
17. Hantusch, B., et al.: Internal images: Human anti-idiotypic Fab antibodies mimic the IgE epitopes of grass pollen allergen Phl p 5a. *Mol. Immunol.*, **43**, 2180–2187 (2006).



## Architecture of Randomly Evolving Idiotypic Networks

Holger Schmidtchen and Ulrich Behn

Institute for Theoretical Physics, University Leipzig, POB 100 920, 04009 Leipzig, Germany;  
Ulrich.Behn@itp.uni-leipzig.de

**Summary.** B lymphocytes express on their surface receptors (antibodies) of a given specificity (idiotype). Crosslinking these receptors by complementary structures, antigens or antibodies, stimulates the lymphocyte. Thus a large functional network of interacting lymphocytes, the idiotypic network, emerges. Idiotypic networks, conceived by Niels Jerne 30 years ago, experience a renewed interest, e.g., in the context of autoimmune diseases.

In a previously proposed minimalistic model idiotypes are represented by bit strings. The population dynamics of the idiootype clones is reduced to a zero-one scheme. An idiootype survives only if it meets enough but not too many complementary structures. We investigate the random evolution of the network towards a highly organized functional architecture which is driven by the influx of new idiotypes, randomly generated in the bone marrow. The vertices can be classified into different groups, which are clearly distinguished, e.g., by the mean life time of the occupied vertices. They include densely connected core groups and peripheral groups of isolated vertices, resembling the central and peripheral parts of the biological network.

We determine the building principles of the observed patterns and propose a description of their architecture, which is easily transferable to other patterns and applicable to different system sizes.

**Key words:** Immune system, B lymphocytes, antibodies, idiotypic interactions, randomly evolving networks.

### 14.1 The Idiotypic Network

The immune system defends the body against threats to its health caused by antigens, e.g., pathogenic cells or substances. A key feature of the immune response is the recognition of foreign invaders. In the humoral immunity, which is considered here, this is achieved by antibodies. Antibodies are proteins with highly specific binding sites, which enable them to bind to complementary sites of an antigen, which are thus marked for further processing, e.g., for eating by macrophages.

Antibodies are produced by B lymphocytes. Each of these cells is capable of producing exactly one specific type (the idiootype) of antibody. On their surface B cells express copies of their antibodies as receptors. When stimulated, i.e., crosslinked by

complementary structures, they proliferate and, after a few cell cycles, differentiate into plasma cells and memory cells, the former secreting large amounts of the useful antibodies. Thus, useful clones survive, while others, lacking stimulation, die. This process is therefore called clonal selection [1].

In 1974 Niels K. Jerne presented his concept of idiotypic network [2]. B lymphocytes with receptors of a given idio type are capable of mutual interaction if their receptors have complementary specificity. Hence, the entirety of the B lymphocyte system forms a functional network, with nodes representing the idiotypes and links between complementary idiotypes. Jerne's concept of idiotypic network got an immediate enthusiastic resonance and earned him the Nobel Prize in 1984. In the following years, B lymphocytes of a given idio type and their anti-idiotypic counterparts were experimentally identified, but the search for deeper network structures was not really successful. Thus, the initial enthusiasm of experimentally working immunologists decayed, parallel with the rapid success of molecular immunobiology. Nevertheless, idiotypic networks stayed attractive for theoretical biologists interested in the systems' behavior and also attracted the interest of theoretical physicists. An excellent review and a thorough discussion of the historical development of immunological paradigms can be found in [3]; for a more personal view cf. also [4]. A review of different modeling approaches written especially for physicists is given in [5].

Today, a new interest in idiotypic interactions has emerged, especially in the context of autoimmune diseases [6, 7], and the progress in experimental methods makes a new generation of experiments feasible. Independently, statistical physicists discovered their interest in the description of networks, especially random and randomly growing networks, with applications in a plethora of different, multidisciplinary fields [8–10].

The estimated size of the potential idiotypic repertoire of humans is of the truly macroscopic order  $10^{12}$ , that of the expressed repertoire is of order  $10^8$  [5, 11]. The interactions between B cells of complementary idio type are genuinely nonlinear. Thus, modeling idiotypic networks is an inviting playground for physicists dealing with statistical physics, nonlinear dynamics, and complex systems.

In a minimalistic model proposed in [12] idiotypes are represented by bit strings as in [13] which can interact with (up to a certain number of mismatches) complementary bit strings. In the model, an idio type population may be either present or absent. For survival it needs stimulation by sufficiently many complementary idiotypes, but it becomes extinct if too many complementary idiotypes are present. The dynamics is driven by the random influx of new idiotypes from the bone marrow. The model has a minimal number of parameters, namely the length of the bit string, the allowed number of mismatches, upper and lower thresholds for stimulation, and the influx of new idiotypes. Hence, it is possible to study the model with special emphasis on the network properties and dynamics. In [12] a first study for one and two allowed mismatches was presented. Interestingly, for certain parameter settings, a random evolution towards a highly nontrivial complex functional architecture of the emerging network was observed. The nodes in this network representing idiotypes can be classified into different groups, which can be clearly distinguished. They include densely connected core

groups and peripheral groups of isolated nodes, resembling the notion of central and peripheral parts of the biological network [14, 15].

In this chapter we aim at investigating the building principles of this architecture and identifying the building blocks, which we shall call pattern modules.

The potential idiotypic network is modeled as in [12, 17] by an undirected base graph  $G = (\mathcal{V}, \mathcal{E})$ . The set of vertices (nodes)  $\mathcal{V}$  represents the potential repertoire of idiotypes a given individual can express. Each idiotypic  $v \in \mathcal{V}$  in the network is characterized by a bit string of length  $d$ :  $\mathbf{b}_d \mathbf{b}_{d-1} \cdots \mathbf{b}_1$  with  $\mathbf{b}_i \in \{0, 1\} \forall i = 1, 2, \dots, d$ . The links  $l \in \mathcal{E}$  connect complementary and almost complementary idiotypes. That is, for every pair of vertices the degree of complementarity is evaluated: If the Hamming distance  $d_H$  between the bit strings of two vertices  $v, w \in \mathcal{V}$  equals the length of the bit string  $d$ , there is a link  $l = \{v, w\}$  representing a perfect match, if  $d_H(v, w) = d-1$ , we call it a one-mismatch link, etc. We allow  $m$  mismatches, for which an interaction of the idiotypes is still possible. In terms of an adjacency matrix we can write the mismatch rule as

$$m_{vw} = \begin{cases} 1 & \text{if } d - d_H(v, w) \leq m \\ 0 & \text{otherwise} \end{cases} . \quad (14.1)$$

$G_d^{(m)}$  then denotes a base graph of vertices with bit strings of length  $d$ , and links between vertices which are complementary except for up to  $m$  bit positions.

At a given moment of time an individual will express only a fraction of the potential repertoire of idiotypes; the corresponding vertices are occupied, and the others are empty. The evolution of the system is driven entirely by the random influx and the internal population dynamics. The update algorithm [12] for the evolution of the system is:

- (i) Choose  $I$  unoccupied sites (holes) randomly and set them occupied. They represent the influx of new idiotypes from the bone marrow.
- (ii) Count the number of occupied vertices  $n(\partial v)$  in the neighborhood of every vertex  $v \in G$ . If  $n(\partial v)$  is outside the window of lower and upper threshold  $(t_l, t_u)$ , the vertex  $v$  will be set empty.

Both updates are parallel, and they are iterated.

In the following section we describe one simple pattern in detail and show that its architecture is based on very few principles. In this context we introduce the notion of pattern modules, which are congruently occupied repeating building blocks of the pattern. In Sect. 14.3 we apply this new concept to more complex patterns and show that it correctly predicts the observed properties of the patterns.

## 14.2 Periodic 2-Cluster Pattern

We performed simulations, in which we measured the behavior of the whole system, as well as the time averaged behavior of every single vertex. We are describing the

**Table 14.1.** Characterization of groups by local quantities for the case  $I = 10$ .

	$S_1$	$S_2$	$S_3$
occupied neighbors $\overline{\langle n(\partial v) \rangle}_{S_i}$	1.16	10.96	53.26
mean life time $\overline{\langle \tau(v) \rangle}_{S_i}$	4699	3	0
mean occupation $\overline{\langle n(v) \rangle}_{S_i}$	0.95	0.01	0.00

latter by characteristic local quantities, finding groups of vertices with equal behavior, and analyzing the network relations between the groups.

The measurements, which will be referred to in the following, were obtained in simulations on base graph  $G_{12}^{(2)}$ , with lower threshold  $t_l = 1$ , upper threshold  $t_u = 10$ . The influx  $I$  was varied in the range of 10 to 800. The system was given a relaxation time of 5000 time steps to reach a steady state. The observation time itself was another 5000 time steps long.

A 2-cluster pattern evolved for  $I = 10$  and  $I = 60$ . It bears great resemblance to the 2-clustered patterns in one-mismatch graphs, which had been investigated before [12]. For both matching rules, i.e., the cases  $m = 1$  and  $m = 2$ , the subgraph of occupied vertices  $\Gamma$  exhibits the characteristic 2-clustered picture for a certain parameter range, which gives both types of configurations their name.

According to the quantitative behavior of the vertices, we can separate them into three groups:  $S_1, S_2, S_3 \subset \mathcal{V}$ . Table 14.1 gives characteristic values of some local quantities, i.e., quantities related to single vertices. We measured the time average for every vertex  $\overline{x(v)}$  and subsequently averaged these mean values over all elements of the respective groups  $\overline{\langle x(v) \rangle}_{S_i}$ .

As in the one-mismatch case there is a group of frequently occupied vertices ( $S_1$ ) and a group of stable holes ( $S_3$ ). Additionally, we now find a group of potential hubs ( $S_2$ ). They are seldom occupied. However, if they are, they function as hubs by linking together up to  $t_u$  2-clusters. For a visualization of the network of occupied vertices  $\Gamma$ , see Fig. 14.1. The sizes of the groups obey  $|S_1| = |S_2|/2 = |S_3|$ .

We made a surprising observation when looking at the vertex indices  $i_v$ . They are given by the decimal number coded in the bit string  $\mathbf{b}_d \mathbf{b}_{d-1} \dots \mathbf{b}_1$ :  $i_v = \sum_{j=1}^d \mathbf{b}_j 2^{j-1}$ . We found that the sum of the two indices in a 2-cluster is constant in the graph  $\Gamma$ . Then a look at the bit strings of the vertices involved in the 2-clusters revealed that they are identical in exactly two bits, say at positions  $k$  and  $l$ . The remaining  $d - 2$  bit positions assume all  $2^{d-2}$  possible values. Inside a cluster both vertices' bit strings are complementary in these positions. Thus, the 2-clusters have a two-mismatch link. We can write

$$\dots \mathbf{b}_k \dots \mathbf{b}_l \dots \quad \text{connects to} \quad \overline{\dots \mathbf{b}_k \dots \mathbf{b}_l \dots}, \tag{14.2}$$

where the overbar denotes the bit inversion.

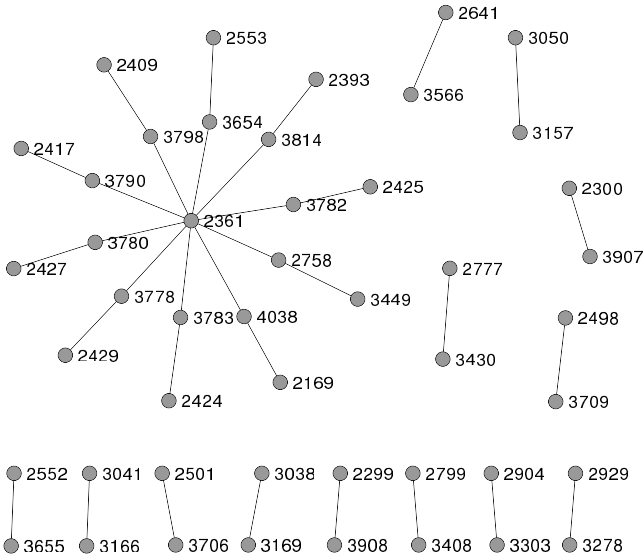


**Fig. 14.1.** A typical pattern found for  $l = 10$ , and one for  $l = 60$ . The occupied vertices form 2-clusters, some of which are interlinked via hubs. The vertices are labeled with the decimal expression of their bit string. The sum of the indices within a 2-cluster is always 6207 in this 2-cluster configuration. The determinant bit positions are 7 and 12. Figure produced using yEd [16].

The other groups,  $S_2$  and  $S_3$ , have similar structural properties. The bit strings of stable holes are also mutually equal in the same two bit positions  $k$  and  $l$ . However, they are inverse to  $b_k$  and  $b_l$  of the occupied vertices. Potential hubs, finally, with respect to the other groups have exactly one deviating and one equal bit in these positions. This can be summarized by

$$\begin{array}{lcl}
 \text{occupied vertices } S_1 & \cdots b_k \cdots b_l \cdots & \\
 \text{potential hubs } S_2 & \cdots \overline{b_k} \cdots \overline{b_l} \cdots & \\
 & \cdots b_k \cdots \overline{b_l} \cdots & \\
 \text{stable holes } S_3 & \cdots \overline{b_k} \cdots \overline{b_l} \cdots & 
 \end{array} \tag{14.3}$$

As only these two bits play the crucial role of determining the pattern, they shall be called determinant bits.

These very few principles suffice to explain all observations made in the simulations, and we are able to construct a perfect 2-cluster pattern, i.e., a configuration in which all vertices of group  $S_1$  are occupied and the others remain empty. It is perfect in the sense that there are no defects but also no hubs.

For such a configuration we can calculate the degeneracy,

$$\text{degeneracy} = 2^2 \times \binom{d}{2}, \tag{14.4}$$

where the first factor represents the choice of the two determinant bits, and the second factor gives the number of possible positions of these bits in the bit string of length  $d$ .

Furthermore, we can compute the generic number of occupied neighbors  $n(\partial v)$  of a vertex  $v$  of any group. As we assume all  $S_1$  to be occupied,  $n(\partial v)$  is given by the number of links between  $v$  and elements of  $S_1$ . In order to establish a link between two vertices, their bit strings need to be complementary except for up to two mismatches. If  $v \in S_1$ , it already has two bits in common with all vertices in  $S_1$ , namely  $\mathbf{b}_k$  and  $\mathbf{b}_l$ . Thus, all remaining bits must be exactly complementary. Hence, there is exactly *one* vertex  $w \in S_1$ ,  $w \neq v$ , which obeys the constraints. If  $v \in S_2$  or  $v \in S_3$ , there is one predetermined mismatch or none, respectively. The remaining mismatches can be distributed among the  $d - 2$  nondeterminant bits. We get

$$n(\partial v) = \sum_{j=0}^1 \binom{d-2}{j} \quad \forall v \in S_2 \quad \text{and} \quad n(\partial v) = 11 \text{ for } d = 12, \quad (14.5)$$

$$n(\partial v) = \sum_{j=0}^2 \binom{d-2}{j} \quad \forall v \in S_3 \quad \text{and} \quad n(\partial v) = 56 \text{ for } d = 12, \quad (14.6)$$

which is in good agreement with the statistical observation, cf. Table 14.1.

Also, the value of the index sum only depends on the determinant bits. If  $(v, w)$ , with  $v, w \in S_1$ , is a pair of vertices forming a 2-cluster as in (14.2), the sum is given by

$$i_v + i_w = \sum_{j \neq k, l} 2^{j-1} + 2\mathbf{b}_k 2^{k-1} + 2\mathbf{b}_l 2^{l-1} \quad \forall (v, w), v, w \in S_1. \quad (14.7)$$

The regularity of the principle underlying this pattern inspired a new description of the structure of the evolving patterns. If we consider the two determinant bits as coordinates of a two-dimensional space, they will define the corners of a two-dimensional hypercube, i.e., a square. In this picture, the corner with coordinates  $(\mathbf{b}_k, \mathbf{b}_l)$  represents an occupied vertex, the opposite corner  $(\overline{\mathbf{b}}_k, \overline{\mathbf{b}}_l)$  is a stable hole, and the neighboring corners of  $(\mathbf{b}_k, \mathbf{b}_l)$  are potential hubs. The two-dimensional hypercube shall be called a pattern module, since it is the smallest, ever-repeating building block of the entire regular configuration. In other words, we can speak of  $2^{d-2}$  congruently occupied parallel worlds.

Fig. 14.2 illustrates the new concept of pattern modules in the smallest possible two-mismatch graph  $G_3^{(2)}$ .

Many results for 2-clustered patterns on the  $G_{12}^{(2)}$  base graph can be generalized to other choices of  $d$  and  $m$ . For instance, the 2-cluster pattern found in [12] can be explained in a similar way. We proved for base graphs  $G_d^{(m)}$ : We can construct 2-cluster patterns by means of pattern modules with exactly one occupied corner. The dimension of the pattern module  $d_M$  equals the number of allowed mismatches  $m$ , the number of qualitatively distinguishable groups is  $d_M + 1$ , and the size of group  $S_i$  is  $2^{d-d_M} \binom{d_M}{i-1}$ . For a 2-cluster pattern to be able to emerge, the lower threshold has to be chosen  $t_l = 1$ , and the upper threshold must obey  $1 \leq t_u \leq d - d_M$ .

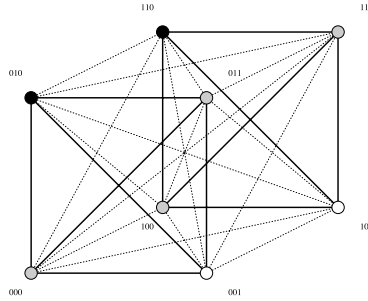


**Fig. 14.2.** The complete graph  $G_3^{(2)}$  with a 2-cluster configuration. On  $G_3^{(2)}$  every vertex is connected to any other. We find two congruently occupied two-dimensional modules (solid links), each consisting of one occupied vertex (black,  $\cdot 10$ ), two potential hubs (gray,  $\cdot 00$  and  $\cdot 11$ ), and one stable hole (white,  $\cdot 01$ ). The upper threshold has to be adjusted to  $t_u = 1$ .

### 14.3 Patterns of Higher Complexity

Besides the 2-cluster pattern described above, a number of different patterns were found in the simulation on  $G_{12}^{(2)}$ . They all appear more complex with respect to the number of qualitatively distinguishable groups and the clustering of their occupied graphs  $\Gamma$ . An elucidating insight into the diversity and some characteristics of the groups is given by Fig. 14.3 showing the average number of occupied neighbors of each vertex. We find distinct regions in dependence of the influx  $I$ . By taking other observable quantities into account, we can describe them as static ( $I < 90$ ), dynamic ( $90 \leq I < 260$ ), dynamic and transient ( $260 \leq I$ ), and random ( $350 \ll I$ ) patterns. Static patterns have groups of occupied vertices, which have a high mean life

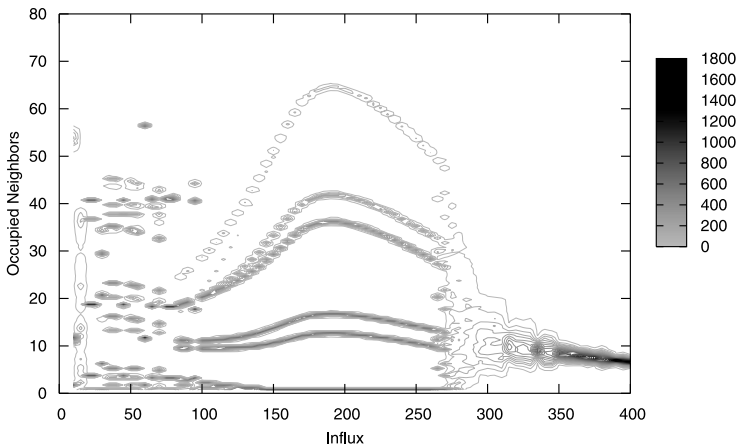


**Fig. 14.3.** We measured the time averages of the number of occupied neighbors of each vertex. The graph shows a top view on histograms giving the frequencies of the average number of occupied neighbors for different values of the main parameter  $I$ .

time  $\overline{\tau(v)}$ . The other groups often are stable holes or sparsely occupied vertices, cf. Table 14.1. In dynamic patterns there still are some stable hole groups; however, we do not find any groups of permanently occupied vertices. The mean life time generally is small, and the graph of occupied vertices  $\Gamma$  changes permanently. While in static and dynamic patterns all vertices remain in their groups, but for high  $l$  the patterns become transient, i.e., groups dissolve and rearrange themselves on the base graph in a different configuration. For very high influxes the dynamics is entirely random.

In the static pattern regime there exists a dominating 8-cluster pattern, in which the clusters of occupied vertices appear as cubes, as well as a 24- and a 30-cluster pattern.

We found that all of these patterns can be explained considering the regular structures which emerge for more than two determinant bits. As explained above, the dimension  $d_M$  of the corresponding pattern module is just the number of determinant bits. Many predictions made for the 2-cluster pattern also hold for the patterns of higher complexity: The number of groups is  $d_M + 1$ , the sizes of the groups are given by  $|S_i| = 2^{d-d_M} \binom{d_M}{i-1}$ . We can arrange these general results as in Table 14.2.

This is, of course, Pascal’s triangle. The bold numbers shall indicate groups which are occupied in the static patterns on  $G_{12}^{(2)}$ . This choice, however, is not unambiguous due to the symmetry of the hypercubic structure of the pattern module, which reflects that vertices with determinant bits  $(b_k, \dots, b_l)$  as well as  $(\overline{b_k}, \dots, \overline{b_l})$  arbitrarily may be labeled as group  $S_1$ .

We also can translate the mismatch rule into the framework of pattern modules: The original rule says that two vertices are connected if their bit strings are complementary except for a maximum of  $m$  mismatches. In terms of the pattern modules, we can formulate that some vertices of group  $S_i$  can connect to some vertices of group  $S_j$ , if the indices obey

$$|i + j - 2 - d_M| \leq m . \tag{14.8}$$

If such links exist, they will have at least  $|i + j - 2 - d_M|$  mismatches.

For example, in Table 14.2 we find that for  $d_M = 2, 4$ , and  $6$  the respective occupied groups  $S_1, S_2$ , and  $S_3$  have vertices which connect to vertices in the same group

**Table 14.2.** Pattern modules in  $G_{12}^{(2)}$ .

$d_M$	$2^{d_M-d}  S_i $ with $i = 1, 2, \dots, d_M+1$						observed clusters in $G_{12}^{(2)}$	
0	1							
1	1		1					
2	<b>1</b>		2	1		2-cluster		
3	<b>1</b>		<b>3</b>	3	1		24-cluster	
4	1		<b>4</b>	6	4	1	8-cluster	
5	1	5	10	10	5	1		
6	1	6	<b>15</b>	20	15	6	1	30-cluster



**Table 14.3.** Characterization of the six empirical groups. Data from [12].

	$\tilde{S}_1$	$\tilde{S}_2$	$\tilde{S}_3$	$\tilde{S}_4$	$\tilde{S}_5$	$\tilde{S}_6$
group size $ \tilde{S}_i $	1124	924	924	134	330	660
life time $\langle \tau(v) \rangle_{S_i}$	0.0	3.8	5.4	10.0	18.1	35.6

via two-mismatch links. In these cases, the connected vertices form the characteristic 2-, 8-, and 30-clusters found in the simulations.

A remarkable pattern found on  $G_{12}^{(2)}$  for  $I = 90$  is the dynamic pattern of a six-group structure. The six groups had been found empirically in [12], cf. Table 14.3.

We now denote the empirically found groups by  $\tilde{S}_i$  to distinguish them from the groups  $S_i$  defined by analyzing the pattern modules.  $\tilde{S}_1$  is the group of stable holes, and  $\tilde{S}_2$  and  $\tilde{S}_3$  are central groups, which have connections with each other, as well as to the peripheral group  $\tilde{S}_5$ .  $\tilde{S}_2$  additionally has links to the other peripheral group  $\tilde{S}_6$ . The group  $\tilde{S}_4$  is somewhat special, because it is entirely surrounded by stable holes. Occupied vertices of this group are sustained solely by the random influx. Fig. 14.4 shows a snapshot of the occupied graph at some time step. We clearly see the central and the peripheral part of the idiotypic network.

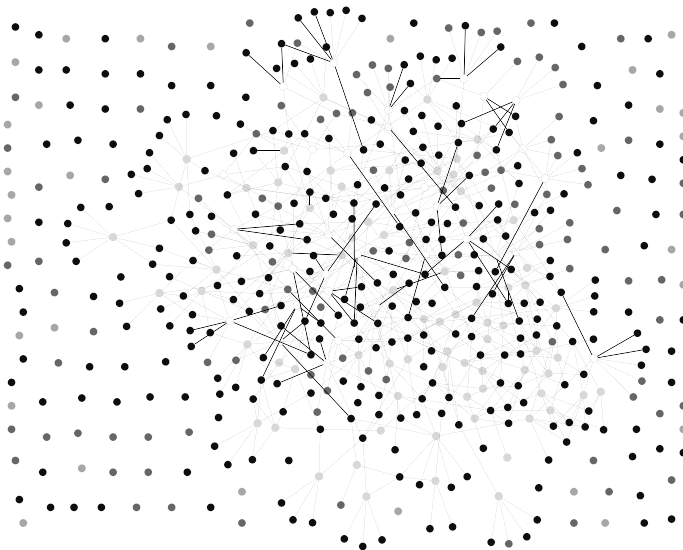


**Fig. 14.4.** Snapshot of the occupied graph  $\Gamma$  of a six-group configuration. The five different shades of gray indicate the mean life time of the different groups  $S_i$  from low (white) to high (black) mean life time. Figure produced using yEd [16].

**Table 14.4.** The pattern module of the six groups structure.

	$S_1$	$S_2$	$S_3$	$S_4$	$S_5$	$S_6$	$S_7$	$S_8$	$S_9$	$S_{10}$	$S_{11}$	$S_{12}$
empirical group	$\tilde{S}_4$	$\tilde{S}_4$	$\tilde{S}_4$	$\tilde{S}_5$	$\tilde{S}_6$	$\tilde{S}_3$	$\tilde{S}_2$	$\tilde{S}_1$	$\tilde{S}_1$	$\tilde{S}_1$	$\tilde{S}_1$	$\tilde{S}_1$
group size	2	22	110	330	660	924	924	660	330	110	22	2

We were able to explain this sophisticated structure by means of an 11-dimensional pattern module. From this we can derive the correct group sizes and, by applying condition (14.8), the observed links between the groups. Also, the observation that  $\tilde{S}_1$  and  $\tilde{S}_4$  further decay into subgroups [18] can be fully understood now. Table 14.4 gives the mapping  $\{S_i\} \rightarrow \{\tilde{S}_j\}$  and the derived group sizes  $|\tilde{S}_j|$ . For example, groups  $S_8, S_9, S_{10}, S_{11}$ , and  $S_{12}$  are the subgroups of the empirical group  $\tilde{S}_1$ . Their calculated size adds to 1124, the statistically measured size of group  $\tilde{S}_1$ .

## 14.4 Perspectives

We achieved a detailed microscopic understanding of the building principles of the very complex structures emerging during the random evolution of a model idiotypic network. For instance, we can calculate the size and the connectivity of the idiotypic groups, which were found empirically by statistical methods in a previous paper [12]. It is worthwhile to note that for a suitable choice of parameters the network comprises a central and a peripheral part, as proposed in [15]. An *ad hoc* architecture similar to the one described here was used in [19] to model the role of the idiotypic network in autoimmunity.

The microscopic understanding now opens the possibility to consider networks of more realistic size. Future steps will include checking whether a similar understanding can be reached for more realistic models. For example, we think of more sophisticated matching rules allowing for bit strings of different lengths, of weighted links for varying binding affinities, of several degrees of population for each idiotypic, and of a delay of takeout modeling memory. Furthermore, we are interested in the evolution of an inserted antigen population.

## References

1. Burnett, F.M.: *The Clonal Selection Theory of Acquired Immunity*. Vanderbilt Univ. Press, Nashville, TN (1959).
2. Jerne, N.K.: Towards a network theory of the immune system. *Ann. Inst. Pasteur Immunol.*, **125C**, 373–389 (1974).
3. Carneiro, J.: Towards a comprehensive view of the immune system. Ph.D. thesis, University of Porto, Oporto, Portugal (1997).

4. Coutinho, A.: A walk with Francisco Varela from first- to second-generation networks: In search of the structure, dynamics and metadynamics of an organism-centered immune system. *Biol. Res.*, **36**, 17–26 (2003).
5. Perelson, A.S., Weisbuch, G.: Immunology for physicists. *Rev. Mod. Phys.*, **69**, 1219–1267 (1997).
6. Shoenfeld, Y.: The idiotypic network in autoimmunity: Antibodies that bind antibodies that bind antibodies. *Nature Medicine*, **10**, 17–18 (2004).
7. McGuire, K.L., Holmes, D.S.: Role of complementary proteins in autoimmunity: an old idea re-emerges with new twists. *Trends in Immunology*, **26**, 367–372 (2005).
8. Strogatz, S.H.: Exploring complex networks. *Nature*, **410**, 268–276 (2001).
9. Dorogovtsev, S.N., Mendes, J.F.F.: *Evolution of Networks: From Biological Nets to the Internet and WWW*. Oxford University Press, Oxford (2003).
10. Barabási, A.L., Albert, R.: Statistical mechanics of complex networks. *Rev. Mod. Phys.*, **74**, 47–97 (2002).
11. Perelson, A.S., Oster, G.F.: Theoretical studies of clonal selection: Minimal antibody repertoire size and reliability of self-non-self discrimination. *J. Theor. Biol.*, **81**, 645–670 (1979).
12. Brede, M., Behn, U.: Patterns in randomly evolving networks: Idiotypic networks. *Phys. Rev. E*, **67**, 031920, 1–18 (2003).
13. Farmer, J.D., Packard, N.H., Perelson, A.S.: The immune system, adaption, and machine learning. *Physica D*, **22**, 187–204 (1986).
14. Coutinho, A.: Beyond clonal selection and network. *Immunol. Rev.*, **110**, 63–87 (1989).
15. Varela, F.J., Coutinho, A.: Second generation immune networks. *Immunology Today*, **5**, 159–166 (1991).
16. yEd - Java<sup>TM</sup> *Graph Editor*, v2.3.1\_02, <http://www.yWorks.com>.
17. Brede, M., Behn, U.: The architecture of idiotypic networks: percolation and scaling behaviour. *Phys. Rev. E*, **64**, 011908, 1–11 (2001).
18. Brede, M.: Random evolution of idiotypic networks: Dynamics and architecture. Ph.D. Thesis, Leipzig University, Leipzig (2003).
19. Sulzer, B., van Hemmen, J.L., Behn, U.: Central immune system, the self and autoimmunity. *Bull. Math. Biol.*, **56**, 1009–1040 (1994).

**Neural Systems and the Brain**

## Analysis of Infectious Mortality by Means of the Individualized Risk Model

Tatiana E. Sannikova

Institute of Numerical Mathematics, Moscow, Russia; tatiana@inm.ras.ru

**Summary.** The goal of this chapter is to describe the mechanism underlying the age-specific increase in death risk related to immunosenescence, to determine the cause-specific hazard rate as a function of immune system characteristics. A mathematical model that allows for the estimation of the age-specific risk of death caused by infectious diseases has been developed. The model consists of three compartments: (1) a model of immunosenescence, (2) a model of infectious disease, and (3) a model giving the relationship between disease severity and the risk of death. The proposed model makes it possible to analyze age-specific mortality from infectious diseases and to predict future changes in mortality due to public health activity. At the same time it can be used for individualized risk assessment.

**Key words:** Immune aging, pneumonia, mortality, antigenic load, infection rate, telomere.

### 15.1 Introduction

The age pattern of mortality from all causes has common traits for different human populations. These traits are relatively high during infancy and early childhood, very low during the reproductive period, increase exponentially from age 35 to 85, and decelerate at very old ages [11,25].

However, the detailed analysis of cause-specific mortality in countries with well-developed health care systems reveals that death rates from major causes do not follow this pattern [11, 12]. For instance, death rates from malignant neoplasms rise at ages 30–54 years and decline afterwards. Mortality from parasitic infections is highest at ages 30–35 years [11]. It has been found that mortality from some cancers levels off around 85–90 years of age, followed by a plateau, or a decline in the last decades of life [4]. Steeply increasing after age 65 years are death rates from respiratory infections and cardiovascular diseases.

All this implies that different systems of the organism become vulnerable in different periods of life. One can suppose that excessive susceptibility to certain diseases or disorders occurs at a period of age-associated remodeling of the system [24].

We propose a new approach to estimate cause-specific risk of death. This approach is based on the modeling of physiological aging of the system responsible for the

lethal disease or disorders. There is some evidence that replicative senescence of T cells results in a growth of mortality caused by respiratory infections [1, 8]. Here we consider age-associated changes in the immune system and the way they influence the course and the outcome of respiratory infection. We develop a model of age-related risk of death from respiratory infections and make an attempt to fit data on pneumonia mortality in some countries.

## 15.2 Model of Age-Related Risk of Death from Respiratory Infections

The principal processes associated with immunosenescence are replacement of naive lymphocytes by memory cells and replicative senescence of lymphocytes. A decrease in the number of naive lymphocytes results in a weak and delayed immune response to new pathogens. Low replicative capacity of lymphocytes leads to a slowed immune response to any challenge as well. The slowed, inadequate immune responses accompanied by widespread damage of target tissues caused by pathogens. Damage of more than a third of vitally important organs (e.g., lung tissue in the case of pneumonia) is related with a high risk of death.

The relationship between immunosenescence and related mortality is represented by the model of age-related risk of death from respiratory infections (see Fig. 15.1). The model consists of three components: a model of immunosenescence [20], a model of infectious disease [13] and a relationship between disease severity and risk of death.

The first model, the mathematical model of immunosenescence, describes the age trend of immune system characteristics such as the concentration of naive and memory T cells and their replicative capacity. The model is represented by a system of ordinary differential equations (ODEs). Numerical solution of the system of ODEs yields the sets of immune characteristics for each age. These characteristics are used in the second model, the model of infectious disease, to determine the value of the lymphocyte concentration at the beginning of disease and the rate of immune response. This model makes it possible to simulate the course of unified infectious disease for each set of immune characteristics or, in other words, for each age. Disease severity is defined as a maximum of target tissue damage in the course of the disease.

The third model is a function of the distribution of resistance in the population, describing population heterogeneity in this characteristic. Infection resistance is defined as a probability of recovery at a certain value of target tissue damage (disease severity). As an output of the model we have risk assessment of lethal outcome in the course of the disease. To estimate the probability of death from certain diseases during a time interval (e.g., during one year) we multiply the risk of lethal outcome in the course of the disease by the probability of becoming infected during the interval under consideration.

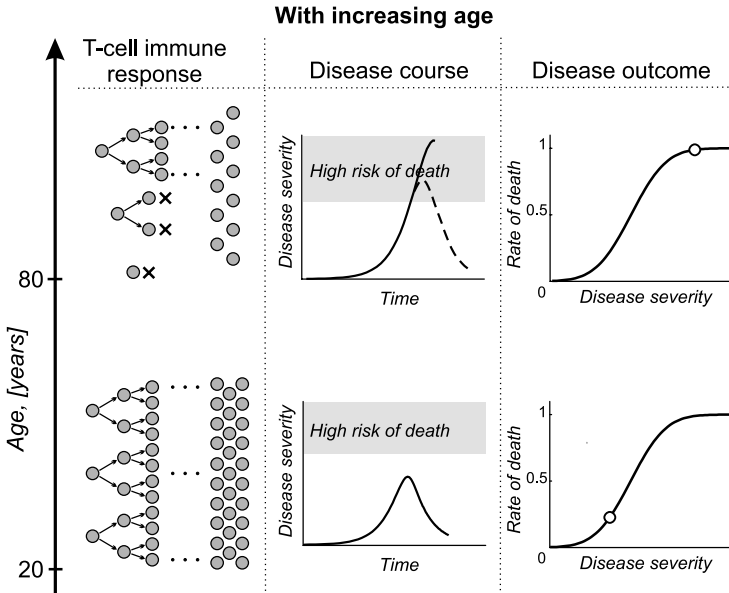


**Fig. 15.1.** The relationship between age-related changes in immune system and increasing risk of death from infectious disease. Proliferative capacity of T cells decreases with age, which results in deceleration of lymphocyte proliferation during immune response. So, the severity of the disease increases with increasing age. The higher the disease severity, the higher risk of lethal outcome.

### 15.2.1 Mathematical Model of Immunosenescence (M1)

The immune system undergoes significant changes in the course of life. According to the environmental challenges and mode of living, subsystems and organs of the immune system are either activated or suppressed. Obviously, the adaptive immune system undergoes more changes than the innate system. There is evidence that some components of the system of innate defense become even more active at older than at young ages. Changes in the population of B cells occur later and to a lesser extent. For simplicity, we consider age-related changes in the population of T cells.

The T cells can be broadly categorized as naive and memory. The specific immune system in the course of self-learning generates memory cells from naive cells. Memory cells are capable of providing a more rapid and effective immune response upon reencounter with antigens than their progenitors. With increasing age the number of memory cells increases, but the rate of naive lymphocyte production declines. So the immune system loses its ability to protect against new pathogens.

At the same time the proliferation potential of all immune cells is decreasing. In older individuals, 30–45% of lymphocytes cannot proliferate in response to antigenic stimuli [7]. Thus, the following processes determine age-related remodeling of the specific immune system: the replacement of naive cells by memory cells, replicative senescence of T cells, and a decrease in volume of lymphoid tissue.

The mathematical model of age-related changes in the immune system is represented by a system of ODEs. The choice of functional forms is based on the law of mass action. Variables of the model are

$N(\tau)$ , the concentration of naive T cells in lymphoid tissue at age  $\tau$ ;

$M(\tau)$ , the concentration of memory T cells in lymphoid tissue at age  $\tau$ ;

$P_N(\tau)$ , the average length of telomere repeats in naive T cell at age  $\tau$ ;

$P_M(\tau)$ , the average length of telomere repeats in memory T cell at age  $\tau$ .

$$\frac{dN}{d\tau} = \frac{N^*}{V} - \alpha_1 \frac{L}{V} N - \mu_N N - \frac{dV}{d\tau} \frac{N}{V}, \quad (15.1)$$

$$\frac{dM}{d\tau} = \rho_1 \alpha_1 \frac{L}{V} N + \rho_2 \alpha_2 \frac{L}{V} M + \mu_M (M^* - N - M) - \frac{dV}{d\tau} \frac{M}{V}, \quad (15.2)$$

$$\frac{dP_N}{d\tau} = (P^* - P_N) \frac{N^*}{NV}, \quad (15.3)$$

$$\frac{dP_M}{d\tau} = \rho_1 \alpha_1 (P_N - P_M - \lambda_N) \frac{L}{V} \frac{N}{M} - (\rho_2 + 1) \alpha_2 \lambda_M \frac{L}{V}. \quad (15.4)$$

The first term in the first equation describes the influx of new naive T cells from the thymus. The rate of influx exponentially decreases with age,

$$N^*(\tau) = N_0^* e^{-k_T \tau}. \quad (15.5)$$

There is evidence that a T cell progenitor loses its proliferative capacity with age [17]. We assume that proliferative capacity is determined by the length of telomeric DNA. Here  $P^*$  is the telomere length in the cells which have recently left the thymus. It decreases with age as

$$P^*(\tau) = (P_0^* - P_{\min}) e^{-k_P \tau} + P_{\min}. \quad (15.6)$$

Lymphoid tissue diminishes with age in both primary (thymus) and in peripheral immune organs (lymph nodes, spleen, and lymphoid tissues draining mucosal surfaces). The volume of the peripheral lymphoid tissue decreases with age as follows:

$$V(\tau) = (V_0 - V_{\min}) e^{-k_V \tau} + V_{\min} \quad (15.7)$$

and compensates for the decline of the total number of T cells.

Initial conditions for system (15.1–15.7) are as follows:

$$N(\tau_0) = N^0; \quad M(\tau_0) = M^0; \quad P_N(\tau_0) = P_N^0; \quad P_M(\tau_0) = P_M^0. \quad (15.8)$$

The physical meaning of model parameters and their estimates were discussed in detail in [20]. Initial conditions and estimates of parameters that allow simulating the normal aging of the immune system are given in Table 15.1. Fig. 15.2 shows age trajectories of the model variables after 18 years. Regimes of normal, slowed, and accelerated immune aging were investigated in [20, 22]. The results of the simulations agree with the clinical observations and with the results of other models of immune processes [1, 2, 6, 16].



**Table 15.1.** Initial conditions and model parameters for simulation of the normal aging of the immune system.

Parameter	Physical meaning and dimension	Estimate
$\alpha_1$	Coefficient of sensitivity of naive T cells to antigen load (ml g <sup>-1</sup> )	$1.5 \cdot 10^4$
$\alpha_2$	Coefficient of sensitivity of memory T cells to antigen load (ml g <sup>-1</sup> )	$1.5 \cdot 10^4$
$\mu_N$	Death rate of naive T cells in the absence of antigen load (day <sup>-1</sup> )	$1.8 \cdot 10^{-4}$
$\mu_M$	Death rate of memory T cells (day <sup>-1</sup> )	0.05
$\rho_1$	Number of memory T cells produced by one naive cell	100
$\rho_2$	Number of memory T cells produced by one memory cell	1.1
$\lambda_N$	Length of telomere repeats lost during transformation of naive cells to memory cell (bp cell <sup>-1</sup> )	1400
$\lambda_M$	Length of telomere repeats lost during self-replication of memory cells (bp cell <sup>-1</sup> )	500
$M^*$	Low limit for normal concentration of memory T cells in lymphoid tissue (cell ml <sup>-1</sup> )	$2.5 \cdot 10^9$
$k_T$	Rate of diminishing of naive T cell production with age (day <sup>-1</sup> )	$1.1 \cdot 10^{-4}$
$k_V$	Relative rate of reduction of lymphoid tissue volume with age (day <sup>-1</sup> )	$2.7 \cdot 10^{-5}$
$k_P$	Relative rate of the telomere repeats reduction in the progenitor of naive T cells (bp day <sup>-1</sup> )	$1 \cdot 10^{-5}$
$L$	Antigen load (g day <sup>-1</sup> ) <sup>1</sup>	
$N_0^*$	The rate of T cell production by the thymus at the age of 18 (cell day <sup>-1</sup> )	$4 \cdot 10^8$
$V_0$	Volume of lymphoid tissue at the age of 18 (ml)	1500
$V_{\min}$	Minimal volume of lymphoid tissue (ml)	100
$P_0^*$	Length of telomere repeats in naive T cells produced at the age of 18 (bp cell <sup>-1</sup> )	$8.3 \cdot 10^3$
$P_{\min}$	Minimal length of telomere repeats in the progenitor of naive T cells	100
$N_0$	The concentration of naive T cells at the age of 18 (cell ml <sup>-1</sup> )	$1.9 \cdot 10^9$
$M_0$	The concentration of memory T cells at the age of 18 (cell ml <sup>-1</sup> )	$6.45 \cdot 10^8$
$P_{N0}$	Length of telomere repeats in naive T cells at the age of 18	$8.8 \cdot 10^3$
$P_{M0}$	Length of telomere repeats in memory T cells at the age of 18	$7.4 \cdot 10^3$

<sup>1</sup> The value of antigenic load characterizes the influence of environmental and behavioral factors on immune system aging and can vary greatly in different individuals. For European populations it was estimated from  $10^6$  g day<sup>-1</sup> to  $2 \dots 10^6$  g day<sup>-1</sup>.

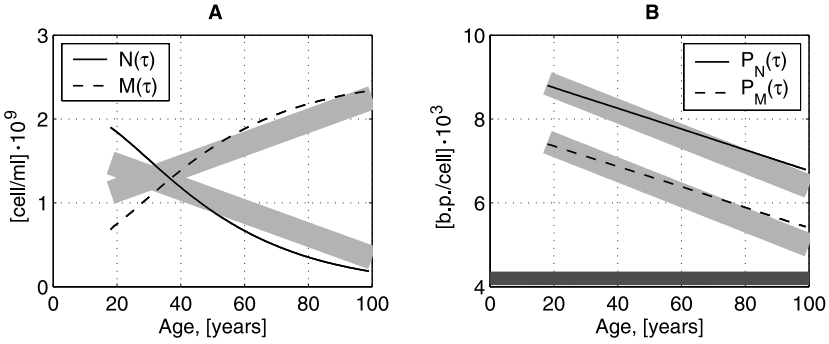


**Fig. 15.2.** Mathematical modeling of age-related changes in peripheral T cell population. (A) the dynamics of concentrations of naive ( $N(\tau)$ ) and memory ( $M(\tau)$ ) T cells in lymphoid tissue; (B) the dynamics of the telomere length in the naive ( $P_N(\tau)$ ) and memory ( $P_M(\tau)$ ) T cells. Wide grey strips depict variance of T cell concentrations and telomere lengths according to clinical observations [10,21]. Horizontal dark grey strip corresponds to the value of critical length for replicative senescence (known as the Hayflick’s limit).

### 15.2.2 Model of Infectious Disease (M2)

A model of infectious disease is used to obtain the estimate of disease severity for age  $\tau$ . The impact of different mechanisms on immune response in the course of pneumonia was studied [19], and it was shown that a decrease in T cell functioning is crucial for respiratory infections usually caused by an ubiquitous pathogen.

This mathematical model describes [13] the processes which determine the beginning, course, and outcome of all infections: invasion and propagation of the pathogen, infection-induced damage of tissues, immune response, elimination of the pathogen and tissue regeneration. The variables of the model are

- $K(t)$ , the concentration of the pathogen in target tissue;
- $C(t)$ , the concentration of specific lymphocytes in draining lymph nodes;
- $F(t)$ , the concentration of specific antibodies in blood;
- $m(t)$ , the fraction of target cells destroyed by pathogen.

The dynamics of the immune response is described by the system of four differential equations,

$$\frac{dK}{dt} = \beta K - \gamma F K, \tag{15.9}$$

$$\frac{dC}{dt} = \alpha(1 - m) F K - \mu_c(C - C^*), \tag{15.10}$$

$$\frac{dF}{dt} = \rho C - \eta \gamma F K - \mu_f F, \tag{15.11}$$

$$\frac{dm}{dt} = \sigma(1 - m) K - \mu_m m. \tag{15.12}$$

with the following initial conditions:

**Table 15.2.** Initial conditions and model parameters for simulation of infectious disease.

Parameter	Physical meaning and dimension	Estimate
$\beta$	Rate of pathogen propagation (day <sup>-1</sup> )	0.35
$\gamma$	Rate of pathogen neutralization by antibodies (ml pt <sup>-1</sup> day <sup>-1</sup> )	$8.5 \cdot 10^{-14}$
$\alpha$	Rate of specific lymphocyte proliferation (ml pt <sup>-1</sup> day <sup>-1</sup> )	$5 \cdot 10^{-11}$
$\mu_C$	Death rate of specific lymphocytes (day <sup>-1</sup> )	0.5
$\rho$	Rate of antibody production by lymphocytes (day <sup>-1</sup> )	$7 \cdot 10^3$
$\eta$	Number of antibodies required to neutralize one pathogen particle	20
$\mu_f$	Death rate of specific antibodies (day <sup>-1</sup> )	0.05
$\sigma$	Rate of target organ damage by the pathogen (ml pt <sup>-1</sup> day <sup>-1</sup> )	$9 \cdot 10^{-9}$
$\mu_m$	Rate of target organ regeneration (day <sup>-1</sup> )	0.4
$K_0$	Infecting dose (pt ml <sup>-1</sup> )	$10^3$
$C^*$	The concentration of specific naive lymphocytes (cell ml <sup>-1</sup> )	—
$C_m$	The concentration of specific memory cells (cell ml <sup>-1</sup> )	—
$k_1$	The fraction of naive T cells involved in immune response	$1.5 \cdot 10^{-6}$
$k_2$	The fraction of memory T cells involved in immune response	$4.3 \cdot 10^{-4}$

$$K(t_0) = K_0; \quad C(t_0) = C_m + C^*; \quad F(t_0) = \frac{\rho(C_m + C^*)}{\mu_f}; \quad m(t_0) = 0. \quad (15.13)$$

To simulate the course of acute pneumonia we use initial conditions and parameter estimates given in Table 15.2 [19]. Note that the expression for initial value of specific lymphocytes contains the concentrations of naive lymphocytes  $C^*$  and memory cells  $C_m$  that are specific to the pathogen under consideration. We assume that the level of specific naive lymphocytes is homeostatic and in the case of natural death of lymphocytes only the excess (cloned) lymphocytes die (see the last term in equation 15.10).

The particular feature of the model of infectious disease is an equation for the dynamics of target tissue damage. Wide tissue damage causes loss of homeostasis and reduces lymphocyte proliferation (the first term in equation 15.10). This distinguishes this model from the models of immune-pathogen dynamics [18,26].

In clinical practice [15] a maximum of tissue damage is interpreted as disease severity  $S$ . In the case of pneumonia, damage to less than 15% of the cells of the three lower segments of the lung corresponds to mild disease with a low risk of death, damage to 35% of the cells of the three lower segments of the lung corresponds to medium severity with a death risk of 0.5, and disease with greater than 45% destroyed target tissue is defined as severe with a very high probability of death ( $\geq 0.77$ ).

Varying the rate of immune response and initial concentration of specific lymphocytes according to the age trend we can simulate the course of infectious disease for different ages. It is assumed that the concentration of specific lymphocytes at the be-

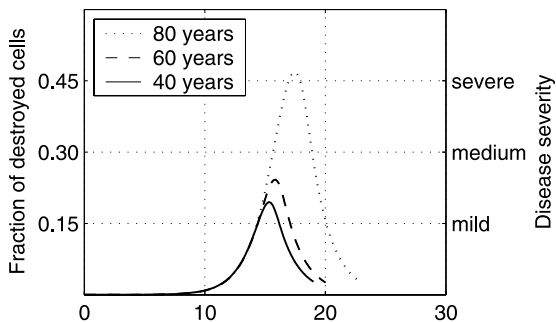


**Fig. 15.3.** The fraction of target cells destroyed by the pathogen in the course of disease for different ages (on the left vertical axis). Disease severity (on the right vertical axis). Disease severity is defined as a maximum of tissue damage.

ginning of the infection depends on the current concentrations of naive and memory T cells as follows:

$$C(t_0, \tau) = C^*(\tau) + C_m(\tau) = k_1 N(\tau) + k_2 M(\tau), \tag{15.14}$$

where  $t_0$  denotes the time of the beginning of disease,  $\tau$  denotes the age.

There is much evidence that the rate of lymphocyte proliferation decreases with age. Denote by  $\alpha^0$  the rate of specific lymphocyte proliferation at age 18 and by  $\alpha(\tau)$  the rate at age  $\tau$ . We assume that the ratio  $\alpha(\tau)/\alpha^0$  is equal to the ratio of replicative capacity of T cells involved in the immune response at age  $\tau$  to the one at age 18. The proliferative capacity of naive T cells involved in the immune response at age  $\tau$  is defined by the concentration and the mean length of their telomeres  $k_1 N(\tau)(P_N(\tau) - H)$ . Here  $H$  is the Hayflick limit—the cell stops division when the telomere becomes shorter than  $H$ . The proliferative capacity of memory T cells can be represented in a similar manner. Then, the expression for  $\alpha(\tau)$  is as follows:

$$\alpha(\tau) = \alpha^0 \frac{k_1 N(\tau)(P_N(\tau) - H) + k_2 M(\tau)(P_M(\tau) - H)}{k_1 N^0(P_N^0 - H) + k_2 M^0(P_M^0 - H)}, \tag{15.15}$$

where  $P_N^0, P_M^0, N^0, M^0$  are values of the respective variables for the age of 18.

Note that the immune processes described in model (15.1)–(15.8) and in equation (15.10) are located in the lymph nodes, equation (15.9) represents changes of pathogen concentration in the target tissue, and equation (15.11) deals with antibody concentration in the blood. We consider variables located in different spatial compartments in order to use reasonable physical constants for modeling cell interaction. All transfer rates are included in the estimates for the rates of interactions (for details see [14]).

In Fig. 15.3 the trajectory of the disease severity is presented for three different ages. It is easy to see that in the interval from 60 to 80 years the severity of simulated disease increases approximately twofold. The higher the disease severity, the higher the risk of lethal outcome.

### 15.2.3 Relationship Between Disease Severity and the Risk of Death (M3)

In our context we define the infection resistance  $Res$  as a probability of recovery at value  $S$  of disease severity. Then, the probability of the lethal outcome is  $p_L = 1 - Res$ . Further, we assume that this characteristic is normally distributed in the population. Hence, the probability of the lethal outcome  $p_L$  at the severity value  $S$  could be represented as the corresponding distribution function

$$p_L(S) = \Phi(S) = \int_0^S \frac{1}{\sigma\sqrt{2\pi}} e^{-(t-a)^2} dt. \tag{15.16}$$

The values of the parameter were estimated based on the clinical observations [15].

Thus, by means of the model of infectious disease and expression (15.16), a relationship between immunosenescence and the risk of death could be established. A constructed model of age-related risk of death from respiratory infections is represented by the flowchart in Fig. 15.4. It has two input parameters—antigenic load and the probability of becoming infected. As output it yields the probability of death from respiratory infections per year.

In the next section we attempt to apply this model to explain differences in pneumonia mortality observed in some developed countries.

## 15.3 Analysis of Pneumonia Mortality

The age patterns of mortality from respiratory infections share common traits in countries with well-developed health care systems. Generally, between ages 20 and 30 the probability of death from respiratory infections is minimal; sometimes it equals zero. The growth of the death rate begins after age 35. The death rates grow exponentially or almost exponentially after the age of 55 years.

WHO data on pneumonia mortality in Austria, Italy, Portugal, the United Kingdom, the USA, and Japan in 1999 are represented by symbols in Fig. 15.5. These

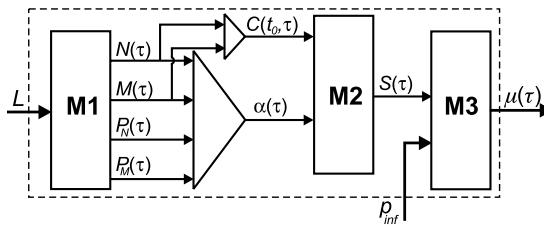


**Fig. 15.4.** Flowchart of the model of age-related risk of death from respiratory infections. **M1**, **M2**, and **M3** denote the model of immunosenescence, the model of infectious disease, and the relationship between disease severity and the risk of death, respectively. The model of age-related risk of death provides as an output mortality curve  $\mu(\tau)$ . The input parameters are antigenic load  $L$  and the probability of becoming infected  $p_{inf}$ .

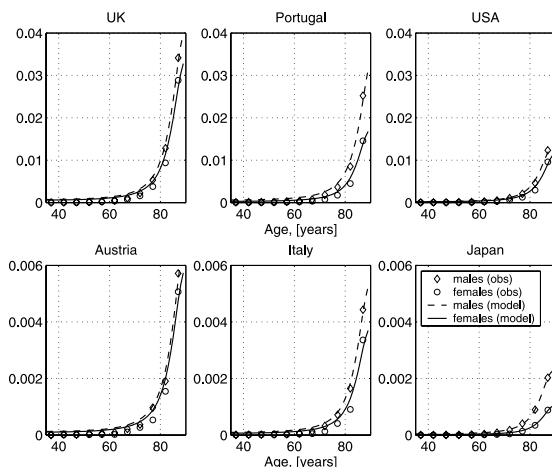


**Fig. 15.5.** Pneumonia mortality (probability of death from pneumonia per year) in Austria, Italy, Portugal, United Kingdom, USA, and Japan in 1999. WHO data are represented by symbols, results of simulation by lines.

countries were chosen because they use the same or coincident categories from the International Classification of Diseases (B-321, ICD-9; or J13, J14, J150–J159, ICD-10). Despite this, the probability of death from pneumonia in the age group 80–84 in the UK is 27 times higher than in Japan and 10 times higher than in Italy.

It could be suggested that higher mortality is associated with total health expenditure but this is not the case (Fig. 15.6). Moreover, life expectancy at birth does not reflect level of pneumonia mortality.

We assume that these populations experience different antigenic load throughout adult life. This can be related to differences in climatic and ecological conditions, modes of living, and national cuisines. We fit the model of age-related risk of death from respiratory infections to the data. The results of the simulations are represented by solid and dashed lines in Fig. 15.5. There is good agreement between the model

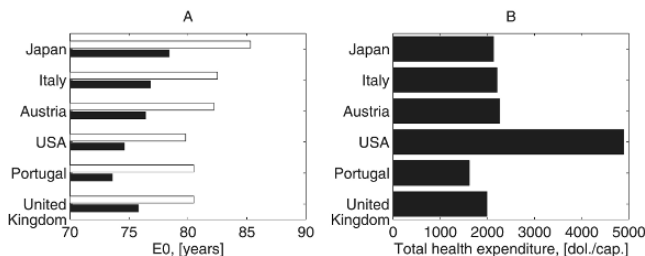


**Fig. 15.6.** (A) Life expectancy at birth (black bars correspond to males, white bars to females) and (B) total health expenditure in the countries under consideration [2000, WHO].

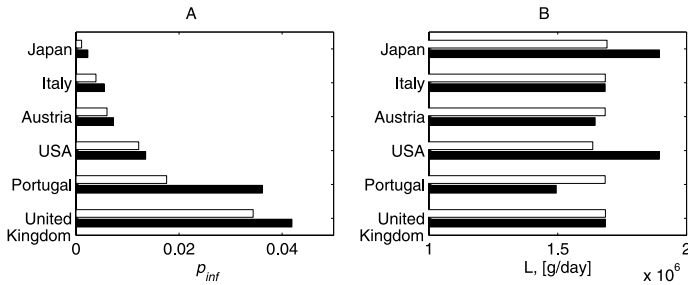


**Fig. 15.7.** Parameter estimates of environmental conditions which influenced immunosenescence in the populations under consideration. (A) Frequency of pneumonia and (B) antigenic load. Black bars correspond to males, white bars to females.

and the data sets for medium and large values of the death rate. For small values (age group 35–39), the estimated risk of death is higher than observed.

To provide a good fit, two parameters of the model were estimated for every population: antigenic load and the frequency of pneumonia (Fig. 15.7). Differences in age-specific mortality between countries are mainly described by variations in the parameter of frequency of pneumonia. Males in Japan and United States experienced a higher antigenic load than males in other countries under consideration. Probably, the higher rate of immunosenescence in the male populations of these countries was related to the dynamic and stressful mode of living [9,23].

## 15.4 Conclusions

The proposed model describes the relation between physiological and demographic aging. According to the proposed model, disease severity is determined by the concentrations of T cells and by the length of their DNA telomeres. After age 60, the course and outcome of infectious disease are highly influenced by the length of T cell telomeres. The existence of an association between higher risk of death from infectious disease and shorter telomere length has been shown [5]. This work describes the influence of heritable and environmental factors on immunosenescence and related mortality.

The values of immune system characteristics are assumed to be population average. In the case of availability of the clinical measurements, the proposed model is transformed into the individualized risk model, which makes it possible to predict consequences of some interventions. There is growing evidence that modification of the immune state by means of vaccination, antiviral and hormonal therapies, stem cell transplantation—and possibly by regulation of telomerase activity [3]—could slow down processes associated with immunosenescence.

In this chapter we demonstrate how this model can be used for analyzing pneumonia mortality. It also allows us to predict future changes in mortality due to public health activity.

## Acknowledgments

The author thanks A.A. Romanyukha and A.I. Yashin for their attention and support. This work is supported by the Russian Foundation for Basic Research grant 04-01-00579a, by Research School Grant 2007-5-1.5-12-02-065) and by the Max Planck Institute for Demographic Research.

## References

1. Aspinall, R.: Longevity and the immune response. *Biogerontology*, **1**, 273–278 (2000).
2. Aviv, A., Levy, D., Mangel, M.: Growth, telomere dynamics and successful and unsuccessful human aging. *Mech. Ageing Dev.*, **124**, 829–837 (2003).
3. Bodnar, A. G., Ouellette, M., Frolkis, M., Holt, S. E., Chiu, C.-P., Morin, G. B., Harley, C. B., Shay, J. W., Lichtsteiner, S., Wright, W. E.: Extension of life-span by introduction of telomerase into normal human cells. *Science*, **279**, 349–352 (1998).
4. Caruso, C., Lio, D., Cavallone, L., Franceschi, C.: Aging, longevity, inflammation, and cancer. *Ann. NY. Acad. Sci.*, **1028**, 1–13 (2004).
5. Cawthon, R. M., Smith, K. R., O'Brien, E., Sivatchenko, A., Kerber, R. A.: Association between telomere length in blood and mortality in people aged 60 years or older. *Lancet*, **361**, 393–395 (2003).
6. De Boer, R. J.: Mathematical model of human CD4+ T-cell population kinetics. *The Netherlands Journal of Medicine*, **60**, 17–26 (2002).
7. Effros, R. B.: Costimulatory mechanisms in the elderly. *Vaccine*, **18**, 1661–1665 (2000).
8. Effros, R. B.: T cell replicative senescence pleiotropic effects on human aging. *Ann NY Acad Sci*, **1019**, 123–126 (2004).
9. Epel, E. S., Blackburn, E. H., Lin, J., Dhabhar, F. S., Adler, N. E., Morrow, J. D., Cawthon, R. M.: Accelerated telomere shortening in response to life stress. *PNAS*, **101**, 17312–17315 (2004).
10. Fagnoni, F. F., Vescovini, R., Passeri, G., Bologna, G., Pedrazzoni, M., Lavagetto, G., Casti, A., Franceschi, C., Passeri, M., Sansoni, P.: Shortage of circulating naive CD8+ T cells provides new insights on immunodeficiency in aging. *Blood*, **95**, 2860–2868 (2000).
11. Horiuchi, S., Finch, C. E., Mesle, F., Vallin, J.: Differential patterns of age-related mortality increase in middle age and old age. *J. Gerontol. A. Biol. Sci. Med. Sci.*, **58**, B495–507 (2003).
12. Horiuchi, S., Wilmoth, J.: Age patterns of the life table aging rate for major causes of death in Japan, 1951–1990. *J Gerontol A Biol Sci Med Sci*, **52**, B67–77 (1997).
13. Marchuk, G.: *Mathematical modelling of immune response in infectious diseases*. Kluwer Academic Publishers, Dordrecht (1997).
14. Marchuk, G., Romanyukha, A. A., Bocharov, G.: Mathematical model of antiviral immune response. II. Parameters identification of acute course of viral hepatitis B data. *J. Theor. Biol.*, **151**, 41–70 (1991).
15. Marchuk, G. I., Berbentzova, E. P.: Acute pneumonia: immunology, severity assessment, clinic, treatment. *Nauka, Moscow* (1989) (in Russian).
16. Mariani, L., Turchetti, G., Franceschi, C.: Chronic antigenic stress, immunosenescence and human survivorship over the 3 last centuries: heuristic value of a mathematical model. *Mech. Ageing Dev.*, **124**, 453–8 (2003).
17. Nikolich-Zugich, J.: T cell aging: naive but not young. *J. Exp. Med.*, **201**, 837–840 (2005).



18. Nowak, M. A., May, R. M.: *Virus Dynamics: Mathematical Principles of Immunology and Virology*. Oxford University Press, Oxford (2000).
19. Romanyukha, A. A., Rudnev, S. G., Sidorov, I. A.: Energy cost of infection burden: An approach to understanding the dynamics of host–pathogen interactions. *J. Theor. Biol.*, **241**, 1–13 (2006).
20. Romanyukha, A. A., Yashin, A.: Age related changes in population of peripheral T cells: towards a model of immunosenescence. *Mech. Ageing Dev.*, **124**, 433–443 (2003).
21. Rufer, N., Brummendorf, T. H., Kolvraa, S., Bischoff, C., Christensen, K., Wadsworth, L., Schulzer, M., Lansdorp, P. M.: Telomere fluorescence measurements in granulocytes and T lymphocyte subsets point to a high turnover of hematopoietic stem cells and memory T cells in early childhood. *J. Exp. Med.*, **190**, 157–168 (1999).
22. Sannikova, T. E., Rudnev, S. G., Romanyukha, A. A., Yashin, A. I.: Immune system aging may be affected by HIV infection: mathematical model of immunosenescence. *Russian Journal of Numerical Analysis and Mathematical Modeling*, **19**, 315–329 (2004).
23. Segerstrom, S. C., Miller, G. E.: Psychological stress and the human immune system: a meta-analytic study of 30 years of inquiry. *Psychol. Bull.*, **130**, 601–630 (2004).
24. Ukraintseva, S. V., Yashin, A. I.: How individual age-associated changes may influence human morbidity and mortality patterns. *Mech. Ageing Dev.*, **122**, 1447–1460 (2001).
25. Vaupel, J. W., Carey, J. R., Christensen, K., Johnson, T. E., Yashin, A. I., Holm, N. V., Iachine, I. A., Kannisto, V., Khazaeli, A. A., Liedo, P., Longo, V. D., Zeng, Y., Manton, K. G., Curtsinger, J. W.: Biodemographic trajectories of longevity. *Science*, **280**, 855–860 (1998).
26. Wigginton, J. E., Kirschner, D.: A model to predict cell-mediated immune regulatory mechanisms during human infection with *Mycobacterium tuberculosis*. *J. Immunol.*, **166**, 1951–1967 (2001).

## Neuromorphological Phenotyping in Transgenic Mice: A Multiscale Fractal Analysis

Andreas Schierwagen,<sup>1</sup> Luciano da Fontoura Costa,<sup>2</sup> Alan Alpar,<sup>3</sup> Ulrich Gärtner,<sup>3</sup> and Thomas Arendt<sup>3</sup>

<sup>1</sup> Institute for Computer Science, University of Leipzig, 04109 Leipzig, Germany; schierwa@informatik.uni-leipzig.de

<sup>2</sup> Institute of Physics at São Carlos, University of São Paulo, Caixa Postal 369, 13560-970 São Carlos, SP, Brazil

<sup>3</sup> Department of Neuroanatomy, Paul Flechsig Institute for Brain Research, University of Leipzig, 04109 Leipzig, Germany

**Summary.** 3D morphological data have been used to quantitatively characterize the morphological phenotype of pyramidal neurons in transgenic mice. We calculated the multiscale fractal dimension (MFD) of reconstructed neuronal cells. Changes in the complexity of neuronal morphology due to permanent activation of p21Ras in the primary somatosensory cortex of transgenic mice correlate with changes in the MFD of dendrites of pyramidal neurons. Transgenic neurons seem slightly less complex (i.e., have lower peak fractal dimension) if compared with the wild type. On the other hand, the enhanced p21Ras activity in transgenic mice may lead to greater variety in the cell morphological phenotype.

**Key words:** Local fractal dimension, multiscale fractal analysis, pyramidal neurons, dendritic morphology, somatosensory cortex, mouse, phenotyping.

### 16.1 Introduction

Transgenic mice mutations provide important means for understanding gene function, as well as for developing therapies for genetic diseases. In these mutants, the gene overexpression may affect several organs and tissues, including the brain. In a specific mouse mutant introduced by [8] a permanently active Ras protein (p21 H-ras<sup>Val12</sup>), in post-mitotic neurons is expressed. Enhanced p21Ras activity results in a dramatically enlarged dendritic tree. In both cortical layers II/III and V, the total surface area and the total volume of dendritic trees is greatly increased. This is mainly caused by increased dendritic diameter and tree degree [1].

The aim of this chapter is to provide further evidence for these findings. For this, quantitative aspects of dendritic tree shape have been analyzed. There are several methods for describing trees by quantitative measures. Neurons are three-dimensional (3D) objects, and the location of their somata within the nervous tissue, as well as the number, spatial dimensioning, branching complexity and 3D embedding of their axonal

and dendritic trees are salient shape characteristics that may significantly distinguish between different cell types.

The branching complexity of neuronal arborizations is determined both by topological and metrical properties (cf. [9]). For topological characterization, a neuronal tree is reduced to a skeleton structure of points (branching or terminal points) and segments between these points. Such a skeleton forms a typical rooted tree out of a finite set of possible different tree types. Dendritic segments can be labeled by centrifugal order (number of segments on the path to the root). Metrical aspects include length and diameter of the segments, path lengths (total length of the path from the dendritic root to a branch point or terminal tip), radial distances of terminal tips from the center of the cell and branching angles. Further details include measures for the irregularity, spatial orientation and curvature of the branches.

Another class of measures is related to the spatial embedding in 3D space, as characterized by the spatial dimensioning, spatial density, spatial orientation and space filling of the structure. In this study, the focus is on space filling or fractal aspects of dendritic tree shape. There are several methods for describing trees by fractal dimensions (see [10, 11] for early fractal analyses of neuronal dendritic trees, and, e.g., [6] for a review).

Multiscale (or *local*) fractal analysis [3, 4, 7] has been demonstrated to be an effective means for characterization of neuronal complexity. This type of analysis seems to be particularly suitable in the present case because the multiscale fractal dimension is independent of size-related parameters like surface area and volume. The aim of this study is to show that observed changes in the complexity of neuronal morphology due to transgenic activation of p21Ras in the primary somatosensory cortex of mice correlate with changes in the multiscale fractal dimensions of dendrites of pyramidal neurons.

## 16.2 Materials and Methods

Two sets of pyramidal neurons (17 cells from wild type and 26 cells from transgenic mice) were reconstructed and digitized using NeuroLucida (MicroBrightField, Inc.) as described elsewhere [1]. The morphology files created with NeuroLucida were processed with CVAPP [2], a freely available program for cell viewing, editing and format converting (Fig. 16.1). Images were thresholded resulting in binary images with 1- and 0-voxels representing the neuron shape and background regions, respectively. Therefore, in digitized 3D binary images, the shape of a neuron is represented by the set of 1-voxels.

The binary images of the neuron shape patterns were used for calculating the multiscale fractal dimension (MFD), a measure related to the image complexity [4, 7]. It is computed through the Minkowski sausage approach, which can be described as follows: Let the neuron shape under study be represented by the set  $S$  of the Cartesian coordinates of each of its 1-voxels. Its exact dilation by a radius  $r$  is defined as the union of all spheres of radius  $r$  centered at each of the elements of  $S$ . A series of dila-

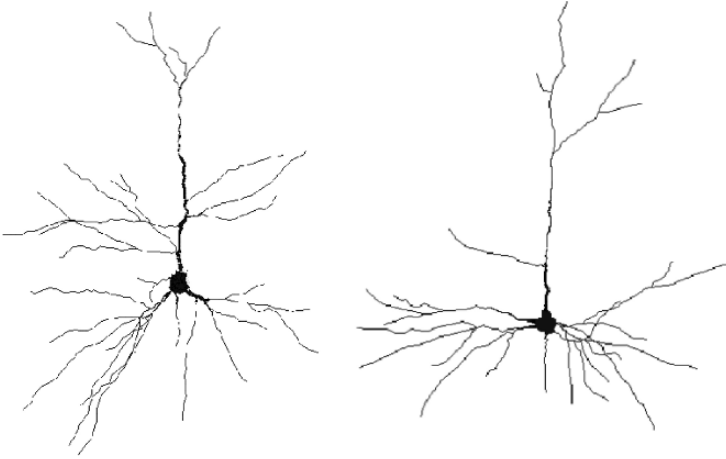


**Fig. 16.1.** Pyramidal cells rendered with CVAPP. Displayed are one example each of transgenic (cell SE15, left) and wild type neurons (cell WT17, right).

tions on the image is made, with radii  $r_i$  equivalent to the intrinsic lattice distances, the so-called exact distances. At each dilation, the volume  $V(r_i)$  of the image is computed.

The volume  $V(r)$  of the shape  $S$  is therefore defined by

$$V(r) = \sum_{i=1}^M V(r_i) \delta(r - r_i), \tag{16.1}$$

where  $\delta(\cdot)$  is the Dirac delta function and  $M$  is the index of the largest exact distance being considered. As  $V(r)$  is a discontinuous function on  $r$ , which is a consequence of the discrete nature of  $r_i$ , it is necessary to interpolate between the Dirac deltas, which is here accomplished by convolving  $V(r)$  with the Gaussian  $g_\sigma(r) = 1/\sigma/\sqrt{2\pi} \exp(-0.5(r/\sigma)^2)$ , yielding the following interpolated volume:

$$v_\sigma(r) = \sum_{i=1}^M V(r_i) g_\sigma(r - r_i). \tag{16.2}$$

It is important to choose a suitable value of the standard deviation parameter,  $\sigma$ , that is large enough just to interpolate between the largest gaps between the exact radii, which occur for small values of  $r$ . The cumulative volume is defined as

$$C(s) = \int_{-\infty}^s v_\sigma(r) dr. \tag{16.3}$$

The Euclidean distance is now represented in terms of its logarithm, leading to the spatial scale parameter  $s = \log(r)$ , so that the exact radii are expressed as  $s_i = \log(r_i)$ . The MFD  $f(s)$  of the set  $S$  of voxel elements can be defined then by

$$f(s) = 3 - \frac{d}{ds} \log(C(s)) = 3 - \frac{C'(s)}{C(s)}. \quad (16.4)$$

While the traditional fractal dimension corresponds to a single scalar value, the MFD becomes a function of the spatial scale parameter  $s$ , providing additional information about the analyzed shapes. Among others, the following measurements quantify meaningful features of the MFD curve: peak fractality,  $f_M$  (the maximum value along the MFD curve), characteristic scale,  $s_M$  (the value of the spatial scale for which  $f_M$  is obtained) and average fractality,  $\langle f \rangle$ . For the computational implementation of this method, see [4].

## 16.3 Results

In Fig. 16.2, an example calculation of the MFD curve for the transgenic cell SE8 is shown. Following the scheme defined in Equations 16.1–16.4, the MFD depending on  $s$  eventually was obtained. As shown there, the fractal dimension decreases at both micro and macro scales, and the peak fractal dimension value,  $f_M$ , is observed at an intermediate scale value,  $s_M$ . This behavior is caused by the finite size of neuron images (see Section 16.4).

The sample histograms of the three parameters utilized,  $f_M$ ,  $s_M$  and  $\langle f \rangle$ , are presented in Fig. 16.3. For  $f_M$ , a bimodal distribution for the transgenic cases results, while wild type cells produced a single mode (Fig. 16.3, top). The distribution of the characteristic scales  $s_M$  observed suggests that the two types of cells are characterized by similar values of this parameter (Fig. 16.3, middle). Finally, the distributions of  $\langle f \rangle$  are bimodal in the case of transgenic cells, and unimodal for wild type cells (Fig. 16.3, bottom).

The scatterplots in Fig. 16.4 depict the mutual relationships between  $f_M$ ,  $s_M$  and

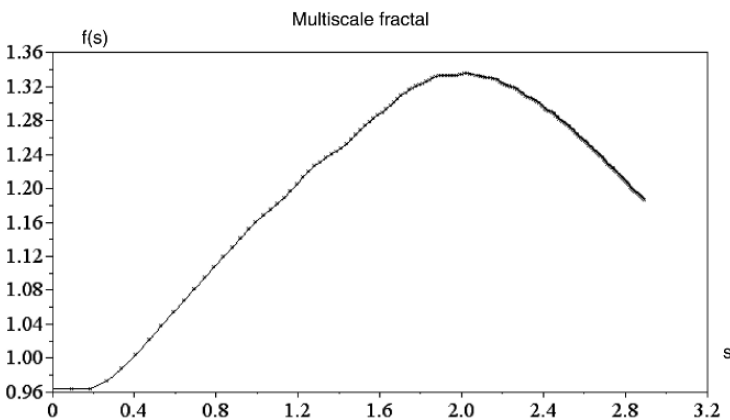


**Fig. 16.2.** Example calculation of MFD for transgenic cell SE8. Shown is the MFD in terms of  $s$ . See text for details.

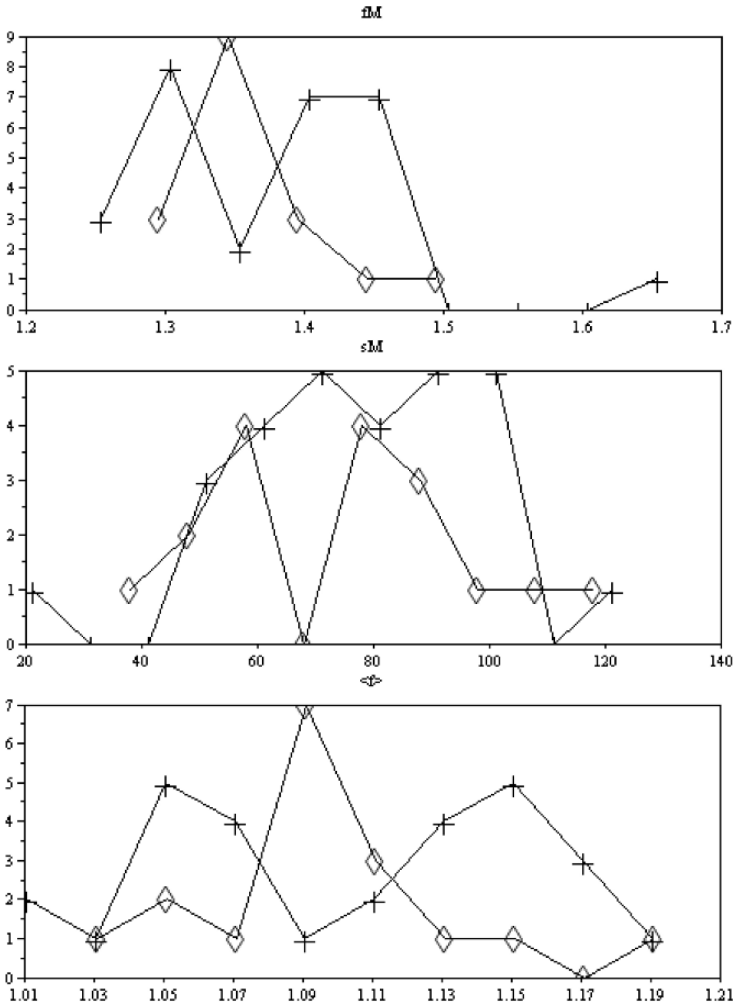


**Fig. 16.3.** Histograms of the three parameters calculated. Presented are numbers of occurrence (ordinate) of peak fractal dimension,  $f_M$ , characteristic scale,  $s_M$ , and average fractal dimension,  $\langle f \rangle$ . Wild type and transgenic cases are identified by diamonds and crosses, respectively.

$\langle f \rangle$ . The strong correlation between peak fractal dimension,  $f_M$ , and maximum fractality scale,  $s_M$ , is obvious.

Fig. 16.5 presents Gaussian densities after principal component analysis for the feature combinations  $(f_M, s_M)$  and  $(f_M, \langle f \rangle)$ , after normal statistical transformation (leading to null mean and unit variance in both cases). By the strong correlation between  $f_M$  and  $s_M$  (Fig. 16.4) the first principal component explains most of the variance and is usable as the measure of complexity. Thus, the feature combination  $(f_M, s_M)$  enables the separation of the two cell types. As indicated in Fig. 16.5, transgenic

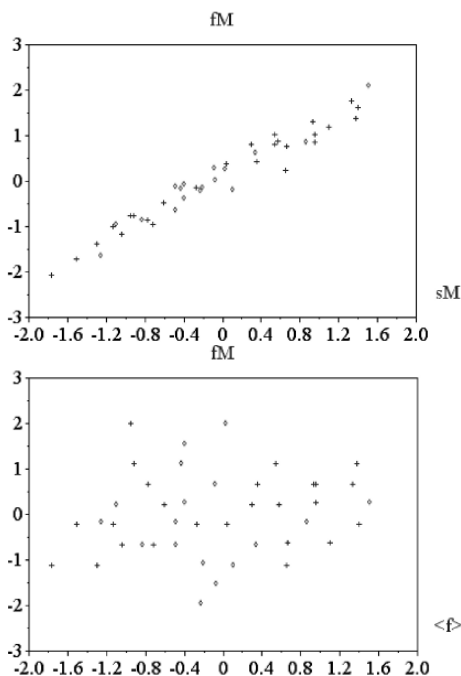


**Fig. 16.4.** Scatterplots of  $f_M$  versus  $s_M$  (top) and  $f_M$  versus  $\langle f \rangle$  (bottom). The meaning of symbols is as in Fig. 16.3.

tend to be less complex as they have a lower fractality, expressing at the same time greater variance.

## 16.4 Discussion

In this chapter 3D data on neuronal morphology has been used to quantitatively characterize the phenotype of transgenic neurons. We calculated the local/multiscale fractal dimension (MFD) of neuronal cells reconstructed in 3D. It is known that the fractality of objects in nature is limited and varies along the spatial scales. On one hand, this is due to the finite size of any real object, leading to behavior close to that of a point for spatial scales much larger than the object diameter. On the other hand, structural properties are usually different at smaller spatial scales. For instance, a cauliflower or a fern has fractal properties only over two or three hierarchical levels, with a smoother characteristic at smaller scales. Moreover, the limited resolution of the image acquisition devices imposes further constraints on the fractal behavior at small spatial scales. The MFD approach explicitly points to this fact.

The advantages of the MFD (a function of the spatial scale) over the traditional fractal dimension (a single scalar value) reside in providing additional information about the analyzed shapes. Thus, we computed complementary features such as the

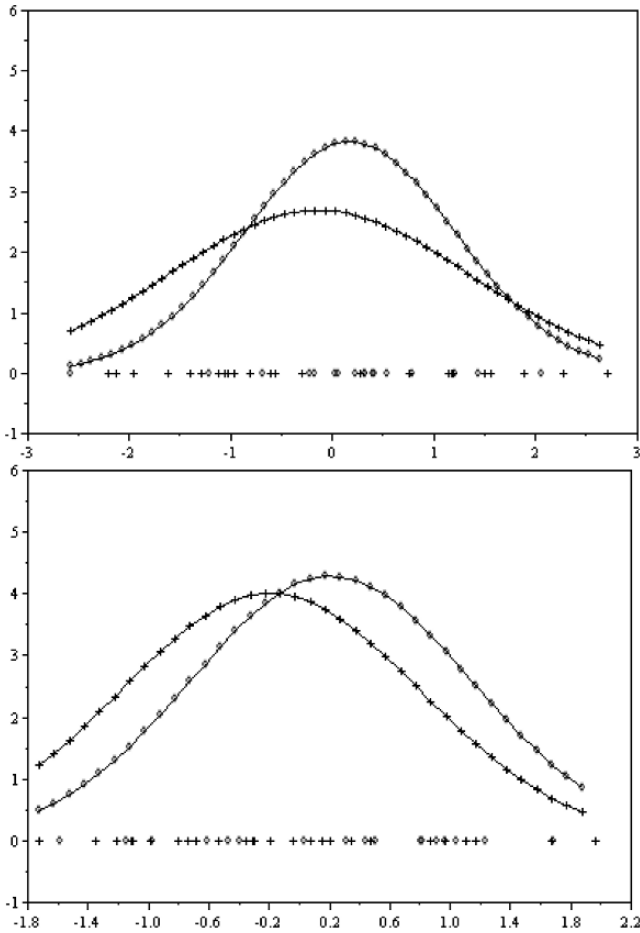


**Fig. 16.5.** Gaussian densities after principal component analysis for  $(f_M, s_M)$  (top) and  $(f_M, \langle f \rangle)$  (bottom). The meaning of symbols is as in Fig. 16.3.

peak fractality, the characteristic scale where it occurs and the average fractality, for quantifying and characterizing the cell types. Two sets of neurons, i.e., pyramidal cells from wild type and p21 H-ras<sup>Val12</sup> transgenic mice, have been analyzed. The results obtained after principal component analysis show that transgenic neurons are slightly less complex, as measured by the peak fractal dimension,  $f_M$ , if compared to their wild type counterpart, while the other two features considered (maximum fractality scale,  $s_M$ , and average fractal dimension,  $\langle f \rangle$ ) did not reveal differences between the two types. Transgenic pyramidal neurons are characterized by increased dispersion if compared to the wild type pyramidal neurons, suggesting that the enhanced p21Ras activity in transgenic mice may lead to greater variety of the cell morphological phenotype.



These findings have recently been substantiated by a percolation analysis accomplished with the same data set. The percolation transform [5] is particularly useful for the characterization of spatial density of distributed points, and it represents an alternative to the multiscale fractal analysis reported here. As the latter, the percolation analysis is independent of size-related parameters like area and volume of the neuronal cells. We were able to verify that changes in the global character of the percolation transform curves derived from the reference points (i.e., dendritic tips and branch points) of the dendrites of pyramidal neurons correlate with changes in the complexity of neuronal morphology due to the activation of p21Ras in the primary somatosensory cortex of transgenic mice.

## Acknowledgments

This study was partly supported by Deutsche Forschungsgemeinschaft (grant GA716/1-1), FAPESP and CNPq.

## References

1. Alpar, A., Palm, K., Schierwagen, A., Arendt, T., Gärtner, U.: Expression of constitutively active p21H-rasVal12 in postmitotic pyramidal neurons results in increased dendritic size and complexity. *J. Comp. Neurol.*, **467**, 119–133 (2003).
2. Cannon, R.C.: Structure editing and conversion with CVAPP (2000). <http://www.compneuro.org/CDROM/nmorph/usage.html>.
3. Costa, L.F., Cesar, R. Jr.: *Shape Analysis and Classification: Theory and Practice*. CRC Press, Boca Raton, FL (2001).
4. Costa, L.F., Manoel, E.T.M., Faucereau, F., Chelly, J., van Pelt, J., Ramakers, G.J.A.: A shape analysis framework for neuromorphometry. *Network: Comput. Neural Syst.*, **13**, 283–310 (2002).
5. Costa, L.F., Barbosa, M.S., Schierwagen, A., Alpar, A., Gärtner, U., Arendt, T.: Active percolation analysis of pyramidal neurons of somatosensory cortex: A comparison of wild type and p21H-rasVal12 transgenic mice. *Int. J. Mod. Phys. C*, **16**, 655–667 (2005).
6. Fernandez, E., Jelinek, H.F.: Use of fractal theory in neuroscience: Methods, advantages, and potential problems. *Methods*, **24**, 309–321 (2001).
7. Havlin, S., Ben-Avraham, D.: Fractal dimensionality of polymer chains. *J. Phys. A: Math. Gen.*, **15**, L311–L316 (1982).
8. Heumann, R., Goemans, Ch., Bartsch, D., Lingenhöhl, K., Waldmeier, P.C., Hengerer, B., Allegrini, P.R., Schellander, K., Wagner, E.F., Arendt, Th., Kamdem, R.H., Obst-Pernberg, K., Narz, F., Wahle, P., Berns, H.: Constitutive activation of Ras in neurons promotes hypertrophy and protects from lesion-induced degeneration. *J. Cell Biol.*, **151**, 1537–1548 (2000).
9. Van Pelt, J., Schierwagen, A.: Morphological analysis and modeling of neuronal dendrites. *Math. Biosciences*, **188**, 147–155 (2004).
10. Schierwagen, A.: Dendritic branching patterns. In: Degn, H., Holden, A.V., Olsen, L.F. (eds) *Chaos in Biological Systems*. Plenum Press, New York and London, 191–193 (1987).
11. Schierwagen, A.: Scale-invariant diffusive growth: A dissipative principle relating neuronal form to function. In: Maynard-Smith, J., Vida, G. (eds) *Organizational Constraints on the Dynamics of Evolution*. Manchester University Press, Manchester, 167–189 (1990).

## A Quantitative Model of ATP-Mediated Calcium Wave Propagation in Astrocyte Networks

William G. Gibson,<sup>1</sup> Les Farnell,<sup>1</sup> and Max R. Bennett<sup>2</sup>

<sup>1</sup> School of Mathematics and Statistics, The University of Sydney, N.S.W. 2006, Australia;  
billg@maths.usyd.edu.au, lesf@maths.usyd.edu.au

<sup>2</sup> Department of Physiology, The University of Sydney, N.S.W. 2006, Australia;  
maxb@physiol.usyd.edu.au

**Summary.** In the past attention has mainly been focused on neurons and the role they play, both individually and as parts of networks, in the functioning of the brain and nervous system. However, glial cells outnumber neurons in the brain, and it is now becoming apparent that, far from just performing supportive and housekeeping tasks, they are also actively engaged in information processing and possibly even learning. Communication in glial cells is manifested by waves of calcium ions ( $\text{Ca}^{2+}$ ) that are released from internal stores, and these waves are observed experimentally using fluorescent markers attached to the ions. The waves can be initiated by stimulation of a single cell, and initially it was assumed that the transmission mechanism involved the passage of an intercellular signalling agent passing through gap junctions connecting the cells. However, a surprising feature is that in many cases the calcium waves can cross cell-free zones, thus indicating the presence of an extracellular messenger.

We have constructed a mathematical model of calcium wave propagation in networks of model astrocytes, these being a subclass of glial cells. The extracellular signalling agent is ATP (adenosine triphosphate) and it acts on metabotropic purinergic receptors on the astrocytes, initiating a G-protein cascade leading to the production of inositol trisphosphate ( $\text{IP}_3$ ) and the subsequent release of  $\text{Ca}^{2+}$  from intracellular stores via  $\text{IP}_3$ -sensitive channels. Stimulation of one cell (by a pulse of ATP or by raising the  $\text{IP}_3$  level) leads to the regenerative release of ATP both from this cell and from neighbouring cells, and hence a  $\text{Ca}^{2+}$  wave. Results are given for the propagation of  $\text{Ca}^{2+}$  waves in two-dimensional arrays of model astrocytes and also in lanes with cell-free zones in between. These theoretical considerations support the concept of extracellular purinergic transmission in astrocyte networks.

**Key words:** Astrocyte, calcium, inositol trisphosphate, ATP, G-protein cascade, extracellular signalling.

### 17.1 Introduction

Since the time of Galvani and Volta in the 18th century neuroscience has been dominated by the paradigm of electrical activity in neurons and other excitable cells, whether it takes the form of action potentials, synaptic potentials, or extracellular currents, etc. However, it has been known for a very long time that many other types of

cells populate the brain and nervous system. Principal among these are the glia: generally classified as Schwann cells, astrocytes, oligodendrocytes, or microglia. Astrocytes, in particular, have many processes that form close contacts with the synaptic connections between neurons and also with the vasculature. However, not too much attention was paid to these cells, as it was thought that they performed mainly a housekeeping role, transporting nutrients and recycling neurotransmitters, etc. Two major discoveries have caused a radical rethink about glia and, in particular, astrocytes. The first is that they have receptors for a wide variety of neurotransmitters and can also release neurotransmitters themselves in response to stimuli (for reviews see [3, 19]). The second is that they display a form of excitability manifested by increases in intracellular  $\text{Ca}^{2+}$  concentration ( $[\text{Ca}^{2+}]$ ). Stimuli that evoke  $[\text{Ca}^{2+}]$  elevation in a single astrocyte pass to adjacent astrocytes, leading to a  $\text{Ca}^{2+}$  wave that can propagate for hundreds of micrometers [4, 6].

The  $\text{Ca}^{2+}$  involved in extracellular communication is thought to come mainly from intracellular stores, principally the endoplasmic reticulum (ER). It is released by the action of  $\text{IP}_3$  upon  $\text{IP}_3$  receptors ( $\text{IP}_3\text{Rs}$ ) on the ER [4]. The  $\text{Ca}^{2+}$  wave can then propagate through neighbouring cells by passive diffusion of  $\text{IP}_3$  through connecting gap junctions. The  $\text{Ca}^{2+}$  itself plays only a minor role in the propagation, as it does not readily pass through gap junctions and also is quickly bound to endogenous buffers in the cell cytosol. An elevated concentration of  $\text{IP}_3$  in a single cell acts on  $\text{IP}_3\text{Rs}$  in the ER causing the release of  $\text{Ca}^{2+}$  into the cytosol which then acts on phospholipase C (PLC) to produce more  $\text{IP}_3$ . The  $\text{IP}_3$  diffuses to neighbouring cells where the regenerative process is repeated. This method of communication in astrocytes has been modelled mathematically [14].

However, this cannot be the only mode of  $\text{Ca}^{2+}$  communication in astrocytes. This is very clear from the work of Hassinger et al. [12] in which  $\text{Ca}^{2+}$  waves were observed to cross cell-free zones up to  $120\ \mu\text{m}$  wide in two-dimensional cultures of astrocytes. The inescapable conclusion is that some extracellular agent is diffusing across this zone and initiating the  $\text{Ca}^{2+}$  wave on the other side. Evidence that this is adenosine triphosphate (ATP) comes from simultaneous imaging of ATP and  $\text{Ca}^{2+}$  waves in two-dimensional cortical astrocyte cultures [21]. Also,  $\text{Ca}^{2+}$  wave propagation is blocked by antagonists of ATP-activated metabotropic purinergic receptors (P2YRs) [7, 11]. These considerations lead to a model of  $\text{Ca}^{2+}$  wave propagation in astrocyte networks that involves an initial stimulus releasing ATP from an astrocyte, and this ATP diffusing in the extracellular space and activating P2YRs on neighbouring astrocytes, which then release further ATP. Thus the mechanism is regenerative, and ATP can act in both an autocrine and a paracrine manner; that is, the released ATP can act both on the cell releasing it and also on neighbouring cells.

It is well established that astrocytes release ATP during  $\text{Ca}^{2+}$  wave propagation [7] and that applying ATP evokes  $\text{Ca}^{2+}$  responses in astrocytes [1, 11]. However, the mechanism by which ATP is released is not known. It appears that  $\text{Ca}^{2+}$  itself is not the activating agent [21], and, in particular, the ATP intercellular wave actually precedes the  $\text{Ca}^{2+}$  wave [17]. Instead, it is likely that  $\text{IP}_3$  is the essential agent, especially as it is generated intracellularly in response to mechanical stimulation, which also induces an intercellular  $\text{Ca}^{2+}$  wave [18]. The model we present below assumes that this  $\text{IP}_3$  then

acts, in an as yet undetermined manner, to release ATP into the extracellular space. This ATP binds to P2YRs on the astrocytes, thereby initiating a G-protein cascade leading to the generation of  $IP_3$  and the liberation of  $Ca^{2+}$  from the ER.

## 17.2 ATP Diffusion Model

### 17.2.1 Introduction

The single-cell model follows that of [15] with some changes. Simplifications have been made: some processes included in that model are not relevant to astrocytes; others are second-order effects and can be omitted with little change to the final results. The main additions that must be made concern the release of ATP into the extracellular space and the diffusion of  $IP_3$  inside the cell and ATP outside the cell. Fig. 17.1 is a schematic diagram showing the main processes that will be used in our model of a single cell.

### 17.2.2 Receptors

A basic model is used in which receptors do not desensitize:

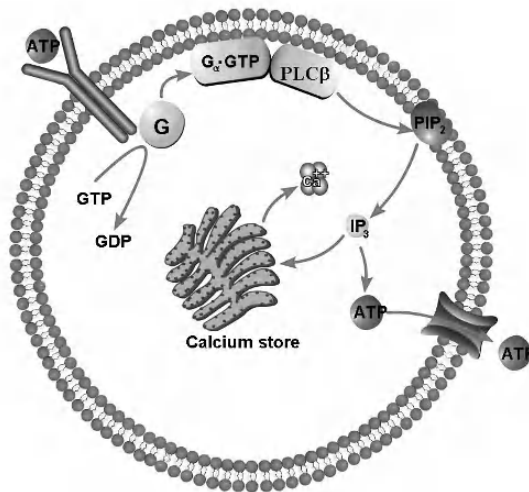
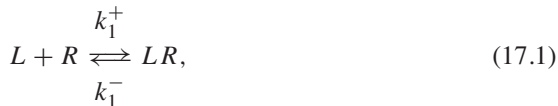


**Fig. 17.1.** Schematic diagram of the pathways used in the model of a single astrocyte. Extracellular ATP binds to P2YRs which then interact with G protein, leading to a subunit  $G_{\alpha} \cdot GTP$  binding to a site on phospholipase C- $\beta$  ( $PLC\beta$ ). This then interacts with membrane-bound phosphatidylinositol 4,5-bisphosphate ( $PIP_2$ ) leading to the hydrolysis of  $PIP_2$  and the production of  $IP_3$ . The latter diffuses into the cytosol where it both binds to  $IP_3$ R on the ER, thus liberating  $Ca^{2+}$  into the cytosol, and also interacts with ATP stores leading to the release of ATP from the astrocyte. This released ATP then diffuses in the extracellular space and can bind to P2YRs both on the original cell and on neighbouring cells.



where  $L$  is ligand and  $R$  is receptor.

The quantity we want is the ratio of bound to total receptors,  $\rho = [LR]/[R_T]$ , where  $[R_T] = [R] + [LR]$  is the total number of receptors. Under the assumption of fast binding kinetics Eq. (17.1) can be assumed to be in equilibrium, leading to

$$\rho = \frac{[ATP]}{K_R + [ATP]}, \quad (17.2)$$

where  $[L] = [ATP]$  is the extracellular ATP concentration and  $K_R = k_1^-/k_1^+$  is the dissociation constant.

### 17.2.3 G-Protein Cascade

The equation describing G-protein activation is ([15], Eq. (16))

$$\frac{d[G]}{dt} = k_a(\delta + \rho)([G_T] - [G]) - k_d[G], \quad (17.3)$$

where  $[G]$  is the amount of activated G-protein,  $[G_T]$  is the total G-protein,  $\rho$  is the fraction of bound receptors as given by Eq. (17.2),  $\delta$  is the ratio of the activities of the unbound and bound receptors (and thus allows for background activity even in the absence of ligand binding, that is, unbound receptors can activate a small amount of G-protein), and  $k_a$  and  $k_d$  are the G-protein activation and deactivation rate parameters, respectively. Again assuming fast kinetics, we obtain

$$G^* = \frac{\rho + \delta}{K_G + \delta + \rho}, \quad (17.4)$$

where  $G^* = [G]/[G_T]$  and  $K_G = k_d/k_a$ .

### 17.2.4 IP<sub>3</sub> Production and Diffusion

IP<sub>3</sub> production, diffusion, and degradation are governed by (cf. [15], Eq. (19))

$$\frac{\partial[\text{IP}_3]}{\partial t} = D_{\text{IP}} \nabla^2[\text{IP}_3] + r_h^* G^* - k_{deg}[\text{IP}_3], \quad (17.5)$$

where  $D_{\text{IP}}$  is the diffusion coefficient for IP<sub>3</sub> and  $r_h^*$  and  $k_{deg}$  are constants; the term  $r_h^* G^*$  is applied only at the cell wall.

### 17.2.5 ATP Production and Diffusion

As stated in Sect. 17.1, the mechanism by which ATP is released by astrocytes has not been established, although there is evidence that  $\text{IP}_3$  is probably involved. We have chosen to use  $\text{IP}_3$  as the agent triggering release, but this is not crucial to the model. ATP production and diffusion are governed by

$$\frac{\partial[\text{ATP}]}{\partial t} = D_{\text{ATP}}\nabla^2[\text{ATP}] + V_{\text{ATP}}\chi(t)\frac{[\text{IP}_3] - [\text{IP}_3]_{\text{min}}}{K_{\text{rel}} + [\text{IP}_3]}, \quad (17.6)$$

where  $D_{\text{ATP}}$  is the diffusion coefficient for ATP. The second term describes the release of ATP into the extracellular space and is applied only if  $[\text{IP}_3]$  is greater than  $[\text{IP}_3]_{\text{min}}$ .  $V_{\text{ATP}}$  and  $K_{\text{rel}}$  are constants and  $\chi(t)$  is a parameter that accounts for depletion of ATP stores inside the cell; it has initial value 1 and decreases according to

$$\frac{d\chi}{dt} = -k_{\text{loss}}\chi(t)\frac{[\text{IP}_3] - [\text{IP}_3]_{\text{min}}}{K_{\text{rel}} + [\text{IP}_3]}, \quad (17.7)$$

where  $k_{\text{loss}}$  is a constant.

### 17.2.6 $\text{Ca}^{2+}$ Release from Internal Stores

The steps leading from  $\text{IP}_3$  production to  $\text{Ca}^{2+}$  release from the ER are based on the theories of [8, 16], as modified by Fink et al. [10]. The  $\text{Ca}^{2+}$  dynamics are governed by

$$\frac{d[\text{Ca}^{2+}]}{dt} = \beta(J_{\text{IP}_3} - J_{\text{pump}} + J_{\text{leak}}), \quad (17.8)$$

where  $[\text{Ca}^{2+}]$  is the cytosolic  $\text{Ca}^{2+}$  concentration,  $J_{\text{IP}_3}$ ,  $J_{\text{pump}}$ , and  $J_{\text{leak}}$  are the rates of  $\text{Ca}^{2+}$  concentration change due to release through  $\text{IP}_3\text{R}$  channels, pump uptake into the ER, and leak from the ER, respectively, and  $\beta$  is a factor describing  $\text{Ca}^{2+}$  buffering. The  $\text{IP}_3$ -induced current is

$$J_{\text{IP}_3} = J_{\text{max}} \left[ \left( \frac{[\text{IP}_3]}{[\text{IP}_3] + K_I} \right) \left( \frac{[\text{Ca}^{2+}]}{[\text{Ca}^{2+}] + K_{\text{act}}} \right) h \right]^3 \left[ 1 - \frac{[\text{Ca}^{2+}]}{[\text{Ca}^{2+}]_{\text{ER}}} \right], \quad (17.9)$$

where  $J_{\text{max}}$  is the maximum rate,  $K_I$  is the dissociation constant for  $\text{IP}_3$  binding to an  $\text{IP}_3\text{R}$ ,  $K_{\text{act}}$  is the dissociation constant for  $\text{Ca}^{2+}$  binding to an activation site on an  $\text{IP}_3\text{R}$ ,  $[\text{Ca}^{2+}]_{\text{ER}}$  is the  $\text{Ca}^{2+}$  concentration in the ER (taken to be constant), and  $h$  satisfies

$$\frac{dh}{dt} = k_{\text{on}}[K_{\text{inh}} - ([\text{Ca}^{2+}] + K_{\text{inh}})h]. \quad (17.10)$$

Here  $k_{\text{on}}$  is the rate of  $\text{Ca}^{2+}$  binding to the inhibitory site on the  $\text{IP}_3\text{R}$  and  $K_{\text{inh}}$  is the corresponding dissociation constant. The ATPase  $\text{Ca}^{2+}$  pump is described by  $J_{\text{pump}} =$

$V_{\max}[\text{Ca}^{2+}]^2/([\text{Ca}^{2+}]^2 + K_p^2)$ , where  $V_{\max}$  is the maximum pumping rate and  $K_p$  is the dissociation constant. The leak is described by  $J_{\text{leak}} = P_L(1 - [\text{Ca}^{2+}]/[\text{Ca}^{2+}]_{\text{ER}})$ , where the constant  $P_L$  is determined by the steady-state flux balance (see Sect. 17.5.2 below). The buffering is described by the steady-state approximation  $\beta = (1 + [B]_{\text{end}}/K_{\text{end}})^{-1}$ , where  $[B]_{\text{end}}$  and  $K_{\text{end}}$  are the concentration and dissociation constant of the endogenous buffer.

### 17.3 Results

The ATP wave in a network of astrocytes is initiated by the application of a pulse of ATP to a single astrocyte. This releases further ATP, which then diffuses in the extracellular space and binds to P2YRs on neighbouring astrocytes, thus causing the release of further ATP. This process can be seen in Fig. 17.2 which shows the ATP concentration profile in a cross section of a two-dimensional array of astrocytes. The solid line shows the wave travelling outwards with “bumps” indicating sites where regenerative release is occurring. This is to be compared with the case where no regeneration occurs, that is, propagation of ATP is by pure diffusion, and this is shown by the broken lines in Fig. 17.2.

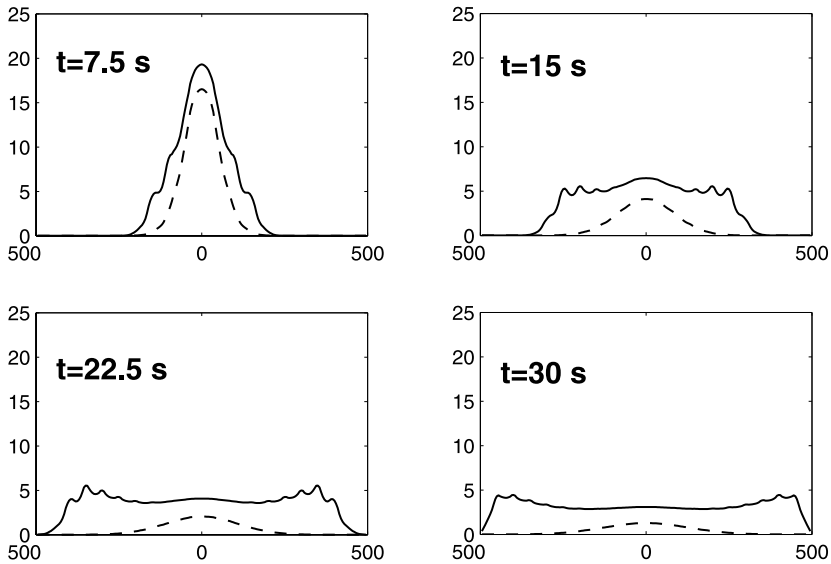
The  $\text{Ca}^{2+}$  profiles corresponding to this situation are shown in Fig. 17.3B, where now the positions of all the cells are shown on the horizontal plane and the height of the bars gives the  $\text{Ca}^{2+}$  concentration in each cell at the given times. The  $\text{Ca}^{2+}$  wave is similar in shape to the ATP wave, but lags slightly behind.

Fig. 17.3A shows the propagation of a  $\text{Ca}^{2+}$  wave in a network containing cell-free zones; specifically, the astrocytes are in parallel lanes 3 cells wide, separated by cell-free lanes 1 cell wide. This means that there is a gap of  $75 \mu\text{m}$  between the surfaces of cells on opposite sides of a cell-free lane, compared to a gap of  $25 \mu\text{m}$  for cells within a lane. The  $\text{Ca}^{2+}$  wave initially moves along the lane of the stimulated cell, but soon ATP diffusing across the cell-free zone initiates  $\text{Ca}^{2+}$  waves in the adjoining lanes, and this process is repeated. Further calculations show that for the same initial conditions the wave will cross cell-free lanes  $125 \mu\text{m}$  wide, but not  $175 \mu\text{m}$  wide.

A comparison between experimental and theoretical  $\text{Ca}^{2+}$  wave amplitude in a lane of astrocytes is shown in Fig. 17.4. In the experimental case, the wave is initiated by mechanical stimulation, but this has been found to be equivalent to exogenous application of ATP. Both the experimental amplitudes (Fig. 17.4B and D) and the theoretical amplitudes (Fig. 17.4E and F) show similar fluctuations, with an initial decline and then a relatively flat tail.

### 17.4 Discussion

As pointed out in Sect. 17.1, there is considerable experimental evidence that extracellular signalling by diffusion of ATP is an important mechanism whereby  $\text{Ca}^{2+}$  waves are produced in astrocyte networks. Our model calculations show that ATP acting on metabotropic purinergic receptors can indeed lead to a propagating  $\text{Ca}^{2+}$  wave. The



**Fig. 17.2.** ATP profiles in a two-dimensional network of model astrocytes. The network consists of a regular array of cells in a plane, the distance apart of the centres of the astrocytes being  $50 \mu\text{m}$  (see also Fig. 17.3B). The ATP wave is initiated by a pulse of ATP of duration  $5 \text{ s}$  and amplitude  $80 \mu\text{M}$  applied at the central astrocyte starting at time zero; other parameters are as given in Sect. 17.5.4. Shown is the ATP concentration as a function of distance along a straight line through the central astrocyte at the times indicated. The horizontal axis gives distance in  $\mu\text{m}$  and the vertical axis gives ATP concentration in  $\mu\text{M}$ . The solid line is calculated using the full model with ATP regeneration included; the broken line gives the corresponding result for pure diffusion with no regeneration.

speed of this wave is about  $17 \mu\text{m s}^{-1}$  for our parameter values and is within the experimental range [11].

The other mechanism whereby  $\text{Ca}^{2+}$  waves can be generated in glial networks involves the diffusion of  $\text{IP}_3$  through gap junctions; for example, in the retina it is thought that astrocytes communicate with each other mainly through gap junctions, but signalling from astrocytes to Müller cells, or between Müller cells, is by extracellular diffusion of ATP [17]. Other systems may use a combination of both methods and the current model could be extended to include gap junction communication, following existing models [14,20].

In the calculations reported above, the  $\text{Ca}^{2+}$  wave extended to the limits of the computational domain, and in fact would continue indefinitely if the domain were extended. This is a consequence of parameter choice; in particular, choosing a larger value of the dissociation constant  $K_R$  causes the wave to have a finite range. Computations can also be made more realistic by using a range of values of  $K_R$  randomly assigned to individual astrocytes, as in the calculation shown in Fig. 17.4, to simulate the random nature of real systems.



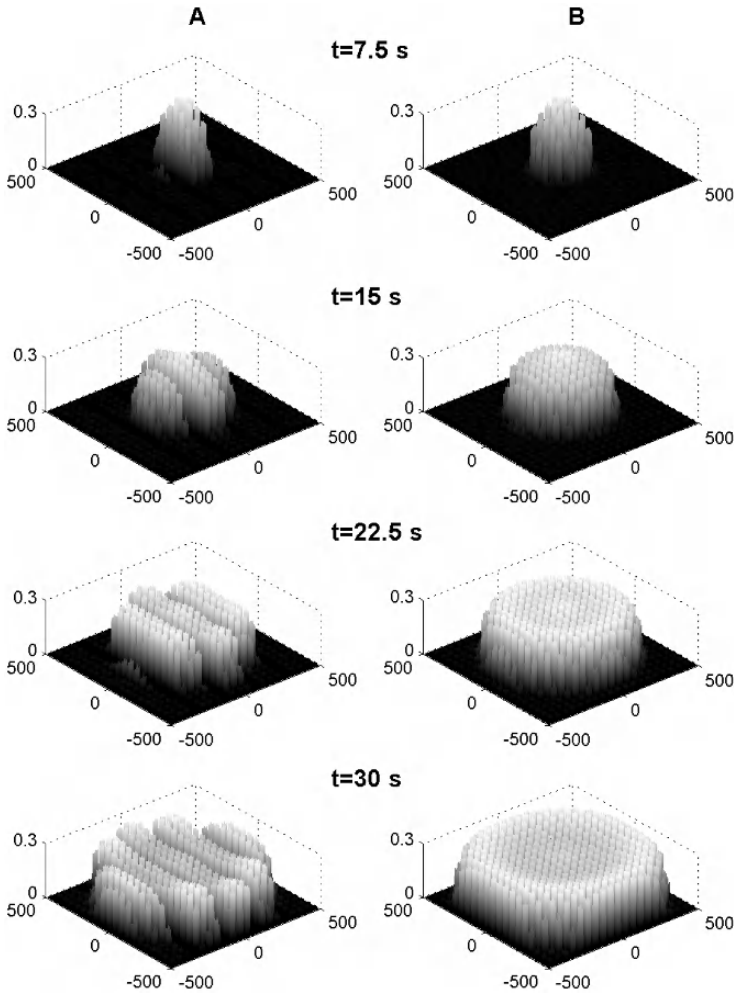


**Fig. 17.3.**  $\text{Ca}^{2+}$  profiles in two-dimensional arrays of astrocytes. In column A the cells are arranged in parallel lanes 3 cells wide separated by cell-free lanes one cell wide; in column B the cells are arranged as for Fig. 17.2. Spacing between cell centres is  $50 \mu\text{m}$  and the  $\text{Ca}^{2+}$  wave is initiated by the application of an  $80 \mu\text{M}$  pulse of ATP for 5 s to the central cell; the full regenerative model is used and other parameters are as given in Sect. 17.5.4. Distances are in  $\mu\text{m}$  and the vertical scale gives  $[\text{Ca}^{2+}]$  in  $\mu\text{M}$ .

While it is abundantly evident that astrocytes release ATP in response to various stimuli, the detailed mechanism underlying this release is not known [2,5]. As pointed out in Sect. 17.1,  $\text{Ca}^{2+}$  itself does not seem to be directly involved so we have chosen instead to use  $\text{IP}_3$  as the activating agent and linked it in an *ad hoc* manner to ATP release (Eq. 17.6). Other pathways could have been used, including linking ATP

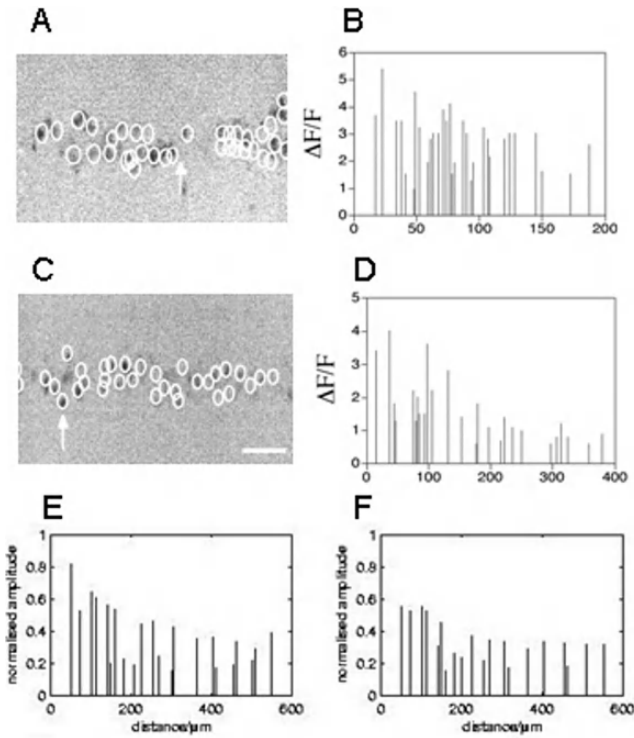


**Fig. 17.4.** Comparison between theoretical and experimental  $\text{Ca}^{2+}$  waves in a lane of astrocytes. A shows a lane of spinal-cord astrocytes plated onto a two-dimensional substrate and mechanically stimulated by a micropipette at the point indicated by the arrow. Only those astrocytes circled in white gave a significant response, as measured by the change in fluorescence of the  $\text{Ca}^{2+}$ -bound dye fluo-3 AM. B shows the corresponding peak fluorescence changes for astrocytes at different distances from the point of stimulation (scale in  $\mu\text{m}$ ). C and D repeat A and B for a different preparation, showing the sort of stochastic variation that can be expected. E shows the result of a theoretical calculation using a lane of astrocytes 5 cells wide and 600  $\mu\text{m}$  long, with a 25  $\mu\text{m}$  spacing between each cell and  $K_R$  values ranging from 25  $\mu\text{M}$  to 125  $\mu\text{M}$  across the lane. The wave was initiated by application of ATP of concentration 80  $\mu\text{M}$  for 5 s to an astrocyte at one end of the lane. F repeats the calculation for a different set of  $K_R$  values.

release to active G-protein concentration. Clearly, this is an area where further input from experiment is needed.

We have so far only modelled interactions between astrocytes. However, an exciting area of current research involves interactions between glia and neurons and, in particular, the *tripartite synapse*, which proposes glial cells as active participants in synaptic transmission between neurons [3]; this has implications for information processing in the brain [9]. This will be a fruitful area for further modelling.

## 17.5 Methods

### 17.5.1 Geometry

Each astrocyte is represented by a cube of side  $25 \mu\text{m}$  and these cubes are arranged in two-dimensional arrays, on the  $xy$ -plane, the minimum spacing between cubes being  $25 \mu\text{m}$ . With this simplified geometry we are not attempting to model the spatial complexity of a real astrocyte; rather this is an “effective” astrocyte in which the processes emanating from a real astrocyte are lumped into a compact space, taken to be cubical for reasons of computational simplicity.

### 17.5.2 Initialization

In the absence of ATP there is still background  $\text{IP}_3$  and  $\text{Ca}^{2+}$  resulting from the activation of a small amount of G-protein by unbound receptors (see Eq. (17.4); in this case,  $\rho = 0$  but  $\delta \neq 0$ ). If diffusion of  $\text{IP}_3$  is neglected, then initial homogeneous concentrations of  $\text{IP}_3$  and  $\text{Ca}^{2+}$ ,  $[\text{IP}_3]_0$  and  $[\text{Ca}^{2+}]_0$  respectively, can be set and the activity ratio  $\delta$  (using Eqs. (17.4) and (17.5)) is given by

$$\delta = \frac{K_G k_{\text{deg}}[\text{IP}_3]_0}{r_h^* - k_{\text{deg}}[\text{IP}_3]_0}. \quad (17.11)$$

The  $\text{Ca}^{2+}$  leak rate,  $P_L$ , is determined by setting  $J_{\text{IP}_3} - J_{\text{pump}} - J_{\text{leak}} = 0$ . Then the  $\text{IP}_3$  equation, Eq. (17.5) is run, as described in the following section, until a steady-state solution is obtained that is close to the homogeneous one. The  $\text{Ca}^{2+}$  equation, Eq. (17.8), is now solved to find the corresponding equilibrium  $\text{Ca}^{2+}$  concentration, which will also be inhomogeneous (even though  $\text{Ca}^{2+}$  does not diffuse) because of the inhomogeneous distribution of  $\text{IP}_3$ .

### 17.5.3 Method of Solution

Each cell is represented by a rectangular Cartesian grid with spacing  $5 \mu\text{m}$ , and thus contains 27 interior grid points and 98 surface grid points. The space between the cells is similarly represented by a rectangular grid with the same spacing of  $5 \mu\text{m}$ . The grid extends to  $\pm 49$  points in the  $z$ -direction. The boundary conditions are ATP sinks at all boundaries. The ER is present at all 125 grid points of each cell and  $\text{Ca}^{2+}$  production and  $\text{IP}_3$  degradation also occur at each of these points. On the other hand,  $\text{IP}_3$  production occurs only at the 98 surface points, as does ATP binding to P2YRs and the production of ATP.

The equations for the diffusion of  $\text{IP}_3$ , Eq. (17.5), and of ATP, Eq. (17.6), are solved using a “leap-frog” method (see the Appendix in [13]). The other differential equations for ATP store depletion, Eq. (17.7),  $\text{Ca}^{2+}$ , Eq. (17.8), and  $h$ , Eq. (17.10), are solved using a standard Runge–Kutta method.

### 17.5.4 Parameter Values

Unless otherwise stated, the parameter values used in the calculations reported here are:  $K_R = 25 \mu\text{M}$ ,  $k_{\text{deg}} = 1.25 \text{ s}^{-1}$ ,  $k_a = 0.017 \text{ s}^{-1}$ ,  $k_d = 0.15 \text{ s}^{-1}$ ,  $r_h^* = 2 \times 10^{-14} \mu\text{mol} \mu\text{m}^{-2} \text{ s}^{-1}$ ,  $D_{\text{IP}} = 280 \mu\text{m}^2 \text{ s}^{-1}$ ,  $V_{\text{ATP}} = 2 \times 10^{-11} \mu\text{mol} \mu\text{m}^{-2} \text{ s}^{-1}$ ,  $K_{\text{rel}} = 10 \mu\text{M}$ ,  $[\text{IP}_3]_{\text{min}} = 0.012 \mu\text{M}$ ,  $k_{\text{loss}} = 30 \text{ s}^{-1}$ ,  $D_{\text{ATP}} = 300 \mu\text{m}^2 \text{ s}^{-1}$ ,  $J_{\text{max}} = 2880 \mu\text{M} \text{ s}^{-1}$ ,  $K_I = 0.03 \mu\text{M}$ ,  $K_{\text{act}} = 0.17 \mu\text{M}$ ,  $k_{\text{on}} = 8.0 \mu\text{M} \text{ s}^{-1}$ ,  $K_{\text{inh}} = 0.1 \mu\text{M}$ ,  $[\text{Ca}^{2+}_{\text{ER}}] = 400 \mu\text{M}$ ,  $V_{\text{max}} = 5.85 \mu\text{M} \text{ s}^{-1}$ ,  $K_p = 0.24 \mu\text{M}$ ,  $\beta = 0.0244$ ,  $[\text{IP}_3]_0 = 0.01 \mu\text{M}$ ,  $[\text{Ca}^{2+}]_0 = 0.05 \mu\text{M}$ .

### Acknowledgments

We thank Dr. Vlado Buljan for providing us with the experimental data. This work was supported by Australian Research Council grant no. DP0345968.

### References

1. Abdipranoto, A., Liu, G.J., Werry, E.L., Bennett, M.R.: Mechanisms of secretion of ATP from cortical astrocytes triggered by uridine triphosphate. *Neuroreport*, **14**, 2177–81 (2003).
2. Anderson, C.M., Bergher, J.P., Swanson, R.A.: ATP-induced ATP release from astrocytes. *J. Neurochem.*, **88**, 246–56 (2004).
3. Araque, A., Parpura, V., Sanzgiri, R.P., Haydon, P.G.: Tripartite synapses: glia, the unacknowledged partner. *Trends Neurosci.*, **22**, 208–215 (1999).
4. Charles, A.C., Merrill, J.E., Dirksen, E.R., Sanderson, M.J.: Intercellular signaling in glial cells: Calcium waves and oscillations in response to mechanical stimulation and glutamate. *Neuron*, **6**, 983–992 (1991).
5. Coco, S., Calegari, F., Pravettoni, E., Pozzi, D., Taverna, E., Rosa, P., Matteoli, M., Verderio, C.: Storage and release of ATP from astrocytes in culture. *J. Biol. Chem.*, **278**, 1354–62 (2003).
6. Cornell-Bell, A.H., Finkbeiner, S.M., Cooper, M.S., Smith, S.J.: Glutamate induces calcium waves in cultured astrocytes: long-range glial signalling. *Science*, **247**, 470–473 (1990).
7. Cotrina, M.L., Lin, J.H., Alves-Rodrigues, A., Liu, S., Li, J., Azmi-Ghadimi, H., Kang, J., Naus, C.C., Nedergaard, M.: Connexins regulate calcium signaling by controlling ATP release. *Proc. Natl. Acad. Sci. U.S.A.*, **95**, 15735–40 (1998).
8. De Young, G.W., Keizer J.: A single-pool inositol 1,4,5-trisphosphate-receptor-based model for agonist-stimulated oscillations in  $\text{Ca}^{2+}$  concentration. *Proc. Natl. Acad. Sci. U.S.A.*, **89**, 9895–9 (1992).
9. Fellin, T., Carmignoto, G.: Neurone to astrocyte signalling in the brain represents a distinct multifunctional unit. *J. Physiol.*, **559**, 3–15 (2004).
10. Fink, C.F., Slepchenko, B., Loew, L.M.: Determination of time-dependent inositol-1,4,5-trisphosphate concentrations during calcium release in a smooth muscle cell. *Biophys. J.*, **77**, 617–628 (1999).
11. Gallagher, C.J., Salter, M.W.: Differential properties of astrocyte calcium waves mediated by P2Y1 and P2Y2 receptors. *J. Neurosci.*, **23**, 6728–39 (2003).

12. Hassinger, T.D., Guthrie, P.B., Atkinson, P.B., Bennett, M.V., Kater, S.B.: An extracellular signaling component in propagation of astrocytic calcium waves. *Proc. Natl. Acad. Sci. U.S.A.*, **93**, 13268–73 (1996).
13. Henery, R., Gibson, W.G., Bennett, M.R.: Quantal currents and potential in the three-dimensional anisotropic bidomain model of smooth muscle. *Bull. Math. Biol.*, **59**, 1047–1075 (1997).
14. Höfer, T., Venance, L., Giaume, C.: Control and plasticity of intercellular calcium waves in astrocytes: a modeling approach. *J. Neurosci.*, **22**, 4850–9 (2002).
15. Lemon, G., Gibson, W.G., Bennett, M.R.: Metabotropic receptor activation, desensitization and sequestration-I: modelling calcium and inositol 1,4,5-trisphosphate dynamics following receptor activation. *J. Theor. Biol.*, **223**, 93–111 (2003).
16. Li, Y-X., Rinzal, J.: Equations for  $\text{InsP}_3$  receptor-mediated  $[\text{Ca}^{2+}]$  oscillations derived from a detailed kinetic model: a Hodgkin-Huxley like formalism. *J. Theor. Biol.*, **166**, 461–473 (1994).
17. Newman, E.A.: Propagation of intercellular calcium waves in retinal astrocytes and Müller cells. *J. Neurosci.*, **21**, 2215–2223 (2001).
18. Niggel, J., Sigurdson, W., Sachs, F.: Mechanically induced calcium movements in astrocytes, bovine aortic endothelial cells and C6 glioma cells. *Membrane Biology*, **174**, 121–134 (2000).
19. Porter, J.T., McMarthy, K.D.: Astrocyte neurotransmitter receptors *in situ* and *in vivo*. *Prog. Neurobiol.*, **51**, 439–455 (1997).
20. Sneyd, J., Wilkins, M., Strahonja, A., Sanderson, M.J. : Calcium waves and oscillations driven by an intercellular gradient of inositol (1,4,5)-trisphosphate. *Biophys. Chem.*, **72**, 101–109 (1998).
21. Wang, Z., Haydon, P.G., and Yeung, E.S.: Direct observation of calcium-independent intercellular ATP signaling in astrocytes. *Anal. Chem.*, **72**, 2001–7 (2000).

## Dynamics of Neural Fields with Distributed Transmission Speeds

Fatihcan M. Atay<sup>1</sup> and Axel Hutt<sup>2</sup>

<sup>1</sup> Max Planck Institute for Mathematics in the Sciences, 04103 Leipzig, Germany;  
atay@member.ams.org

<sup>2</sup> Humboldt University at Berlin, Newtonstr. 15, 12489 Berlin, Germany;  
axel.hutt@physik.hu-berlin.de

**Summary.** We consider the continuous field model of neural populations with the addition of a distribution of transmission speeds. The speed distribution arises as a result of the natural variability of the properties of axons, such as their degree of myelination. We analyze the stability and bifurcations of equilibrium solutions for the resulting field dynamics. Using a perturbation approach, we show that the speed distribution affects the frequency of bifurcating periodic solutions and the phase speed of traveling waves. The theoretical findings are illustrated by numerical calculations.

**Key words:** Neural field, delay, bifurcations, pattern formation, traveling waves.

### 18.1 Introduction

In recent years, several models of coupled neurons have attracted much attention, including networks involving spatial structures, describing a continuous, synaptically coupled neural field extended in space [1–5]. The dynamics of these fields are governed by integro-differential equations. Since the signal transmission along the axons occurs at a finite speed, the neural field shows retarded interaction due to distance-dependent delays between two spatial locations [6]. However, such delays have not always been included in field models. Some recent works have taken delays into account by using a fixed value  $v$  for axonal transmission speed [3, 7, 8], or two different values of  $v$  for excitatory and inhibitory connections [9]. On the other hand, the propagation speed along the axon depends on a number of factors, such as its myelination. The myelin is a fatty material, composed mainly of lipids and lipoproteins, that encloses certain axons and nerve fibers and affects their electrical conductance. The natural diversity in the degree of myelination of the axons leads to a diversity in the propagation speeds. Experimental studies reveal statistically distributed speeds in cortico-cortical connections in rats [6] and in intracortical connections in the visual cortex of cats and monkeys [10, 11]. Fig. 18.1 shows the distribution of speeds obtained in these studies. The maximum speed is between 5 m/s and 12 m/s in rats and at about 0.2 m/s in the cat and monkey brain;

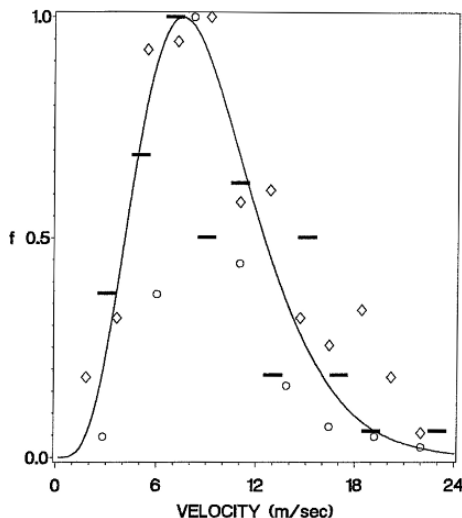


**Fig. 18.1.** Experimentally obtained neural transmission speed values, fitted by a gamma distribution (after Nunez [6], printed with permission of the author and Oxford University Press, Inc.).

however, a marked variance of speeds is observed about the peak values, and the histogram of speed values seems to follow a gamma distribution [6]. Distributed speeds have been considered in simple neural models; for instance, Nunez [6] studied an integral equation model, similar to (18.1) but without the temporal differentiation operator (see also [5]). In this chapter, we introduce a distribution of signal transmission speeds into the classical field model of neural dynamics [1]. Our emphasis is on an analytical investigation of the effects of distributed speeds on the dynamics through the stability of equilibria and the bifurcations leading to spatial patterns and oscillations.

We first give a brief introduction to the neural field models, which are based on the fact that neurons have a large spatial density ( $\sim 10^4$  neurons/mm<sup>3</sup>) and are derived by considering ensemble activity at a larger spatial scale. A detailed review of the derivation can be found in, e.g., [9]. The basic activity can be formulated in terms of the input-output behavior of synapses, which convert incoming pulses to postsynaptic potentials. In the coarse-grained population model, at time  $t$  and some point  $x$  in the field, ensembles of excitatory and inhibitory chemical synapses respond to incoming pulse activity and yield an effective postsynaptic potential  $V(x, t)$ . In classical models of a homogeneous field, the dynamics of  $V$  can be described by [3]

$$\frac{\partial}{\partial t} V(x, t) + V(x, t) = \bar{\alpha} \int_{\Omega} K(|x - y|) S(V(y, t - |x - y|/v)) dy + I(x, t).$$

Here  $\Omega$  is a spatial domain, which is taken to be the one-dimensional line here. The kernel  $K$  gives the spatial distribution for excitatory and inhibitory synaptic connections. The nonlinear transfer function  $S$  represents the ensemble pulse activity generated by

the effective membrane potential [12] and is monotone increasing. For unimodally distributed firing thresholds of the neurons in the population,  $S$  is typically taken to have a sigmoidal shape [9]. Furthermore,  $I$  is the external stimulus,  $\bar{\alpha}$  represents the synaptic efficacy, and  $v$  is the transmission speed along axons between the population neurons. In this chapter, we extend previous studies of neural populations by considering a distribution of axonal transmission speeds, and thus introducing a speed distribution  $g(v)$  into the above model to obtain

$$\frac{\partial}{\partial t} V(x, t) + V(x, t) = \bar{\alpha} \int g(v) \int_{-\infty}^{\infty} K(|x - y|) S(V(y, t - |z|/v)) dy dv + I(x, t). \quad (18.1)$$

We take  $g$  to be an arbitrary probability density function, that is,  $g(v) \geq 0$  and  $\int g(v) dv = 1$ . Typically, physical considerations impose positive lower and upper bounds,  $v_l$  and  $v_h$ , to biologically possible transmission speeds. In this case, the density  $g$  will be zero outside of the interval  $[v_l, v_h]$ .

## 18.2 Equilibrium Solutions and Bifurcations

We begin the analysis of the model (18.1) by studying its equilibrium solutions and their stability. For the case of a constant input  $I(x, t) \equiv E^*$ , a spatially uniform equilibrium solution  $V(x, t) \equiv V^*$  of (18.1) satisfies the equation

$$V^* = \bar{\alpha} \kappa S(V^*) + E^*, \quad (18.2)$$

where  $\kappa = \int_{-\infty}^{\infty} K(z) dz$ . There may be one or more solutions  $V^*$  satisfying (18.2), depending on the shape of  $S$ . For small variations  $u(x, t) = V(x, t) - V^*$  about any such equilibrium solution, the dynamics are governed by the linear equation

$$\frac{\partial}{\partial t} u(x, t) + u(x, t) = \alpha \int g(v) \int_{-\infty}^{\infty} K(z) u(x + z, t - |z|/v) dz dv, \quad (18.3)$$

where

$$\alpha = \bar{\alpha} S'(V^*) \geq 0. \quad (18.4)$$

Note that by (18.4), the parameter  $\alpha$  contains information about the particular equilibrium solution under study, as well as the value of the external input  $E^*$ , since the latter affects  $\alpha$  through the value of  $V^*$  from (18.2).

Substituting  $u(x, t) = e^{\lambda t} e^{ikx}$  into (18.3), where  $\lambda \in \mathbf{C}$  and  $k \in \mathbf{R}$ , a dispersion relation is obtained between the temporal and spatial modes:

$$\lambda + 1 = \alpha \int g(v) \int_{-\infty}^{\infty} K(z) e^{-\lambda|z|/v} e^{-ikz} dz dv. \quad (18.5)$$

Note that the solution  $\lambda$  has a negative real part for  $\alpha = 0$ , which implies that  $V^*$  is asymptotically stable for  $\alpha = 0$ , and thus also for small  $\alpha$ . If  $\alpha$  increases further,



the stability of the equilibrium solution can be lost as an eigenvalue  $\lambda$  crosses the imaginary axis. At the critical transition, there is an eigenvalue  $\lambda = i\omega$ , with  $\omega \in \mathbf{R}$ . The bifurcating solutions can be qualitatively classified as stationary or oscillatory depending on whether  $\omega = 0$  or  $\omega \neq 0$ , respectively, and as spatially homogeneous or inhomogeneous depending on whether  $k = 0$  or  $k \neq 0$ , respectively.

It is easy to see that stationary bifurcations are independent of the delays introduced by finite propagation speeds. Indeed, letting  $\lambda = 0$  in (18.5) gives

$$\begin{aligned} 1 &= \alpha \int g(v) dv \int_{-\infty}^{\infty} K(z) e^{-ikz} dz \\ &= \alpha \hat{K}(k), \end{aligned} \tag{18.6}$$

where  $\hat{K}$  denotes the Fourier transform of  $K$ . Hence, conditions for stationary bifurcations depend solely on the value of  $\alpha$  and the properties of the kernel  $K$ . In particular, one obtains Turing modes when (18.6) holds for some  $k \neq 0$ . On the other hand, the delays turn out to be important in oscillatory bifurcations [8, 9]. Because of the importance of oscillatory activity in neural processing, the oscillatory bifurcations and their relation to delays is particularly relevant for the present study. Oscillatory bifurcations can be spatially homogeneous ( $\omega \neq 0$  and  $k = 0$ ), corresponding to spatially uniform, or synchronous, oscillations, or spatially inhomogeneous ( $\omega \neq 0$  and  $k \neq 0$ ), corresponding to traveling waves. In the latter case,  $\omega/k$  gives the corresponding wave speed.

### 18.3 Reduced-Order Models

The analysis of the bifurcations by solving (18.5) is difficult in general. In order to obtain results applicable for arbitrary connectivity and speed distributions, we use a perturbation approach. To this end, we introduce the power series expansion

$$u(x+z, t-|z|/v) = \sum_{m=0}^{\infty} \frac{(-|z|/v)^m}{m!} \frac{\partial^m}{\partial t^m} u(x+z, t)$$

into (18.3). The infinite series can be truncated to yield an approximation for the dynamics, and the error committed is small when the transmission speeds are sufficiently large and the connection kernel  $K$  decays sufficiently fast [8]. The advantage gained is that, for the reduced equation obtained by neglecting terms of order  $N+1$  and higher, the relation (18.5) has the form of a polynomial in  $\lambda$ . Namely, one obtains

$$\lambda + 1 = \alpha \sum_{m=0}^N \frac{(-1)^m}{m!} \lambda^m E[v^{-m}] \hat{K}_m(k),$$

where  $E[v^{-m}] = \int v^{-m} g(v) dv$  is the expected value of  $v^{-m}$ , and

$$\hat{K}_m(k) = \int_{-\infty}^{\infty} |z|^m K(z) e^{-ikz} dz$$

denotes the Fourier transforms of the moments of  $K$ . The zeroth moment  $\hat{K}_0$  is simply the Fourier transform of  $K$ , for which we continue using the more conventional notation  $\hat{K}$ . Taking  $N = 0$  is equivalent to neglecting all propagation delays in the field, while  $N = 1$  gives an equation that depends only on the mean value of propagation speeds and not their distribution. The lowest-order approximation that retains the effects of distributed speeds is obtained by taking  $N = 2$ . For this case, the dispersion relation (18.5) reduces to a quadratic equation in  $\lambda$ :

$$p_k(\lambda) = c_2(k)\lambda^2 + c_1(k)\lambda + c_0(k) = 0 \quad (18.7)$$

with coefficients

$$\begin{aligned} c_0(k) &= 1 - \alpha \hat{K}(k) \\ c_1(k) &= 1 + \alpha E[v^{-1}] \hat{K}_1(k) \\ c_2(k) &= -\frac{1}{2} \alpha E[v^{-2}] \hat{K}_2(k). \end{aligned}$$

The analysis of (18.7) gives qualitative information about the behavior of the full dispersion relation (18.5) at nearby parameter values.

The bifurcation conditions are easy to determine for the case  $N = 2$ . Hence, for stationary bifurcations, we see that the pair  $(\lambda, k)$  with  $\lambda = 0$  satisfies (18.7) if and only if

$$\alpha \hat{K}(k) = 1, \quad (18.8)$$

which is the same as (18.6), and is independent of propagation delays. For oscillatory bifurcations, the pair  $(\lambda, k)$  with  $\lambda = i\omega$ ,  $\omega > 0$ , satisfies (18.7) if and only if

$$\alpha E[v^{-1}] \hat{K}_1(k) = -1 \quad (18.9)$$

and

$$\omega^2 = 2 \frac{\alpha \hat{K}_0(k) - 1}{\alpha E[v^{-2}] \hat{K}_2(k)} > 0. \quad (18.10)$$

As noted above, the equilibrium solution is stable for small  $\alpha$ , since the bifurcation conditions (18.8) and (18.9) do not hold. As  $\alpha$  is further increased, stability can be lost through a stationary or oscillatory bifurcation, characterized by the conditions (18.8), (18.9), and (18.10), respectively. Note that in the case of instantaneous signal propagation ( $v = \infty$ ), one has  $E[v^{-1}] = 0$ , and by (18.9) oscillatory bifurcations cannot occur. Thus, stability can be lost through an oscillatory bifurcation only in the case of delayed signal propagation.

## 18.4 Effects of Speed Distributions

In order to study the effects of distributed transmission speeds on the dynamics, we keep the mean value  $E[v^{-1}]$  fixed and change the variance  $\text{Var}[v^{-1}]$ . We consider the

case  $N = 2$ , that is, the simplest reduced model which exhibits the effect of speed distributions. It follows from the conditions (18.8) and (18.9) that the stability of the equilibrium solution is unaffected by the variances, and the bifurcations occur at (approximately) the same parameter values. In particular, the wave number  $k^*$  at bifurcation does not depend on the variance of speed distribution. The main effect of the variances is on the frequency  $\omega$  of oscillatory bifurcations, as given by (18.10). Since  $E[v^{-2}] = \text{Var}[v^{-1}] + E^2[v^{-1}]$ , we see that the frequency  $\omega^*$  at bifurcation will decrease with increasing variance  $\text{Var}[v^{-1}]$ . In the case of bifurcating traveling waves, an increase in  $\omega^*$  corresponds to an increase in the speed  $\omega^*/k^*$  of the waves since  $k^*$  is unaffected by the variance of speeds. We conclude that the spread of the speed distribution affects the frequency of bifurcating oscillatory solutions and the phase speed of traveling waves.

For numerical calculations, we take the spatial domain  $\Omega$  to be the circle with circumference  $C$  (or equivalently the interval  $[0, C]$  with periodic boundary conditions). We choose the connectivity kernel as

$$K(z) = \frac{a_e}{2} e^{-|z|} - \frac{a_i}{2} r e^{-r|z|},$$

where  $r$  denotes the relation of excitatory and inhibitory spatial ranges, and  $a_e$  and  $a_i$  represent excitatory and inhibitory synaptic weights. For instance, when  $r > a_e/a_i$ , the neural field exhibits local inhibition and lateral excitation and thus facilitates traveling waves in the case of a single propagation speed [13]. The transfer function has been chosen as the logistic function  $S(V) = 10/(1 + \exp(-1.8(V - 3.0)))$ . The distribution of propagation speeds is described by the truncated gamma density

$$g(v) = \frac{N_{p,q}}{q^p \Gamma(p)} v^{p-1} \exp(-v/q), \quad p > 2, q > 0$$

in the speed range  $0 < v_l \leq v \leq v_h$ , where  $N_{p,q}$  is the normalization factor arising from the truncation. This choice of  $g(v)$  reflects experimental findings [6, 10, 11]. Fig. 18.2 shows gamma distributions for various  $p$ . It is easy to show that  $g(v)$  has its maximum at  $v_m = q(p - 1)$ ,  $E[v^{-1}] = N_{p,q}/(N_{p-1,q} v_m)$ , and  $\text{Var}[v^{-1}] = N_{p,q}(p - 1) / (N_{p-2,q}(p - 2)v_m^2) - E^2[v^{-1}]$ .

We fix  $q$  as  $q = v_m/(p - 1)$  and thus parametrize the transmission speed distribution by  $p$  and  $v_m$ . We determine the phase speed  $\omega/k$  of bifurcating waves from (18.10). In Fig. 18.3, the resulting phase speed is plotted with respect to  $v_m$  and  $\text{Var}[v^{-1}]$ . It can be seen that the phase speed is lower than  $v_m$  for all speed distribution widths, and it grows roughly linearly with  $v_m$ . This relation of the wave speed and the transmission speed is similar to previous findings for single transmission speeds [8, 13, 14]. In addition, we see here that increasing  $\text{Var}[v - 1]$  decreases the phase speed of the waves; that is, the broader the speed distribution, the lower the resulting phase speed for bifurcating waves.

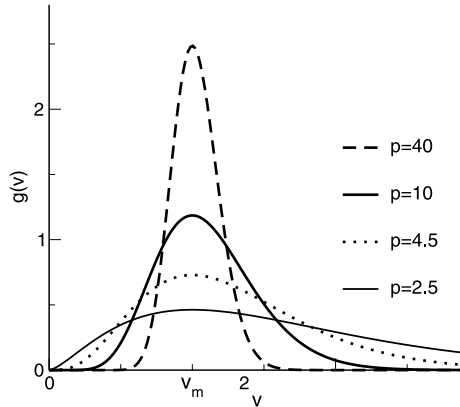


**Fig. 18.2.** Gamma-distributed transmission speeds.

### 18.5 Conclusion

We have introduced transmission speed distributions to the standard neural population model and studied their effects on the stability and bifurcations of equilibrium solutions. An important feature of the analysis is the relation between the connectivities and delays. We have presented an approximation method to gain some insight into this relationship and study the bifurcation structure. The method is applicable to general field connectivities and speed distributions with sufficiently high mean value. As an application, we have shown that the shape of the speed distribution affects the speed of traveling waves and the frequency of synchronous oscillations. For the second-order approximate model derived here, we explicitly calculate the effects of the distribution and show that a larger variance of propagation speeds yields a smaller wave speed for

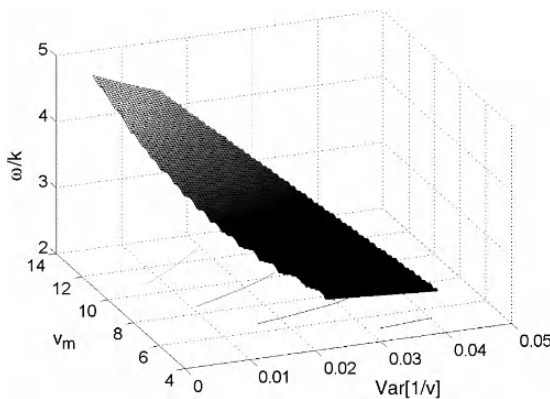


**Fig. 18.3.** The propagation speed of bifurcating traveling waves. The bottom horizontal plane depicts the contour lines for the speed. Parameter values are  $r = 3$ ,  $a_e = 100$ ,  $a_i = 99$ ,  $v_l = 4$ ,  $v_h = 100$ .

traveling waves. Higher-order approximations and global behavior may reveal richer effects. For instance, in the second-order approximation, the stability of the equilibrium is unaffected by the variance of the speed distribution. However, the variance of delays is known to affect stability in several other systems [15, 16], so the possibility is not ruled out that higher-order terms in the approximation may introduce stability changes. We have also neglected some details of the model, such as long-range feedback loops and the corresponding delay distributions; the reader is referred to [17] for a detailed account. At any rate, the result that distributed speeds affect oscillatory dynamics clearly shows the importance of including speed distributions in neural models.

## References

1. Wilson, H.R., Cowan, J.D.: Excitatory and inhibitory interactions in localized populations of model neurons. *Biophys. J.*, **12**, 1–24 (1972).
2. Amari, S.: Dynamics of pattern formation in lateral-inhibition type neural fields. *Biol. Cybernetics*, **27**, 77–87 (1977).
3. Bressloff, P.C., Coombes, S.: Physics of the extended neuron. *Int. J. Mod. Phys. B*, **11**, 2343–2392 (1997).
4. Gerstner, W.: Time structure of the activity in neural network models. *Phys. Rev. E*, **51**, 738–758 (1995).
5. Jirsa, V.K.: Connectivity and dynamics of neural information processing. *Neuroinformatics*, **2**, 183–204 (2004), large review paper.
6. Nunez, P.L.: *Neocortical Dynamics and Human EEG Rhythms*. Oxford University Press, New York, Oxford (1995).
7. Pinto, D.J., Ermentrout, G.B.: Spatially structured activity in synaptically coupled neuronal networks: I. Travelling fronts and pulses. *SIAM J. Appl. Math.*, **62**, 206–225 (2001).
8. Atay, F.M., Hutt, A.: Stability and bifurcations in neural fields with finite propagation speed and general connectivity. *SIAM J. Appl. Math.*, **65**, 644–666 (2005).
9. Hutt, A., Atay, F.M.: Analysis of nonlocal neural fields for both general and gamma-distributed connectivities. *Physica D*, **203**, 30–54 (2005).
10. Bringuier, V., Chavane, F., Glaeser, L., Fregnac, Y.: Horizontal propagation of visual activity in the synaptic integration field of area 17 neurons. *Science*, **283**, 695–699 (1999).
11. Girard, P., Hupe, J.M., Bullier, J.: Feedforward and feedback connections between areas V1 and V2 of the monkey have similar rapid conduction velocities. *J. Neurophysiol.*, **85**, 1328–1331 (2001).
12. Freeman, W.J.: Tutorial on neurobiology: From single neurons to brain chaos. *International Journal of Bifurcation and Chaos*, **2**, 451–482 (1992).
13. Hutt, A., Bestehorn, M., Wennekers, T.: Pattern formation in intracortical neuronal fields. *Network: Comput. Neural Syst.*, **14**, 351–368 (2003).
14. Coombes, S., Lord, G.J., Owen, M.R.: Waves and bumps in neuronal networks with axo-dendritic synaptic interactions. *Physica D*, **178**, 219–241 (2003).
15. Atay, F.M.: Distributed delays facilitate amplitude death of coupled oscillators. *Phys. Rev. Lett.*, **91**, 094101 (2003).
16. Jirsa, V.K., Ding, M.: Will a large complex system with time delays be stable? *Phys. Rev. Lett.*, **93**, 070602 (2004).
17. Atay, F.M., Hutt, A.: Neural fields with distributed transmission speeds and non-local feedback delays. *SIAM J. Appl. Dynamical Systems*, **5**(4), 670–698 (2006).

# Estimation of Differential Entropy for Positive Random Variables and Its Application in Computational Neuroscience

David Hampel

Department of Applied Mathematics, Masaryk University Brno, Janackovo namesti 2a, 662 95 Brno, Czech Republic; 12235@mail.muni.cz

**Summary.** We use the differential entropy concept and methods related to differential entropy estimation in this chapter. In the beginning, we define the basic terms: entropy, differential entropy, the Kullback–Leibler distance and the refractory periods. We show relations between differential entropy and the Kullback–Leibler distance as well.

Hereafter a detailed description of the methods used is given. These methods can be divided into three groups: parametric methods of entropy estimation, “plug-in” entropy estimators based on nonparametric density estimation and direct entropy estimators. The formulas for direct entropy estimation based on the first four sample moments are introduced.

The results are illustrated by comparing the methods of the entropy estimation, combined with two refractory period estimates. We compare the estimates based on the histogram, the kernel density estimator, the sample spacing method, Vasicek’s method, the nearest neighbor distance method and the methods based on sample moments.

**Key words:** Interspike intervals, refractoriness, differential entropy estimation, Kullback–Leibler distance.

## 19.1 Introduction

With the differential entropy concept we can identify (as with frequency characteristics) changes in neuron behavior or compare the behavior of two and more neurons under different experimental situations. For this purpose it is necessary to have a good estimate of the differential entropy. It follows from the definition of the differential entropy that the task is closely related to the problem of how to identify a probability density function from sampled realizations of a random variable. The estimates of the differential entropy can be used for calculating the Kullback–Leibler distance, which finally reflects the changes in the neuronal behavior.

When the neuronal activity is recorded, the interspike intervals (ISIs) are registered. These can be considered as realizations of an independent positive random variable  $x_1, \dots, x_n$ , for which the entropy has to be estimated. Taking into account refractoriness in neuronal firing, this positive random variable is shifted for an unknown

constant. Thus, this shift has to be estimated as well. Primarily, we are interested in how the refractoriness affects the estimate of the differential entropy.

## 19.2 The Theory

We first define the basic terms of this chapter. We define the entropy of a random variable  $X$  with a probability mass function  $p(x) = P(X = x)$ ,  $x \in \mathcal{X}$  by

$$H(X) = - \sum_{x \in \mathcal{X}} p(x) \log_2 p(x). \quad (19.1)$$

The entropy is measured in bits (see [2]). The entropy  $H(X)$  measures the “randomness” of the distribution. For example, if we have a Bernoulli distribution with parameter  $p = 0.5$ , we have the biggest uncertainty as to what can happen. The entropy is maximized in this situation. If we set parameter  $p$  to 0 or 1, we have sureness as to what can happen and the entropy is minimized in this situation (it is equal to 0).

An extension for a continuous distribution can be proposed; in addition the usage of the natural logarithm is common. Thus, what we call the differential entropy is given as

$$H(f) = - \int_S f(x) \ln f(x) dx, \quad (19.2)$$

where  $S$  is a support of the density  $f(x)$  (see [2]). The differential entropy can be expressed by using the distribution function  $F(x) = P(X \leq x)$  (see [6]) as

$$H(f) = \int_0^1 \ln \left\{ \frac{d}{dp} F^{-1}(p) \right\} dp. \quad (19.3)$$

Later in the chapter we will use the term “entropy” in the sense of “differential entropy.”

An exponential distribution maximizes the differential entropy among all densities with the same support and the same mean value. We can say that exponentially distributed ISIs are generated in “the most stochastic” manner. This situation can be interpreted as a “state of idle communication” between neurons; only a minimum of information is transported and the receiving neuron is kept in “maximal attention.”

Although the equation (19.2) seems like an analogy of (19.1), the interpretation and the properties of the differential entropy are a little different (for example, differential entropy can be negative). To avoid difficulties connected with differential entropy interpretation the Kullback–Leibler (K–L) information distance between densities  $f$  and  $g$  is defined as

$$KL(f, g) = \int_0^\infty f(t) \ln \frac{f(t)}{g(t)} dt. \quad (19.4)$$

The K–L distance is a “measure” of similarity between two densities. It is nonnegative. When support  $g$  contains support  $f$ , the K–L distance is finite (see [2], [4]).

The distance between the densities defined on the positive half line and the exponential density plays a significant role in the K–L distance interpretation. The K–L distance between exponential density  $f_e$  with parameter  $\lambda$  and density  $f$  can be expressed from (19.4) as

$$KL(f, f_e) = \lambda E(X) - \ln \lambda - H(f), \tag{19.5}$$

where  $E(X)$  is the mean value of the distribution with density function  $f(x)$ . This expression can be interpreted as a “measure of randomness reduction” or a “measure of information gain” in comparison with idle communication.

If the means of densities  $f$  and  $f_e$  are the same ( $E(X) = E(X_e) = \frac{1}{\lambda}$ ), we get from (19.5)

$$KL(f, f_e) = 1 - \ln \lambda - H(f) = H(f_e) - H(f). \tag{19.6}$$

This means that the problem of how to determine the K–L distance is reduced to differential entropy determination in this case (due to [4]).

According to physiological models we cannot suppose that a neuron can fire for a short time after the spike. This property is called “refractoriness.” An absolute refractory period begins after the spike generation, when it is impossible to emit a spike under even a strong stimulus. Then begins a relative refractory period, when the spike can be emitted for an extremely strong stimulus only.

So, ISIs cannot be arbitrarily small, but they should have a minimal duration  $\Delta > 0$ . From a statistical point of view we can say that the density describing ISIs will be positive on the interval  $(\Delta, \infty)$ , not  $(0, \infty)$ .

### 19.3 The Methods

It is possible to benefit from the relations between (19.1) and (19.2). We can use approximate techniques for differential entropy estimation based on sampling (see Paninsky, L. 2003, Estimation of entropy and mutual information. *Neural Comput.* 15, 6, pp. 1191–1253). We don’t use such techniques for our differential entropy estimation problem; we are interested in the following groups of methods, which are directly intended for differential entropy estimation.

#### 19.3.1 Parametric Methods

Under the assumption about the distribution of ISIs we estimate its parameters  $\theta_1, \dots, \theta_k$  (most often by the maximum likelihood method). By using them and the equation (19.2) we can calculate the entropy estimation analytically or numerically from the expression

$$\hat{H}(f) = - \int_S \hat{f}(x) \ln \hat{f}(x) dx, \tag{19.7}$$

where  $\hat{f}(x)$  is a density estimator  $f(x, \hat{\theta}_1, \dots, \hat{\theta}_k)$ . The parametric estimate will be good in the case when the assumption about the distribution is correct.



### 19.3.2 Plug-In Estimators

If we cannot say anything about the ISI distribution, we can use one of the nonparametric methods. Instead of using parameters of distribution, we will estimate the density directly. The entropy estimation will be obtained from (19.7) again. For this purpose we can use the histograms

$$\hat{f}_{\text{hist}}(x) = \sum_{j=2}^m \frac{1}{nd_{j-1}} I_{[t_{j-1}, t_j)}(x) \left[ \sum_{i=1}^n I_{[t_{j-1}, t_j)}(x_i) \right] + \frac{1}{nd_m} I_{[t_m, t_{m+1})}(x) \left[ \sum_{i=1}^n I_{[t_m, t_{m+1})}(x_i) \right], \quad x \in \mathcal{R} \quad (19.8)$$

with  $m$  equidistant or nonequidistant dividing subintervals of length  $d_j, j = 1, \dots, m$ , with borders  $t_1 < t_2 < \dots < t_m < t_{m+1}$ . The index function  $I_{[a,b)}(x)$  is defined as

$$I_{[a,b)}(x) = \begin{cases} 1 & \text{for } x \in [a, b), \\ 0 & \text{for } x \notin [a, b). \end{cases} \quad (19.9)$$

The histogram construction requires the setting of at least three constants: two borders and the number of dividing subintervals. According to previous simulation studies<sup>1</sup> we can say that the best results for the plug-in histogram estimator were reached with the histogram with nonequidistant dividing subintervals. The number of these subintervals is equal to the biggest  $m$  for which the following holds:

$$2[n/m] > n - [n/m](m - 1), \quad (19.10)$$

where  $n$  is the number of observations and  $[c]$  denotes the whole part of the real number  $c$  (for 50 observations  $m = 8$ , for 250  $m = 18$ , for 1250  $m = 42$ ). The number of the observations in particular subintervals is the same, except in the last subinterval. The histogram is constructed on the interval  $[\min(X), \max(X)]$  or a similar interval.

More sophisticated are the kernel estimators,

$$\hat{f}_{\text{kern}}(x) = \frac{1}{nh} \sum_{i=1}^n K \left( \frac{x - x_i}{h} \right) \quad x \in \mathcal{R}, \quad (19.11)$$

where the function  $K$  is the kernel. The kernel function  $K : \mathcal{R} \rightarrow (0, \infty)$  is symmetric and bounded and

$$\int_{-\infty}^{\infty} K(x) dx = 1 \quad \text{and} \quad \lim_{x \rightarrow \pm\infty} |x|K(x) = 0. \quad (19.12)$$

---

<sup>1</sup> We explored the dependence of particular methods of entropy estimation on selected parameters (histogram: number of dividing intervals, latitude of dividing intervals, borders of histogram; kernel estimates: smoothing parameter, type of kernel).

We have to choose the proper kernel as well as the most suitable constant  $h$ . This constant essentially affects the quality (accuracy) of the kernel estimate of the density. In practice, we can solve this problem using the cross-validation method. We are looking for the constant  $h$ , which maximizes likelihood  $L(h) = \prod_{i=1}^n f_i(x_i)$ , where

$$f_i(x) = \frac{1}{nh} \sum_{(j=1), (j \neq i)}^n K\left(\frac{x - x_j}{h}\right) \quad x \in \mathcal{R} \tag{19.13}$$

and we get  $h$  as the optimal kernel width.

A further possibility is to use the moment-based density estimators. We use the notation from [3] for their introduction. Let  $f(x)$  be a density function with mean value  $\mu$ , dispersion  $\sigma^2$ , skewness  $\gamma_1$ , kurtosis  $\gamma_2$  and cumulants  $\kappa_1, \kappa_2, \dots$ . Then function

$$c(x) = \exp\left[\sum_{j=1}^{\infty} \frac{e_j(-D)^j}{j!}\right] f(x), \tag{19.14}$$

where  $e_j$  are constants depending on a particular  $f(x)$ ,  $D$  is a differential operator and  $D^j f(x) = \partial^j f(x)/\partial x^j$ , will have cumulants  $\kappa_1 + e_1, \kappa_2 + e_2, \dots$ .

When using (19.14) the exponential must be expanded in a series as

$$\exp\left[\sum_{j=1}^{\infty} \frac{e_j(-D)^j}{j!}\right] \approx \sum_{i=0}^{\infty} \frac{\left[\sum_{j=1}^{\infty} \frac{e_j(-D)^j}{j!}\right]^i}{i!}. \tag{19.15}$$

Using the standardized quantity  $y = (x - \mu)/\sigma$  and the normal density as  $f(x)$  we get  $e_1 = 0, e_2 = 0, e_3 = \gamma_1$  and  $e_4 = \gamma_2$ .

Finally, when we make the summation for  $j = 1, 2, 3, 4$  and  $i = 0, 1$ , using the standardized quantity  $y$  and the density of normal distribution as  $f(x)$  in the right side of equation (19.15), we get the Gram–Charlier density estimate

$$\hat{f}_{GC}(y) = (2\pi)^{-\frac{1}{2}} e^{-\frac{1}{2}y^2} \left[1 + \frac{\gamma_1}{6}(y^3 - 3y) + \frac{\gamma_2}{24}(y^4 - 6y^2 + 3)\right]. \tag{19.16}$$

Further, the Edgeworth density estimate will be obtained by summation over  $j = 1, 2, 3, 4, i = 0, 1, 2$ , using the standardized quantity  $y$  and the density of normal distribution as  $f(x)$ . In addition, we leave out members of order less than  $1/n$  in the expansion series. We express the Edgeworth estimate as

$$\begin{aligned} \hat{f}_{\text{Edg}}(y) &= (2\pi)^{-\frac{1}{2}} e^{-\frac{1}{2}y^2} \\ &\times \left[1 + \frac{\gamma_1}{6}(y^3 - 3y) + \frac{\gamma_2}{24}(y^4 - 6y^2 + 3) + \frac{\gamma_1^2}{72}(y^6 - 15y^4 + 45y^2 - 15)\right]. \end{aligned} \tag{19.17}$$

In general, the Edgeworth density estimate is not better than the Gram–Charlier density estimate. With a knowledge of  $\mu, \sigma, \gamma_1$  and  $\gamma_2$ , we can approximate  $f(x)$  as

$$f(x) \approx \frac{1}{\sigma} \hat{f} \left( \frac{x - \mu}{\sigma} \right), \tag{19.18}$$

where for  $\hat{f}$  we use (19.16) or (19.17).

It is possible to construct estimates based on distributions different from normal. For an ISI distribution, we have supposed the gamma distribution will be a good base for moment estimates of the ISI's density, because it is defined on  $(0, \infty)$  as well as the distributions we are interested in. In addition, in [5] it is stated that we can approximate many models of ISIs very well by the gamma distribution. Unfortunately, these estimates are very sensitive to the estimates of the moments, so we cannot use them because of the relatively small number of observations.

### 19.3.3 Direct Entropy Estimators

As the first estimator of this sort, we have the “sample-spacing” estimator. Suppose  $x_{[1]}, \dots, x_{[n]}$  are a realization of order statistics  $(x_{[1]} < \dots < x_{[n]})$  corresponding to  $x_1, \dots, x_n$ . Then  $x_{[i+m]} - x_{[i]}$  is called a spacing of order  $m$  or  $m$ -spacing ( $1 \leq i < i + m \leq n$ ). Depending on these spacings we can construct an  $m$ -spacing entropy estimator for  $m$  fixed as

$$H_s = \frac{1}{n} \sum_{i=1}^{n-m} \ln \left( \frac{n}{m} (x_{[i+m]} - x_{[i]}) \right) - \psi(m) + \ln m, \tag{19.19}$$

where  $\psi(m) = -(\ln \Gamma(m))'$  is the digamma function. This entropy estimator is consistent under some conditions (see [1]).

Next from the group of direct estimate methods we have Vasicek's entropy estimators. The estimator of (19.3) can be constructed by substituting empirical distribution function  $F_n$  instead of distribution function  $F$  and using the difference operator in place of the differential operator. The derivative of  $F^{-1}(p)$  is then estimated by  $(x_{[i+m]} - x_{[i-m]})n/(2m)$  for  $(i - 1)/n < p \leq i/n, i = m + 1, m + 2, \dots, n - m$ , where  $m$  is a positive integer smaller than  $n/2$ . One-sided differences of type  $x_{[i+m]} - x_{[1]}$  or  $x_{[n]} - x_{[i-m]}$  are used in place of  $x_{[i+m]} - x_{[i-m]}$  when  $p \leq m/n$  respectively  $p > (n - m)/n$ . This produces estimate  $H_V$  of entropy  $H(f)$ ,

$$H_V = n^{-1} \sum_{i=1}^n \ln \{ (x_{[i+m]} - x_{[i-m]})n/(2m) \}, \tag{19.20}$$

where  $x_{[i]} = x_{[1]}, i < 1$  and  $x_{[i]} = x_{[n]}, i > n$ . Vasicek in [6] transcribes this sum into three components, shows their properties and due to bias elimination recommends the modified estimator

$$H'_V = H_V - \left( \ln n - \ln 2m + \left( 1 - \frac{2m}{n} \right) \psi(2m) - \psi(n + 1) + \frac{2}{n} \sum_{i=1}^m \psi(i + m - 1) \right), \tag{19.21}$$

where  $m$  is small, maximally equal to  $n/2$ .

The next of the direct estimators is the nearest neighbor distance estimator. Let  $\rho_{n,i}$  be the distance from  $x_i$  to its nearest neighbor,  $\rho_{n,i} = \min_{j \neq i, j \leq n} |x_i - x_j|$ . Entropy estimation depending on the nearest neighbor distance is defined as

$$H_n = \frac{1}{n} \sum_{i=1}^n \ln(n\rho_{n,i}) + \ln 2 + C_E, \tag{19.22}$$

where  $C_E$  is the Euler constant  $C_E = -\int_0^\infty e^{-t} \ln t dt (\approx 0.577215)$ . A similar estimator is described in the paper: Kozachenko, L. F., Leonenko, L., Sample estimate of the entropy of a random vector, *Problems of Information Transmission*, 23, 95–101 (1987).

As the last method of the group of direct entropy estimation methods we introduce exact formulas derived from the Gram–Charlier and the Edgeworth concept (19.16) and (19.17). The expression based on the Gram–Charlier expansion is denoted below. At first we identify

$$\begin{aligned} A_1 &= \frac{1}{4}(1 + \ln(2\pi\sigma^2)) \left( 1 + \operatorname{erf} \left( \frac{\mu}{\sqrt{2}\sigma} \right) \right), \\ A_2 &= \frac{-\gamma_1(8\sigma^5 + 4\mu^4\sigma + 4\mu^2\sigma^3) + \gamma_2(\mu^5 - \mu^3\sigma^2) + 24\mu\sigma^4}{\sigma^5} \\ &\quad + \frac{\ln(2\pi\sigma^2)(\gamma_1 4(\sigma^3 - \mu^2\sigma) + \gamma_2(\mu^3 - 3\mu\sigma^2))}{\sigma^3}, \\ A_3 &= \frac{\gamma_1}{12} \frac{\mu^2 - \sigma^2}{\sigma^2} - \frac{\gamma_1^2 \mu}{72} \frac{\mu^4 - 10\mu^2\sigma^2 + 15\sigma^4}{\sigma^5} - \frac{\gamma_2 \mu}{48} \frac{-3\sigma^2 + \mu^2}{\sigma^3} \\ &\quad + \frac{\gamma_1 \gamma_2}{144} \frac{45\sigma^4 \mu^2 + \mu^6 - 15\sigma^2 \mu^4 - 15\sigma^6}{\sigma^6} \\ &\quad - \frac{\gamma_2^2 \mu}{1152} \frac{105\sigma^4 \mu^2 - 105\sigma^6 + \mu^6 - 21\sigma^2 \mu^4}{\sigma^7}, \\ A_4 &= \exp \left( -\frac{\mu^2}{2\sigma^2} \right) \sqrt{\frac{2}{\pi}}, \end{aligned}$$

where

$$\operatorname{erf}(x) = \frac{2}{\sqrt{\pi}} \int_0^x e^{-t^2} dt. \tag{19.23}$$

Now the estimator based on the Gram–Charlier expansion can be expressed as

$$E_{GC} = A_1 - A_4 \left( \frac{A_2}{96} + A_3 \right). \tag{19.24}$$

The expression based on the Edgeworth expansion is identified by

$$\begin{aligned}
A_1 &= \frac{1}{4}(1 + \ln(2\pi\sigma^2)) \left( 1 + \operatorname{erf} \left( \frac{\mu}{\sqrt{2}\sigma} \right) \right), \\
A_2 &= \frac{\gamma_1}{12} \frac{\mu^2 - \sigma^2}{\sigma^2} - \frac{\gamma_1^2 \mu}{72} \frac{\mu^4 - 10\mu^2\sigma^2 + 15\sigma^4}{\sigma^5} \\
&\quad - \frac{\gamma_2 \mu}{48} \frac{-3\sigma^2 + \mu^2}{\sigma^3} + \frac{\gamma_1 \gamma_2}{144} \frac{45\sigma^4 \mu^2 + \mu^6 - 15\sigma^2 \mu^4 - 15\sigma^6}{\sigma^6} \\
&\quad - \frac{\gamma_2^2 \mu}{1152} \frac{105\sigma^4 \mu^2 - 105\sigma^6 + \mu^6 - 21\sigma^2 \mu^4}{\sigma^7} \\
&\quad + \frac{\gamma_1^3}{864} \frac{105\sigma^8 - 28\mu^6 \sigma^2 + 210\mu^4 \sigma^4 - 420\mu^2 \sigma^6}{\sigma^8} \\
&\quad - \frac{\gamma_1^2 \gamma_2}{3456} \frac{-36\mu^6 \sigma^2 + 378\mu^4 \sigma^4 - 1260\mu^2 \sigma^6 + 945\sigma^8 + \mu^8}{\sigma^9}, \\
A_3 &= \frac{\ln(2\pi\sigma^2)(\gamma_1^2(10\mu^3\sigma^2 - \mu^5 - 15\mu\sigma^4))}{\sigma^5} \\
&\quad + \frac{\gamma_2(-3\mu^3\sigma^2 + 9\mu\sigma^4) + 12\gamma_1(\mu^2\sigma^3 - \sigma^5)}{\sigma^5}, \\
A_4 &= \frac{72\sigma^6\mu + \gamma_1^2(5\mu^3\sigma^4 - 8\mu^5\sigma^2 + \mu^7) + 3\gamma_2(\mu^5\sigma^2 - \mu^3\sigma^4)}{\sigma^7} \\
&\quad - \frac{12\gamma_1(\mu^2\sigma^5 + 2\sigma^7 + \mu^4\sigma^3)}{\sigma^7}, \\
A_5 &= \exp \left( -\frac{\mu^2}{2\sigma^2} \right) \sqrt{\frac{2}{\pi}},
\end{aligned}$$

and finally

$$E_{\text{Edg}} = A_1 + A_5 \left( \frac{1}{288}(A_3 - A_4) - A_2 \right). \quad (19.25)$$

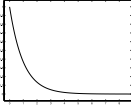
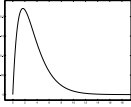
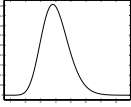
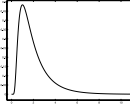
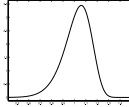
The formulas are long but computationally fast. Both are assigned for the densities on positive half line. They are not unbiased, but the error is negligible. We tested these formulas on a wide range of distributions. We got very good results for distributions with the coefficient of variation  $CV < 0.8$  except for the inverse Gaussian distribution. The results for this distribution are not very good in the ranges  $CV < 0.05$  and  $0.55 < CV < 0.8$ , but for  $0.05 < CV < 0.55$  we get very good results.

## 19.4 Analysis of Simulated Data

Now we compare 12 methods of entropy estimation combined with two refractory period estimates

$$\tilde{\Delta} = \min(X) \quad (19.26)$$

**Table 19.1.** Distributions used for generating simulations: exponential, gamma, inverse Gauss and Weibull distributions.

Distribution	Exp(1)	Gam.(0.6,2)	Gam.(5,20)	Inv.Gauss(2,4)	Weib.(0.5,10)
Graph of density					
CV	1	0.7071	0.2236	0.7071	0.1203
Entropy	1	2.0880	1.2905	1.4556	-0.7138

and

$$\hat{\Delta} = \max \left\{ \min(X) - \sqrt{\frac{\widehat{\text{var}}(X)}{n}}, 0 \right\}. \tag{19.27}$$

The density estimation based methods use the density renormalized on the desired interval. We use shift  $0.3 \times \text{mean}$  value. We have 10 repetitions with 50 or 250 observations. As a comparative criterion we use the mean square error. The simulations were generated from the distributions in Table 19.1.

The following entropy estimation methods are used:

1. Parametric. Using maximum likelihood method, we calculate distribution parameters and then entropy estimation by (19.7). We suppose the distribution type is known.
2. Plug-in: Histogram. We use histogram (19.8) constructed according to the rule (19.10) on the interval  $[\min(X), \max(X)]$ .
3. Plug-in: Histogram. Like the method above, but on the interval  $[\max\{\min(X) - (\widehat{\text{std}}(X)/\sqrt{n}), 0\}, \max(X) + (\widehat{\text{std}}(X)/\sqrt{n})]$ .
4. Plug-in kernel estimate based on (19.11). We use often-used Epanechnikov kernel  $((3/4)(1 - x^2)$  for  $x \in [-1, 1]$  and 0 elsewhere), smoothing parameter is determined via cross-validation method.
5. Plug-in estimate based on the Edgeworth density estimation (19.17).
6. Plug-in estimate based on the Gram–Charlier density estimation (19.16).
7. Direct estimate based on “sample-spacings” (19.19). We use  $m = 1$ .
8. Direct: The Vasicek estimate (19.20). We use  $m = 6$  for 50 observations and  $m = 13$  for 250 observations.
9. Direct: The improved Vasicek estimate (19.21). We use  $m = 4$ .
10. Direct estimate based on nearest neighbor distance (19.22).
11. Direct moment estimate based on the Gram–Charlier concept (19.24).
12. Direct moment estimate based on the Edgeworth concept (19.25).

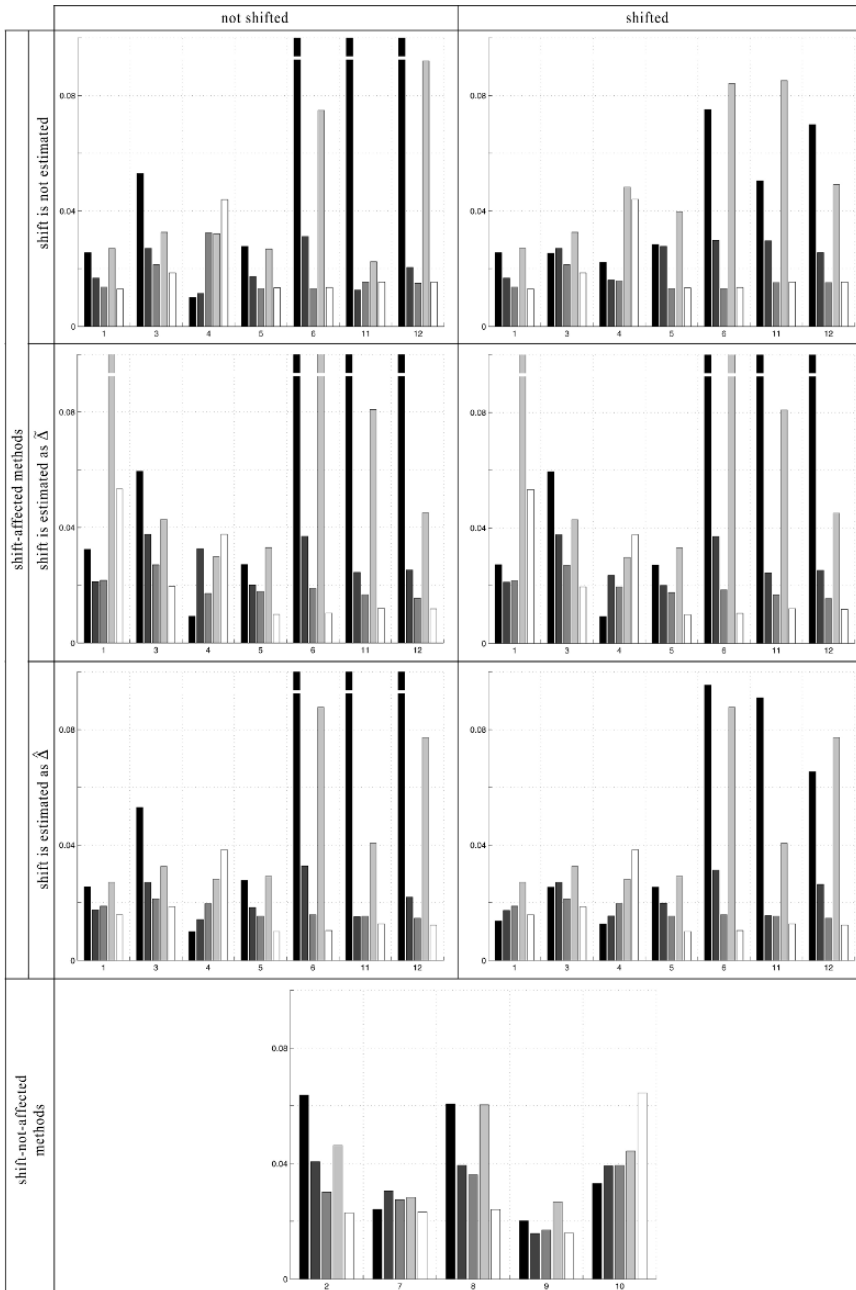


**Fig. 19.1.** The comparison of mean squared error for entropy estimation methods. We use 50 valued simulations from Table 19.1. Black columns are used for exponential distribution, dark gray for gamma(0.6,2), gray for gamma(5,20), light gray for the inverse Gaussian and white for the Weibull distribution. The numbers under the bars denote methods described above.

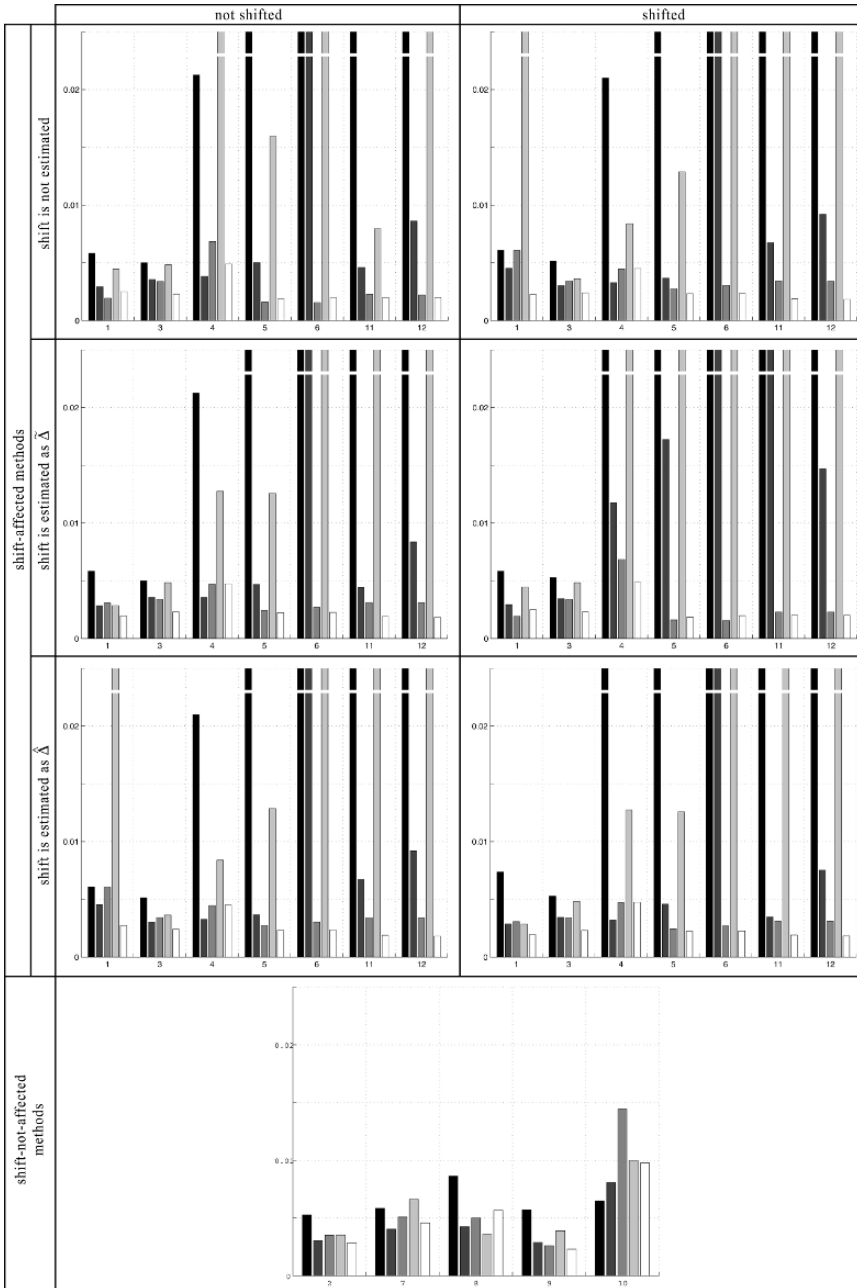


**Fig. 19.2.** The comparison of mean squared error for entropy estimation methods. We use 250 valued simulations from Table 19.1. Black columns are used for exponential distribution, dark gray for gamma(0.6,2), gray for gamma(5,20), light gray for the inverse Gaussian and white for the Weibull distribution. The numbers under the bars denote methods described above.



In our work, we can differentiate among six situations: We have no shift and we don't estimate it or estimate it by  $\tilde{\Delta}$  or by the  $\hat{\Delta}$  estimator; we have shifted data and again we don't estimate it or estimate it by  $\tilde{\Delta}$  or by the  $\hat{\Delta}$  estimator. Of course, there is the group of methods which are shift independent.

## 19.5 Results

In Fig. 19.1 and 19.2 there are results depicted for 50 valued simulations and 250 valued simulations. From these figures, we can state the following conclusions:

- The direct moment estimate based on the Gram–Charlier concept gives results as good as those of the parametric estimate and other good estimates, but for distributions with CV ranges given in Section 19.3.3 only. We obtain good estimates for the 50-valued sample as well. This estimate is strongly shift-affected. Analogously, the estimate based on Edgeworth's concept is a bit worse in general.
- The histogram constructed according to rule (19.10) gives asymptotically good results. There is not a significant difference between the methods marked 2 and 3.
- The improved Vasicek estimate seems to be the best estimate of entropy of all the mentioned methods.
- Shift estimator  $\min(X)$  is too rough (the real shift is overestimated) and may cause marked degradation of the entropy estimation. The estimator (19.27) reduces this overestimation and can improve mainly density-based entropy estimation methods except for the cases of exponential distribution and some parameter combinations of the inverse Gaussian distribution.

## References

1. Beirlant, J., Dudewicz, E. J., Györfi, L., van der Meulen, E. C.: Nonparametric entropy estimation: an overview. *Int. J. Math. Stat. Sci.*, **6**, 17–39 (1997).
2. Cover, T. M., Thomas, J. A.: *Elements of Information Theory*. John Wiley & Sons, New York (1991).
3. Johnson, N. L., Kotz, S.: *Distributions in Statistics—Continuous Univariate Distributions—1*. John Wiley & Sons, New York (1970).
4. Kostal, L., Lansky, P.: Similarity of interspike interval distributions and information gain in stationary neuronal firing. *Biol. Cybernet.*, **94(2)**, 157–167 (2006).
5. Reeke, G. N., Coop, A. D.: Estimating the temporal interval entropy of neuronal discharge. *Neural Computation*, Massachusetts Institute of Technology, **16**, 941–970 (2004).
6. Vasicek, O.: A test for normality based on sample entropy. *J. Statist. Soc. B*, **38**, 54–59 (1976).

## Dynamics of Integrate-and-Fire Models

Joanna Tyrcha

Department of Mathematical Statistics, Institute of Mathematics, Stockholm University, S-106 91 Stockholm, Sweden; joanna@math.su.se

**Summary.** A model for the generation of action potentials by a neuron is presented. This model is based on standard and commonly accepted properties of excitable cells (neurons). The novelty is that under quite natural assumptions the generation of action potentials is described as a special case of a general model for systems generating recurrent biological events. A formula for a density function of the membrane potential distribution in the firing times of the neuron is derived. An analysis of time intervals between spikes is of special interest. Three different interspike interval distributions are found, where one of them is close to the stable distribution. It is consistent with the well-known hypothesis that stable interspike intervals form part of the neural chain in which information is being preserved.

**Key words:** Neuron, action potential, interspike intervals, integrate-and-fire model.

### 20.1 Introduction

Integrate-and-fire models have enjoyed great popularity in the modelling of many types of biological processes where there is evidence that some state variable must reach a threshold before an event is initiated. One of the many research domains where these models have been highly utilized is a brain and nerve system, particularly ion channel dynamics.

Ion channels are found in all cell membranes. They are believed to be the molecular basis, at the cellular level, for excitability in many tissues, especially nerve and muscle. The theoretical foundations for our present understanding of nerve membrane ion currents were laid down by Hodgkin and Huxley [5]. Their ideas determined experimental approaches before the development of the patch-clamp technique of Neher and Sakmann [12], which permitted the possibility of measuring ion currents through individual ion channels. From this time on, many detailed conductance neuron models, sometimes termed Hodgkin–Huxley models, were developed. Unfortunately, because of their intrinsic complexity, these models are usually difficult to analyse and are computationally expensive in numerical implementations. For this reason, simple phenomenological spiking neuron models such as integrate-and-fire models [2,4,7,8,15,16] are in high use. In formal spiking neuron models, action potentials

are generated by a threshold process. The neuron fires whenever the membrane potential of the neuron reaches a threshold.

We present a model for the generation of action potentials by a neuron which is not based on the classical integrate and fire models [2,4,7,8,15,16] but is some special case of a general model for systems generating recurrent biological events [9]. We derive a formula for a density function of the membrane potential distribution in the firing times of the neuron. We are especially interested in an analysis of the time intervals between spikes (interspike intervals). Depending on different assumptions in our model, we consider different distribution functions of interspike intervals.

The chapter is organized as follows. In Section 20.2 we present a general model for systems generating recurrent biological events [9]. In Section 20.3 we define a model for the generation of action potentials by a neuron and show how it is related to the general model described in Section 20.2. Section 20.4 contains an analysis of interspike intervals in the action potentials model. Depending on specific assumptions in the action potentials model, we find three different interspike interval distributions and show that one of them is close to a stable distribution. The idea of a stable interspike intervals distribution was first proposed by Holden [6]. He suggested that neurons with stable interspike intervals form part of the neural chain in which information is being preserved. We present his ideas in Section 20.5.

## 20.2 A Model for Systems Generating Recurrent Biological Events

We consider a biological system that produces events. We assume that, in addition to the usual laboratory (clock) time  $t$ , the system also has an internal physiological time that resets from the value  $\tau$ . When an event appears, the physiological time resets from the value  $\tau = \tau_{\max}$  to  $\tau = 0$ . The rate of maturation  $d\tau/dt$  depends on the amount of an activator  $a$ , i.e.,

$$\frac{d\tau}{dt} = \phi(a), \quad \phi \geq 0. \quad (20.1)$$

We further assume that the activator is produced by a dynamics described by the solution to the differential equation

$$\frac{da}{dt} = g(a), \quad g \geq 0. \quad (20.2)$$

The solution of (20.2) satisfying the initial condition  $a(0) = r$  is denoted by  $a(t) = \Pi(t, r)$ , and we assume that it is defined for all  $t \geq 0$ .

When an event is produced at a time  $\tau = \tau_{\max}$  and an activator level  $a_{\max}$ , then a portion  $\delta(a_{\max})$  of  $a_{\max}$  is consumed in the production of the event. Thus after the event the activator resets to the level

$$a = a_{\max} - \epsilon(a_{\max}). \quad (20.3)$$

We assume that this function is invertible and denote its inversion by  $\lambda$ . We also assume that the survival function of  $\tau_{\max}$  is independent of the initial value of the activator.

With these assumptions, we can derive a recurrence relation for the values of the activator at times when events occur [9], namely

$$a_{n+1} = \lambda^{-1}(Q^{-1}(Q(a_n) + \tau_n)) \quad n = 0, 1, \dots, \quad (20.4)$$

where

$$Q(z) = \int_0^z q(y)dy, \quad q(y) = \frac{\phi(y)}{g(y)}.$$

By assumption,  $a_n$  and  $\tau_n$  are independent and thus we may consider (20.4) as a discrete time dynamical system with stochastic perturbations by  $\tau_n$ . The behaviour of this system from a statistical point of view may be described by the sequence of distributions

$$F_n(x) = \text{Prob}(a_n < x)$$

for  $n = 0, 1, \dots$  and their densities. The recurrence formula for the densities  $f_n = dF_n/dx$  appears as follows:

$$f_{n+1}(x) = \lambda'(x)q(\lambda(x)) \int_0^{\lambda(x)} h(Q(\lambda(x)) - Q(y))f_n(y)dy,$$

where  $h$  is the density function of the distribution of  $\tau_n$ . Introducing the operator  $P$  defined by

$$Pf(x) = \int_0^{\lambda(x)} \left( -\frac{\partial}{\partial x} H(Q(\lambda(x)) - Q(y)) \right) f(y)dy, \quad (20.5)$$

we may write these relations in the more abbreviated forms  $f_{n+1} = Pf_n$  and  $f_n = P^n f_0$  ( $H$  is the survival function of the distribution of  $\tau_n$ ). Under some simple regularity conditions concerning  $\lambda$ ,  $Q$  and  $H$ , equation (20.5) defines a Markov operator on the space  $L^1(R_+)$  of all integrable functions defined on the half line  $R_+ = [0, \infty)$ . These assumptions are formulated in the paper [9] where we also examined the convergence properties of the  $f_n$  densities.

In the next section we will show how the presented model could be used for modelling of action potential generation by a neuron.

### 20.3 A Model for Action Potential Generation

We consider a single cell subject to a time invariant depolarizing current  $I$ , derived either from an external source or internally if the cell is a pacemaker cell. In the absence of any depolarizing input, the membrane potential  $V$  will spontaneously return to the resting potential if perturbed from that point. In the presence of the current  $I$ , the membrane potential is assumed to have dynamics described by

$$\frac{dV}{dt} = \bar{V} - G(V), \quad (20.6)$$

where  $\bar{V}$  is the constant depolarizing potential induced by the current  $I$ , and  $G(V)$  is directly related to the nonlinear voltage-dependent ionic currents through the membrane [9].

With some other natural assumptions, the generation of action potentials can be described as a special case of equation (20.4) with  $\tau_n$  exponentially distributed. The activator of our general model is identified now with the membrane potential  $a(t) = V(t)$ . Thus, equation (20.6) can be written in the form

$$\frac{dV}{dt} = g(V)$$

with  $g(V) = \bar{V} - G(V)$ . If we assume a linear approximation, then it would be

$$\frac{dV}{dt} = \bar{V} - kV.$$

Because of the nature of  $G(V)$ , there is a unique positive value of  $V = V_M$ , such that  $g(V_M) = 0$  (in the linear case  $V_M = \bar{V}/k$ ). We assume that during an action potential there is a sequence of channel openings and closings so the membrane potential resets by a constant amount  $V_R$ , i.e.,

$$\lambda^{-1}(x) = x - V_R, \quad V_R > 0.$$

The form of the function  $\phi$  is  $\phi(x) = 0$  for  $x < V_T$ ,  $\phi(x) > 0$  for  $x \geq V_T$  where  $V_T$  is a constant threshold such that  $V_T > V_R$ .

Using these assumptions, it was shown that [9]:

- there is a minimum period of time between action potentials (known as a refractory period);
- the correlation coefficient between successive interspike intervals ( $\Delta t_n$ ) is negative;
- the correlation coefficient becomes small when the mean of  $\Delta t_n$  becomes large;
- the recurrence relation becomes

$$V_{n+1} = Q^{-1}(\tau_n) - V_R, \quad n = 0, 1, \dots, \quad (20.7)$$

where

$$Q(x) = \begin{cases} 0 & 0 \leq x < V_T \\ \int_{V_T}^x q(y)dy & V_T \leq x \leq V_M, \end{cases}$$

$q(y) = \phi(y)/g(y)$  and the internal times  $\tau_n$  are distributed with the exponential density  $e^{-x}$ .

## 20.4 Distributions of Interspike Intervals

If the densities  $f_n$  in our general model are given, then it is easy to find the density function of the distribution of the interevent intervals, i.e., the time intervals  $\Delta t_n =$

$t_{n+1} - t_n$  between the  $n$ th and  $(n + 1)$ st events [9]. Namely, the density of interevent intervals is

$$\alpha_n(x) = \int_0^\infty h \left( \int_0^x \phi(\Pi(s, r)) ds \right) \phi(\Pi(x, r)) f_n(r) dr. \quad (20.8)$$

A spike train can be represented by the sequence of intervals between spikes; this is characterized by the interval statistics (in the time domain by probability distributions and in the frequency domain by spectral densities). In the literature [1] we can find two schemes of spike generation. The first produces a renewal process that has no memory of the excitation because the system resets itself each time a spike is generated. Here, there is no correlation between successive spike intervals. The second scheme generates a nonrenewal spike train, with correlations between adjacent intervals. We consider the distribution of time intervals between spikes as a special case of equation (20.8).

### 20.4.1 Exponential Distribution

Let us come back to the model for action potential generation. The variables  $\tau_n$  in equation (20.7) are distributed with the exponential density  $e^{-x}$ , so the variables  $Q^{-1}(\tau_n)$  are distributed with the density

$$s(x) = \frac{dQ(x)}{dx} e^{-Q(x)} = \begin{cases} 0 & 0 \leq x < V_T \\ q(x)e^{-Q(x)} & V_T \leq x < V_M \end{cases}.$$

If we assume that the function  $\phi(x)$  is constant, i.e.,

$$\phi(x) = \begin{cases} 0 & x < V_T \\ p & x \geq V_T \end{cases},$$

then

$$Q(x) = \int_{V_T}^x \frac{\phi(y)}{g(y)} dy = \int_{V_T}^x \frac{p}{\bar{V} - ky} dy = -\frac{p}{k} \ln \left( \frac{V_M - x}{V_M - V_T} \right). \quad (20.9)$$

The density function for  $V_n$  is then

$$f_{V_n}(x) = -\frac{p}{k} \cdot \frac{1}{(x - V_M + V_R)} \cdot \left( \frac{x - V_M + V_R}{V_T - V_M} \right)^{p/k}.$$

Now we can easily calculate the interspike interval distribution using formula (20.8). First, we have

$$\int_0^x \phi(\Pi(s, r)) ds = \int_{V_T}^x p ds = p(x - V_T),$$

and putting this into equation (20.8) gives

$$\begin{aligned} \alpha_n(x) &= \int_{V_T - V_R}^{V_M - V_R} e^{-p(x - V_T)} \cdot p \cdot \left(-\frac{p}{k}\right) \cdot \left(\frac{1}{V_T - V_M}\right)^{p/k} (r - V_M + V_R)^{p/k - 1} dr \\ &= pe^{-p(x - V_T)}. \end{aligned} \tag{20.10}$$

As we see, this is the density function of the exponential distribution with a parameter  $p, p > 0, x > V_T$ .

This distribution is one of a few interspike interval distributions considered in the literature [17].

### 20.4.2 Rayleigh Distribution

If we assume that the function  $\phi(x)$  is a linear function, i.e.,

$$\phi(x) = \begin{cases} 0 & x < V_T \\ px & x \geq V_T \end{cases},$$

then

$$Q(x) = \int_{V_T}^x \frac{\phi(y)}{g(y)} dy = \int_{V_T}^x \frac{py}{V - ky} dy = p \left(\frac{V_T - x}{k}\right) + \ln \left(\frac{V_M - V_T}{V_M - x}\right)^{\frac{pV_M}{k}}$$

and

$$\int_0^x \phi(\Pi(s, r)) ds = \int_{V_T}^x ps ds = \frac{px^2 - pV_T^2}{2}.$$

After some calculations, we get the density function for  $V_n$ ,

$$f_{V_n}(x) = \left(\frac{1}{V_M - V_T}\right)^{\frac{pV_M}{k}} \frac{p(x - V_T)}{k} (V_M - x + V_R)^{\frac{pV_M}{k} - 1} e^{-p(V_T - x + V_R)}$$

and the density function of the time intervals between spikes,

$$\begin{aligned} \alpha_n(x) &= \int_0^\infty h \left(\int_0^x \phi(\Pi(s, r)) ds\right) \phi(\Pi(x, r)) f_{V_n}(r) dr \\ &= \int_{V_T - V_R}^{V_M - V_R} e^{-\frac{p}{2}(x^2 - V_T^2)} \cdot px \cdot f_{V_n}(r) dr = px e^{-\frac{p}{2}(x^2 - V_T^2)}. \end{aligned} \tag{20.11}$$

The obtained density function is the density function of the distribution known in the literature as a Rayleigh distribution.

The Rayleigh distribution is a continuous probability distribution with the density function defined in general as [18]

$$f(x | \sigma) = \frac{x \cdot \exp\left(\frac{-x^2}{2\sigma^2}\right)}{\sigma^2} \quad \text{for } x \geq 0,$$

where  $\sigma > 0$  is a parameter. The expected value is equal to  $\sigma\sqrt{\pi/2}$ , and the variance is  $[(4 - \pi)/2]\sigma^2$ . In equation (20.11) the parameter  $p = 1/\sigma^2$  and the density function is defined for  $x \geq V_T$ .

We reiterate some useful properties of the Rayleigh distribution:

- If a random variable  $X$  has an exponential distribution with a parameter  $\lambda$ , then  $Y = \sqrt{2X\sigma\lambda}$  has a Rayleigh distribution with a parameter  $\sigma$ ;
- If  $X$  and  $Y$  are independent random variables normally distributed,  $X \in N(0, \sigma^2)$  and  $Y \in N(0, \sigma^2)$ , then  $R = \sqrt{X^2 + Y^2}$  is a Rayleigh distributed random variable with a parameter  $\sigma^2$ ;
- The Rayleigh distribution with  $\sigma = 1$  is a  $\chi^2$  distribution with two degrees of freedom;
- The Weibull distribution is a generalization of the Rayleigh distribution. The Weibull distribution is often used to model the time until a given technical device fails or in general to model lifetimes of objects.

So, the Rayleigh distribution as a special case of the Weibull distribution seems to be a quite natural candidate for modelling of the time intervals between spikes.

**20.4.3 Pareto Distribution**

Let us now consider the function  $\phi(x)$  having the following form:

$$\phi(x) = \begin{cases} 0 & x < V_T \\ \frac{p}{x} & x \geq V_T \end{cases} .$$

So, we can calculate

$$Q(x) = \int_{V_T}^x \frac{\phi(y)}{g(y)} dy = \int_{V_T}^x \frac{p}{y(\bar{V} - ky)} dy = \ln \left( \frac{x(V_M - V_T)}{V_T(V_M - x)} \right)^{\frac{p}{kV_M}}$$

and

$$\int_0^x \phi(\Pi(s, r)) ds = \int_{V_T}^x \frac{p}{s} ds = \ln \left( \frac{x}{V_T} \right)^p .$$

In a similar way as before we can now get the density function of the membrane potential distribution,

$$f_{V_n}(x) = \left( \frac{V_T}{V_M - V_T} \right)^{\frac{p}{kV_M}} \frac{p}{k} \cdot \frac{1}{x - V_R} (V_M - x + V_R)^{\frac{p}{kV_M} - 1} ,$$

and using formula (20.8) the density function of the time intervals between spikes, namely

$$\alpha_n(x) = \int_{V_T - V_R}^{V_M - V_R} e^{-\ln\left(\frac{x}{V_T}\right)^p} \cdot \frac{p}{x} \cdot f_{V_n}(r) dr = \frac{p(V_T)^p}{x^{p+1}} . \tag{20.12}$$

The last function is the density function in the Pareto distribution with parameters  $V_T$  and  $p$  ( $V_T > 0, p > 0, x \geq V_T$ ).

The Pareto distribution is found in a large number of real-world situations. This continuous distribution is also known as the Bradford distribution. If  $X$  is a random



variable with a Pareto distribution, then the probability distribution of  $X$  is characterized by the statement [18]

$$P(X > x) = \left(\frac{x}{x_m}\right)^{-k},$$

where  $x$  is any number greater than  $x_m$ , which is the (necessarily positive) minimum possible value of  $X$ , and  $k$  is a positive parameter. The family of Pareto distributions is parametrized by two quantities,  $x_m$  and  $k$ . The probability density is then

$$f(x | k, x_m) = k \cdot \frac{x_m^k}{x^{k+1}} \quad \text{for } x \geq x_m. \tag{20.13}$$

The expected value of a random variable following a Pareto distribution is  $x_m \cdot k / (k - 1)$  (if  $k \leq 1$ , the expected value is infinite) and the variance is  $x_m^2 k / [(k - 1)^2 (k - 2)]$ . In equation (20.12) the parameter  $p = k$  and  $V_T = x_m$ .

### 20.4.4 Stable Distributions

Stable distributions are a rich class of probability distributions that allow skewness and heavy tails, and they have many intriguing mathematical properties. The class was characterized by Paul Lévy in his study of sums of independent identically distributed random variables [10]. A stable distribution is a distribution where sums of random variables have the same distribution as the original. We now define it more formally

**Definition 1** A random continuous  $X$  is said to have a stable distribution if, for any  $n \geq 2$ , there is a positive number  $C_n$  and a real number  $D_n$  such that

$$X_1 + X_2 + \dots + X_n \stackrel{d}{=} C_n X + D_n,$$

where  $X_1, X_2, \dots, X_n$  are independent realizations of  $X$ , and  $\stackrel{d}{=}$  means that the variables have the same distribution.

Different authors have provided different definitions of stable distributions that often lead to confusion. We introduce only one more definition that specifies a stable distribution more formally.

**Definition 2** A stable probability distribution is defined by the Fourier transform of its characteristic function  $\psi(t)$ :

$$f(x | \alpha, \beta, c, \mu) = \frac{1}{2\pi} \int_{-\infty}^{\infty} \psi(t) e^{-itx} dt,$$

where  $\psi(t)$  is given by

$$\psi(t) = \exp[it\mu - |ct|^\alpha (1 - i\beta \text{sign}(t)\Psi)]$$

and  $\Psi = \tan(\pi\alpha/2)$  for all  $\alpha$  except  $\alpha = 1$  in which case  $\Psi = -(2/\pi) \ln |t|$ .

This definition shows that a general stable distribution requires four parameters:

- an index of stability or characteristic exponent  $\alpha \in (0, 2]$ ,
- a skewness parameter  $\beta \in [-1, 1]$ ,
- a scale parameter  $c > 0$ , and
- a location parameter  $\mu \in R$ .

For  $\alpha = 2$  the distribution reduces to a Gaussian distribution with variance  $2c^2$  and mean  $\mu$  and the skewness parameter  $\beta$  has no effect. For  $\alpha = 1, \beta = 0$  the distribution reduces to a Cauchy distribution with scale parameter  $c$  and location parameter  $\mu$ .

Only one of the stable maximally skewed distributions, i.e., the distribution with  $\alpha = 1/2$ , can be expressed through elementary functions. This distribution has density

$$f_{1/2} = \frac{1}{x\sqrt{2\pi x}} \exp\left(\frac{-1}{2x}\right).$$

Two more maximally skewed distributions, for  $\alpha = 2/3$  and  $\alpha = 3/2$ , can be expressed through special functions called Whittaker functions [21].

The probability density function for the stable distribution with  $\alpha = 2/3, \beta = 1$  is

$$f_{2/3}(x) = \frac{\sqrt{3}}{x\sqrt{\pi}} \exp\left(\frac{-16}{27x^2}\right) W_{1/2, 1/6}\left(\frac{32}{27x^2}\right), \quad x > 0,$$

where  $W_{1/2, 1/6}$  is a Whittaker function [3].

The Whittaker function  $W_{k, \mu}$  can be calculated using the confluent hypergeometric function  $U(a, b, z)$  [19]:

$$W_{k, \mu} = \frac{z^{0.5+\mu} U(0.5 - k + \mu, 1 + 2\mu, z)}{e^{0.5z}},$$

where

$$U(a, b, z) = \frac{1}{\Gamma(a)} \int_0^\infty e^{-zt} t^{a-1} (1+t)^{b-a-1} dt.$$

A similar expression for  $f_{3/2}(x)$  can be found in [21].

Though stable distributions usually cannot be summarized via elementary functions, their tails often allow fairly simple approximations [20]. Also, there are now reliable computer programs to compute stable densities, distribution functions and quantiles [11, 13, 20]. With these programs, it is possible to use stable models in a variety of practical problems.

Stable distributions have been proposed as a model for many types of biological, physical and economic systems. There are several reasons for using a stable distribution to describe a system. The first is the presence of solid theoretical reasons for expecting non-Gaussian stable behaviour. The second reason is the generalized central limit theorem, which states that the only possible nontrivial limit of normalized sums of continuous random variables is a stable law [14]. A third argument for the use of stable distributions in modelling systems is empirical: many large data sets exhibit heavy tails and skewness.

There is yet another property of a stable distribution that is particularly important in modelling of action potential generation. The asymptotic behaviour is described by

$$\lim_{|x| \rightarrow \infty} f(x) = \frac{\alpha C^\alpha}{|x|^{\alpha+1}}, \quad (20.14)$$

where  $f$  is the density function of a stable distribution and  $C$  is proportional to  $c$  of Definition 2. We see that the above equation is very close to equations (20.12) and (20.13), so this means that the form of the asymptotic density function of a stable distribution is very similar to that of the density function of a Pareto distribution. We must remember that if we assume that in the model of action potential generation the function  $\phi(x)$  is inversely proportional to the membrane potential, then the interspike interval distribution is a Pareto distribution. The fact that the distribution of the time intervals between spikes is close to the stable distribution is very interesting and was considered previously in the literature [6]. The theoretical ground for the stable interspike interval is presented in the next section.

## 20.5 Stable Distributions in the Nervous System

Transmission of information in the nervous system is made by a series of action potentials. Since all the action potentials are identical, except in their times of occurrence, the information content of the signal is dependent only on the patterns of times of occurrence of the action potentials. If adjacent interspike intervals are independent, the interspike interval probability density function  $\alpha(x)$  completely characterizes the process and contains the same amount of information as the spike train.

In any sensory pathway in the nervous system information will be transmitted through a cascade of neurons  $\dots, j-1, j, j+1, \dots$ . If each neuron is treated as a perfect integrator with instantaneous reset, the probability density function of the output from the  $j$ th neuron  $f_j(x)$  will be the convolution of the probability density function of its input,  $f_{j-1}(x)$ . Since the information content of the spike train is equivalent to the information content of its probability density function, this information will only be preserved as the signal passes up the neural cascade if  $f_j(x)$  has a form which is invariant under convolution with itself. But as we mentioned in Section 20.4.4, a probability density function which has a form which is invariant under convolution with itself is said to have a stable distribution function.

It is important to remark that the preservation of information does not mean error-free transmission, but that the signals of subsequent neurons are coding the same qualitative aspect of the stimulus, e.g., its intensity. Holden [6] stated the following hypothesis:

*If action potential trains on a cascade of sensory neurons have stable distributions, the sensory system is preserving information, and its converse:*

*If action potential trains in a cascade of sensory neurons do not have stable distributions, the sensory system is not preserving information, but is extracting features of interest from the stimulus pattern, or processing information.*

## 20.6 Conclusion

We have proposed a model for the generation of action potentials by a neuron, which is a special case of a model for systems generating recurrent events. Depending on the form of the rate of maturation, we get three possible distributions of time intervals between spikes. One of them is a Pareto distribution which is simultaneously an asymptotic distribution of a stable distribution. This is consistent with a hypothesis known before in the literature that the information in a spike train is preserved when the probability density function is stable under convolution with itself. This hypothesis means that stable interspike interval distributions characterize a simple information transmission pathway, and nonstable interval distributions suggest more complex information processing functions.

## References

1. Chacron, M.J., Linder, B., Longtin, A.: Noise shaping by interval correlations increases information transfer. *Phys. Rev. Lett.*, **92**, 080601 (2004).
2. Geisler, C., Goldberg, A.: A stochastic model of the repetitive activity of neurons. *Biophys. J.*, **6**, 53–69 (1966).
3. Gradshteyn, I.S., Ryzhik, I.M.: *Table of Integrals, Series and Products*. Academic Press, New York (1980).
4. Hill, A.: Excitation and accommodation in nerve. *Proc. R. Soc. Lond B Biol. Sci.*, **119**, 305–355 (1936).
5. Hodgkin, A.L., Huxley, A.F.: A quantitative description of membrane current and its application to conduction and excitation in nerve. *J. Physiol. (Lond.)*, **117**, 500–544 (1952).
6. Holden, A.V.: A note on convolution and stable distributions in the nervous system. *Biol. Cybernetics*, **20**, 171–173 (1975).
7. Jolivet, R., Lewis, T.J., Gerstner, W.: Generalized integrate-and-fire models of neuronal activity approximate spike trains of a detailed model to a high degree of accuracy. *J. Neurophysiol.*, **92**, 959–976 (2004).
8. Lapicque, L.: Recherches quantitatives sur l'excitation électrique des nerfs traitée comme une polarisation. *J. Physiol. Pathol. Gen.*, **9**, 620–635 (1907).
9. Lasota, A., Mackey, M.C., Tyrcha, J.: The statistical dynamics of recurrent biological events. *J. Math. Biol.*, **30**, 775–800 (1992).
10. Lévy, P.: Sur certains processus stochastiques homogènes. *Comp. Math.*, **7**, 283 (1940).
11. McCulloch, J.H., Panton, D.B.: In: Adler, R.J., Feldman, R.E., Kim, J.R.: *A Practical Guide to Heavy Tails: Statistical Techniques and Applications*. Birkhäuser, Boston, 501–507 (1998).
12. Neher, E., Sakmann, B.: Single-channel currents recorded from membrane of denervated frog muscle fibres. *Nature (Lond.)*, **260**, 779–802 (1976).
13. Nolan, J.P.: *Stable Distributions*. Math/Stat Department, American University, Washington, D.C. (2005).
14. Samorodnitsky, G., Taqqu, M.S.: *Stable Non-Gaussian Random Processes: Stochastic Models with Infinite Variance*. Chapman & Hall, New York (1994).
15. Stein, R.: A theoretical analysis of neuronal variability. *Biophys. J.*, **5**, 173–194 (1965).
16. Tuckwell, H.: *Introduction to Theoretical Neurobiology*. Cambridge University Press, London (1988).

17. Tuckwell, H.: *Stochastic Processes in the Neuroscience*. Society for Industrial and Applied Mathematics, Philadelphia, PA (1989).
18. Wikipedia, the free encyclopedia.
19. Wolfram, S.: *The Mathematica Book*. Cambridge University Press, London (1999).
20. Zaliapin, I.V., Kagan, Y.Y., Schoenberg, F.P.: Approximating the distribution of Pareto sums. *Pure Appl. Geophys.*, **162**, 1187–1228 (2005).
21. Zolotarev, V.M.: *One-Dimensional Stable Distributions*. Amer. Math. Soc. Providence, RI, 284 (1983).

## A Monte Carlo Method Used for the Identification of the Muscle Spindle

Vassiliki K. Kotti and Alexandros G. Rigas

Democritus University of Thrace, Department of Electrical and Computer Engineering,  
GR-67100 Xanthi, Greece; vkotti@ee.duth.gr, rigas@ee.duth.gr

**Summary.** In this chapter we describe the behavior of the muscle spindle by using a logistic regression model. The system receives input from a motoneuron and fires through the Ia sensory axon that transfers the information to the spinal cord and from there to the brain. Three functions which are of special interest are included in the model: the threshold, the recovery and the summation functions. The most favorable method of estimating the parameters of the muscle spindle is the maximum likelihood approach. However, there are cases when this approach fails to converge because some of the model's parameters are considered to be perfect predictors. In this case, the exact likelihood can be used, which succeeds in finding the estimates and the exact confidence intervals for the unknown parameters. This method has a main drawback: it is computationally very demanding, especially with large data sets. A good alternative in this case is a specific application of the Monte Carlo technique.

**Key words:** Exact logistic regression, likelihood function, Monte Carlo technique, muscle spindle.

### 21.1 The Biological System

The system we examine is a complex biological system called the muscle spindle, which is part of the skeletal muscles and is responsible for the initiation of movement and the maintenance of muscle posture. The effects of the imposed stimuli on the muscle spindle's fibers are transmitted to the spinal cord by the axons of sensory nerves closely associated with the muscle spindle. The discharge of the sensory axons is also modified by action potentials carried by the axons of a group of cells called motoneurons. The action potential is a localized voltage change that occurs across the membrane surrounding the nerve cell and axon, with amplitude approximately 100 mV and duration 1 ms. In this chapter we are interested in the discharge that occurs in the presence of an alpha motoneuron.

Let  $Y_t$  describe the firing process of the system. By choosing the sampling interval  $h$ , the observations of the output can be written as follows:

$$y_t = \begin{cases} 1, & \text{when a spike occurs in } (t, t + h] \\ 0, & \text{otherwise,} \end{cases}$$

where  $t = h, \dots, Nh$  and  $T = Nh$  is the time interval in which the process is observed. We usually choose  $h = 1$  ms. The input  $X_t$  imposed by the alpha motoneuron on the system consists of the observations  $x_t$  defined similarly.

### 21.2 System Modeling

In this section we present the logistic regression model that can be used for the identification of the system under the influence of an alpha motoneuron. This model extends the work of [2] and [3] used for the identification of neuronal firing systems. The firing of the system we study occurs when the potential of the membrane that surrounds the sensory axon exceeds a critical level called the threshold. The membrane’s potential at the trigger zone is influenced both by internal and external processes.

The internal processes are responsible for the spontaneous firing of the system. This is an ability of the system to produce a series of nerve pulses on its own, by increasing the resting potential to the level of the threshold. Let  $\phi_t$  denote the threshold potential level at the trigger zone at time  $t$  by  $\phi_t = \theta_0 + \epsilon_t$ , where  $\epsilon_t$  is the unknown noise process that includes contributions of unmeasured terms that influence the firing of the system and  $\theta_0$  represents an unknown constant threshold. Other forms of threshold can also be considered that allow the threshold to vary with time [7]. Let  $V_t$  represent the recovery function which is described by a polynomial function of order  $k$  given by

$$V_t = \sum_{i=1}^k \theta_i \gamma_t^i,$$

where  $\gamma_t$  is the time elapsed since the system last fired and  $\theta_i$  are the unknown coefficients.

External processes are responsible for the firing of the system when it is affected by external parameters such as the presence of a motoneuron. The function representing the effect of an alpha motoneuron on the muscle spindle at any given time  $t$  is based on a summation described by a set of coefficients  $\{a_u\}$ . The summation function is defined by

$$SF_t = \sum_{u \leq t} a_u x_{t-u},$$

where  $x_{t-u}$  is the observation of the input at time  $t - u$ .

The logistic regression model that describes the effect of the covariates incorporated in the recovery and the summation function at any given time  $t$  is expressed as

$$\log\left(\frac{\pi_t}{1 - \pi_t}\right) = \sum_{u \leq t} a_u x_{t-u} + \sum_{i=1}^k \theta_i \gamma_t^i - \theta_0, \tag{21.1}$$

where  $\pi_t$  denotes the probability of an output spike to occur. The unknown parameters that have to be estimated are the coefficients  $\{a_u\}$ , the recovery function parameters  $\theta_i$  and the constant threshold  $\theta_0$ . More details about the logistic model given by (21.1) and the covariates included are given in [6].

## 21.3 Methods

### 21.3.1 The Maximum Likelihood Approach

The likelihood function is defined as the joint probability of the random variables whose realizations constitute the sample. For a sample of size  $n$  with observations  $(y_1, \dots, y_n)$ , the corresponding random variables are  $(Y_1, \dots, Y_n)$ . The probability density function of  $Y_t$  describes the contribution to the likelihood function of every single observation and is given by  $P\{Y_t = y_t\} = \pi_t^{y_t}(1 - \pi_t)^{1-y_t}$ ,  $y_t = 0, 1$ . Since the observations are assumed to be independent, the likelihood function is the joint probability

$$L_0 = P(Y_1 = y_1, Y_2 = y_2, \dots, Y_n = y_n) = \prod_{t=1}^n \pi_t^{y_t} (1 - \pi_t)^{1-y_t}, \quad (21.2)$$

where  $\pi_t = \pi(x_{1t}, x_{2t}, \dots, x_{pt})$  is the conditional probability that  $Y_t$  equals 1, given  $x_t$ , where  $p$  is the number of covariates included in the model. It is however more convenient to use the log of the likelihood function and therefore we have

$$l(y_t, \pi_t) = \log L_0 = \sum_{t=1}^n \left[ y_t \log \left( \frac{\pi_t}{1 - \pi_t} \right) + \log(1 - \pi_t) \right]. \quad (21.3)$$

The probability  $\pi_t$  is related with the unknown parameters of the model through (21.1) and thus the likelihood function is considered as a function of the unknown parameters.

### 21.3.2 Drawbacks of the Maximum Likelihood Approach

The maximum likelihood approach is the most favorable method of estimation, but unfortunately it can fail completely or produce poor results in terms of the unknown parameters and their standard errors. These problems are caused by certain structures in the data, which occur when we deal with data sets that are small, or data sets that are large, but sparse. The most common numerical problem occurs when a collection of covariates separates the outcome, so that there is no overlap in the distribution of the covariates between the two possible outcome values. This phenomenon is called complete or quasi-complete separation and in these cases the maximum likelihood estimators do not exist as was demonstrated in [1] and [11]. The separation can be identified by the existence of one or more empty cells in the corresponding contingency tables. (An example of quasi-complete separation is described in Table 21.2. The empty cell where  $X_{t-13} = 1$  and  $Y = 1$  indicates quasi-complete separation.)



### 21.3.3 The Exact Logistic Regression

An alternative solution is to obtain the exact estimates of the unknown parameters. The idea of exact logistic regression (ELR) is to estimate some of the parameters of the model by replacing the remaining parameters in the likelihood function by their sufficient statistics. The likelihood function given by (21.2) can be written in the following form:

$$P(Y_1 = y_1, Y_2 = y_2, \dots, Y_n = y_n) = \frac{\exp(\sum_{s=0}^p \beta_s w_s)}{\prod_{t=1}^n (1 + \exp(x_t \beta))}, \quad (21.4)$$

where  $w_s = \sum_{i=1}^n x_{is} y_i$  are the sufficient statistics,  $\beta$  is a vector of the unknown parameters and  $\beta^T = (\beta_0, \beta_1, \dots, \beta_p)$ . In our case the vector  $\beta$  includes the coefficients  $\{a_u\}$ ,  $\theta_i$  ( $i = 1, 2, \dots, k$ ) and  $\theta_0$ . Suppose that we are interested in one of the regression parameters, regarding the remainder as a nuisance. Without loss of generality, we choose the parameter of interest to be  $\beta_p$ . It can be proved (see [8]) that the conditional likelihood is given by

$$f(w_p | \beta_p) = \frac{c(w_0, w_1, \dots, w_p) \exp(\beta_p w_p)}{\sum_u c(w_0, w_1, \dots, w_{p-1}, u) \exp(\beta_p u)}, \quad (21.5)$$

where the summation in the denominator is over all the values of  $u$  for which  $c(w_0, w_1, \dots, w_{p-1}, u) \geq 1$ . The initial theory about ELR proposed by Cox in 1970 (see [4]) was considered computationally infeasible for many years and, despite the availability of fast numerical algorithms developed later (see [5] and [12]), there are cases where the data set is too large and the exact estimates cannot be obtained easily. This case corresponds to our example presented later, where we shall see that the requirements in computing time and memory are restrictive, because the data set is too large (15870 observations). A good alternative in this case is to obtain estimates of the exact results by using Monte Carlo techniques.

### 21.3.4 The Monte Carlo Approach

When it is not possible to store the exact permutational distribution, we could obtain Monte Carlo samples from this distribution. One naive approach would be to follow conventional Monte Carlo methods that lead to massive rejection of the samples that do not satisfy the constraints of the conditional distribution. This approach is easy to implement and does not require computer memory. However, it becomes inefficient very quickly even for relatively small samples. In this case one can use a network-based direct Monte Carlo sampling approach discussed in [10] which stores a network of vectors that satisfy the constraints of the conditional distribution given by (21.5). The samples are then drawn from this network and therefore this method is more efficient than the conventional Monte Carlo sampling. There is however a disadvantage as far as the memory is required for the construction and the storage of the network. The memory required depends on the specifics of the problem such as the sample size, the number of covariates in the model, the number of covariate groups and the proportion of responses. This technique is available on LogXact (see [9]).

**Table 21.1.** Table of the results.

	Estimates			95% Confidence Interval	
	Asymptotic(s.e.)	Exact	Monte Carlo	Exact	Monte Carlo
$\theta_0$	-3.4186 (0.1317)	-3.4493	-3.4475	(-3.9435, -2.9905)	(-3.9551, -2.9655)
$\theta_1$	0.0967 (0.0105)	0.0986	0.1002	( 0.0629, 0.1351)	( 0.0632, 0.1364)
$a_1$	0.2168 (0.2447)	0.2134	0.2142	(-0.7897, 1.0618)	(-0.7827, 1.1123)
$a_7$	1.7565 (0.1722)	1.7414	1.7534	( 1.0975, 2.3617)	( 1.1006, 2.4187)
$a_{13}$	-7.7503 (6.6326)	-2.2142	-2.2736	( $-\infty$ , -0.4818)	( $-\infty$ , -0.4877)
$a_{19}$	-7.8191 (6.7208)	-2.2480	-2.4730	( $-\infty$ , -0.5272)	( $-\infty$ , -0.4757)
$a_{25}$	-8.1085 (6.6810)	-2.5503	-2.3280	( $-\infty$ , -0.8199)	( $-\infty$ , -0.6439)
$a_{31}$	-8.1542 (6.7425)	-2.5838	-2.5827	( $-\infty$ , -0.8594)	( $-\infty$ , -0.8981)
$a_{37}$	-8.2998 (6.6745)	-2.7224	-2.7851	( $-\infty$ , -0.9879)	( $-\infty$ , -0.7965)
$a_{43}$	-2.7278 (0.7167)	-2.4404	-2.4465	( $-\infty$ , -0.6608)	( $-\infty$ , -0.6909)
$a_{49}$	-0.3193 (0.2464)	-0.3413	-0.3395	(-1.3670, 0.5291)	(-1.3919, 0.5245)

## 21.4 Results

In this section we provide a neurophysiological example which causes a breakdown in the maximum likelihood estimation. The data set includes two time series which consist of 259 input and 356 output spikes, recorded in a time interval of 15870 ms. The input is imposed to the muscle spindle by an alpha motoneuron and the output contains the discharge of the muscle spindle’s sensory axon.

The attempt to fit the logistic regression model given by (21.1) using the maximum likelihood approach results in misleading conclusions, which are shown in Table 21.1. It is obvious that the estimates and the standard errors of the coefficients  $a_{13}$ ,  $a_{19}$ ,  $a_{25}$ ,  $a_{31}$ , and  $a_{37}$  are very large compared with the other estimates, denoting a *problematic area* on the summation function. This occurs because of the quasi-complete separation, as illustrated in Table 21.2. This situation causes problems to the maximum likelihood estimation, which considers that the covariate  $X_{t-13}$  is a perfect predictor. The same situation applies for all the covariates of the *problematic area* and it causes the maximum likelihood method to diverge. A solution in this case is to perform exact estimation. The exact results and the confidence intervals are also shown in Table 21.1. The lower confidence bound for the estimates of the problematic

**Table 21.2.**  $2 \times 2$  contingency table between  $Y$  and  $X_{t-13}$ .

	$Y = 0$	$Y = 1$
$X_{t-13} = 0$	4677	356
$X_{t-13} = 1$	257	0

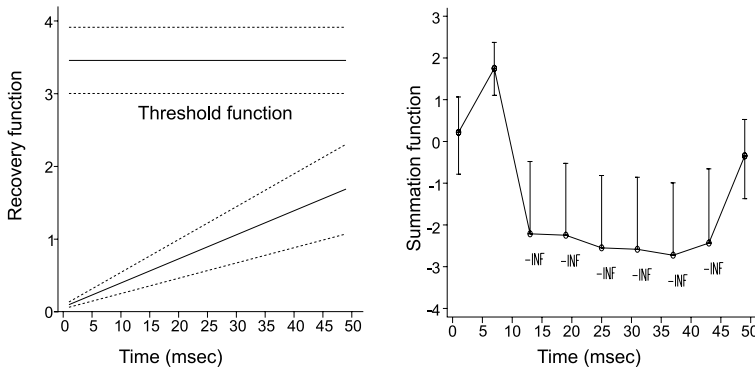


**Fig. 21.1.** (a) Monte Carlo estimates of the threshold and the recovery function. The dotted lines correspond to 95% confidence intervals. The recovery function does not cross the threshold, but the increase may be indicative of possible spontaneous firing. (b) Monte Carlo estimates of the summation function. The vertical bars represent the 95% confidence intervals of the  $a_u$  coefficients. The summation function accelerates for a very short period during the first 10 ms, and afterwards decelerates. This inhibitory behavior blocks the response of the system for about 40 ms.

area is  $-\infty$ , indicating that the data set contains observations at the extreme points of the sample space for these coefficients. An alternative solution is to perform Monte Carlo estimation by sampling 10,000 times from the appropriate conditional distribution. The estimates and their confidence intervals obtained by performing Monte Carlo estimation are shown in Table 21.1 and a graphical presentation is given in Fig. 21.1. All computations were performed on a Pentium, 1000 MHz PC. For consistency all the results are displayed to four decimal digits. The maximum likelihood estimates are compared with those of the ELR and the Monte Carlo respectively. The Monte Carlo estimation required 1/4 of the exact estimation computing time and 1/10 of the exact estimation memory requirements.

### 21.5 Discussion

In this chapter we have used a logistic regression model in order to describe the behavior of the muscle spindle when it is affected by an alpha motoneuron. The estimated coefficients of the summation function are positive for a very short period in the beginning, indicating an acceleration of the system’s firing. However in the interval between 11–50 ms the system is blocked by the presence of the alpha motoneuron and its behavior is inhibitory. This becomes obvious from the negative values of the estimated coefficients. The recovery function is modelled by a first-order polynomial. The graphical presentation of the recovery function shows an increase, which tends to cross the threshold level. This fact indicates a tendency for possible activity of the system.

## References

1. Albert, A., Anderson, J.A.: On the existence of maximum likelihood estimates in logistic models. *Biometrika*, **71**, 1–10 (1984).
2. Brillinger, D.R.: Maximum likelihood analysis of spike trains of interactive nerve cells. *Biological Cybernetics*, **59**, 189–200 (1988).
3. Brillinger, D.R.: Nerve cell spike train data analysis: a progression of technique. *J. Am. Stat. Assoc.*, **87**, 260–271 (1992).
4. Cox, D.R.: *Modelling Binary Data*. Chapman & Hall, New York (1970).
5. Hirji, K.F., Mehta, C.R., Patel, N.R.: Computing distributions for exact logistic regression. *J. Am. Stat. Assoc.*, **82**, 1110–1117 (1987).
6. Kotti, V.K., Rigas, A.G.: Identification of a complex neurophysiological system using the maximum likelihood approach. *J. Biol. Syst.*, **11**, 189–204 (2003).
7. Kotti, V.K., Rigas, A.G.: A nonlinear stochastic model used for the identification of a biological system, In: Capasso, V. (ed.) *Mathematical Modeling & Computing in Biology and Medicine*. The Miriam Project Series, Progetto Leonardo, Escapulario. Co., Bologna, Italy (2003).
8. Kotti, V.K., Rigas, A.G.: Logistic regression methods and their implementation. In: Edler, L., Kitsos C.P. (eds.) *Recent Advances in Quantitative Methods for Cancer and Human Risk Assessment*. Wiley, New York (2005).
9. LogXact-5 for Windows, *User Manual*, Cytel Software (2002).
10. Mehta, C.R., Patel, N.R., Senchaudhuri, P.: Efficient Monte Carlo methods for conditional logistic regression, *J. Am. Stat. Assoc.*, **95**, 99–108 (2000).
11. Santner, T.J., Duffy, D.E.: A note on A. Albert's and J.A. Anderson's conditions for the existence of maximum likelihood estimates in logistic regression models. *Biometrika*, **73**, 755–758 (1986).
12. Trichler, D.: An algorithm for exact logistic regression. *J. Am. Stat. Assoc.*, **79**, 709–711 (1984).

## Mechanisms of Coincidence Detection in the Auditory Brainstem: Examples

Petr Marsalek<sup>1,2</sup> and Marek Drapal<sup>1</sup>

<sup>1</sup> Charles University Prague, Department of Pathological Physiology, U nemocnice 5, CZ-128 53, Praha 2, The Czech Republic; marsalek@cesnet.cz, drapal@email.cz

<sup>2</sup> Corresponding author. Czech Technical University in Prague, Faculty of Biomedical Engineering, nam. Sitna 3105, CZ-272 01, Kladno, The Czech Republic

**Summary.** The auditory brainstem in mammals contains a neural circuit for sound localization. The exact functioning of this circuit is still under controversy. Two spike generation mechanisms studied previously, excitatory coincidence detection and inhibitory coincidence detection, are studied here regarding the input-output relationship of the spike time densities. We propose that synchronous binary multiplication operation on spikes is the underlying process of these two variants of coincidence detection. A derivation of time to the spike is shown, which enables us to estimate the contribution of the neural circuit in the auditory brainstem to the overall reaction time of sound localization. The brainstem contribution is minute compared to the conduction delays in the mammalian neocortex. Finally, the skewness of the resulting output spike time densities is discussed in both the excitatory and inhibitory cases and the inhibitory case is shown to be close to the normal density with a standard goodness-of-fit test for the normal probability density function.

**Key words:** Coincidence detection, directional hearing, interaural time delay, stochastic neuronal model.

### 22.1 Introduction

The auditory brainstem in mammals contains a neural circuit for sound localization. When the direction of incoming sound changes, so do the differences of some of its parameters between the two ears (interaural parameters). Sound localization is based on these sound parameters: interaural spectral difference, interaural intensity difference and interaural time difference (ITD). In this chapter we deal only with the ITD. The ITD changes when there is a change of the angle of the line from the sound source to the center of the head with the left-right symmetry plane. The discrimination threshold of this angle change in humans corresponds to a time difference in the range of 10 microseconds. Alternatively, such a short time difference can be described as a sound phase difference. Of course, such short time differences are not perceived subjectively. They are only employed in the sound localization circuit in the brainstem.

In the brainstem of birds the ITD is processed by a delay line [16], as it was suggested more than half a century ago in a visionary work of Jeffress [5]. However, such a delay line has not been found in mammals and recent experiments [1, 4, 12] and [15] indicate that the mechanism of the ITD processing in mammals does not work as the delay line. Yet in both birds and mammals the microsecond ITD has to be somehow detected by a unit (by a neuron, or by a neural circuit) acting as a coincidence detector. Without the coincidence detection none of the circuits in both birds and mammals would work.

This chapter presents a stochastic model of the coincidence detection (CD) in the auditory brainstem neural circuits. We have studied the feed-forward processing in the brainstem previously [8, 10, 11]. Here we present a not yet published example of CD using the beta density as a probability density of input spike occurrences in time. We stated previously that in the brainstem circuitry two types of CD take place, based on the polarity of the synaptic transmission. We call these two types of CD the excitatory CD and the inhibitory CD [10].

In [14] the CD was proposed as a mechanism for multiplication of firing rates within a limited spiking frequency range of asynchronous spike trains in a compound eye of a crab. Since in our synchronous cases the frequency is a sub-harmonic of sound, in our versions of spike operations only binary and not continuous multiplication with spikes is implemented.

## 22.2 Results

### 22.2.1 Conditions of Coincidence Detection

Following [14], we denote input from one side A, and from the other side B. The CD is realized when input spikes from both sides are closer in time than the fixed value of  $\Delta$ , which is a constant of the neural circuit. During neuronal relaying, spikes are subject to a delay with a random component. We assume that the random delays on sides A and B are mutually independent and identically distributed non-negative random variables  $D$  with a maximum value of  $\delta$ :

$$0 \leq D \leq \delta. \quad (22.1)$$

For relevant sound frequencies and delays the length of the window for CD  $\Delta$  is not longer than the maximum delay  $\delta$  and the delay  $\delta$  is not longer than the sound period  $T$ :

$$0 \leq \Delta \leq \delta \leq T. \quad (22.2)$$

In the excitatory CD the spike is generated only when the two spikes from sides A and B meet in a time interval shorter than  $\Delta$ , in other words when the two spike delays  $D_A$  and  $D_B$  are closer in time than  $\Delta$ :

$$|D_A - D_B| \leq \Delta. \quad (22.3)$$

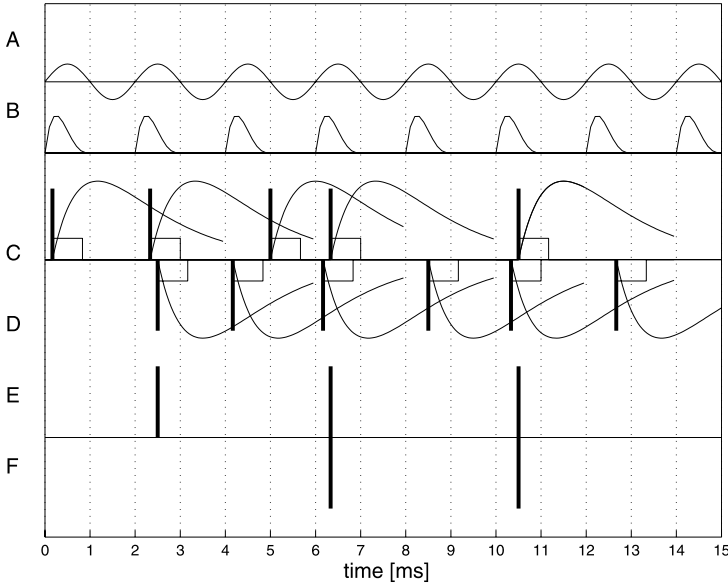


**Fig. 22.1. Generation of the output spike trains of the CD mechanisms.** Trace A: Sound with the frequency 500 Hz. Trace B: Series of spike time densities  $f(x)$  phase locked to the sound rising phase. Traces C and D: The windows of length  $\Delta$  (thin rectangles) are triggered by the leading edges (thick horizontal bars) of the spikes. These spikes (thin smooth functions with cut off tails) are postsynaptic potentials of the two inputs. The D trace is flipped vertically to show the overlaps of the coincidence detection windows. Trace E: The spike train of the excitatory CD is generated by placing the output spike aligned with the later of the two spikes of C and D, if the two windows of length  $\Delta$  overlap in time. Trace F: For the output spike in the spike train of the inhibitory CD, all the conditions for the excitatory CD are necessary and furthermore the (inhibitory) spike from the contra-lateral side (trace D) must arrive sooner in time than the spike from the ipsi-lateral side (trace C). The F trace is also flipped vertically.

In the inhibitory CD the condition expressed in equation (22.3) is modified. Spikes must arrive in the right succession. The excitatory spike from side A must come after the inhibitory spike from side B. This is formulated as

$$0 \leq D_A - D_B \leq \Delta. \tag{22.4}$$

Mechanisms showing how these excitatory CD and inhibitory CD are generated are shown in Fig. 22.1. The example sound frequency is 500 Hz in the figure. The postsynaptic potentials of the two inputs from cochlear nuclei are the series of alpha functions,  $x \exp(-x/\tau)$ , with  $\tau = 1$  ms. The window duration is  $\Delta = 0.66$  ms, mean delays are  $E(D_A) = E(D_B) = 0.33$  ms and their standard deviation is 0.18 ms. Note the longer duration of these alpha functions, compared to the CD windows, even though their time constant  $\tau$  is shorter than typical biological time constants of postsynaptic potentials. Durations of all the events depicted in Fig. 22.1 are only loosely to scale.

Further, we denote the probability of events described by inequalities (22.3) and (22.4) as  $P(\Delta)$ . For  $\Delta = 0$  it holds that  $P(\Delta) = 0$ . In the case of  $\Delta = \delta$ ,  $P(\Delta) = 1$ , and since  $P(\Delta)$  monotonically increases with  $\Delta$ ,  $P(\Delta)$  as a function of  $\Delta$  is a cumulative distribution function. Random variables  $D$  are distributed in accordance with a given probability density function  $f(x)$ . Then for the excitatory CD,  $P(\Delta) = \text{Prob}(|D_A - D_B| \leq \Delta)$  can be calculated. Analogously for the inhibitory CD,  $P(\Delta) = \text{Prob}(0 \leq D_A - D_B \leq \Delta)$ . The output spike is emitted at the moment of the latter input spike. The output time density for specific examples of  $D$  and  $f(x)$  and the rationale behind these examples are given in Section 22.2.3. In Fig. 22.1, beta density  $B_{24}$  discussed in Section 22.2.3 is shown as the example of the density  $f(x)$ .

### 22.2.2 Further Sources of Probabilistic Spiking

Under conditions (22.3) or (22.4), respectively, when  $\Delta < \delta$ , the spike generation probability is lower than 1. In [11] we showed that lowered spiking probability is also due to the process of sub-harmonic spike generation, which progressively lowers the spiking probability towards higher frequencies. We also gave a formula for dependence of this probability on the main sound frequency in that paper. Let us denote the net spiking probability set by the processes mentioned above as  $p$ . Further, one could ask: How many sound cycles and how much time does it take before the output spike is generated with desired reliability? Let us study the 50% and the 95% reliability. The processing time will determine the processing speed and therefore the reaction time for the sound localization circuit as a whole.

The procedure to calculate the processing time is shown in Fig. 22.2 for the two example values of  $p = 0.4$  and  $0.8$ .  $N$  is the number of sound cycles from 1 up to the cycle in which spikes at both neurons A and B are generated together at some time. Let  $P(n)$  denote the probability that  $N \leq n$ .  $P(n)$  is a discrete cumulative distribution function of  $n$ . Using the spike delivery probability  $p$  we calculate a probability of how many cycles it will take for the mechanisms of the excitatory CD and of the inhibitory CD to generate their output. From this we will characterize the processing time by the two example values of  $N$ : by the number of cycles at which there is a 50% reliability of generating the output spike and by the number of cycles needed to reach a 95% reliability that the output spike is generated. The processing times to the first spike of the 50% and 95% reliabilities are  $NT$ , for the sound period  $T$  and for the two example values of  $N$ . The larger of the last two delays  $D$  in the last sound cycle is not included in these formulas, see [11] for details. In calculating these processing times we also set the coincidence detection probability in (22.3) to  $P(\Delta) = 1$ . Other cases, with  $P(\Delta) < 1$ , would be calculated analogously.

The  $N$  is the minimal  $n$  such that the probability  $P$  of spike generation in cycle  $n$  is  $P(n) \geq R$  (where reliability  $R$  is 0.5 or 0.95). This  $N$  is found as the occurrence of a success in a partial trial of a set of Bernoulli trials. This scheme does not exclude the occurrence of a success in some other partial trial. Consequently, the probability of the event that a success occurs in at least one partial trial of  $n$  trials does not equal  $np^2$ , as one might naively expect, but the probability equals to  $1 - (1 - p^2)^n$ . Therefore we seek the minimal natural number  $N$  satisfying inequality



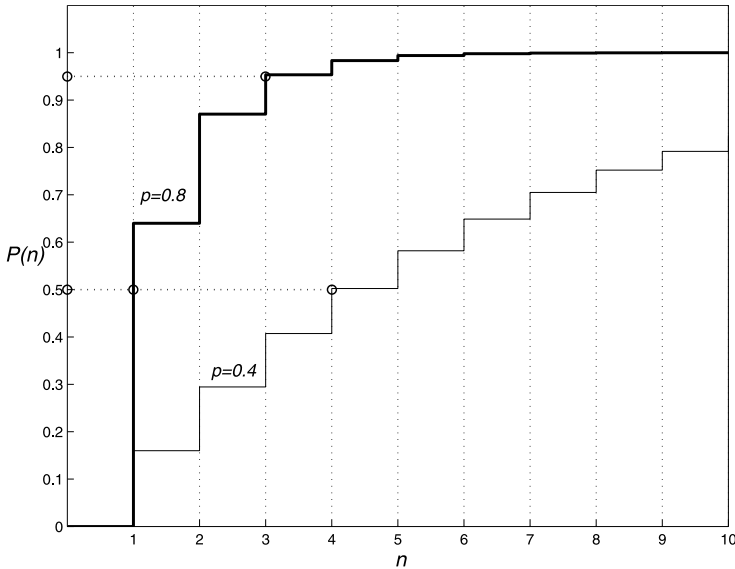


**Fig. 22.2. Determining processing time counted in sound cycles from  $P(n)$ .**  $P(n)$  is discrete and is discretized by the sound period steps. The values of  $P(n)$  are the following: during the first cycle  $P(1) = p^2$ , during the second cycle  $P(2) = p^2 + (1 - p^2)p^2$ , in the  $n$ th cycle  $P(n) = \sum_0^{n-1} (1 - p^2)^i p^2$  and this sum gives the left side in inequality (22.5).  $P(n) = 1$  for  $n \rightarrow \infty$ . Intersection of these staircases with horizontals at  $R = 0.5$  and  $R = 0.95$ , respectively, gives the values of natural number  $N$ . Examples with  $p = 0.4$ , light line, and  $p = 0.8$ , bold line, are shown, the latter in order to demonstrate that  $N$  can even be equal to 1 for the value of  $p > \sqrt{2}/2$  and the reliability value of  $R = 0.5$ .

$$1 - (1 - p^2)^N \geq R \tag{22.5}$$

for unknown  $N$  and for the values of  $R$  equal to 0.5 and to 0.95. Solving this inequality for  $N$  we obtain  $N$  as

$$N = \left\lceil \frac{\log(1 - R)}{\log(1 - p^2)} \right\rceil, \tag{22.6}$$

where  $\lceil \cdot \rceil$  denotes rounding towards the nearest larger natural number. The base of the logarithm in both the numerator and the denominator can be arbitrary. Some numerical examples are shown in Fig. 22.2 and some others are used as parameters in a table in [11].

### 22.2.3 Examples of Input and Output Density Functions

For the input spike time probability density function we will use the beta density. We will write the beta density in a standard form, as

$$B_{ab} = \begin{cases} x^{a-1}(1 - x)^{b-1} B(a, b)^{-1}, & \text{for } x \in [0, 1] \\ 0 & \text{otherwise,} \end{cases} \tag{22.7}$$

where the parameters  $a, b > 0$  and  $B(a, b)$  is the beta function. The beta density with  $a, b \geq 1, a < b$ , which means nonzero skewness, fits well to experimental data. This is also because its nonzero value is confined to the range of  $[0, 1]$  and this guarantees the assumption (22.2), namely that the spike fits into one sound cycle, after the cycle length  $[0, T]$  is normalized to  $[0, 1]$ . We substitute the beta density  $B_{ab}$  with parameters  $a, b$  for the probability density function  $f(x)$  of  $D_A$  and  $D_B$  in equation (22.3). For  $a = 1, b = 1$ , the probability density function becomes the uniform density. The uniform density was used as a choice for  $f(x)$  in [10]. Next we will use parameters  $a = 2$  and  $b = 4$  as the example:

$$B_{24}(x) = \begin{cases} 20x(1 - x)^3, & \text{for } x \in [0, 1] \\ 0 & \text{otherwise.} \end{cases} \tag{22.8}$$

To calculate the probability of the CD the condition (22.3) has to be fulfilled. Therefore for the excitatory CD we seek a density  $u$  of the random variable  $W = |D_A - D_A|$ , where  $D_A$  and  $D_B$  are distributed in accordance with equation (22.8). As the intermediary step giving out the density for the inhibitory CD we set

$$Z = D_A - D_B, \tag{22.9}$$

with its density denoted  $q(z)$ .

We substitute  $f(x) = B_{24}(x)$  and  $g(x) = B_{24}(x)$  into the standard convolution formula for the sum of two random variables,  $q(z) = \int_{-\infty}^{\infty} f(x)g(x - z)dx$ . The piecewise evaluated integral  $q(z)$  is

$$\begin{aligned} q(z) &= \int_{\max(z-1,0)}^{\min(z,1)} f(x)g(z - x)dx \\ &= \int_{z \in [-1,0]} f(x)g(z - x)dx + \int_{z \in [0,1]} f(x)g(z - x)dx \\ &= \int_0^z f(x)g(z - x)dx + \int_{z-1}^1 f(x)g(z - x)dx. \end{aligned}$$

Obviously,  $q(z)$  is an even function. We substitute into these integrals for  $f$  and  $g$  from (22.8) and we obtain the sum of two ninth-degree polynomials in two variables  $x$  and  $z$  when starting with a fourth-degree polynomial  $B_{24}$ . This would require tedious calculation without the use of a symbolic manipulator software package (we used the Symbolic Math Toolbox of the Matlab package).

In summary, using (22.3) and assuming that  $D_A$  and  $D_B$  are distributed with density (22.8), then  $Z = D_A - D_B$  for the inhibitory CD has the following density:

$$q_{24}(z) = \begin{cases} -0.6349z^9 + 2.8571z^7 - 20z^4 + 33.33z^3 \\ \quad -17.1429z^2 + 1.5873, & \text{for } x \in [0, 1], \\ 0.6349z^9 - 2.8571z^7 - 20z^4 - 33.33z^3 \\ \quad -17.1429z^2 + 1.5873, & \text{for } x \in [-1, 0] \\ 0 & \text{otherwise.} \end{cases} \tag{22.10}$$

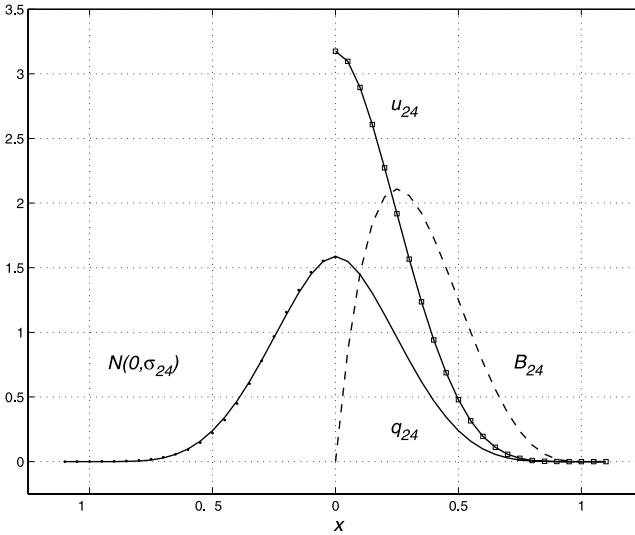


**Fig. 22.3. Densities of input and output time in one sound cycle.**  $B_{24}$ , broken line, is the input beta density with parameters of  $a = 2, b = 4$ . The intermediate result of calculations,  $q_{24}$ , is the solid line, in fact consisting of the two separate but aligned polynomials for  $x$  in  $[-1, 0]$  and in  $[0, 1]$ , respectively, of (22.10). Dots, superimposed on the left branch, denoted  $N(0, \sigma_{24})$ , belong to the normal density with the respective mean and standard deviation and are close to the solid lines of  $q_{24}$ . Solid line marked with squares is the output density  $u_{24}$ , which is zero outside the range of  $[0, 1]$ .

The variable calculated as the absolute value of  $W = |D_A - D_B|$  for the excitatory CD then has the resulting density  $u_{24}(w), u_{24}(w) = 2q_{24}(w)$  for  $w \in [0, 1]$  and  $u_{24}(w) = 0$  otherwise.

Starting from  $B_{24}$ , for enough sample data points, the numerically calculated density of  $q_{24}(z)$  is close to the normal density. Testing 500 data points of the density  $q_{24}(z)$  for the samples of normal density gives the positive answer with a significance level of  $10^{-15}$ . This was in the Jarque–Bera test [2] for goodness of fit to, or departure from, the normal density, based on the sample kurtosis and skewness.

Therefore the normal density  $N(\mu, \sigma)$  with zero mean and adjusted standard deviation of  $\sigma_{24} = 0.2518$  can replace the density  $q_{24}$ . For maximal delay  $\delta$  the range of  $x$  is  $x \in [0, \delta]$ , in other words we should substitute  $x/\delta$  for  $x$ . This renormalization will match to the  $B_{24}$  with nonzero values from  $[0, 1]$  and the standard deviation of  $N(\mu, \sigma_{24})$  will be equal to  $\sigma_{24} = 0.2518/\delta$ . The nonzero but close to zero values of  $N(\mu, \sigma_{24})$  outside the range of  $[-1, 1]$  are negligible, as shown by the above-mentioned significance level. Densities  $B_{24}, q_{24}, u_{24}$  and  $N(\mu, \sigma_{24})$  are shown in Fig. 22.3. In the next section we comment on the prospective use of the normal density in the description of output density. Even though the input beta density is used specifically because the input spike trains are generated by a sound stimulus, the output density  $q_{24}$  for the inhibitory CD is close to the normal density. The signs in the gener-

ation of the excitatory CD do not cancel, the algorithm is not symmetric in this sense. Therefore its output density  $u_{24}$  is also not symmetric and has a nonzero skewness.

## 22.3 Discussion

The wiring of the brainstem circuits for the CD is described in detail in previous works [11] and reviews [5]. We will discuss only the differences between the excitatory and inhibitory CD below. Of all the experimental literature which calls for an alternative to a delay line theory in mammals we list just the representative papers [1,4,12].

Concerning the difference in the summation sign between the excitatory and inhibitory CDs, we should note that the polarity change is possible in a neural circuit only by chaining the excitatory and inhibitory synapse in series. In addition, negative and positive amplitudes which are summed at a postsynaptic neuron have exactly two origins: (1) the excitatory and inhibitory synapses at the same postsynaptic neuron and (2) depolarization and hyperpolarization currents at the same neuron [3,4] and [15].

All spike generation is discussed with respect to one sound cycle. Spikes are generated synchronously with a sub-harmonic oscillation and a limit frequency is imposed to the output frequency. This frequency limit, also mentioned at the beginning of Section 22.2.2, was used in [6] before. The processing time discussed in this section as a contribution to the reaction time would be just a minute contribution to the cortical processing in humans. However, the smaller the experimental animal is, the faster is its cortical processing and then the processing time may be more important. These reaction and processing times may also be of interest for an experimenter, who could devise further experiments elucidating the functioning of the brainstem neural circuitry.

The prediction of the output density type is useful in the description of propagation of the spike timing jitter into higher-order neurons within the auditory pathway. Most authors choose normal density, sometimes because there is no prior knowledge about the density. In the examples of output excitatory and inhibitory densities we show how such knowledge can be derived. Other examples of densities can be found in [7,9] and [13].

## Acknowledgments

Thanks to Michal Andrlík, Nick Dorrell and Petr Lánský. Special thanks to Eduard Kurišćák and Martin Zápotocký. Supported by the GAUK grant no. 32/2005 and by the MSM grant no. 6840770012.

## References

1. Batra, R., Kuwada, S., Fitzpatrick, D. C.: Sensitivity to interaural temporal disparities of low- and high- frequency neurons in the superior olivary complex. I. Heterogeneity of responses. II. Coincidence detection. *J. Neurophysiol.*, **78**, 1222–1247 (1997).

2. Bera, A., Jarque, C.: Efficient tests for normality, heteroscedasticity and serial independence of regression residuals: Monte Carlo evidence. *Economics Letter*, **7**, 313–318 (1981).
3. Borisyuk, A., Semple, M. N., Rinzel, J.: Adaptation and inhibition underlie responses to time-varying interaural phase cues in a model of inferior colliculus neurons. *J. Neurophysiol.*, **88**, 2134–2146 (2002).
4. Brand, A., Behrend, O., Marquardt, T., McAlpine, D., Grothe, B.: Precise inhibition is essential for microsecond interaural time difference coding. *Nature*, **417**, 543–547 (2002).
5. Joris, P. X., Smith, P. H., Yin, T. C. T.: Coincidence detection in the auditory system: 50 years after Jeffress. *Neuron*, **21**, 1235–1238 (1998).
6. Kral, A., Majernik, V.: Neural networks simulating the frequency discrimination of hearing for non-stationary short tone stimuli. *Biol. Cybern.*, **74**, 359–366 (1996).
7. Lansky, P.: Sources of periodical force in noisy integrate-and-fire models of neuronal dynamics. *Phys. Rev. E*, **55**, 2040–2043 (1997).
8. Marsalek, P.: Coincidence detection in the Hodgkin-Huxley equations. *Biosystems*, **58**, 83–91 (2000).
9. Marsalek, P., Koch, C., Maunsell, J.: On the relationship between synaptic input and spike output jitter in individual neurons. *Proc. Natl. Acad. Sci. USA*, **94**, 735–740 (1997).
10. Marsalek, P., Kofranek, J.: Sound localization at high frequencies and across the frequency range. *Neurocomputing*, **58–60**, 999–1006 (2004).
11. Marsalek, P., Lansky, P.: Proposed mechanisms for coincidence detection in the auditory brainstem. *Biol. Cybern.*, **92**, 445–451 (2005).
12. McAlpine, D., Jiang, D., Palmer, A. R.: A neural code for low-frequency sound localization in mammals. *Nat. Neuroscience*, **4**, 396–401 (2001).
13. Reed, M. C., Blum, J. J., Mitchell, C. C.: Precision of neural timing: effects of convergence and time windowing. *J. Comput. Neurosci.*, **14**, 34–47 (2002).
14. Srinivasan, M. V., Bernard, G. D.: A proposed mechanism for multiplication of neural signals. *Biol. Cybern.*, **21**, 227–236 (1976).
15. Szalisznyo, K., Zalanyi, L.: Role of hyperpolarization-activated conductances in the auditory brainstem. *Neurocomputing*, **58–60**, 401–407 (2004).
16. Wagner, H., Brill, S., Kempster, R., Carr, C. E.: Microsecond precision of phase delay in the auditory system of the barn owl. *J. Neurophysiol.*, **94**, 1655–8 (2005).

## Multi-Scale Analysis of Brain Surface Data

Thomas Hübsch<sup>1</sup> and Marc Tittgemeyer<sup>2</sup>

<sup>1</sup> Max-Planck-Institute for Human Cognitive and Brain Sciences, Leipzig, Germany;  
huebsch@cbs.mpg.de

<sup>2</sup> Max-Planck-Institute for Neurological Research, Cologne, Germany;  
mark.tittgemeyer@nf.mpg.de

**Summary.** The human brain is characterized by complex convolution patterns. Analyzing the variability of these patterns among human subjects can reveal information for the detection of diseases that affect the human brain. This chapter presents a novel method to visualize the brain surface and its folding pattern at different scales. The analysis steps involved are the transformation of the cortical surface from high resolution magnetic resonance tomography images (MRI) to an initial representation as a triangulated mesh and finally to a representation as a series of spherical harmonic basis functions. The spherical harmonic parameterization of the surface is translation, rotation and scaling invariant. The parametric representation gives a multidimensional coefficient vector for each cortical surface. The technique allows easier recognition of convolutional patterns. The method is a first step toward a statistical multi-scale analysis of the brain surface.

**Key words:** Brain surface visualization, shape analysis, spherical harmonic.

### 23.1 Introduction

The brain surface (specifically the cortical surface) is highly convoluted. Human subjects show great inter-individual variability in their convolutional patterns [1, 2]. We propose a method to simplify and visualize these convolutional patterns. Surfaces are usually simplified by smoothing techniques. This removes unnecessary details while keeping the coarse structure of the surface. Besides smoothing, our method transforms the surface from the three-dimensional (3D) spatial domain to the frequency domain. This will reveal important information on the convolutional patterns at different scales [3, 4]. These scales represent the brain development [5] during fetal and embryonic stages [6] up to the fully convoluted brain [7, 8]. With the advent of neuroimaging procedures, the cortex can be visualized using noninvasive techniques like magnetic resonance imaging (MRI). Through an image processing tool chain (see Materials and Methods) the raw MRI data is converted to a 3D volume dataset. From this dataset, the cortical surface is extracted [9] to a triangulated mesh consisting of several hundred thousand vertices. This mesh structure describes the visible shape of the cortex and so its convolutional pattern. However, to assess the different scales in the cortical surface

the mesh has to be transformed to a new domain. A transformation to the spherical domain has been done in [10] with smoothing based on linear diffusion. The surfaces are restricted to being star shaped but this restriction had been eliminated in [11]. Flat maps are commonly used to transform a 3D cortical surface into the 2D Euclidean domain [12]. Transforming the cortical surface to the structural domain [13] represents the convolutions as a graph structure revealing quantitative properties previously not visible in the original 3D object domain. Our method is based on the transformation to the spherical and frequency domains using spherical harmonic basis functions. Spherical harmonics are commonly used for the decomposition of shapes equal to a deformed sphere. Any object that is topologically equivalent to a sphere (no holes) can be represented as a series of spherical harmonics basis functions. This transformation will allow us to keep almost every detail in the fine cortical structure but also generate a multi-scale description from coarse to fine convolutional patterns.

## 23.2 Materials and Methods

### 23.2.1 Surface Reconstruction

To reconstruct a cortical surface we follow a multistep approach: First 3D T1-weighted MR volumes (192x250x250) at 1 mm resolution were acquired from 160 healthy subjects (80 male, 80 female, age 20–30 years). Then the MR volumes were reoriented to the plane of anterior and posterior commissure and transformed to the standard Talairach stereotactic coordinate system [23]. Upon reorientation, the images were processed for gray-scale normalization and removal of intensity inhomogeneities. A fuzzy C-means algorithm was used to segment the tissue types [14]. The cortical surfaces are generated as smooth triangular meshes [15, 22], where brain substructures such as brain stem and cerebellum have been removed [16].

### 23.2.2 Parameterization

The parameterization step fits a surface  $S: R^2 \rightarrow R^3$  to a set of data points  $P_{i,i=1,\dots,N}$ . The cortical surface can be described after a topological correction as a closed genus zero surface [17], i.e., a deformed sphere. This makes the sphere the most natural parameterization domain for the cortical surface [18, 19]. Choosing the sphere has advantages, as no boundaries for a surface are defined on the sphere as in flat maps [20] and an ideal basis set exists, the spherical harmonics. The mapping of the vertices from the cortical surface to the sphere can be challenging since the cortical surface is usually not star shaped. There have been different approaches for the spherical mapping algorithm. Quicken [24] maps a triangulated mesh by a constrained optimization procedure. The constraints include area preservation and distortion minimization of the mapped triangles. A hierarchical optimization is used, taking multiresolution versions from coarse- to fine-grained of the initial mesh as an input to the optimization procedure. Fischl [15] establishes a surface-based coordinate system by transforming each hemisphere of the cortical surface to a parameterized surface on the sphere. The

mapped surface on the sphere is optimal with respect to metric distortions and degree of folding. The spherical coordinate system (longitude, colatitudes) is used to describe a point  $(x, y, z)$  on the original surface with its coordinates on the sphere. We use the algorithm from Fischl implemented in FreeSurfer [15] which is computationally feasible even for mesh resolutions up to 250,000 vertices and large subject sets.

### 23.2.3 Decomposition

Spherical harmonics form a complete orthonormal basis over the surface of the unit sphere. Any radial function  $f$  can be expanded in terms of complex spherical harmonics [11]:

$$f(\theta, \phi) = \sum_{l=0}^{\infty} \sum_{m=-l}^l C_l^m Y_l^m(\theta, \phi), \quad (23.1)$$

where  $l, m$  integers,  $l \geq m \geq 0$ ,  $\theta \in [0, \pi]$ ,  $\phi \in [0, 2\pi]$ . The spherical harmonics  $Y$  are defined as

$$Y_l^m(\theta, \phi) \equiv \sqrt{\frac{2l + l(l - m)!}{4\pi(l + m)!}} P_l^m(\cos \theta) e^{im\phi}. \quad (23.2)$$

$P_l^m$  are the associated Legendre polynomials of order  $m$  and degree  $l$  and can be expressed in terms of the unassociated Legendre polynomials:

$$P_l^m(x) = (-1)^m (1 - x^2)^{m/2} \frac{d^m}{dx^m} P_l(x). \quad (23.3)$$

A surface can be expressed in terms of spherical harmonics with the decomposition into the three coordinate functions:

$$(X(\theta, \phi), Y(\theta, \phi), Z(\theta, \phi)) = \sum_{l=0}^{\infty} \sum_{m=-l}^l C_l^m Y_l^m(\theta, \phi). \quad (23.4)$$

The coefficients  $C_l^m$  are three-dimensional vectors for the three coordinate functions  $X, Y, Z$  and can be computed by [21]

$$C_l^m = \langle f(\theta, \phi), Y_l^m(\theta, \phi) \rangle = \int_0^\pi \int_0^{2\pi} f(\theta, \phi) Y_l^m(\theta, \phi) d\phi \sin \theta d\theta. \quad (23.5)$$

For a surface mesh, the function  $f(\theta, \phi)$  is only defined at the  $N$  mesh vertices. Therefore, the method adopted by Brechbühler [21] is chosen where all the values needed for the basis function are arranged in matrix  $B$ ,  $b_{ij(l,m)} = Y_l^m(\theta_i, \phi_i)$ , the surface data points  $(x, y, z)$  are arranged in a matrix  $X$  and the coefficients in a matrix  $C$ ,  $c_{ij(l,m)} = (C_l^m x, C_l^m y, C_l^m z)$ . This results in the linear equation system  $B \cdot C = X$ , with the coefficients matrix  $C$  as the solution. After the parameterization the surface is now represented in the coefficient space within the spherical harmonic basis function



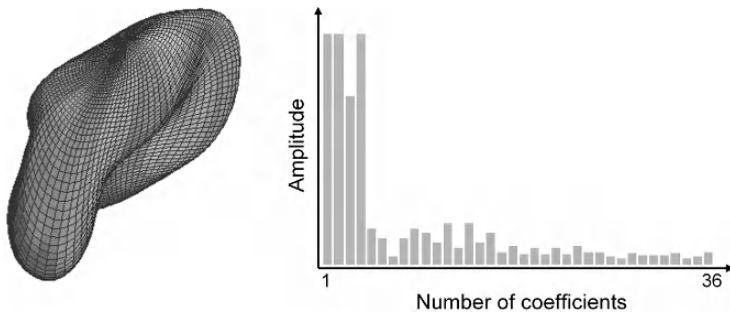


**Fig. 23.1.** Cortical surface of right hemisphere and first 36 coefficients.

coordinate system completely scaling, rotation and translation invariant. It allows the visualization and analysis at multiple scales. Fig. 23.1 shows the coarse-scale visualization of the right hemisphere from an individual subject and the associated spherical harmonic coefficients. The convolutional patterns are hidden, only the cortical outline shape is visible. For statistical analysis a feature vector  $v$  is extracted for each cortical surface  $m$  from the spherical harmonics coefficients:

$$v_m = \bigcup_{k=1}^K c_{m,k}, \tag{23.6}$$

where  $K$  is the number of coefficients, and  $c_{m,k}$  is the coefficient  $k$  in subject  $m$ . Grouping the coefficients of all surfaces together results in the feature matrix  $F$ :

$$F = \begin{pmatrix} c_{1,1} & c_{1,2} & c_{1,3} & \dots & c_{1,k} \\ c_{2,1} & c_{2,2} & c_{2,3} & \dots & c_{2,k} \\ \dots & \dots & \dots & \dots & \dots \\ c_{m,1} & c_{m,2} & c_{m,3} & \dots & c_{m,k} \end{pmatrix}, \tag{23.7}$$

where  $c_{m,k}$  is the coefficient  $k$  in subject  $m$ .

The feature vector  $v_m$  and the feature matrix  $F$  will be used in subsequent analysis steps.

## 23.3 Results

### 23.3.1 Surface Visualization

Comparing subjects according to their convolutional pattern is much easier at the coarse scale. Fig. 23.2 shows one subject’s right hemisphere at different scales from coarse (upper left) to fine convolutional patterns (lower right). The surface is visualized as a series of spherical harmonic coefficients instead of the original triangulated mesh. This new representation requires 1/10 of the original storage for the mesh, since only the coefficients for each surface have to be stored. Fig. 23.3 depicts three subjects

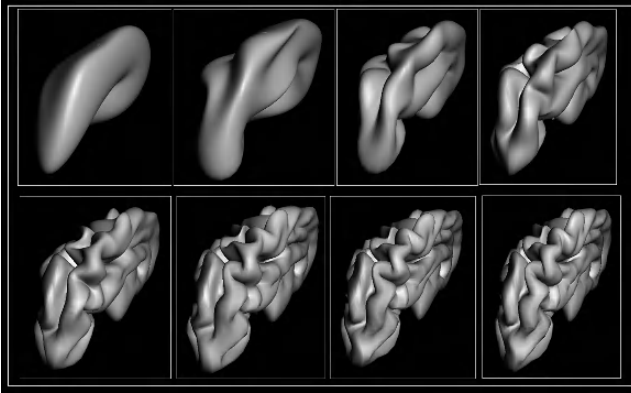


**Fig. 23.2.** Subject's right hemisphere at eight different scales.

at three different scales. The left column reveals their difference in the inferior frontal cortex (white arrow). In the middle column additional differences in the Sylvian fissure (white arrow) become visible. At the full scale (right column) the differences are numerous, taking into account all convolutions in their final complexity. In a first step toward a statistical multi-scale analysis, each surface is described by its feature vector and the mean shape in the coefficient representation is computed.

### 23.3.2 Pattern Analysis

In order to compare cortical surfaces from different subjects the feature matrix  $F$  containing the feature vectors is statistically analyzed. A shape characterized by its feature vector  $v$  can be interpreted as a point in a high dimensional vector space. A distance measure can now be applied to all of these points. The  $L_p$  distance between two points

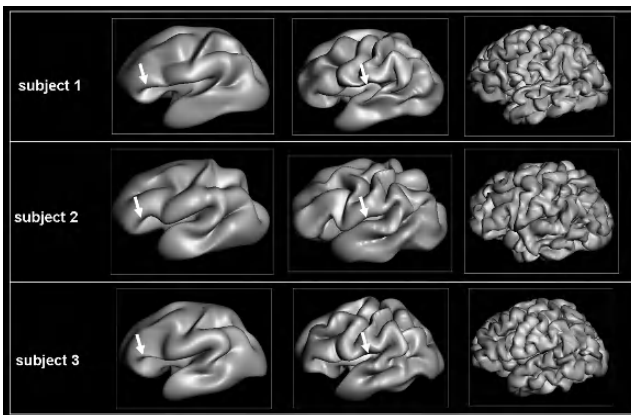


**Fig. 23.3.** Three male subjects visualized at three different scales.

$x, y \in R^K$  is used ( $K$  is the number of coefficients):

$$L_P(x, y) = \left( \sum_{i=0}^N |x_i - y_i|^P \right)^{1/P} \quad (23.8)$$

with  $P = 1$  the  $L_1$  distance,

$$L_1(x, y) = \left( \sum_{i=0}^N |x_i - y_i| \right) \quad (23.9)$$

between two feature vectors used as a similarity measure. As seen in the Fig. 24.1 the coefficients are decreasing in amplitude from low to high frequencies. Low frequencies have high impact in the distance between feature vectors. Low frequencies encode overall shape and extend the cortical surface; therefore, the similarity measure is sensitive to match these properties first when comparing two cortical surfaces. To overcome this limitation a Spearman rank correlation matrix between all subjects is established:

$$R = \begin{pmatrix} r_{1,1} & r_{1,2} & \dots & r_{1,j} \\ r_{2,1} & r_{2,2} & \dots & r_{2,j} \\ \vdots & & & \vdots \\ r_{i,1} & r_{i,2} & \dots & r_{i,j} \end{pmatrix}, \quad r_{ij} = 1 - \frac{6 \sum_{k=1}^K (d_{k,i} - d_{k,j})^2}{K(K^2 - 1)}, \quad (23.10)$$

where  $d_{k,i}$  is the statistical rank of coefficient  $k$  in subject  $i$ .

The nonparametric Spearman rank correlation is used in favor of the Pearson correlation, because the coefficients in feature vector  $v$  are already ordered from low to high frequencies. The overestimation of low frequencies can be avoided since the statistical rank differences between coefficients and not their absolute value are used in the measure.

**Combining statistical measures.** Both statistical measure  $L_1$  distance and Spearman rank correlation are combined to define a similarity measure for the feature vectors:

$$rl_{i,j} = (1 - r_{i,j}) l_{i,j}, \quad (23.11)$$

where  $r_{i,j}$  is the Spearman rank correlation between feature vector of subjects  $i$  and  $j$ , and  $l_{i,j}$  is the distance between feature vector of subjects  $i$  and  $j$ .

Through a cluster analysis the cortical shapes are organized into groups according to their shape properties. This could potentially lead together with neuronal and cellular properties of the cortex to a taxonomy of brain surfaces. Since there is no a priori hypothesis about cluster groups of cortical surfaces, a hierarchical cluster analysis is employed. The joining tree clustering joins together feature vectors of cortical surfaces into successively larger groups. The joining operation requires some similarity or distance measure. The combined  $L_1$  distance and Spearman rank correlation is used as the measure. Each step in the clustering algorithm joins together two objects. The value of  $rl_{i,j}$  chooses the two closest objects. As more objects are grouped together the cluster becomes larger and contains more dissimilar elements according to

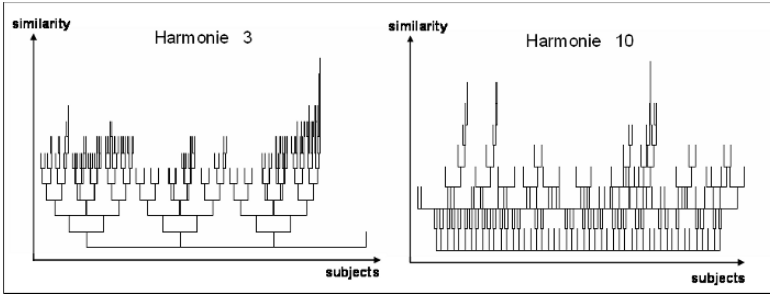


**Fig. 23.4.** Cluster groups for 80 male subjects for 3 and 10 harmonies.

the measure  $rl_{i,j}$ . The algorithm operates as follows. In the first step each object resides in its own cluster, the distance between two objects is  $rl_{i,j}$ . In subsequent steps two clusters with more than one element have to be compared. The linkage rule which decides if two clusters are similar is determined by the matrix  $R$ , the subjects being the union of the two clusters' subjects. The two objects with the maximal correlation are computed as well as their  $L_1$  norm. If the value  $rl_{i,j}$  is below the threshold then the minimum correlation and maximum  $L_1$  norm between all subjects in the newly formed cluster are computed. If these are also below the threshold the new cluster is formed. This prevents the cluster from becoming too heterogeneous according to the similarity measure  $rl_{i,j}$ .

At three harmonies only 16 coefficients from the spherical harmonic series are used; therefore, only the coarse shape is reconstructed and clustered. Fig. 23.4 shows that three cluster groups have emerged at three harmonies. At 10 harmonies primary folding patterns are visible, the cluster groups have been spread out and the dissimilarity among the cortical surfaces is much higher—therefore smaller clusters have been formed. Fig. 23.5 shows subjects at 3 and 5 harmonies from the same cluster group as well as the same subjects at 10 harmonies in different clusters.

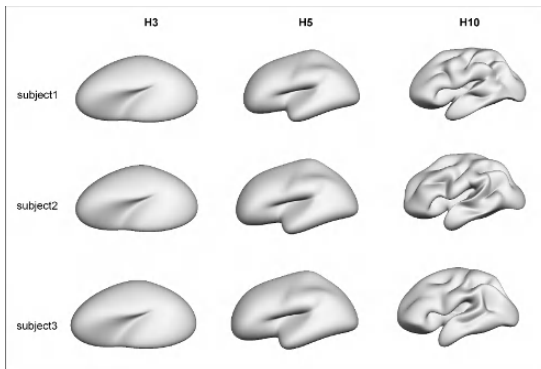


**Fig. 23.5.** Individual subjects at 3, 5 and 10 harmonies. At 3 and 5 harmonies all subjects belong to the same cluster. At 10 harmonies the subjects fall into different clusters.

## 23.4 Conclusion

The method allows variable scale analysis and visualization of the cortical surface despite differences in size and shape of the convolutional patterns. Each surface is transformed from the common spatial domain representing the cortex in three-dimensional coordinates, to the frequency domain representing the cortex as spherical harmonic coefficients. In the frequency domain cortical folds are expressed through low frequencies forming the coarse shape and high frequencies adding finer folding details. The spherical harmonic transformation reduces the complexity of the cortical surface. Simplified cortical surfaces allow easier comparisons of cortical convolutions. Cortical surfaces expressed as an ordered series of spherical harmonic coefficients make statistical analysis in large group studies possible. The statistical analysis can group surfaces into clusters according to their shape properties and folding patterns.

## References

1. Hofman, M.A.: The fractal geometry of convoluted brains. *J. Hirnforsch.*, **32**, 103–11 (1991).
2. Kennedy, D.N., et al.: Gyri of the human neocortex: an MRI-based analysis of volume and variance. *Cereb. Cortex*, **8**, 372–84 (1998).
3. Prothero, J.: Small brain, large brain—a quest for nature’s scale-up rules. *J. Hirnforsch.*, **39**, 335–47 (1999).
4. Prothero, J.W., Sundsten, S.W.: Folding of the cerebral cortex in mammals. A scaling model. *Brain Behav. Evol.* **24**, 152–67 (1984).
5. Richman, D.: Mechanical model of brain convolutional development. *Science*, **189**, 18–21 (1975).
6. Price, D., Willshaw, D.: *Mechanisms of Cortical Development*, 1st edition. Oxford: Oxford University Press (2000).
7. Hofman, M.A.: Size and shape of the cerebral cortex in mammals. I. The cortical surface. *Brain Behav. Evol.*, **27**, 28–40 (1985).
8. Hofman, M.A.: Size and shape of the cerebral cortex in mammals. II. The cortical volume. *Brain Behav. Evol.*, **32**, 17–26 (1988).
9. Joshi, M., et al.: Brain segmentation and the generation of cortical surfaces. *Neuroimage*, **9**, 461–76 (1999).
10. Blow, T.: Spherical diffusion for 3d surface smoothing. 1st International Symposium on 3D Data Processing, Visualization and Transmission, Padova, Italy, 449–458 (2002).
11. Brechbühler, C., Gerig, G., Kübler, O.: Parametrization of closed surfaces for 3-d shape description. *CVIU*, **61**, 154–170 (1995).
12. Van Essen, D.C., Drury, H.A.: Structural and functional analyses of human cerebral cortex using a surface-based atlas. *J. Neurosci.*, **17**, 7079–102 (1997).
13. Riviere, D., et al.: Automatic recognition of cortical sulci of the human brain using a congregation of neural networks. *Med. Image Anal.*, **6**, 77–92 (2002).
14. Pham, D.L., Prince J.L.: An adaptive fuzzy C-means algorithm for image segmentation in the presence of intensity inhomogeneities. *Pattern Recognition Letters*, **20**, 57–68 (1999).
15. Fischl, B., Sereno, M.I., Dale, A.M.: Cortical surface-based analysis. II: Inflation, flattening, and a surface-based coordinate system. *Neuroimage*, **9**, 195–207 (1999).

16. Kelemen, A., Szekely, G., Gerig, G.: Elastic model-based segmentation of 3-D neuroradiological data sets. *IEEE Trans. Med. Imaging*, **18**, 828–39 (1999).
17. Griffin, L.D.: The intrinsic geometry of the cerebral cortex. *J. Theor. Biol.*, **166**, 261–73 (1994).
18. Haker, S., et al.: Conformal surface parameterization for texture mapping. *IEEE Trans. Visualization and Computer Graphics*, **6**, 181–189 (2000).
19. Yu, P., et al.: Shape analysis of neuroanatomical structures based on spherical wavelets. 11th Annual Meeting of the Organization for Human Brain Mapping (OHBM), Toronto, Canada (2005).
20. Van Essen, D.C., et al.: Functional and structural mapping of human cerebral cortex: solutions are in the surfaces. *Adv. Neurol.*, **84**, 23–34 (2000).
21. Brechbuehler, C.: Description and analysis of 3-D shapes by parametrization of closed surfaces. Diss., ETH Zurich, (1995).
22. Thompson, P.M., Schwartz, C., Toga, A.W.: High-resolution random mesh algorithms for creating a probabilistic 3D surface atlas of the human brain. *Neuroimage*, **3**, 19–34 (1996).
23. Lohmann, G., et al.: LIPSIA—a new software system for the evaluation of functional magnetic resonance images of the human brain. *Comput. Med. Imaging Graph.*, **25**, 449–57 (2001).
24. Quicken, M., Brechbühler, C., Hug, J., Blattmann, H., Szekely, G.: Parameterization of closed surfaces for parametric surface description. *Computer Vision and Pattern Recognition CVPR* (2000).

## The Spike Generation Processes: A Case for Low Level Computation

Tjeerd olde Scheper

Department of Computing, Oxford Brookes University, Oxford, OX33 1HX, UK;  
tvolde-scheper@brookes.ac.uk

**Summary.** Over the last couple of years, it can be said that the focus of the computational aspects of neurons has moved from synaptic weight and firing rate encoding to temporal firing encoding. On the other hand, several elements of these models have been based on some conceptual assumptions that imply relative simple dynamic behaviour of neuronal membrane activity in an active-passive process. In line with recent advances that have produced a better understanding of the biochemical processes that occur within cells, it is proposed that the processes that are involved in a membrane depolarisation cascade are less static than have been assumed so far. In particular, the possibilities of low level computation at the membrane level need to be explored more extensively. In this chapter some computational properties of the spike generation processes are explored using phenomenological models.

**Key words:** Neuronal membrane, computation, Hindmarsh–Rose model, chaotic control, synchronisation.

### 24.1 Introduction

The limited dynamic behaviour that exists within models currently studied for spike generation is partly due to the fact that little is known about the low level interaction of the components that generate the depolarisation cascade. Even though it has been known for a long time that the ionic channel dynamics is voltage gated as well as gated by other mechanisms, the interaction between different transmembrane components and intracellular processes is less well known [1, 7]. This may, in part, be attributed to the difficulty of measuring accurately the exact state of individual channels and the difficulty of acquiring information about the subcellular processes that are involved in the spike generation cascade of living cells. The construction of theoretical models of these channels has already produced a large body of knowledge about the conductance behaviour of ionic channels. This knowledge is, however, limited by the underlying assumptions of the models. The stable state of most conductance models, such as the well-known Hodgkin–Huxley system, does not include further dynamical aspects beyond mere responses to global changes in voltage. By developing abstract models of more complex systems with the specific aim to produce systems that are capable of

some level of computation and comparing the performances with biological systems, a much more detailed understanding of the possible processes may be reached.

## 24.2 Membrane Elements as Computational Units

To achieve a better understanding of the processes involved in the possible computations performed at the molecular level in the neuronal membrane, a membrane computational unit can be defined. A membrane computational unit (MCU) is formed by a collection of ionic channels and other transmembrane proteins that contribute to the formation of a single depolarising spike in a neuronal membrane at that point. The composite elements are not evenly distributed nor is it assumed that they are all in a similar state. Indeed, these states may be responsible for a localised mechanism that may be capable of some types of computation. The advantages of such mechanisms are extensive. A combination of localised membrane-specific computation and global computational activity of the entire neuron will allow a staggering amount of processing elements. Furthermore, each MCU does not have to be specifically defined but can be organised in response to local dynamic behaviour.

Local state changes of the complex interactions of membrane depolarising units have not been considered to be very relevant in the overall theory of neuronal computation. Indeed, an emphasis appears to exist to reduce the membrane components of an electrically active cell to mere conductive elements with the computation solely provided by intercellular communication [1]. This model of cellular activity is based on single and population channel dynamics in an enforced fixed state. However, if one considers that the interaction of all the channel proteins are of an extremely complex nature, as can be derived from the rest of the biochemical pathways [2], it appears to be more likely that localised states and state-induced processing are not only possible but functional.

The biophysical structure of the membrane may be described as a mosaic of ionic channels and other membrane-bound proteins. The biophysical organisation of the neuronal membrane mosaic determines the properties of the membrane, such as conductance [3]. This is depicted schematically in Fig. 24.1 where the octagons represent an ionic channel organisation and the circles molecules that are capable of inducing adaptation. In a static model environment, the adaptation may cause the global neuronal behaviour to change in response to a depolarisation input current. In a temporal and spatially dynamic model the localised adaptation may cause the local environment to change in response to local and global effect. This includes both local adaptation as activity-induced adaptation of the membrane mosaic (Fig. 24.2 and 24.3).

The conductance models, as currently used in systems of computational neurons, are generally based on the original models (or variations of it) as defined according to the Hodgkin–Huxley dynamics [6, 15]. This describes each ionic channel as a continuous state variable whose dynamic behaviour in time is described by first-order kinetics. Each channel equation has an increasing term and a decreasing term of the conductance dependent state variable  $n$ , e.g.,  $dn/dt = \alpha_n(V) \times (1 - n) - \beta_n(V) \times n$ .



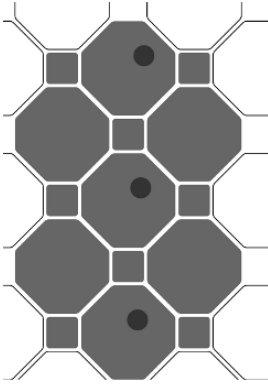


**Fig. 24.1.** The biophysical mosaic.

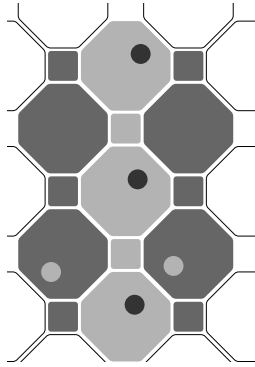


**Fig. 24.2.** Local response of conductive elements in presence of adaptation.

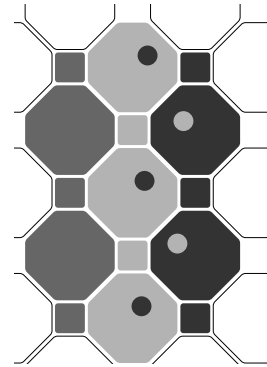


**Fig. 24.3.** Activity-induced adaptation in nearby conductive elements in a biophysical mosaic.

The activation and inactivation rate functions  $\alpha_n(V)$  and  $\beta_n(V)$  were then experimentally determined by varying the voltage. The resulting equations were subsequently derived from the experimental data set by fitting elementary arithmetical operations as functions of the voltage. There are several assumptions made within this model that may now be considered to be too unassuming.

The possible states of the ionic channels can be primarily determined by the conductance but the existence of additional states is not impossible. It could be considered that other states, such as a blocked state, are part of the normal state transitions that occur. The kinetic dynamics of the molecular interactions are rarely of first order within other biochemical reactions and this may be recognised by considering the subdomains and co-proteins of the ionic channel as part of the kinetic equation. The rate of opening and closing as described by the  $\alpha(V)$  and  $\beta(V)$  functions only describes the channel dynamics but does not explain the mechanisms by which these dynamics have emerged. Furthermore, the functions, as currently used to describe the spike generation process, are incapable of exhibiting other dynamics than fixed state dynamics (by external periodic forcing and similar mechanisms, some more complex dynamic behaviour of the voltage may be produced but these do not change the stable state of the Hodgkin–Huxley system itself).

It can be argued that the localised dynamics exist by virtue of the biochemical processes involved. In other words, the enzymatically controlled chemical reactions and the membrane processes controlled by secondary and tertiary molecular structural changes do allow more complex dynamics to occur. The observation of noisy oscillations is not precluded by this assumption. It may also be considered that if the highly controlled processes that can be found in the biochemical pathways were not present in the proteins involved in the formation of the depolarisation cascade, they would form a complete separate part of the entire biochemical system. An uncontrolled and noisy

process, such as the depolarisation cascade, is simply not energetically favourable if by controlling the process, energy can be saved. The next step in process control, in the sense of allowing some depolarising currents to result in a spike or of blocking such currents locally, seems to be a mere optimisation of the complete controlled process. True localised computation may then follow readily and it can then be possible to define a spatially and dynamically bound unit which forms the minimally required computational element or MCU.

Ideally, one would like to describe all processes and molecules involved at the biophysical level and study the system using the physical properties of those processes. The complexity of such a modelling system is of very high order and, by assuming that the underlying computational process is not dependent on unique physical circumstances, the use of more phenomenological models is justified with the aim of understanding what is required to achieve some particular computational process.

### 24.3 Membrane Computational Unit Model

With the aim of simulating computational processes within an MCU, several biologically relevant phenomenological models are combined. Each model of an MCU has at least two different components that act together to produce a system which is capable of complex emergent behaviour. One is a spike generation component and the other a controlled chaotic drive component. The spike formation component has been derived from the Hindmarsh–Rose (HR) model [5] but includes a fourth slow recurrent equation which represents the slow calcium exchange between intracellular stores and the cytoplasm [10]. This makes the modified HR model more like a chaotic Hodgkin–Huxley (HH) model of stomatogastric ganglion neurons [10]. The four-dimensional HR can therefore be accurately interpreted as a phenomenological model of the conductance-based HH model. The parameter values for the four-dimensional Hindmarsh–Rose (HR4) model are  $a = 1$ ,  $b = 3$ ,  $c = 1$ ,  $d = 1$ ,  $e = 1$ ,  $f = 5$ ,  $g = 0.0275$ ,  $u = 0.00215$ ,  $s = 4$ ,  $v = 0.001$ ,  $k = 0.9573$ ,  $r = 3.0$ ,  $m = 1$ ,  $n = 1$  and rest potential  $x_0 = 1.605$ . The variable  $I$  represents the input to the unit which can be external square input pulses or input from other units. With these parameter values the model is stable in the resting potential but shows low dimensional chaos in the bursting patterns [10].

$$\frac{dx}{dt} = ay + bx^2 - cx^3 - dz + I \quad (24.1)$$

$$\frac{dy}{dt} = e - fx^2 - my - gw \quad (24.2)$$

$$\frac{dz}{dt} = u(s(x + x_0) - nz) \quad (24.3)$$

$$\frac{dw}{dt} = v(r(y + l) - kw) \quad (24.4)$$

It is also possible to add another inactivation current which competes with the third current to return the system to the equilibrium state. The third equation of the

HR4 model (24.3) is then complemented with a fifth equation resulting in the five-dimensional Hindmarsh–Rose model HR5. The effect of the faster inactivation current  $z_f$  (24.8), compared to the slower inactivation current as used in HR4, is that the system tends to burst less. The faster current makes the system return faster towards the equilibrium where only a larger (re)activation current can cause the system to burst. In the MCU model, the HR5 system allows the temporal separation of spikes by increasing the refractory period. Parameter values for (24.8) are  $s_{f_1} = 8, s_{f_2} = 1, n_f = 4$  and the parameter  $d_f = 0.5$  in (24.5). The parameters  $s_s = 4$  and  $n_s = 1$  have the same value as the equivalent parameters in (24.3).

$$\frac{d x}{d t} = a y + b x^2 - c x^3 - d_s z_s - d_f z_f + I \quad (24.5)$$

$$\frac{d y}{d t} = e - f x^2 - m y - g w \quad (24.6)$$

$$\frac{d z_s}{d t} = u (s_s (x + x_0) - n_s z_s) \quad (24.7)$$

$$\frac{d z_f}{d t} = u ((s_{f_1} (x + x_0) - s_{f_2} x^2) - n_f z_f) \quad (24.8)$$

$$\frac{d w}{d t} = v (r (y + l) - k w) \quad (24.9)$$

Connecting these HR models will result in different types of behaviour, such as stable periodic and chaotic synchronised and unsynchronised behaviour [10]. These depend on continuous, relatively large, inputs to the model. It is possible to make continuous connections of HR4 models that change the chaotic spike bursting into slow oscillations [12]. However, the system need not be purely chaotic to make use of some of the properties of chaotic systems, such as control and synchronisation. A *controlled* chaotic system is a system which is inherently chaotic but is limited to a controlled state such that the resulting dynamic behaviour is indistinguishable from periodic behaviour [14]. For some types of control, such as rate control and Ott–Grebogi–Yorke (OGY) control [8, 14], the chaotic system is only perturbed into the unstable periodic orbit during very small periods of its evolution. Outside the control period, the controlled system is still capable of synchronisation [9]. This feature allows the use of a stable controlled period generated by a *controlled* chaotic system to synchronise to another system even if they have different periods.

To introduce the required controlled chaotic behaviour in either of the HR models, a scaled and inverted Rössler system has been used [13]. This is necessary because the normal Rössler model has a different time scale from the HR4 model. As can be seen in Table 24.1, the scaled variables are proportional to the normal Rössler parameter values. It is possible to map the time scale of the modified Rössler (R3) model to fit the time scale of the HR4 model and use the R3 system to generate patterns. In addition to the scaling, the  $u_r$  variable has been inverted to enable the convenient use of this variable as the drive for the HR4 model.

$$\frac{d x_r}{d t} = -b_r y_r - d_r u_r \quad (24.10)$$

**Table 24.1.** Scaled parameter values compared to normal Rössler model values.

Parameter	Normal value	Scaled value
$a_r$	$\frac{1}{5}$	$\frac{1}{75}$
$b_r$	1	$\frac{1}{15}$
$c_r$	1	$\frac{1}{15}$
$d_r$	1	$\frac{1}{50}$
$k_r$	5.7	-0.57
$w_r$	$\frac{1}{5}$	$-\frac{1}{75}$
$p_r$	1	-1

$$\frac{d y_r}{d t} = c_r x_r + a_r y_r \tag{24.11}$$

$$\frac{d u_r}{d t} = p_r u_r x_r + k_r u_r + w_r \tag{24.12}$$

The R3 system is controlled into an unstable periodic orbit using a chaotic rate control mechanism [8]. This mechanism allows the system to exhibit different periodic orbits by limiting the rate of change of equation (24.12). The rate control variable  $\sigma$  is only different from 1 if the variables  $x$  and  $u$  are diverging rapidly, i.e., when the chaotic manifold is stretching or folding. Equation (24.12) is modified to (24.14) as shown below. The rate control parameter  $\mu$  determines the strength of the rate limiting function and the parameter  $\xi$  can have different values but is usually  $-2 \leq \xi < 0$ . This chaotic control mechanism is very effective at stabilising different unstable periodic orbits, but not for any given value of  $\mu$  and  $\xi$ . Typically used values are  $\mu = 6$  and  $\xi = -1$  or  $\xi = -2$ .

$$\sigma(x, u) = e^{\frac{\xi(xu)}{u+x+\mu}} \tag{24.13}$$

$$\frac{d u_r}{d t} = \sigma(x_r, u_r) p_r u_r x_r + k_r u_r + w_r. \tag{24.14}$$

The controlled chaotic system is now connected to the four-dimensional Hindmarsh-Rose system via the HR4  $z$  variable. Equation (24.3) is subsequently modified to become

$$\frac{d z}{d t} = u (s (x + x_0) - q u_r z). \tag{24.15}$$

Because the  $u_r$  variable of the scaled Rössler R3 system is always negative, the parameter  $q$  in equation (24.15) is negative:  $q = -12$ .

Finally, different HR-type systems may be connected electrically by summation of the two main currents. It is possible to extend this to all currents but this does not seem to have a significant effect on the qualitative behaviour of the two connected systems.

By adding the total differences in activity of the HR models'  $x$  and  $y$  variables as follows, depending on the choice of  $\alpha$ , different dynamic behaviour will result:

$$I_i(x) = \alpha_i(x) \sum_j (x_j - x_i) \tag{24.16}$$

$$I_i(y) = \alpha_i(y) \sum_j (y_j - y_i). \tag{24.17}$$

For example, for  $\alpha(x), \alpha(y) > 0$  the resulting HR system will act as a logical AND of the input spikes. With  $\alpha(x) = 0$  and  $\alpha(y) > 0$ , the resulting HR system acts as an AND-NOT gate, i.e., it is only active if one of the inputs has produced a spike but not if both spike together and not if only the other input has a spike. This may be used to detect both coincidental spikes as well as single spikes from one source only.

### 24.4 SyncMCU

The different computational elements described may be combined to construct an ensemble of computational elements capable of solving computational problems. For example, consider Fig. 24.4 where five computational units are linked. Here, units HR4R3-1 and 2 are made from four-dimensional HR systems, driven by a controlled scaled Rössler system R3. Unit HR5-AND consists of a single HR5 system, without a controlled chaotic drive, but electrically connected to units HR4R3-1 and 2 using (24.16) and (24.17) with  $\alpha(x), \alpha(y) > 0$ . Unit HR4-ANDNOT consists of a four-dimensional HR4 system but with a scaled R3 drive. It receives input from units HR4R3-1 and 2 but with  $\alpha(x) = 0$  and  $\alpha(y) > 0$ . Lastly, unit HR4 is a normal HR4 system without an R3 drive, that only receives input from unit HR5-AND. All the R3 drive systems are controlled in the same unstable periodic orbit but the driving scalar

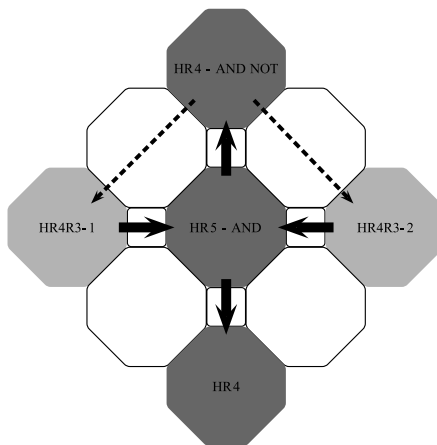


**Fig. 24.4.** Schematic representation of the SyncMCU model.

is small such that by itself it does not cause the system to fire. The R3 systems may therefore act as a localised subcellular clock that can be in or out of sync with other units.

The configuration shown in Fig. 24.4 may act as a detector of desynchronisation of two input signals. Given an additional external input to the units HR4R3-1 and 2, which are combined in unit HR5-AND and then passed on to unit HR4, the unit HR4-ANDNOT will detect if unit HR4R3-2 fires but HR4R3-1 does not. Note that if they both fire, HR4-ANDNOT does not fire unless it has fired recently. We can now use this to attempt to synchronise unit HR4R3-2 with unit HR4R3-1 even if they have completely different periods.

To enable unit HR4-ANDNOT to synchronise the units HR4R3-1 and 2, a synchronisation function is defined as

$$\frac{dS}{dt} = \kappa_1(x_r^1 - x_r^2)\theta(x) - \kappa_2S, \quad (24.18)$$

where  $\kappa_1$  and  $\kappa_2$  are the growth and decay parameters, and  $x_r^n$  are the  $x_r$  variables of the controlled chaotic scaled Rössler systems of the units that are synchronised. The function  $\theta(x)$  is a threshold function on the  $x$  variable of the HR4 system of the unit HR4-ANDNOT. Parameters for (24.18) are  $\kappa_1 = -0.75$ ,  $\kappa_2 = 0.5$  with the threshold set at  $-0.5$ .

## 24.5 Results

In Fig. 24.5 and 24.6 can be found the results of the SyncMCU model. The model is integrated using different time steps and verified with several numerical integrators, such as the fifth-order Runge–Kutta and Prince–Dormand Runge–Kutta integrators, which all produced qualitatively similar results. Because the model cannot start from an *a priori* established initial stable state, the model is run for 5000 time steps without chaotic control to allow the Rössler model to reach the domain of its strange attractor. At time step 5000, the chaotic control is enabled, resulting in subthreshold activity which ensures that the model is in a stable periodic orbit before external input is presented. At time step 10000, the external input is enabled which generates pulses of width 10 with period 290 for HR4R3-1 and period 400 for HR4R3-2.

In both Fig. 24.5 and 24.6, the  $x$  variables of HR4R3-1 and 2 are shown for the first 25000 time steps only. This enables the period, due to the combined effect of the controlled chaotic drive and the external input, to become visible. They are verified to continue in the same multiorbit for very long runs. As can be seen in Fig. 24.5(c) and (d), in the unsynchronised case, units HR5-AND and HR4-ANDNOT show spiking patterns at the combined harmonic input periods. Because the system is responding to the effects of the external input combined with its internal controlled chaotic drive, the emerging patterns appear fairly noisy.

In the synchronised case, as shown in Fig. 24.6(c) and (d), the emerging patterns are corrected by the synchronisation pulses shown in 24.7(b) on the internal unit controlled chaotic drive, and the patterns are much less noisy than in the unsynchronised case.

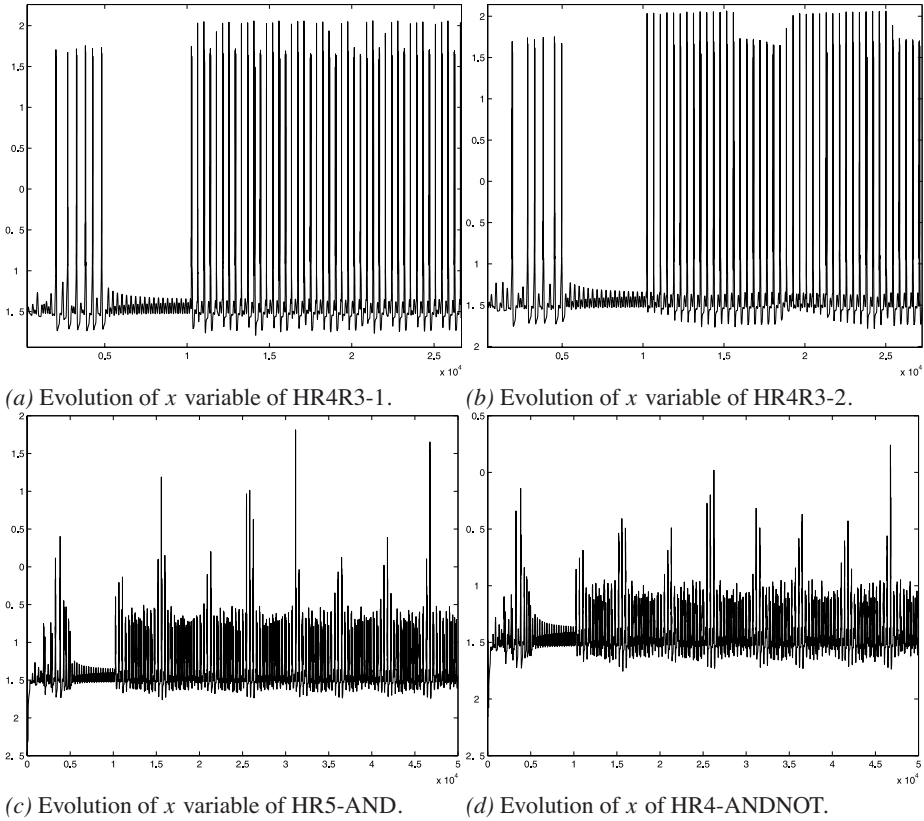
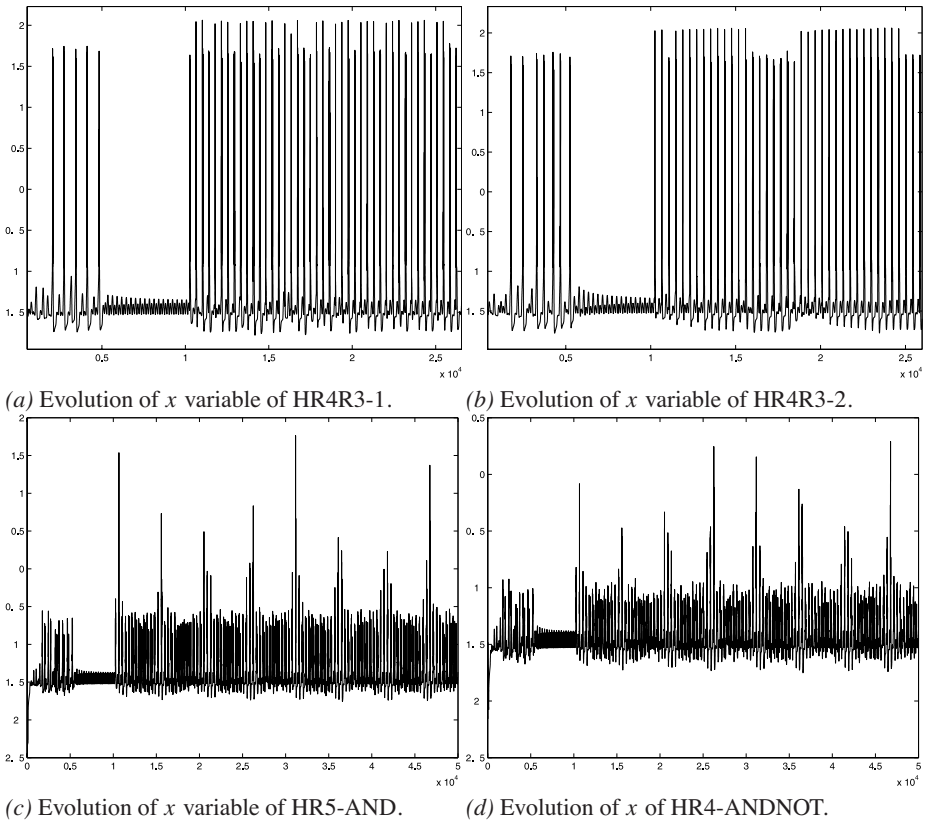


Fig. 24.5. SyncMCU model without synchronisation.

By superimposing the synchronised and unsynchronised unit HR4-ANDNOT in Fig. 24.7(a) the extent of synchronisation correction becomes more clear, indicating that the correction made by the synchronisation function is effective even though the periods of the external input patterns are very much different.

## 24.6 Conclusion

Using a combination of phenomenological models, it may become possible to study computational aspects of neuronal membrane functions. The computational aspects that can be modelled using the MCU paradigm can give indications of biophysical features that may be hidden from the experimentalist at this moment. It can also extend the computational ability of neural and neuronal networks by more distributed computation and the use of simple computational steps to perform important signal processing functions.

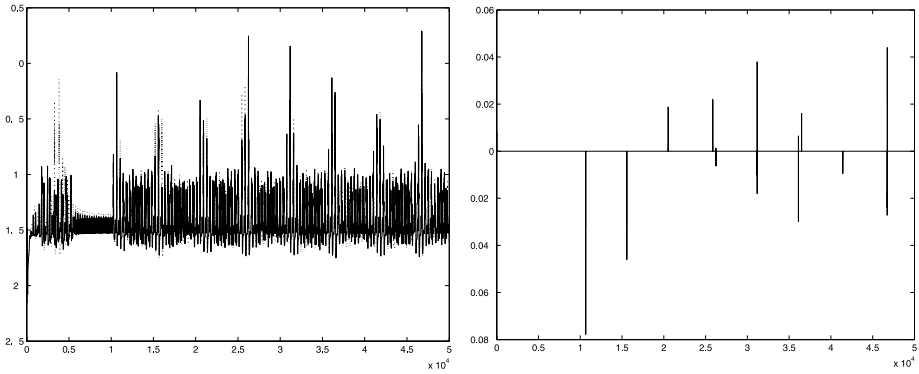


**Fig. 24.6.** Response of Membrane Computational Units to different input frequencies to units HR4R3 in the SyncMCU model.

The synchronisation model is based on the synchronisation capabilities of the controlled chaotic internal drive. Even though the underlying internal drive is based on a scaled chaotic Rössler model, the resulting system is stable periodic due to the control. The emergent behaviour of the model is due to the interaction of the different periodic external inputs to HR4R3-1 and HR4R3-2 with the stable periodic controlled drive which is summed in HR5-AND and filtered through HR4-ANDNOT, resulting in a synchronisation pulse to HR4R3-2. This, finally, causes the internal controlled drive to synchronise to the difference between the inputs to HR4R3-1 and HR4R3-2. Introducing white Gaussian noise in the external input frequencies does not prevent the system from synchronising although more correcting synchronisation pulses are needed (not shown).

Results from conceptual models as presented may provide indications to identify localised computation in the neuron. Recent experimental results in the subunits of thin dendrites [11] indicate the possible important role of spatial compartmentalisation. Additionally, experimental results, obtained by looking at learning by geometrical shape





(a) Evolution of  $x$  variables of HR4-ANDNOT, solid line synchronised, dotted line unsynchronised. (b) Synchronisation pulses of the synchronisation function  $S$  when synchronising unit HR4R3-2.

**Fig. 24.7.** Effect of Synchronization pulses which synchronises unit HR4R3-2 with HR4R3-1.

changes of dendritic spikes, have shown that a single spike event is capable of modulation of the signal transmission [4]. The MCU paradigm may provide a computational framework from which the computational abilities of dendritic structures can be studied.

## Acknowledgments

Many thanks to Dr. Nigel Crook and Professor Cyriel Pennartz for their valuable contributions and discussion.

## References

1. Dayan, P., Abbott, L.F.: *Theoretical Neuroscience, Computational and Mathematical Modeling of Neural Systems*. MIT Press, Cambridge, MA (2001).
2. Fell, D.A.: *Understanding the Control of Metabolism*. Portland Press, London (1997).
3. Graham, L.J., Kado, R.T.: *The Handbook for Brain Theory and Neural Networks*. Chapter: The neuron's biophysical mosaic and its computational relevance. MIT Press, Cambridge, MA, 2nd edition (2002), 170–175.
4. Herzog, A., Spradvedlyvyy, V., Kube, K., Schnabel, R., Korkotian, E., Braun, K., Michaelis, B.: Learning by geometrical shape changes of dendritic spikes. In: Proceedings of European Symposium on Artificial Neural Networks 2004 (2004), 385–390.
5. Hindmarsh, J.L., Rose, R.M.: A model of neuronal bursting using three coupled first order differential equations. *Proc. R. Soc. Lond.*, **B 221**, 87–102 (1984).
6. Hodgkin, A.L., Huxley, A.F.: A quantitative description of membrane current and its application to conduction and excitation in nerve. *J. Phys.*, **117**, 500–544 (1952).
7. Maass, W., Bishop, C.M. (eds.): *Pulsed Neural Networks*. MIT Press, Cambridge, MA (2001).

8. olde Scheper, T.: Rate control of chaotic systems. in preparation (2007).
9. Pecora, L.M., Carroll, T.L.: Synchronization in chaotic systems. *Phys. Rev. Lett.*, **64**, 821–824 (1989).
10. Pinto, R.D., Varona, P., Volkovskii, A.R., Szucs, A., Abarbanel, H.D.I., Rabinovich, M.I.: Synchronous behavior of two coupled electronic neurons. *Phys. Rev. E*, **62** (N2 PTB), 2644–2656 (2000).
11. Polsky, A., Mel, B.W., Schiller, J.: Computational subunits in thin dendrites of pyramidal cells. *Nature Neuroscience*, **7**, 621–627 (2004).
12. La Rosa, M., Rabinovich, M.I., Huerta, R., Abarbanel, H.D.I., Fortuna, L.: Slow regularization through chaotic oscillation transfer in a unidirectional chain of Hindmarsh–Rose models. *Phys. Lett. A*, **266**, 88–93 (2000).
13. Rössler, O.E.: An equation for continuous chaos. *Phys. Lett.*, **57A**, 397–398 (1976).
14. Schuster, H.G. (ed): *Handbook of Chaos Control*. Wiley-VCH Verlag GmbH (1999).
15. Traub, R.D.: *Neuronal Networks of the Hippocampus*. Cambridge University Press, London (1991).

**Innovative Mathematical Methods and Education**

## Offdiagonal Complexity: A Computationally Quick Network Complexity Measure—Application to Protein Networks and Cell Division

Jens Christian Claussen

Institut für Theoretische Physik und Astrophysik, Christian-Albrechts-Universität zu Kiel, Leibnizstr.15, D-24098 Kiel, Germany; claussen@theo-physik.uni-kiel.de

**Summary.** Many complex biological, social, and economical networks show topologies drastically differing from random graphs. But what is a complex network, i.e., how can one quantify the complexity of a graph? Here the Offdiagonal Complexity (OdC), a new, and computationally cheap, measure of complexity is defined, based on the node-node link cross-distribution, whose nondiagonal elements characterize the graph structure beyond link distribution, cluster coefficient, and average path length. The OdC approach is applied to the *Helicobacter pylori* protein interaction network and randomly rewired surrogates thereof. In addition, OdC is used to characterize the spatial complexity of cell aggregates. We investigate the earliest embryo development states of *Caenorhabditis elegans*. The development states of the premorphogenetic phase are represented by symmetric binary-valued cell connection matrices with dimension growing from 4 to 385. These matrices can be interpreted as adjacency matrices of an undirected graph, or network. The OdC approach allows us to describe quantitatively the complexity of the cell aggregate geometry.

**Key words:** Complexity, graphs, networks, development, metabolic networks, degree correlations, computational complexity.

### 25.1 Complex Networks

From a series of seminal papers (Watts and Strogatz [1], Barabasi and Albert [2–4], Dorogovtsev and Mendes [5], Newman [6], see also [7] for an overview), since 1999, small-world and scale-free networks have been a hot topic of investigation in a broad range of systems and disciplines.

Metabolic and other biological networks, collaboration networks, www, internet, etc., have in common that the distribution of link degrees follows a power law, and thus has no inherent scale. Such networks are termed “scale-free networks.” Compared to random graphs, which have a Poisson link distribution and thus a characteristic scale, they share a lot of different properties, especially a high clustering coefficient, and a short average path length. However, the question of *complexity* of a graph is still in its

infancy. A “blind” application of other complexity measures (as for binary sequences or computer programs) does not account for the special properties shared by graphs and especially scale-free graphs as they appear in biological and social networks.

Mathematically, a graph (or synonymously in this context, a network) is defined by a (nonempty) set of nodes, a set of edges (or links), and a map that assigns two nodes (the “end nodes” of a link) to each link. In a computer, a graph may be represented either by a list of links, represented by the pairs of nodes, or equivalently, by its adjacency matrix  $a_{ij}$  whose entries are 1 (0) if nodes  $i, j$  are connected (disconnected). Useful generalizations are weighted graphs, where the restriction of  $a_{ij}$  is relaxed from binary values to (usually nonnegative) integer or real values (e.g., resistor values, travel distances, interaction coupling), and directed graphs, where  $a_{ij}$  no longer needs to be symmetric, and the link from  $i$  to  $j$  and the link from  $j$  to  $i$  can exist independently (e.g., links between webpages, or scientific citations). In this chapter the discussion will be kept limited to binary undirected graphs.

## 25.2 Complexity Measures in Biology

In biological sciences, the evolution of life is studied in detail and at large, and it is observed qualitatively that evolution creates, on average, organisms of increasing complexity. If one wants to quantify an increase of complexity, one has to define suitable complexity measures. In some sense, the number of cells may be an indicator, but it quantifies body size rather than complexity. Instead one may observe the number of organelles, the size of the metabolic network, the behavioural complexity of social organisms, or similar properties. To have a time series of the complexity distribution of all organisms during evolution on earth would be highly interesting for the test of models of evolution, speciation, and extinctions. But apart from such academic questions, there are many areas of practical use of complexity measures in biology and medicine, such as the complexity of morphological structures, cell aggregates, metabolic or genetic networks, or neural connectivities.

## 25.3 Other Complexity Measures

For text strings (as in computer programs, or DNA) there are common complexity measures in theoretical computer science, such as *Kolmogorov complexity* (and the related *Lempel–Ziv complexity* and *algorithmic information content* AIC) [8]. For example, AIC is defined by the length of the shortest program generating the string. For random structures, thus also for random graphs, these measures indicate high complexity. A distinction of complex structured (but still partly random) structures from completely random ones usually is prohibitive for this class of measures. For this reason, measures of *effective complexity* [9] have been discussed; usually these are defined as an entropy (or description length) of “a concise description of a set of the entity’s regularities” [9]. Here we are mainly interested in this second class, and straightforwardly one would try to apply existing measures, e.g., to the link list or to the adjacency matrix. However,

mathematically it is not straightforward to apply these text string based measures to graphs, as there is no unique way to map a graph onto a text string.

Thus one desires to use complexity measures that are defined directly for graphs. Two classical measures are known from graph theory; *graph thickness* and *coloring number* have a low “resolution” and their relevance for real networks is not clear. Two new complexity measures recently have been proposed for graphs, *Medium Articulation* [10] for weighted graphs (as they appear in foodwebs) and a measure for directed graphs by Meyer-Ortmanns [11] based on the *network motif* concept [12]). Unfortunately, the latter two complexity measures are computationally quite costly. A computational complexity approach has been defined by Machta and Machta [13] as *computational depth* of an *ensemble of graphs* (e.g., small-world, scale-free, lattice). It is defined as the number of processing time steps a large parallel computer (with an unlimited number of processors) would need to generate a *representative* member of that graph ensemble. Unlike other approaches, it does not assign single complexity values to each graph, and again is nontrivial to compute.

Table 25.1 gives a qualitative assessment of the behaviour of some of the mentioned complexity measures for lattices in two- and three-dimensional complex and random structures. Note that especially the ability to distinguish nonrandom complex structures from pure randomness differs between the approaches. Hence, a *simpler estimator* of graph complexity is desired, and one possible approach, the Offdiagonal Complexity (OdC), is proposed here. A striking observation of the node-node link correlation matrices of complex networks [14, 15] is that entries are more evenly spread among the offdiagonals, compared to both regular lattices and random graphs. This can now be used to define a complexity measure for undirected graphs [14, 15].

This chapter is organized as follows. In Section 25.4 OdC is defined and illustrated with an example. Sections 25.5 and 25.6 investigate the application of OdC to two quite different biological problems: a protein interaction network, compared with randomized surrogates, and a temporal sequence of spatial cell adjacency during early *Caenorhabditis elegans* development, quantifying the temporal increase of complexity.

**Table 25.1.** Qualitative Assessment of Various Complexity Measures.

	2D, 3D	complex structures	random structures
AIC, Kolmogorov	$o(1)$	large	maximal
effective complexity	$o(1)$	large	$o(1)$
coloring number	2, 2	$\simeq 3 - 4$	$\simeq 3 - 4$
graph thickness	$2, N^{1/3}$	$\simeq 2 - 5$	$\simeq 3 - 4$
motif count	$o(1)$	large	large
Machta	$o(1)$	large	$o(1)$
OdC	0	large	low

### 25.4 Definition of the Offdiagonal Complexity (OdC)

**Definition** (Offdiagonal Complexity). Let  $g_{ij}$  be the adjacency matrix of a graph with  $N$  nodes, i.e.,  $g_{ij} = 1$  if nodes  $i$  and  $j$  are connected, else  $g_{ij} = 0$ .

- (i) For each node  $i$  of the graph, let  $l(i)$  be the node degree, i.e., the number of edges (links),

$$l(i) := \sum_{j=0}^{N-1} g_{ij}. \tag{25.1}$$

- (ii) Let  $c_{mn}$  be the number of edges between all pairs of nodes  $i$  and  $j$ , with node degrees  $m = l(i)$ ,  $n = l(j)$  with  $l(j) \geq l(i)$  (ordered pairs), i.e.,

$$c_{mn} := \sum_{j=0}^{N-1} \sum_{i=0}^{N-1} g_{ij} \delta_{m,l(i)} \delta_{n,l(j)} H(l(i) - l(j)). \tag{25.2}$$

Here  $\delta$  is the Kronecker symbol and  $H(x) = 1$  for  $x \leq 0$  and  $H(x) = 0$  for  $x > 0$ . Due to the pair ordering, the matrix  $c_{mn}$  has entries only on the main diagonal and above. Thus,  $c_{mn}$  is a (not normalized) node-node link correlation matrix.

- (iii) Summation over the minor diagonals, or offdiagonals, i.e., all pairs with the same  $k_i - k_j$  up to  $k_{\max} = \min_i \{l(i)\}$ , and normalization, gives us

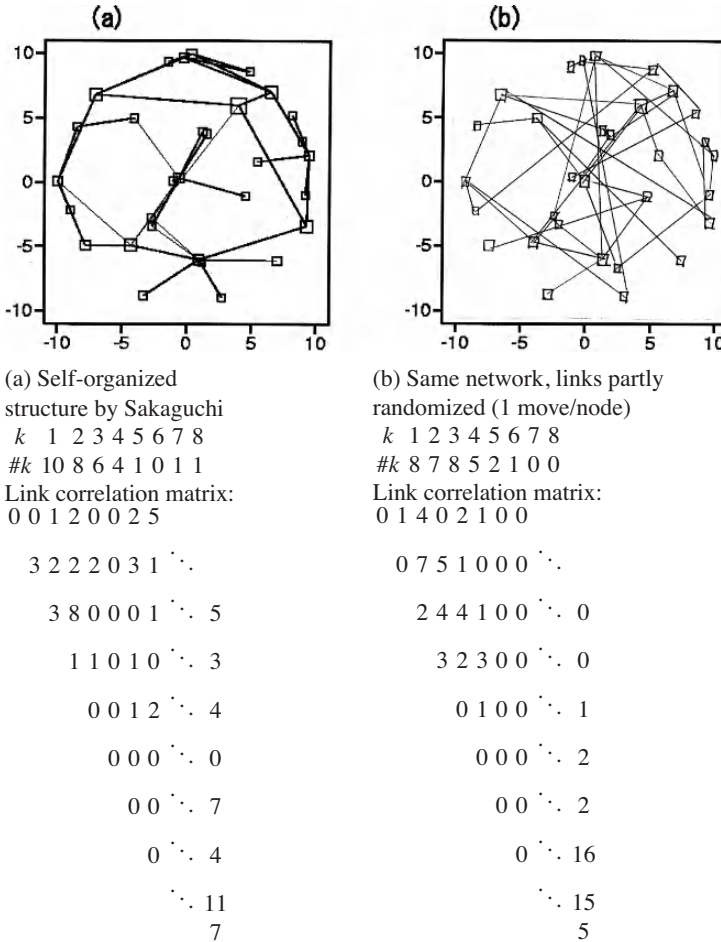
$$\tilde{a}_k = \sum_{i=0}^{k_{\max}-k} c_{i,k+i}, \quad A := \sum_{k=0}^{k_{\max}} \tilde{a}_k, \quad \forall k \ a_k := \tilde{a}_k / A. \tag{25.3}$$

- (iv) Then OdC is defined as an entropy measure on this normalized distributions (here it is understood that  $0 \ln(0) = 0$ ),

$$\text{OdC} = - \sum_{k=0}^{k_{\max}} a_k \ln a_k. \tag{25.4}$$

**Examples.** For a  $d$ -dimensional orthogonal lattice, all nodes have degree  $2d$ , and the node-node link correlation matrix has only one nonzero entry at row  $2d$  and column  $2d$ . For a fully connected graph, the single entry is at row  $N$  and column  $N$ . Obviously, for regular graphs (where all nodes have a fixed degree  $k$ )  $\text{OdC} = 0$  holds in general.

OdC is an approximative complexity estimator that takes as values zero for a regular lattice, zero for a fully connected graph, low values for a random graph, and higher values for “apparently complex” structures. One main advantage is that it does not involve costly (high-order or NP-complete) computations.



(a) Self-organized structure by Sakaguchi  
*k* 1 2 3 4 5 6 7 8  
 #*k* 10 8 6 4 1 0 1 1  
 Link correlation matrix:  
 0 0 1 2 0 0 2 5

3 2 2 2 0 3 1 ∴ ∴  
 3 8 0 0 0 1 ∴ ∴ 5  
 1 1 0 1 0 ∴ ∴ 3  
 0 0 1 2 ∴ ∴ 4  
 0 0 0 ∴ ∴ 0  
 0 0 ∴ ∴ 7  
 0 ∴ ∴ 4  
 ∴ ∴ 11  
 7

The vector of diagonal sums is (7,11,4,7,0,4,3,5).  
 Resulting entropy: OdC = 1.858622

(b) Same network, links partly randomized (1 move/node)  
*k* 1 2 3 4 5 6 7 8  
 #*k* 8 7 8 5 2 1 0 0  
 Link correlation matrix:  
 0 1 4 0 2 1 0 0

0 7 5 1 0 0 0 ∴ ∴  
 2 4 4 1 0 0 ∴ ∴ 0  
 3 2 3 0 0 ∴ ∴ 0  
 0 1 0 0 ∴ ∴ 1  
 0 0 0 ∴ ∴ 2  
 0 0 ∴ ∴ 2  
 0 ∴ ∴ 16  
 ∴ ∴ 15  
 5

The vector of diagonal sums is (5,15,16,2,2,1,0,0).  
 Resulting entropy: OdC = 1.376939

The random reshuffling lowers the OdC entropy away from OdC<sub>max</sub> = 2.550838.

**Fig. 25.1.** (a) Self-organized structure by Sakaguchi. (b) Randomly rewired network.

### 25.4.1 Illustration with a Spatial Network

A spatial hierarchical network emerging from a self-organizing process has recently been introduced by Sakaguchi [16], as shown in Fig. 25.1a. This snapshot example is now taken to illustrate how the node-node link correlation matrix and the OdC entropy are modified under a random reshuffling of links.



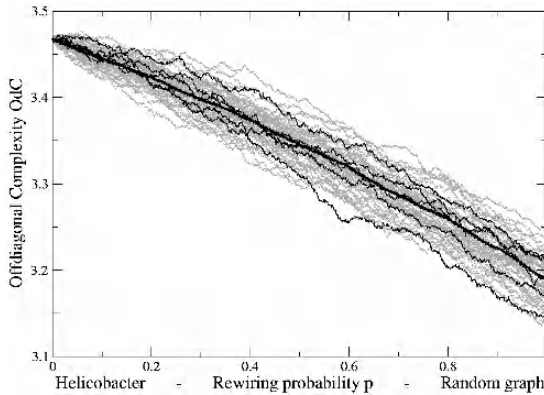


**Fig. 25.2.** OdC for random reshufflings of the *Helicobacter pylori* network (left,  $p = 0$ ) up to a rewiring probability of  $p = 1$  (right). The bold line shows the average; five OdC trajectories along a rewiring path are shown for illustration (thin lines).

## 25.5 Application to the *Helicobacter pylori* Protein Interaction Graph and Reshuffling to a Random Graph

To demonstrate that OdC can distinguish between random graphs and complex networks, the *Helicobacter pylori* protein interaction graph [17] has been chosen. For different rewiring probabilities  $p$  and  $10^2$  realizations each, the links have been reshuffled, ending up with a random graph for  $p = 1$ . As can be seen in Fig. 25.2, rewiring in any case lowers the OdC.

## 25.6 Application to Spatial Cell Division Networks

The tiny (1 mm) nematode worm *C. elegans* looks like a quite primitive organism, but it nevertheless has a nervous system and muscles, and thus shares functional organs with higher-developed animals. More importantly, it shows a morphogenetic process from a single-cell egg through morphogenesis to an adult worm. Towards an understanding of the genetic mechanisms of the cell division cycle in general, *C. elegans* has become one of the genetically best-studied animals. Despite that, little is known (in the sense of a dynamical model) about how the cell division and spatial reorganization take place. Not even the spatial organization of cells during morphogenesis is well described.

### 25.6.1 Early Development of *C. elegans*

The earliest embryo development states of *Caenorhabditis elegans* have recently been recorded experimentally and described quantitatively [18]. The cell division development has been described in simplicial spaces, and the cell division operations are described by operators in finite linear spaces [19].

### 25.6.2 Topological Structure During Premorphogenesis

The premorphogenetic phase of development runs until the embryo reaches a state of about 385 cells. The detailed division times and spatial cell movement trajectories follow with high precision a mechanism prescribed in the genetic program. While many of the genetic mechanisms are known especially for *C. elegans*, we are a long way from a mathematical modelling of the cell division and spatial organization directly from the genome. Thus it is still desired to develop mathematical models for this spatiotemporal process, and to compare it with quantitative experimental data.

With good reliability, the cell adjacency is known experimentally [18,19] in a number of intermediate steps, which in the remainder we call cell states. Here we focus on the adjacency matrices of the cells describing each intermediate state between cell divisions and cell migrations and investigate the complexity of neighborhood relations.

### 25.6.3 Increasing Complexity of *C. elegans* States

The results for 28 state matrices are shown in Fig. 25.3. The dashed line shows the supremum value  $(-\ln N)$  a graph of the same size could reach, despite the fact that, due to combinatorial reasons, this supremum is not necessarily always reached.

The moderate decay in the last two states may be due to the fact that (at least for Poisson-like link distributions) the summation implies some self-averaging if one wants to compare networks of different size. One way to avoid this problem is to define the complexity measure from all  $k_{\max} \cdot (k_{\max} - 1)$  entries,

$$\text{FOdC} := - \sum_{i=0}^{k_{\max}} \sum_{j=i}^{k_{\max}} c_{ij} \ln(c_{ij}). \tag{25.5}$$

This can be called the Full Offdiagonal Complexity (FOdC), as the full set of matrix entries is taken into account. The result for FOdC is shown in Fig. 25.3.

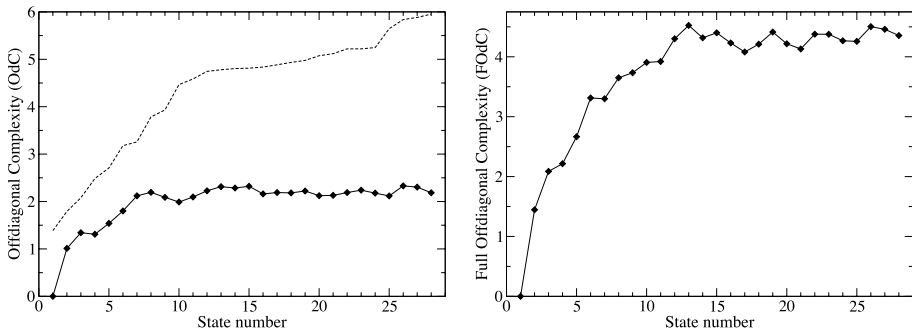


**Fig. 25.3.** Left: Offdiagonal Complexity of the network states. The dashed line shows the maximal complexity a graph of the same number of nodes could reach. Right: Full Offdiagonal Complexity. Here all possible pairs of nodes contribute to the complexity.

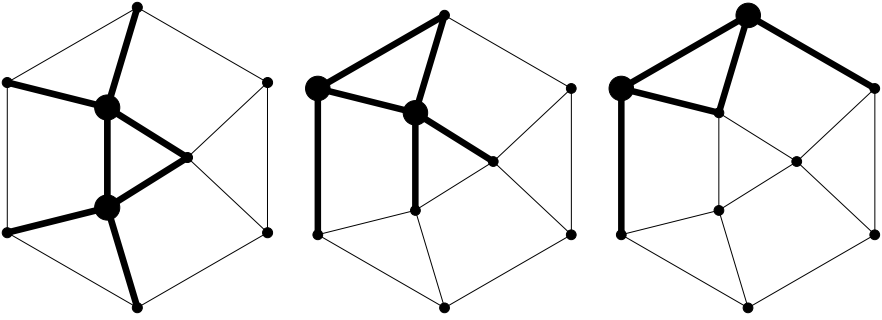


**Fig. 25.4.** Intuitive explanation of saturation for large homogeneous spatial networks. From left to right: Bulk-bulk, bulk-surface, and surface-surface are the typical pairs of node degrees. For large cell aggregates, surface and bulk cells are more homogeneous, i.e., the variation of the neighborhood degree decreases.

#### 25.6.4 Saturation for Large Network Size

As expected, the complexity of the spatial cell structure increases along the first premorphogenetic phase. Compared to the maximal possible complexity that could be reached by a graph of the same number of node degrees (but not for a three-dimensional cell complex), the complexity, as measured by OdC, saturates. This has a straightforward explanation. The limiting case of a large homogeneous cell agglomerate would end up with roughly two classes of cells (at surface and within bulk) and thus three classes of neighborhood pairs: bulk-bulk, bulk-surface and surface-surface (see Fig. 25.4). As the coordination numbers within bulk and surface fluctuate, this effectively delimits the growth of possible different neighborhood geometries. After initial growth, FOdC resolves fluctuations corresponding to the effect of alternating cell division and spatial reorganization.

### 25.7 Conclusions and Outlook

A new complexity measure for graphs and networks has been proposed. Contrary to other approaches, it can be applied to undirected binary graphs. The motivation of its definition is twofold: One observation is that the binning of link distributions is problematic for small networks. The second observation is that if one uses instead of the (plain) entropy of link distribution, which is insignificant for scale-free networks, a “biased link entropy,” it has an extremum where the exponent of the power law is met.

The central idea of OdC is to apply an entropy measure to the link correlation matrix, after summation over the offdiagonals. This allows for a quantitative, yet still approximative, measure of complexity. OdC is roughly “hierarchy sensitive” and has the main advantage of being computationally not costly.

## Acknowledgments

J.C.C. thanks Christian Starzynski for the simulation code for Fig. 25.2, and A. Krämer for kindly providing the experimental data of the cell adjacency matrices.

## References

1. Watts, D.J., Strogatz, S.H.: Collective dynamics of ‘small-world’ networks. *Nature*, **393**, 440–442 (1998).
2. Barabasi, A.L., Albert, R.: Emergence of scaling in random networks. *Science*, **286**, 509–512 (1999).
3. Albert, R., Barabasi, A.-L.: Statistical mechanics of complex networks. *Reviews of Modern Physics*, **74**, 47–97 (2002).
4. Barabasi, A.-L.: *Linked*. Plume Books, New York (2003).
5. Dorogovtsev, S.N., Mendes, J.F.F.: Evolution of networks. *Adv. Phys.*, **51**, 1079 (2002).
6. Newman, M.E.J.: The structure and function of complex networks. *cond-mat/0303516*. *SIAM Review*, **45**, 167–256 (2003).
7. Bornholdt, S., Schuster, H.-G. (eds): *Handbook of Graphs and Networks*. Wiley-VCH, Berlin (2002).
8. Gell-Mann, M., Lloyd, S.: Information measures, effective complexity, and total information. *Complexity*, **2**(1), 44–52 (1996).
9. Gell-Mann, M.: What is complexity? *Complexity*, **1**(1), 16–19 (1995).
10. Wilhelm, T.: An elementary dynamic model for nonbinary food-webs. *Ecol. Model.*, **168**, 145–152 (2004).
11. Meyer-Ortmanns, H.: Functional complexity measure for networks. *Physica A*, **337**, 679–690 (2004).
12. Milo, R., Shen-Orr, S., Itzkovitz, S., Kashtan, N., Chklovskii, D., Alon, U.: Network motifs: simple building blocks of complex networks. *Science*, **298**, 824–827 (2002).
13. Machta, B., Machta, J.: Parallel dynamics and computational complexity of network growth models. *Phys. Rev. E*, **71**, 026704 (2005).
14. Claussen, J.C.: AKSOE 3.10, Verhandl. Deutsche Phys. Ges., Regensburg (2004), extended version of unpublished talk draft, Nov. 11, 2003.
15. Claussen, J.C.: Characterization of networks by the Offdiagonal Complexity, *Physica A*, **375**, 365–373 (2007). doi:10.1016/j.physa.2006.08.067.
16. Sakaguchi, H.: Self-organization of hierarchical structures in nonlocally coupled replicator models. *Phys. Lett. A*, **313**, 188–191 (2003).
17. *Helicobacter pylori* data, <http://www.cosin.org>, <http://www.helico.com>.
18. Krämer, A.: PhD thesis, Kiel 2002, [http://e-diss.uni-kiel.de/diss\\_617](http://e-diss.uni-kiel.de/diss_617).
19. Krämer, A.: unpublished; Betten, A., Betten, D.: The proper linear spaces on 17 points. *Discr. Appl. Math.*, **95**, 83–108 (1999).

# An Analytically Solvable Asymptotic Model of Atrial Excitability

Radostin D. Simitev<sup>1,2</sup> and Vadim N. Biktashev<sup>2</sup>

<sup>1</sup> Department of Mathematics, University of Glasgow, Glasgow G12 8QW, UK;  
r.simitev@maths.gla.ac.uk

<sup>2</sup> Applied Mathematics, Department of Mathematical Sciences, The University of Liverpool,  
Liverpool L69 7ZL, UK; V.N.Biktashev@liverpool.ac.uk

**Summary.** We report a three-variable simplified model of excitation fronts in human atrial tissue. The model is derived by novel asymptotic techniques from the biophysically realistic model of Courtemanche *et al.* [11] in an extension of our previous similar models. An iterative analytical solution of the model is presented which is in excellent quantitative agreement with the realistic model. It opens new possibilities for analytical studies as well as for efficient numerical simulation of this and other cardiac models of similar structure.

**Key words:** Cardiac modelling, asymptotics, excitation, wave front.

## 26.1 Introduction

The mechanical activity of the heart is controlled by electrical impulses propagating regularly through it during one's entire lifespan [22]. A disturbance in the regular propagation may lead to life-threatening *cardiac arrhythmias* [31]. Sudden cardiac death, for instance, accounts for 300,000 to 400,000 deaths annually in the United States alone [14,23], i.e., more than for AIDS, and breast and lung cancer. This entails intensive research into the mechanisms of heart functioning and failure. The accumulated information reveals an overwhelming complexity of the patterns of electrical cardiac activity.

A true understanding of the experimental data requires the development of qualitative cardiac models [10,19,20]. One approach to cardiac modelling is to take into account the various levels of membrane, cellular and myocardial structure and their interactions and to model the *action potential* (AP) on the basis of experimental measurements of ion fluxes in as much detail as possible. The resulting models are known as *realistic* or *detailed ionic models*. The first example of this type of models was developed by Noble [25,26] and now such models exist for various cardiac cells in different species, e.g., [3,12,21,27,35] and many others. However, since these models are very complex and highly nonlinear, it is difficult to assess the contribution of specific model components to different patterns of activity. Furthermore, their computation is arduous

because it contains a large number of equations and small parameters. They become very expensive and time consuming especially when large volumes of tissue are simulated. One possible alternative is to search for simplified models which could mimic the most important AP properties, allow analytical studies and reduce the computing requirements. Many simplified models have been suggested, either phenomenologically, or based on the structure of the realistic models, [1, 4, 13, 15, 18], etc. However, all of these models contain arbitrary elements in the sense that they are not derived from any of the realistic biophysical cell models and lack explicit correspondence with the biophysical structure of the cardiac tissues. For example, van der Pol and van der Mark modelled heartbeat as an electronic relaxation oscillator [28].

Our recent studies [7, 8, 32, 33] have demonstrated a serious disadvantage of the most popular and successful simplified generic model of cardiac excitability: the FitzHugh–Nagumo (FHN) equations [17, 24]. It cannot describe adequately the one feature of excitation propagation which is most important for medical applications, namely the way regular propagation fails and arrhythmias occur. An excitation wave in real cardiac tissue, or in a realistic model, may fail to propagate if the temporal gradient of the transmembrane voltage at the front becomes too small to excite the tissue ahead of it, e.g., if the wave fails to propagate fast enough [8]. Then the wave front loses its sharp spatial gradient and its further spread is purely diffusive, i.e., the front dissipates. This happens long before the back of the excitation impulse catches up with the front. This type of propagation failure does not exist in a FHN-type model [6] since it is known that the propagation of a wave front in this system may be slowed down, halted or even reversed [16]. This phenomenon is illustrated in Fig. 26.1: a temporary block of excitability halts the FHN wave only temporarily, but completely disrupts propagation in the realistic model, even though it lasts a much shorter time than the AP.

Earlier we proposed novel asymptotic methods of reduction of cardiac equations [9]. In this chapter we use these methods to derive a three-component description of the propagating excitation fronts and their dissipation. The virtue of our model is that it reproduces propagation failure unlike the FHN models because it is derived in a reliable way from the realistic ionic model. We also report an analytical solution for this three-component model. The analytical solution is constructed as an iterative procedure and it may be seen as a generalisation in which the caricature solutions presented in our earlier papers [5, 6, 30] appear as first approximations. This is, to our knowledge, the first analytical solution, albeit in quadratures, which gives a numerically accurate prediction of the front propagation velocity (within 16%) and its profile (within 0.7 mV) in human atrial tissue.

## 26.2 Mathematical Formulation of the Problem

### 26.2.1 Atrial Tissue Model

In our study atrial tissue is a one-dimensional, homogeneous and isotropic medium satisfying a system of *reaction-diffusion equations*

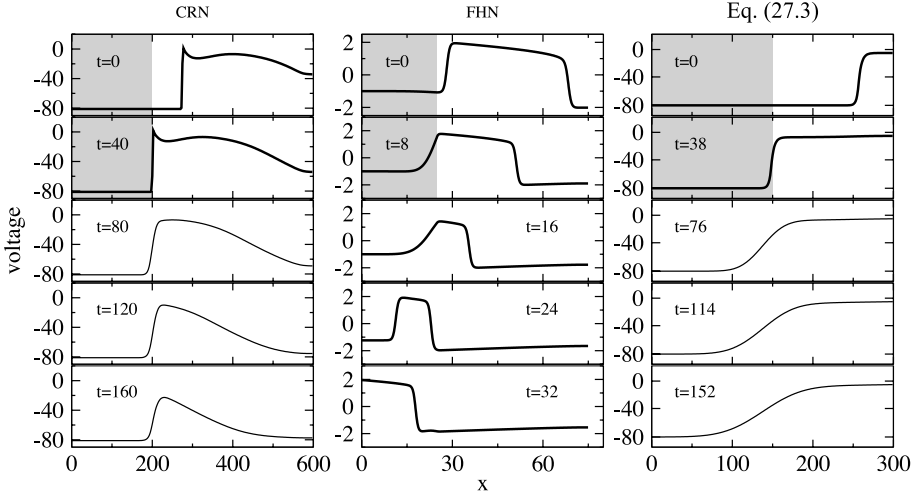


**Fig. 26.1.** Propagation of excitation in the models of Courtemanche *et al.* [11] (first column), FitzHugh–Nagumo (second column) and equations (26.3) (third column), through a temporary block of excitability, introduced by artificially reducing the value of a parameter representing the main excitatory ionic current responsible for the initiation of the front. For example, in the three-variable model (26.3) this parameter is  $j$  which was decreased from the normal value of 0.9775 to 0.28 during the block. In FHN, propagation resumes after the block is removed; in CRN and (26.3) it does not.

$$\partial_T \mathbf{u} = \hat{\mathbf{D}} \cdot \partial_X^2 \mathbf{u} + \mathbf{F}(\mathbf{u}), \quad (26.1)$$

where  $\mathbf{F}(\mathbf{u})$  is a vector defined according to the atrial single-cell realistic CRN model [11],  $\mathbf{u} = (V, m, h, j, \dots)^T \in \mathbb{R}^{21}$  is the vector of all dynamic variables of the model and  $\hat{\mathbf{D}} = \text{diag}(D, 0, 0, \dots)$  is the tensor of diffusion in which only the coefficient of the voltage  $V$  is nonzero. This simplified description focuses on the excitation and propagation of impulses, while ignoring the effects due to geometry, anisotropy and heterogeneity of a real atrium.

### 26.2.2 Asymptotic Reduction

In order to reduce the dimension and complexity of the problem, we perform a formal analysis of the time scales of dynamic variables. For the system (26.1) we define characteristic *time scale* functions,  $\tau_i(u_1, \dots, u_{21}) \equiv |(\partial F_i / \partial u_i)^{-1}|$  and compare their magnitudes obtained numerically for a space-clamped version of the system as shown in Fig. 26.2. The variables, whose time scales  $\tau_i$  are relatively small, are *fast variables* since they change significantly during the upstroke of a typical AP, while all other variables, whose time scales  $\tau_i$  are relatively large, are *slow variables* because they change only slightly during this period. Fig. 26.2(a) demonstrates that the variables  $V, m, h, u_a, w, o_a, d$  are fast variables comparable with the time scale of the AP upstroke.

A specific feature of system (26.1) is that of the various ionic currents in the system only the sodium current  $I_{\text{Na}}$  is significantly large during the AP upstroke, whereas

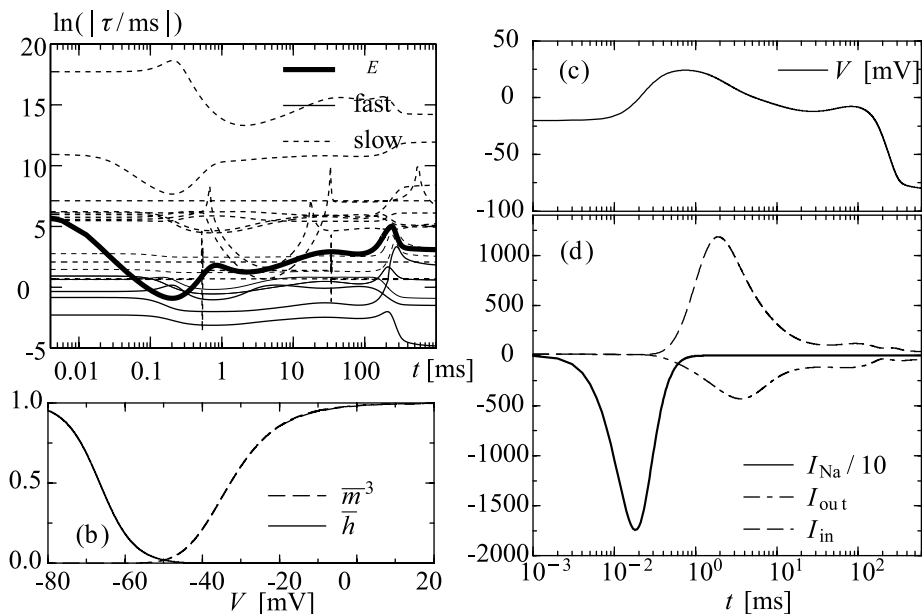


**Fig. 26.2.** Asymptotic properties of the atrial CRN model [11]. (a) Time scale functions of dynamical variables vs. time. (b) Quasi-stationary values of the gating variables  $\bar{m}$  and  $\bar{h}$ . (c) Transmembrane voltage  $V$  as a function of time. (d) Main ionic currents:  $I_{\text{Na}}$  is the fast sodium current (shown scaled by a factor 0.1),  $I_{\text{in}} = I_{\text{b,Na}} + I_{\text{NaK}} + I_{\text{Ca,L}} + I_{\text{b,Ca}} + I_{\text{NaCa}}$  is the sum of all other inward currents and  $I_{\text{out}} = I_{\text{p,Ca}} + I_{\text{K1}} + I_{\text{to}} + I_{\text{Kur}} + I_{\text{Kr}} + I_{\text{Ks}} + I_{\text{b,K}}$  is the sum of all outward currents; the individual currents are described in [11]. The results are obtained for a space-clamped version of the model at values of the parameters as given in [11]. A typical AP was triggered by initialising the transmembrane voltage to nonequilibrium value of  $V = -20$  mV.

other currents are small at this stage as can be seen in Fig. 26.2(d). Secondly, the fast sodium current  $I_{\text{Na}}$  is only large during the AP upstroke, and almost vanishes otherwise, because either gate  $m$  or gate  $h$  or both are nearly closed outside the upstroke since their quasi-stationary values  $\bar{m}(V)$  and  $\bar{h}(V)$  are small there as illustrated in Fig. 26.2(b).

To formalise the distinction between fast and slow terms we perform an *asymptotic embedding* of system (26.1). We introduce an artificial parameter  $\epsilon$  into the system so that for  $\epsilon = 1$  the original system is recovered, while in the limit  $\epsilon \rightarrow 0$  only the terms comparable with the time scale of the AP upstroke are retained,

$$\partial_T V = D \partial_X^2 V - \frac{(\epsilon^{-1} I_{\text{Na}}(V, m, h, j) + \Sigma'_I(V, \dots))}{C_M},$$

$$\partial_T m = \frac{(\bar{m}(V; \epsilon) - m)}{\epsilon \tau_m(V)}, \quad \bar{m}(V; \epsilon) = \begin{cases} \bar{m}(V), & \epsilon = 1, \\ \theta(V - V_m), & \epsilon = 0, \end{cases}$$



$$\begin{aligned}
\partial_T h &= \frac{(\bar{h}(V; \epsilon) - h)}{\epsilon \tau_h(V)}, & \bar{h}(V; \epsilon) &= \begin{cases} \bar{h}(V), & \epsilon = 1, \\ \theta(V_h - V), & \epsilon = 0, \end{cases} \\
\partial_T y &= \frac{(\bar{y}(V) - y)}{\epsilon \tau_y(V)}, & y &= u_a, w, o_a, d, \\
\partial_T \mathbf{U} &= \mathbf{W}(V, \dots), & &
\end{aligned} \tag{26.2}$$

where  $\theta(\cdot)$  is the Heaviside function,  $\Sigma'_I(\cdot)$  is the sum of all currents except the fast sodium current  $I_{\text{Na}}$ , the dynamic variables  $V, m, h, u_a, o_a$  and  $d$  are defined in [11],  $\mathbf{U} = (j, o_i, \dots, \text{Na}_i, K_i, \dots)^T$  is the vector of all other, slower variables, and  $\mathbf{W}$  is the vector of the corresponding right-hand sides. Novel features of the asymptotic embedding (26.2), nonstandard in comparison with the theory of fast-slow systems [2,29,34], are (a) the introduction of the asymptotic factor  $\epsilon^{-1}$  only at one term  $I_{\text{Na}}$  on the right-hand side of the equation for  $V$  whereas the standard factor  $\epsilon$  at the derivative would be equivalent to factor  $\epsilon^{-1}$  at the whole right-hand side, and (b) that in the limit  $\epsilon \rightarrow 0$ , functions  $\bar{m}(V)$  and  $\bar{h}(V)$  have to be considered zero in certain overlapping intervals  $V \in (-\infty, V_m]$  and  $V \in [V_h, +\infty)$ , and  $V_h \leq V_m$ , hence the representations  $\bar{m}(V; 0) = \theta(V - V_m)$  and  $\bar{h}(V; 0) = \theta(V_h - V)$ . These aspects, as applied to the fast sodium current, have been shown to be crucial for the correct description of the propagation block [5]. A more detailed discussion of the parameterisation (26.2) can be found in reference [9].

The exact value of  $D$  is not essential for the theoretical analysis, as its change is equivalent to rescaling of the spatial coordinate. To operate with dimensional velocity, we assume the values  $D = 0.03125$ , as in [8,9], and  $C_M = 1 \mu\text{F cm}^{-1}$ . We perform the scaling  $t = \epsilon^{-1}T$ ,  $x = (\epsilon D)^{-1/2}X$ , take the limit  $\epsilon \rightarrow 0$  and notice that the equations for the variables denoted by  $y$  in (26.2) decouple from the voltage equation. Thus, we arrive at the conclusion that only the following three-variable system needs to be considered for a description of the propagation of an AP front or its failure:

$$\partial_t V = \partial_x^2 V + \overline{I_{\text{Na}}}(V) j h m^3, \tag{26.3a}$$

$$\partial_t h = (\theta(V_h - V) - h) / \tau_h(V), \tag{26.3b}$$

$$\partial_t m = (\theta(V - V_m) - m) / \tau_m(V). \tag{26.3c}$$

In other words, we consider the fast time scale on which the upstroke of the AP occurs, neglect the variations of slow variables during this period as well as all transmembrane currents except  $I_{\text{Na}}$ , as they do not make a significant contribution during this period, and replace  $\bar{m}$  and  $\bar{h}$  with zero when they are small. The parameters and functions in (26.3) are defined as in [11], namely

$$\overline{I_{\text{Na}}}(V) = g_{\text{Na}}(V_{\text{Na}} - V), \tag{26.4a}$$

$$\tau_k(V) = (\alpha_k(V) + \beta_k(V))^{-1}, \quad k = h, m, \tag{26.4b}$$

$$\bar{k}(V) = \alpha_k(V) / (\alpha_k(V) + \beta_k(V)), \quad k = h, m,$$

$$\alpha_h(V) = 0.135 e^{-(V+80)/6.8} \theta(-V - 40),$$

$$\beta_h(V) = \left( 3.56 e^{0.079V} + 3.1 \times 10^5 e^{0.35V} \right) \theta(-V - 40)$$

$$\begin{aligned}
 & + \theta(V + 40) (0.13(1 + e^{-(V+10.66)/11.1}))^{-1}, \\
 \alpha_m(V) &= \frac{0.32(V + 47.13)}{1 - e^{-0.1(V+47.13)}}, \\
 \beta_m(V) &= 0.08e^{-V/11}, \\
 g_{Na} &= 7.8, \quad V_{Na} = 67.53, \quad V_h = -66.66, \quad V_m = -32.7.
 \end{aligned}$$

Two new “gate threshold” parameters  $V_h$  and  $V_m$  appear in the system and are chosen from the conditions  $\bar{h}(V_h) = 1/2$  and  $\bar{m}^3(V_m) = 1/2$ . As follows from the derivation, variable  $j$ , the slow inactivation gate of the fast sodium current, acts as a parameter of the model. It is the only one of all the slow variables included in the vector  $\mathbf{U}$  that affects our fast subsystem. We say that it describes the *excitability* of the tissue.

### 26.2.3 Travelling Waves and Reduction to ODE

We look for solutions in the form of a front propagating with a constant speed and shape. So we use the ansatz  $F(z) = F(x + ct)$  for  $F = V, h, m$  where  $c$  is the dimensionless wave speed of the front, related to the dimensional speed  $C$  by  $c = (\epsilon/D)^{1/2}C$ . Then equations (26.3) reduce to

$$V'' = cV' - \bar{I}_{Na}(V) j h m^3, \tag{26.5a}$$

$$h' = (c \tau_h(V))^{-1} (\theta(V_h - V) - h), \tag{26.5b}$$

$$m' = (c \tau_m(V))^{-1} (\theta(V - V_m) - m), \tag{26.5c}$$

where the boundary conditions are given by

$$V(-\infty) = V_\alpha, \quad h(-\infty) = 1, \quad m(-\infty) = 0, \tag{26.6a}$$

$$V(+\infty) = V_\omega, \quad h(+\infty) = 0, \quad m(+\infty) = 1. \tag{26.6b}$$

Here  $V_\alpha$  and  $V_\omega$  are the pre- and post-front voltages, and  $V_\alpha < V_h < V_m < V_\omega$ .

Equations (26.5) represent a system of fourth order so its general solution depends on four arbitrary constants. Together with constants  $V_\alpha, V_\omega$  and  $c$  this makes seven constants to be determined from the six boundary conditions in (26.6). Thus, we should have a one-parameter family of solutions, i.e., one of the parameters ( $V_\alpha, V_\omega, c$ ) can be chosen arbitrary from a certain range.

### 26.2.4 Comparison of the Three-Variable Model (27.5) with the Realistic CRN Model [11]

The simplified three-variable model (26.3) and its ODE version (26.5) provide an excellent approximation to the fronts of the action potential in human atrial tissue as demonstrated in Fig 26.3 where a comparison with the solution of the realistic CRN model [11] is presented. As must be expected, the voltage in the simplified model remains constant after reaching its post-front value  $V_\omega$  while the voltage in the CRN

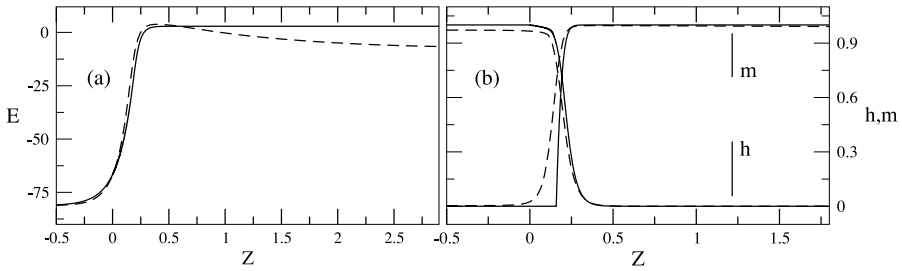


**Fig. 26.3.** (a) The AP potential and (b) the gating variables  $h$  and  $m$  as functions of the travelling wave coordinate  $Z = z\sqrt{D}$ . The solution of the CRN model [11] is given by broken lines and that of the three-variable model of (26.5) by solid lines. The pre-front voltage and the excitation parameter in (26.5) are chosen as  $V_\alpha = -81.18$  mV and  $j = 0.956$ , respectively, and correspond to the equilibrium values in the realistic model. The gates  $h$  and  $m$  are indicated in the plot. The iterative analytical solution (26.14) is indistinguishable from the numerical solution of (26.5) after 30 iterations.

model assumes a shape typical for an action potential. To quantify further the comparison between the two models below we list the values of the wave speed, the post-front voltage and the maximum rate of AP rise. For the realistic model [11] these values are  $C = 0.2824$  mm/ms,  $V_\omega = 3.60$  mV and  $(dV/dt)_{\max} = 173.83$  V/s. The respective values for the simplified model (26.5) are  $C = 0.2372$  mm/ms,  $V_\omega = 2.89$  mV and  $(dV/dt)_{\max} = 193.66$  V/s. The relative errors made by the simplified model in estimating the wave speed and the the maximum rate of AP rise are 16% and 11%, respectively, and the absolute error in estimating the post-front voltage is  $-0.7$  mV.

We recall that our main motivation for the derivation of the three-variable simplified model was to reproduce the realistic front dissipation behaviour of atrial tissue as it appears for example in the CRN model [11]. The third column of Fig. 26.1 illustrates the dissipation of a propagating front in equations (26.3) in response to a temporary block of excitability. It is observed that the dissipation behaviour of the simplified system resembles the one of the realistic CRN model. In this aspect of the behaviour our model is superior to the simplified models of FHN type.

## 26.3 Iterative Analytical Solution

### 26.3.1 Exact Solution for $V \leq V_m$

For  $V \leq V_m$  the reduced model (26.5), (26.6) has a two-parameter family of exact solutions, with parameters  $V_\alpha$  and  $c$ . Since the boundary condition  $m(-\infty) = 0$  is an equilibrium point of (26.5c),  $m(z) = 0$  remains a solution for all  $z \leq \xi$ . It follows that (26.5a) is a constant-coefficient linear homogeneous equation in this interval, and its solution

$$V(z) = V_\alpha + (V_h - V_\alpha) e^{cz}, \tag{26.7}$$

satisfies boundary conditions  $V(-\infty) = V_\alpha$ ,  $V(0) = V_h$  and  $V(\xi) = V_m$ , provided that the internal boundary point  $\xi$  is located at

$$\xi = \frac{1}{c} \ln \left( \frac{V_m - V_\alpha}{V_h - V_\alpha} \right). \tag{26.8}$$

Finally,  $h(V) = 1$  is a solution of (26.5b) with boundary condition  $h(V_\alpha) = 1$  in the interval  $V \leq V_h$ , because it belongs to its equilibrium set. In the interval  $V \geq V_h$ , (26.5b) can be rewritten in the form

$$\frac{d}{dV}(\ln h) = -\frac{1}{c^2 (V - V_\alpha) \tau_h(V)}, \tag{26.9}$$

and its solution can be immediately obtained,

$$h(V) = \exp \left( -\frac{1}{c^2} \int_{V_h}^V \frac{dV}{(V - V_\alpha) \tau_h(V)} \right). \tag{26.10}$$

### 26.3.2 Approximate Solutions for $V \geq V_m$

For  $V \geq V_m$ , we rewrite (26.5) as

$$\frac{d}{dz} \left( \frac{dV}{dz} e^{-cz} \right) = f(z) e^{-cz}, \tag{26.11a}$$

$$\frac{d}{dz}(\ln h) = -\frac{1}{c \tau_h(z)}, \tag{26.11b}$$

$$\frac{d}{dz}(\ln(1 - m)) = -\frac{1}{c \tau_m(z)}, \tag{26.11c}$$

where

$$f(z) = -\overline{I_{Na}}(V(z)) j h(z) m^3(z). \tag{26.12}$$

The boundary conditions are

$$V(\xi) = V_m, \tag{26.13a}$$

$$V'(\xi) = c (V_m - V_\alpha), \tag{26.13b}$$

$$h(\xi) = h_0 = \exp \left( -\frac{1}{c^2} \int_{V_h}^{V_m} \frac{dV}{(V - V_\alpha) \tau_h(V)} \right), \tag{26.13c}$$

$$m(\xi) = 0, \tag{26.13d}$$

$$V'(\infty) = 0. \tag{26.13e}$$

This problem is equivalent to the following system of integral equations:

$$m(z) = 1 - \exp \left( -\frac{1}{c} \int_\xi^z \frac{d\sigma}{\tau_m(V(\sigma))} \right), \tag{26.14a}$$

$$h(z) = h_0 \exp \left( -\frac{1}{c} \int_{\xi}^z \frac{d\sigma}{\tau_h(V(\sigma))} \right), \tag{26.14b}$$

$$V(z) = V_m - \frac{1}{c} \left[ \int_{\xi}^z f(\sigma) (1 - e^{c(\xi-\sigma)}) d\sigma - (e^{cz} - e^{c\xi}) \int_z^{+\infty} f(\sigma) e^{-c\sigma} d\sigma \right] \tag{26.14c}$$

$$c = \frac{1}{V_h - V_\alpha} \int_{\xi}^{+\infty} f(\sigma) e^{-c\sigma} d\sigma. \tag{26.14d}$$

The last equation (26.14d) imposes an additional relationship between parameters  $V_\alpha$  and  $c$ , so the ultimate solution depends only on one arbitrary parameter, say  $V_\alpha$ , which in reality may be determined by the pre-history of the medium through which the excitation front propagates.

The system (26.14) can be solved by iterations, starting from a suitable initial approximation. The iterations converge for a number of various initial approximations, see Fig. 26.4. In Section 26.4 we discuss two selected initial approximations. The first of them, **A1**, is favourable from a numerical point of view. The second one, **A2**, is important in the context of our recent work [30] since it leads to an even further formal simplification of problem (26.5) to a system which allows exact solution and extensive analytical study.

## 26.4 Selected Initial Approximations

### 26.4.1 A1: The Small-Diffusion Initial Approximation

A simple initial approximation may be obtained by considering a space-clamped version of (26.5) corresponding to the limit  $D \rightarrow 0$  of a very small constant of diffusion in equations (26.2) (note that this is applied only to the solution in the interval  $V \geq V_m$ ) and replacing the gating variable  $m$  with its quasi-stationary value  $\bar{m}$  which in our asymptotic limit and for  $V \geq V_m$  equals 1. Hence, an initial approximation may be chosen to satisfy

$$\frac{dE}{dt} = \bar{I}_{Na}(V) j h, \tag{26.15a}$$

$$\frac{dh}{dt} = -h/(\tau_h(V)). \tag{26.15b}$$

This system can be solved in quadratures,

$$h(V) = h_0 - \int_{V_0}^V \frac{dV}{\bar{I}_{Na}(V) j \tau_h(V)}, \tag{26.16a}$$

$$t = \int_{V_0}^V \frac{dV}{\bar{I}_{Na}(V) j h(V)}, \tag{26.16b}$$

where the initial conditions  $V_0$  and  $h_0$  are given by equations (27.13a) and (27.13c).

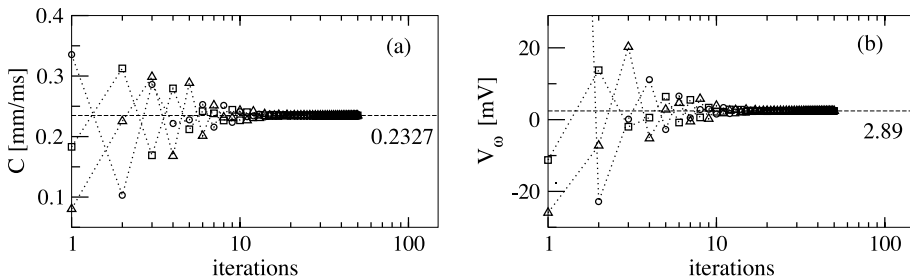


**Fig. 26.4.** Convergence of the iterative solution (26.14), starting from initial approximation **A1** (triangles), same as **A1** but with the equation for  $m$  gate retained (squares) and **A2** with  $V^{(0)} = V_m$  (circles). The excitation parameter and the pre-front voltage are  $j = 0.9775$  and  $V_\alpha = -81.18$  mV. The values on the right-hand side y-axis represent the numerical solution of the boundary-value problem (26.5).

### 26.4.2 A2: The “Caricature” Initial Approximation

An even simpler initial approximation is

$$V = V^{(0)} = \text{const.} \tag{26.17}$$

In this case functions of voltage  $\overline{I_{Na}}(V)$ ,  $\tau_h(V)$  and  $\tau_m(V)$  take constant values  $\overline{I_{Na}}(V^{(0)})$ ,  $\tau_h(V^{(0)})$  and  $\tau_m(V^{(0)})$ , respectively. Then quadratures (26.14) for the results of the first iteration are obtained in explicit formulae; moreover, (26.14d) is resolved explicitly. These explicit formulae have been reported in our recent work [30] (see formulae (10) of that paper). There this piecewise-linear simplification was considered only as an arbitrary “caricature” with the purpose of merely analysing qualitative features of the solution set. Here we note that it actually appears naturally as a step of the iterative procedure leading to a numerically accurate solution.

The iterative analytical solution (26.14) obtained from these initial approximations is indistinguishable from the numerical solution of (26.5) after some 30 iterations and has the shape of a travelling front as shown in Fig. 26.3.

### 26.4.3 Convergence and Uniqueness of the Iterative Solution (27.14)

The iteration procedure produced by (26.14) is nonlinear and nonmonotonic, and we do not have a rigorous proof of its convergence from any given initial approximation. Likewise, we do not have a rigorous proof that the solution of the boundary-value problem (26.13) is unique. However, it is straightforward to see that if the iterations converge, the result is a solution of the boundary-value problem, due to the above-mentioned equivalence of (26.13) and the system of integral equations (26.14). Fig. 26.4 illustrates that the first several iterations obtained from different initial approximations oscillate about the correct numerical solution of the problem and ultimately converge to it. The “small diffusion” initial approximation **A1** is particularly interesting because the results of the second iteration are already very close to the accurate

numerical values for the wave speed and the post-front voltage. Indeed, if the excitability parameter and the pre-front voltage are chosen at their physiological resting values  $j = 0.9775$  and  $V_\alpha = -81.18$  mV, respectively [11], at the second step of the iterations the value of the dimensional wave speed is  $C = 0.2255$  mm/ms, which has only 20% relative error compared to the value 0.2824 mm/ms of the realistic ionic model 26.2 and 5% relative error compared to the value 0.2372 mm/ms obtained numerically from equations (26.5). Similarly, the post-front voltage  $V_\omega = -7.22$  mV compares well with the value 3.36 mV of the CRN model 26.2. Clearly, the second iteration obtained from initial approximation **A1** introduces certain errors. Numerically, however, it is immensely superior to any other numerical scheme because it involves only a single evaluation of formulae (26.16) and a twofold evaluation of formulae (26.14). In addition, the dangers of numerical divergence associated with many of the alternative numerical schemes for solving problems (26.2) or (26.5) are avoided since the above expressions are mathematically well behaved.

The two initial approximations discussed above are essentially different. In the small-diffusion approximation the initial guess for the voltage  $V(z)$  is a function  $V^0 = v(z)$  while in the “caricature” approximation it is a constant  $V^0 = \text{const}$ . The fact that two essentially different initial approximations give the same limits is a strong indication that the iterative procedure leads to a unique solution. To support this claim further we have performed calculations starting from initial approximation **A2** with initial values  $V^{(0)} = -28, -30, -32, -34, -36, -38$ . In all cases the iterations converged to the same solution, in a similar manner to those shown on Fig. 26.4. The small-diffusion initial approximation is not discussed here because its initial guess  $V^0 = v(z)$  is the unique solution (26.16) of equations (26.15) and thus it does not depend on any arbitrary parameters.

So, although we cannot exclude the possibility that the iteration procedure may not converge from some “bad” initial guess, the examples considered provide evidence that a reasonable initial approximation always gives converging iterations, and the solution is unique.

## 26.5 Discussion

We have presented an analytical approach to the description of the speed and the structure of an excitation front in a model of human atrial tissue [11]. We have identified small parameters in the realistic model and used asymptotic arguments to obtain a simplified three-variable model of the excitation front. Although we have explicitly used certain quantitative features of atrial tissue [11], the main properties used are generic for cardiac excitation models so the approach should be applicable, possibly with suitable modifications, to other cardiac equations models too. Our model takes the form of a nonlinear eigenvalue problem with a piecewise right-hand side defined over three voltage intervals. This model is solved explicitly in the first two intervals, and in the last interval we have suggested an analytical iterative procedure capable of producing a solution with a good accuracy already after the first iteration. The iterative procedure can be started from reasonably chosen simple initial approximations and converges

to a unique solution which differs only within a few percent from the solution of the realistic ionic atrial model.

An important feature of our approach is that it is capable of correctly describing the excitation propagation at reduced excitabilities, up to a complete block of propagation via a “front dissipation” mechanism, which is completely unachievable by traditional analytical approaches based on FHN type equations. This aspect has been analysed in our earlier publications [5, 6, 9, 30]. In particular, our recent study [30] is devoted to a discussion of one practical application of our approach. There we have used a numerical solution of the simplified three-variable model (26.5) to propose a simple criterion for break-up and self-termination of spiralling waves and have confirmed our predictions by numerical simulations of the realistic model of Courtemanche *et al.* However, the important question of finding an analytical solution of our simplified model (26.5) has now been solved here.

The possibility of obtaining numerically reasonable analytical approximations to front solutions in realistic cardiac equations, demonstrated here, opens the way for analytical description and, possibly, a better understanding of more complicated regimes in excitable media, such as wave break-ups and spiral waves.

## Acknowledgment

This study is supported by EPSRC grant GR/S75314/01.

## References

1. Aliev, R. R., Panfilov, A. V., A simple two-variable model of cardiac excitation, *Chaos Solitons and Fractals*, **7**, 293–301, 1996.
2. Arnol'd, V. I., ed., *Dynamical Systems IV*, Springer, Berlin, 1994.
3. Beeler, G. W., Reuter, H., Reconstruction of the action potential of ventricular myocardial fibres, *J. Physiol.*, **268**, 177–210, 1977.
4. Bernus, O., Wilders, R., Zemlin, W., Verschelde, H., Panfilov, A. V., A computationally efficient electrophysiological model of human ventricular cells, *Am. J. Physiol.*, **282**, H2296–H2308, 2002.
5. Biktashev, V. N., Dissipation of the excitation wavefronts, *Phys. Rev. Lett.*, **89** (16), 168102, 2002.
6. Biktashev, V. N., A simplified model of propagation and dissipation of excitation fronts, *Int. J. Bif. Chaos*, **13**(12), 3605–3620, 2003.
7. Biktashev, V. N., Suckley, R., Non-Tikhonov asymptotic properties of cardiac excitability, *Phys. Rev. Lett.*, **93**(16), 168103, 2004.
8. Biktasheva, I. V., Biktashev, V. N., Dawes, W. N., Holden, A. V., Saumarez, R. C., M.Savill, A., Dissipation of the excitation front as a mechanism of self-terminating arrhythmias, *IJBC*, **13**(12), 3645–3656, 2003.
9. Biktasheva, I. V., Simitev, R., Suckley, R., Biktashev, V. N., Asymptotic properties of mathematical models of excitability, *Phil. Trans. Roy. Soc. A*, **364**, 1283–1298, DOI: 10.1098/rsta.206.1770, 2006.



10. Clayton, R. H., Computational models of normal and abnormal action potential propagation in cardiac tissue: linking experimental and clinical cardiology, *Physiol. Meas.*, **22**, R15–R34, 2001.
11. Courtemanche, M., Ramirez, R., Nattel, S., Ionic mechanisms underlying human atrial action potential properties: insights from a mathematical model, *Am. J. Physiol.*, **275**, H301–H321, 1998.
12. Demir, S. S., Clark, J. W., Murphey, C. R., Giles, W. R., A mathematical model of a rabbit sinoatrial node cell, *Am. J. Physiol.*, **266**, C832–C852, 1994.
13. Duckett, G., Barkley, D., Modeling the dynamics of cardiac action potentials, *Phys. Rev. Lett.*, **85**, 884–887, 2000.
14. Engelstein, E. D., Zipes, D. P., Sudden cardiac death, in *The Heart, Arteries and Veins*, eds. R. W. Alexander, R. C. Schlant, V. Fuster, pp. 1081–1112, McGraw-Hill, New York, 1998.
15. Fenton, F., Karma, A., Vortex dynamics in three-dimensional continuous myocardium with fiber rotation: Filament instability and fibrillation, *Chaos*, **8**, 20–47, 1998.
16. Fife, P. C., Pattern formation in reacting and diffusing systems, *J. Chem. Phys.*, **64**, 554–564, 1976.
17. FitzHugh, R. A., Impulses and physiological states in theoretical models of nerve membrane, *Biophys. J.*, **1**, 445–466, 1961.
18. Hinch, R., An analytical study of the physiology and pathology of the propagation of cardiac action potentials, *Progress in Biophysics and Molecular Biology*, **78**, 45–81, 2002.
19. Holden, A. V., Panfilov, A. V., Modelling propagation in excitable media, in *Computational Biology of the Heart*, eds. A. V. Holden, A. V. Panfilov, pp. 65–99, Wiley, New York, 1997.
20. Kohl, P., Noble, D., Winslow, R. L., Hunter, P. J., Computational modelling of biological systems: tools and visions, *Phil. Trans. R. Soc. Lond. A*, **358**, 579–610, 2000.
21. Luo, C.-H., Rudy, Y., A dynamic model of the cardiac ventricular action potential. I. Simulations of ionic currents and concentration changes, *Circulation Res.*, **74**, 1071–1096, 1994.
22. Mohrman, D. E., Heller, L. J., *Cardiovascular Physiology*, McGraw-Hill, New York, 2003
23. Myerburg, R. J., Castellanos, A., Cardiac arrest and sudden death, in *Heart Disease: A Textbook of Cardiovascular Medicine*, ed. Braunwald E., pp. 742–779, WB Saunders, Philadelphia, PA, 1997.
24. Nagumo, J., Arimoto, S., Yoshizawa, S., An active pulse transmission line simulating nerve axon, *Proc. IRE*, **50**, 2061–2070, 1962.
25. Noble, D., Cardiac action and pacemaker potentials based on the Hodgkin–Huxley equations, *Nature*, **188**, 495–497, 1960.
26. Noble, D., A modification of the Hodgkin–Huxley equations applicable to Purkinje fibre action and pace-maker potentials, *J. Physiol.*, **160**, 317–352, 1962.
27. Nygren, A., Fiset, C., Firek, L., Clark, J. W., Lindblad, D. S., Clark, R. B., Giles, W. R., Mathematical model of an adult human atrial cell: the role of  $K^+$  currents in repolarization, *Circulation*, **82**, 63–81, 1998.
28. van der Pol, B., van der Mark, J., The heartbeat considered as a relaxation oscillation, and an electrical model of the heart, *Lond. Edinb. Dublin Phil. Mag. J. Sci.*, **6**, 763–775, 1928.
29. Pontryagin, L. S., The asymptotic behaviour of systems of differential equations with a small parameter multiplying the highest derivatives, *Izv. Akad. Nauk SSSR, Ser. Mat.*, **21**, 107–155, 1957.
30. Simitev, R. D., Biktashev, V. N., Conditions for propagation and block of excitation in an asymptotic model of atrial tissue, *Biophys. J.*, **90**, 2258–2269, 2006.
31. Spooner, P. M., Rosen, M. R., eds., *Foundations of Cardiac Arrhythmias: Basic Concepts and Clinical Approaches*, Marcel Dekker, New York, 2000.
32. Suckley, R., Biktashev, V. N., The asymptotic structure of the Hodgkin–Huxley equations, *Int. J. Bif. Chaos*, **13(12)**, 3805–3826, 2003.

33. Suckley, R., Biktashev, V. N., Comparison of asymptotics of heart and nerve excitability, *Phys. Rev. E*, **68**, 011902, 2003.
34. Tikhonov, A. N., Systems of differential equations, containing small parameters at the derivatives, *Mat. Sbornik*, **31**, 575–586, 1957.
35. Varghese, A., Winslow, R. L., Dynamics of abnormal pacemaking activity in cardiac Purkinje fibers, *J. Theor. Biol.*, **168**, 407–420, 1994.

# A Bayesian Approach to the Quantitative Polymerase Chain Reaction

Nadia Lalam<sup>1</sup> and Christine Jacob<sup>2</sup>

<sup>1</sup> EURANDOM, P.O. Box 513, 5600 MB Eindhoven, The Netherlands;  
lalam@eurandom.tue.nl

<sup>2</sup> INRA, Unit of Applied Mathematics and Informatics,  
78352 Jouy-en-Josas Cedex, France; christine.jacob@jouy.inra.fr

**Summary.** The quantitative polymerase chain reaction aims at determining the initial amount  $X_0$  of a specific portion of DNA molecules from the observation of the amplification process of the DNA molecules' quantity. This amplification process is achieved through successive replication cycles. It depends on the efficiency  $\{p_n\}_n$  of the replication of the molecules,  $p_n$  being the probability that a molecule will duplicate at replication cycle  $n$ . Modelling the amplification process by a branching process and assuming  $p_n = p$  for all  $n$ , we estimate the unknown parameter  $\theta = (p, X_0)$  using Markov chain Monte Carlo methods under a Bayesian framework.

**Key words:** Branching process, Bayesian inference, quantitative polymerase chain reaction.

## 27.1 Introduction

The polymerase chain reaction (PCR) first described by Saiki et al. [16] is an in vitro enzymatic reaction of molecular biology capable of amplifying the number of copies of a specific DNA fragment called the target. The PCR is widely used since it allows one to detect a very low abundance of DNA. Protocols that not only detect rare nucleic acids but quantitate them as well are increasingly used. The monitoring of DNA molecules as they replicate during the PCR is known as a real-time or kinetic PCR. The quantitative PCR (Q-PCR) aims at determining the initial amount of specific DNA present in a sample. This presents many applications spanning from gene expression studies to forensic medicine [2].

The PCR consists in the succession of typically 30 to 50 replication cycles. The number of copies of the target DNA is doubled at most at each replication cycle, but in practice, the probability that a molecule will be successfully duplicated after one replication cycle, known as the efficiency of the reaction, is less than one. Early replication cycles of the PCR are characterized by an exponential increase in target amplification. Then, possibly because of a depletion of reaction components or because of a decline in the polymerase enzyme activity (Liu and Saint [9]), the reaction efficiency slows down and eventually ceases, leading to a saturation phase decomposed into a linear phase and a plateau phase.

In the literature, under the assumption of constant reaction efficiency, the theory of Bienaymé–Galton–Watson branching processes in discrete time, the time step being a replication cycle, has been introduced to model the PCR exponential phase for estimating replication errors of the DNA polymerase (Krawczak et al. [7], Piau [15], Sun [19]). A simulation analysis using the coalescence theory has been performed by Weiss and von Haeseler [20] providing the maximum likelihood estimator of the replication error rate. There also exists an extensive literature involving branching processes and ignoring the replication errors (mutations in a site of the target for instance), that is, assuming that all the duplicated molecules are identical to the target template. In this setting that we will consider henceforth, Stolovitzky and Cecchi [18] studied the number of cycles during which the amplification process undergoes an exponential phase and may therefore be modelled by a single-type supercritical Bienaymé–Galton–Watson branching process for which the reaction efficiency at replication cycle  $n$ , denoted by  $p_n$ , satisfies  $p_n = p$  for all  $n$ . They proposed a method for inferring the initial number of DNA molecules  $X_0$  when considering two sets of samples  $S_1$  and  $S_2$ , each with a given number of  $d$  identical preparations. They considered observations of the molecule numbers at replication cycle  $n_1$  (resp.  $n_2$ ) belonging to the exponential phase in all the  $d$  preparations of sample  $S_1$  (resp.  $S_2$ ) which they denoted by  $X_{n_1,i}$  in the sample preparation  $i$  (resp.  $X_{n_2,i}$ ). Computing the average  $v_1 = (1/d) \sum_{i=1}^d X_{n_1,i}$  (resp.  $v_2$ ), they proposed to estimate the initial DNA molecules number  $X_0$  by the quantity  $v_1^{-n_2/(n_1-n_2)} v_2^{n_1/(n_1-n_2)}$  and the reaction efficiency  $p$  by  $v_1^{1/(n_1-n_2)} v_2^{-1/(n_1-n_2)} - 1$ . Here and in what follows, let us denote by  $X_k$  the number of DNA molecules present at replication cycle  $k$ . Relying on a single trajectory of the PCR amplification process in its exponential phase modelled by a Bienaymé–Galton–Watson branching process, Jacob and Peccoud [5] built conditional least squares estimators (CLSEs) of the reaction efficiency  $p$  based on  $n - h + 1$  successive observations of  $X_h, \dots, X_n$  with either  $h$  or  $n - h$  fixed as  $n$  tends to infinity. They also built the moment estimator of the initial DNA molecules number  $X_0$  and constructed its asymptotic confidence interval. Olofsson [11] gave maximum likelihood estimators of the quantities  $p$  and  $X_0$  using a censored Bienaymé–Galton–Watson process. Based on the PCR enzymological approach of Schnell and Mendoza [17], Jagers and Klebaner [6] modelled the amplification process using a near-critical population-size-dependent branching process with efficiency  $p_n = p(X_{n-1}) = K/(K + X_{n-1})$ , where  $K$  is a Michaelis–Menten type constant of the reaction. The authors then explained theoretically the existence of the linear part of the saturation phase observed by experimentalists on real-time PCR data. Lalam et al. [8] studied the CLSE of  $\{p_n\}_n$  in the framework of a population-size-dependent branching process with a reaction efficiency model generalizing the one proposed by Jagers and Klebaner [6].

The previous statistical analyses of the Q-PCR were made in a frequentist setting. The aim of this chapter is to perform a Bayesian analysis in order to estimate the reaction efficiency of the exponential phase  $p$  and the initial DNA molecules number  $X_0$  from a single amplification trajectory. We will use some prior information on the parameter  $\theta = (p, X_0)$  and we will rely on a stochastic modelling of the PCR amplification process during the exponential phase. The model will be a supercritical

Bienaymé–Galton–Watson branching process for which the reaction efficiency and the initial number of DNA molecules are random variables. We construct Bayesian estimators and sets of credibility of the parameter  $\theta$  by Markov chain Monte Carlo (MCMC) methods. MCMC techniques enable one to carry out simulations from a distribution by embedding it as a limiting distribution of a Markov chain and simulating from the Markov chain until it approaches equilibrium (Gamerman [3]).

Recall that we will not take into account replication errors during the amplification process and assume therefore that, when the duplication of a target DNA molecule is successful, this creates two DNA molecules identical to the target. We will also consider that the DNA molecule numbers which are accounted for in the inference analysis are observed without measurement errors.

We introduce our Bayesian approach for real-time Q-PCR in Section 27.2 and we specify it in Section 27.3. Simulation results are given in Section 27.4. Section 27.5 contains further perspectives.

## 27.2 Bayesian Approach

Recall that  $X_k$  represents the number of DNA molecules present at replication cycle  $k$ , and  $p_k$  the replication probability of a molecule at cycle  $k$ . During the exponential phase, the reaction efficiency is assumed to satisfy  $p_k = p$ , for all  $k$ . With probability  $p$ , if the duplication has been successful, a DNA molecule gives rise to two DNA molecules at the end of a replication cycle. Otherwise, with probability  $1 - p$ , a DNA molecule remains unchanged. This may be modelled by a branching process

$$X_k = \sum_{i=1}^{X_{k-1}} Y_{k,i},$$

where  $Y_{k,i}$  is the number of descendants in cycle  $k$  of the  $i$ th molecule from cycle  $k - 1$ . The random variable  $Y_{k,i}$  takes values in  $\{1, 2\}$ :  $Y_{k,i} = 1$  if the replication of molecule  $i$  fails and  $Y_{k,i} = 2$  if the replication of molecule  $i$  is successful. We assume that  $\{Y_{k,i}\}_{k,i}$  are independent and identically distributed (i.i.d.) with  $P(Y_{k,i} = 2) = p = 1 - P(Y_{k,i} = 1)$ , where  $0 < p < 1$ . The cases  $p = 0$  (the molecules never replicate) and  $p = 1$  (all the molecules always replicate) are excluded from the analysis since they never occur in real-time PCR experiments. We therefore consider a supercritical Bienaymé–Galton–Watson branching process  $\{X_k\}_k$  modelling the exponential phase of the PCR amplification process defined by

$$\begin{cases} X_0 \\ X_k = X_{k-1} + \text{Bin}(X_{k-1}, p), & k \geq 1 \end{cases}$$

with unknown parameter  $\theta = (p, X_0)$ , where  $p$  is the reaction efficiency of the exponential phase and  $X_0$  is the initial number of DNA molecules. The notation  $\text{Bin}(N, p)$  stands for a random variable following a binomial distribution with parameters  $N$  and  $p$ .

We consider a Bayesian framework: we use both some prior information about the model parameter  $\theta$  and the observation of  $\{X_k\}_k$  in the inference process. Bayesian inference is drawn by constructing the probability distribution of the parameter  $\theta$ , based on all that is known about it, given the data. The probability distribution of  $\theta$  given the data is called the posterior distribution of the parameter  $\theta$ . In the following study, we aim at determining the posterior distribution of  $\theta$ . Let  $\Theta$  be the parameter set in which  $\theta$  takes its values and denote by  $x_k$  the realization of the random variable  $X_k$ . Let  $\pi(\theta)$  be the prior distribution of the parameter  $\theta$  and let  $\pi(x_h, \dots, x_n | \theta)$  be the likelihood conditionally to  $\theta$  based on the observations  $(x_h, \dots, x_n)$ . The choice of the cycle  $h$  will be explained in Subsection 27.3.2. According to the Bayes rule, the posterior distribution of  $\theta$  is

$$\pi(\theta | x_h, \dots, x_n) = \frac{\pi(\theta)\pi(x_h, \dots, x_n | \theta)}{\int_{\theta' \in \Theta} \pi(\theta')\pi(x_h, \dots, x_n | \theta')}. \quad (27.1)$$

The Bayesian estimator of  $\theta$  that we consider is the posterior mean. We also construct the credibility set of  $\theta$  which is the confidence interval of the posterior distribution of  $\theta$ .

## 27.3 Model Specification

We compute the posterior distribution of  $\theta$  defined by (27.1) after the introduction of the prior distributions and the likelihood of the observations given below.

### 27.3.1 Prior Distributions

During the exponential phase, the reaction efficiency  $p$  is assumed to be independent of  $X_0$ . This entails that the prior distribution of  $\theta = (p, X_0)$  satisfies  $\pi(\theta) = \pi(p)\pi(X_0)$ , where  $\pi(p)$  (resp.  $\pi(X_0)$ ) is the prior distribution of  $p$  (resp.  $X_0$ ).

**Prior for  $p$ .** In view of the definition of the branching process  $\{X_k\}_k$  in Section 27.2, we have  $X_k - X_{k-1} = \text{Bin}(X_{k-1}, p)$ : the reaction efficiency  $p$  of the exponential phase is a parameter of a binomial distribution. Relying on the fact that, in the setting of i.i.d.  $\text{Bin}(N, p)$  random variables with  $N$  known, a usual non-informative prior for  $p$  is the beta distribution with parameters 0.5 and 0.5, we propose to use here this distribution as a prior for  $p$  although we are not in the simple i.i.d.  $\text{Bin}(N, p)$  case. We will denote this distribution, whose density is  $1/(\pi\sqrt{p(1-p)})$ , by  $\text{Beta}(0.5, 0.5)$ .

**Prior for  $X_0$ .** The initial DNA molecules number  $X_0$  is obtained by extraction of DNA from a biological sample. This can be accounted for by a Poisson distribution (Nedelman et al. [10]). We therefore propose a Poisson distribution with parameter  $\lambda$ , denoted by  $\text{Poisson}(\lambda)$ , for the prior distribution  $\pi(X_0)$ . We assume that  $\lambda$  is a random variable with uniform distribution of fixed support  $[a, b]$ . The prior distribution  $\pi(X_0)$  thus defined is called a two-stage or hierarchical prior; that is, a prior for  $\lambda$ , known as a hyper-prior, is put on the parameter of the prior  $\text{Poisson}(\lambda)$ . The choice of the support  $[a, b]$ , where  $a$  and  $b$  are constants, will be specified by the experimenter.

### 27.3.2 Likelihood

We will consider successive observations from the exponential phase ranging from replication cycles  $h$  to  $n$ , with  $h \geq 1$ . The starting replication cycle  $h$  is chosen such that, from this cycle on, the measurement error is relatively negligible when considering real-time PCR data. It is well known that the early observations of real-time PCR trajectories are extremely noisy and that the relative error starts to decrease as the reaction proceeds (Peccoud and Jacob [12], Peirson et al. [14]). As already indicated, we assume that  $\{X_k\}_{h \leq k \leq n}$  is observed with no measurement error.

Let us recall that  $X_k = X_{k-1} + \text{Bin}(X_{k-1}, p)$ . Then, for  $k \geq 2$ ,

$$\begin{aligned} P(X_k = x_k \mid X_{k-1} = x_{k-1}, \theta) &= P(X_k = x_k \mid X_{k-1} = x_{k-1}, p) \\ &= P(X_{k-1} + \text{Bin}(X_{k-1}, p) = x_k \mid X_{k-1} = x_{k-1}, p) \\ &= P(\text{Bin}(X_{k-1}, p) = x_k - X_{k-1} \mid X_{k-1} = x_{k-1}, p) \\ &= C_{x_{k-1}}^{x_k - x_{k-1}} p^{x_k - x_{k-1}} (1 - p)^{2x_{k-1} - x_k}. \end{aligned}$$

Hence the density of  $X_h, \dots, X_n$  given  $\theta$  is equal to

$$\pi(x_h, \dots, x_n \mid \theta) = \left[ \prod_{k=h+1}^n C_{x_{k-1}}^{x_k - x_{k-1}} p^{x_k - x_{k-1}} (1 - p)^{2x_{k-1} - x_k} \right] \times \pi(x_h \mid \theta),$$

where  $\pi(x_h \mid \theta) = \sum_{x_1, \dots, x_{h-1}} \prod_{k=2}^h P(X_k = x_k \mid X_{k-1} = x_{k-1}, \theta)$  if  $h \geq 2$ , and if  $h = 1$ ,  $\pi(x_1 \mid \theta) = \pi(X_0 + \text{Bin}(X_0, p) = x_1 \mid \theta) = C_{X_0}^{x_1 - X_0} p^{x_1 - X_0} (1 - p)^{2X_0 - x_1}$ .

### 27.3.3 Posterior Distribution of $\theta$

We deduce from Subsections 27.3.1 and 27.3.2 the expression of the posterior distribution of  $\theta$  denoted by  $\pi(\theta \mid x_h, \dots, x_n)$ . This quantity combines information from the priors and the sample. In view of (27.1),

$$\begin{aligned} \pi(\theta \mid x_h, \dots, x_n) &\propto \pi(\theta) \pi(x_h, \dots, x_n \mid \theta) \\ &= \pi(p) \pi(X_0) \pi(x_h, \dots, x_n \mid \theta) \\ &\propto \int 1_{a \leq \lambda \leq b} \frac{\lambda^{X_0}}{X_0!} e^{-\lambda} d\lambda \frac{1}{\sqrt{p(1-p)}} \\ &\quad \cdot \left[ \prod_{k=h+1}^n C_{x_{k-1}}^{x_k - x_{k-1}} p^{x_k - x_{k-1}} (1 - p)^{2x_{k-1} - x_k} \right] \cdot \pi(x_h \mid \theta) \\ &= \frac{1}{X_0!} \int_a^b \lambda^{X_0} e^{-\lambda} d\lambda \frac{1}{\sqrt{p(1-p)}} \\ &\quad \cdot \left[ \prod_{k=h+1}^n C_{x_{k-1}}^{x_k - x_{k-1}} \right] \left[ \frac{p}{1-p} \right]^{x_n - x_h} (1 - p)^{\sum_{k=h}^{n-1} x_k} \cdot \pi(x_h \mid \theta). \end{aligned}$$

Let  $J(X_0) = \int_a^b \lambda^{X_0} e^{-\lambda} d\lambda$ . Integration by parts yields the relationship  $J(X_0) = F(X_0) + X_0 J(X_0 - 1)$ , where  $F(X_0) = a^{X_0} e^{-a} - b^{X_0} e^{-b}$ . By iteration, we deduce that

$$J(X_0) = F(X_0) + X_0 F(X_0 - 1) + X_0(X_0 - 1)F(X_0 - 2) + \dots + X_0!F(1) + X_0!F(0).$$

Therefore, the posterior distribution of  $\theta$  satisfies

$$\pi(\theta | x_h, \dots, x_n) \propto \frac{J(X_0)}{X_0!} \frac{1}{\sqrt{p(1-p)}} \cdot \left[ \prod_{k=h+1}^n C_{x_{k-1}}^{x_k - x_{k-1}} \right] \left[ \frac{p}{1-p} \right]^{x_n - x_h} (1-p)^{\sum_{k=h}^{n-1} x_k} \cdot \pi(x_h | \theta). \tag{27.2}$$

This posterior distribution does not have a form belonging to some known distributions family. Due to the analytical intractability of the posterior distribution, a simulation study is necessary (Chen et al. [1]). This will allow one to sample  $\theta$  from its posterior distribution and to determine the corresponding Bayesian estimator based on the posterior distribution together with credibility intervals. We will use the software WinBUGS<sup>3</sup> in order to implement our simulations. WinBUGS approximates the posterior distribution of  $\theta$  by MCMC techniques. The MCMC numerical integration technique is widely used for implementation of the Bayes procedure (Gilks et al. [4]). This allows one to simulate a Markov chain whose stationary distribution is the joint posterior probability distribution of the parameters of the model. The software WinBUGS uses the Gibbs sampling method as a means for stochastic simulation using Markov chains. The parameters are first assigned arbitrary initial values, and the chain is simulated until it converges to the stationary distribution. Observations from the chain at stationarity are subsequently used to estimate the joint posterior probability of the parameters. This allows one to compute credibility intervals of  $\theta$ .

### 27.4 Simulation Results

We run 10,000 MCMC cycles after a burn-in period of 10,000 cycles, the burn-in cycles being discarded from the analysis. We consider a PCR trajectory consisting of 30 replication cycles for which the true values of the parameters are  $p = 0.7$  and  $X_0 = 50$ .

Recall that the Bayesian estimator of  $\theta$  that we consider is the mean of the posterior distribution. The estimation summary of the posterior distribution that will be provided consists of the marginal posterior means and 95% credibility intervals of  $p$  and  $X_0$  based on the observations from cycles  $h$  to  $n$  and based on the priors

$$\pi(p) \sim \text{Beta}(0.5, 0.5)$$

---

<sup>3</sup> The software WinBUGS is publicly available at <http://www.mrc-bsu.cam.ac.uk/bugs>.



**Table 27.1.** Summary of the results for the parameter  $p$  according to  $[h, n]$ .

$h$	$n$	Mean	Standard deviation	MC error	2.5%	97.5%
1	30	0.7	$1.836 \cdot 10^{-5}$	$2.173 \cdot 10^{-7}$	0.6999	0.7
10	15	0.6994	$1.005 \cdot 10^{-3}$	$1.135 \cdot 10^{-5}$	0.6974	0.7014
10	20	0.7002	$2.613 \cdot 10^{-4}$	$3.002 \cdot 10^{-6}$	0.6996	0.7007
10	25	0.7001	$6.922 \cdot 10^{-5}$	$8.158 \cdot 10^{-7}$	0.7	0.7002
15	20	0.7002	$2.664 \cdot 10^{-4}$	$3.051 \cdot 10^{-6}$	0.6997	0.7007
15	25	0.7001	$6.932 \cdot 10^{-5}$	$8.169 \cdot 10^{-7}$	0.7	0.7002

$$\pi(X_0) \sim \text{Poisson}(\lambda) \quad \text{with } \lambda \sim \text{Uniform}(30, 70).$$

For different values of  $h$  and  $n$ , we present the marginal posterior means, standard deviations, MC errors, and 95% credibility intervals for  $p$  (resp.  $X_0$ ) in Table 27.1 (resp. Table 27.2). The MC error is the computational accuracy of the mean and standard deviation. This means that the reported values of the mean and standard deviation are computationally accurate to about  $\pm$  the value of the MC error.

The more observations we consider, that is the wider  $[h, n]$ , the better the Bayesian estimate of  $p$  since its standard deviation decreases and its 95% credibility interval becomes narrower around the true value of  $p$ . For a given amplitude of  $[h, n]$ , the estimator of  $p$  is more accurate when  $n$  is larger: for example, for  $[h, n] = [10, 15]$ , the standard deviation is of the order of  $10^{-3}$ , whereas for  $[h, n] = [15, 20]$ , the standard deviation is of the order of  $10^{-4}$ . This suggests a consistency property of the Bayesian estimator of  $p$  as  $n$  increases analogous to the strong consistency of the CLSE of  $p$  proved in the frequentist setting in [5]. But  $[h, n]$  has hardly any influence on the estimate of  $X_0$ , as can be viewed from formula (27.2) in which the marginal posterior density of  $X_0$  does not depend on the observations from cycles  $[h, n]$ . Indeed, the only term of (27.2) in which  $[h, n]$  is used, namely  $\prod_{k=h+1}^n C_{x_{k-1}}^{x_k - x_{k-1}} p^{x_k - x_{k-1}} (1 - p)^{2x_{k-1} - x_k}$ , does not depend on  $X_0$  and therefore disappears when computing the marginal posterior distribution of  $X_0$ . This remark is in accordance with the fact indicated by Jacob

**Table 27.2.** Summary of the results for the parameter  $X_0$  according to  $[h, n]$ .

$h$	$n$	Mean	Standard deviation	MC error	2.5%	97.5%
1	30	56.74	9.292	0.1678	44	77
10	15	56.71	9.286	0.1583	44	77
10	20	56.78	9.3	0.1629	44	77
10	25	56.74	9.929	0.1654	44	77
15	20	56.77	9.301	0.1625	44	77
15	25	56.74	9.295	0.1654	44	77

**Table 27.3.** Summary of the results for the parameters  $p$  and  $X_0$  according to  $[a, b]$ .

Parameter	$a$	$b$	Mean	Standard deviation	MC error	2.5%	97.5%
$p$	20	60	0.7001	$6.923 \cdot 10^{-5}$	$7.202 \cdot 10^{-7}$	0.7	0.7002
$X_0$	20	60	52.79	6.873	0.09281	44	69
$p$	1	100	0.7001	$6.841 \cdot 10^{-5}$	$7.077 \cdot 10^{-7}$	0.7	0.7002
$X_0$	1	100	63.46	12.71	0.3341	44	87

and Peccoud [5] that there is no consistent estimator of  $X_0$  as the number of observations  $n - h + 1$  tends to infinity when considering the frequentist setting. This can also be noticed from the study of Olofsson [11], who indicated that the maximum likelihood estimator of  $X_0$  based on a censored process  $(X_c, \dots, X_n)$  is of the order of  $X_c / (1 + p)^c$ . This entails that increasing  $n$  does not have an impact on the behavior of this estimator.

Let  $h = 10$  and  $n = 25$ . If we take another support  $[a, b]$  for the hyper-parameter  $\lambda$  of the Poisson( $\lambda$ ) prior distribution of  $X_0$ , then we get the results indicated in Table 27.3.

The interval  $[a, b]$  has an impact on the estimation of  $X_0$  but not on  $p$  as can be deduced from (27.2) giving the posterior density of  $\theta$ . The information for estimating  $p$  is brought by the amplification process, that is, by the observations of  $\{X_k\}_{h \leq k \leq n}$ .

### 27.5 Concluding Remarks

We used the classical modelling of the evolution in time of DNA molecule numbers undergoing the PCR exponential phase by a supercritical Bienaymé–Galton–Watson branching process  $\{X_k\}_{0 \leq k \leq n}$ . Relying on this modelling, we performed a Bayesian statistical analysis providing the construction of Bayesian estimators and credibility sets for the parameter  $\theta = (p, X_0)$ . Our study suggests that the Bayesian estimator of  $p$  is consistent. This asymptotic behavior would be similar to the strong consistency of the frequentist CLSE of  $p$  proved by Jacob and Peccoud [5]. Another remark coming from the study of Table 1.2 is that the Bayesian estimator of  $X_0$  is not consistent since the credibility set does not improve as  $n$  increases. This is also analogous to the remark from [5] made in the frequentist approach that there is no consistent estimator of  $X_0$ .

It would be interesting to carry out a similar Bayesian statistical analysis when considering another non-informative prior for  $p$ , namely Jeffrey’s prior, which is based on the Fisher information matrix and which presents the advantage of being invariant under reparameterization.

The aim of the Q-PCR is to determine the initial DNA molecules’ quantity. In a frequentist framework, Jacob and Peccoud [5] constructed an asymptotic confidence interval of  $X_0$ , as the replication cycle  $n$  tends to infinity. It would be of interest to compare this asymptotic confidence interval, when estimating  $X_0$  by the frequentist moment estimator, with the credibility intervals built in our Bayesian approach.

The Bayesian estimators of  $p$  and  $X_0$  constructed here were based on  $\{X_k\}_{h \leq k \leq n}$ , where  $h$  is a replication cycle such that the observations are above the background noise level. The initial real-time PCR data are very noisy, so the statistical analysis of the process should not include the first observations which are not reliable. In our study, we made the strong assumption that the process  $\{X_k\}_k$  was observed without measurement errors. For real-time PCR data whose noisy observations are expressed in fluorescence units, the observed fluorescence  $F_k$  at replication cycle  $k$  may be modelled by

$$F_k = \alpha X_k + \varepsilon_k \quad (27.3)$$

with unknown proportionality constant  $\alpha$  and disturbance  $\varepsilon_k$ , as proposed by Peccoud and Jacob [13] assuming normality of the noise  $\{\varepsilon_k\}_k$ . Future work consists in using a Bayesian approach to deal with real-time PCR data  $\{F_k\}_{h \leq k \leq n}$  using the model defined by (27.3).

## References

1. Chen, M.-H., Shao, Q.-M., Ibrahim, J. G.: *Monte Carlo Methods in Bayesian Computation*. Springer-Verlag, New York (2000).
2. Ferré, F. (ed): *Gene Quantification*. Birkhäuser, New York (1998).
3. Gamerman, D.: *Markov Chain Monte Carlo: Stochastic Simulation for Bayesian Inference*. Chapman & Hall, London (1997).
4. Gilks, W. R., Richardson, S., Spiegelhalter, D. J.: *Markov Chain Monte Carlo in Practice*. Chapman & Hall, London (1996).
5. Jacob, C., Peccoud, J.: Estimation of the parameters of a branching process from migrating binomial observations. *Adv. Appl. Prob.*, **30**, 948–967 (1998).
6. Jagers, P., Klebaner, F.: Random variation and concentration effects in PCR. *J. Theoret. Biol.*, **224**, 299–304 (2003).
7. Krawczak, M., Reiss, J., Schmidtke, J., Rosler, U.: Polymerase chain reaction: replication errors and reliability of gene diagnosis. *Nucleic Acids Res.*, **17**, 2197–2201 (1989).
8. Lalam, N., Jacob, C., Jagers, P.: Modelling of the PCR amplification process by a size-dependent branching process and estimation of the efficiency. *Adv. Appl. Prob.*, **36**, 602–615 (2004).
9. Liu, W., Saint, D. A.: Validation of a quantitative method for real time PCR kinetics. *Biochemical and Biophysical Research Communications*, **294**, 347–353 (2002).
10. Nedelman, J., Heagerty, P., Lawrence, C.: Quantitative PCR: procedures and precisions. *Bull. Math. Biol.*, **54**, 477–502 (1992).
11. Olofsson, U.: Branching processes: Polymerase Chain Reaction and mutation age estimation. Ph.D. Thesis, Department of Mathematical Statistics, Chalmers University of Technology, Göteborg, Sweden (2003).
12. Peccoud, J., Jacob, C.: Theoretical uncertainty of measurements using quantitative Polymerase Chain Reaction. *Biophysical Journal*, **71**, 101–108 (1996).
13. Peccoud, J., Jacob, C.: Statistical estimations of PCR amplification rates. In: Ferré, F. (ed) *Gene Quantification*. Birkhäuser, New York (1998).
14. Peirson, S. N., Butler, J. N., Foster, R. G.: Experimental validation of novel and conventional approaches to quantitative real-time PCR data analysis. *Nucleic Acids Res.*, **31**, e73 (2003).

15. Piau, D.: Confidence intervals for nonhomogeneous branching processes and polymerase chain reactions. *Ann. Probab.*, **33**, 674–702 (2005).
16. Saiki, R., Scharf, S., Faloona, F., Mullis, K., Horn, G. T., Ehrlich, H. A., Arnheim, M.: Enzymatic amplification of  $\beta$ -globin genomic sequences and restriction site analysis for diagnosis of sickle cell anemia. *Science*, **239**, 487–491 (1985).
17. Schnell, S., Mendoza, C.: Enzymological considerations for a theoretical description of the Quantitative Competitive Polymerase Chain Reaction. *J. Theor. Biol.*, **184**, 433–440 (1997).
18. Stolovitzky, G., Cecchi, G.: Efficiency of DNA replication in the polymerase chain reaction. *Biophysics*, **93**, 12947–12952 (1996).
19. Sun, F.: The PCR and branching processes. *J. of Computational Biology*, **2**, 63–86 (1995).
20. Weiss, G., von Haeseler, A.: A coalescent approach to the Polymerase Chain Reaction. *Nucleic Acids Res.*, **25**, 3082–3087 (1997).

## A Model of Poplar (*Populus* sp.) Physiology and Morphology Based on Relational Growth Grammars

Gerhard Buck-Sorlin,<sup>1</sup> Ole Kniemeyer,<sup>2</sup> and Winfried Kurth<sup>2</sup>

<sup>1</sup> Crop and Weed Ecology Group, Wageningen UR, Haarweg 333, 6709 RZ Wageningen, The Netherlands; gerhard.buck-sorlin@wur.nl

<sup>2</sup> Brandenburgische Technische Universität Cottbus, Chair for Graphics Systems, P.O. Box 101344, D-03013 Cottbus, Germany; {okn—wk}@informatik.tu-cottbus.de

**Summary.** Functional-structural plant models (FSPMs), combining the physiological function of a plant with its architecture, require precise and transparent specifications. This can be seen as a new challenge to the design of programming languages. Here we introduce, exemplarily for a model of young poplar trees, our new formalism of relational growth grammars (RGGs), which extend the well-known Lindenmayer (L-)systems to a specific sort of node- and edge-labelled graph grammars. The model has been written in the programming language XL, which extends standard Java by rule-based programming with RGGs and overcomes many of the disadvantages of L-systems. RGGs can bridge different scales: In our model, morphogenetic rules in L-system style are combined with rules describing a regulatory network of hormone biosynthesis and rules updating photosynthate concentrations of shoot modules, all in one and the same formalism.

**Key words:** Formal language, graph grammar, physiological model, functional-structural plant model (FSPM), poplar, *Populus* sp.

### 28.1 Introduction

Typical models in plant physiology so far have often been limited to simple statistical approaches (not necessarily based on causal relationships), or to process-oriented models of reaction or transport (usually simplifying spatial structures strongly), or to structural models imitating a fixed arrangement of plants, organs or cells. The epistemological value of such isolated models is often small, and they tend to miss the systemic character of the organism to be modelled.

Recently, functional-structural plant models (FSPMs) [1] have provided a promising perspective to overcome these restrictions. However, in order to master the complexity of the resulting models, a tailor-made model specification language is an essential prerequisite. It is a decisive disadvantage of the majority of present FSPMs that their model specification is comprehensible only to programmers and computer scientists. This slows down the key processes of modelling (conception and structuring in programme modules, parameterisation, calibration and validation) and discourages potential users of the model.

Currently, the most widespread formalism for specifying the architectural development of plants are L-systems. Introduced by the biologist Aristid Lindenmayer in 1968 to model the growth of filamentous organisms, they became popular first among theoretical researchers in the field of automata and formal languages. Later, they were combined with a graphical 3D interpretation of strings and used for structural models of higher plants (e.g., [5]). From the perspective of a programmer, an L-system is essentially a rule-based system similar to those long used in the field of “artificial intelligence.” However, L-systems lack some of the features which are nowadays expected from a model specification language—particularly the support of object-oriented concepts, a high degree of interactivity, and the possibility of writing multiscaled models. Furthermore, the topology of the structures resulting from the standard graphical interpretation of L-systems is restricted to locally 1D, tree-like branching, which does not suffice to produce more complex structures like, e.g., networks.

We have therefore developed a new modelling formalism, “relational growth grammars” (RGGs) [4]. These are graph grammars which generalise L-systems and rewrite node-labelled graphs with an arbitrary number of edge types (relations). The embedding of the programming language Java additionally provides procedural and object-oriented constructs for modelling with RGG (programming language “XL”: [4]). A similar approach—yet based on C++ instead of Java and based on conventional L-systems instead of graph grammars—is being pursued by [2] in the form of the language “L+C”.

RGGs have been shown to be suitable for the modelling of cereal crops (barley, [3]). In this model, the external shape and its temporal dynamics (morphology), the effect of single major genes and the dynamics of metabolic regulatory networks that control morphogenesis (i.e., the development of shape) could all be represented within one and the same formal frame.

We will first define the notion of RGGs somewhat more precisely. To demonstrate their capacities, we will then briefly describe an RGG-based FSPM of poplar (*Populus* sp.), a fast-growing, commercially valuable temperate tree that has become the model species of forest genetics and physiology.

## 28.2 Relational Growth Grammars

An RGG rule is formally a quintuple  $(L, C, E, R, P)$  with  $L \cup C \neq \emptyset$ .  $L$ , the *left-hand side proper* of the rule, is a set of *graphs* with node labels and edge labels. It represents the part of the structure which is to be transformed. A *derivation step* of an RGG involves the removal of a copy (“match”) of one rule’s  $L$  from a (usually) larger graph and the insertion of the corresponding  $R$ , the *right-hand side proper* of the rule, which is also a set of graphs (with the underlying node sets not necessarily disjoint from those of  $L$ ).  $R$  is the result of the transformation of the substructure  $L$ .  $C$  is again a set of graphs (with the node set possibly but not necessarily overlapping with that of  $L$ ) and is called the *context* of the rule. For a rule, in order to be applicable the set  $C$  must match with a set of subgraphs of the given graph in a way which is consistent with the match of  $L$ , but in the derivation step the context is not removed

(except for the parts that are also in  $L$ ). This notion of context generalises the “left” and “right contexts” of context-sensitive L-systems [5] and enables a flexible control of subgraph replacement:  $L$  can only be transformed if it is embedded in the necessary context.  $E$  is a set of logical expressions in Java syntax which usually contain some parameters referring to node labels from  $L \cup C$  and are interpreted as *conditions* which must be met before the rule can be applied. Finally,  $P$  is a (possibly empty) list of Java commands, possibly involving parameters referring to node labels from  $L \cup C \cup R$  and parameters from  $E$ .  $P$  specifies an imperative piece of code which is executed after rule application. We write RGG rules in the form  $(* C *) , L , (E) ==> R \{P\}$ ; the order of the  $C$ ,  $L$  and  $E$  parts being indeterminate. An edge with label  $a$  between nodes  $x$  and  $y$  is written  $x - a - > y$ .

An RGG is a set of RGG rules. In the language XL, RGG rules can be put together in blocks, thus enabling an additional hierarchy of rules and an explicit control of their order of application, like in table L-systems. An RGG-based *derivation* is a sequence of discrete, successive derivation steps, starting from a given initial graph (axiom). In each step, one or all matching rules are applied, depending on the chosen mode of rule application. *Sequential* and *parallel* modes of application are well known from Chomsky grammars and L-systems, respectively. In most biological applications, the parallel mode is more appropriate. However, parallelism requires the specification of a *conflict resolution strategy* for overlapping matches of left-hand sides. Future extensions of the RGG formalism will provide explicit support for the most common conflict resolution schemes. So far, we have considered only a special case: the multiple matching of  $L$  with one and the same copy of  $L$  itself in the graph (occurring when  $L$  has internal symmetries). The standard mode of rule application realised in XL, which is basically the well-known single-pushout approach from graph grammar theory, tries to apply the rule to every match.

Our mechanism for *embedding* the right-hand side into the surrounding graph simply transfers incoming (resp. outgoing) edges of the textually leftmost (resp. rightmost) nodes of  $L$  to the textually leftmost (resp. rightmost) nodes of  $R$ . Future versions of XL will allow other embedding strategies (e.g., by specifying anchor nodes in  $R$  without using the somewhat arbitrary textual arrangement of nodes).

We have shown in [6] that it is straightforward to represent typical standard data structures like sets, multisets, lists or multiple-scaled trees (cf. [7]) as labelled graphs. The RGG formalism provides standard types of edges (i.e., special edge labels) to represent common relations occurring in these data structures, like the successor relation in lists or the membership in sets. Particularly, *strings* are special graphs where all nodes are connected in linear order by successor edges (hence, L-systems are a special case of RGG). Because the successor relation is used so frequently, it is denoted by a blank in our notation, i.e.,  $a b$  is equivalent to  $a - \text{successor} - > b$ . Additionally, the user can define new relations using, e.g., algebraic operators like the transitive hull, which can be employed in RGG rules in the same way as edges.

RGGs were partly inspired by the PROGRES system [8]. Furthermore, features from parametric L-systems were included in the RGG formalism, particularly commands from turtle geometry (cf. [5]), which are allowed as nodes and can be used to interpret the derived graphs in 3D space.

The inclusion of an imperative part ( $P$  in our definition) allows the execution of code from a conventional object-oriented language. Additionally, in XL such a language (Java) serves as a framework for the whole RGG and allows the user to define constants, variables, classes and methods. Furthermore, graph nodes in XL are Java objects and can carry arbitrary additional information and functionalities, e.g., concerning geometry, visual appearance or animated behaviour.

### 28.3 The Modelling Platform GroIMP

To facilitate model development, simulation and visualisation, we have developed the software GroIMP (growth grammar-related interactive modelling platform); see also [9]. GroIMP was designed with special emphasis on user-friendliness and interactivity in order to achieve a maximum of acceptance in the community of biological and agronomical users who are interested in FSPMs. The language XL constitutes the main modelling machinery of GroIMP. It is entirely embedded; particularly, the source code can be written using the integrated text editor jEdit, and automatically compiled. An error message panel as well as hypertext links to error sites in the source code facilitate debugging.

Concerning graphical output, GroIMP is equipped with a full range of 3D geometric classes for modelling and visualisation, including turtle commands, a set of graphical primitives (spheres, cones, cylinders, boxes, light sources) and spline surfaces (NURBS). The latter can be created using several techniques like sweeping surfaces or rotating lines. Furthermore, realistic-looking materials can be designed using texture files or procedural textures, as normal for current 3D graphics software. The visual output of a model can be displayed within GroIMP itself (real-time graphical rendering based on OpenGL), or outsourced to the free raytracer POV-Ray. At every stage of a simulation, the user can interact with the model to, e.g., select, modify or delete elements or to change parameters. An example for user interaction in a running growth simulation is shown in Fig. 28.1.

GroIMP is an open-source software, licensed under the terms of the GNU General Public License and available at [www.grogra.de](http://www.grogra.de). A collection of simple example models can also be found there.

### 28.4 The Poplar Model

We can only give an incomplete description of the model here. A commented source code of the model and further information may be obtained from the authors. The RGG model presented here is based in part on ECOPHYS [10], a process model that simulates the development of one-year-old unbranched poplar saplings during the establishment year. Similar, young unbranched poplar seedlings (*Populus canescens*) were cultivated in a greenhouse and destructively measured on one occasion for biometric parameters used in the model described below: leaf blade area, leaf stalk and internode length. Local temperature and light (photosynthetic photon flux density) measurements



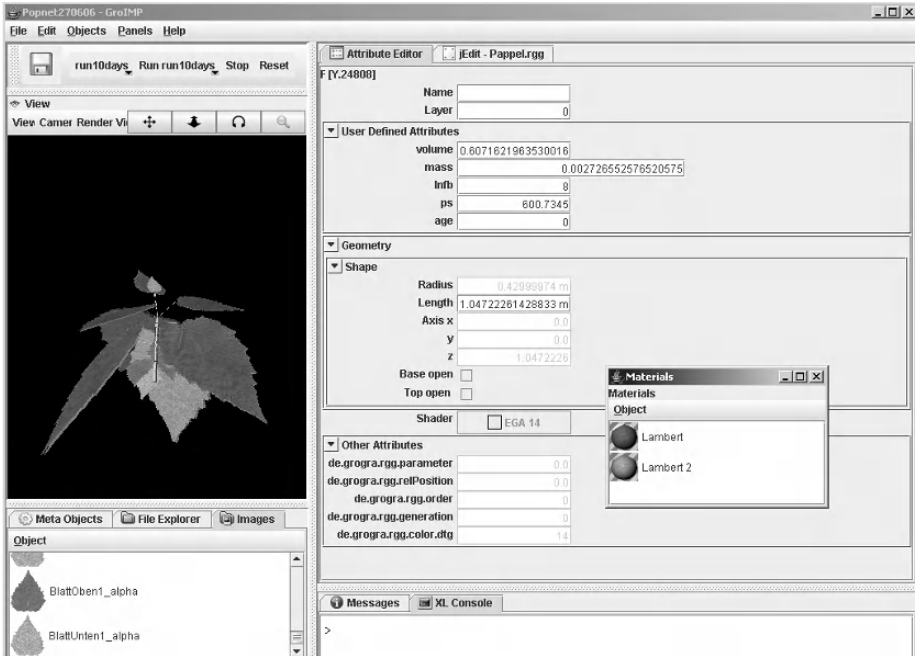


**Fig. 28.1.** Screenshot of the GroIMP graphical user interface, showing the 3D view, the material panel and the attribute editor. All components are fully interactive.

were used as input variables. Characteristic photosynthetic parameters related to leaf maturity (see below) were determined using the same plant material two weeks before the destructive harvest.

The RGG model runs with hourly time steps, and the environmental input variables are the daily courses of light intensity (photosynthetically active radiation) and temperature. Taking these input variables, plus the current area of each simulated leaf, the hourly production of photosynthates (PS; in terms of primary carbohydrates) is computed at every other time step. These PS are the building blocks for the growth and extension of all simulated organs.

In our RGG implementation, the simulated poplar grows from seed (the seed contains a certain amount of storage PS to kick off growth). Transport of PS along the simulated structures (internodes (= stem sections), leaf blades and petioles (= leaf stalks)) takes place at alternate steps at which growth pauses. This artificial alternation of growth and transport steps avoids conflicts in parameter updating and thus ensures a smooth operation of the model.

Growth consists in the production of new leaves and internodes at certain time intervals (plastochrons) from a growing tip (meristem), plus the extension/unfolding of existing organs according to the amount of PS available locally or imported from neighbouring organ modules. The model has furthermore been equipped with a metabolic regulatory network describing the biosynthesis of the plant hormone gib-

berellic acid ( $GA_1$ ) and two of its metabolic precursors as used in [3], where also the rules specifying the network topology and dynamics are described at length. The variables needed to parameterise the network have been taken over from [3] or derived from [11]. The following set of two RGG rules determines the behaviour of a meristem during and after a plastochron (i.e., the time, in hours, between the formation of two successive leaves):

```

Meristem(r, p), (p>0) ==> if (r <= 55) ( Meristem(r, p-1) );
x:Meristem(r, p), (p==0) ==> if (r <= 55) (
Internode(0,0,r+1,0) [ GA19(0.01) ][ GA20(0.01) ][ GA1(0.001) ]
[ ap(apmax[r]) Petiole(0.001, 0.01, 0) RH(1a)
Leaf(1, 2880, 3.0, 5.0, 0.1, 0.01, r) ab(abmax[r]) RL(1)
blade { numLeaves++; ori = irandom(0, 5);} ]
RH(azi[x.r]) RU(ori) Meristem(r+1,plast) );

```

The symbol `Meristem` occurring on the left-hand side of both rules refers to a previously defined class. Biologically, it represents a growing tip (or meristem). The `x` in front of `Meristem` (in the second rule) signifies a concrete instance of the class `Meristem`, whose parameter `r` (rank) is accessed in a turtle command (RH) on the right-hand side, with the azimuth angle `azi[x.r]` depending on leaf rank and taken from a table. In the first rule, the internal parameter `p` is counted down with a step size of one. This variable is initiated with the declared variable `plast` (length of the plastochron in hours; see last code line). Thus, the first rule ensures that a new metamer (i.e., internode, leaf blade and petiole) is only produced after one plastochron (on average 15 hours in our data set) has passed. The condition (`r <= 55`) limits the total number of metamers to 55. When a plastochron has passed (`p==0`, rule 2), a `Meristem` is transformed into an `Internode`, a `Petiole`, a `Leaf` (with a blade as the graphically visible part in the image), and finally a further terminal growing tip `Meristem`, initiated with a new parameter `p = plast` and an incremented leaf rank, `r`. The parameterised nodes RL, RU and RH are turtle graphics commands for the relative orientation of the newly initiated organs in space. `ab` and `ap` are auxiliary symbols determining the dynamics (zero to maximum value) of the angle between petiole and blade, respectively internode and petiole—each symbol being initiated with its own leaf rank (`r`)-specific maximum value, `abmax[r]` and `apmax[r]`. Note, in braces, procedural Java code that can be interspersed anywhere on the right-hand side of an XL-rule. In this case it serves to define a new parameter needed for a turtle command and to increment a leaf counter.

Each new instance of `Internode` is provided with three further objects symbolising the three substance classes (`GA19`, `GA20`, `GA1`) that are considered in the  $GA$ -biosynthesis network (see also Results and Discussion below) [3], with the numbers in parentheses indicating the initial concentrations of these substances. Using a further rule, an internode extends as a direct function of the local concentration of  $GA_1$ ; likewise, the  $GA_{19}$  pool is locally replenished using the time-dependent function `ga19Prod`:

```

y:Internode [ga19:GA19][ga20:GA20][ga1:GA1] ::>
{

```

```

ga19[concentration] := ga19Prod (time) * DELTA_T;
y[length] := (float) ga1[concentration];
}

```

The above rule is called an *execution* rule, as signified by the special transformation symbol `::>` between the left- and the right-hand side of the rule: such a rule is used to update certain parameters of nodes within the graph, without replacing them (as would be done in traditional L-systems).

In accordance with [10], each newly formed leaf undergoes four developmental stages or maturity classes (undeveloped, recently formed, mature, overmature) with different photosynthetic characteristics, the latter also being input variables to the functions in the form of coefficients. The maturity classes are a function of the rate of leaf production.

A simple shading function allows the distinction between unshaded and shaded leaves:

```

boolean isShaded (Node s)
{
    return exist ((* f:Leaf,
        ((f != s) && isInsideCone (f, s, 40*DEG))*));
}

```

The function is declared largely within the source code of the model itself, thus conveying maximal transparency to the user. A node `s` (usually a leaf) of the graph produced so far is taken as an input. Using this, a query is then conducted into the neighbourhood of `s`, by traversing the graph according to a search pattern specified within the context brackets, `(* and *)`: First of all, nodes (named `f`) of type `Leaf` are searched for. A further restriction is that `f` be not equal to `s` itself, i.e., the “looking” node cannot cast shade upon itself. Also, as an additional condition, the shading leaf `f` must be located within a cone with an opening angle of  $40^\circ$  emerging with a vertical central axis from `s`. The function `isShaded` is typically invoked in the conditional part of a rule:

```

b:Leaf ::> if ((numLeaves - b.r - 1 < 5) && (!isShaded(b)))
{ /* conduct photosynthesis at normal rate and grow */}
else
{ /* conduct photosynthesis at lowered rate and grow less */}

```

The first alternative of this execution rule is applied to the five uppermost leaves `b`, provided they are unshaded; `numLeaves` is a global leaf counter, whereas `b.r` is the rank of leaf `b`. The PS pools and sizes (areas) of these leaves are updated (code not shown).

As mentioned above, we have implemented rules for the acropetal (upwards) and basipetal (downwards) transport of PS and combined these to a method `transport()`, which runs in alternation with a further method combining the growth rules. Several techniques for the modelling of substance transport along a forming structure could be envisaged. We implemented a method by which pairs of neighbouring nodes in our graph data structure are identified using a general context query and then

the concentration parameters are modified accordingly, by incrementing/decrementing them with the amount to be transported:

```

b:Leaf -ancestor-> c:Internode ::>
{
float r;
r = (b.ps - c.ps) * 0.1;
b[ps] += -r;
c[ps] += r;
}

```

The execution rule ensures the basipetal transport of a certain amount  $r$  of PS from the PS-pool of a leaf  $b$  to the internode  $c$  it is attached to. This relation is symbolised with the relation edge `-ancestor->`. The last two statements of the rule update the PS-pools of the leaf and the internode. As a specialty of XL, we encounter here the *quasi-parallel* assignment operator `+=`. It ensures that the two statements are executed in parallel, i.e., the changes they cause are not visible until all rules of the currently active rule set have been applied.

## 28.5 Results and Discussion

In order to demonstrate the capability of RGGs to represent different hierarchical and procedural scales within one formalism, the poplar model was designed to contain both morphogenetic rules and a “plugged-in” metabolic regulatory network. The idea was that, by modifying certain parameters of the network, a new metabolic equilibrium should arise, which in turn should have an effect on certain morphogenetic rules, thereby ultimately changing the resulting visible morphology of the plant.

For our purposes, we chose an example provided by [11]: This study describes a transgenic hybrid poplar mutant, in which the gene encoding the enzyme GA 2-oxidase is overactivated by a transcriptional enhancer. GA 2-oxidase is a catabolising enzyme that degrades the bioactive form of gibberellic acid ( $GA_1$ ) into its inactive form,  $GA_8$ . The extension of internodes after their formation by the meristem depends upon the concentration of  $GA_1$ . Some graphical output of the poplar model is shown in Fig. 28.2. As can be seen on the right-hand side of the picture, the simulated mutant reproduces the phenotypic effect of the real mutant: due to a low concentration of  $GA_1$ , the internodes hardly extend, leading to a stunted (or “stumpy,” name of the mutant) appearance, while the number of leaves produced remains unaffected.

The current stage of the model presented here has not been designed to solve specific scientific questions regarding poplar physiology and genetics, though a later version might well be developed to be apt for this purpose. We rather intended to show here that our new formalism is in principle suitable to represent a wide range of biological processes at different scales while at the same time strictly keeping to a clear and concise format. We have already identified circumstances that require the extension of our formalism, especially at the cellular level where the processes involved in cell division and extension cannot be tackled using traditional node replacement rules, but

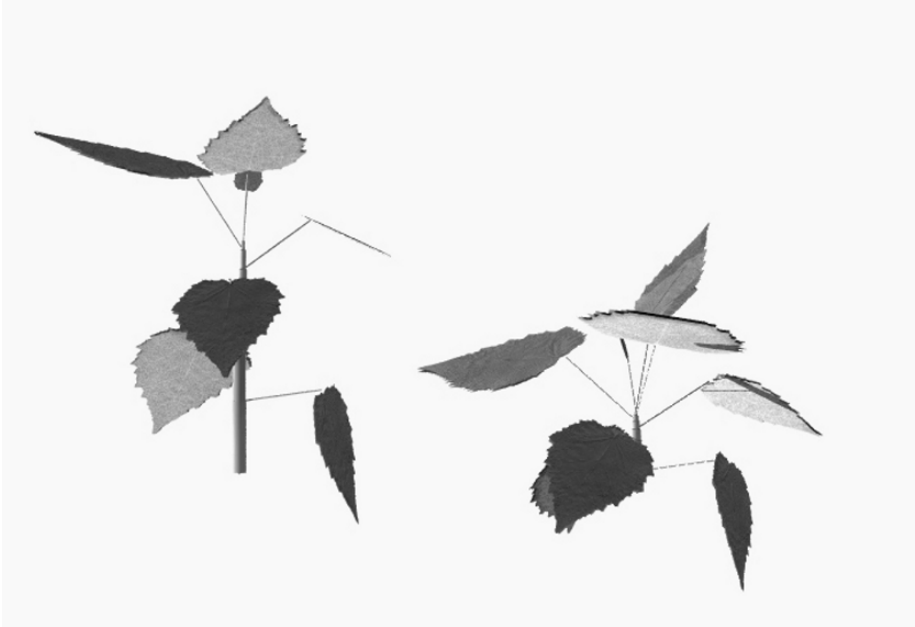


**Fig. 28.2.** Two simulation results of the RGG poplar model (240 steps, about 10 days). The wild type (left) exhibits normally extended internodes, the “stumpy” mutant (right) stunted internodes.

where we have to deal with a set of rather complicated edge or cell wall replacement rules (cf. [5]). However, as the data structure of RGGs are true graphs (and not a 1D string as in conventional L-systems), the dynamic representation of a cellular tissue as a 3D graph would be much easier in our formalism. Furthermore, the transport of substances along the simulated structure currently takes place in a discretised fashion and at a fixed meso-scale (i.e., from one botanical module to the next): the simulation of a continuous transport and of scaleable concentration gradients necessitates an extension of RGGs towards the optimised solution of ordinary and partial differential equations.

## Acknowledgments

The principal author would like to express his sincere gratitude to Patrick Schweizer (IPK) for providing working facilities. Financial support by DFG (grant Ku 847/5) is gratefully acknowledged.

## References

1. Godin, C., Hanan, J.S., Kurth, W., Lacoïnte, A., Takenaka, A., Prusinkiewicz, P., Dejong, T., Beveridge, C., Andrieu, B. (eds): 4th International Workshop on Functional-Structural Plant Models. Abstract Volume. Montpellier France: UMR AMAP (2004).

2. Karwowski, R., Prusinkiewicz, P.: Design and implementation of the L+C modeling language. *El. Notes Theor. Comp. Sci.*, **86**, 19pp. (2003).
3. Buck-Sorlin, G.H., Kniemeyer, O., Kurth, W.: Barley morphology, genetics and hormonal regulation of internode elongation modelled by a relational growth grammar. *New Phytol.*, **166**, 859–867 (2005).
4. Kurth, W., Kniemeyer, O., Buck-Sorlin, G.: Relational growth grammars—a graph rewriting approach to dynamical systems with a dynamical structure. In: J.-P. Banâtre, P. Fradet, J.-L. Giavitto, O. Michel (eds) *Unconventional Programming Paradigms*. L. N. Comp. Sci., **3566**, Springer, Berlin, 56–72 (2005).
5. Prusinkiewicz, P., Lindenmayer, A.: *The Algorithmic Beauty of Plants*. Springer, New York (1990).
6. Kniemeyer, O., Buck-Sorlin, G., Kurth, W.: A graph grammar approach to Artificial Life. *Artif. Life*, **10**, 413–431 (2004).
7. Godin, C., Caraglio, Y.: A multiscale model of plant topological structure. *J. Theor. Biol.*, **191**, 1–46 (1998).
8. Schürr, A., Winter, A.J., Zündorf, A.: The PROGRES approach: Language and environment. In: G. Rozenberg (ed): *Handbook of Graph Grammars and Computing by Graph Transformation, Vol. 2, Applications, Languages and Tools*. World Scientific, Singapore, 487–550 (1999).
9. Kniemeyer, O., Buck-Sorlin, G., Kurth, W.: GroIMP as a platform for functional-structural modelling of plants. In: J. Vos, L.F.M. Marcelis, P.H.B. de Visser, P.C. Struik, J.B. Evers (eds) *Functional Structural Plant Modelling in Crop Production*. Springer, Dordrecht, 43–52 (2007).
10. Host, G.E., Rauscher, H.M., Isebrands, J.G., Dickmann, D.I., Dickson, T.R., Crow, T.R., Michael, D.A.: *The ECOPHYS User's Manual*. Rhinelander, WI, North Central Forest Experiment Station (1990), 50 pp.
11. Busov, V.B., Meilan, R., Pearce, D.W., Ma, C., Rood, S.B., Strauss, S.H.: Activation tagging of a dominant gibberellin catabolism (*GA 2-oxidase*) from poplar that regulates tree stature. *Plant Physiol.*, **132**, 1283–1291 (2003).

---

## Asymptotic Behavior of a Two-Dimensional Keller–Segel Model with and without Density Control

Vincent Calvez<sup>1</sup> and Yasmin Dolak-Struß<sup>2</sup>

<sup>1</sup> Département de Mathématiques et Applications, Ecole Normale supérieure, 45 rue d’Ulm, 75005 Paris, France; vincent.calvez@ens.fr

<sup>2</sup> Faculty of Mathematics, University of Vienna, Nordbergstr. 15, 1090 Vienna, Austria; yasmin.dolak-struss@univie.ac.at

**Summary.** We study the Keller–Segel model for chemotaxis, consisting of a drift-diffusion equation describing the evolution of the cell density coupled to an equation for the chemoattractant. It is known that in the classical Keller–Segel model solutions can become unbounded in finite time. We present recent analytical results for this model, and compare its behavior in two space dimensions numerically to the behavior of a model accounting for the finite volume of cells. This modified Keller–Segel model relies on the assumption that cells stop aggregating when their density is too high, and thus allows for the global existence of solutions. We characterize the slow movement of a certain class of plateau-shaped solutions and perform numerical experiments for both models, showing that solutions of the classical (before blow-up) and of the density control model share common features: regions of high cell density are attracted by each other and, under suitable boundary conditions, by the domain boundaries.

**Key words:** Chemotaxis, Keller–Segel model, blow-up, volume filling.

### 29.1 Introduction

The survival of most living organisms depends on their ability to detect and react to external signals. In particular, numerous creatures, ranging from bacteria and protozoa to tissue cells or multicellular organisms, respond to variations in chemical concentrations in order to find food, mates, or new habitats. *Chemotaxis*, the oriented movement towards or away from chemical gradients, has become an intense field of experimental studies as well as of mathematical modelling. One of the earliest and most successful attempts to describe chemotaxis mathematically has become known as the *Keller–Segel (KS) model for chemotaxis*. Whereas the first equation was already derived in 1953 by Patlak [23] from a random walk problem, the full system was introduced by E. Keller and L.A. Segel to describe aggregation of the slime mold amoeba *Dictyostelium discoideum* [18, 19]. The resulting model exhibits an extremely interesting and diverse behavior. It has not only become the basis for the mathematical description of phenomena like tumor growth or embryonic development, but its mathematical

analysis has also become a field of interest on its own. In this chapter, we will discuss two different versions of the model and compare their asymptotic behavior. More precisely, for  $x \in \Omega \subset \mathbb{R}^2$  and  $t > 0$ , we will analyze the system

$$\partial_t \rho + \nabla_x \cdot (\chi(\rho)\rho \nabla_x S) = \epsilon \Delta \rho \quad (29.1)$$

$$-\Delta S = \rho - S, \quad (29.2)$$

subject to the initial condition

$$\rho(x, 0) = \rho_I(x) \quad (29.3)$$

and boundary conditions

$$\frac{\partial \rho}{\partial n} - \chi \rho \frac{\partial S}{\partial n} = 0, \quad \frac{\partial S}{\partial n} = 0 \text{ or } S = 0 \quad \text{on } \partial \Omega \quad (29.4)$$

for two different choices of the function  $\chi(\rho) \geq 0$ . Here, equation (29.1) describes the temporal evolution of the cell density  $\rho(x, t)$ , which is governed by migration in direction of the gradient of the chemical concentration  $S(x, t)$  and random movement of the cells. The chemical  $S$  is subject to diffusion as well as degradation and production by the cells themselves. The system presented here is actually a special case of the original model. First of all, the evolution of the chemical is classically described by a parabolic instead of an elliptic equation. By using the elliptic equation (29.2), we assume implicitly that the evolution of the chemoattractant is fast compared to the evolution of the cell density. Additionally, the equations are already given in their nondimensionalized form, such that there remains only one dimensionless parameter  $\epsilon$  representing the ratio between the diffusivity of the cells and the typical length and time scales of the problem. In the following, we will confine ourselves to the case  $\epsilon \ll 1$ , i.e., we will assume that the influence of cell diffusion is small compared to the chemotactic flux. The *chemotactic sensitivity*  $\chi$  describes how strongly cells react to the chemical gradient.

In this chapter, we will investigate two important cases:  $\chi = 1$ , and  $\chi = 1 - \rho$ . Models featuring a constant chemotactic sensitivity have been studied by a large number of authors, and we will discuss this case in Section 29.2. We will give a summary on recent analytical results and present conditions for the global existence of solutions. The second choice of  $\chi$ , where  $\chi$  is a monotonically decreasing function of the cell density, will be studied in Section 29.3. In particular, we will discuss the asymptotic behavior of solutions. Numerical experiments for both systems will show that concerning certain aspects, the two models behave qualitatively in a similar way. Finally, we will compare and discuss our results in Section 29.4.

## 29.2 The Classical Model: $\chi = 1$

This section is devoted to the classical model, where the diffusion coefficient and the chemotactic sensitivity are chosen to be constant, i.e.,



$$\partial_t \rho + \nabla_x \cdot (\rho \nabla S) = \epsilon \Delta \rho, \tag{29.5}$$

$$-\Delta S = \rho - S. \tag{29.6}$$

As mentioned above, the KS model was introduced to model the aggregation of a population of cells. It is therefore of interest to answer the question whether solutions can become unbounded in finite time (*blow-up*) or not. This phenomenon is now well understood, and we start with a brief survey of the main results in this area (not in chronological order). For the sake of simplicity in the theoretical overview we will slightly modify the equation for the chemoattractant. This does not affect the qualitative behavior of the whole system. However, we will keep (29.5), (29.6) for numerical simulations (Fig. 29.1, 29.2, 29.3).

### 29.2.1 Global Existence or Blow-Up: A Threshold

We replace the equation for the chemical (29.6) by the Poisson equation, that is, we consider

$$\begin{cases} \partial_t \rho + \nabla_x \cdot (\rho \nabla S) = \epsilon \Delta \rho, \\ -\Delta S = \rho - \langle \rho \rangle, \quad x \in \Omega \subset \mathbb{R}^2, \quad t > 0, \end{cases} \quad \frac{\partial S}{\partial n} = 0 \text{ on } \partial\Omega, \tag{29.7}$$

with  $\langle \cdot \rangle$  denoting the mean value over the bounded domain  $\Omega$ . This reduction does not change the general behavior of the system, but it facilitates the presentation of some short computations and basic ideas [17]. We also define the total mass of cells  $M$ , which is conserved.

The KS system (29.7) comes with an energy structure [3, 11], namely

$$\mathcal{E}(t) = \epsilon \int \rho \log \rho - \frac{1}{2} \int \rho S, \quad \frac{d\mathcal{E}}{dt} \leq 0. \tag{29.8}$$

Because of the balance between the diffusion and the chemotactic processes—resp. the positive and the negative terms in (29.8)—it is not possible to deduce, e.g., any estimate on the cell density. It is therefore necessary to compare the opposite terms using refined inequalities [3, 10, 11, 27].

Although we will not consider the case  $\Omega = \mathbb{R}^2$  in the numerics, it provides a good understanding of the KS model. Intuitively, the diffusion counterbalances the phenomenon of blow-up. Indeed, there exists a threshold: if  $8\pi\epsilon > M$ , solutions exist for all time, otherwise if  $8\pi\epsilon < M$ , solutions blow up in finite time [4, 10]. The proof of this theorem is divided into two parts: first the existence and the precise value of the threshold from below are derived from the logarithmic version of the Hardy–Littlewood–Sobolev inequality [8]. In a second step, it is shown that the second moment of  $\rho$  vanishes in finite time if  $8\pi\epsilon < M$ . Consequently, the solution does not exist further in the classical sense.

On a bounded domain  $\Omega$  the situation is similar, but there are several thresholds due to boundary effects (we refer to [15] for a complete and precise review of this case). If  $\Omega$  is smooth (typically  $\mathcal{C}^2$ ), the global existence of solutions is ensured if

$4\pi\epsilon > M$  [3, 11]. If the diffusion coefficient  $\epsilon$  is below this threshold,  $4\pi\epsilon < M$ , blow-up may occur, either on the boundary or inside the domain [13, 21].

If  $\Omega$  is piecewise  $C^2$  and  $\Theta$  denotes the smallest angle, solutions are global if  $4\Theta\epsilon > M$  [11]. Below this threshold solutions may blow-up.

### 29.2.2 Interaction Between Several Peaks

What happens after blow-up? Assuming that there is a natural way to define solutions after the time of blow-up, how do several peaks interact? A first answer to these questions is provided by the work of Velázquez [28]. He considers the following equation for the cell density:

$$\partial_t \rho + \nabla_x \cdot \left( G_\delta(\rho) \nabla S \right) = \Delta \rho, \quad x \in \mathbb{R}^2, \tag{29.9}$$

where typically  $G_\delta(u) = u/(1 + \delta u)$ . This approximation eventually leads to concentration regions of high density, but solutions are global in time for any  $\delta > 0$  (see next paragraph). Using matched asymptotic expansion methods, he derives the following vortex-like equations for the movement of peaks:

$$\dot{x}_i(t) = -\Gamma(M_i(t)) \sum_{\substack{j=1 \\ j \neq i}}^N \frac{M_j(t)}{2\pi} \cdot \frac{x_i(t) - x_j(t)}{|x_i(t) - x_j(t)|^2} + \text{regular part.} \tag{29.10}$$

Here  $x_i$  denotes the trajectory of the  $i$ th peak and  $M_i$  is the mass contained in this peak. The function  $\Gamma$  depends on the particular nonlinearity  $G$  opted for in (29.9). This approach can be considered as a way of continuing the solutions of (29.9) for  $\delta = 0$  beyond the blow-up time. Note that this would imply that even after blow-up, peaks of cell density are attracting each other.

### 29.2.3 Volume Effects and Global Existence

Blow-up of the cell density in finite time partially answers the question of aggregation, but it restricts the modelling. Therefore, nonlinearities have been introduced into the KS model [12, 14, 16, 20, 22], particularly into the chemosensitivity  $\chi$  (see the next section for a saturating effect in the chemotactic response). This naturally raises the following question: how can such nonlinearities preventing blow-up be characterized? Adapting the energy methods to the nonlinear case,

$$\partial_t \rho + \nabla_x \cdot \left( \chi(\rho) \rho \nabla S - \nabla d(\rho) \right) = 0 \quad t \geq 0, \tag{29.11}$$

there is a naturally emerging quantity which plays the role of a reduced diffusion  $\mathcal{D}$  [7], given by

$$\mathcal{D}'(u) = \frac{d'(u)}{\chi(u)}, \quad \mathcal{D}(0) = 0.$$

In addition, let us define the reduced pressure function  $\mathcal{H}: \mathcal{D}'(u) = u\mathcal{H}'(u)$ ,  $\mathcal{H}(1) = 0$ . In accordance with the linear case (where  $\mathcal{H}(u) = \epsilon \log(u)$ ) there is a threshold condition, namely

$$\exists \delta > 0 \exists U \geq 0 \quad \forall u \geq U \quad 4\pi\mathcal{H}(u) \geq (M + \delta) \log u,$$

which guarantees global existence of solutions.

### 29.2.4 Numerical Experiments

To solve system (29.5), (29.6) numerically, we use a classical finite difference scheme on a square regular grid. Inspired by the method of Scharfetter and Gummel [25] derived for the numerical solution of semiconductor models, we write the evolution equation as

$$\partial_t \rho = \epsilon \nabla_x \cdot (e^{S/\epsilon} \nabla \rho e^{-S/\epsilon}), \tag{29.12}$$

and discretize the flux accordingly. We proceed successively: for each time step we first solve the equation for  $S$  using a finite difference scheme; then we solve the advection-diffusion equation associated with zero-flux boundary conditions.

As we have seen, different thresholds for blow-up depending on the shape of the domain have been derived analytically. Concordantly, our numerical simulations show that if the diffusion is large enough, but still sufficiently small for solutions to blow-up, aggregation occurs on the boundary. Furthermore, vertices with smaller interior angles (basically the corners of a square) are more attractive for peaks in the cell density. An example is shown in Fig. 29.1, where we plot several isolines  $\rho = \alpha \rho_{\max}$  of the solution, for successive times and a given value of  $\alpha \in [0, 1]$  (see the figure caption). On the same figure we also plot the trajectory of the peak of the cell density. Simulations featuring homogeneous Dirichlet boundary conditions for  $S$  (see Fig. 29.2) show that the shifting of the cell density towards the boundary is closely related to the Neumann boundary conditions for the chemical. Indeed, this is also indicated by analytical results for system (29.7): in the case of Dirichlet boundary conditions together with  $-\Delta S = \rho$ , there is a unique threshold for blow-up ( $8\pi\epsilon \geq M$ ) [3]. This can be understood intuitively: bundles of cells are pushed away from the boundary due to the orientation of the gradient of the chemical.

Finally, the phenomenon of attracting aggregates is illustrated in Fig. 29.3. Note that if a peak lies initially too close to the boundary, it feels its attractive effect and the phenomenon is biased.

## 29.3 The Volume Filling Model: $\chi = 1 - \rho$

If the aggregation behavior of cells is to be described in more detail, models allowing for the global existence of solutions are of special interest. The finite volume of cells implies that there is a maximal value for the cell density in an aggregate, where cells

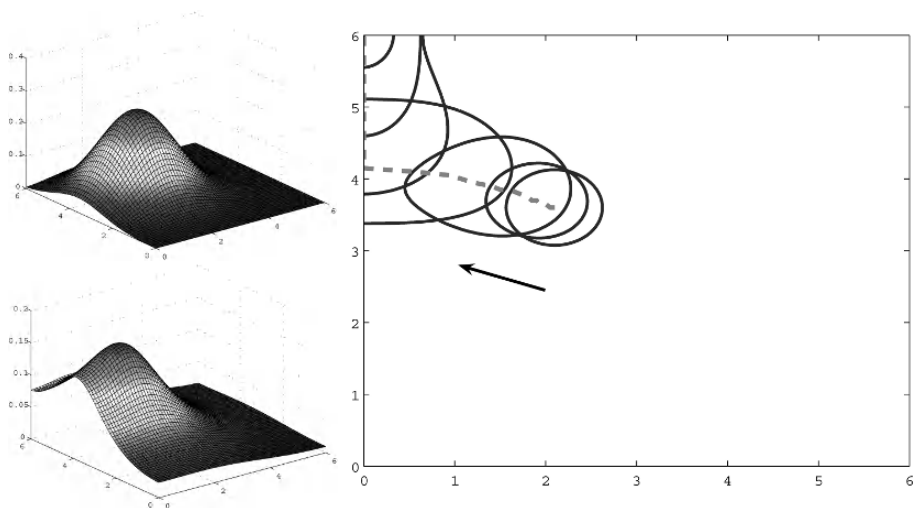


**Fig. 29.1.** The classical KS model (29.5), (29.6) with Neumann boundary conditions for  $S$ . (left) The cell density for times  $t = 0$  and  $t = 60$ . (right) Successive isolines of the cell density  $\rho$  between  $t = 0$  and  $t = 144$ , with a cut-off coefficient  $\alpha = 5/6$ . The trajectory of the peak is plotted in a dashed line. Initial condition is a Gaussian centered on  $(x_0, y_0) = (2.1, 3.6)$ , with total mass  $M = 2$ . The diffusion coefficient is  $\epsilon = 0.05$ , such that  $4\pi \times \epsilon \approx 0.63 < M$ . The blow-up time is approximately  $T_{bu} = 160$ .

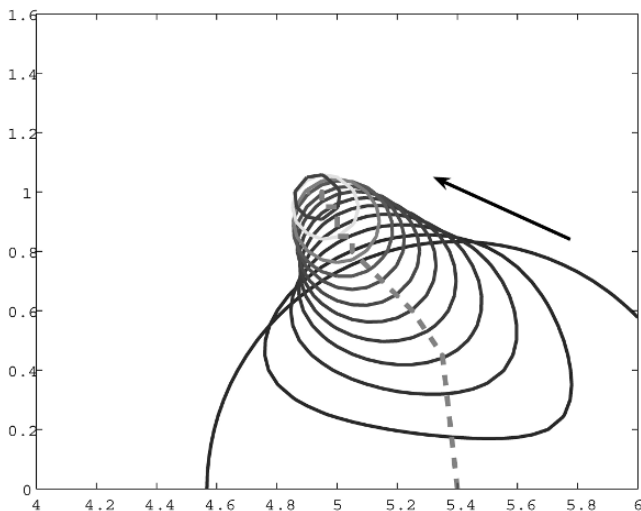


**Fig. 29.2.** The classical KS model (29.5), (29.6) with Dirichlet boundary conditions for  $S$ . Successive isolines between times  $t = 0$  and  $t = 20$  are displayed, with a cut-off coefficient  $\alpha = 1/2$ . Initial condition is a Gaussian centered on the boundary. Total mass is  $M = 1.6$ , and  $\epsilon = 0.05$ , such that  $8\pi \times \epsilon \approx 1.26 < M$ . The blow-up time is approximately  $T_{bu} = 25$ .

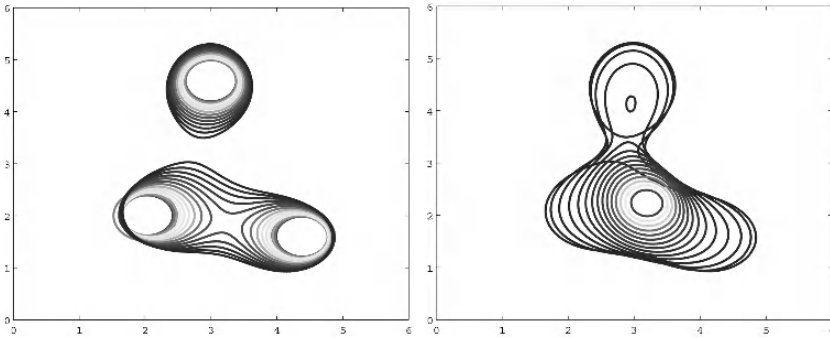


**Fig. 29.3.** Interaction between several peaks in the classical KS model (29.5), (29.6) with Neumann boundary conditions for  $S$ . Successive isolines are displayed between times (*left*)  $t = 0$  and  $t = 16$ , (*right*)  $t = 16$  and  $t = 44$ , with a cut-off coefficient  $\alpha = 0.4$ . Initial conditions are three Gaussian-like peaks with total mass  $M = 3.6$ , the diffusion coefficient is  $\epsilon = 0.05$ . Time of blow-up is approximately  $T_{bu} = 50$ .

are tightly packed. Assuming that cells stop to react chemotactically when the density becomes too large leads to a model where  $\chi = 1 - \rho$  in (29.1), i.e.,

$$\begin{cases} \partial_t \rho + \nabla_x \cdot (\rho(1 - \rho)\nabla_x S) = \epsilon \Delta \rho \\ \Delta S = S - \rho. \end{cases} \tag{29.13}$$

First introduced in [14] and later derived from a microscopic approach in [22], the model has since been studied in several papers with both an elliptic [5,9] or a parabolic [24] equation for the chemical concentration. Mathematically, the specific choice of  $\chi$  leads to the global existence of solutions. In particular, if the initial conditions are chosen such that  $0 \leq \rho_I(x) \leq 1$ , then also  $0 \leq \rho(x, t), S(x, t) \leq 1, \forall t > 0$ . For a more detailed discussion of results, see for instance [5].

### 29.3.1 Asymptotic Behavior

Stability analysis and numerical simulations show that if  $\epsilon$  is small enough, a nonconstant initial condition leads to the formation of distinct patterns. In particular, plateau-like structures are formed (see Fig. 29.4), where regions of high cell density ( $\rho \approx 1$ ) alternate with regions where it is almost zero. In [9], the asymptotic behavior of these solutions was studied in one space dimension by the method of exponential asymptotics. Two distinct time scales can be observed: plateaus move towards each other exponentially slowly, i.e., their velocity is of order  $\mathcal{O}(e^{-c/\epsilon})$ . If two plateaus approach each other too closely, the smaller one loses its shape and merges with the larger one on an  $\mathcal{O}(1)$ -time scale. This metastable behavior can also be found in phase-separation models like the Cahn–Hilliard or the Allen–Cahn equation (see references in [29]). The merging process continues until only one single plateau, typically situated at one of the domain boundaries, is left. In [6], the same model is treated for multiple space dimensions  $d > 1$ . As it turns out, the time scale of movement is no longer exponentially large but of order  $\mathcal{O}(\epsilon^{-1})$ .

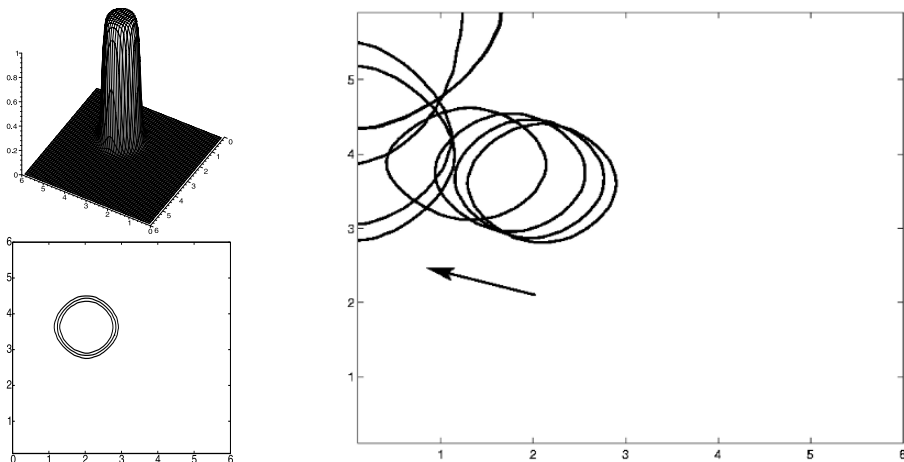


**Fig. 29.4.** The KS model with density control with homogeneous Neumann boundary conditions for  $S$ . (left) Side view and contour plot of the cell density  $\rho$  as a solution of the KS model with density control at  $t = 25$ ; isolines are shown at  $\rho = 0.2, 0.5$ , and  $0.8$ . (right) Contour plot of the level set  $\rho = 0.5$  for successive times ( $t = 0$  to  $t = 3500$ ). Initial conditions as described in the text, with  $r_0 = 0.8$ ,  $(x_0, y_0) = (3.6, 2.1)$ , with total mass  $M = 2$ . The diffusion coefficient is  $\epsilon = 0.01$ .

Before we present numerical simulations for the system in two space dimensions, we will briefly study its long-time behavior. For an asymptotic analysis of the present system in multiple space dimensions we refer to [6].

We rescale (29.13) onto the slow time scale  $\tau = \epsilon t$  to obtain the equations

$$\epsilon \partial_\tau \rho = \nabla_x \cdot (\epsilon \nabla_x \rho - \rho(1 - \rho) \nabla_x S) \tag{29.14}$$

$$\Delta S = S - \rho, \tag{29.15}$$

where the rescaled quantities  $\rho$  and  $S$  are now functions of  $(x, \tau)$ . In the following analysis, we describe the motion of the interface between a region of high density of  $\rho$  and the surrounding low-density region, i.e., the level set  $\Gamma(\tau) = \{x \mid \rho(x, \tau) = 1/2\}$ , where we will assume that  $\Gamma(\tau)$  is smooth.

We introduce a new, local coordinate system (see for instance [1]): let  $z$  be the signed distance to the interface  $\Gamma(\tau)$  oriented along the unit outer normal  $n$ , and let  $\sigma$  be a curvilinear coordinate oriented according to the tangent unit vector to the interface, where we choose  $\sigma$  to be the arc length of  $\Gamma(\tau)$ . Due to the fact that the interface is not stationary, these new coordinates depend explicitly on time, i.e.,  $\sigma = \sigma(\tau)$  and  $z = z(\tau)$ .

Denoting points on the interface by  $\Gamma(\tau) = \{X(\sigma(\tau), \tau)\}$ , any point in space with Cartesian coordinates  $x \in \mathbb{R}^2$  that is sufficiently close to the interface can be uniquely expressed in terms of the new coordinates by  $x = X(\sigma(\tau), \tau) + z(\tau)n(\sigma(\tau), \tau)$  such that this change of coordinates is well defined in a neighborhood of  $\Gamma(\tau)$ . From this relation it follows that

$$\frac{\partial x}{\partial z} = n \quad \text{and} \quad \frac{\partial x}{\partial \sigma} = \partial_\sigma X + z \partial_\sigma n = (1 + z(\partial_\sigma n \cdot \partial_\sigma X)) \partial_\sigma X, \quad (29.16)$$

where the rightmost equality is due to the fact that  $\partial_\sigma n$  has no component in the normal direction and  $|\partial_\sigma X| = 1$ . Equation (29.16) defines the unit vectors of the new coordinate system, i.e.,  $n$  and  $\partial_\sigma X$ , respectively.

On the other hand, considering the new coordinates as functions of the old ones, we can determine the vectors  $\nabla_x \sigma(x, \tau)$ ,  $\nabla_x z(x, \tau)$  by applying the chain rule

$$\frac{\partial x}{\partial q_i} \cdot \nabla_x q_j = \sum_{k=1}^2 \frac{\partial x_k}{\partial q_i} \frac{\partial q_j}{\partial x_k} = \frac{\partial q_j}{\partial q_i} = \delta_{ij}, \quad q = (\sigma, z), \quad i = 1, 2. \quad (29.17)$$

This implies

$$\nabla_x z = n, \quad \nabla_x \sigma = \partial_\sigma X \left| \frac{\partial x}{\partial \sigma} \right|^{-1}. \quad (29.18)$$

As a next step, we express the density as a function of the new variables  $\rho(\sigma, z, \tau)$ , thus transforming equation (29.14) into

$$\begin{aligned} &\epsilon(\partial_\tau \rho + \partial_\sigma \rho \partial_\tau \sigma + \partial_z \rho \partial_\tau z) + (\nabla_x \sigma \partial_\sigma + \nabla_x z \partial_z) \\ &\cdot \left[ \rho(1 - \rho)(\nabla_x \sigma \partial_\sigma S + \nabla_x z \partial_z S) - \epsilon(\nabla_x \sigma \partial_\sigma \rho + \nabla_x z \partial_z \rho) \right] = 0. \end{aligned} \quad (29.19)$$

To capture the dynamics in the thin region around the interface, we introduce the boundary layer variable  $\zeta = z/\epsilon$  and make the two-scale ansatz  $\rho(\sigma, z, \tau) = \bar{\rho}(\sigma, z, \tau) + \tilde{\rho}(\sigma, \zeta, \tau) - \lim_{\epsilon \rightarrow 0} [\bar{\rho}(\sigma, \eta/\sqrt{\epsilon}, \tau) + \tilde{\rho}(\sigma, -\eta/\sqrt{\epsilon}, \tau)]$ , where the last term represents the common limit of the outer solution  $\bar{\rho}$  and the inner solution  $\tilde{\rho}$  (the intermediate variable  $\eta$  is  $\mathcal{O}(1)$  in the region between the boundary layer and the outer regions). Both  $\bar{\rho}$  and  $\tilde{\rho}$  solve (29.19). We expand both contributions asymptotically,

$$\begin{aligned} \bar{\rho}(\sigma, z, \tau) &= \bar{\rho}_0(\sigma, z, \tau) + \epsilon \bar{\rho}_1(\sigma, z, \tau) + \mathcal{O}(\epsilon^2), \\ \tilde{\rho}(\sigma, \zeta, \tau) &= \tilde{\rho}_0(\sigma, \zeta, \tau) + \epsilon \tilde{\rho}_1(\sigma, \zeta, \tau) + \mathcal{O}(\epsilon^2). \end{aligned}$$

In the following, we impose an important restriction on the outer solution  $\bar{\rho}$ : we will only be interested in solutions satisfying

$$\bar{\rho}_0 = \begin{cases} 1 & \text{for } z < 0 \\ 0 & \text{for } z > 0, \end{cases} \quad \bar{\rho}_i \equiv 0 \quad \text{for } i \geq 1. \quad (29.20)$$

Away from the boundary layer, this choice solves equation (29.19) to all orders of  $\epsilon$ , and is motivated by the fact that only this type of solution can be observed in numerical simulations.

Analogously to the ansatz for  $\rho$ , we can also consider the chemical  $S$  as the sum of an outer and an inner contribution, where  $\bar{S}(\sigma, z, \tau)$  and  $\tilde{S}(\sigma, \zeta, \tau)$  solve equation (29.15) with  $\bar{\rho}$  and  $\tilde{\rho}$  as source terms, respectively. However, inserting  $\tilde{S}$  into (29.15) and writing the Laplacian in the new variables  $\sigma$  and  $\zeta$  yields

$$\partial_\zeta^2 \tilde{S} + \epsilon(\partial_\sigma X \cdot \partial_\sigma n) \partial_\zeta \tilde{S} + \epsilon^2 \partial_\sigma^2 \tilde{S} = \epsilon^2(\tilde{S} - \tilde{\rho}) + \mathcal{O}(\epsilon^3),$$

which implies that the influence of the boundary layer terms  $\tilde{\rho}$  on  $S$  is only of order  $\mathcal{O}(\epsilon^2)$ . Since the  $\mathcal{O}(\epsilon)$  contributions of the outer solution  $\bar{S}$  are also zero due to the special choice of  $\bar{\rho}$  given in (29.20), we have

$$\begin{aligned} S(\sigma, z, \tau) &= \bar{S}_0(\sigma, z, \tau) + \mathcal{O}(\epsilon^2) = \bar{S}_0(\sigma, \epsilon\zeta, \tau) + \mathcal{O}(\epsilon^2) \\ &= \bar{S}_0(\sigma, 0, \tau) + \epsilon\zeta \partial_z \bar{S}_0(\sigma, 0, \tau) + \mathcal{O}(\epsilon^2). \end{aligned} \tag{29.21}$$

Before we proceed by solving the inner equations, we must first calculate  $\nabla_x \sigma$  as a function of  $\zeta$  and compute the dot products between  $\nabla_x \sigma$ ,  $\nabla_x z$  and their derivatives with respect to  $\sigma$  and  $\zeta$ . From (29.16) and (29.18), it follows that

$$\begin{aligned} \nabla_x \sigma &= \partial_\sigma X (1 + \epsilon\zeta(\partial_\sigma n \cdot \partial_\sigma X))^{-1} \\ &= \partial_\sigma X (1 - \epsilon\zeta(\partial_\sigma n \cdot \partial_\sigma X) + \epsilon^2 \zeta^2 (\partial_\sigma n \cdot \partial_\sigma X)^2 + \mathcal{O}(\epsilon^3)). \end{aligned}$$

Thus, we can calculate

$$\begin{aligned} \nabla_x \sigma \cdot \partial_\sigma \nabla_x \sigma &= \partial_\sigma |\nabla_x \sigma|^2 = \mathcal{O}(\epsilon), & \nabla_x \sigma \cdot \partial_\sigma \nabla_x z &= \partial_\sigma n \cdot \partial_\sigma X + \mathcal{O}(\epsilon), \\ \nabla_x z \cdot \partial_\zeta \nabla_x \sigma &= 0, & \nabla_x z \cdot \partial_\zeta \nabla_x z &= 0. \end{aligned}$$

Inserting the expansion of the inner solution into (29.19), we obtain a hierarchy of equations of ascending order of  $\epsilon$ . To the lowest order,

$$\mathcal{O}(\epsilon^{-1}) : \quad \partial_\zeta(\tilde{\rho}_0(1 - \tilde{\rho}_0)\partial_z \bar{S}_0 - \partial_\zeta \tilde{\rho}_0) = 0,$$

where  $\partial_z \bar{S}_0$  is evaluated at  $(\sigma, 0, t)$ . Since the outer and inner solution need to be matched,  $\partial_\zeta \tilde{\rho}_0 \rightarrow 0$  as  $\zeta \rightarrow \pm\infty$ , and integration with respect to  $\zeta$  yields

$$\partial_\zeta \tilde{\rho}_0 = \tilde{\rho}_0(1 - \tilde{\rho}_0)\partial_z \bar{S}_0. \tag{29.22}$$

From (29.22) we can see that the asymptotic approximation is only valid as long as the condition  $\partial_z \bar{S}_0 > 0$  holds true.

To the next order, we have

$$\begin{aligned} \mathcal{O}(1) : \quad &\partial_\zeta \tilde{\rho}_0 \partial_\tau z + \partial_\sigma(\tilde{\rho}_0(1 - \tilde{\rho}_0)\partial_\sigma \bar{S}_0) + (\partial_\sigma n \cdot \partial_\sigma X)(\tilde{\rho}_0(1 - \tilde{\rho}_0)\partial_z \bar{S}_0 - \partial_\zeta \tilde{\rho}_0) \\ &+ \partial_\zeta(\tilde{\rho}_0(1 - \tilde{\rho}_0)\zeta \partial_z^2 \bar{S}_0 + \tilde{\rho}_1(1 - 2\tilde{\rho}_0)\partial_z \bar{S}_0 - \partial_\zeta \tilde{\rho}_1) = 0. \end{aligned} \tag{29.23}$$

From (29.22), the third term vanishes.

We integrate (29.23) with respect to  $\zeta$  from  $-\infty$  to  $+\infty$ . Since  $\tilde{\rho}$  and  $\tilde{\rho}$  have to be matched as  $\zeta \rightarrow \pm\infty$ , it follows from the particular choice of  $\bar{\rho}$  (29.20) and (29.22) that  $\tilde{\rho}_0(\infty) = 0$ ,  $\tilde{\rho}_0(-\infty) = 1$ ,  $\tilde{\rho}_1(\pm\infty) = \partial_\zeta \tilde{\rho}_1(\pm\infty) = 0$ , and the integral of the fourth term in (29.23) vanishes. Concerning the second term in the integral, we can deduce from (29.22) that

$$\int_{-\infty}^{\infty} \tilde{\rho}_0(1 - \tilde{\rho}_0) d\zeta = \int_{-\infty}^{\infty} \frac{\partial_\zeta \tilde{\rho}_0}{\partial_z \bar{S}_0} d\zeta = -\frac{1}{\partial_z \bar{S}_0}.$$



Hence, we obtain a condition on the remaining terms, i.e., the equation

$$\partial_\tau z + \partial_\sigma \left( \frac{\partial_\sigma \bar{S}_0}{\partial_z \bar{S}_0} \right) = 0. \tag{29.24}$$

Since the quantity  $\partial_\tau z$  is the negative value of the interface velocity in normal direction  $V_n$ , this is the sought-for equation describing the dynamics of the curve  $\Gamma(\tau)$ . Coupled to the evolution equation for  $\bar{S}_0$ , the motion of the interface is hence given by

$$\begin{aligned} V_n &= \partial_\sigma \left( \frac{\partial_\sigma \bar{S}_0}{\partial_z \bar{S}_0} \right) \text{ on } \Gamma(\tau) \times (0, T) \\ -\Delta \bar{S}_0 &= \bar{\rho}_0 - \bar{S}_0 \text{ in } \Omega \times (0, T). \end{aligned} \tag{29.25}$$

The gradient flow structure of this system as well as the stability of stationary solutions of (29.25) are discussed detail in [6].

### 29.3.2 Numerical Experiments

The above derived system (29.25) falls into the class of surface diffusion models, and although numerical methods for this type of model have been developed recently (see for instance [26, 2]), the numerical solution of (29.25) is—due to the coupling to the chemical  $\bar{S}_0$ —absolutely nonstandard. Hence, we confine ourselves to solving the full system (29.13) numerically. Again, for each time step,  $S$  is first computed using a finite difference discretization of the elliptic equation, then the cell density  $\rho$  is calculated using the updated value for  $S$ . Due to the nonlinearity in  $\rho$ , the Scharfetter–Gummel algorithm described above cannot be generalized in a straightforward way, and we use an upwind scheme for the cell density equation instead.

Our numerical experiments are analogous to those in Section 29.2, where we now choose the initial conditions

$$\rho_I(x, y) = \begin{cases} 1 & \text{for } (x - x_0)^2 + (y - y_0)^2 \leq r_0, \\ 0 & \text{else.} \end{cases}$$

Fig. 29.4 shows successive contour plots of a solution  $\rho$  for parameter values as given in the caption. Just as in the case where  $\chi = 1$ , we see that the aggregation moves first towards and then along the nearest boundary until it has reached the nearest corner. Fig. 29.5 shows the solution of (29.13) under the same conditions as in Fig. 29.4, but with homogeneous Dirichlet boundary conditions for  $S$ . Just as in the classical model, the peak moves away from the boundary, to the middle of the domain. Finally, in Fig. 29.6, the merging of two maxima under Neumann boundary conditions is shown. Since the plateaus are approximately of the same size, both deform until they join as one single, large peak. This peak eventually behaves like the plateau in Fig. 29.4 and travels towards the boundary (data not shown).

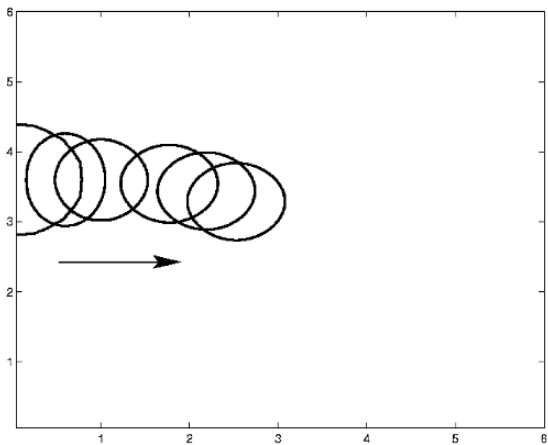


**Fig. 29.5.** The KS model with density control with homogeneous Dirichlet boundary conditions for  $S$ . Contour plot of the cell density  $\rho$  for  $t = 0$  to  $t = 12500$ . Parameter values are the same as in Fig. 29.4.

### 29.4 Conclusion

In the last decades, a large number of articles has been dedicated to the mathematical analysis of the Keller–Segel model for chemotaxis. In particular, the phenomenon of blow-up of solutions has been a focus of interest in the mathematical community, and precise conditions for its occurrence have been derived. On the other hand, several

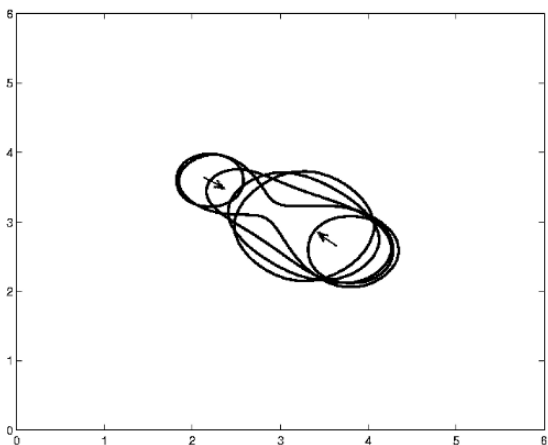


**Fig. 29.6.** The KS model with density control with homogeneous Neumann boundary conditions for  $S$ . Contour plot of two merging peaks for successive times (isolines shown for  $t = 0$  to  $t = 500$ ). Initial conditions are  $r_0 = 0.4, (x_0, y_0) = (3.6, 2.2)$  for the first,  $r_0 = 0.5, (x_0, y_0) = (2.6, 3.8)$  for the second peak. Total mass  $M = 2, \epsilon = 0.005$ .

modifications of the classical KS model have been proposed to prevent overcrowding and thus to guarantee the global existence of solutions. The aim of this work was to review recent rigorous and formal results on the asymptotic behavior of both the classical KS model and a related model featuring a density control mechanism, leading to a nonlinear flux term in the equation for the cell density.

The dominating qualitative effect in the classical KS model is the blow-up in finite time. In contrast to this, the solutions of the nonlinear KS model form plateau-shaped regions of high cell density that move on a slow time scale inversely proportional to  $\epsilon$ , as was shown above for space dimension  $d = 2$ .

We also presented numerical simulations of both models, showing that, despite the differences, solutions of the classical and the volume filling model also share common features. If we focus on regions corresponding to high cell density (respectively moving areas where blow-up occurs and plateaus) we observe that they are attracted by each other (compare Fig. 29.3 and 29.6). Our numerical approach is restricted to the time before blow-up, but studies of Velazquez [28] indicate that even after blow-up, peaks are attracted by each other. Another phenomenon to be observed in the numerical simulations is that in both models, peaks are attracted by the domain boundaries (compare Fig. 29.1 and 29.4): for a variety of initial conditions tested, peaks or plateaus of high cell density first move towards the nearest boundary to then approach a region where the curvature of the boundary is high, for instance the corners of a rectangle. This is an interesting phenomenon that is not completely understood so far, but is apparently closely connected to homogeneous Neumann boundary conditions for the chemical. If homogeneous Dirichlet conditions are chosen instead, the peaks or plateaus move away from the boundary. Intuitively, this can be explained by the fact that the Neumann boundary conditions act like a mirror, “reflecting” variations in the cell density; hence, the phenomena of two peaks merging and one peak being attracted by the boundary are indeed a result of the same mechanism.

## Acknowledgments

VC especially thanks Francis Filbet for his fruitful help during CEMRACS’04. YDS wants to thank Christian Schmeiser for valuable discussions and suggestions.

## References

1. Arfken, G., Weber, H.: *Mathematical Methods for Physicists*. Academic Press, San Diego, CA (1995).
2. Bänsch, E., Morin, P., Nochetto, R.: A finite element method for surface diffusion: The parametric case. *J. Comput. Phys.*, **203**, 321–343 (2005).
3. Biler, P., Nadzieja, T.: Existence and nonexistence of solutions for a model of gravitational interaction of particles. *Colloq. Math.*, **66**, 319–334 (1994).
4. Blanchet, A., Dolbeault, J., Perthame, B.: Two-dimensional Keller–Segel model: optimal critical mass and qualitative properties of the solutions. *Electron. J. Differential Equations*, No. 44 (electronic) (2006).

5. Burger, M., Di Francesco, M., Dolak-Struß, Y.: The Keller–Segel model for chemotaxis with prevention of overcrowding: Linear vs. nonlinear diffusion. *SIAM J. Math. Anal.*, **38**, 1288–1315 (electronic) (2006).
6. Burger, M., Dolak-Struß, Y., Schmeiser, C.: Asymptotic analysis of an advection-dominated chemotaxis model in multiple spatial dimensions. Preprint (2006).
7. Calvez, V., Carrillo, J.A.: Volume effects in the Keller–Segel model: energy estimates preventing blow-up. *J. Math. Pures Appl.*, **86**, 155–175 (2006).
8. Carlen, E., Loss, M.: Competing symmetries, the logarithmic HLS inequality and Onofri’s inequality on  $S^n$ . *Geom. Funct. Anal.*, **2**, 90–104 (1992).
9. Dolak, Y., Schmeiser, C.: The Keller–Segel model with logistic sensitivity function and small diffusivity. *SIAM J. Appl. Math.*, **66**, 595–615 (2005).
10. Dolbeault, J., Perthame, B.: Optimal critical mass in the two dimensional Keller–Segel model in  $\mathbb{R}^2$ . *C. R. Math. Acad. Sci. Paris*, **339**, 611–616 (2004).
11. Gajewski, H., Zacharias, K.: Global behavior of a reaction-diffusion system modelling chemotaxis. *Math. Nachr.*, **195**, 77–114 (1998).
12. Gamba, A., Ambrosi, D., Coniglio, A., de Candia, A., Di Talia, S., Giraud, E., Serini, G., Preziosi, L., Bussolino, F.: Percolation, morphogenesis, and Burgers dynamics in blood vessels formation. *Phys. Rev. Lett.*, **90**, 118101 (2003).
13. Herrero, M.A., Velázquez, J.J.L.: Chemotactic collapse for the Keller–Segel model. *J. Math. Biol.*, **35**, 177–194 (1996).
14. Hillen, T., Painter, K.: Global existence for a parabolic chemotaxis model with prevention of overcrowding. *Adv. in Appl. Math.*, **26**, 280–301 (2001).
15. Horstmann, D.: From 1970 until present: The Keller–Segel model in chemotaxis and its consequences. Part I. *Jahresbericht der DMV*, 105:103:165 (2003).
16. Horstmann, D., Winkler, M.: Boundedness vs. blow-up in a chemotaxis system. *J. Differential Equations*, **215**, 52–107 (2005).
17. Jäger, W., Luckhaus, S.: On explosions of solutions to a system of partial differential equations modelling chemotaxis. *Trans. Amer. Math. Soc.*, **329**, 819–824 (1992).
18. Keller, E.F., Segel, L.A.: Initiation of slime mold aggregation viewed as an instability. *J. Theor. Biol.*, **26**, 399–415 (1970).
19. Keller, E.F., Segel, L.A.: Model for chemotaxis. *J. Theor. Biol.*, **30**, 225–234 (1971).
20. Kowalczyk, R.: Preventing blow-up in a chemotaxis model. *J. Math. Anal. Appl.*, **305**, 566–588 (2005).
21. Nagai, T.: Blow-up of radially symmetric solutions to a chemotaxis system. *Adv. Math. Sci. Appl.*, **5**, 581–601 (1995).
22. Painter, K., Hillen, T.: Volume-filling and quorum sensing in models for chemosensitive movement. *Canad. Appl. Math. Quart.*, **10**, 280–301 (2003).
23. Patlak, C.S.: Random walk with persistence and external bias. *Bull. Math. Biophys.*, **15**, 311–338 (1953).
24. Potapov, A.B., Hillen, T.: Metastability in chemotaxis models. *J. Dyn. Diff. Eq.*, **17**, 293–330 (2005).
25. Scharfetter, D., Gummel, H.: Large signal analysis of a Silicon Read diode oscillator. *IEEE Trans. Electron Devices*, **ED-16**, 64–77 (1969).
26. Smereka, P.: Semi-implicit level set methods for curvature and surface diffusion motion. *J. Sci. Comput.*, **19**, 438–456 (2003).
27. Suzuki, T.: *Free Energy and Self-Interacting Particles*. Progress in Nonlinear Differential Equations and their Applications, 62. Birkhäuser, Boston (2005).
28. Velázquez, J.J.L.: Point dynamics in a singular limit of the Keller–Segel model. I. Motion of the concentration regions. *SIAM J. Appl. Math.*, **64**, 1198–1223 (2004).

29. Ward, M.: Exponential asymptotics and convection-diffusion-reaction models. In *Analyzing Multiscale Phenomena Using Singular Perturbation Methods*. Proceedings of Symposia in Applied Mathematics, **56**, 151–184 (1998).

## Saturation Effects in Population Dynamics: Use Branching Processes or Dynamical Systems?

Christine Jacob

Applied Mathematics and Informatics unity, INRA, 78352 Jouy-en-Josas Cedex, France;  
christine.jacob@jouy.inra.fr

**Summary.** This chapter deals with the behavior of a branching population undergoing saturation effects when it becomes too large. We study in particular the limits of the prediction given in the setting of the deterministic dynamical system related to the stochastic branching process modeling the evolution of the population. We also generalize the usual Markovian branching processes of order one to size-dependent branching processes that may have a longer memory and give conditions leading to an almost sure extinction of the process while the dynamical system is persistent. The notion of reproductive rate is explained and generalized. We give some examples, in particular the amplification process in the polymerase chain reaction (PCR).

**Key words:** Branching process, dynamical system, reproductive rate, saturation, PCR, logistic.

### 30.1 Introduction

Every biological population needs some suitable resources for surviving both from the quality point of view and from the quantity point of view. When the available resources are not appropriate, the population dies out or, when possible, it migrates towards a more favorable environment or undergoes mutations allowing its survival. The persistence of a population depends on some balance between the renewing rate of the populations sharing the same resources and the regeneration rate of the resources. When this balance occurs with some delay, it generally creates random cycles. The classical lynx-hare population dynamics is such a generic example ([20]). Epidemics are other examples.

The prediction of the behavior of the population dynamics and in particular the question of persistence or extinction requires a modeling approach. Branching processes and, more specifically, size- (or density-, or more generally, state-) dependent branching processes and derived models are the appropriate models for population dynamics. Our main goal here is to study the limits of the prediction given in the setting of the deterministic dynamical system related to a stochastic process modeling the

evolution of a population undergoing saturation effects. We show that when the population is very large and its dynamic is density dependent relative to some normalization that depends on the initial size of the population or on the time, or on both quantities, that the normalized process may behave asymptotically before extinction as the related (deterministic) dynamical system. But this result is neither valid for the nonnormalized process, nor in general for the concentration process when the process itself increases to  $\infty$ , as  $n \rightarrow \infty$ , and increasing bias between the two models may be observed. Moreover in all the cases, when the initial conditions are favourable to the growth of the population, but the saturation effects concern both births and deaths, then, while the dynamical system persists as time tends to infinity, the stochastic process dies out with probability 1. It is therefore crucial to study not only the behavior of the process conditioned on nonextinction but also the law of its extinction time since the extinction of a population may support the implementation of immigrant populations.

We also generalize the current Markovian processes of order one to state-dependent branching processes that may have a longer memory and give conditions leading to an a.s. (almost sure) extinction of the process while the dynamical system is persistent. The notion of reproductive rate is explained and generalized in this frame.

We finally give some examples. The first example, which is the most detailed, concerns the amplification process in the polymerase chain reaction (PCR). In this case, the saturation effects are assumed to concern only the “births” since the molecules obtained by replication are assumed indestructible during the experiment time. The other examples concern the evolution of bacteria populations in a more or less limited (i.e., closed) environment. Details of the proofs and additional simulations may be found in ([6]).

### 30.2 Markovian Branching Processes of Order One

First consider a single type population, the size evolution of which,  $\{N_n\}_n$ , is modeled by a Markovian branching process of order one. If  $\mathcal{F}_n$  denotes the  $\sigma$ -algebra generated by the process until time  $n$ ,  $N_0$  being given, then  $\{N_n\}_{n \geq 1}$  is essentially defined by

$$N_n = \sum_{i=1}^{N_{n-1}} Y_{n,i}; \quad \{Y_{n,i}\}_i \text{ i.i.d. given } \mathcal{F}_{n-1}, \tag{30.1}$$

$$E(Y_{n,1} | \mathcal{F}_{n-1}) = m(N_{n-1}), \quad \text{Var}(Y_{n,1} | \mathcal{F}_{n-1}) = \sigma^2(N_{n-1}), \tag{30.2}$$

where  $Y_{n,i}$  is the offspring size of the individual  $i$ .

In the multitype case with  $d$  types, (30.1) becomes

$$N_n^k = \sum_{h=1}^d \sum_{i=1}^{N_{n-1}^h} Y_{n,i}^{h,k}; \quad k = 1, \dots, d, \tag{30.3}$$

where  $Y_{n,i}^{h,k}$  is the size of offspring with the type  $k$  whose “parent” is  $i$  with type  $h$ . We denote  $M(N_{n-1})$  the matrix of expectations  $\{E(Y_{n,i}^{h,k} | \mathcal{F}_{n-1})\}_{h,k}$ . In what follows,  $M(\cdot)$  (resp.  $m(\cdot)$ ) are continuous functions.

The simplest and most ancient model is the well-known BGW ([1]) (Bienaymé–Galton–Watson) process which is not size dependent and therefore cannot model saturation effects. Another well-known size-dependent Markovian class is the class of ABGW (asymptotically BGW with  $\lim_N M(N) = M$ ). Let  $\mathbf{N}_n^t = (N_n^1, \dots, N_n^d)$  and  $\xi^h(\mathbf{N}_{n-1}) = (\xi^{h,1}(\mathbf{N}_{n-1}), \dots, \xi^{h,d}(\mathbf{N}_{n-1}))$ , where  $\xi^{h,k}(\mathbf{N}_{n-1}) = \sum_{i=1}^{N_{n-1}^h} (Y_{n,i}^{h,k} - M(\mathbf{N}_{n-1})[h, k])$ , then (30.1) or more generally (30.3) may also be written in an autoregressive way,

$$\mathbf{N}_n^t = \mathbf{N}_{n-1}^t M(\mathbf{N}_{n-1}) + \sum_{h=1}^d \xi^h(\mathbf{N}_{n-1}). \tag{30.4}$$

Since  $\xi^h(\mathbf{N}_{n-1})$  is a martingale difference, that is  $E(\xi^h(\mathbf{N}_{n-1}) \mid \mathcal{F}_{n-1}) = 0$ , (30.3) leads to the natural dynamical system

$$\mathbf{X}_n^t = \mathbf{X}_{n-1}^t M(\mathbf{X}_{n-1}), \quad \mathbf{X}_0 = \mathbf{N}_0. \tag{30.5}$$

### 30.2.1 Large Initial Population

When the initial population is very large and the offspring at time  $n$  depends on the density  $N_{n-1}^\mu = N_{n-1} \mu_{n-1, N_0}^{-1}$ , where  $\mu_{n, N_0} \rightarrow \infty$  as  $N_0 \rightarrow \infty$ , we may compare the behavior of  $\{N_n^\mu\}_n$  to that of  $\{X_n^\mu\}_n$  defined by  $X_n^{\mu \ t} = X_{n-1}^\mu M(X_{n-1}^\mu)$ ,  $n \geq 1$ , where  $X_0^\mu = N_0^\mu = \text{constant}$ , for all  $N_0$ . In a natural way,  $\mu_{n, N_0} = V_0$  (initial volume), or equivalently  $N_0$ , when assuming a constant initial density  $d_0 = N_0/V_0$ , or in the multitype case,  $N_n$  (total size of the population at time  $n$ ). But other normalizations are possible. For example, in the single type BGW case, a natural normalizing quantity is  $\mu_{n, N_0} = N_0 m^n$  since  $\lim_{N_0} \lim_n N_n [N_0 m^n]^{-1} \stackrel{\text{a.s.}}{=} \lim_{N_0} W \stackrel{\text{a.s.}}{=} 1$ , for  $m > 1$  ([1]), which leads to  $\lim_{N_0} \lim_n (N_n^\mu - X_n^\mu) \stackrel{\text{a.s.}}{=} 0$ , where  $X_n^\mu = X_0^\mu = N_0^\mu = 1$ , for all  $n$ . Denoting  $[N_n] = N_n V_0^{-1}$  (or equivalently  $N_n N_0^{-1}$ ), and assuming an initial constant density  $d_0 = N_0 V_0^{-1}$ , and since when  $[N_n] = N_n N_0^{-1}$ ,  $E[N_n] = [X_n] = m^n$  with  $\text{Var}([N_n] - [X_n]) = m^{2n} O(N_0^{-1})$ , we get  $\lim_{N_0} ([N_n] - [X_n]) \stackrel{\text{a.s.}}{=} 0$ , but  $\lim_{N_0} \lim_n |[N_n] - [X_n]|$  is in general infinite. In the size-dependent case such that the deterministic model is persistent while the stochastic one dies a.s. to 0, Klebaner ([12]) studied the model with a threshold  $K$  such that  $m(N_{n-1}/K) = 0$  when  $N_{n-1} > K$ . The normalized process is  $N_n^K = N_n K^{-1} = d_n d_{\max}^{-1}$  where  $d_n = N_n V_0^{-1}$  (or  $N_n N_0^{-1}$ ),  $d_{\max} = K V_0^{-1}$  (or  $K N_0^{-1}$ ). Assuming  $d_0$  and  $d_{\max}$  constant, for any  $N_0$ , then  $X_0^K = N_0^K = d_0 d_{\max}^{-1}$  is constant for all  $K$  (or equivalently all  $N_0$ ). The author proved that the quasi-stationary distribution  $\lim_n \mathcal{L}(N_n^K \mid N_n^K \neq 0)$  exists and concentrates as  $K \rightarrow \infty$  around the stable limit points of  $\{X_n^K\}_n$  ([12]). This result allows us to use the asymptotic behavior of  $\{X_n^K\}_n$  as an approximation of the asymptotic behavior of the process  $\{N_n^K\}_n$  until extinction. It would not be the case if the results concerned  $\lim_n \lim_K \mathcal{L}(N_n^K \mid N_n^K \neq 0)$  instead of  $\lim_K \lim_n \mathcal{L}(N_n^K \mid N_n^K \neq 0)$ .

In 1997, Högnäs ([4]) defined a stochastic Ricker model with  $m(N_{n-1}) = \exp(r - \gamma N_{n-1})$ . Its deterministic counterpart is  $X_n = X_{n-1} \exp(r - \gamma X_{n-1})$ ,  $n \geq 1$ ,  $X_0 = N_0$ ,



equivalent, for  $\gamma \neq 0$ , to  $d_n = d_{n-1} \exp(r - d_{n-1})$ , where  $d_n = \gamma X_n$ . Defining  $\gamma = V_0^{-1}$  (or  $N_0^{-1}$ ), where  $d_0$  is constant, for any  $\gamma$ , then  $d_n$  is the population density at time  $n$ . The author proved that for any given  $\gamma$ , the process of densities  $\{\gamma N_n\}_n$  has a unique quasi-stationary distribution  $\Pi_\gamma$  and, for  $d_0$  fixed,  $\lim_\gamma \Pi_\gamma$  exists and is a uniform law on the unique (weakly) stable cycle of  $\{d_n\}_n$ .

In the multitype case, assuming that  $M(\cdot)$  only depends on the empirical probability vector  $\widehat{\mathbf{P}}_{n-1} = (\mathbf{N}_{n-1}/N_{n-1})1_{\{N_{n-1} \neq 0\}}$ , where  $N_{n-1} = \sum_h N_{n-1}^h$  is the size of the population, and using the autoregressive approach, Jacob and Viet ([8]) proved  $\lim_{N_0} \widehat{\mathbf{P}}_n \stackrel{\text{a.s.}}{=} \mathbf{P}_n$ , where  $\{\mathbf{P}_n\}_n$  is solution of a dynamical system. Therefore  $\lim_n \lim_{N_0} \widehat{\mathbf{P}}_n \stackrel{\text{a.s.}}{=} \lim_n \mathbf{P}_n$ . They also showed that in a closed population, the limit in  $n$  and in  $N_0$  cannot be exchanged. However we have the following property in a supercritical population.

**Proposition 1** *Assume that  $\{N_n\}_n$  is a supercritical BGW process with  $E(Y_{n,1}^{h,0}) = m > 1$ ,  $\text{Var}(Y_{n,1}^{h,0}) = \sigma^2$ ,  $\sum_k \text{Var}(Y_{n,i}^{h,k} \mid \mathcal{F}_{n-1}) < \tilde{\sigma}^2$ , for all  $h$ , where  $Y_{n,i}^{h,0} = \sum_k Y_{n,i}^{h,k}$ , and that  $\|F(\mathbf{x}) - F(\mathbf{y})\|_{L^1} \leq \|\mathbf{x} - \mathbf{y}\|_{L^1}$ , where  $F(\mathbf{x}) = \mathbf{x}^t M(\mathbf{x})m^{-1}$ . Then  $\lim_{N_0} \|\widehat{\mathbf{P}}_n - \mathbf{P}_n\|_{L^1} \stackrel{P}{=} 0$  and  $\lim_{N_0} \lim_n \|\widehat{\mathbf{P}}_n - \mathbf{P}_n\|_{L^1} \stackrel{P}{=} 0$ , where the probabilities  $\{\mathbf{P}_n\}_n$  are solutions of  $\mathbf{P}_n^t = F(\mathbf{P}_{n-1})$ ,  $n \geq 1$ ,  $\mathbf{P}_0 = \widehat{\mathbf{P}}_0$  being assumed fixed as  $N_0 \rightarrow \infty$ .*

### 30.2.2 Small Initial Population

We study here the behavior of the nonnormalized process  $\{N_n\}_n$ . Since the study of the asymptotic behavior of a state-dependent (not size-dependent ABGW) branching process is an open problem, we consider the single type model (30.1) and its deterministic counterpart  $X_n = m(X_{n-1})X_{n-1}$ ,  $X_0 = N_0$ . Since a population starting with a small size is by definition not yet well implemented, it is crucial to determine the conditions which lead either to the persistence or to the extinction of the branching process and to compare these conditions to those related to the dynamical system.

Assume  $m(X) > 0$ , for all  $X > 0$ , and recall that  $m(X)$  is a continuous function of  $X$ . Then  $\{X_n\}_n$  persists as  $n \rightarrow \infty$  if 0 is unstable, and its asymptotic extinction is possible if 0 is asymptotically stable (attracting from some neighborhood)([2]). Moreover the extinction is guaranteed if 0 is globally asymptotically stable (attracting from all the space). Defining the current reproductive rate  $R(X_{n-1}) = X_n X_{n-1}^{-1} = m(X_{n-1})$ , the bifurcation parameter for  $\{X_n\}_n$  is  $R_0 = \lim_{X \rightarrow 0} R(X)$ , since, for  $R_0 > 1$ , 0 is unstable and for  $R_0 < 1$ , 0 is (locally) asymptotically stable ([2]). Considering then process (30.1), (30.2), we may define the current reproductive rate  $R^s(N_{n-1}) = E(N_n \mid N_{n-1})N_{n-1}^{-1} = m(N_{n-1})1_{\{N_{n-1} \neq 0\}}$ . Since  $\{N_n\}_n$  is a homogeneous Markov chain on  $\mathbb{N}$ , it satisfies the classical behavior  $P(\lim_n N_n = 0 \cup \lim_n N_n = \infty) = 1$  (see Section 30.3). This implies that the long-term persistence is possible if  $P(\lim_n N_n = \infty) > 0$ , which depends on the value of  $R_\infty^s = \lim_{N \rightarrow \infty} R^s(N)$ . In the particular case  $m(\cdot) = m$ , which is the case of the BGW process, we have  $R_\infty^s = R_0 = m$ . For an ABGW process,  $R_\infty^s = m \neq R_0$ . This is still true in a more general case.

Compare first  $\{N_n\}_n$  with  $\{X_n\}_n$  on  $\{\lim_n N_n = \infty\}$ . The optimal known results, in the meaning that the asymptotic behavior of trajectories of the process is the most

similar to the deterministic trajectory, are obtained in the near-critical size-dependence case ([10]) when  $\lim_n N_n X_n^{-1} \stackrel{\text{a.s.}}{=} 1$ , equivalent to  $\lim_n (N_n - X_n) X_n^{-1} \stackrel{\text{a.s.}}{=} 0$ . But this does not imply  $\lim_n (N_n - X_n) = 0$  (see Section 30.2.3 for an example). In the BGW case, the results are even weaker since  $\lim_n N_n X_n^{-1} \stackrel{\text{a.s.}}{=} W$  (which leads to  $\lim_n |N_n - X_n| = \infty$  on the nonextinction set, for  $m > 1$ ).

Compare now the behavior of the two models on  $\{\lim_n N_n = 0\}$ . This question may be studied using the distribution of the process conditioned on nonextinction  $\mathcal{L}(N_n | N_n \neq 0)$ . The existence of  $\lim_n \mathcal{L}(N_n | N_n \neq 0)$ , called a quasi-stationary distribution, is more particularly studied in the literature. First results were given by Kolmogorov and Yaglom in the BGW case ([14, 21]): for  $m < 1$ ,  $\lim_n P(N_n = K | N_n \neq 0) = \alpha_K$ ,  $\sum_K \alpha_K = 1$ ; for  $m = 1$ ,  $\lim_n P(N_n [0.5\sigma^2 n]^{-1} \leq x | N_n \neq 0) = 1 - \exp -x$ . Moreover for  $m = 1$ , the extinction time  $T$  satisfies  $0 < \lim_{t \rightarrow \infty} t P(T > t) < \infty$  ([5]), and for  $m < 1$ ,  $P(T > n) \simeq C m^n$  ([19]) (for more details and results, see [3]). These results show that the asymptotic behavior of the BGW process conditioned on nonextinction may be larger than its deterministic counterpart since  $X_n = N_0 m^n$  with  $\lim_n X_n = 0$ , in the subcritical case  $m < 1$ , and  $X_n = N_0$  in the critical case  $m = 1$ . The behavior of  $\{N_n\}_n$  conditioned on nonextinction and the extinction time distribution are particularly crucial quantities for processes that die out a.s. and for which the related deterministic model is persistent. The critical BGW case is a well-known trivial example of such processes since the process dies out a.s. while  $X_n = N_0$ . But there exists a class of nontrivial size-dependent processes that also satisfy these properties. These processes check  $R_\infty^\infty < 1$  while  $R_0 > 1$  (see Section 30.3). In Section 30.2.1 we saw such examples of saturation models that die out a.s.: the model with a threshold introduced by Klebaner ([13]) and the stochastic Ricker model introduced by Högnäs ([4]).

### 30.2.3 A Particular Example of Partial Saturation: The Polymerase Chain Reaction (Saiki, R.K., Scharf, S., Faloona, F.A., Mullis, K.B., Horn, G.T., Erlich, H.A., and Arnheim, N. Enzymatic amplification of beta-globulin genomic sequences and restriction site analysis for diagnosis of sickle cell anemia. *Science*, 230(4732), 1350–1354 (1985). Mullis, K.B. and Faloona, F.A. Specific synthesis of DNA *in vitro* via a polymerase-catalyzed chain reaction. *Methods Enzymol.*, 155, 335–350 (1987).)

The PCR technology is based on an amplification *in vitro* of a given DNA (or RNA) fragments population, called the target, through successive replication cycles. At cycle  $n$ , the number of DNA fragments similar to the target is such that  $N_n = 2N_{n-1}$ , if all the replications succeed. But in practice,  $N_n < 2N_{n-1}$ , since some replications may fail. The goal of a PCR experiment is the estimation of the unobservable initial population size  $N_0$  from observable amplified populations  $\{N_n, N_{n+1}, \dots, N_n\}$ . This technology has many applications, e.g., in gene expression, virus detection and quantification, and GMO detection and quantification.

**Modeling the Amplification Process by a Size-Dependent Branching Process.** The modeled period corresponds to the experiment period. For simplification, we assume

that each new molecule never disappears and consequently that  $N_n \geq N_{n-1}$ . Then the amplification process may be modeled by  $N_n = N_{n-1} + \sum_{i=1}^{N_{n-1}} \delta_{n,i}$ , where  $\delta_{n,i} = 1$  with probability  $p(N_{n-1})$  if replication of  $i$  succeeds, and  $\lim_N p(N) = 0$ . This implies  $m(N_{n-1}) = E(1 + \delta_{n,1} \mid \mathcal{F}_{n-1}) = 1 + p(N_{n-1})$ , and  $\sigma^2(N_{n-1}) = p(N_{n-1})(1 - p(N_{n-1}))$ . The assumptions  $\lim_N p(N) = 0$  with  $N_n \geq N_{n-1}$  imply that  $\{N_n\}_n$  is a near-critical process with  $P(\lim_n N_n = \infty) = 1$ . Jagers and Klebaner ([9]) used Schnell–Mendoza’s model for the efficiency ([18]):  $p(N_{n-1}) = K(K + N_{n-1})^{-1}$ , where  $K = V_0 K_M$ ,  $K_M$  being the Michaelis–Menten constant of the reaction, that is, the concentration of substrate leading to a rate of reaction equal to half the maximum rate. The authors proved  $\lim_n N_n n^{-1} \stackrel{\text{a.s.}}{=} K$ ;  $\lim_n N_n X_n^{-1} \stackrel{\text{a.s.}}{=} 1$ , where  $X_n = m(X_{n-1})X_{n-1}$ ,  $X_0 = 1$  or  $X_0 = N_0$ . In this model, the saturation begins theoretically at the first cycle but is really taken into account in simulations when  $N_{n-1}$  becomes nonnegligible with respect to  $K$ . This model may be generalized in a statistical way in order to introduce a saturation threshold greater than  $N_0$ , leading to a theoretical exponential phase with efficiency  $p < 1$ . For example ([15]):

$$p(N_n) = \left[ \frac{K}{K + S(N_n)} \right] \left[ \frac{1 + \exp(-C(S(N_n)S^{-1} - 1))}{2} \right]$$

$$S(N) = S1_{\{N < S\}} + N1_{\{N \geq S\}}, \quad S : \text{threshold of saturation.}$$

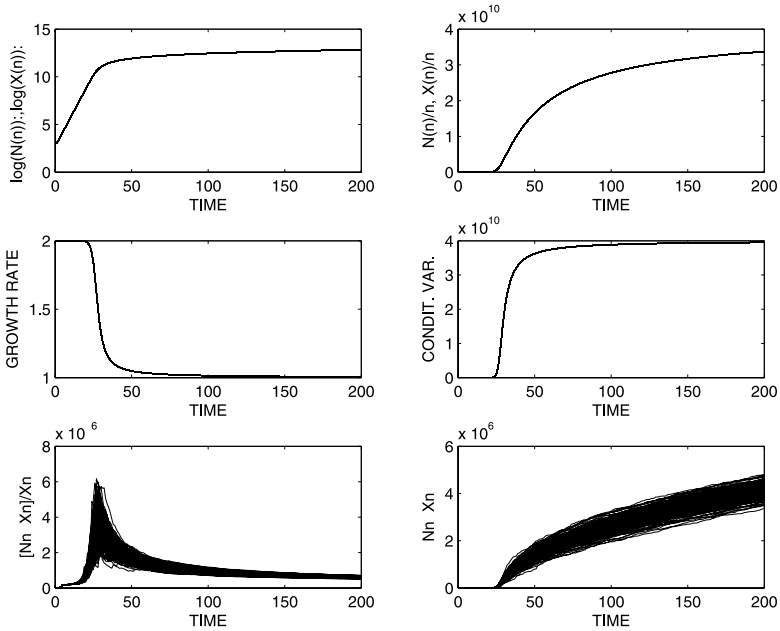
The particular case  $C = 0, S = N_0$  corresponds to Schnell and Mendoza’s model. The asymptotic behavior of the generalized process is

$$\lim_{n \rightarrow \infty} N_n n^{-1} \stackrel{\text{a.s.}}{=} K_C; \quad \lim_n N_n X_n^{-1} \stackrel{\text{a.s.}}{=} 1, \tag{30.6}$$

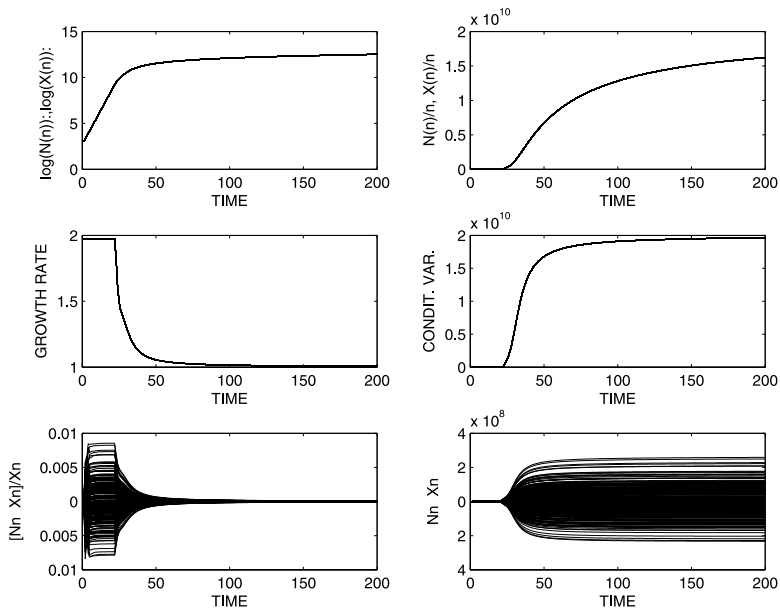
where  $K_C = K\delta_C, \delta_C = (1/2)1_{\{C \neq 0\}} + 1_{\{C=0\}}, X_0 = N_0$  or  $X_0 = 1$ . In this model, the exponential phase ends abruptly when the saturation threshold  $S$  is reached. Result (30.6) shows that  $\lim_n (N_n^\mu - X_n^\mu) \stackrel{\text{a.s.}}{=} 0$ , for  $\mu_{n,N_0} = nK_C$ . Since  $K_C = V_0 \delta_C K_M$ , then  $N_n^\mu = [N_n](n\delta_C K_M)^{-1}$  and  $X_n^\mu = [X_n](n\delta_C K_M)^{-1}$ , where  $[N]$  and  $[X]$  are concentrations. Therefore  $\lim_n [N_n]n^{-1} - [X_n]n^{-1} \stackrel{\text{a.s.}}{=} 0$ , but  $[N_n] - [X_n]$  seems to increase indefinitely with  $n$  according to Fig. 30.1, which forbids in Schnell–Mendoza’s model under a fixed  $d_0, \lim_{V_0} \lim_n ([N_n] - [X_n]) = 0$ . In Fig. 30.2 relative to the generalized Schnell–Mendoza model, the exponential phase ends abruptly, which is visible on the growth rate graphic. On the last line, the bias between the process and the deterministic model is now centered. This comes from  $E(N_n - X_n)/X_n = 0$  in the exponential phase, where  $X_n = m^n N_0$ .

Fig. 30.3 is similar to Fig. 30.1 except that now  $X_0 = 1$  and only a single trajectory of the branching process is taken into account in all the graphics. We see especially on the growth rate curve, the time needed for forgetting the initial conditions  $N_0 \neq X_0$ .

**Statistical Problem in QPCR: Estimation of  $N_0$ .** Due to  $\lim_n N_n X_n^{-1} \stackrel{\text{a.s.}}{=} 1$  with  $X_0 = 1$  which implies that the information on  $N_0$  disappears in the plateau phase (defined by  $m(\cdot) \simeq 1$ ), and since the accuracy of observation of the amplification process increases as  $n \rightarrow \infty$ , a “good” estimator of  $N_0$  will be based on observations from the end of the exponential phase to the end of the linear phase (phase between the



**Fig. 30.1.** Simulations from Schnell–Mendoza’s stochastic and deterministic models;  $N_0 = X_0 = 1000$ ,  $K = 4 \cdot 10^{10}$ . In the last line, 100 trajectories of  $\{N_n\}_n$  are represented.



**Fig. 30.2.** Simulations from the generalized stochastic and deterministic models with  $N_0 = X_0 = 1000$ ,  $K = 4 \cdot 10^{10}$ ,  $S = 10^9$ ,  $C = 0.6$ .

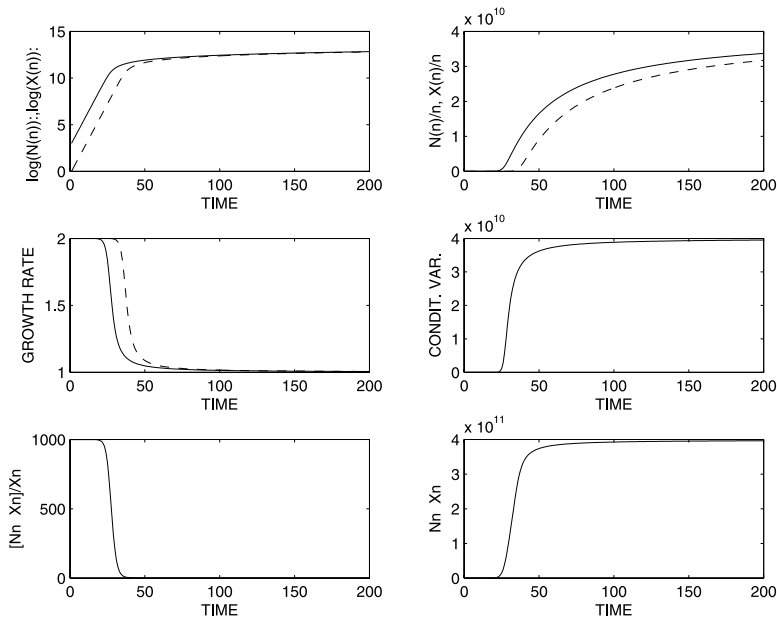


**Fig. 30.3.** Simulations from Schnell–Mendoza’s stochastic and deterministic model;  $N_0 = 1000, X_0 = 1, K = 4 \cdot 10^{10}$ .

exponential phase and the plateau phase). The simplest estimator is  $\hat{N}_{0,n} = N_n m^{-n}$  which satisfies  $E(\hat{N}_{0,n} | N_0) = N_0$ . The asymptotic law of this estimator allows the construction of a confidence interval of  $N_0$  ([17], [7]). In ([16]) the censored maximum likelihood estimator based on observations from cycle  $n$  is shown to be very closed to this estimator, which forbids any consistency property. Since  $\hat{N}_{0,n}$  depends on  $m^n$ , the unknown parameter  $m = 1 + p$  needs to be accurately estimated. We use the CLSE (conditional least squares estimator) based either on the exponential phase ([7], [16]) or better on both the exponential phase and the linear phase. We have ([15]) the asymptotic properties of the CLSE of  $K$  as  $n \rightarrow \infty$  while this parameter disappears as  $n \rightarrow \infty$ . In Fig. 30.4, the estimation is done on a real PCR trajectory.

### 30.3 A Size-Dependent Branching Process for Saturation Phenomena with a Long Memory

Assume now that the resources consumed by the population may need a long time to be regenerated. Then the evolution of the population size may be modeled by (30.1) with  $E(Y_{n,1} | \mathcal{F}_{n-1}) = m(F_{n-1}), \text{Var}(Y_{n,1} | \mathcal{F}_{n-1}) = \sigma^2(F_{n-1}), F_{n-1} = (N_{n-1}, \dots, N_0)$ .

**Proposition 2** Assume A1:  $P(Y_{n,i} = 0 | N_{n-1} = N, \mathcal{F}_{n-1}) \geq f(N) > 0$ , for all  $N$ . Then  $P(\lim_n N_n = 0 \cup \lim_n N_n = \infty) = 1$ .

**Proposition 3** Define  $R_\infty^s = \overline{\lim}_{n \rightarrow \infty} \overline{\lim}_{\|F_{n-1} \rightarrow \infty\|} m(F_{n-1})$ . Assume A1 and A2:  $R_\infty^s < 1$ . Then  $P(\lim_n N_n = \infty) = 0$ .

Moreover if there exists  $c < 1$  such that  $\overline{\lim}_N f(N) > 1 - cm_*^{-1}$ , where  $m_* = \overline{\lim}_{n \rightarrow \infty} \overline{\lim}_{\|F_{n-1} \rightarrow \infty\|} E(Y_{n,1} | Y_{n,1} > 0, \mathcal{F}_{n-1})$ , then  $R_\infty^s \leq c < 1$ .

**30.3.1 Example: Logistic Saturation Model for Bacteria Division**

Assume first a single population of bacteria (or cells)  $\{N_n\}_n$  satisfying the previous model with a long memory, where  $P(Y_{n,i} = 2 | \mathcal{F}_{n-1}) = p(F_{n-1})$  (efficiency of the division) and  $P(Y_{n,i} = 0 | \mathcal{F}_{n-1}) = 1 - p(F_{n-1})$ . We assume here a generalized form of Schnell–Mendoza’s model:  $p(F_{n-1}) = pK(K + \sum_{l=1}^{d_n} \mu^l N_{n-l})^{-1}$ ,  $0 \leq \mu \leq 1$ , where  $p$  is the division efficiency when there is no saturation effect,  $K$  is related to the saturation threshold, and  $d_n$  represents the memory size. The related deterministic model defined by  $X_n = m(X_{n-1})X_{n-1}$  satisfies  $X_n = 2pKX_{n-1}(K + \sum_{l=1}^{d_n} \mu^l X_{n-l})^{-1}$ .

Assume first  $d_n = 1$ . This model is called the Pielou logistic equation ([2]). Moreover if  $n$  corresponds to a real time  $n\Delta t$ , then it corresponds to the continuous time Verhulst–Pearl model ([2]):  $X'_t = X_t(a - bX_t)$ ,  $a\Delta t = \ln 2p$ ,  $b\Delta t = (\ln 2p)\mu K^{-1}(2p - 1)^{-1}$ .  $X_n$  has an explicit form when  $d_n = 1$  ([2]). Moreover for  $2p \neq 1$ ,  $\lim_n X_n = X_* = (2p - 1)K\mu^{-1}$ , and for  $2p = 1$ ,  $\lim_n X_n = X_* = 0$ , implying that  $X_*$  is globally asymptotically stable.

Now, assume  $d_n = d$ . Then  $\mathbf{X}_n = M(\mathbf{X}_{n-1})\mathbf{X}_{n-1}$ , where the first line of  $M(\mathbf{X}_{n-1})$  is  $(m(\mathbf{X}_{n-1}), 0, \dots, 0)$  and the  $k$ th line, for  $k > 1$ , contains 1 in the  $k - 1$ th position and 0 elsewhere;  $R(\mathbf{X}_{n-1})$  is the first eigenvalue of  $M(\mathbf{X}_{n-1})$ , that is,  $R(\mathbf{X}_{n-1}) = m(\mathbf{X}_{n-1})$ , implying  $R_0 = \lim_{\mathbf{X}_{n-1} \rightarrow 0} R(\mathbf{X}_{n-1}) = 2p$ . When  $2p > 1$ , 0 is unstable, implying the persistence of  $\{X_n\}_n$ , as  $n \rightarrow \infty$ . Moreover there is an equilibrium point  $X_* = K\mu^{-1}(2p - 1)(1 - \mu)(1 - \mu^d)^{-1}$ , if  $\mu \neq 1$ , and  $X_* = K(2p - 1)d^{-1}$ , if  $\mu = 1$ . When  $2p < 1$ ,  $\{X_n\}_n$  is decreasing until it reaches the only nonnegative fixed point 0, and 0 is globally stable.

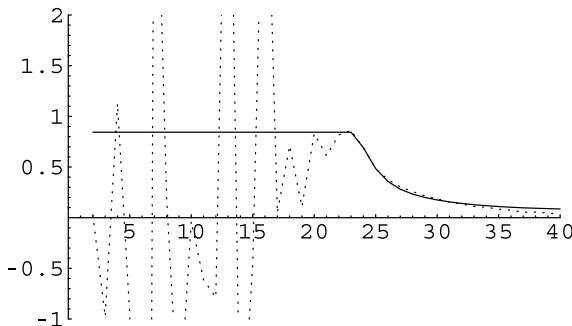


**Fig. 30.4.** Estimation in the generalized model:  $h = 21$ ,  $n = 25$ ,  $\hat{n}_s = 23$ ,  $\hat{K}_{h,n} = 0.38055$ ,  $\hat{S}_{h,n} = 0.070553$ ,  $\hat{C}_{h,n} = 0.6$ ,  $\hat{p}_{h,n} = 0.843599$ . Dashed line, the empirical efficiency, continuous line, the CLSE.

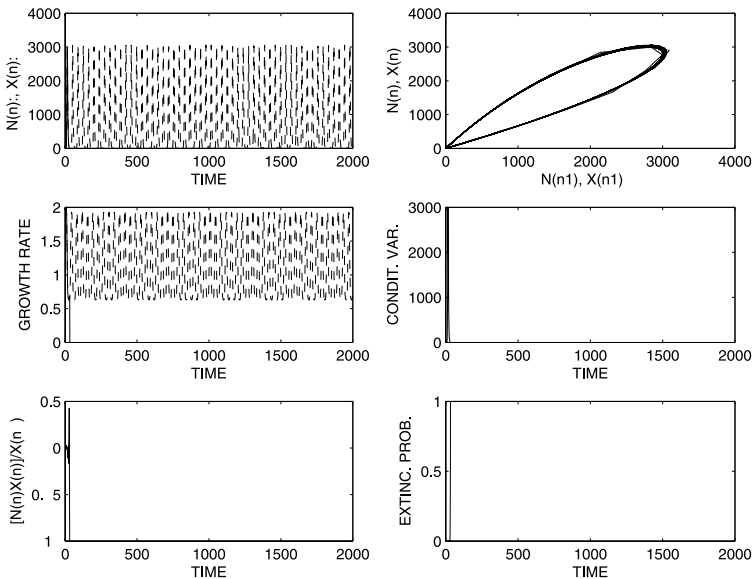


Fig. 30.5.  $N_0 = 1, K = 10^4, p = 1, \mu = 1, d_n = 20$ .

Finally, when  $d_n = n$  with  $\mu = 1$ , then  $\lim_n X_n = 0$  with  $X_n$  decreasing.

Consider now the branching process. According to Proposition 2 we have  $P(\lim_n N_n = 0 \cup \lim_n N_n = \infty) = 1$  since A1 is checked with  $f(N) = (K\mu^{-1}(1 - p) + N)(K\mu^{-1} + N)^{-1}$ . Moreover according to Proposition 3, since  $\lim_N f(N) = 1$ , we have  $P(\lim_n N_n = \infty) = 0$ . The conditional probability of extinction  $q(F_{n-1}) = P(N_n = 0 \mid F_{n-1}, N_{n-1} \neq 0)$  satisfies  $q(F_{n-1}) \geq \exp(-pK\mu^{-1})$ , for  $N_{n-1}$  large enough,  $q(F_0) = (K\mu^{-1}(1 - p) + 1)(K\mu^{-1} + 1)^{-1}$ ,  $F_0 = (1, 0, 0, \dots)$ . Consequently  $K\mu^{-1}$  plays a key role both in the rate of extinction of the stochastic process and in  $X_*$ . The behavior of  $\{N_n\}_n$  before extinction will be studied here by simulations.

On the first line of Fig. 30.5, the graph on the left shows the oscillations of  $\{X_n\}_n$  in dashed lines and a trajectory of  $\{N_n\}_n$  in continuous lines. This one dies out after a single oscillation. The difference between Fig. 30.5 and Fig. 30.6 concerns the value of  $K$ . The extinction time is much larger for  $K = 10^6$  than for  $K = 10^4$ , since after 2000 simulation times, the trajectory of the stochastic process is not yet extinct. The relative difference now exhibits important oscillations as the time increases (left graph, bottom line).

Assume now two populations  $a, b$ , sharing the same resources with  $\{N_n^h\}_n, h \in \{a, b\}$ , defined by  $N_n^h = \sum_{i=1}^{N_{n-1}^h} Y_{n,i}^h, \{Y_{n,i}^h\}_i$  i.i.d. given  $F_{n-1}$  with  $p_h(F_{n-1}) = P(Y_{h,n,i} = 2 \mid F_{n-1}) = p_h K_h (K_h + \sum_{l=1}^{d_n} \mu^l [N_{n-l}^a + N_{n-l}^b])^{-1}$ . As in the single population case, we have  $P(\lim_n N_n = 0) = 1$ , where  $N_n = N_n^a + N_n^b$ . We simulate this model with  $N_0^a = N_0^b$  and identical parameters for the two populations. See Fig. 30.7. The graphs of the left column concern population  $a$  while those of the right column concern population  $b$ . The variability of the random oscillations are much larger than

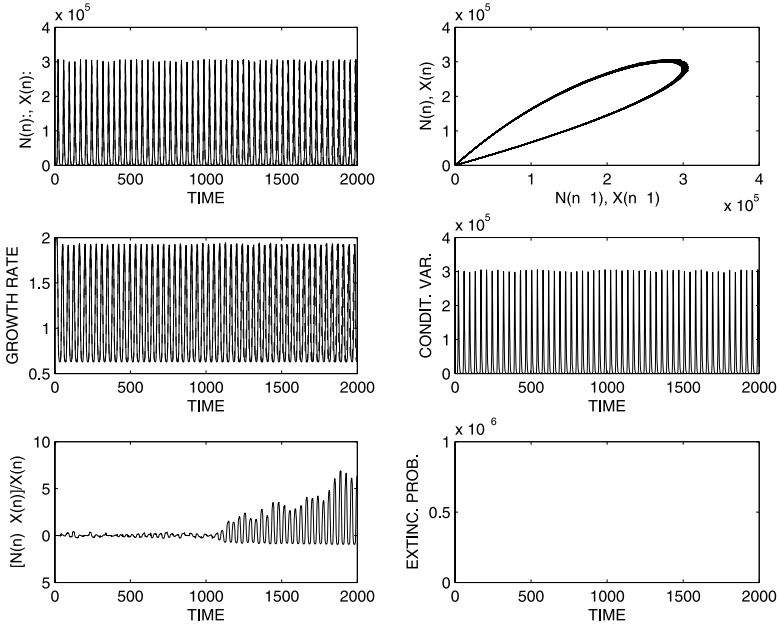


Fig. 30.6.  $N_0 = 1, K = 10^6, p = 1, \mu = 1, d_n = 20$ .

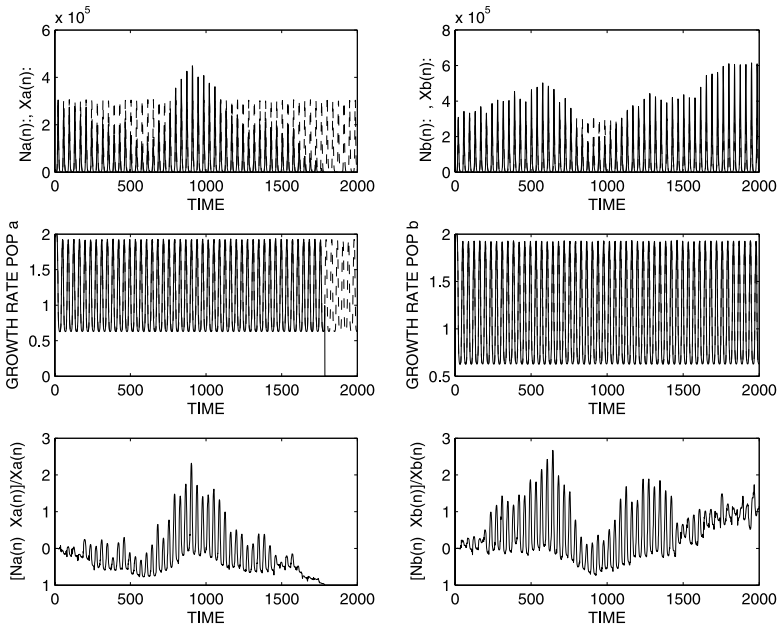


Fig. 30.7.  $N_0 = 1, K_a = K_b = 10^6, p_a = p_b = 1, \mu = 1, d_n = 20$ .



in the single population case. The deterministic models persist as  $n \rightarrow \infty$ , whereas the extinction occurs around time 1800 for population  $a$  and after time 2000 for population  $b$ . The extinction of population  $a$  here allows the growth of population  $b$ . It could also allow the invasion by some exogenous populations. It is therefore crucial to work in the stochastic frame rather than in the deterministic one when the question concerns biodiversity.

## References

1. Athreya, K.B., Ney, P.E.: *Branching Processes*. Dover Publications, Inc., Mineola, NY (2004), xii+287pp.
2. Elaydi, S.: *An Introduction to Difference Equations*. Third edition. Undergraduate Texts in Mathematics. Springer, New York (2005), xxii+539pp.
3. Haccou, P., Jagers, P., Vatutin, V.A.: *Branching Processes Variation, Growth, and Extinction of Populations*. Cambridge Studies in Adaptive Dynamics, Cambridge (2005), 316pp.
4. Högnäs, G.: On the quasi-stationary distribution of a stochastic Ricker model. *Stochastic Process Appl.*, **70**, 243–263 (1997).
5. Holte, J.M.: Extinction probability for a critical general branching process. *Stochastic Processes Appl.*, **2**, 303–309 (1974).
6. Jacob, C.: Population dynamics: modeling by branching processes or by dynamical systems? Technical Report 2005–7, MIA unity, INRA, Jouy-en-Josas, France (2005).
7. Jacob, C., Peccoud, J.: Estimation of the parameters of a branching process from migrating binomial observations. *Adv. Appl. Probab.*, **30**, 948–967 (1998).
8. Jacob, C., Viet, A.F.: Epidemiological modeling in a branching population. Particular case of a general SIS model with two age classes. *Math. Biosci.*, **182**, 93–111 (2003).
9. Jagers, P., Klebaner, F.: Random variation and concentration effects in PCR. *J. Theoret. Biol.*, **224**, 299–304 (2003).
10. Klebaner, F.C.: Population-size-dependent branching process with linear rate of growth. *J. Appl. Probab.*, **20**, 242–250 (1983).
11. Klebaner, F.C.: On population-size-dependent branching processes. *Adv. in Appl. Probab.*, **16**, 30–55 (1984).
12. Klebaner, F. C., Lazar, J., Zeitouni, O.: On the quasi-stationary distribution for some randomly perturbed transformations of an interval. *Ann. Appl. Probab.*, **8**, 300–315 (1998).
13. Klebaner, F. C., Zeitouni, O.: The exit problem for a class of density-dependent branching systems. *Ann. Appl. Probab.*, **4**, 1188–1205 (1994).
14. Kolmogorov, A.N., Savostyanov, B.A.: The calculation of final probabilities for branching random processes. *Doklady Akad. Nauk SSSR (N.S.)*, **56**, 783–786 (1947) 60.0X.
15. Lalam, N., Jacob, C., Jagers, P.: Modelling the PCR amplification process by a size-dependent branching process and estimation of the efficiency. *Adv. in Appl. Probab.*, **36**, 602–615 (2004).
16. Olofsson, U.: Branching processes: Polymerase Chain Reaction and mutation age estimation. Thesis, Department of Mathematical Statistics, Chalmers University of Technology, Göteborg, Sweden (2003).
17. Peccoud, J., Jacob, C.: Theoretical Uncertainty of Measurements Using Quantitative Polymerase Chain Reaction. *Biophysical J.*, **71**, 101–108 (1996).
18. Schnell, S., Mendoza, C.: Enzymological Considerations for a Theoretical Description of the Quantitative Competitive Polymerase Chain Reaction (QC-PCR). *J. Theor. Biol.*, **184**, 433–440 (1997).

19. Seneta, E.: Functional equations and the Galton-Watson process. *Advances in Appl. Probability*, **1**, 1–42 (1969).
20. Stenseth, N.C., Falck, W., Bjornstad, O.N., Krebs, C.J.: Population regulation in snowshoe hare and Canadian lynx: Asymmetric food web configurations between hare and lynx. *Proc. Natl. Acad. Sci. USA*, **94**, 5147–5152 (1997).
21. Yaglom, A.M.: Certain limit theorems of the theory of branching random processes. *Doklady Akad. Nauk SSSR (N.S.)*, **56**, 795–798 (1947), in Russian.

# Modelling and Simulation by Stochastic Interacting Particle Systems

Tobias Klauß, Anja Voß-Böhme

Institut für Math. Stochastik, Technische Universität Dresden, Dresden, Germany;  
tobias.klauss@tu-dresden.de, anja.voss-boehme@tu-dresden.de

**Summary.** Stochastic interacting particle systems (IPSs) are individual-based models, which include stochastic local interactions on a spatial lattice. In this respect an IPS works similarly to a cellular automaton. However, IPSs are continuous-time Markov processes, hence there is a large background of analytical methods. Further, one has the possibility to simulate the system on a finite lattice, which is what we focus on in this work. We explain the modelling steps broadly and by means of examples. Finally, we state the core of a simulation algorithm. The ideas is to convince the reader that IPSs can be used to set up and simulate sophisticated and applicable models but allow an analytical approach as well.

**Key words:** Simulation, modelling, interacting particle systems, local stochastic interaction, individual-based model, spatially extended system.

## 31.1 Introduction

In the mathematical modelling of biological problems, individual-based models become increasingly important, since new experimental techniques allow one to follow up and quantitatively describe the behavior of individual molecules, genes, cells or whole organisms. By now, there are huge amounts of data describing the behavior of single components of a system and the interaction between these components. In general, the single components of a system are spatially distributed and interact with each other. Often this interaction is local, which means that each single component only interacts with other components of its direct neighborhood. Nevertheless, the system as a whole shows very complex behavior or patterns in a certain way. Mathematical modelling aims at explaining this complex outcome on the basis of the local behavior.

A first insight into the model behavior can be obtained by computer simulations. Discretizing space and time, one can use cellular automata (CA) or lattice gas cellular automata (LGCA) to describe the phenomena at hand on a computer and to study the expected outcome for given parameter specifications. However, it is often difficult to analyze these models since there are only few rigorous studies of CA and LGCA. In the frame of Markov chain theory the discreteness of time causes additional problems.

Other important models that are widely used are partial differential equations (PDEs) which are time- and space-continuous models. They are well studied and allow analytical results as well as numerical solutions, but they can only be used when one abstracts from the individual nature of the interaction. Moreover, the equations are often set up rather ad hoc, and it is often not clear how the PDE system relates to the behavior of the single components.

We would like to draw attention to interacting particle systems (IPSS), which model individual interaction between the components of a system. Here space is discretized but time is kept continuous. IPSS are analytically tractable but can nevertheless be quite easily simulated on a computer, as this chapter shows. In some cases, they allow the rigorous derivation of a PDE description of the system. In those cases, the form of the differential equations and the values of the parameters are directly related to the individual interaction of the components.

The main goal of this chapter is to guide the reader from an intuitive understanding of the individual behavior of spatially distributed systems to setting up a well-defined IPS that models this behavior. In addition, we will detail how this system can be effectively run on a computer to simulate the model behavior. The reader can then turn to the vast literature on IPSS for analytical results. There are some well-studied simplified models which can suggest the expected qualitative behavior, as well as general methods for the analysis of particle systems. Of course the analysis of more complicated systems is often of a delicate nature.

To illustrate the course of reasoning we have chosen two biological examples: the spread of epidemics and predator-prey competition. We do not claim new modelling ideas here, but we hope that most readers' familiarity with these examples will help them to understand our special approach: IPSS are individual models that are easy to establish and comprehend, which can be well simulated on a computer and which allow rigorous analysis. We hope that the reader will notice that much more complicated models can be set up and simulated without problems.

**Example A 1 (Spread of Epidemics)** *We consider individuals that can be either healthy or infected. Healthy individuals become infected at a rate which is proportional to the number of infected neighbors. Infected individuals recover at a constant rate.*

**Example B 1 (Predator-Prey Competition, see [4])** *We consider two interacting populations: predator and prey.*

*We assume that all individuals migrate with a certain constant rate, that is they move to a randomly chosen neighboring location if this location is empty.*

*Individuals of each species are born or die at rates that depend on the number of predator and prey individuals in the direct neighborhood. This dependence is given by the following matrix:*

	<i>predator</i>	<i>prey</i>
<i>predator</i>	<i>a</i>	<i>b</i>
<i>prey</i>	<i>k</i>	<i>l</i>

The parameters in this table give the net birth rates (or death rates, if negative) of an individual of a certain type when surrounded mainly by neighbors of another type. For instance,  $a$  is the net birth rate of a predator individual in an environment dominated by predator and  $b$  is the net birth rate of a predator individual in an environment dominated by prey. Hence, in classical models  $a$  is assumed to be smaller than  $b$ .

## 31.2 Set Up the IPS Model

### 31.2.1 State Space

We want to model the temporal evolution of a population of spatially distributed individuals that interact with each other. We assume that those components are located on the nodes of some regular  $d$ -dimensional lattice  $S \subset \mathbb{Z}^d$ . This means that we have discretized the space. In the case where only one individual is allowed per node, we speak of *volume exclusion*. Each individual is in a certain state or has a certain type (orientation, mass, color, sensitivity, etc.). We assume that the set  $W$  of possible states is a finite set. We describe the state of the whole system by *configurations*  $\eta \in X = W^S$ . This means that  $\eta = (\eta(x))_{x \in S}$ , where  $\eta(x)$  describes the state of the individual at node  $x$ . Sometimes the value 0 is assigned to a given node, if this node is not occupied by any individual.

*Comment.* In general, the set  $W$  of possible states can even be infinite. In this case, we require  $W$  to be a compact metric space. Note that any finite  $W$  equipped with the discrete metric is compact. The product space  $X = W^S$  with the product topology is compact. Convergence in the product topology is equivalent to pointwise convergence, i.e.,  $\eta_n \rightarrow \eta$  if and only if  $\eta_n(x) \rightarrow \eta(x)$  for any  $x \in S$ .

**Example A 2 (Spread of Epidemics)** We assume that each site of the lattice  $S$  is occupied by exactly one individual which can be either healthy or infected. Thus we set  $W := \{0, 1\}$  with the interpretation that  $\eta(x) = 1$  if the individual at site  $x$  is infected and  $\eta(x) = 0$  if the individual at  $x$  is healthy. Note that a system with state space  $\{0, 1\}^S$  and in which only one coordinate changes in each transition is often referred to as a spin system.

**Example B 2 (Predator-Prey Competition)** Each site of the lattice  $S$  can be empty, occupied by a predator individual or occupied by a prey individual. Therefore, we set  $W := \{0, 1, 2\}$  with 0 for an empty site, 1 for predator individuals and 2 for prey individuals.

### 31.2.2 Transitions

The evolution of our system shall consist of *transitions*

$$\eta \rightarrow \tau_T(\eta, v),$$

where

$$T \subset S, \quad \eta \in X = W^S, \quad v \in W^T$$

and

$$\tau_T : W^S \times W^T \rightarrow W^S : \tau_T(\eta, v)(x) := \begin{cases} v(x), & x \in T \\ \eta(x), & x \notin T. \end{cases}$$

The interpretation is as follows: The transition only affects nodes in the spatial area  $T$ . The actual configuration in  $T$ , that is  $\eta|_T = (\eta(x))_{x \in T}$ , is replaced by a new local configuration  $v \in W^T$ .

We assume that  $T$  is always a finite set. Often one poses further restrictions on the set of possible  $T$ . For instance, one requires  $T$  to consist only of one single element or to consist only of pairs of neighboring nodes. The set of all finite  $T \subset S$  is denoted by  $\mathcal{T}$ , whereas the set of all finite  $T \subset S$  which are allowed as transition areas is denoted by  $\mathcal{T}_0$ .

**Example A 3 (Spread of Epidemics)** *A given configuration of healthy and infected individuals changes when a healthy individual becomes infected or an infected individual recovers. This means that transitions take place on single nodes, i.e.,  $\mathcal{T}_0 := \{\{x\}; x \in S\}$ . The transitions are described by*

$$\tau_x(\eta)(s) = \begin{cases} \eta(s) & : s \neq x \\ 1 - \eta(x) & : s = x \end{cases}, \quad \eta \in \mathcal{X}, x \in \mathcal{T}_0. \tag{31.1}$$

Note that such transitions are called spin-flip transitions.

**Example B 3 (Predator-Prey Competition)** *A given configuration may change by birth and death of individuals or by migration of already existing individuals. Birth and death affect only one coordinate, whereas migration to a neighboring site changes the configuration at two adjacent sites at once. Therefore, we have  $\mathcal{T}_0 := \{\{x\}; x \in S\} \cup \{\{x, y\}; x \in S, y \in \mathcal{U}(x)\}$ . Here, for given  $x \in S, \mathcal{U}(x) := \{s \in S : \|x - z\| = 1\}$  denotes the set of neighboring sites for  $x$  in the Euclidian distance.*

1. Population development—consisting of birth and death of individuals—is described by transitions  $\tau_x(\eta, i)$ . They describe the transition from the given configuration  $\eta \in \mathcal{X}$  into a new configuration  $\tau_x(\eta, i)$  which is obtained by substituting into  $\eta$  the value  $i$  at site  $x$ . In detail,

$$\tau_x(\eta, i)(s) = \begin{cases} \eta(s) & : s \neq x \\ i & : s = x. \end{cases} \tag{31.2}$$

2. The possible transitions for the migration processes are the same as for an exclusion process. See [1] or [2]. We consider only transitions where an individual at  $x$  moves to a neighboring  $y$  if  $y$  is vacant. If  $y$  is occupied, it shall remain at  $x$ . So

$$\tau_{xy}(\eta)(s) = \begin{cases} \eta(y) & : s = x \\ \eta(x) & : s = y \\ \eta(s) & : s \notin \{x, y\} \end{cases}, \quad \eta \in \mathcal{X}, x, y \in S, \|x - y\| = 1. \tag{31.3}$$

*Comment.* Note that the definition of possible transitions is one of the important ingredients next to the choice of the configuration space. Here the restriction is that the transitions change the given configuration only within finite subsets of the lattice. However, one can model possible transitions with a large freedom.

### 31.2.3 Transition Rates

The next step to define the IPS is to give the rates of the possible transitions. This adds the probabilistic part to the model. We suppose that the system’s dynamic is *Markovian*, which means that the rate for a transition from the actual configuration  $\eta$  to a new configuration  $\zeta$  does not depend on the temporal history of the system but on the present configuration  $\eta$  and the future configuration  $\zeta$ . In particular, we denote the rate for a transition from  $\eta$  to  $\zeta = \tau_T(\eta, v)$  by  $c_T(\eta, v)$ . One can think of the rates as a weighting of the possible transitions. So the dynamics of our system is completely described by the family  $\mathcal{T}_0$  of possible transition areas and a family  $(c_T(\eta, \cdot))_{T \in \mathcal{T}_0}$  of transition rates. Note that

$$c_T : X \times W^T \rightarrow [0, \infty), \quad T \in \mathcal{T}.$$

*Comment.* The transition rates can often be derived from direct observation of the component’s interaction.

**Example A 4 (Spread of Epidemics)** For current  $\eta \in \mathcal{X}$ , the state in the node  $x$  is flipped from “healthy” to “infected” with a rate that is proportional to the number of infected individuals in the direct neighborhood, and it is flipped from “infected” to “healthy” with constant rate. This is modelled by

$$c_x(\eta, 1 - \eta(x))(s) = \begin{cases} \lambda \sum_{y \in \mathcal{U}(x)} \eta(y) & : \eta(x) = 0 \\ 1 & : \eta(x) = 1, \end{cases} \quad (31.4)$$

where  $\lambda$  is a real non-negative parameter.

### Example B 4 (Predator-Prey Competition)

1. We first define the transition rates for the birth and death transitions. Therefore, put for  $\eta \in \mathcal{X}$   $\eta_1(x) := \sum_{z \in \mathcal{U}(x)} \mathbb{1}_{\{1\}}(\eta(z))$  and  $\eta_2(x) := \sum_{z \in \mathcal{U}(x)} \mathbb{1}_{\{2\}}(\eta(z))$ . Obviously,  $\eta_1(x)$  is the number of predators in  $\mathcal{U}(x)$  and  $\eta_2(x)$  is the number of prey in  $\mathcal{U}(x)$  for given configuration  $\eta$  and node  $x$ . For simplicity, we assume that the parameters  $a, b, k, l$  that were introduced in Example B 1 are non-negative. Note that the model can be easily adjusted if some of the parameters are negative. So the transition rates for the birth processes as defined in (31.2) are given by

$$c_x(\eta, i) = \begin{cases} a\eta_1(x) + b\eta_2(x) & : \eta(x) = 0, i = 1 \\ k\eta_1(x) + l\eta_2(x) & : \eta(x) = 0, i = 2 \\ 0 & : \text{otherwise,} \end{cases} \quad (31.5)$$

for any  $\eta \in \mathcal{X}$ ,  $i \in W$  and  $x \in S$ .

2. We define the rates for the migration transitions that were defined in (31.3). An individual at  $x$ —supposing there is one—chooses with equal probability one of its neighboring sites and jumps to this place, if it is empty. Thus, for  $x, y \in S$ , we set  $p(x, y) = |\mathcal{U}(x)|^{-1} = 1/(2d)$  and define

$$c_{xy}(\eta, v) = \begin{cases} p(x, y) & : \eta(x) \in \{1, 2\}, \eta(y) = 0, v = \tau_{xy}(\eta)|_{\{x,y\}} \\ 0 & : \text{otherwise.} \end{cases} \quad (31.6)$$

Note that the migration rates are the same rates as for the exclusion process in [1] with stochastic matrix  $p(x, y)$ .

### 31.2.4 Finite Range Condition

In the case that the spatial lattice  $S$  is finite, the above transition rates supplemented with boundary conditions lead to a well-defined IPS. However, many analytical properties of such a particle system only reveal if the corresponding system on the infinite lattice  $\mathbb{Z}^d$  is studied. Since the state space  $W^{\mathbb{Z}^d}$  is not countable even for finite  $W$ , special care has to be taken that the rates lead to a well-defined Markov process for an infinite lattice. A sufficient condition for this is the *finite range condition* which we will state now. In applications with local interactions, this condition is fulfilled naturally. Note that this condition can be considerably relaxed. See [1] for details.

Let a family  $(c_T(\eta, \cdot))_{T \in \mathcal{T}_0}$  of transition rates be given. We define

$$c_T(\eta, W^T) = \sum_{v \in W^T} c_T(\eta, v).$$

One can interpret this value as the total rate at which a transition takes place that changes the actual configuration  $\eta$  by alteration of the coordinates in  $T$ . Let

$$c_T = \sup_{\eta \in \mathcal{X}} c_T(\eta, W^T). \quad (31.7)$$

The value  $c_T$  plays quite an important role in the context of IPS in general but also for our goal to set up a simulation method. In addition, we define a value  $c$  by maximizing over the set  $\mathcal{T}_0$  in which transitions can take place,

$$c := \max_{T \in \mathcal{T}_0} (c_T). \quad (31.8)$$

This value is particularly important if transitions can take place in differently shaped  $T$ 's. The quantity

$$c_T(z) := \sup_{v \in W^T} \sup_{\eta, \zeta \in \mathcal{X}} \{ |c_T(\eta, v) - c_T(\zeta, v)| : \eta(x) = \zeta(x) \text{ for all } x \neq z \}$$

measures the degree to which the transition rate  $c_T(\cdot, \cdot)$ ,  $T \in \mathcal{T}$  depends on the coordinate  $z \in S$ .



**Definition 1** *The family  $(c_T(\eta, \cdot))_{T \in \mathcal{T}_0}$  of transition rates satisfies the finite range condition, if there exists an  $N > 0$  such that*

- (a)  $c_T = 0$ , if  $T$  contains two points  $x, y$  with  $|x - y| > N$  and
- (b)  $c_T(z) = 0$ , if  $\min_{x \in T} |x - z| > N$ .

In fact, the finite range condition is often very easily verified. Part *a*) says that the transition areas are bounded, that is, only the coordinates in a region of diameter at most  $N$  are changed at once. Part *b*) says that the rate  $c_T(\eta, \cdot)$  for a transition (involving the coordinates in  $T$ ) depends on  $\eta$  only through the values  $\eta(x)$  with  $x$  from the distance- $N$ -neighborhood of  $T$  and not from the values of  $\eta$  at more distant coordinates. One can easily see that this condition holds for our examples.

### 31.2.5 Generator

This paragraph is devoted to the mathematical background of an IPS. We just state one important existence theorem and omit the framework. The reader who is mainly interested in simulating a stochastic IPS can skip this part. An explicit description of the theory is given in [1].

Formally, one can write the expression for an operator  $A$  which acts on the set  $D$  of all functions  $f : X \rightarrow \mathbb{R}$  that depend on only finitely many coordinates. Often  $D$  is also referred to as the set of *cylinder* or *tame* functions [1]. In particular,

$$Af(\eta) = \sum_{T \in \mathcal{T}_0} \int_{v \in W^T} c_T(\eta, dv)[f(\tau_T(\eta, v)) - f(\eta)]. \tag{31.9}$$

**Theorem 1** *If the family of transition rates  $(c_T(\eta, \cdot))_{T \in \mathcal{T}_0}$  satisfies the finite range condition, then  $A$  is a Markov pregenerator. The closure  $A$  of  $A$  is a Markov generator, see [1].*

*Comment.* It follows directly from the theorem that any IPS with finite range transition rates is a well-defined Markov process.

## 31.3 The Dynamics of the Finite IPS

We understand a *finite IPS* to be an IPS on a finite lattice. Hence, we assume that  $|S| < \infty$ . As before, we suppose that  $|W| < \infty$ . Thus, the state space  $X = W^S$  is finite. Let a family  $(c_T(\eta, \cdot))_{T \in \mathcal{T}_0}$  together with  $\mathcal{T}_0$  be given. Due to the finiteness of  $X$ , the finite range condition holds trivially and the corresponding Markov process generated by  $A$  is a (continuous-time) Markov chain. Further, the space of (continuous) functions  $f : X \rightarrow \mathbb{R}$  is a finite dimensional vector space. Since the generator  $A$  is a linear operator it has a matrix representation, which we will determine within this paragraph. In the sequel, we will identify  $A$  with its matrix representation. Now, the

problem is that we have a continuous-time model but want to establish a simulation method. This means we need to understand the dynamics in a sequential or algorithmic way. In order to do so we interpret the Markov chain dynamics in two different ways by applying standard methods to the Markov process generated by  $A$ .

### 31.3.1 Representation of the Generator $A$

Before we present the results of our calculation we need to fix some notation. As above, we write  $\eta|_U$  for  $\{\eta(x); x \in U\}$ , the restriction of some configuration  $\eta$  to the coordinates of  $U \subseteq S$ . Further, put

$$N_{\mathcal{T}_0} := |\mathcal{T}_0|,$$

the number of elements of  $\mathcal{T}_0$ . We define

$$A_T f(\eta) := \sum_{v \in W^T} c_T(\eta, v)[f(\tau_T(\eta, v)) - f(\eta)]. \tag{31.10}$$

Then  $A$  decomposes into

$$A f(\eta) = \sum_{T \in \mathcal{T}_0} A_T f(\eta). \tag{31.11}$$

As mentioned,  $A$  and  $A_T$  are linear maps and hence possess a matrix representation denoted by  $(a_{\eta\xi})$ ,  $(a_{\eta\xi}^T)$ , respectively.

**Lemma 1** *Let  $\eta \in \mathcal{X}$ ,  $T \in \mathcal{T}_0$ . Then the matrix representation of  $A_T$  satisfies condition (Q) in the next section, and*

$$\begin{aligned} a_{\eta\eta}^T &= -c_T(\eta, W^T) + c_T(\eta, \eta|_T) \\ a_{\eta\xi}^T &= \begin{cases} c_T(\eta, \xi|_T) & \text{if } \eta|_{S \setminus T} = \xi|_{S \setminus T} \\ 0 & \text{if } \eta|_{S \setminus T} \neq \xi|_{S \setminus T}. \end{cases} \quad (\eta \neq \xi) \end{aligned}$$

The proof of this lemma can be found in the Appendix. The key idea is to insert the indicator functions  $\mathbb{1}_\eta, \eta \in \mathcal{X}$  into (31.10).

Note that

$$a_{\eta\eta}^T = - \sum_{\substack{v \in W^T \\ v \neq \eta|_T}} c_T(\eta, v). \tag{31.12}$$

With (31.11) we obtain the following.

**Corollary 1** *The matrix representation of  $A$  satisfies condition (Q), where*

$$a_{\eta\eta} = - \sum_{T \in \mathcal{T}_0} c_T(\eta, W^T) \tag{31.13}$$

and

$$a_{\eta\xi} = \sum_{T \in \mathcal{T}_0} c_T(\eta, \xi|_T) \mathbb{1}_{(\xi|_{S \setminus T})}(\eta|_{S \setminus T}) \quad (\eta, \xi \in \mathcal{X}, \eta \neq \xi). \tag{31.14}$$

### 31.3.2 Two Concepts for Continuous-Time Markov Chains

Let  $Q = (q_{ij})_{i,j \in X}$  be the generator of some continuous-time Markov chain with countable state space  $X$ . The following condition holds:

$$q_{ij} \geq 0 \text{ for } i \neq j; \quad q_{ii} \leq 0 \quad \text{and} \quad -q_{ii} = \sum_{j \neq i} q_{ij}. \quad (Q)$$

For the analysis of the dynamics of an IPS we mention two results that can be found in many relevant text books.

**1. The compound Poisson process.** Let  $I$  be the identity mapping  $\mathcal{X} \rightarrow \mathcal{X}$ . Suppose that  $(N_t)_{t \in [0, \infty)}$  is a Poisson process with parameter  $\alpha \in (0, \infty)$  and  $(X_n)_{n \in \mathbb{N}_0}$  is some discrete-time Markov chain independent of  $(N_t)_{t \in [0, \infty)}$  and with the one-step transition probabilities  $\mathbf{p}$ . By

$$(X_t^N)_{t \in [0, \infty)} \quad (31.15)$$

we denote the process with event times according to  $(N_t)_{t \in [0, \infty)}$  and which performs transitions according to  $\mathbf{p}$  at the event times. Then the stochastic process  $(X_t^N)_{t \in [0, \infty)}$  is a Markov process with generator equal to  $\alpha(\mathbf{p} - I)$ .

**2. The embedded chain.** Since the complete presentation is quite extensive we refer to [3]. The idea is that a continuous-time Markov chain can be decomposed into exponentially distributed holding times, where no transition takes place, and a discrete-time Markov chain. The parameter of the holding times as well as the transition probability matrix of the discrete-time chain can be concluded from the generator  $Q$ .

### 31.3.3 Interpretations of IPS Dynamics

Let  $(\eta_t)_{t \in [0, \infty)}$  be some finite IPS generated by  $A$  as given in (31.11). The following algorithmic understanding of this process is derived by considering the embedded chain and by interpreting  $(\eta_t)_{t \in [0, \infty)}$  as a compound Poisson process.

**1. We use the embedded chain arguments.** Let  $\eta$  be the current configuration of the IPS, and let  $T \in \mathcal{T}_0$ . One could imagine an alarm clock at  $T \in \mathcal{T}_0$ . The holding time until  $\eta$  changes involving the coordinates in  $T$  is exponentially distributed with parameter  $-a_{\eta\eta}^T$ , see (31.12). Let  $v \in W^T$ . The probability of a transition from  $\eta$  to  $\tau_T(\eta, v)$  is given by

$$\frac{c_T(\eta, v)}{-a_{\eta\eta}^T}.$$

After the transition has taken place, the alarm will be reset. The global behavior of the process can be interpreted as the *superposition of transitions* taking place locally in all possible  $T \in \mathcal{T}_0$  as described above, since  $Af(\eta) = \sum_{T \in \mathcal{T}_0} A_T f(\eta)$ .

**2. We use the statement of the compound Poisson process.** In the following, we construct a compound Poisson process with generator  $A$ . Let  $\eta \in \mathcal{X}$ . We define

$$(p_{\eta\xi}^T)_{\eta, \xi \in \mathcal{X}} = \mathbf{p}^T \quad (31.16)$$

by

$$\begin{aligned}
 p_{\eta\eta}^T &:= 1 + \frac{1}{c}a_{\eta\eta}^T \\
 &= 1 - \frac{1}{c}c_T(\eta, W^T) \text{ with Lemma 1, and further} \\
 p_{\eta\xi}^T &:= \frac{1}{c}a_{\eta\xi}^T \quad \xi \in \mathcal{X}, \eta \neq \xi \\
 &= \frac{1}{c}c_T(\eta, \xi|_T)\mathbb{1}_{(\xi|_{S\setminus T})}(\eta|_{S\setminus T}), \text{ likewise with Lemma 1.}
 \end{aligned}$$

One easily verifies that  $\mathbf{p}^T$  is a stochastic matrix with Lemma 1. Moreover, the definition of  $\mathbf{p}^T$  is such that the equation

$$A_T = c(\mathbf{p}^T - I) \tag{31.17}$$

is valid. From (31.17) we conclude

$$\begin{aligned}
 A &= \sum_{T \in \mathcal{T}_0} A_T = c \left( \sum_{T \in \mathcal{T}_0} \mathbf{p}^T - \sum_{T \in \mathcal{T}_0} I \right), \\
 &= c \left( \sum_{T \in \mathcal{T}_0} \mathbf{p}^T - N_{\mathcal{T}_0} \cdot I \right), \\
 &= c \cdot N_{\mathcal{T}_0} \left( \frac{1}{N_{\mathcal{T}_0}} \sum_{T \in \mathcal{T}_0} \mathbf{p}^T - I \right) \\
 &= \alpha \left( \frac{1}{N_{\mathcal{T}_0}} \mathbf{p} - I \right), \quad \text{where } \mathbf{p} := \sum_{T \in \mathcal{T}_0} \mathbf{p}^T \text{ and } \alpha := c \cdot N_{\mathcal{T}_0}. \tag{31.18}
 \end{aligned}$$

Note that  $(1/N_{\mathcal{T}_0})\mathbf{p}$  is also a stochastic matrix. Let  $(Y_n)_{n \in \mathbb{N}_0}$  be a discrete Markov chain on  $\mathcal{X}$  with transition probability matrix  $(1/N_{\mathcal{T}_0})\mathbf{p}$ . Let  $\alpha$  be the parameter of iid<sup>1</sup> exponentially distributed holding times  $(h_n)_{n \in \mathbb{N}_0}$  and let  $(N_t)_{t \in [0, \infty)}$  be the Poisson process corresponding to the holding times  $(h_n)_{n \in \mathbb{N}_0}$ . Then,  $(N_t)_{t \in [0, \infty)}$  is a Poisson process with parameter  $\alpha$ . We obtain that  $(X_t^N)_{t \in [0, \infty)}$ , see (31.15), has a generator equal to  $A$ . This allows the following interpretation of the IPS generated by  $A$ .

Let  $\eta$  be the current configuration of  $(\eta_t)_{t \in T}$ . After an exponentially distributed waiting time with parameter  $\alpha$  the IPS performs a transition according to  $(1/N_{\mathcal{T}_0})\mathbf{p}$ , i.e.,

$$\frac{1}{N_{\mathcal{T}_0}}p_{\eta\xi} = \frac{1}{N_{\mathcal{T}_0}} \sum_{T \in \mathcal{T}_0} p_{\eta\xi}^T \quad (\xi \in \mathcal{X}) \tag{31.19}$$

---

<sup>1</sup> Identically independently distributed.

is the probability for such a transition from  $\eta$  to  $\xi$ . This can be interpreted as follows. A uniformly distributed random variable with probability density equal to  $(1/N_{\mathcal{T}_0})$  picks out the region  $T \in \mathcal{T}_0$  where a transition from  $\eta$  shall take place, and the “local” transition in this  $T$  is then performed according to  $\mathbf{p}^T$ .

We want to point out a difference in the interpretations of  $(\eta_t)_{t \in \mathbf{T}}$  given in **1** and **2**. In **1**, the holding times are not identically distributed. The stochastic matrix which controls the transitions at the event times has only diagonal elements equal to 0. Hence, there are no transitions of a current configuration  $\eta$  in itself. On the other hand, the construction in **2** allows *fake events*, i.e., transitions of the form  $\tau_T(\eta, \eta|_T)$  for a current configuration  $\eta$  and  $T \in \mathcal{T}_0$ , with positive probability. But the holding times are distributed iid.

## 31.4 Simulating the Finite IPS

### 31.4.1 Preparations

We take the general assumptions of Section 31.3. In this section we present an algorithm that can be used to implement an IPS given that all the modelling steps as described in the previous sections are performed. In other words, we assume that the possible transitions  $\tau_T(\eta, v)$  from  $\eta \in \mathcal{X}$  are defined, where  $T \in \mathcal{T}_0$  and  $v \in W^T$ , and that these transitions occur with a rate  $c_T(\eta, v)$ . Recall that the set  $\mathcal{T}_0$  holds the subsets of the lattice in which transitions can take place. We define

$$W_+^T := \{v \in W^T; v \neq \eta|_T \text{ and } c_T(\eta, v) > 0\} \quad \eta \in \mathcal{X}.$$

In words, this is all  $v \in W^T$  such that the transition  $\tau_T(\eta, v)$  is no fake event and has a strictly positive rate for given  $\eta$ . We say that a *transition is possible* if  $W_+^T$  is not empty for given  $T$ . Since  $W$  and  $T$  are finite we denote  $W_+^T = \{v_1, \dots, v_n\}$ . The algorithm corresponds to *one* local transition (update) of the system. In other words it explains the transition from one  $\eta$  to a certain  $\tilde{\eta}$ . We do not take care of any graphical output or terminating condition of the algorithm. Such details are usually strongly connected to the particular model. The algorithm is related almost one-to-one to the interpretation in the sense of **2** of Section 31.3. Recall (31.19). It starts with any given configuration  $\eta$ , which is called the initial condition for now. We formulate two random experiments that are part of the flowchart presented in the next section. The reader may translate these experiments into program code as desired. Further, we explain the decision **Dec** that is part of the flowchart.

- 1. Exp1:** Choose some  $T \in \mathcal{T}_0$  with uniform distribution on  $\mathcal{T}_0$ .
- 2. Dec:** Decide whether transition is possible in the chosen  $T$ . Transition is possible, if  $W_+^T$  is not empty for given  $T$ . In other words, the system updates with a strictly positive rate.
- 3. Exp2:** The second random experiment is modelled as follows. The random variable maps into  $W_+^T \cup \{\eta|_T\} = \{v_1, \dots, v_n, \eta|_T\}$ . So, the state space of this experiment is the set  $W_+^T$  enlarged with the element  $\eta|_T$  of  $W^T$ . Recall (31.8) and (31.16).

If  $v = \eta|_T \in W^T$ , the transition  $\tau_T(\eta, v)$  is a fake event and its probability is given by the diagonal element  $p_{\eta\eta}^T$  of (31.16). Thus, the density of the distribution (single point probabilities) of the random experiment is given according to (31.16) by

$$P = \left( \frac{c_T(\eta, v_1)}{c}, \frac{c_T(\eta, v_2)}{c}, \dots, \frac{c_T(\eta, v_n)}{c}, 1 - \sum_{i=1}^n \frac{c_T(\eta, v_i)}{c} \right).$$

The probability on the right-hand side in the above parentheses is the probability of the mentioned fake event.

### 31.4.2 Flowchart for One Transition

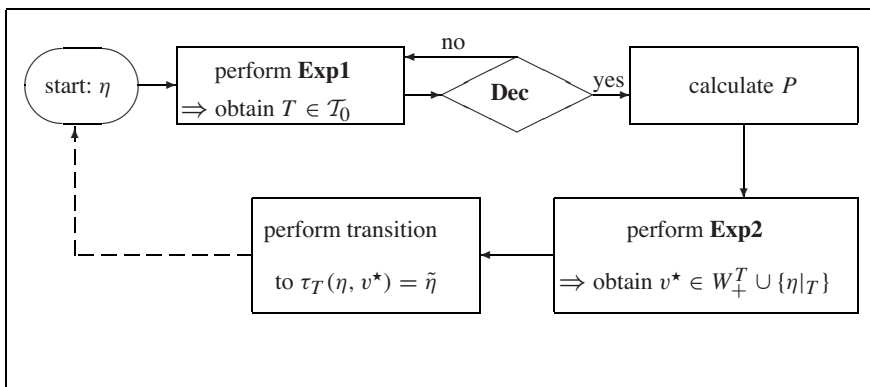


Fig. 32.1. Visualization of the simulation scheme.

**Example B 5 (Predator-Prey Competition)** We illustrate the local update procedure for the Predator-Prey Example.

**Exp1:** Choose the transition area  $T$  from  $\mathcal{T}_0$ , that is in our case, choose either a single node  $\{x\} \subset S$  or a pair of neighboring sites  $\{x, y\} \subset S$ . The probability to select a certain transition area shall be  $1/|\mathcal{T}_0|$ , i.e., each area has the same chance to be chosen. Note that the number  $|\mathcal{T}_0|$  of possible transition areas depends only on the structure and size of  $S$ .

**Dec:** In the case that a single node has been chosen for  $T$ , transition is possible if the node  $x$  is empty, see (31.5). Then a new individual—either predator or prey—can be born at this node. In the case that a pair of neighboring sites has been chosen for  $T$ , then transition is possible if one site is occupied by predator or prey and the other one is empty. Then the individual can migrate from the first site to the other one.

**Exp2:** Remember that the system is in the actual configuration  $\eta$ . Note that the value  $c$  depends on the parameters  $a, b, k, l$  and the lattice dimensionality  $d$  and that  $c$  can be calculated by the formulas (31.8) and (31.7).

In the case that  $T = \{x, y\}$  was chosen, a migration is performed with chance  $1/(2dc)$  and the configuration is left unchanged (fake event) with probability  $1 - [1/(2dc)]$ . Any other transition corresponding to the transition area  $T$  has chance zero. This means that the vector  $P$  has only two non-zero entries:  $1/2dc$  for the local

configuration  $v$  with  $v(x) = \eta(y)$  and  $v(y) = \eta(x)$  and  $1 - [1/(2dc)]$  for the local configuration  $v_0$  with  $v(x) = \eta(x)$  and  $v(y) = \eta(y)$  (fake event).

In the case that  $T = \{x\}$  was chosen, calculate  $\eta_1(x)$  and  $\eta_2(x)$ , the number of predator and prey individuals in the neighborhood of  $x$ , as defined in Example B 4. The birth of a predator individual at  $x$  is described by replacement of  $v(x) = 1$  instead of  $\eta(x) = 0$  and it occurs with probability  $(a\eta_1(x) + b\eta_2(x))/c$ . Analogously, the transition to the local configuration  $v(x) = 2$  (birth of prey) has chance  $(k\eta_1(x) + l\eta_2(x))/c$ . The only other possibility is  $v(x) = 0$ , the fake event, with chance  $1 - (a\eta_1(x) + b\eta_2(x))/c - (k\eta_1(x) + l\eta_2(x))/c$ .

### 31.4.3 The Simulation Clock

The fact that IPSs are time-continuous models allows us to explicitly relate the number of simulation updates to real time. To illustrate this we go back to the interpretation 2 of Section 31.3, and formula (31.18). There it is stated that the clock pulse for the transitions is given by a Poisson process  $(N_t)_{t \in [0, \infty)}$  with parameter  $\alpha := c \cdot N_{\mathcal{T}_0}$ . This means that the waiting times in between such transitions are iid distributed with an exponential distribution with parameter  $\alpha$  and the number # of simulation updates up to time  $t$  equals  $N_t$ . We conclude from the law of large numbers that  $N_t \approx \alpha t$  for large  $t$ . Therefore, we can estimate the real time  $t$  from the number # of simulation updates by

$$t \approx \frac{1}{\alpha} \cdot \#. \quad (31.20)$$

This estimate is more precise the larger the number of updates is.

There are two interesting facts which we point out. First, the parameter  $\alpha = c \cdot N_{\mathcal{T}_0}$  depends on the lattice size. This reflects the connection between the local nature of the single transitions and the global simulation clock pulse. Note that a certain fixed transition area is expected to be chosen once during  $N_{\mathcal{T}_0}$  simulation updates. Second, two systems, where the dynamics is essentially the same but the rates of the second system are increased by a constant factor compared to the first system, are simulated exactly the same way. Only the clock pulse for the second system is increased by the mentioned factor in comparison with the first system. In fact, one would implement both systems identically and account for the relation to real time by formula (31.20).

## 31.5 Discussion

IPSs are continuous-time Markov processes. They allow us to model the local interaction of spatially distributed individuals. Therefore, they are particularly suited for the modelling of many biological systems. We have stated the main modelling steps that are necessary to establish an IPS model for a given biological problem.

There is a long history of IPS-modelling in the physical sciences which is accompanied by a large interest in IPSs from the mathematical side. Therefore, there exist many

well-studied IPSs that can be used for reference, as well as a variety of mathematical methods that can be used to analytically study new IPSs. However, the analytical properties of an IPS are often not revealed until one studies the corresponding system on an infinite lattice. If the finite range condition is satisfied for the transition rates, then even the infinite IPS is a well-defined Markov process.

Many studies start with a computer simulation of the model. Therefore, it is necessary to translate the dynamics of the particle system into a sequential algorithm that can be implemented on a computer. We have developed the core of a simulation algorithm for any finite IPS.

Proportionally increased transition rates result in a speedup of the system dynamics. The simulation algorithm remains essentially unchanged. We have worked out the relation of the number of simulation steps to real time.

We want to point out that the simulation algorithm is closely related to (asynchronous) cellular automata. An advantage of an IPS model is that it falls into a class of mathematically well-studied systems, so that the model can be analyzed rigorously in many cases. For instance, sometimes it is possible to derive a PDE from the IPS model by sending the lattice spacing to zero in a suitable way. Then the parameters of the resulting PDE are directly related to the parameters of the individual interaction.

## Appendix

### A.1 The Proof of Lemma 1

*Proof* Let  $T \in \mathcal{T}_0$  and  $\eta \in \mathcal{X}$ . Then

$$\begin{aligned} a_{\eta\eta}^T &= A_T \mathbb{1}_\eta(\eta) = \sum_{v \in W^T} c_T(\eta, v) [\mathbb{1}_\eta(\tau_T(\eta, v)) - \mathbb{1}_\eta(\eta)] \\ &= - \sum_{v \in W^T} c_T(\eta, v) + \sum_{v \in W^T} c_T(\eta, v) \mathbb{1}_\eta(\tau_T(\eta, v)) \\ &= - \sum_{v \in W^T} c_T(\eta, v) + c_T(\eta, \eta|_T). \end{aligned}$$

Further, we have  $\sum_{\xi, \xi \neq \eta} a_{\eta\xi}^T = \sum_{\xi, \xi \neq \eta} A_T \mathbb{1}_\xi(\eta)$ , where for  $\eta \neq \xi$

$$\begin{aligned} A_T \mathbb{1}_\xi(\eta) &= \sum_{v \in W^T} c_T(\eta, v) [\mathbb{1}_\xi(\tau_T(\eta, v)) - \mathbb{1}_\xi(\eta)] \\ &= \sum_{v \in W^T} c_T(\eta, v_k) \mathbb{1}_\xi(\tau_T(\eta, v)) \\ &= \begin{cases} c_T(\eta, v) & \text{if } \tau_T(\eta, v) = \xi \\ 0 & \text{if } \tau_T(\eta, v) \neq \xi \end{cases} \\ &= \begin{cases} c_T(\eta, \xi|_T) & \text{if } \eta|_{S \setminus T} = \xi|_{S \setminus T} \\ 0 & \text{if } \eta|_{S \setminus T} \neq \xi|_{S \setminus T}. \end{cases} \end{aligned}$$



We conclude

$$\begin{aligned}
 \sum_{\{\xi \in \mathcal{X}; \xi \neq \eta\}} a_{\eta\xi}^T &= \sum_{\{\xi \in \mathcal{X}; \xi \neq \eta, \eta|_{S \setminus T} = \xi|_{S \setminus T}\}} c_T(\eta, \xi|_T) \\
 &= \sum_{v \in W^T, v \neq \eta|_T} c_T(\eta, v) \\
 &= c_T(\eta, W^T) - c_T(\eta, \eta|_T).
 \end{aligned}$$

Since  $c_T(\eta, v) \geq 0$  ( $\eta \in \mathcal{X}$ ,  $v \in W^T$ ) the first assertion is proved.  $\square$

## Acknowledgments

We thank Andreas Deutsch for inspiring discussions. We thank Wilfried Schenk for helpful advice. We thank David Wierse, who works with the predator-prey model.

## References

1. Liggett, T.M.: *Interacting Particle Systems*. Springer, New York (1985).
2. Liggett, T.M.: *Stochastic Interacting Particle Systems: Contact, Voter and Exclusion Processes*. Springer, Berlin (1999).
3. Bhattacharya, R.N., Waymire, E.C.: *Stochastic Processes with Applications*. John Wiley & Sons, Inc., New York (1990).
4. Durrett, R., Levin, S.: The importance of being discrete (and spacial). *Theoretical Population Biology*, 46 (1994).

## Teaching Mathematical Biology in a Summer School for Undergraduates

Gerda de Vries and Thomas Hillen

Department of Mathematical and Statistical Sciences, University of Alberta, Edmonton, AB, T6G 2G1, Canada; devries@math.ualberta.ca, thillen@math.ualberta.ca

**Summary.** For the past four years, the University of Alberta has hosted a summer school on mathematical biology, aimed at undergraduate students who have completed 2–3 years of study in mathematics or a similar quantitative science. The aim of this summer school is to introduce the students to mathematical modelling and analysis applied to real biological systems. In the span of 10 days, students attend lectures and exercise sessions, learn how to set up mathematical models, and use analytical and computational tools to relate them to biological data. They experience the modelling process by working on a research project. In this chapter, we explain our teaching philosophy, share some unique features of our summer school, and exemplify key course components.

**Key words:** Education, undergraduate, modelling.

### 32.1 Introduction

Mathematical modelling of biological systems requires a wide variety of methods and skills from multiple disciplines. Traditionally, these skills are taught separately in standard courses in mathematics, biology, and computer science, but rarely are they integrated into a single undergraduate-level course that focusses on the modelling process.

At the Centre for Mathematical Biology at the University of Alberta, inspired by a similar summer school at the University of Tübingen, we have developed a 10-day summer school for motivated undergraduate students that integrates the methods of applied mathematics in the context of mathematical biology.

The summer school addresses questions of utmost importance to the mathematical biologist, namely what type of model to use, how to develop a mathematical model, how to relate a model to experimental data, and how to validate and/or evaluate the model.

Our primary goal then is to teach the development of models based on biological observations and experimental data, and the interpretation of model results in order to make predictions, suggestions for further experiments, and suggestions for control measures or treatments. We include qualitative model analysis, model simulation, and model validation.

In this chapter, we describe how we accomplish all of the above in the short time of 10 days. In Section 32.2, we provide an overview of the summer school, describing the schedule, typical participants, and prerequisites for the course. The bulk of the chapter is devoted to describing the course content, in Section 32.3. We conclude with our perspectives on the benefits and impact of the summer school in Section 32.4, and a brief discussion in Section 32.5.

## 32.2 Overview of the Summer School

We aim to introduce undergraduate students to mathematical modelling and analysis in the context of real biological systems and to provide them with a simulated research experience. To that end, our summer school consists of three integrated components:

1. Through **lectures and exercises**, focussing on four main topics (difference equations, ODEs, PDEs, and stochastic models and parameter estimation), students are introduced to various techniques of mathematical modelling.
2. Through a **self-guided tutorial**, students learn how to use Maple to simulate mathematical models and relate them to biological data.
3. Through **projects**, students experience the modelling process.

The summer school consists of 10 instructional days. The schedule we use is shown in Table 32.1. During the first 5 days, students attend lectures, work through exercises, and complete the self-guided computer tutorial. The last 5 days are devoted to the research projects.

The summer school is attended by 15–25 students each year. In addition to lecturing, our summer school involves a significant amount of one-on-one mentoring and interaction with students. For that reason, we cap enrollment at approximately 25.

Typical students have completed 2–3 years of undergraduate study in mathematics or a similar quantitative science. While the majority of attendees major in mathematics, some already are enrolled in a degree program combining mathematics or computer science and biology. Undergraduates in their third year are especially encouraged to attend. Beginning graduate students in the biological and medical sciences interested in mathematical modelling are welcome as well, and in fact serve as an excellent complement to the group composition.

The prerequisites for attending our summer school are a basic knowledge of calculus, linear algebra, and differential equations. Although not necessary, we have found that some knowledge of computer programming is extremely helpful.

We typically run the summer school with four core instructors, one high-profile guest instructor, secretarial support staff, and approximately 20 volunteers (graduate students and postdoctoral fellows). The core instructors give the lectures and guide the exercise sessions during the first half of the summer school, and serve as primary project consultants for 2–3 student teams during the second half. The guest instructor attends the summer school for the last few days only, delivers a keynote address, and serves as roaming project consultant, interacting with each student team. The graduate students and postdoctoral fellows help with all aspects of the summer school.

**Table 32.1.** Schedule for the mathematical biology summer school.

	9:00–10:30	11:00–12:30	1:30–3:00	3:30–5:00	Evening
<b>Day 1</b>	Introduction	Discrete I	Maple Lab	Discrete II	Homework
<b>Day 2</b>	Exercises	ODE I	Maple Lab	ODE II	Homework
<b>Day 3</b>	Exercises	PDE I	Maple Lab	PDE II	Homework
<b>Day 4</b>	Exercises	Stochastic I	Maple Lab	Stochastic II	Homework
<b>Day 5</b>	Exercises	Maple Lab	Maple Lab	Maple Lab	Project Intro
<b>Day 6</b>	DAY OFF				
<b>Days 7–10</b>	Projects	Projects	Research Lecture	Projects	
<b>Day 11</b>	Presentations	Presentations	Presentations	Presentations	Graduation

## 32.3 Course Content

In this section, we elaborate on the three course components, namely lectures and homework, the computer tutorial, and research projects.

### 32.3.1 Part I: Lectures and Homework

We integrate theory and modelling in the lectures and homework component of the summer school. We begin with a brief presentation on the history of mathematical biology. The modelling lectures begin with a review of the importance of distinguishing between dependent and independent variables, and probabilities and rates, as well as an overview of the most common model classes.

We elaborate on four of the model classes (difference equations, ODEs, PDEs, and stochastic models and parameter estimation) in four units of lectures and homework sessions. Each unit consists of 3 hours of lecturing and 1.5 hours of tutorial sessions

during which homework problems (assigned during the lectures) are discussed. Students receive extensive course notes that fill in details not covered in the lectures. The course notes have been edited and published [2].

The unit on difference equations covers scalar and two-dimensional systems, both linear and nonlinear. Students are introduced to the concept of a fixed point, as well as the notions of stability and instability. For scalar equations, we teach both graphical stability analysis (cobwebbing) and linear stability analysis. The latter is extended to two-dimensional systems. We give a full treatment of the discrete logistic equation, including period-doubling and the Feigenbaum diagram, thereby introducing students to the concept of a bifurcation.

The unit on ordinary differential equations builds on the previous unit, and covers direction fields, nullclines, and phase plane analysis. Applications include the investigation of 2-species interaction models such as predator-prey or competition models, as well as standard susceptible-infected-removed (SIR) epidemiological models.

The unit on partial differential equations covers an age-structured population model and reaction-diffusion equations. In particular, we focus on the critical domain size problem and travelling waves.

The last unit covers stochastic modelling and parameter estimation. The section on stochastic models covers random walk models and birth-death processes. The section on parameter estimation includes the log-likelihood method, the Akaike information criterion (AIC), and the likelihood ratio test.

The following exercise, drawn from the lectures on difference equations, illustrates our approach to integrating theory and modelling:

*Consider the following model for drug prescription:*

$$a_{n+1} = a_n - ka_n + b,$$

*where  $a_n$  is the amount (in mg) of a drug in the bloodstream after administration of  $n$  dosages at regular hourly intervals.*

- (a) *Discuss the meaning of the model parameters  $k$  and  $b$ . What can you say about their size and sign?*
- (b) *Perform cobwebbing analysis for this model. What happens to the amount of drug in the bloodstream in the long run? How does the result depend on the model parameters?*
- (c) *Sketch a graph of  $a_n$  versus  $n$ . How should  $b$  be chosen to ensure that the drug is effective, but not toxic?*

In this exercise, students are given the equation of the model, but they are asked to figure out the structure of the model themselves, by determining the meaning of each of the model parameters. In other exercises, students are asked to construct their own model, based on explicitly stated assumptions. The experience gained from working through exercises such as these prepare students for the project work later during the summer school.

### 32.3.2 Part II: Self-Guided Maple Tutorial

The structure of the Maple tutorial [2] follows the lectures. The tutorial supports the material discussed in the lecture and provides a different perspective on biological problems, but also covers topics not discussed in the lectures. In particular, we use the tutorial to introduce students to data analysis, covering linear regression and dealing with data sets, as well as numerical solutions of differential equations.

The computational software of our choice is Maple. The point is not to learn Maple *per se*, but to extend the range of interesting problems within the grasp of students through computation. Other software, such as Mathematica, Matlab, or even C++, could be used instead.

Each student has access to a computer and works through the tutorial document at his/her own pace. We typically schedule about 12 hours of lab time for the Maple tutorial. An instructor and several teaching assistants are present during the Maple lab sessions to provide help when needed.

The tutorial is extensive and contains many examples and exercises, ranging from trivial to challenging in difficulty. We do not expect every student to complete the entire tutorial, although each year there are a few who do (primarily advanced students with some computer programming background). Occasionally, a student already has some background with Maple. Those students are free to skip sections of the tutorial with material that is familiar to them. We have found that the tutorial is sufficiently wide ranging and challenging to keep the interest of those students.

Following is a sample exercise from the Maple tutorial illustrating the use of data analysis in the modelling process:

*Consider the Ricker model, written in the following form:*

$$x_{n+1} = ae^{-bx_n}x_n.$$

- (a) *Fit the Ricker model to Barlow's data on the number of nests per hectare for a population of the common wasp *Vespula vulgaris* [1], shown below.*

1988	1989	1990	1991	1992
8.6	31.1	7.0	11.7	10.2

*That is, find the values of the parameters  $a$  and  $b$  that best fit the data.*

- (b) *Check the fit for the data two ways: (1) in a plot of  $\ln(x_{n+1}/x_n)$  versus  $x_n$ , and (2) in a plot of  $x_{n+1}$  versus  $x_n$ .*
- (c) *What behaviour is predicted for the wasp population, based on the results of your earlier bifurcation analysis of the Ricker model?*

This exercise is one in which we expect students to integrate knowledge obtained in preceding exercises. In particular, students learned linear regression in an earlier set of exercises. Here, students are expected to recognize the linear relationship  $\ln(x_{n+1}/x_n) = \ln(a) - bx_n$ , and then use linear regression to obtain the best-fit values for  $\ln(a)$  and  $b$ . In another set of preceding exercises, students were asked to systematically investigate the behaviour of the Ricker model written in the form  $y_{n+1} = ry_n e^{-y_n}$

over a range of the parameter value  $r$ , and summarize the behaviour in a bifurcation diagram. Here, they are asked indirectly to determine the relationship between the two forms of the Ricker model, and use the results of the bifurcation analysis to predict the behaviour of the model obtained for the wasp population.

### 32.3.3 Part III: Research Projects

Students choose a modelling problem from a set of approximately 25 project descriptions, loosely grouped in four topic areas (epidemic models, population dynamics, models for spatial spread, and physiology) [2].

Students work in teams of 2–3, under the guidance of one of the instructors. Students are expected to develop a model, analyze and/or simulate their model, and prepare a presentation.

Many of the problems have not been studied previously with a mathematical model, and are open ended, with no “right solution” *per se*. Because of the open-ended nature of the research projects, instructors are flexible. Very often, students take the project in different, sometimes better, directions than the instructor might have.

In many cases, students will need to simplify their problem and build a hierarchy of models, each model incorporating additional realism from the original problem at hand. We emphasize to students that success is not measured in terms of the end product, but in terms of the amount of learning that is taking place during the model development and analysis. It is not uncommon that the team apparently making the slowest progress actually is learning the most.

For some of the projects, we provide some supplementary reference materials. For others, students easily can obtain additional information from the internet. We do not require students to study the biological topic at length (we believe that initial efforts in mathematical modelling require only the identification of basic mechanisms). The point of the project work is not to produce publishable results, but rather for students to experience the modelling process.

Sample project topics include the spread of HIV in Cuba, cholera in South Africa, the extinction of a wolf population in Sweden, the pupil control system, and radiation treatment of cancer. The complete set of project descriptions can be found in [2].

Following is a sample project description, dealing with the outbreak of yellow fever in Senegal:

*Yellow fever (YF) is a viral disease transmitted to primates (including humans) by infected mosquitoes. The disease is endemic in populations of monkeys living in the jungle. The disease is spread into the human population in three stages:*

1. *Sylvatic transmission occurs when mosquitoes which have fed on infected monkeys next bite a human working in the jungle.*
2. *Intermediate transmission occurs when mosquitoes pass the virus among humans living in rural areas.*
3. *Urban transmission occurs when mosquitoes pass the virus among humans living in urban areas.*

*Below is a data set of YF cases reported during an outbreak in the city of Touba in Senegal in 2002 [4]. As soon as the virus was identified (October 11), a vaccination program was started. YF vaccine is safe and effective, and provides immunity within one week in 95% of those vaccinated.*

Date	Jan 18	Oct 4	Oct 11	Oct 17	Oct 24	Oct 31	Nov 20	Nov 28
Cases (total)	18	12	15	18	41	45	57	60
Deaths (total)	0	0	2	2	4	4	10	11

*Develop a model for the three stages of YF as outlined above, including vaccination in urban areas, and fit your model to the data. Would you expect that the disease dies out or that it becomes persistent? What would have happened without vaccination?*

The student team that tackled this problem in one of our recent summer schools decided to simplify the problem significantly, and focussed on the outbreak of YF within urban areas only. They constructed a model describing the transmission of the virus within the population of mosquitoes and from mosquitoes to humans. The mosquito population was divided into two classes (susceptible and infective), and the human population was divided into five classes (susceptible, exposed, infective, recovered, and vaccinated). Parameterizing a model of this size is a daunting task, even for experienced researchers. The students were able to obtain estimates for a number of parameters (such as the biting rate of mosquitoes) from the internet and journal articles, and adjusted the value of remaining parameters with a “fit-by-eye” procedure. They obtained a reasonable fit of the model to the data supplied, and then investigated the predictive power of the model in terms of suggesting strategies for controlling the outbreak of the disease.

Projects such as this one allow students to experience the entire modelling process, from model development to simulation/analysis to the interpretation of results.

### 32.4 Benefits and Impact of the Summer School

Students are very enthusiastic about the summer school. They are grateful for the challenging extracurricular experience and appreciative of the opportunity to interact with other bright and motivated students from varied educational backgrounds. Following are examples of typical comments received from students upon the completion of the summer school:

*I think the biggest thing I got out of the workshop was an appreciation of the wide variety of modeling applications (especially through the projects)—and also the immense power of a relatively limited set of techniques.*

*This workshop not only helped me to gain experience in Mathematical Biology, but also to decide my direction in my academic career.*



*It gave me a good overall look at math modeling . . . I now know what a “mathematical model” is. It’s a phrase I hear a lot, but wasn’t exactly sure what that meant. I also now have a clearer vision of a direction that I’d like to take in graduate studies.*

The comments quoted above illustrate that the summer school is highly useful to these students in guiding them towards future studies or careers in mathematical biology. Indeed, a significant number of past participants have continued their graduate studies in mathematical biology. To our knowledge, at least 12 out of 64 participants have found a place at different Canadian or US institutions.

The immediate benefits of the summer school for both the core and guest instructors are infectious enthusiasm and exposure to potential graduate students committed to the field of mathematical biology. But there are additional benefits. In particular, the instructional materials developed for the summer school have grown over the years, and now are published as an undergraduate textbook [2]. Also, we are starting to use modules developed for the summer school in our regular classes, and have plans to offer an undergraduate course on mathematical biology in the near future using the same philosophy that we use in the summer school.

Last, but not least, the summer school contributes significantly to the career development of the many graduate students and postdoctoral fellows who help run it. Both graduate students and postdoctoral fellows participate as teaching assistants for the exercise sessions and Maple labs during the first half of the summer school. In addition, the postdoctoral fellows serve as project consultants during the second half.

## 32.5 Discussion

Our summer school is an academically stimulating program that teaches the following applied math skills in the context of mathematical biology: theory, modelling, analysis, computation, data fitting, and prediction. Through lectures and exercises, the Maple tutorial, and project work, participants not only gain a wide knowledge of mathematical biology, but also are introduced to research.

Although our formal instructional time with the students is very limited, we cover enough aspects of modelling that students can find and learn required advanced techniques while working on their projects. In fact, students relish the challenge provided in the projects, and it is during this part of the summer school that we observe a phenomenal increase in knowledge and skill development. Participants are highly motivated and often achieve much more than expected.

For more information about the summer school, and to view student work, we invite readers to visit our website [3].

## Acknowledgments

We thank our colleagues Mark Lewis (University of Alberta), Frithjof Lutscher (University of Ottawa), Johannes Müller (Technical University of Munich), and Birgitt Schöfnisch (University

of Tübingen), who all have contributed significantly to the development of the summer school. We are grateful to the guest instructors: Pauline van den Driessche (University of Victoria), Leah Edelstein-Keshet (University of British Columbia), Michael Mackey (McGill University), Rebecca Tyson (University of British Columbia Okanagan), Gary de Young (Kings University College), Michael Li (University of Alberta), and Alex Potapov (University of Alberta). We also thank our graduate students, postdoctoral fellows, and secretarial support staff for their helpful suggestions and feedback. Most of all we thank the enthusiastic participants of the summer school who have made it a highlight of our academic year. Last, but not least, we are grateful to the institutions and organizations who have provided funding for the workshop, namely the Pacific Institute for the Mathematical Sciences (PIMS), Alberta Science and Research Authority (ASRA), the Mathematics for Information Technology and Complex Systems (MITACS) National Centre for Excellence, the Centre for Mathematical Biology, and the Department of Mathematical and Statistical Sciences at the University of Alberta.

## References

1. Barlow, N.D., Moller, H., Beggs, J.R.: A model for the effect of *Sphecoptera vesparum* as a biological control agent of the common wasp (*Vespula vulgaris*) in New Zealand. *Journal of Applied Ecology*, **33**, 31–34 (1996).
2. de Vries, G., Hillen, T., Lewis, M., Müller, J., Schönfisch, B.: *A Course in Mathematical Biology: Quantitative Modelling with Mathematical and Computational Methods*. SIAM, Society for Industrial and Applied Mathematics, Philadelphia, PA (2006).
3. Centre for Mathematical Biology (University of Alberta). <http://www.math.ualberta.ca/~mathbio/summerworkshop/>.
4. World Health Organization. [www.who.int](http://www.who.int).

---

# Index

- action potential, 225, 228, 235
  - generation, 229
- adenosine triphosphate (ATP), 194
  - production and diffusion of, 197
- adjacency matrix, 280
- age, 169
- allergen, 147
- analysis
  - bifurcation, 147, 150, 205, 208, 209, 342, 372
  - linear stability, 372
  - stability, 205
- antibody, 157, 173
- antigen, 133
  - load, 169
  - stimulus, 140
- antigen-presenting cell (APC), 133
- Aron model, 3
- artificial intelligence, 255
- atrocyte, *see* cell
- astrocytes
  - ATP waves, 198
  - Ca<sup>2+</sup> waves, 198
- asymptotic
  - approximation, 332
  - behavior, 324, 329, 335, 342
  - embedding, 289, 292
- atrial
  - excitability, 289
  - tissue, 295
- autocrine effect, 147
- automaton, *see* model
- average fractality, 188, 191
- aversiveness, 38
- axon myelination, 205
- bacteria, 109, 340
  - aerobic, 110
  - anaerobic, 110
  - Helicobacter pylori*, 284
  - Listeria monocytogenes*, 110
  - Pseudomonas putida*, 109, 110
  - Staphylococcus aureus*, 23
- Bayesian
  - analysis, 303, 304
  - estimator, 308
  - inference, 310
- Bernoulli
  - distribution, *see* distribution
  - trial, 248
- bifurcation, *see* analysis
- binary image, 186
- biodiversity, 101
  - migration, 101, 102
  - target of representation, 102, 103
- bionic, 255
  - application, 265
- birth-death process, 372
- brain, 193, 237
  - folding pattern, 259
  - surface data, 255
  - surface reconstruction, 256
- branching process, 303, 310, 342
  - Bienaymé–Galton–Watson, 304
  - density-dependent, 339
  - size-dependent, 339
  - state-dependent, 329

*Caenorhabditis elegans*, 279

calcium ( $\text{Ca}^{2+}$ )

release from endoplasmic reticulum, 194,  
197

wave, 194

cancer, 374

cardiac arrhythmias, 289

carrying capacity, 17, 54, 57

cat, 205

cauliflower, 190

cell

adjacency, 285

astrocyte, 194

B lymphocyte, 157

dendritic, 136

division, 279, 284

memory T lymphocyte, 136, 172

microglia, 194

naïve T lymphocyte, 136, 145, 172

neuronal, *see* neuron

ogliodendrocyte, 194

T-helper, 145

T lymphocyte, 133

Th1–Th2 regulation, 145

wild type, 188

chaos, 269

characteristic scale, 186, 188, 191

chemical gradient, 324

chemotactic sensitivity, 324

chemotaxis, 323

cicada, 75

clonal

expansion, 133, 134

selection, 158

cognitive thinking, 259, 261

coincidence detection, 246

competition, 372

competitive exclusion, 75, 76, 133, 134

complexity, 185, 189, 192, 279

measure, 280, 285

of networks, 279

computation, 265

mixed-integer programming, 104

multimicroprocessor, 265

computational

neuroscience, 213

conceptual presentation, 255

confocal microscope image, 111

connectivity kernel, 210

conservation biology, 101

bird conservation, 104

continuous-time Markov chain, 359

algorithmic interpretation, 360

control, 265, 269

convolution pattern, 255

correlated inheritance, 53

correlation

coefficient, 228

degree, 279

cryptic, 37

prey, 47

cytokine network, *see* network

Darwinian selection, 63

decision making, 259

degree distribution, *see* distribution

delay, 205

interaural time, 245

demographic stochasticity, 50

dendritic

morphology, 185

tree, 186

density function, 227

Gaussian, 189

interspike intervals, 229, 231

probability, 249

Rayleigh, 230

stable, 233

development, 279

Diamond's theorem, 93

*Dictyostelium discoideum*, 323

diffusion, 11, 12, 198, 297, 326

coefficient, 16

density-dependent, 111

Fickian, 13

nonlinear, *see* nonlinear

of  $\text{IP}_3$ , 202

directional hearing, 245

Dirichlet condition, 13, 327

Dirichlet–Neumann condition, 112

disease

allergy, 145

cholera, 374

HIV, 374

infectious, 169

malaria, *see* malaria

methicillin-resistant *S. aureus* (MRSA), 23

mortality, 170, 177

- pneumonia, 169
- severity, 171
- yellow fever, 374
- dispersal, 11, 102
  - long range, 16
  - mechanism, 21
- dispersion relation, 207
- distance
  - Euclidian, 23, 28, 29, 39, 187
  - exact, 186
  - Hamming, 159
  - Kullback–Leibler, 213
- distribution
  - Bernoulli, 214
  - Bradford, 231
  - Cauchy, 233
  - degree, 60
  - exponential, 228, 229, 231
  - gamma, 210, 218
  - Gaussian, 233
  - interspike intervals, 225, 228, 235
  - inverse Gaussian, 223
  - normally distributed, 231
  - Pareto, 231, 234, 235
  - Poisson, 306
  - Rayleigh, 230
  - speed, 206
  - stable, 225, 232, 234
  - Weibull, 223, 231
- DNA, 303, 343
- dynamic
  - programming, 102, 105
  - separatrix, 145
  - system, 339
- dynamical system, 339
- ecological stability, 49
- ecosystem, 49
- Edgeworth density, 217
- education
  - modelling, 369
  - summer school, 369
  - undergraduate, 369
- effective complexity, 280
- electrical conductance, 205
- emotional
  - effect, 255
  - influence, 255
- entropy, 214, 218
- differential, 214
- estimator, 213, 216
- moment estimator, 219
- Vasicek’s estimator, 218
- enzyme, 320
- epidemics, 12, 339, 354
  - fungal, 11
  - nosocomial infections, 26
- equation
  - Allen–Cahn, 329
  - Cahn–Hilliard, 329
  - difference, 121
  - differential, 133
  - discrete logistic, 372
  - finite difference, 115
  - FitzHugh–Nagumo (FHN), 290
  - integro-differential, 205
  - master, 24
  - mean field, 138
  - ordinary differential (ODE), 134, 137, 294, 371
  - ordinary differential with impulses, 87
  - partial differential (PDE), 354, 371
  - reaction-diffusion, 301, 302
  - Vanderplank, 12
- evolution, 280
  - coevolution, 37
  - ecological time scale, 49
  - quasi-stable strategy (q-ESS), 51, 54
  - stability, 38
  - stable strategy (ESS), 37, 38, 65
- evolutionary
  - ecology, 49
  - game theory, 65
- Ewens’s concept, 68
- excitability, 290, 294
- excitable media, 300
- excitatory chemical synapse, 206
- exopolysaccharide (EPS), 109
- exponential asymptotics, 329
- extinction, 49, 56, 58, 101, 340
- extracellular messenger, 193
- feed-forward processing, 246
- feedback
  - autocrine, 145
- Feigenbaum diagram, 372
- fern, 190
- Fickian diffusion, *see* diffusion

- Fisher's selection model, 66
- Fisher's theorem, 63, 64, 67
- fitness, 63
  - density-dependent, 54
  - density-independent, 55
  - intrinsic, 54
- fluctuation, 286
- folding pattern analysis, 259
- formal languages, 314
- Fourier transform, 208, 232
- fractal dimension, 185
  - local, 190
  - multiscale (MFD), 186, 190
- Fujiyama landscape, 53
- full offdiagonal complexity, 285
- functional-structural plant model, 313
  - genetics, 320
  - poplar, 314, 316, 320
- fungal epidemics, *see* epidemics
- fungus, 11
- G-protein, 195
  - cascade, 193
- gap junction, 193
- Gaussian
  - distribution, *see* distribution
  - estimation, 25
  - noise, 274
- gene
  - genotype space, 50
- generalized central limit theorem, 233
- gibberellic acid, 320
- Gillespie algorithm, *see* method
- Gram–Charlier
  - concept, 224
  - density estimate, 217
- graph grammar, 313
- growth
  - aerobic, 113
  - anaerobic, 113
- Hamming distance, *see* distance
- Hassel model, *see* model
- heart, 289
- hyposensitization therapy, 145
  - ultra-rush protocol, 153
- idiotype, 157
- idiotypic interaction, 157
- imaging, 194
- immigration, 54
- immune
  - aging, 169
  - system, 4, 157
- immunology, 133
- immunosenescence, 169, 170
- infanticide, 63
- infection, 23
  - rate, 169
- information processing, 193
- inhibitory
  - chemical synapse, 206
  - connection, 205
- inositol trisphosphate (IP<sub>3</sub>), 194
  - diffusion through gap junctions, 199
  - production and diffusion of, 196
  - receptor (IP<sub>3</sub>R), 195
- interaction, 51
  - local, 357
  - matrix, 54
  - predator-prey, 354
- interaural time difference, 245
- interface propagation, 113, 115
- interspike interval, 213
- intra-specific competition, 54
- ion channel, 225
- Jacobian, 6
- Keller–Segel model, *see* model, 196
- kinetics, 196
  - Monod, 112
- Kullback–Leibler distance, *see* distance, 196
- L-system, 314, 315, 319, 321
  - context-sensitive, 315
  - parametric, 315
  - table, 315
- Laplacian, 331
- lattice model, *see* model
- learning, 193
- Leslie matrix, 76
- lifetime, 58
- likelihood curve, 25
- Lindenmayer system, *see* L-system
- lipid, 205
- lipoprotein, 205
- localization
  - sound, 245

- lowest-order approximation, 209
- Lyapunov function, 75
  - average Lyapunov function, 83
- Lyapunov functional, 113
- lymph node, 136
- lymphatic network, 133
- lymphocyte, *see* cell
- magnetic resonance imaging (MRI), 255
- malaria, 3
  - duration of infection, 3
  - rate of infection, 3
  - vaccine efficacy, 3
- Malthusian parameter, 93
- Markov
  - operator, 227
  - process, 340, 359
- master equation, *see* equation
- mean degree, 59
- mean field
  - equation, *see* equation
  - model, *see* model
- measure
  - algorithmic information content, 280
  - coloring number, 281
  - graph thickness, 281
  - Kolmogorov complexity, 280
  - Lempel–Ziv complexity, 280
  - network motif concept, 281
- membrane, 266
  - computational unit (MCU), 266, 268
  - potential, 225–228, 231
- memory, 255, 257
  - T-cell, *see* cell
  - training, 255
- metabolic regulatory network, *see* network
- method
  - $\eta$ -ball, 23
  - Gibbs sampling, 308
  - Gillespie algorithm, 26, 28
  - leap-frog, 202
  - logistic regression, 239
  - maximum likelihood, 239
  - Monte Carlo, 240
  - Prince–Dormand Runge–Kutta integrator, 272
  - Runge–Kutta, 272
  - shape transformation, 256
  - spherical harmonics decomposition, 256
  - Vasicek’s, 213
- mice, 186
  - transgenic, 185, 191, 192
  - wild type, 191
- Michaelis–Menten constant, 123
- migration, 53, 54
- mildew, 13
- Minkowski sausage, 186
- mixing, 13
- model
  - agent-based, 133, 134
  - automata-based, 133
  - automaton, 314
  - bit string, 158
  - blow-up, 323, 326, 334
  - cellular automaton (CA), 110, 133, 353
  - compartmental, 12
  - continuous-time Markov process, 354, 365
  - discrete, 87
  - epidemic, 374
  - for action potential generation, 227
  - for recurrent biological events, 225, 235
  - game theory, 37
  - FSPM, *see* functional-structural plant model
  - Hassell, 96
  - Hindmarsh–Rose, 265, 268
  - HIV, 4
  - Hodgkin–Huxley, 225, 265
  - individual-based, 50, 111
  - integrate-and-fire, 225, 226
  - interacting particle system (IPS), 353
  - IPS generator, 359
  - Keller–Segel, 323
  - lattice, 355, 358
  - lattice gas cellular automaton (LGCA), 353
  - Leslie matrix, 75
  - logistic, 347
  - logistic regression, 238
  - lottery, 121
  - Markov chain Monte Carlo (MCMC), 305
  - mean field, 136
  - microscopic, 133
  - minimalistic, 57, 60, 289
  - network, 194
  - neuron, 225
  - of replicator dynamics, 63
  - phase-separation, 329
  - physiological, 313

- random walk, 372
- realistic cardiac, 289
- Ricker, 341, 373
- Rössler, 269, 272
- semiconductor, 327
- spatial spread, 374
- spatial Tangled Nature, 52
- stochastic, 27, 371
- stochastic neuronal, 246
- susceptible-exposed-infected-removed (SEIR), 11
- susceptible-infected-empty beds (SIB), 26
- susceptible-infected-removed (SIR), 372
- Tangled Nature, 49
- volume filling, 335
- Webworld, 49
- model development, 316
- monkey, 205
- Monod, *see* kinetics
- Monte Carlo method, *see* method
- morphogenesis, 284, 314
- mortality, 41, 169
- mosquito, 4, 375
- MRT images, 255
- multi-scale analysis, 255
- mutant group, 40
- mutation, 49
  
- naive T cell, *see* cell
- neighborhood degree, 286
- neoplasm, 169
- nervous system, 193
- network, 193
  - astrocytes, 194
  - biological, 280
  - cell division, 284
  - complex, 279
  - cytokine, 145
  - degree distribution, 57
  - genetic, 280
  - idiotypic, 157
  - mean degree, 56
  - metabolic, 280
  - metabolic regulatory, 314
  - of interactions, 49
  - random, 279
  - randomly evolving, 157
  - scale-free, 286
  - social, 280
  
- Neumann boundary conditions, 330
- neural circuit, 245
- neural field, 205
- neuron, 185, 225, 235
  - auditory, 245
  - axon, 205
  - motoneuron, 237
  - muscle spindle, 237
  - myelin, 205
  - pyramidal, 185, 186, 191, 192
  - synaptic efficacy, 207
  - transgenic, 190, 191
- neuronal morphology, 190
- neurotransmitter, 194
- non-autonomous system, 121, 145
- non-Gaussian stable behaviour, 233
- nonlinear, 112
  - diffusion, 109, 113
  - eigenvalue problem, 311
- nosocomial infection, 23
- numerical simulation, 109, 111, 327, 353
  - Markov chain Monte Carlo, 308
  - of interacting particle systems, 363
  
- Offdiagonal Complexity, 279, 282
- optimization model, 105
- ordinary differential equation (ODE), *see* equation
- oscillation
  - bifurcation, 208
  - population dynamics, 348
  - relaxation, 290
  
- pacemaker cell, 227
- parameter estimation, 23, 369, 371
  - $\eta$ -ball method, 24
  - joint, 30
- parameter identification, 21
- partial differential equation (PDE), *see* equation
- Pascal's triangle, 164
- patch-clamp technique, 225
- pathogen, 23, 173
- pattern formation, spatio-temporal, 205
  - front dissipation, 295, 300
  - spiral wave, 300
  - traveling wave, 21, 205, 208, 211, 294
  - Turing, 208
  - wave break-up, 300



- wave front, 289
- pattern module, 162
- pattern perception, 255, 261
- pattern recognition, 255
- peak fractality, 191
- peptide, 134
- permanence, 75
- perturbation approach, 205
- pest management, 11
- phenotype, 56, 63
- phenotyping, 185
- phosphatidylinositol 4,5-bisphosphate (PIP<sub>2</sub>), 195
- photosynthesis, 317
- physiological model, *see* model
- physiology, 374
- plankton, 109
- plant epidemics, 23
- polymerase chain reaction (PCR), 339, 343
  - exponential phase, 344
  - linear phase, 344
  - plateau phase, 344
  - quantitative (Q-PCR), 303, 310
- population
  - basic reproductive index, 14
  - dynamics, 87, 121, 339, 350, 374
  - lynx-hare dynamics, 339
  - oscillation, 348
  - predator-prey, 354, 372
  - prey equation, 134
  - reproductive rate, 339
  - winter conditions, 87
- Populus* sp., 313
- postsynaptic potential, 206, 247
- power law, 56, 58
- probabilistic spiking, 248
- probability density function, *see* density function
- problem solving, 261
- procaryote, 109
- process
  - birth-death, *see* birth-death
  - branching, *see* branching
  - continuous birth, 92
- proliferative capacity, 172
- protein interaction graph, 284
- pupil control, 374
- pyramidal neuron, *see* neuron
- quasi-steady-state condition, 134
- random graph, 280, 284
- reaction-diffusion equation, *see* equation
- refractoriness, 213
- refractory period, 213, 215
- regeneration, 198
- relational growth grammars, 313–318, 320, 321
  - graph data structure, 321
  - interactive modelling platform (GroIMP), 316
  - morphogenetic rules, 313, 320
  - regulatory network, 320
- relaxation oscillator, *see* oscillation
- replicator dynamics, 63
- reserve selection, 101
- Ricker model, *see* model
- Rössler model, *see* model
- Routh–Hurwitz criterion, 15
- saturation, 339, 343
- scale-free graphs, 280
- secondary defence, 38, 47
- semelparity, 75
- semelparous population, 76
- sensitization, 153
- sensory axon, 237
- separation, quasi-complete, 239
- separatrix, 147
- shape analysis, 255
- sigmoidal function, 139
- signaling
  - aposematic, 37
  - extracellular, 193
- simulation, *see* numerical simulation
- SIR epidemiological model *see* model
- skewness, 232
- soma, 185
- somatosensory cortex, 185
- space, 121
- spatial
  - heterogeneity, 122
  - network, 283, 286
- spatio-temporal pattern, *see* pattern formation
- species abundance distribution (SAD), 49
- species interaction network, 59
- species-area relation (SAR)
  - z*-value of, 52

- species-area relationship (SAR), 49
- speed distribution, 205
- speed of traveling wave, 211
- spherical harmonic, 255
  - basis functions, 256
- spike
  - generation, 265
  - time intervals, 225
  - train, 246
- spinal cord, 237
- stability condition, 40
- stable manifold, 152
- stochastic model, *see* model
- stochastic perturbation, 227
- stochastic programming, 101
  - L-shaped method, 104
  - scenario generation, 106
- stroboscopic map, 146, 148
- survival, 323
- synchronization, 208, 266
  
- T lymphocyte, *see* cell
- telomere, 169
- theorem of natural selection, 63
- therapy
  - hyposensitization, 145
  - immunotherapy, 145
  - radiation treatment, 374
- thinking process, 255
- time
  - asymptotic behavior, 14, 341
  - discrete time dynamical system, 227
  - physiological, 226
- toxicity, 47
- toxin, 38
  
- trait variable, 58
- transgenic, 188
  - activation, 186
  - cell, 186, 188
  - mice, 185
- transmembrane currents, 293
- transmission speed, 205
- traveling wave, *see* pattern formation
- Turing, *see* pattern formation
  
- Uncinula necator*, 11
- undergraduate education, 369
- universal computer, 265
- traveling wave, *see* pattern formation
- Turing, *see* pattern formation
  
- vaccination program, 7
- Vanderplank equation, *see* equation
- Vasicek's method, *see* method
- venom immunotherapy, 145, 152
- vine, 11, 20
- visual cortex, 205
- visualization, 258
- volume filling, 323
  - model, *see* model
  
- wave amplitude, 198
- Webworld model, *see* model
- Weibull distribution, *see* distribution
- weight function, 51
- Whittaker function, 233
- wolf population, 374
  
- yellow fever, *see* disease
- Young's inequality, 15